ASME
SETTING THE STANDARD
1880 2005

Transactions of the ASME, Journal of Fluids Engineering (ISSN 0098-2202) is published bimonthly (Jan., Mar., May, July, Sept., Nov.) by The American Society of Mechanical Engineers, Three Park Avenue, New York, NY 10016. Periodicals postage paid at New York, NY and additional mailing offices.
POSTMASTER: Send address changes to Transactions of the ASME, Journal of Fluids Engineering, c/o THE AMERICAN SOCIETY OF MECHANICAL ENGINEERS, 22 Law Drive, Box 2300, Fairfield, NJ 07007-2300.
CHANGES OF ADDRESS must be received at Society headquarters seven weeks before they are to be effective. Please send old label and new address.

Journal of Fluids Engineering

Published Bimonthly by ASME

VOLUME 127 • NUMBER 6 • NOVEMBER 2005

TECHNICAL PAPERS

(Contents continued on inside back cover)

This journal is printed on acid-free paper, which exceeds the ANSI Z39.48-1992 specification for permanence of paper and library materials. ♾™
♻ 85% recycled content, including 10% post-consumer fibers.

Journal of Fluids Engineering Volume 127, Number 6 NOVEMBER 2005

TECHNICAL BRIEFS

The ASME Journal of Fluids Engineering is abstracted and indexed in the following:

Applied Science & Technology Index, Chemical Abstracts, Chemical Engineering and Biotechnology Abstracts (Electronic equivalent of Process and Chemical Engineering), Civil Engineering Abstracts, Computer & Information Systems Abstracts, Corrosion Abstracts, Current Contents, Ei EncompassLit, Electronics & Communications Abstracts, Engineered Materials Abstracts, Engineering Index, Environmental Engineering Abstracts, Environmental Science and Pollution Management, Excerpta Medica, Fluidex, Index to Scientific Reviews, INSPEC, International Building Services Abstracts, Mechanical & Transportation Engineering Abstracts, Mechanical Engineering Abstracts, METADEX (The electronic equivalent of Metals Abstracts and Alloys Index), Petroleum Abstracts, Process and Chemical Engineering, Referativnyi Zhurnal, Science Citation Index, SciSearch (The electronic equivalent of Science Citation Index), Shock and Vibration Digest, Solid State and Superconductivity Abstracts, Theoretical Chemical Engineering

Prediction of Flutter of Turbine Blades in a Transonic Annular Cascade

Ivan McBean
Alstom Power, Switzerland

Kerry Hourigan

Mark Thompson

Monash University, Australia

Feng Liu
University of California, Irvine, California

A parallel multiblock Navier-Stokes solver with the k-ω turbulence model is used to solve the unsteady flow through an annular turbine cascade, the transonic Standard Test Case 4, Test 628. Computations are performed on a two- and three-dimensional model of the blade row with either the Euler or the Navier-Stokes flow models. Results are compared to the experimental measurements. Comparisons of the unsteady surface pressure and the aerodynamic damping are made between the three-dimensional, two-dimensional, inviscid, viscous simulations, and experimental data. Differences are found between the stability predictions by the two- and three-dimensional computations, and the Euler and Navier-Stokes computations due to three-dimensionality of the cascade model and the presence of a boundary layer separation, respectively. [DOI: 10.1115/1.2060731]

Introduction

Aeroelasticity in turbomachinery has been recognized as one of the most important problems presently facing the designers of turbomachinery blades. The structural instability is due to the interaction between the unsteady aerodynamics and the structural dynamics of the blades. In the aeronautical industry, demand for lighter and more efficient machines is developing. In the power generation industry, there is a drive to increasingly large exhaust areas of low-pressure steam turbines, leading to longer blades. Under both of these conditions, turbine blades of present-day designs are more likely to react to the effects of dynamic loading due to unsteady aerodynamics. The coupling between the fluid and structure can lead to blade failure if in the design phase attention is not paid to the possibility of aeroelastic interaction.

The aeroelastic interaction may be regarded as falling into one of two groups. One is forced response where the blades vibrate under periodic aerodynamic force of neighboring blade rows; however, there is sufficient mechanical or aerodynamic damping to limit the amplitude of the vibration. Blades under these conditions may fail under low- or high-cycle fatigue. The second is an unstable situation where there is insufficient damping in the system, and the amplitude of a self-excited vibration increases over time, until the blade fails. This second type of configuration is the focus of the models investigated in this paper.

Although experimental studies play an important role in the research into this phenomenon, computational simulations provide a number of key advantages. These include the ability to represent the flow in the whole flow-field at significantly lower cost. Thus results may be studied, in detail, providing insights into flow behavior and flow structures. Marshall and Imregun [1] provide a review of both classical and more modern numerical methods for aeroelastic predictions.

Sophisticated simulation models that involve fully coupled and time-accurate fluid-structure computations have been developed for turbomachinery blade rows in recent years, where the motion of the blades are computed by computational structural dynamics under aerodynamic forcing while the flow is computed by an Euler or a Navier-Stokes flow solver with moving boundaries to accommodate the motion of the blades. Vahdati and Imregun [2] presented a methodology for the three-dimensional aeroelasticity analysis of turbomachinery blades using an unstructured Navier-Stokes solver for the fluid and a modal model for the structure. Sayma et al. [3] and Vahdati et al. [4] extended the method for forced response predictions. Carstens et al. [5] developed a structured-grid Navier-Stokes solver coupled with structural model for flutter simulations. Doi and Alonso [6] coupled an unsteady flow solver with a commercially available finite element code for the structure. Liu et al. [7] developed a multiblock, multigrid, and parallel time-accurate Navier-Stokes solver coupled with a modal model for the structures for flutter simulations of airfoils and wings. The method was also extended to turbomachinery blade vibrations Sadeghi et al. [8].

Although the aforementioned approaches represent a new step in computational analysis, their applications in a practical design environment still await development of faster computers, more efficient numerical algorithms, or both; and validation of such direct time-domain simulations remains to be fully investigated because of the lack of measurement data. In addition, experience with such codes by the design engineer must be developed. Consequently, more efficient methods using two-dimensional models, or Euler equations, and the energy method to determine flutter boundaries are still the major tools used in the design of turbomachinery blades. Discussions of these methods can be found in [1,9–11]. Under certain conditions, it is questionable that such approaches adequately represent turbine blade behavior under operating conditions. A major difficulty in the simulation of three-dimensional aeroelasticity in turbomachinery is the lack of experimental measurements to validate numerical computations. Bell and He [12] designed experiments and performed computations to study three-dimensional effects on blade flutter. Their studies, however, are limited to low sub-sonic conditions. The purpose of this paper is to quantify and document the differences between two- and three-dimensional computations and those between Euler and Navier-Stokes computations by comparing all of them with a relatively well-defined experimental test case, the transonic Standard Test Case 4, Test 628. The annular cascade geometry was investigated in a previous paper [13] for the subsonic flow conditions. The investigation presented in this paper involves transonic flow conditions.

Model of Aeroelastic Configuration

The model configuration was chosen so that it could be compared to experimental measurements thus providing a validation of the simulation and realistic boundary conditions. The case is known as Test 628, of standard configuration 4 of the standard

Contributed by the Fluids Engineering Division for publication in the JOURNAL OF FLUIDS ENGINEERING. Manuscript received by the Fluids Engineering Division November 2, 2004; final manuscript received: May 29, 2005. Associate Editor: Akira GOTO

Table 1 Aeroelastic parameters for standard configuration 4, Test 628

Condition	Experiment
Typical reference velocity U_{ref}	65 m/s
Bending mode direction δ	63.0°
Bending mode amplitude at hub h_c	3.15×10^{-3}
Bending mode amplitude at midspan h_c	4.03×10^{-3}
Bending mode amplitude at casing h_c	4.91×10^{-3}
Reynolds number	5.9×10^{5}
Outlet Mach number Ma_{is2}	1.43
Reduced frequency k_c	0.0779

configurations developed to demonstrate flutter in turbomachinery [14]. This has a low aspect ratio, is well documented in terms of the experimental measurement, and exhibits both transonic and significant viscous flow characteristics.

The standard configurations rely on Lane's [15] traveling wave model where a single vibrational mode shape is considered, with an interblade phase angle (IBPA) assumed between adjacent blade passages. Since there are a finite number of possible IBPAs for a rotor of finite radius, only a limited number are required to be modeled.

In the present numerical model, the annular or linear cascade is truncated at the lowest number of passages required for flow periodicity; periodic conditions are assumed at the circumferential boundaries of the cascade.

The experimental configuration is characterized by the flow conditions summarized in Table 1. The flow at the inlet is subsonic and almost incompressible, whereas at the exit absolute Mach number it is well above unity. Surface pressure measurements were taken only at midspan.

The experimental apparatus involved an annular cascade of blades that were translated in an oscillatory manner to model the vibration of turbine blades undergoing flutter. The aeroelasticity was modeled in the experiment by rotating the blade about a spanwise pivot, toward the hub of the apparatus. The amplitude of the vibration was kept constant, as was the frequency of oscillation. The phase difference was modified between neighboring blades to identify the most critical interblade phase angle. This was determined by the energy method, where the unsteady pressure is integrated over time. The model may be related to a simple spring-mass system. If energy in the system is damped, the system remains stable. Conversely if the energy adds to the total energy of the system over time, it is unstable.

During the experiments, which involved a number of different configurations and flow conditions, Schlieren photography was performed and a strong passage shock was located on the blade suction side. The exact position of the shock wave was not noted for this particular set of conditions.

The experiment was modeled numerically through both a three- and two-dimensional geometry. In the case of the two-dimensional configuration, the midspan flow conditions were specified at the inlet and outlet of the domain. Periodic flow conditions were specified in the circumferential or blade-to-blade direction. Where the aeroelastic configurations were modeled, sufficient blade passages were required to maintain time periodicity as well as spatial periodicity. For example, for the interblade phase angle of 90 deg, four passages would be required, with periodic conditions applied at the outer blade passage boundaries.

In the case of the three-dimensional geometry, the amplitude of the blade oscillation was varied linearly over the span to model the rotation of the blade about the pivot, as in the experiment. The tip gap was not modeled.

There are two different geometric configurations considered. The first is a two-dimensional cascade model where the dimensions of the two-dimensional slice are taken to be at midspan of the experiment. The second involves three-dimensional annular passages. The inlet and outlet plane lies one chord upstream and downstream of the blade's leading and trailing edges, respectively. Although the overall distribution of the inlet total pressure profile was specified, the details of the boundary layer profile were not provided. Thus, a constant level of total pressure was specified to the wall. The boundary layer thickness developed over the end walls between inlet and the blade leading edge.

Modeling Method

The numerical implementation of the fluid model involves a finite volume spatial discretization of the compressible Reynolds-averaged Navier-Stokes equations. They are solved simultaneously with the k-ω turbulence equations for model closure. The fluid model governing equations are solved in a time accurate manner using a dual-time approach [7,16]. The artificial diffusion scheme of Jameson et al. [17] is applied for smoothing oscillations due to the discretization of the convective terms and nonlinearities in the flow field, such as shock waves and stagnation points.

The solver has been implemented to operate on parallel computer facilities using MPI. A moving mesh implementation adapts the fluid mesh to the oscillation of the turbine blades [18]. The numerical implementation has been validated by applying the code to a number of simplified flutter configurations. This process of validation has been reported previously [13,19].

Results and Discussion

Because of the complicated nature of the flow for this particular configuration, it was necessary to perform a detailed study under steady flow conditions to ensure that the results were not unduly affected by the grid geometry. This investigation also gave indication about some of the physical behavior that could be expected of the aeroelastic configuration.

Steady Flow. A grid resolution study was first performed on the steady configuration, with no oscillation of the blade profile. Although an H-grid was adequate for modeling the subsonic turbine configurations, it had some major deficiencies when applied to the modeling of transonic cascade flow. A comparison between the passage Mach number distribution and cell distribution for two-dimensional steady simulations with an outlet Mach number of 1.4 was investigated for two different types of mesh geometries [13]. Each mesh had a comparable cell count, with the O–H grid having 152 cells and the H-grid having 160 cells on the blade surface, respectively. The most notable difference was the resolution of the trailing edge shock. The wake region in the case of the H-grid was also less distinct. This was the most compelling reason for the use of the O–H mesh for the modeling of this flow regime. The low resolution of shock waves on the blade suction side could lead to significant inaccuracies in the reproduction of the unsteady flow field.

An O–H mesh was further refined in the throat region, which led to better resolution of the passage shock. A simulation involving the new mesh of four times the number of cells exhibited shock-induced boundary-layer separation at about 70% of chord on the blade suction side. A mesh of twice the cell density was produced involving 85,000 cells per spanwise plane and 736 cells on the blade surface, displayed little further change in results. The inlet average flow angle condition measured in the experiment was given in the cross section normal to the cascade axis 10% axial chord upstream of the blade leading edge, where there exists considerable circumferential and radial nonuniformity due to the proximity to the blades. In the case of the computations, the inlet plane is one chord length ahead of the blade leading edge and a uniform inlet angle of −26 deg is used instead of the −12 deg measured at the 10% chord location ahead of the blade leading edge in the experiment. The surface pressure coefficient for these

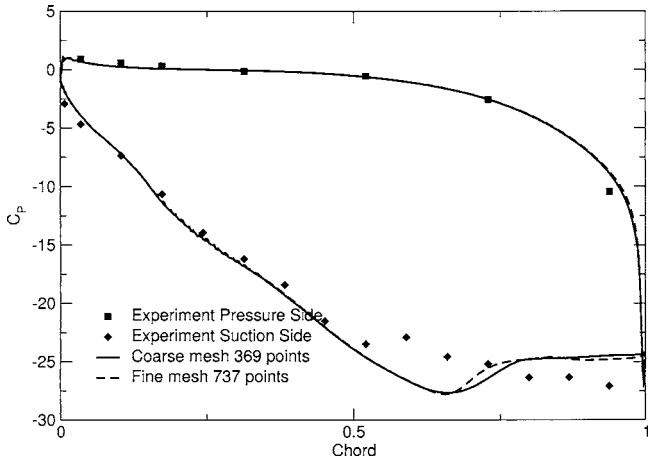

Fig. 1 Surface pressure coefficient for coarse and fine meshes

two meshes is shown in Fig. 1. There is some difference in the separation region, however the distribution through the passage shock at 70% chord is similar between the two simulations.

Schlieren distributions of the simulated flow field may be represented by contours of density gradient. They are useful for identifying shock features, wake regions, and boundary layers in compressible flow. The density gradient was calculated for the simulations. Comparisons of this quantity for the coarse and fine meshes showed that they were similar for the two-dimensional simulations, with little difference between the flow features.

A comparison of the surface pressure coefficient at midspan for the three-dimensional, two-dimensional Navier-Stokes, and Euler simulations is made in Fig. 2. Both Navier-Stokes simulations predict the impingement of the passage shock on the blade suction-side at about 65% chord, with the position predicted by the two-dimensional simulation slightly forward of that predicted by the three-dimensional simulation. The two-dimensional Euler simulation predicts the shock impingement further forward again, at 60% chord. In the experimental results shown in the same figure, it appears that the passage shock impinges on the blade at 50% of chord, given that the passage shock is identified by a local minimum in the surface pressure coefficient. It is not obvious whether the experimental results involve a separation zone at the trailing edge. Experiments in a linear cascade with the same profile at the higher outlet Mach number of 1.68 show what appears to be a separated zone after the passage shock on the suction side

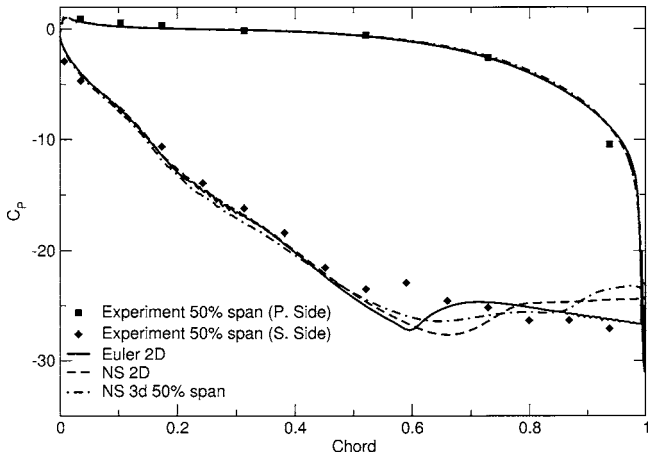

Fig. 2 Surface pressure coefficient for Euler, and two- and three-dimensional configurations

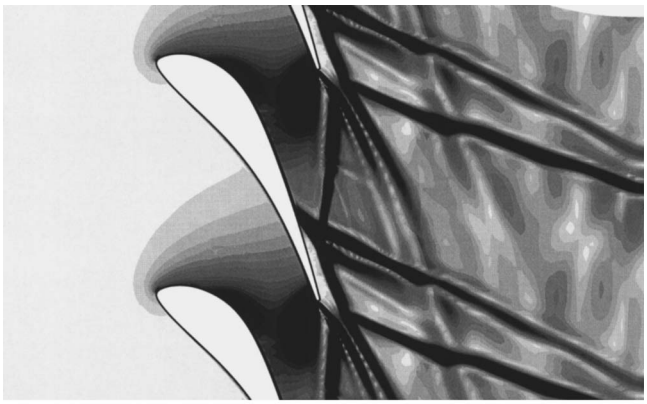

(a) Two-dimensional simulation

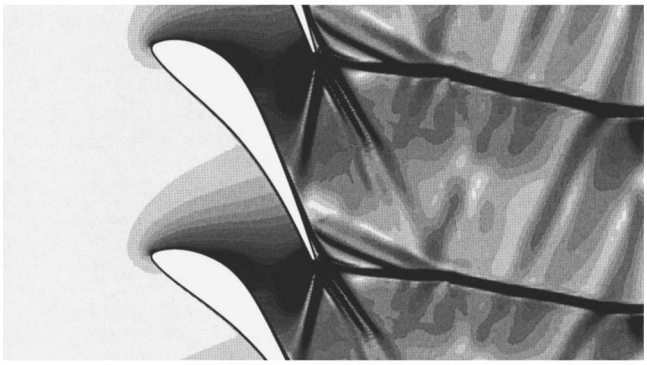

(b) Three-dimensional simulation

Fig. 3 Schlieren distributions for steady Navier-Stokes simulations

in a plot of surface isentropic Mach number [14].

The Schlieren distribution in Fig. 3 were calculated for the two- and three-dimensional Navier-Stokes simulations to identify differences between the two results. The Schlieren distribution for the three-dimensional case is at midspan. The flow is quite complex and involves a number of different phenomena.

In the two-dimensional case the point of flow separation coincides with the passage compression shock at about 70% chord. An oblique shock wave emanates from the separation point at −30 deg from the machine axis. Another oblique shock wave extends from the blade trailing edge toward the outlet at an angle of −20 deg from the machine axis. The wake is characterized by a fork like region, extending in the flow direction from the trailing edge.

The three-dimensional simulations differ in the point of separation and the geometry of the shock waves. The passage shock is also visible but does not coincide with the separation point on the blade suction side; the flow separates further down stream at about 85% chord. A shock wave also occurs at the point of separation at a similar angle to that in the two-dimensional case, but it merges shortly downstream with the shock from the trailing-edge.

A three-dimensional contour plot of the steady pressure coefficient on the blade suction side for the simulation is shown in Fig. 4. In the trailing-edge region of the blade in the figure, the white region represents the separation bubble; this is where the flow has negative axial velocity at the first mesh point adjacent to the blade surface. The pressure distribution varies significantly in the spanwise direction from midchord toward the trailing edge, as does the size of the separation bubble. On inspection, the flow in circumferential plane at the 75% span region more closely resembles the two-dimensional simulation compared with the midspan three-dimensional distribution.

The spanwise variation in pressure coefficient is also compared

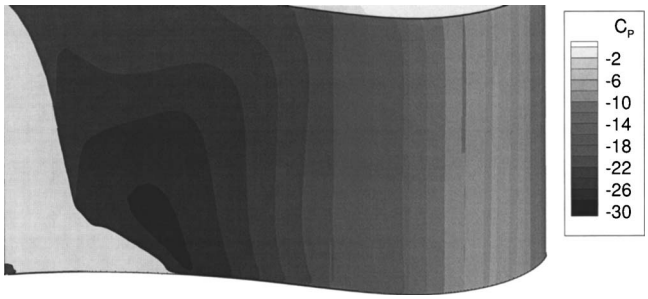

Fig. 4 Steady pressure coefficient and separated zone on blade suction side for three-dimensional simulation

with experimentally measured values in Fig. 5. Once again, the impingement of the passage shock on the blade suction side is identified by a local minimum in the pressure coefficient, in the neighborhood of midchord. The point of impingement of the passage shock in the simulation is 70% chord at 25% span, 65% chord at midspan, and 55% chord at 75%. It is more difficult to identify the position of the shock in the experimental measurements due to lack of resolution. At 25% span the shock may be at about 65% chord, midspan at 50% chord, and at 75% span at 45% chord. The simulation predicts a shock position that is 10% further aft on average than the experiment. Therefore, the in-passage flow conditions in the simulations are at higher Mach number than in the experiment.

There are some differences between the steady simulations, between the two- and three-dimensional simulations, and also with experiment. The next section investigates the way in which these differences affect the results for the simulations of the aeroelastic configuration. The surface pressure distributions do not compare well between the two- and three-dimensional configurations. The way in which this affects the aeroelastic stability of the configuration is investigated in the following section.

Unsteady Surface Pressure and Aerodynamic Damping. The aeroelastic configuration involved the oscillation of the blade profile in a translational mode, as described in model section. The flow conditions were similar to those applied in the steady simulations described above.

Because of the higher mesh density of the mesh required to resolve the passage shock, only an interblade phase angle of 180 deg was investigated, given the limits of the available computer resources. The mesh for this particular case involves a grid density of ~5 million cells, run under unsteady flow conditions. This is a large simulation for state-of-the-art workstations and medium-sized parallel, computer clusters.

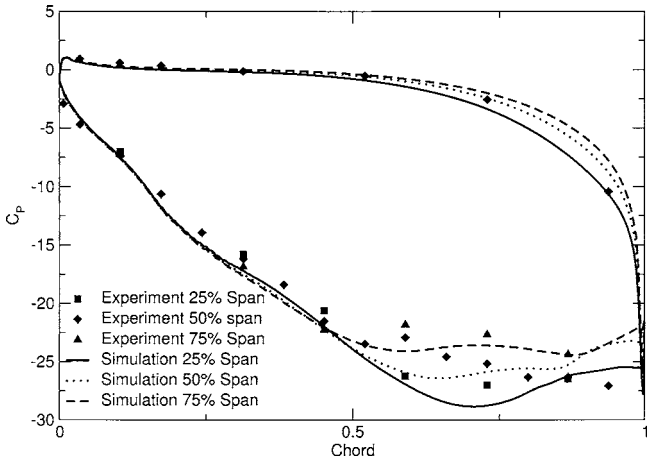

Fig. 5 Distribution of steady pressure coefficient for 3-dimensional simulation versus experiment

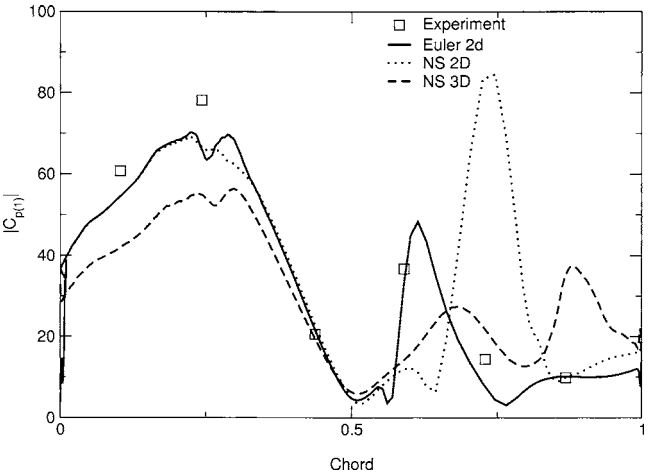

Fig. 6 First harmonic magnitude of unsteady pressure for blade suction side at midspan

The unsteady pressure on the blade due to the oscillation of the blade is analyzed by performing a fast-Fourier-transform of the fluctuating static pressure on the blade surface. The first harmonic of this quantity is typically the largest and is at the same frequency as the blade oscillation, with a phase shift that depends on the local flow conditions. The phase shift is critical in determining the stability of the configuration. The experimental measurements were analyzed in a similar way. A configuration where the integrated unsteady pressure over the blade surface leads the oscillation of the blade in terms of phase is unstable and will lead to failure of the blade where there is insufficient mechanical damping.

A comparison is made between Euler and Navier-Stokes simulations for the two- and three-dimensional geometries at midspan in Figs. 6–8. The blade surface distributions of the first harmonic of unsteady pressure are shown. The magnitude of the second harmonic of unsteady pressure was found to be insignificant. For the peak unsteady pressure on the blade suction side at 20% chord, there is some deviation between the two- and three-dimensional geometries. In the forward half of the blade, the predictions of unsteady pressure phase compare well with experiment for both models and both surfaces. Beyond midchord on the blade

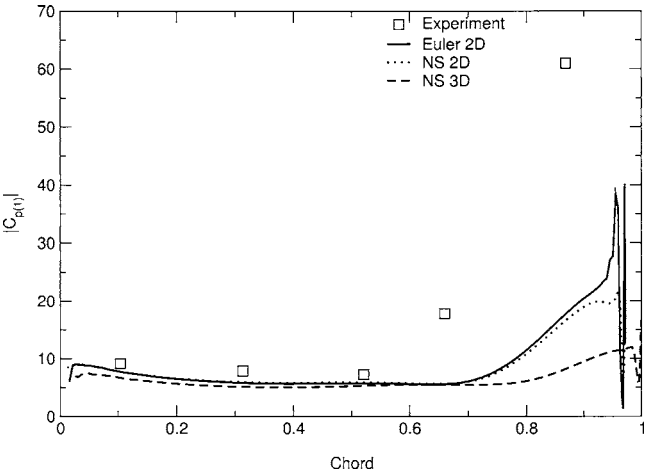

Fig. 7 First harmonic magnitude of unsteady pressure on blade pressure side at midspan

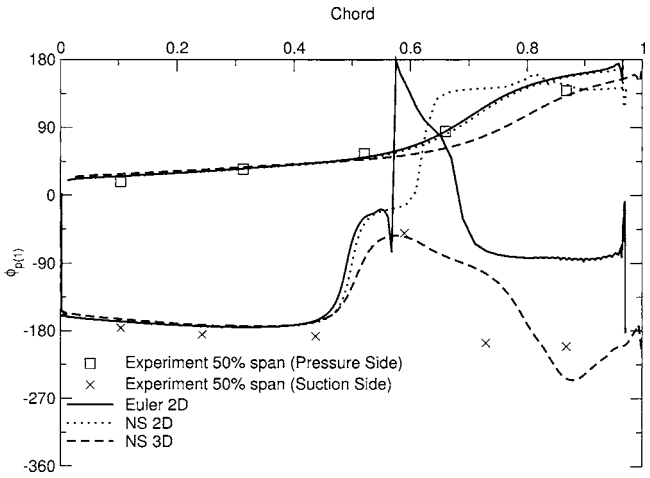

Fig. 8 Phase of first harmonic of unsteady pressure at midspan

suction side, however, there are more significant differences.

The passage shock is evident in the experiment and the simulation results by a local maximum on the blade suction side between 60% and 70% chord. The two-dimensional Euler simulation predicts the shock impingement position closest to the experiment as it did in the steady simulations. For the two-dimensional Navier-Stokes simulations it is difficult to distinguish between the shock impingement and the separation point at 70% chord. The three-dimensional Navier-Stokes simulation predicts the impingement at ~65% chord as in the steady simulation. The flow separation is the cause of the second maximum at about 85% chord.

There are significant differences in phase for the flow models on the blade suction side toward the trailing edge; however, the three-dimensional result gives the best prediction of phase in this region. In the experiment, the phase on the blade suction side returns to similar values to the forward section after the neighborhood of the passage shock, whereas both two-dimensional fluid models predict a phase almost a half cycle from the experimentally measured value.

The distribution on the blade of the unsteady pressure and phase for the three-dimensional Navier-Stokes simulation is shown in Figs. 9 and 10. The separation line is visible in both plots toward the blade trailing edge. The impingement of the passage shock is also visible in the plot of phase, as a local maximum at 70% chord. Because of the complicated nature of the spanwise variation in unsteady pressure, a two-dimensional simulation cannot reproduce this type of behavior.

The shock induced boundary layer separation or any other flow separation on the blade suction side cannot be well predicted by inviscid simulations. Navier-Stokes simulations, however, tend to be conservative in the prediction of flow separation. Usually they predict flow separation at more extreme conditions than is required in reality. A grid-independent prediction of the flow separation on the blade suction side proved to be a significant challenge. As the spatial grid and time resolution are refined, unsteady vortex shedding may appear at time scales much smaller than that of the blade oscillation frequency. The suitability of the turbulence model under such conditions is questionable. Other authors have investigated the performance of turbulence simulations with separated flow with mixed results [20].

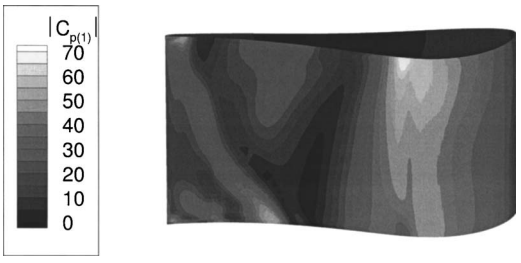

Fig. 9 Magnitude of first harmonic of unsteady pressure for three-dimensional configuration

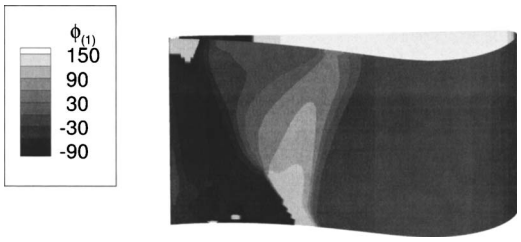

Fig. 10 Phase of first harmonic of unsteady pressure for three-dimensional configuration

Deviations of the results from the experimental results may also be due to other important factors, such as the effect of tip leakage at the outer casing and the lack of resolution of the flow conditions at the simulation inlet and outlet planes, taken from the experimental measurements.

Despite the aforementioned issues, the present computational results indicate the importance of the use of a three-dimensional model and a Navier-Stokes code for the accurate prediction of the unsteady pressures, especially the phase of the unsteady pressure after flow separation, which is critical for the correct prediction of flutter stability of the blades.

A comparison is made between the different configurations for damping coefficient in Fig. 11. Even though the three-dimensional Navier-Stokes simulation predicts a significant difference in the peak unsteady pressure magnitude at 20% chord, the damping coefficient it predicts is closest to experiment since the damping coefficient is mostly determined by phase angle.

Conclusion

A parallel multiblock Navier-Stokes solver with the k-ω turbulence model is used to study the unsteady flow through an annular turbine cascade. Two different configurations are used in the computations, one two-dimensional, the other three-dimensional. In addition, computations are also performed with both the Euler and the Navier-Stokes flow models. The computational results of the two- and three-dimensional configurations and with either the

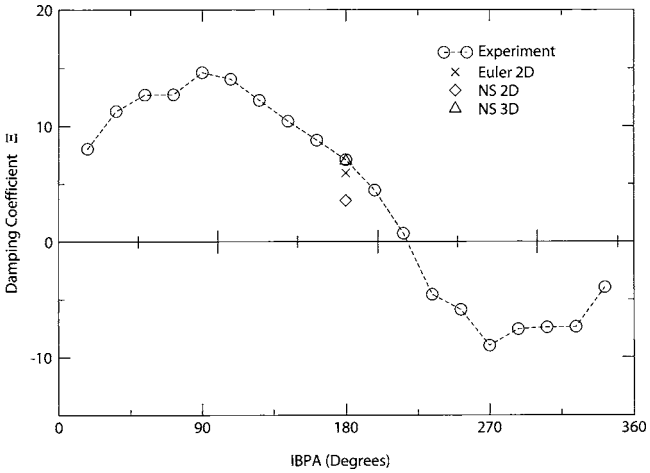

Fig. 11 Damping coefficient for different simulations versus experiment

Euler or the Navier-Stokes models are compared to available experimental data to document the effects of viscosity and three-dimensionality on the prediction of unsteady pressure and aerodynamic damping for the vibration of the blades. The comparisons reveal that, where flow separation occurs, only the Navier-Stokes computation gives the correct phase-angle distribution of the unsteady pressure, which is critical for the prediction of flutter through the computation of aerodynamic damping. Furthermore, there are significant three-dimensional effects in both amplitude and phase of the surface unsteady pressures on the blade. Not surprisingly, the three-dimensional Navier-Stokes computation yields the best prediction of the aerodynamic damping compared to experimental data. This result questions the reliance of the design engineer on the general applicability of two-dimensional, inviscid, or both two-dimensional and inviscid computations for flutter predictions, despite their advantage in computational efficiency.

Acknowledgments

The authors wish to thank the Australian Partnership for Advanced Computing (APAC) and the Victorian Partnership for Advanced Computing for provision of the computer equipment and partial support of the project.

Nomenclature

$b=c/2$ = semi-chord

c = chord of turbine blade

$Cp=(p-p_{\mathrm{ref}})/(p_0-p_{\mathrm{ref}})$ = time average surface pressure coefficient

$Cp(n)=p_{(n)}/(h_c(p_0-p_{\mathrm{ref}}))$ = nth harmonic of the unsteady pressure coefficient

h_c = bending amplitude, nondimensional with chord

$k_c=\omega c/2U_{\mathrm{ref}}$ = reduced frequency, based on semi-chord

Ma = Mach number

Ma_{is2} = isentropic Mach number at outlet

p = static pressure

p_{ref} = reference static pressure at a position designated by experiment

$p_{(n)}$ = nth harmonic of unsteady pressure

p_0 = total pressure

$\mathrm{Re}=\rho U_{\mathrm{ref}} c/\mu$ = Reynolds number

$u^*=\sqrt{\tau_{\mathrm{wall}}}/\sqrt{\rho_{\mathrm{wall}}}$ = friction velocity

U_{ref} = velocity at reference position

$y+=yu^*/\nu$ = dimensionless distance, scaled with sublayer

δ = direction of bending amplitude from machine axis

$\phi_{(n)}$ = phase of nth harmonic of unsteady pressure coefficient

μ = coefficient of dynamic molecular viscosity

ν = coefficient of kinematic molecular viscosity

ρ = density

τ_{wall} = shear stress at wall

ω = angular frequency

ω_α = natural frequency of pitching axis

Ξ = blade aerodynamic damping coefficient

References

[1] Marshall, J. G., and Imregun, M., 1996, "A Review of Aeroelasticity Methods With Emphasis on Turbomachinery Applications," J. Fluids Struct., **10**, pp. 237–267.

[2] Vahdati, M., and Imregun, M., 1996, "A Nonlinear Aeroelasticity Analysis of a Fan Blade Using Unstructured Dynamic Meshes," Proc. Inst. Mech. Eng., Part C: J. Mech. Eng. Sci., **210**(6), pp. 549–564.

[3] Sayma, A. I., Vahdati, M., and Imregun, M., 2000, "An Integrated Nonlinear Approach for Turbomachinery Forced Response Prediction, Part I: Formulation," J. Fluids Struct., **14**(1), pp. 87–101.

[4] Vahdati, M., Sayma, A. I., and Imregun, M., 2000, "An Integrated Nonlinear Approach for Turbomachinery Forced Response Prediction, Part II: Case Studies," J. Fluids Struct., **14**(1), pp. 103–125.

[5] Carstens, V., Kemme, R., and Schmitt, S., 2003, "Coupled Simulation of Flow-Structure Interaction in Turbomachinery," Aerosol Sci. Technol., **7**(4), pp. 298–306.

[6] Doi, H., and Alonso, J., 2002, "Fluid/Structure Coupled Aeroelastic Computations for Transonic Flows in Turbomachinery," In: *Proc. of ASME Turbo Expo 2002*, ASME, New York, ASME Paper No. GT-2002-30313.

[7] Liu, F., Cai, J., Zhu, Y., Wong, A. S. F., and Tsai, H. M., 2001, "Calculation of Wing Flutter by a Coupled Fluid-Structure Method," J. Aircr., **38**(2), pp. 334–342.

[8] Sadeghi, M., and Liu, F., 2005, "Coupled Fluid-Structure Simulation for Turbomachinery Blade Rows," *43rd AIAA Aerospace Sciences Meeting and Exhibit*, Reno, AIAA Paper No. 2005-0018.

[9] Imregun, M., 1998, "Recent Developments in Turbomachinery Aeroelasticity," Computational Fluid Dynamics '98, pp. 524–533.

[10] Verdon, J., 1993, "Review of Unsteady Aerodynamic Methods for Turbomachinery Aeroelastic and Aeroacoustic Applications," AIAA J., **31**(2), pp. 235–250.

[11] Srinivasan, A. V., 1997, "Flutter and Resonant Vibration Characteristics of Engine Blades," ASME J. Eng. Gas Turbines Power, **119**, pp. 741–775.

[12] Bell, D. L., and He, L., 2000, "Three-Dimensional Unsteady Flow for an Oscillating Turbine Blade and the Influence of Tip Leakage," ASME J. Turbomach., **122**, pp. 93–101.

[13] McBean, I., 2002, "Simulation of 3-Dimensional Aeroelastic Effects in Turbomachinery Cascades," Ph.D. thesis, Monash University.

[14] Bölcs, A., and Fransson, T. H., 1986, "Aeroelasticity in Turbomachines: Comparison of Theoretical and Experimental Cascade Results," EPFL Lausanne.

[15] Lane, F., 1956, "System Mode Shapes in the Flutter of Compressor Blade Rows," J. Aeronaut. Sci., **23**, pp. 54–66.

[16] Liu, F., and Ji, S., 1996, "Unsteady Flow Calculations with a Multigrid Navier-Stokes Method," AIAA J., **34**(10), pp. 2047–2053.

[17] Jameson, A., Schmidt, W., and Turkel, E., 1981, "Numerical Solutions of the Euler Equations by Finite Volume Methods Using Runge-Kutta Time-Stepping Schemes," *Proc. AIAA 14th Fluid and Plasma Dynamics Conf.*, AIAA, Washington, DC, AIAA Paper 81-1259.

[18] Tsai, H. M., Wong, A. S. F., Cai, J., Zhu, Y., and Liu, F., 2001, "Unsteady Flow Calculations With a Parallel Multi-Block Moving Mesh Algorithm," AIAA J., **39**(6), pp. 1021–1029.

[19] McBean, I., Liu, F., Hourigan, K., and Thompson, M., 2002, "Simulations of Aeroelasticity in an Annular Cascade Using a Parallel 3-Dimensional Navier-Stokes Solver," *Proc. of ASME Turbo Expo 2002*, ASME, New York, ASME Paper No. GT-2002-30366.

[20] Fransson, T. H., Jöcker, M., Bölcs, A., and Ott, P., 1998, "Viscous and Inviscid Linear/Nonlinear Calculations Versus Quasi-3D Experimental Data for a New Aeroelastic Turbine Standard Configuration," ASME Turbo Expo 1998, ASME, 98-GT-490.

Prediction of Cascade Flows With Innovative Second-Moment Closures

Domenico Borello
Dopartimento di Meccanica ed Aeronautica,
Università di Roma "La Sapienza," Via
Eudossiana 18, Rome, Italy
e-mail: borello@dma.ing.uniroma1.it

Kemal Hanjalic
Department of Multi-scale Physics, TU Delft,
Lorentzweg 1, Delft, The Netherlands
e-mail: hanjalic@ws.tn.tudelft.nl

Franco Rispoli
Dipartimento di Meccanica ed Aeronautica,
Università di Roma "La Sapienza," Via
Eudossiana 18, Rome, Italy
e-mail: franco.rispoli@uniroma1.it

*We report on the performances of two second-moment turbulence closures in predicting turbulence and laminar-to-turbulent transition in turbomachinery flows. The first model considered is the one by Hanjalic and Jakirlic (HJ) [Comput. Fluids, **27**(2), pp. 137–156 (1998)], which follows the conventional approach with damping functions to account for the wall viscous and nonviscous effect. The second is an innovative topology-free elliptic blending model, EBM [R. Manceau and K. Hanjalic, Phys. Fluids, **14**(3), pp. 1–11 (2002)], here presented in a revised formulation. An in-house finite element code based on a parallel technique is used for solving the equation set [Borello et al., Comput. Fluids, **32**, pp. 1017–1047 (2003)]. The test cases under scrutiny are the transitional flow on a flat plate with circular leading edge (T3L ERCOFTAC-TSIG), and the flow around a double circular arc (DCA) compressor cascade in quasi-off-design condition* ($i = -1.5°$) *[Zierke and Deutsch, NASA Contract Report 185118 (1989)]. The comparison between computations and experiments shows a satisfactory performance of the HJ model in predicting complex turbomachinery flows. The EBM also exhibits a fair level of accuracy, though it is less satisfactory in transition prediction. Nevertheless, in view of the robustness of the numerical formulation, the relative insensitivity to grid refinement, and the absence of topology-dependent parameters, the EBM is identified as an attractive second-moment closure option for computation of complex 3D turbulent flows in realistic turbomachinery configurations.* [DOI: 10.1115/1.2073267]

Keywords: Second Moment Closures, Stabilized Finite Element Methods, Transition, Turbomachinery Flows

Introduction

The major impediment to the trustworthy use of computational fluid dynamics (CFD) in the aerodynamic design of turbomachinery is still the large degree of uncertainty in turbulence closure modeling. Predicting accurately flow separation and reattachment on a turbomachinery blade, effects of streamline curvature and pressure gradient, and, especially, the laminar-to-turbulent transition is still a challenge. The transition is of primary concern because of the dramatic changes induced in the skin friction, heat transfer, and pressure distribution.

The transition from laminar to turbulent flow can be classified into three types [1]. The first is the natural transition where turbulence develops gradually by natural amplification of perturbations and local instabilities of laminar flows. In a by-pass transition, turbulence is diffused into the boundary layer from the free-stream or from a local turbulent source, whereas in a separation-induced transition, turbulence is generated by the separation of a laminar boundary layer, primarily in the shear layer around the separation bubble and near the reattachment point. The prediction of natural transition is beyond the scope of Reynolds averaged Navier Stokes (RANS) models. However, in turbomachinery flows, this mechanism is quite rare. On the other hand, the by-pass and separation induced transitions are common and can in principle be modeled by RANS approaches.

Eddy-viscosity models (EVMs), adopting either linear or nonlinear stress-strain relationship, have shown not to be very satisfactory in reproducing transition in turbomachinery flows, despite occasional claims of success. The well-known deficiencies of linear models in reproducing the near-wall stress anisotropy, streamline curvature effects, and in responding to extra strain rates make them unsuited for predicting transitional flows others than on a flat plate. Nonlinear EVMs were expected to overcome these shortcomings. However, it is difficult to choose a suitable model among a variety of existing nonlinear EVMs at different levels of closure, some involving quadratic or cubic in terms of mean strain rates and vorticity, with several coefficients that are often treated as functions of mean-flow and turbulence parameters. Craft et al. [2] reported successful applications of their cubic eddy-viscosity model, closed by an additional transport equation for the stress anisotropy invariant; the test cases also included some transitional flows. Chen et al. [3,4] considered several transitional flows using the same three-equation model of Craft et al., as well as its two-equation derivative [5], but their conclusions indicate the need for further improvements. Recently, Corsini and Rispoli [6] and Borello and Rispoli [7] computed the flow around an ERCOFTAC T3L profile using the same cubic eddy viscosity model of Craft et al. [5] and obtained fair results, albeit only for a large (7%) free-stream turbulence. Similar success has been achieved in predicting the 2D DCA and 3D NACA compressor cascades [7], such as encountered in non-free-vortex axial rotors [8].

Major challenges in computing transitional flow are the accurate prediction of the evolution of the turbulence and the location of the transition incipience. Linear EVMs, especially those that use damping functions in terms of nondimensional wall distance, are known to fail in this respect because of inadequate account for realistic viscosity effects and stress anisotropy evolution. Various remedies have been introduced to cure the problem, the most frequent being the artificial triggering of transition (i.e., switch-on of a turbulence model) at an a priori specified location based on some empirical information. Another approach, supposedly more general, is the introduction of an intermittency function, evaluated from an algebraic correlation or from the solution of an empirical transport differential equation (e.g., [9]), but all such models are

Contributed by the Fluids Engineering Division of ASME for publication in the JOURNAL OF FLUIDS ENGINEERING. Manuscript received August 5, 2004; final manuscript received: July 11, 2005. Assoc. Editor: Akira Goto.

Table 1 Details of SMC formulations

	HJ	EBM
Φ_{ij}	$\Phi_{ij1}+\Phi_{ij2}+\Phi^w_{ij1}+\Phi^w_{ij2}$	$(1-\alpha^2)\Phi^w_{ij}+\alpha^2\Phi^h_{ij}$
ε_{ij}	$f_s\varepsilon^w_{ij}+(1-f_s)\varepsilon\delta_{ij}$	$(1-\alpha^2)\frac{\overline{u_iu_j}}{k}\varepsilon+\alpha^2\frac{2}{3}\varepsilon\delta_{ij}$
D^t_ϕ	$\frac{\partial}{\partial x_k}\left((C_\phi T\overline{u_ku_l})\frac{\partial\phi}{\partial x_l}\right)$	$\frac{\partial}{\partial x_k}\left((C_\phi T\overline{u_ku_l})\frac{\partial\phi}{\partial x_l}\right)$
P_ε	$C_{\varepsilon1}\frac{P_k}{T}$	$C_{\varepsilon1}\frac{P_k}{T}+\left(c(1-\alpha^2)\sqrt{\frac{k}{\overline{u_iu_jn_in_j}}}\right)\frac{P_k}{T}$
ε_ε	$C_{\varepsilon2}f_\varepsilon\frac{\tilde{\varepsilon}}{T}$	$C_{\varepsilon2}\frac{\varepsilon}{T}$
ψ	$C_{\varepsilon3}\nu T\overline{u_ku_j}\frac{\partial^2U_i}{\partial x_j\partial x_l}\frac{\partial^2U_i}{\partial x_k\partial x_l}$	0

burdened with high empiricism and most showed to be inappropriate for the application to flows with complex geometries.

The negative experience with the eddy-viscosity models has prompted the use of second-moment closures (SMCs) with incorporated low-Re-number and wall proximity effects. The first model of this kind was proposed by Hanjalic and Launder [10] almost three decades ago, but, despite promising results, the model has not been widely accepted primarily because of high demand on fine grid clustering in the wall vicinity. Subsequent variants proposed by Shima [11], and Lai and So [12] experienced a similar destiny. None of these models was tested in turbomachinery flows. More recently, Chen and Leschziner [13] discussed a hybrid EVM/SMC formulation for the simulation of two compressors and the VKI turbine cascades. Whereas an improvement with respect to EVMs can be noted, the authors indicated the need for further development. Gerolymos et al. [14] reported improved predictions of several complex turbomachinery flows with their new low-Re SMC. The authors claim that their solutions required only 30%–50% more computing time, as compared to a linear EVM. Although their model looks rather complex, and gives just a marginal improvement in cases with weak separation as compared to the standard low-Re k-ε model, its high computational efficiency and robustness, comparable to nonlinear EVMs, deserve attention and bring new support in favor of SMCs.

In this paper we report on the performance of two second-moment closures in selected turbomachinery flows. The first model considered is the well-established and broadly tested low-Re SMC of Hanjalic and Jakirlic [15], dubbed HJ. This model showed good performances in a number of flows featuring strong adverse and favorable pressure gradients (the latter including also relaminarization) [16], in separating [15], rotating, and swirling flows [17,18], as well in by-pass and separation-induced laminar-to-turbulent transition [19]. Its performance in complex 3D turbomachinery flows has been recently assessed [20]. The second model considered is an innovative elliptic blending model (EBM, [21]), which proved to be very robust and not very demanding on fine grid clustering, thus seemingly suited for complex turbomachinery configurations. The EBM is a topology-free model, with an innovative approach to the modeling of the pressure-strain term, employing blending between the near-wall and away-from-wall ("homogeneous") pressure-strain models, in terms of a blending function obtained from the solution of an elliptic equation akin to Durbin's elliptic relaxation model (ERM, [22]). In contrast to the ERM where elliptic equations are to be solved for each stress component, EBM introduces just one scalar equation while maintaining a comparable level of accuracy. This model has been shown to perform very well in channel flows, backward-facing steps, and single and multiple-impinging jets [23], but has not been tested before in turbomachinery flows.

The test and comparison of the EBM and HJ performance in turbomachinery flows is the main target of the present paper. The potential of the two SMCs with low-Re and wall-proximity provisions are systematically assessed in several benchmark flows including the T3L round-leading edge and a DCA compressor cascade flow. The equations are solved using an in-house parallel stabilized finite element code [24]. Numerical predictions are compared with available experimental databases.

Turbulence Models

There are two important prerequisites for predicting laminar-to-turbulent transition in wall-bounded flows. These are the accurate prediction of true viscosity effect (low-Reynolds number) which has a scalar character (as it damps equally the turbulence fluctuations in all directions) and of the nonviscous, wall-orientation-biased wall-blocking effects, which primarily suppresses the turbulence fluctuations normal to the wall. The latter has a strong effect on the overall turbulence anisotropy close to a solid wall, which—with the exception of the elliptic relaxation model of Durbin [25] and some higher-order nonlinear formulations—is hardly tractable by any eddy-viscosity models. On the other hand, the accurate reproduction of the stress anisotropy (and, especially, of the wall-normal component) has proved to be crucial in predicting the laminar-to-turbulent transition [19]. A full second-moment closure offers much better prospects for reproducing the stress anisotropy, and thus the effects of streamline curvature and rotation and—with an appropriate low-Re treatment—the laminar-to-turbulent transition.

Both SMCs considered here have been designed to account separately for viscous and nonviscous wall-proximity effects. In the HJ model, this has been achieved by introducing two types of wall-topology-free damping functions into a baseline high Reynolds number (high-Re) closure, one solely in terms of the turbulence Reynolds number for the true-viscosity effects, and the other in terms of stress- and dissipation-rate anisotropy invariants. Because the near-wall turbulence anisotropy is primarily due to inviscid wall blocking, one can argue that the anisotropy invariants can be used to model the nonviscous wall effects, though indirectly. A further distinction is made between large-scale motions, accounted for with the stress-anisotropy invariants, and small-scale motions, treated in terms of the dissipation-anisotropy invariants.

The elliptic blending model follows a different rationale. In analogy with Durbin's elliptic relaxation method [22], here the inviscid wall blocking effect is introduced via the elliptic relaxation concept, whereas viscous effects are accounted for by introducing the Kolmogorov time and length scales as the lower scale bounds. The latter proved to be satisfactory for modeling viscous damping in the near-wall region, but apparently not fully adequate for capturing laminar-to-turbulent and reverse transition, as it will be shown later.

Table 2 HJ model coefficients

$C_{\varepsilon1}=1.44$	$C_{\varepsilon2}=1.92$	$C_{\varepsilon3}=0.25$	$C_2=0.8A^{1/2}$	$C^w_1=\max(1.0-0.7C;0.3)$	$C^w_2=\min(A_2;0.3)$
$C_{\overline{u_iu_j}}=0.22$	$C_\varepsilon=0.18$	$C_1=C+\sqrt{A}E^2$	$C=2.5AF^{1/4}f$	$f=\min\left[\left(\frac{\mathrm{Re}_t}{150}\right)^{3/2};1\right]$	$F=\min(0.6;A_2)$

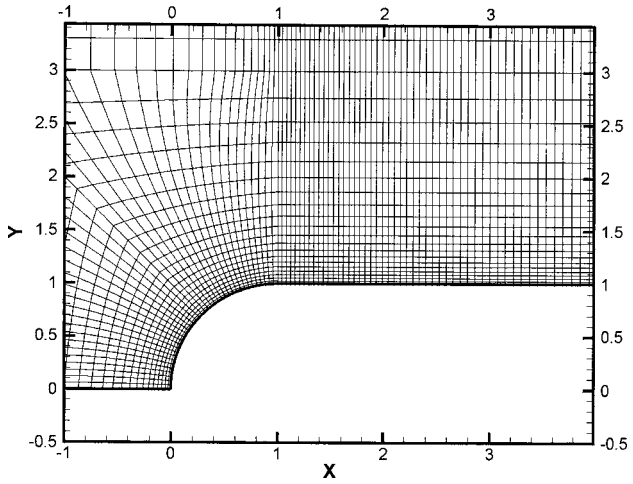

Fig. 1 T3L-Mesh detail

It is worthwhile to note that the presented SMC closures lead to an increase in the CPU time up to 80% as compared with the standard low-Re closure.

The Reynolds stress ($\overline{u_i u_j}$) and dissipation-rate (ε) transport equations can be written in a general form

$$\frac{D\overline{u_i u_j}}{Dt} = P_{ij} + D_{ij}^{\nu} + D_{ij}^{t} - \varepsilon_{ij} + \Phi_{ij} \tag{1a}$$

$$\frac{D\varepsilon}{Dt} = P_{\varepsilon} + D_{\varepsilon}^{\nu} + D_{\varepsilon}^{t} - \varepsilon_{\varepsilon} + \psi \tag{1b}$$

where the terms on the left-hand sides denote the material derivative, P_ϕ denotes production, D_ϕ^ν and D_ϕ^t are molecular and turbulent diffusion, respectively, ε_ϕ is molecular destruction, Φ_{ij} is the pressure-strain term, and ψ is the gradient production term in the ε equation. A comparative overview of both the HJ and EBM formulations is given below, with a focus on the modified version of the EBM that offers a robust framework for computations of complex flows.

A Conventional Damping-Functions Approach As a representative of the conventional approach to model the viscous and wall-blocking effects, we consider the model of Hanjalic and Jakirlic [15]. This model was originally based on the standard high-Re second-moment closure with simple linear pressure strain modeling (Rotta's return-to-isotropy model for the slow term and Noat et al.'s isotropization-of-production model for the rapid term) with Gibson-Launder (GL, [26]) wall-echo model. Despite its simplicity and deficiencies in some flows (impinging, rotating), this basic model has proven over the years to be reasonably successful in a variety of flows and was selected by HJ to serve as the high-Re asymptote. The GL wall-echo model contains the wall-normal unit vectors **n** and wall-distance function $f_w(d_w)$, which have been regarded as inconvenient for flows in complex geometries, though both **n** and d_w can be easily evaluated in the preprocessing phase. Other pressure-strain models can also be used as a high-Re basis, e.g., Craft and Launder [27] modified wall-echo term for flows with stagnation regions, or topology-free high-Re SMC, such as Speziale, Sarkar, and Gatski (SSG, [28]), though possibly with some minor retuning of the coefficients. It is noted, however, that the SSG model is inferior to the GL model in reproducing the near-wall anisotropy [29], at least in generic channel and boundary layer flows.

The adopted full pressure-strain model can be written as

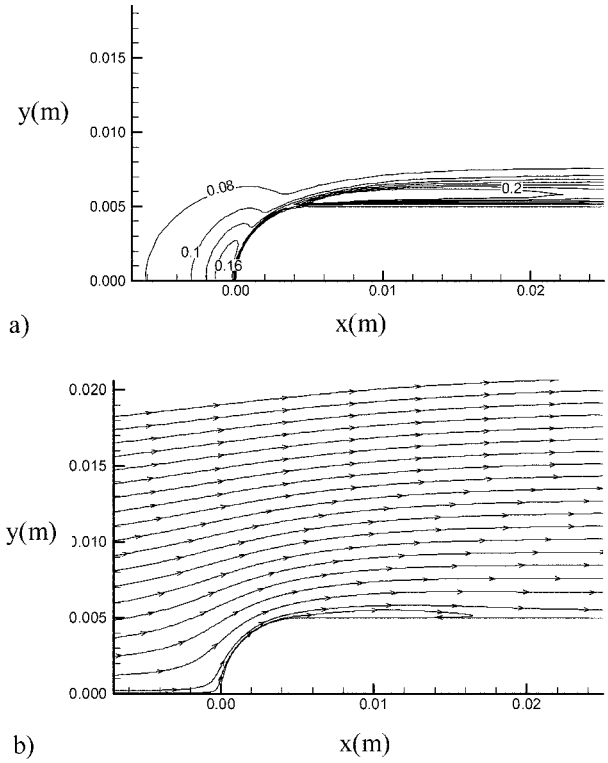

Fig. 2 EBM—coarse grid: (*a*) turbulence intensity and (*b*) streamlines distribution

$$\Phi_{ij} = \Phi_{ij1} + \Phi_{ij2} + \Phi_{ij1}^{w} + \Phi_{ij2}^{w} = -C_1\varepsilon a_{ij} - C_2\left(P_{ij} - \frac{2}{3}P_k\delta_{ij}\right) + C_1^w f_w \frac{\varepsilon}{k}\left[\overline{u_k u_m} n_k n_m \delta_{ij} - \frac{3}{2}(\overline{u_k u_i} n_k n_j + \overline{u_k u_j} n_k n_i)\right] + C_2^w f_w \frac{\varepsilon}{k}\left[\phi_{km,2} n_k n_m \delta_{ij} - \frac{3}{2}(\phi_{ik,2} n_k n_j + \phi_{jk,2} n_k n_i)\right] \tag{2}$$

where $f_w = \min(k^{3/2}/2.5\varepsilon d_w; 1.4)$.

The HJ submodels for the viscous and wall-proximity effects draw on the early low-Re SMC of Hanjalic and Launder [10], but with modifications that makes it possible to discern viscous from inviscid wall influences. This has been achieved by expressing the coefficients in the pressure-strain model in terms of the local turbulence Reynolds number $\mathrm{Re}_t = k^2/(\nu\varepsilon)$ to account for viscosity, and in terms of the invariants of the stress anisotropy $[a_{ij} = \overline{u_i u_j}/k - (2/3)\delta_{ij}]$ and dissipation rate anisotropy $[e_{ij} = \varepsilon_{ij}/\varepsilon - (2/3)\delta_{ij}]$ [15].

In analogy to the pressure-strain term, also the dissipation tensor ε_{ij} (Table 1) is modeled as a blending of the near-wall and away-from-wall terms [30]. The blending function is made dependent upon the flatness factors of the stress (A) and dissipation (E) anisotropy $[A = 1 - (9/8)(A_2 - A_3),\ E = 1 - (9/8)(E_2 - E_3)$, where $A_2 = a_{ij}a_{ij},\ A_3 = a_{ij}a_{jl}a_{li},\ E_2 = e_{ij}e_{ij},\ E_3 = e_{ij}e_{jl}e_{li}]$ to account separately for large- and small-scale turbulence anisotropy:

$$\varepsilon_{ij} = f_s\varepsilon_{ij}^w + (1 - f_s)\varepsilon\delta_{ij} \text{ where } f_s = 1 - \sqrt{A}E^2. \tag{3}$$

This formulation has been calibrated to reproduce the near-wall ε_{ij} components as obtained by DNS results for channel flow. The high-Re term is expressed as in the standard formulation.

The proposed near-wall term reads as

$$\varepsilon_{ij}^w = \frac{1}{T}\frac{[\overline{u_i u_j} + (\overline{u_i u_k} n_j n_k + \overline{u_j u_k} n_i n_k + \overline{u_l u_k} n_l n_k n_i n_j) f_d]}{1.0 + 1.5(\overline{u_i u_k} n_l n_k/k) f_d} \tag{4}$$

Table 3 EBM coefficients

$C_{\varepsilon 1}=1.44$	$C_{\varepsilon 2}=1.83$	$c=0.03$	$C_L=0.161$
$C_{\overline{u_i u_j}}=0.21$	$C_\varepsilon=0.18$	$C_\eta=80.0$	$C_T=6.0$

where $f_d=(1+0.1\mathrm{Re}_t)^{-1}$, $T=k/\varepsilon$.

Note that the flatness parameters A and E in f_s become unity in isotropic turbulence, whereas they approach zero in the two-component limit. However, although both parameters attain identical limits, they are not equal nor proportional to each other. Because small-scale dissipative motions are affected by the wall to a lesser extent than large scale eddies, the parameter E approaches its isotropic value of unity much faster than A when moving away from a solid wall [15]. In view of these features, A and E are convenient parameters to account for large- and small-scale turbulence anisotropy, especially when approaching the two-component limit.

In HJ, the dissipation equation (1*b*) takes the standard form with the low-Re modifications of Hanjalic and Launder [10]. The submodels for the various terms are summarized in Table 1, with the function f_ε in the viscous destruction term defined as

$$f_\varepsilon = 1 - \frac{C_{\varepsilon 2}-1.4}{C_{\varepsilon 2}} \exp\left[-\left(\frac{\mathrm{Re}_t}{6}\right)^2\right]. \tag{5}$$

The turbulent diffusion D^t_ϕ is for simplicity modeled using the Daly-Harlow formulation [31]. In Table 2 the HJ coefficients are reported.

Elliptic Blending Model. The basic idea of the EBM is to use a scalar elliptic function to accommodate the homogeneous pressure-strain and stress-dissipation rate models to meet the wall conditions [21]. This approach has its roots in the elliptic-relaxation second-moment closure of Durbin [22], but instead of solving a *tensorial* elliptic equation for the function f_{ij}, here the pressure-strain term is modeled by blending a homogeneous and a near-wall model through the expression

$$\Phi_{ij} = (1-\alpha^2)\Phi^w_{ij} + \alpha^2 \Phi^h_{ij} \tag{6}$$

using a *scalar* elliptic blending function α, obtained by solving an elliptic equation

$$\alpha - L^2\nabla^2\alpha = 1. \tag{7}$$

The parameter α is positive defined: it is set to zero at a solid wall, while approaching unity in the free-stream nearly-homogeneous regions, following an elliptic law depending only on the local length scale L. For the homogeneous part Φ^h_{ij}, any known pressure-strain model can be applied. In this work the Speziale et al. (SSG [28]) pressure-strain model for homogeneous conditions is used; this model has been shown to reproduce fairly well the stress redistribution in several homogeneous, as well in some inhomogeneous near-equilibrium flows, including those along solid walls, though not in the region very close to the wall

$$\Phi^h_{ij} = -\left(g_1 + g_1^* \frac{P_k}{\varepsilon}\right)\varepsilon b_{ij} + (g_3 - g_3^*\sqrt{b_{kl}b_{kl}})kS_{ij} + g_4 k\left(b_{ik}S_{jk} + b_{jk}S_{ik} - \frac{2}{3}b_{im}S_{im}\delta_{ij}\right) + g_5 k(b_{ik}\Omega_{jk} + b_{jk}\Omega_{ik}) \tag{8}$$

Table 4 T3L—convergence iterations

Convergence iterations	EBM	HJ
Coarse grid	438	415
Fine grid	245	257

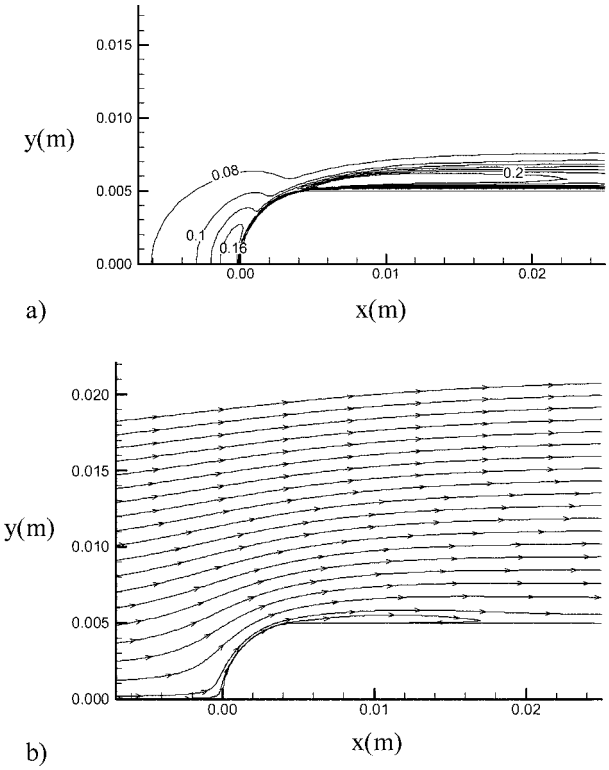

Fig. 3 EBM—fine grid: (*a*) turbulence intensity and (*b*) streamlines distribution

where $g_1=3.4$, $g_1^*=1.8$, $g_3=0.161$, $g_3^*=1.3$, $g_4=1.25$, $g_5=0.4$.

Manceau and Hanjalic [21] derived a new model for the near-wall counterpart Φ^w_{ij}, which satisfies the wall-limiting constraints and the balance of all terms in the transport equations for each stress component

$$\Phi^w_{ij} = -5\frac{\varepsilon}{k}\left(\overline{u_i u_k}n_j n_k + \overline{u_j u_k}n_i n_k - \frac{1}{2}\overline{u_k u_l}n_k n_l(n_i n_j + \delta_{ij})\right). \tag{9}$$

The need for modeling complex geometries militates against a frame-related definition of the wall-normal direction. As the gradient of α becomes normal to the wall in its proximity, $\mathbf{n}$ is here defined in a topologically free fashion as

$$\mathbf{n} = \frac{\nabla\alpha}{\|\nabla\alpha\|}. \tag{10}$$

The ε_{ij} term has been constructed in a similar manner by adopting a nonisotropic formulation in the wall region, which asymptotes to the isotropic form in the free-stream where $\alpha=1$:

$$\varepsilon_{ij} = (1-\alpha^2)\frac{\overline{u_i u_j}}{k}\varepsilon + \frac{2}{3}\alpha^2\varepsilon\delta_{ij}. \tag{11}$$

With regard to the ε equation, the production term has been recast, with the coefficient $C_{\varepsilon l}$ expressed as a function of α and the ratio of turbulence kinetic energy and the wall-normal stress component

$$P_\varepsilon = C_{\varepsilon 1}\frac{P_k}{T} + \left(c(1-\alpha^2)\sqrt{\frac{k}{\overline{u_i u_j}n_i n_j}}\right)\frac{P_k}{T}. \tag{12}$$

This modification aims at compensating for the omission of the low-Re ψ term. This intervention is akin to Durbin's modification in his k-ε-v^2-f model, and it is motivated by the numerical stiffness of the ψ term, which in the original form contains the second derivative of the mean velocity, thus requiring a very fine mesh in the near-wall region. This modification makes the model robust

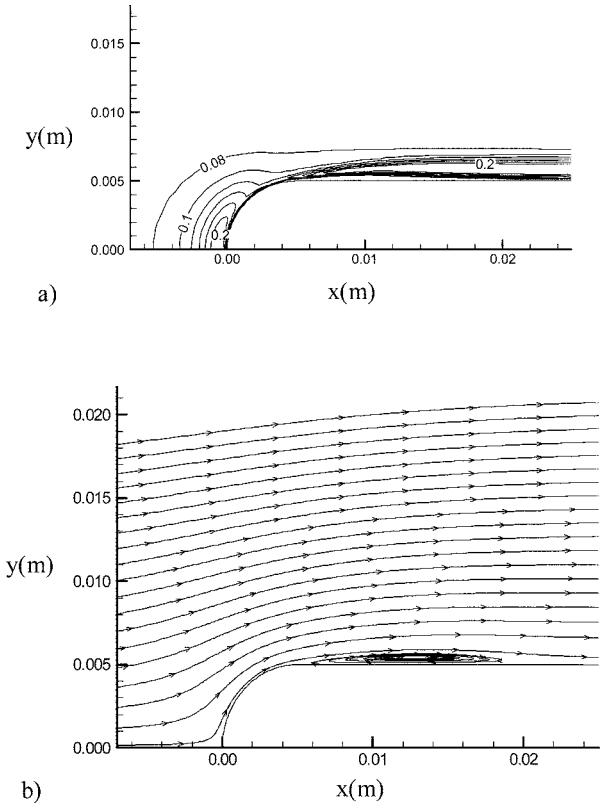

Fig. 4 HJ—coarse grid: (*a*) turbulence intensity and (*b*) streamlines distribution

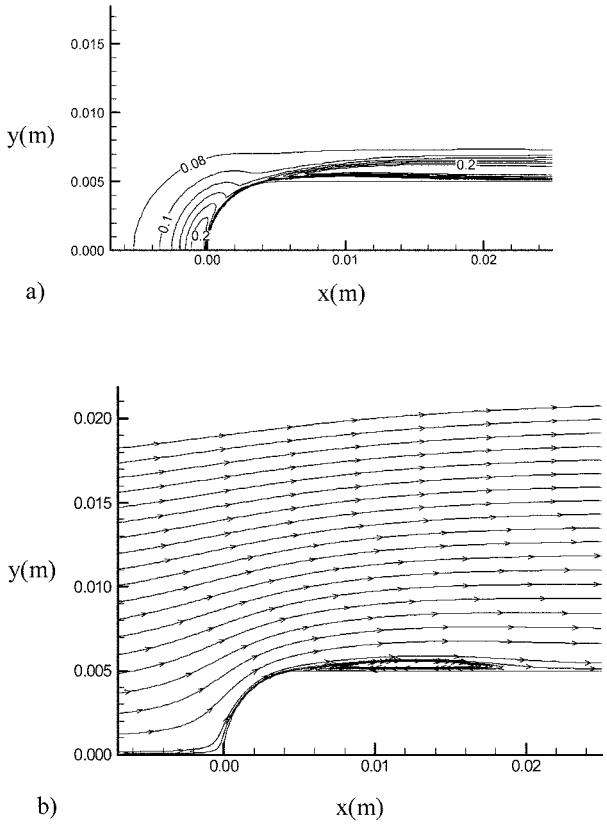

Fig. 5 HJ—fine grid: (*a*) turbulence intensity and (*b*) streamlines distribution

and—within reasonable limits—rather insensitive to the near-wall mesh refinement, enabling the first grid point to be placed at a distance, in terms of y^+, up to 3.

Finally, the length and time scales in the EBM are defined in the conventional manner in terms of k and ε for the high-Re regions, but, following Durbin [25], are bounded by the Kolmogorov scales in the low Reynolds number limit:

$$L = C_L \max\left(\frac{k^{3/2}}{\varepsilon}; C_\eta \frac{\nu^{3/4}}{\varepsilon^{1/4}}\right) \tag{13a}$$

$$T = \max\left(\frac{k}{\varepsilon}; C_T \frac{\nu^{1/2}}{\varepsilon^{1/2}}\right). \tag{13b}$$

The lower scale bounds become effective very close to the wall, thus introducing viscous effects into the model, though these modifications do not appear capable of fully reproducing laminar-to-turbulent transition. The other coefficients are reported in Table 3.

Numerical Techniques

The RANS equation set complemented with the turbulence closure equations has been solved by using an implicit SUPG/PSPG stabilized finite element approach [32,33]. The linearization of the equations system has been solved by adopting a fixed-point strategy. The solution of a preliminary standard low-Re k-ε model is used to produce a set of initial conditions for the RSM calculations. The equations of motion and continuity are solved in a fully coupled fashion. The Reynolds stress gradients have been directly implemented in the momentum equation as a source term without any numerical difficulties. This contrasts the common procedure practiced by other authors who found it necessary to introduce some temporary artificial eddy viscosity to cure numerical instabilities and convergence problems in the solution of momentum equation when passing from eddy viscosity models to Reynolds stress models [34]. The stabilized finite element approach here applied has guaranteed stable and monotonic convergence in the prediction of the investigated flow fields. In order to prevent the occurrence of nonphysical values of turbulent variables, during the solution procedure a lower positive bound (*clipping*) has been placed for the turbulent terms that are positive definite ($u_i u_i, \varepsilon$). It is important to note that *clipping* is adopted *only* during the solution procedure to enforce realizability and clipped variables are not present in the final results.

The convergence threshold parameters here adopted are

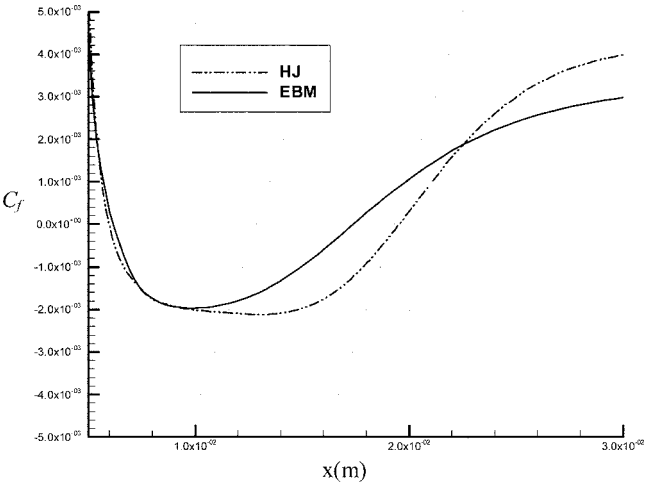

Fig. 6 T3L—friction factor along the leading edge for fine grid

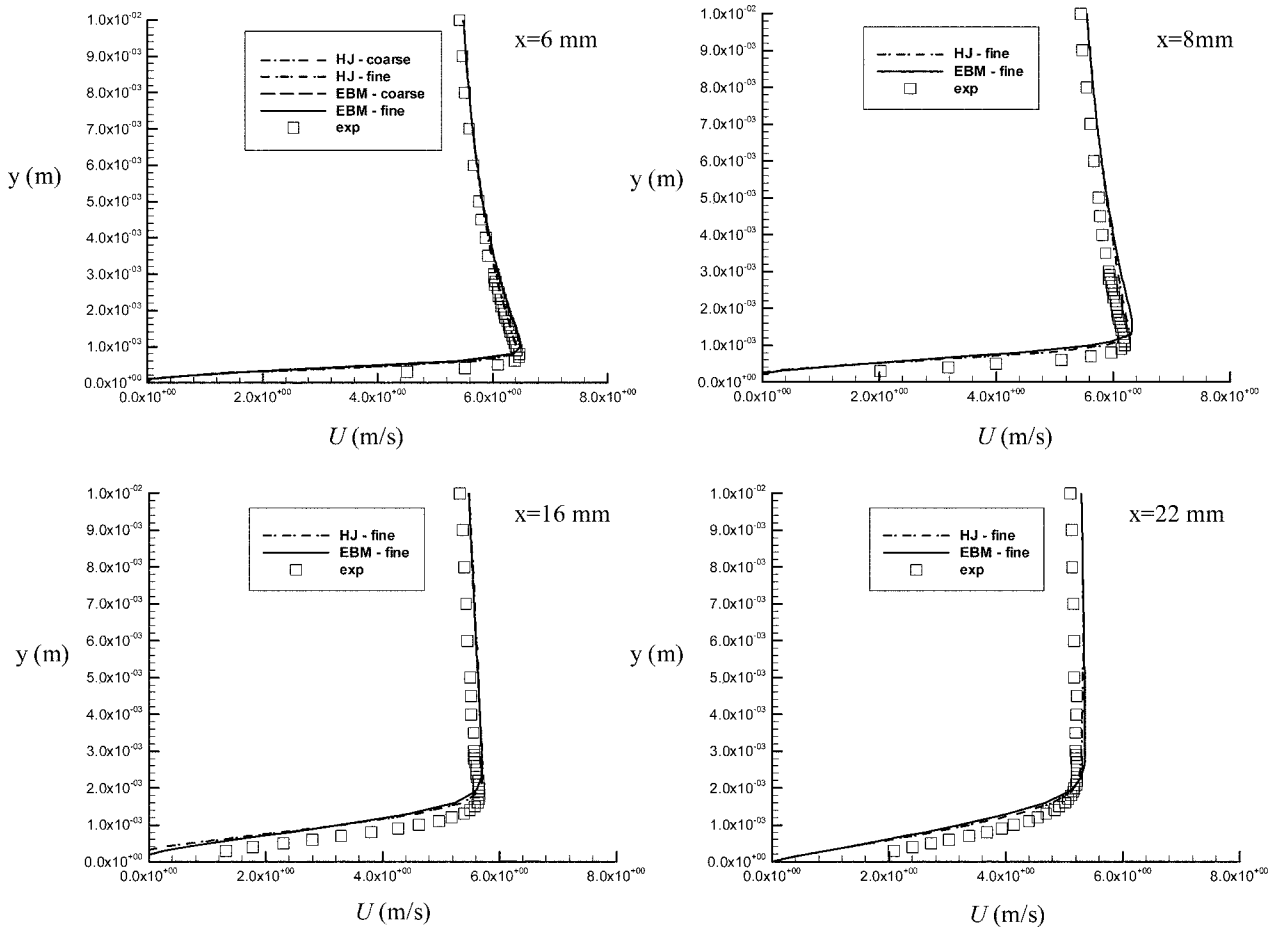

Fig. 7 T3L—boundary layer velocity profiles at four stations: (*a*) *x*=6 mm; (*b*) *x*=8 mm; (*c*) *x*=16 mm; (*d*) *x*=22 mm

$$\|r\|/\|r^0\| < rtol; \quad \|\bar{U}_i^n - \bar{U}_i^{n-l}\|/\|\bar{U}_i^n\| < stol$$

where $\|r\|$ and $\|r^0\|$ are, respectively, actual and initial residual norms, while $\bar{U}_i$ is the generic unknown quantity and the superscripts refer to the nonlinear iteration. Both prescribed threshold parameters are set to 10^{-5}.

The adopted numerical solution is based on a MPI-based parallel FGMRes solver running on a LINUX cluster with 16 processors and 8 Gb RAM [24,35].

Discussion of Results

The proposed low-Re SMC models has been fully validated in reference test cases [20]. Here the following turbomachinery flow cases are investigated.

T3L Round-Leading Edge Flow. Computations of flow over a flat plate with a semi-circular leading edge are compared to the experimental results produced in the framework of the ERCOFTAC SIG on transition modeling [36]. The Reynolds number, based on the inlet free-stream velocity (5 m/s) and the leading edge radius r (5 mm), is 1660. Because of symmetry, only the upper part of the 2D computational domain is considered. The latter extends $15r$ in the transverse direction, whereas the inlet and outlet sections are located $10r$ upstream and $44r$ downstream of the leading edge stagnation point. Two block-structured H–O grids with 16,951 and 24,881 nodes, respectively, are used. The O-connected region around the plate includes 41 nodes normal to the wall, clustered to give $y^+=1.0$ for the near-wall point. Figure 1 shows details of the impingement region.

At the inlet section of the computational domain, the experimental free-stream, uniform mean velocity profile is used. A uniform profile is also assumed for the normal Reynolds stresses, computed after the measured free-stream turbulence intensity ($TI=7\%$) by using the experimental anisotropy relationships [36]: $\overline{vv}=0.75\overline{uu}$ and $\overline{ww}=\overline{vv}$. Free boundary conditions are used for the tangential Reynolds stress $\overline{uv}$. Finally, the inflow dissipation rate is obtained as $\varepsilon=k^{3/2}/l_m$ where the length scale (l_m) has been tuned to 18 mm in order to match the measured decay of the free-stream turbulence level. No slip conditions are enforced at the wall for all the variables except for ε, which is instead defined by using the wall limit in terms of the kinetic energy gradient $[\varepsilon_w=2\nu(\partial\sqrt{k}/\partial x_j)^2]$. Von Neumann boundary conditions are enforced at the symmetry line for all variables except for the normal velocity component, which is set to zero. Finally, von Neumann conditions are applied to all variables at the remaining boundaries.

In Table 4 the nonlinear convergence iterations have been reported for both the models. It is worth noting that on the coarse grid a uniform flow field for all the variables is set as initial condition. For the fine grid computations, an interpolation of the coarse grid predictions is used as the initial field.

In order to assess the predicting capabilities of the considered SMC models as far as capturing of the separation-induced transition is concerned, the turbulence intensity contours and streamlines around the stagnation point are analyzed.

As a preliminary remark it is important to note that no substantial difference has been noted between the coarse and fine grids for both models. The EBM (Figs. 2 and 3) overpredicts the turbulence level near the impingement zone, which induces excessive mixing and somewhat suppresses the separation, as indicated by the streamline distribution. When the fine grid is adopted instead

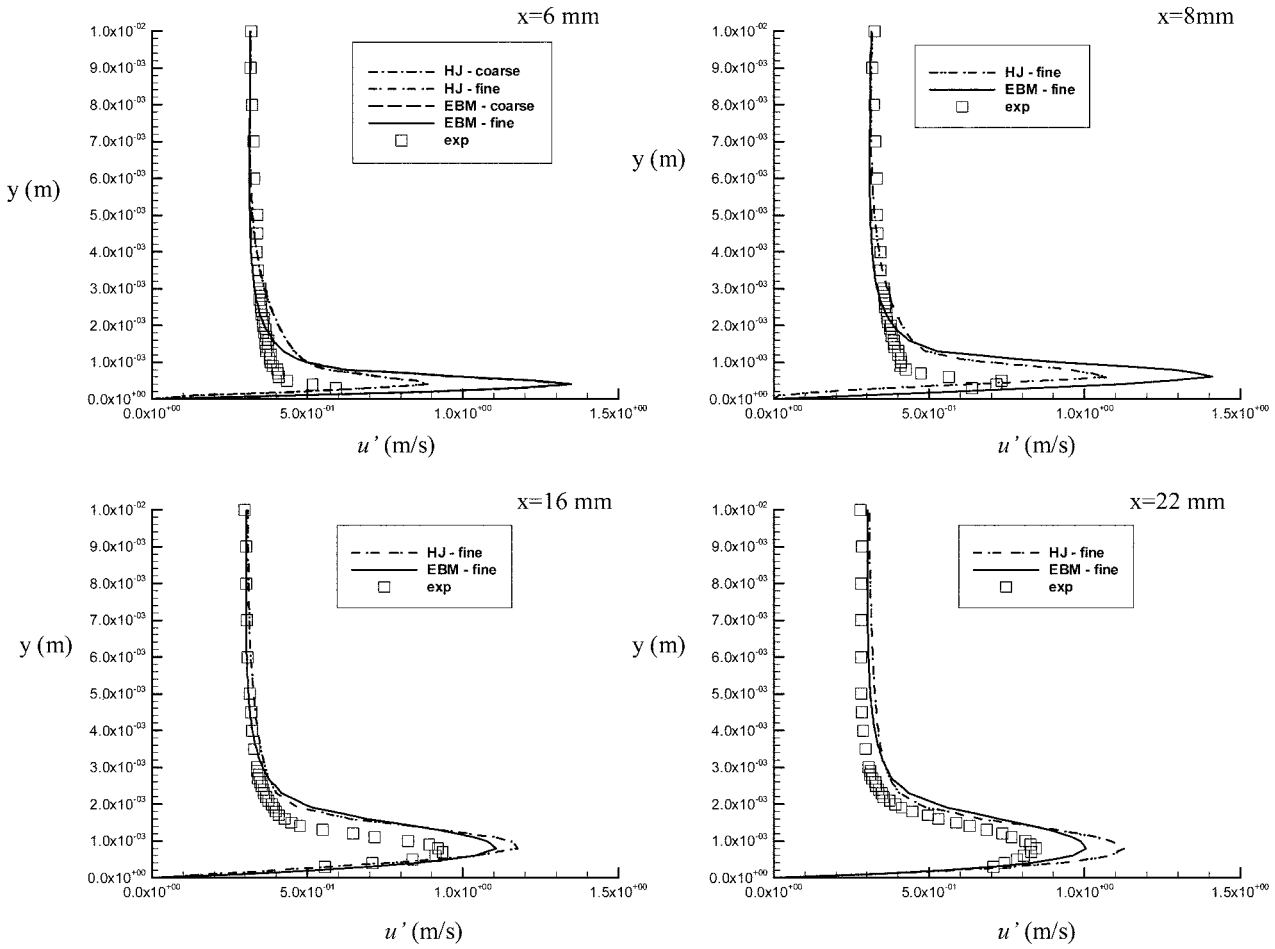

Fig. 8 T3L—boundary layer velocity fluctuations u' profiles at four stations: (*a*) x=6 mm; (*b*) x=8 mm; (*c*) x=16 mm; (*d*) x=22 mm

(Fig. 3), the EBM resolves fairly well the near-wall zone. The turbulence level near the impingement point is lower than with the coarse grid, and a recirculation bubble appears 6 mm downstream of the leading edge, extending up to 15 mm. Results obtained with the HJ model with the coarse grid (Fig. 4) feature drawbacks similar to the EBM, though predicting a smaller turbulence peak near the impingement point. As expected, on the fine grid the HJ model (Fig. 5) returns the best results, consistent with the rationale of the model, which is aimed at capturing transition and separation. A recirculation zone extending from 6 to 18 mm is captured, in fair accord with experimental results.

The above results indicate that both models generate stable results on very coarse grids as well. However, as expected, a very fine clustering towards the wall ($y^+=1.0$) is required to properly predict near-wall turbulence effects in the impingement region.

Figure 6 reports the distribution of the friction factor C_f along the profile. It is worth noting that, according to the streamline plot, the EBM predicts a smaller recirculation region, ranging in between 5 and 17 mm, whereas the HJ predicts a back-flow region near the wall ranging in between 5 to 19 mm. Both results are in satisfactory agreement with Palikaras et al. [36] extrapolations, which locate the recirculation bubble in between 6 and 17 mm downstream of the leading edge.

In Fig. 7, the boundary layer mean velocity (U) profiles are compared at four sections, located just downstream from the round region (6 mm) near the inception of the recirculation zone (x=8 mm), in the reattachment point (x=16 mm) and in the recovering region (x=22 mm), respectively. In the first section, results of both grids for both models are presented. It is clearly evident that a grid independent solution has been achieved. Both models give satisfactory results; the second and the third sections clearly show the presence of a recirculation region as already displayed by the C_f distribution and the experimental results. Nevertheless, the thickness of the boundary layer seems to be somewhat overestimated.

The profiles of the rms of the velocity fluctuations (u') at the same four locations are presented in Fig. 8. At the first location, the HJ simulation gives improved results in the near-wall region as compared with the EBM. On the other hand, the EBM simulation returns a better turbulence peak in the near-wall region further downstream (Fig. 3), though in other respects the above noticed superiority of the HJ simulation is not replicated. Nevertheless, the EBM predictions are quite satisfactory in view of its simplicity (and, consequently, numerical robustness), featuring a plausible reproduction of the reattachment and recovery zones.

The global performance of the models under consideration is evaluated by the integral parameters at the above cross sections, as shown in Fig. 9. It is noted that in the integral parameters calculations the upper limit of the boundary layer has been assumed as the location (on a line directed normally to the profile) where the flow velocity (U_e) is equal to 99% of the maximum velocity calculated along the same cross section. The displacement thickness distribution $\delta[=\int_0^\infty(1-U/U_e)dy]$ (Fig. 9(*a*)) shows an acceptable behavior (especially for HJ), although an overestimation of the boundary layer height, already observed in Fig. 7, is noticed. The momentum thickness $\vartheta[=\int_0^\infty U/U_e(1-U/U_e)dy]$

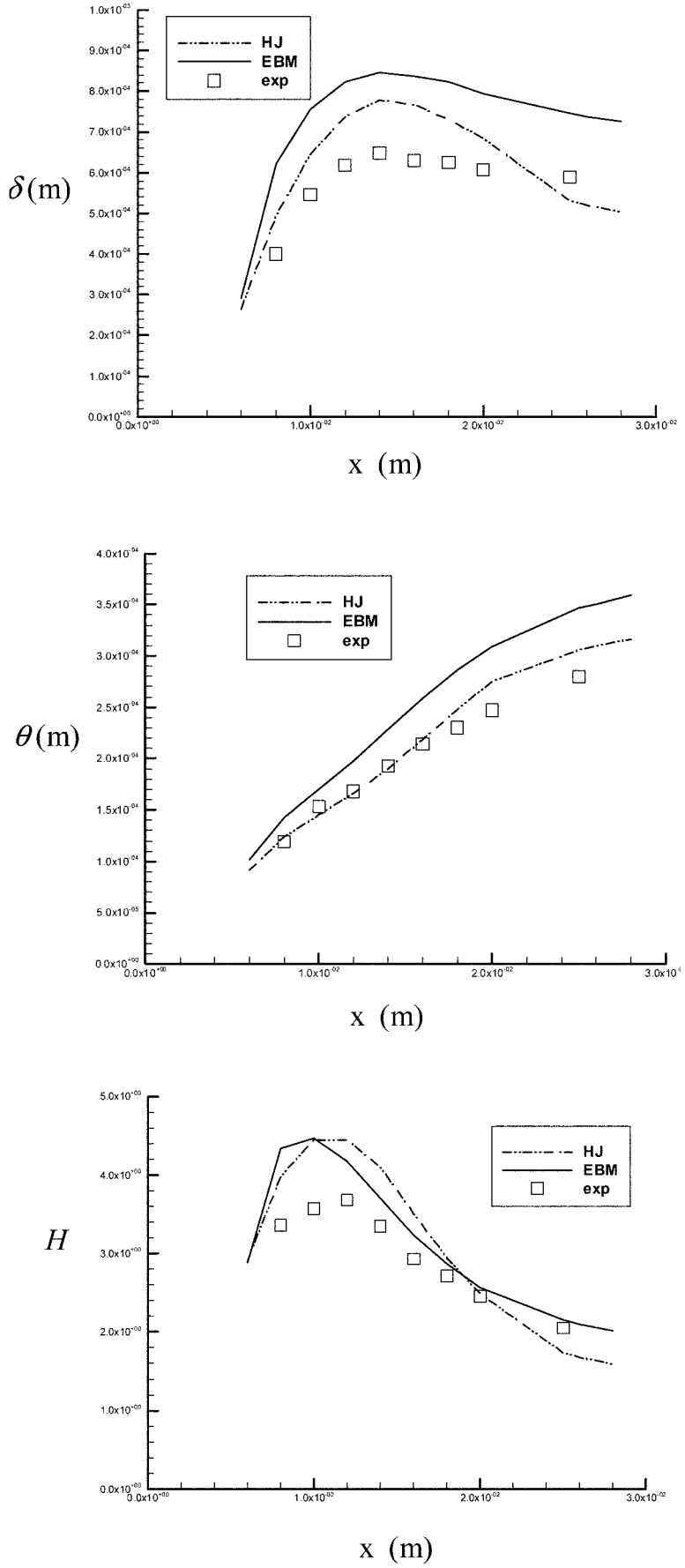

Fig. 9 T3L—integral parameters (*a*) displacement thickness; (*b*) momentum thickness; (*c*) shape factor

Table 5 DCA—cascade geometry

Camber angle	65°
Stagger angle	20.5°
Solidity	2.14
Chord length	228.6 mm
Inlet velocity	32.88 m/s
Chord based Reynolds number	501,000
Inlet Mach number	0.1

(Fig. 9(*b*)) distribution confirms that the momentum losses in the boundary layer are very well predicted by the HJ model. The predictions obtained with the EBM can also be regarded as satisfactory.

The value of the shape factor $H(=\delta/\vartheta)$ (Fig. 9(*c*)) indicates that EBM better estimates the length of the transition region and it shows a more accurate description of the mean flow properties in the region far downstream from the leading edge.

Double Circular Arc Cascade Flow. The second test case refers to a DCA compressor cascade flow, investigated experimentally by Zierke and Deutsch [37]. The cascade geometrical parameters are summarized in Table 5.

The cascade operation under scrutiny corresponds to a weak off-design condition with an incidence angle of −1.5°. Although the flow is at an inlet angle close to design, it is highly challenging due to the presence of strong transition and separation phenomena arising along the blade surfaces.

The two adopted computational grids contain up to 69,792 nodes, and a combined H–O topology is used to mesh the solution domain. The boundary layer is included within the O-connected region where 61 nodes are allocated normal to the blade surface. Near the solid wall y^+ is set to a value of about 1 for both grids; a different number of nodes is used for the profile discretization; in the coarser grid 585 nodes are adopted, while in the finest one 721 nodes are placed along the blade skin. Figure 10 shows the coarser grid, with details of the leading and trailing edge.

In the inflow section, located a chord upstream of the blade leading edge, uniform distributions for all the variables are assumed, i.e., the experimental free-stream velocity, a turbulence intensity value TI=2.0%, and a characteristic length scale l_m =16 mm. The inflow normal Reynolds stresses are modulated as indicated for the T3L test case. No-slip conditions are used at the blade surfaces, with the exception of the dissipation rate ε, which is set to the wall value ε_w. Homogeneous von Neumann boundary

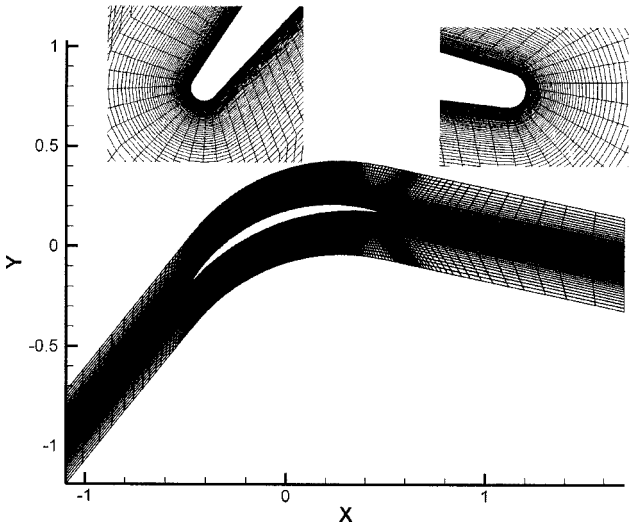

Fig. 10 DCA cascade—computational mesh (coarse discretization)

Table 6 DCA—convergence iterations

Convergence iterations	EBM	HJ
Coarse grid	370	356
Fine grid	452	420

conditions are enforced at the outlet section (one chord downstream from the leading edge), and flow periodicity is assumed on the permeable boundaries midway between adjacent vanes.

In Table 6 the nonlinear convergence iterations for both grids have been reported.

The distributions of the calculated C_p $[C_p=(p-p_{in})/(\rho U^2/2)]$, where p is the current pressure value and p_{in} is the pressure at the inlet section, are compared in Fig. 11. In Fig. 11(*a*) the HJ model plausibly reproduces the experimental results with both grids. However, the finer grid results match better the measurements. On the suction side, HJ captures the negative peak at the impingement point and the pressure spike that leads to the separation-induced transition of boundary layer, related to the favorable pressure gradient (extending up to 8% of chord). After that, a strong adverse pressure gradient develops at the blade portion ranging up to about 75% of the chord. The HJ reproduces fairly well this region, showing sensitivity to the streamline curvature and boundary layer development under such an adverse pressure gradient. This enables us to correctly predict the pressure plateau located around 75% of the chord, indicating the inception of a separation region

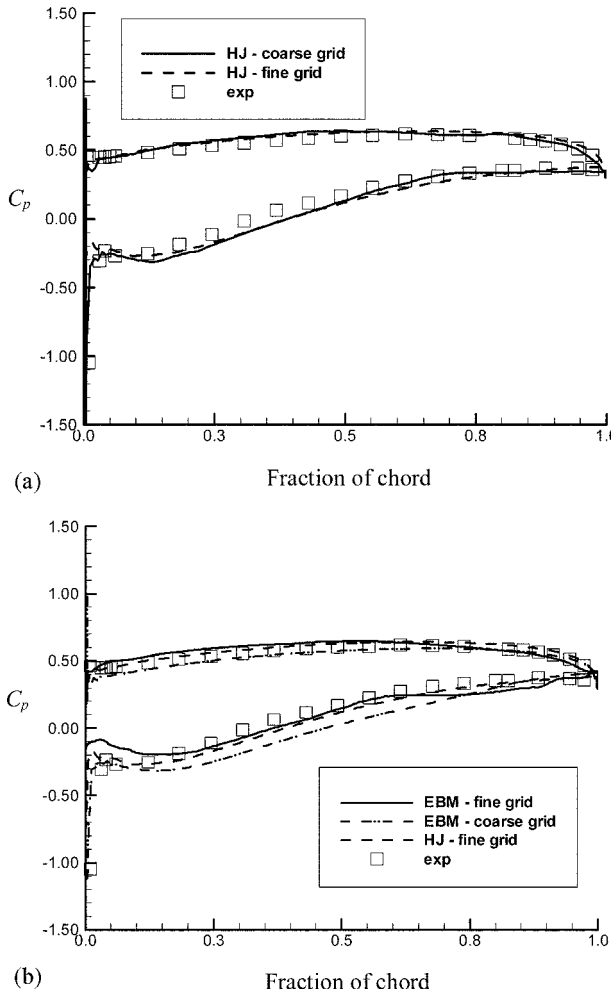

Fig. 11 DCA cascade—C_p distribution: (*a*) HJ simulations and (*b*) EBM simulations

that extends up to the trailing edge. On the pressure side, HJ returns an accurate prediction of the C_p distribution, indicating the presence of a large blade portion subjected to weak adverse pressure gradient (up to 65%), followed by a zone affected by a favorable pressure gradient.

EBM [Fig. 11(*b*)] shows some discrepancies with respect to HJ (the HJ results on the fine grid are used as reference) especially in the suction side. In particular, on the coarse grid the accuracy of C_p predictions is not satisfactory. The finer grid predictions show a clear improvement. However, at the inlet a too steep pressure gradient is present, leading to an early transition to turbulence and a misrepresentation of the pressure spike at 5% of chord. This behavior is related to the lack of sensitivity of the EBM to transition phenomena which cannot be accounted only by the low-Re scale bounds, which is the only low-Re-number remedy in the EBM. Nevertheless, the adverse pressure gradient region is correctly predicted up to 70% of the chord. The downstream trailing edge plateau is also captured, indicating that the model is capable of predicting the separation process, as indicated also by the sharp pressure recovery predicted in the trailing edge. On the pressure side, only minor discrepancies are noticed between EBM and experiments. The fine performance of EBM is attributed to the lesser importance of adverse pressure gradient. The present comparisons with data in the literature allow us to argue that the fine grid results could be assumed as grid indipendent. Hence, in the following only the finer grid results are considered for discussion.

Figures 12 and 13 compare the streamwise velocity profiles and the predicted turbulence intensity (TI) profiles at two stations along the blade suction side. To exploit the capabilities of the SMCs as compared with to the eddy-viscosity closures, the velocity and turbulence intensity profiles obtained with the cubic Craft, Launder, and Suga—CLS—model [35] are reported in Figs. 12 and 13. At the first station (19.7% of the chord), the HJ model returns a boundary layer velocity prediction close to measurements. The EBM produces an increased thickness (1 mm wider) of the boundary layer. This outcome could be related to the early transition in the first station already noted in Fig. 11(*b*).

The turbulence intensity profiles [Fig. 13(*a*)] confirm the capabilities of HJ in predicting the turbulence statistics in nonequilibrium boundary layers. The near wall region is very well predicted up to a distance of about 3 mm. Moving farther away from the wall, the turbulence intensity remains higher than the experimental one until about 20 mm from the blade surface (not shown in the figure). In contrast, the EBM shows a relatively high level of turbulence in the boundary layer. However, the TI profile is correctly predicted outside the boundary layer. The CLS results show that the boundary layer at this station is still almost laminar. As stated in Borello et al. [35], this should be related to the cubic turbulence attenuation operators. At the second station, located in final portion of the blade (90.3%), the HJ velocity profile shows very good prediction of the velocity and other mean features of the boundary layer [Fig. 12(*b*)] in terms of both its thickness and the extension of the recirculation region. A similar behavior is observed for the turbulence intensity profiles [Fig. 13(*b*)], though the distribution within the boundary layer does not capture the double peak of the TI. It is worth noting that, in the near-wall region, Zierke and Deutsch [37] report an experimental scatter much larger than the mean value of the local turbulence intensity. This implies that, at this location, the measurements can be relied upon only farther than 5 mm from the blade. The EBM results show that the model response to adverse pressure gradient not completely satisfactory. As a consequence of the drawbacks already evident in section at 19.7% of chord, the boundary layer thickness is about 5 mm wider than in the experiments. Despite this deficiencies in the velocity and turbulence intensity, the boundary layer thickness predicted by the EBM can be considered as satisfactory if compared with the results of the CLS model.

An overall estimation of the both SMCs accuracy in reproducing the boundary layer development can be obtained by analyzing

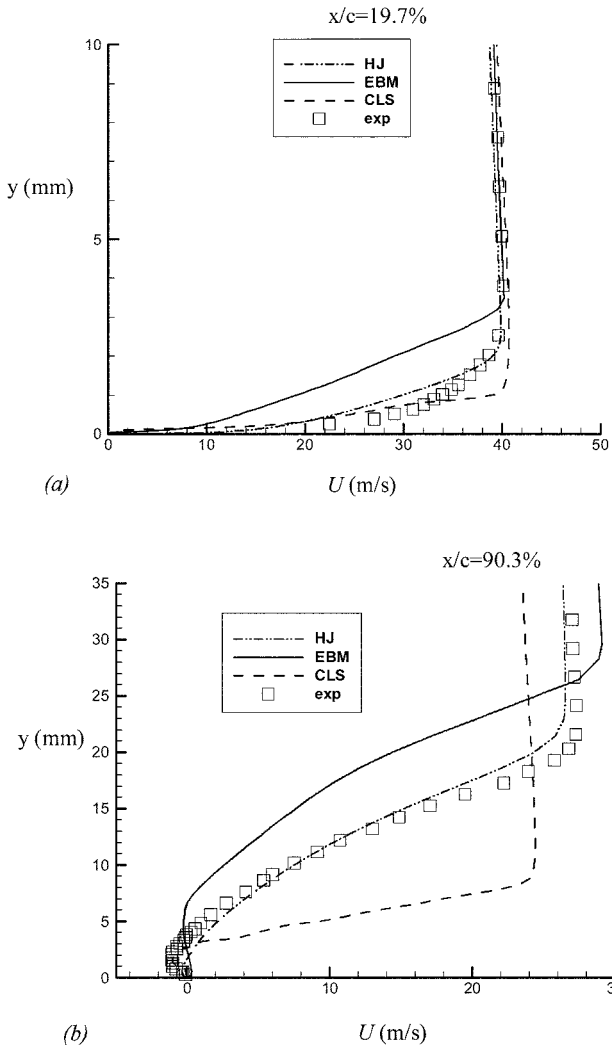

Fig. 12 DCA cascade—boundary layer-velocity profiles in two stations (*a*) 19.7% of chord; (*b*) 90.3 % of chord

the integral parameters (Fig. 14). HJ shows very good agreement with experiments. This confirms the fair response of the boundary layer to the adverse pressure gradient and the streamline curvature.

EBM shows a wider thickness of the boundary layer along all the suction side. At the first station, the measured shape factor ($H \approx 2$) indicates a transitional boundary layer due to a leading edge separation bubble near the measuring station. In contrast, both SMCs predict an early leading edge separation (very close to the leading edge, some 3% of the chord upstream with respect to experiments). Then, at the first measurement station (where $H \approx 1.3$) the computed boundary layer is already fully turbulent. This is due to the high level of turbulence enforced at the inlet section, in analogy to the settings of Chen et al. [13], aimed at sustaining turbulence upstream of the blade. Nevertheless, in downstream sections all the integral parameters show a steep rise that, in accord with experiments, indicate the presence of a large recirculation region. As a conclusive step of the discussion, global cascade parameters have been compared with experiments in Table 7. The blade loading was assessed in terms of the diffusion factor $\hat{D}=1-U_{out}/U_{in}+\Delta U_t/(2\sigma U_{in})$, where U_{in}, U_{out}, and ΔU_t are the mean values of the inlet velocity, the outlet velocity (measured 31.9% of chord downstream the leading edge), and the variation in the tangential velocity, while σ is the cascade solidity. Also considered is the static pressure coefficient $\hat{C}_p=(p_{out}$

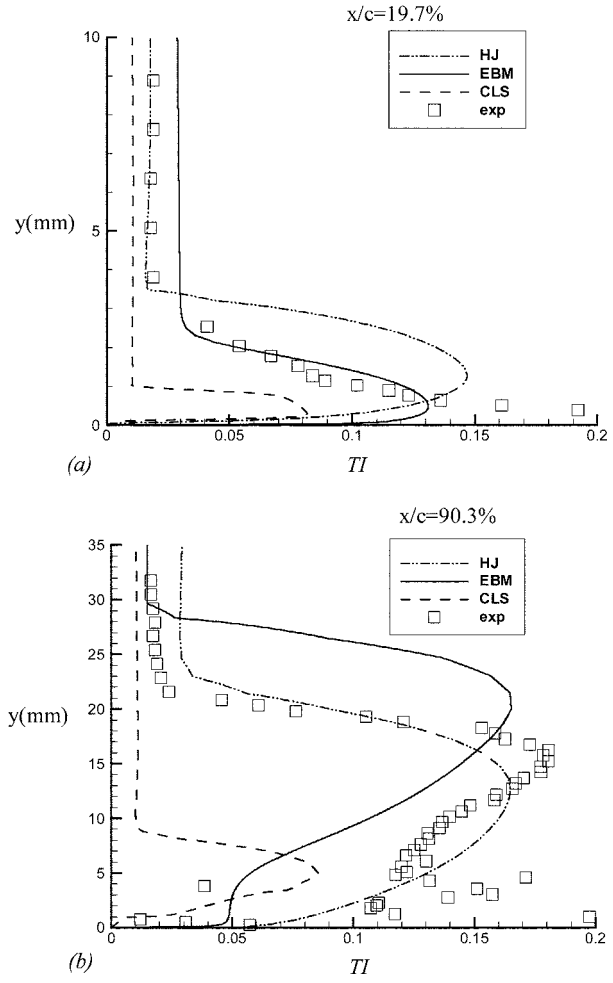

Fig. 13 DCA cascade—boundary layer velocity *TT* profiles in two stations: (*a*) 19.7% of chord; (*b*) 90.3% of chord

$-p_{in})/(0.5\rho U_{in}^2)$ where p_{out}, p_{in} are the mean values of the static pressure at the inlet and outlet sections, respectively, and ρ is the mean density, as well as the total pressure loss coefficient $\hat{\omega} = (p_{0in} - p_{0out})/(0.5\rho U_{in}^2)$, where p_{0out}, p_{0in} are the mean values of the total pressure.

We argue that the HJ results are in very good agreement with experiments. On the other hand, the EBM shows an accurate prediction of the diffusion factor, while the description of the static total pressure loss coefficients deteriorates and, with regards to these parameters, does not show a clear improvement as compared with the CLS.

Conclusions

The paper provides an assessment of two second-moment turbulence closures in predicting compressor cascade flows. Both models allow integration up to the wall accounting separately for the viscous and wall-blocking nonviscous effects. The focus is on the elliptic blending model (EBM), which provides a simple but robust framework for treating flows in complex geometries. In parallel, the tests have also been carried out with a well-established SMC closure of Hanjalic and Jakirlic (HJ), here applied for the first time to turbomachinery flows.

The performance of each model can be summarized as follows.

The HJ model gives quite good predictions of the flow field for the flow over a round leading edge flat plate, demonstrating its ability to capture boundary layer development, transition inception, and small recirculation region in the presence of streamlines

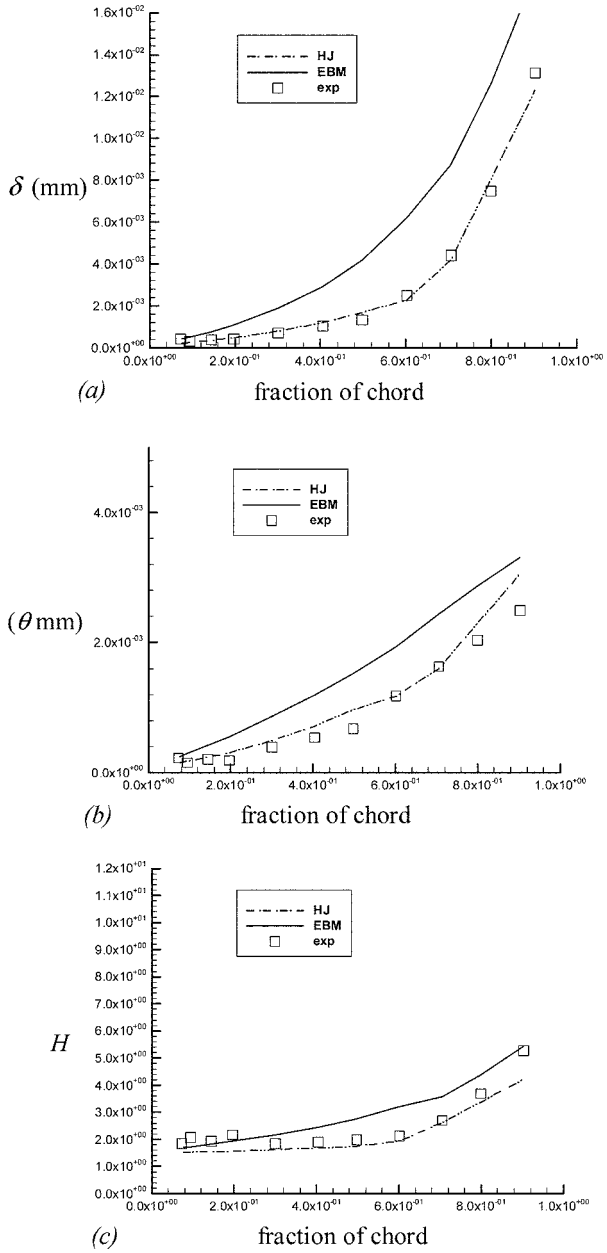

Fig. 14 DCA cascade—suction side integral parameters: (*a*) displacement thickness; (*b*) momentum thickness; (*c*) shape factor

curvature and zero pressure gradient. The double circular arc simulation shows that, even in the presence of an adverse pressure gradient, the HJ model is capable in reproducing the boundary layer development (i.e., velocity and turbulence profiles, plus integral parameters) and the presence of large recirculation regions.

The EBM simulations generally return satisfactory results, despite lacking specific Reynolds-number-dependent provisions for

Table 7 DCA—cascade loading parameters

Loading parameters	Experiments	HJ	EBM	CLS
$\hat{D}$	0.555	0.553	0.559	0.561
$\hat{C}_p$	0.473	0.472	0.409	0.528
$\hat{\omega}$	0.094	0.139	0.205	0.082

capturing laminar-to-turbulent and reverse transition. In the T3L case, although failing to reproduce the proper transition location, EBM gives performance comparable to the HJ model. In the DCA simulation, several important flow features have been predicted with the EBM as accurately as with the HJ model. Despite the less satisfactory prediction of C_p, the EBM simulation reproduces acceptably well the velocity and turbulent intensity profiles along the suction side. The integral parameters in this test case show that the EBM tends to overestimate the boundary layer thickness due to an inappropriate prediction of transition and the subsequent downstream turbulence recovery.

Based on these findings (and an earlier test in a variety of flows) we conclude that the HJ model can be identified as a suitable and accurate tool for CFD of turbomachinery flows. Despite the need for a fine grid clustering in the near-wall region and the presence of a wall-distance-dependent function f_w in the baseline GL model that serves as the high-Re-number asymptote, the HJ model has been successfully applied to the simulation of complex 3D turbomachinery flows bounded by complex wall topology (see also [20]). The EBM, on the other hand, shows great potential for computing complex flows. Its plausible physical rationale with a wall-sensing elliptic equation that is capable of identifying complex wall configuration and its effects on pressure-strain and dissipation, together with its simple and robust, topology-free formulation, as well as its relative insensitivity to grid refinement, makes it an attractive proposition for computing 3D flow phenomena in real complex geometries. However, it requires still improvements in the description of the laminar-to-turbulent and reverse transition as well as for proper capturing of the effects of the adverse pressure gradient on the boundary layer development.

Acknowledgments

The authors would like to thank MIUR (COFIN 2003) for the financial support and University of Roma "La Sapienza" for support to cooperation under the "Visiting Professors Programme."

References

[1] Mayle, R. E., 1991, "The Role of Laminar-Turbulent Transition in Gas Turbine Engines," ASME J. Turbomach., **113**, pp. 509–517.
[2] Craft, T. J., Launder, B. E., and Suga, K., 1997, "Prediction of Turbulent Transition Phenomena with a Nonlinear Eddy-Viscosity Model," Int. J. Heat Fluid Flow, **17**, pp. 108–155.
[3] Chen, W. L., Lien, F. S., and Leschziner, M. A., 1998, "Non-Linear Eddy-Viscosity Modeling of Transitional Boundary Layers Pertinent to Turbomachine Aerodynamics," Int. J. Heat Fluid Flow, **19**, pp. 297–306.
[4] Chen, W. L., Lien, F. S., and Leschziner, M. A., 1998, "Computational Prediction of Flow Around Highly Loaded Compressor Cascade Blades with Non-Linear Eddy-Viscosity Models," Int. J. Heat Fluid Flow, **19**, pp. 307–319.
[5] Craft, T. J., Launder, B. E., and Suga, K., 1996, "Development and Application of a Cubic Eddy-Viscosity Model of Turbulence," Int. J. Heat Fluid Flow, **17**, pp. 108–155.
[6] Corsini, A., and Rispoli, F., 2002, "Anisotropic Turbulence Modeling of Near Wall Effects Pertinent to Turbomachinery," ASME Paper FEDSM02, Montreal.
[7] Borello, D., and Rispoli, F., 2003, "Improved Non-Equilibrium Turbulence Closure Modeling for Axial Flow Compressors Simulation," *ASME IGTI03*, Atlanta, GA.
[8] Corsini, A., and Rispoli, F., 2005, "Flow Analyses in a High-Pressure Axial Ventilation Fan with a Non-Linear Eddy Viscosity Closure," Int. J. Heat Fluid Flow, **26**, pp. 349–361.
[9] Lodefier, K., Merci, B., De Langhe, C., and Dick, E., 2003, "Transition Modelling with the SST Turbulence Model and an Intermittency Transport Equation," *ASME IGTI03*, Atlanta, GA.
[10] Hanjalic, K., and Launder, B. E., 1976, "Contribution Towards a Reynolds-Stress Closure for Low-Reynolds-Number Turbulence," J. Fluid Mech., **74**, pp. 593–610.
[11] Shima, N., 1988, "A Reynolds-Stress Model for Near-Wall and Low-Reynolds-Number Regions," ASME J. Fluids Eng., **110**, pp. 38–44.
[12] Lai, Y. G., and So, M. C., 1990, "On Near-Wall Turbulent Flow Modelling," J. Fluid Mech., **221**, pp. 641–673.
[13] Chen, W. L., and Leschziner, M. A., 1999, "Modelling Turbomachine-Blade Flows with Non-Linear Eddy-Viscosity Models and Second Moment Closure," MechE Paper C557/131/99, A, pp. 189–199.
[14] Gerolymos, G. A., Neubauer, J., Sharma, V. C., and Vallet, I., 2002, "Improved Prediction of Turbomachinery Flows Using Near-Wall Reynolds-Stress Model," ASME J. Turbomach., **124**, pp. 86–99.
[15] Hanjalic, K., and Jakirlic, S., 1998, "Contribution Towards the Second Moment Closure Modelling of Separating Turbulent Flows," Comput. Fluids, **27**(2), pp. 137–156.
[16] Hanjalic, K., Hadzic, I., and Jakirlic, S., 1999, "Modeling Turbulent Wall Flows Subjected to Strong Pressure Variation," ASME J. Fluids Eng., **121**, pp. 57–64.
[17] Jakirlic, S., and Hanjalic, K., 2002, "A New Approach to Modelling Near-Wall Turbulence Energy and Stress Dissipation," J. Fluid Mech., **459**, pp. 139–166.
[18] Jakirlic, S., Hanjalic, K., and Tropea, C., 2002, "Modeling Rotation and Swirling Turbulent Flows: a Perpetual Challenge," AIAA J., **40**, pp. 1980–1996.
[19] Hadzic, I., and Hanjalic, K., 1999, "Separation Induced Transition to Turbulence," Flow, Turbul. Combust., **63**, pp. 153–173.
[20] Borello, D., Hanjalic, K., and Rispoli, F., 2005, "Numerical Simulation of Turbulent Flows in 3D Decelerating Cascade Using Second Moment Closure Modeling," 6th European Congress on Turbomachinery, March 2005, Lille, France.
[21] Manceau, R., and Hanjalic, K., 2002, "Elliptic Blending Model: a New Near-Wall Reynolds-Stress Turbulence Closure," Phys. Fluids, **14**(3), pp. 1–11.
[22] Durbin, P. A., 1993, "A Reynolds Stress Model for Near-Wall Turbulence," J. Fluid Mech., **249**, pp. 465–486.
[23] Thielen, L., Hanjalic, K., Jonker, H., and Manceau, R., 2005, "Prediction of Flow and Heat Transfer in Multiple Impinging Jets with Elliptic Blending Model" Int. J. Heat Mass Transfer, **48**(8), pp. 1583–1598.
[24] Borello, D., Migliarese Caputi, M., and Rispoli, F., 2003, "A Parallel Multilevel Finite Element Solver for Axial Compressor CFD," *Parallel Computational Fluid Dynamics-New Frontiers and Multi-Disciplinary Applications*, Kyto, Matsuno, K., Ecer, A., Periaux, J., Satofuka, N., and Fox, P., eds., Elsevier Science, Amsterdam.
[25] Durbin, P. A., 1991, "Near Wall Turbulence Closure Modelling Without Damping Functions," Theor. Comput. Fluid Dyn., **3**, pp. 1–13.
[26] Gibson, M. M., and Launder, B., 1978, "Ground Effects on Pressure Fluctuations in the Atmospheric Boundary Layer," J. Fluid Mech., **86**, pp. 491–511.
[27] Craft, T. J., and Launder, B. E., 1992, "New Wall-Reflection Model Applied to the Turbulent Impinging Jet," AIAA J., **30**, pp. 2970–2972.
[28] Speziale, C. G., Sarkar, S., and Gatski, T. B., 1991, "Modeling the Pressure-Strain Correlation of Turbulence: An Invariant Dynamical System Approach," J. Fluid Mech., **227**, pp. 245–272.
[29] Hadzic, I., 1999, "Second-Moment Closure Modelling of Transitional and Unsteady Turbulent Flows," Ph.D. thesis, TUDelft.
[30] Hanjalic, K., and Jakirlic, S., 1993, "A Model of Stress Dissipation in Second Moment Closures," Appl. Sci. Res., **51**, pp. 513–518.
[31] Daly, B. J., and Harlow, F. H., 1970, "Transport Equation of Turbulence," Phys. Fluids, **13**, pp. 2634–2649.
[32] Borello, D., Borrelli, P., Quagliata, E., and Rispoli, F., 2001, "A Multigrid Additive and Distributive Parallel Algorithm for FEM Turbomachinery CFD," *ECCOMAS CFD 2001*, Swansea, UK.
[33] Corsini, A., Rispoli, F., and Santoriello, A., 2005, "A Variational Multiscale Higher-Order Finite Element Formulation for Turbomachinery Flow Computations," *Computer Methods for Applied Mechanics and Engineering*, **194**, pp. 4797–4823
[34] Hanjalic, K., 1999, "Second Moment Turbulence Closure for CFD: Needs and Prospects," Int. J. Comput. Fluid Dyn., **12**, pp. 67–97.
[35] Borello, D., Corsini, A., and Rispoli, F., 2003, "A Finite Element Overlapping Scheme for Flows on Parallel Platform," Comput. Fluids, **32**, pp. 1017–1047.
[36] Palikaras, A., Yakinthos, K., and Goulas, A., 2002, "Transition on a Flat Plate with a Semi-Circular Leading Edge Under Uniform and Positive Shear Free-Stream Flow," Int. J. Heat Fluid Flow, **23**, pp. 455–470.
[37] Zierke, W. C., and Deutsch, S., 1989, "The Measurement of Boundary Layers on a Compressor Blade in Cascade," NASA Contract Report 185118.

A Quantitative Comparison of Delta Wing Vortices in the Near-Wake For Incompressible and Supersonic Free Streams

Frank Y. Wang
USDOT John A. Volpe National Transportation Systems Center,
Cambridge MA 02142

Ivana M. Milanovic
University of Hartford,
Department of Mechanical Engineering,
West Hartford CT 06117

Khairul B. M. Q. Zaman

Louis A. Povinelli

NASA John H. Glenn Research Center at Lewis Field,
Cleveland OH 44135

When requiring quantitative data on delta wing vortices for design purposes, low-speed results have often been extrapolated to configurations intended for supersonic operation. This practice stems from a lack of database in high-speed flows due to measurement difficulties. In the present paper an attempt is made to examine this practice by comparing data from an incompressible flow experiment designed specifically to correspond to an earlier experiment in supersonic flows. The comparison is made for a 75° sweptback delta wing at angles of attack of 7° and 12°. For the incompressible flow, detailed flow-field properties including vorticity and turbulence characteristics are obtained by hot-wire and pressure probe surveys. The results are compared, wherever possible, with available data from the earlier Mach 2.49 experiment. The results indicate that quantitative similarities exist in the distributions of total pressure and swirl velocities. Qualitative similarities also exist in other properties, however, many differences are observed. The vortex core is smaller and rounded at low speed. At high speed, it is elongated in the spanwise direction near the trailing edge but goes through "axis switching" within a short distance downstream. The vortex is located farther outboard, i.e., the spacing between the two legs of the vortex pair is larger, at low speed. The axial velocity distribution within the core is significantly different in the two flow regimes. A "jet-like" profile, observed at low speed, either disappears or becomes "wake-like" at high speed. The axial velocity characteristics are examined in the light of an analytical model. [DOI: 10.1115/1.2060732]

1 Introduction

After more than five decades of research, investigations of delta wing vortices continue to be of both practical and academic importance. However, a quantitative comparison of these vortices between incompressible and supersonic regimes has remained illusive due to a limited database. Such a comparison is attempted in the present paper with a focus on the flow field extending from the trailing edge up to about one chord downstream. A summary of the current understanding of incompressible and supersonic delta wing vortices, and hypotheses on how they may compare, are first provided.

For a sharp-edged delta wing (also referred to as "planform" in the following) in a low-speed stream, the overall vorticity dynamics is reasonably understood based on visualization as well as quantitative experiments. Flow from windward (pressure) side spilling over the leeward (suction) side separates along the leading edges. The resulting shear layers then roll up into a pair of large counter-rotating swirls above the delta wing. These are commonly referred to as either "primary" or "leading edge" vortices. The primary vortex pair often would induce a smaller pair of secondary vortices of opposite sign. Sometimes even a pair of tertiary vortices, induced by the secondary pair, can be observed. However, with increasing distance from the planform, the latter vortices decay quickly. Consequently, within a short distance, the leading edge vortex pair remains as the salient feature of the wake. The process usually completes within about two root chords from the planform (Spreiter and Sacks [1]; Hummel [2]; Hiremath et al. [3]; Kedzie and Griffin [4]). With sharp leading edges, since the flow separation location is fixed, the topology of the ensuing vortical flow is also known to be insensitive to Reynolds number (Carcaillet et al. [5]; Luckring [6]).

In the supersonic flow regime, a quantitative investigation has been very rare in comparison to its low-speed counterpart (Sforza [7]; Wood et al. [8]; Milanovic and Wang [9]). This is due mainly to experimental difficulties encountered in high-speed flows. Flow topology has been analyzed based on visualization studies (Miller and Wood [10]; Seshadri and Narayan [11]). In visualization studies, under the condition of "subsonic leading edge" and in the absence of cross-flow shock waves, the overall leeward flow topology has been found to be insensitive to Mach and Reynolds numbers (Stanbrook and Squire [12]; Stromberg et al. [13]; Erickson et al. [14]; Kraft [15]; Örnberg [16]; Rom [17]; Monnerie and Werlé [18]; Green [19]). The "subsonic leading edge" condition refers to a subsonic Mach number normal to the leading edge, first discussed by Stanbrook and Squire [12]. The vortex flow downstream in the wake likewise exhibits topological similarities between supersonic free stream under subsonic leading edge condition and its low-speed counterpart (Spreiter and Sacks [1]; Centolanzi [20]; Walker and Stivers [21]; Wetzel and Pfyl [22]; Spahr and Dickey [23]; Ganzer and Szodruch [24]). These findings provided a justification for extrapolating a low-speed database to configurations intended for supersonic operation (Stromberg et al. [13]; Erickson et al. [14]; Kraft [15]).

For the supersonic wake, limited quantitative data can be found in previously classified literature, such as in the works of Centolanzi [20], Walker and Stivers [21], Wetzel and Pfyl [22] and Spahr and Dickey [23]. The emphasis of these measurements, made at generous spatial intervals, was not to provide details of the flow field but to evaluate theoretical models for a downwash

Contributed by the Fluids Engineering Division for publication in the JOURNAL OF FLUIDS ENGINEERING. Manuscript received by the Fluids Engineering Division December 2, 2004. Final manuscript received July 12, 2005. Associate Editor: Hamid Johari.

prediction in the wake. Although these measurements yielded useful gross information, overall, data for supersonic flow remain rare.

Even though the vortices in the two flow regimes are qualitatively similar, Green [19] conjectures that quantitative details are surely different as are the associated aerodynamic effects. Dissimilarities have been noted in some studies. For example, the onset of vortex asymmetry and breakdown are found to occur at much lower angles of attack in the supersonic regime (Rom [17]; Green [19]; Fellows and Carter [25]; Craven and Alexander [26]). An obvious difference stems from compressibility effects. Crossflow shock waves can emerge to interact with the primary vortices. Significant density gradient variation exists, as indicated by shadowgraph flow visualizations. Thus, it is possible that baroclinic torque could be an additional source of vorticity in the compressible flow regime. Differences are also inferred from leeward surface pressure measurements. For a fixed angle of attack, the magnitude of the primary suction peak has been shown to reduce with an increasing free-stream Mach number (Wendt [27]; Stallings [28]). This could imply a corresponding decrease in vortex strength. The primary vortex core over the wing, as visualized by vapor screen technique, "flattens" in the direction of the span with increasing Mach number (Stanbrook and Squire [12]; Vorropoulos and Wendt [29]; McGregor [30]). Downstream in the wake, visualization suggests that the primary vortex can experience substantial stretch in the direction normal to the span, and that secondary vortices persist farther at a higher Mach number (Ganzer and Szodruch [24]).

There are certain physical differences between the two flow regimes that could impact the structure of the vortices in the wake. In the low-speed case, the Kutta condition dictates that the leeward flow slows down after the initial acceleration as the trailing edge is approached. Thus, the leading edge vortices are subjected first to a favorable followed by an adverse pressure gradient. In the supersonic case, on the other hand, the flow on the leeward surface continually expands until it is abruptly decelerated by the shock wave from the trailing edge.

In light of the preceding discussion, it is apparent that there are ambiguous views on how the near-wake vortical structures in the two flow regimes may differ. The literature lacks a direct quantitative comparison needed not only for a clearer understanding but also for validating theoretical and computational studies. Such a comparison constitutes the main objective of the present paper. During the course of literature survey, it also became apparent that details of the vortical structure even in a low-speed wake were lacking (Hummel [2]; Hiremath et al. [3]; Rom [17]; Green [19]). A detailed documentation of the wake at low speed, particularly for the turbulence and vorticity characteristics, forms the other objective of the paper.

2 Experimental Setup

Both the earlier supersonic and the present incompressible experiments were performed with delta wings of common geometric proportion, but of two different sizes. The delta wings had 75° sweepback, thus, the apex angle was 30°. Each was of a "flat-top" shape, having a four percent thickness-to-root-chord ratio and a chamfer of 30° along all edges. A top-view schematic is shown in Fig. 1. The model root chords (c) for the Mach 2.49 and incompressible experiments were 152.4 and 237.0 mm, respectively. The corresponding Reynolds numbers based on c were 6.5×10^6 and 1.0×10^5.

The low-speed experiments were carried out in an open circuit tunnel at NASA Glenn Research Center. The free-stream velocity was nominally 8 ms^{-1}. The 0.76 m wide $\times$ 0.51 m high test section was preceded by a 16:1 contraction ratio inlet and the blower was located downstream. The wing was mounted near the beginning of the test section and the measurement domain was within one test-section height. Thus tunnel wall effects on the data are considered insignificant. A streamlined strut, with 57 mm chord and 3.2 mm thickness, supported the wing. The strut was attached centrally on the pressure surface of the wing. The effect of the wake of the strut was also considered insignificant in the measurement domain.

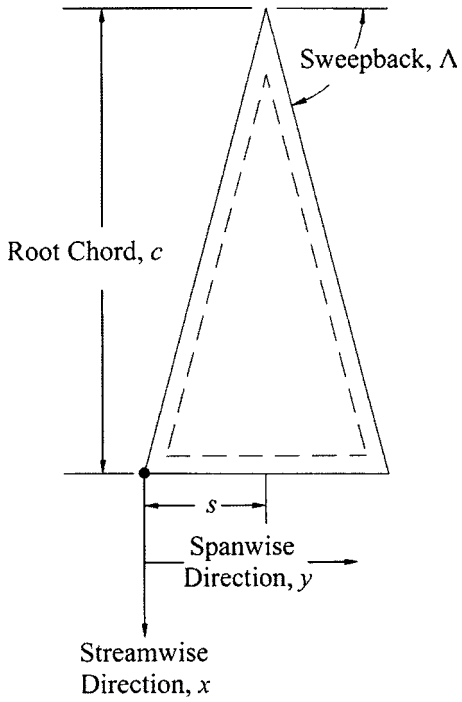

Fig. 1 Top-view schematic of the planform and the illustration of coordinate notations

Two adjacent crossed hot-wires (Dantec R.51), one placed in the "u-v" and the other in the "u-w" orientation, were traversed under automated computer control to step through the same grid points. The appropriate relative shift of the two datasets yielded the distribution of all three components of velocity and turbulence intensities on a given cross-sectional plane. The v and w data were corrected for the error introduced by the u gradients and the finite separation of the sensors in each X probe. The probes were calibrated *in situ* and the outputs from the four sensors were least-squares fitted with fourth-order polynomials as a function of the tunnel velocity. The polynomial coefficients were later used to calculate the velocities using cosine law. The survey plane at the trailing edge involved strongest secondary motion and flow angularity as much as 22° was noted. No yaw or pitch correction has been applied. An earlier study in the same facility (Foss and Zaman [31]) indicates that the errors introduced in v and w due to such angularity should be within 5%. The most significant contributor to the uncertainty in the data was the drift in hot-wire calibration. During data acquisition the tunnel velocity (u_∞) was monitored constantly. If there was more than 1% deviation, the acquisition was stopped. Data normalization was done by an updated value of u_∞. The uncertainty in the normalized u velocity is estimated to be within 2%. The probe traverse had a resolution of 0.025 mm. Uncertainty in the mean streamwise vorticity is estimated to be about 20%. Further details of the facility and hot-wire procedure can be found in the cited paper. An approximately 0.8 mm i.d. thin-walled Pitot probe, connected to a 0.01 psig (69 Pa) range pressure transducer, was used to acquire the total pressure data in separate runs. Uncertainty in the measured Pitot pressure is estimated to be within 2% of the dynamic pressure. Data were obtained at 7° and 12° angles of attack. Detailed cross-sectional measurements were carried out in the near wake at six streamwise locations. Both Pitot and hot-wire surveys employed a minimum spatial grid spacing of 1.52 mm.

The supersonic experiments were conducted in the Mach 2.49 blowdown facility at the Polytechnic University in Farmingdale, New York; the results were summarized by Milanovic and Kalkhoran ([32,33]). The 0.381 m $\times$ 0.381 m square test section was 1.27 m long. As with the low-speed experiment, the wing was mounted on a streamlined strut attached to the pressure surface. Measurements were carried out with a five-hole miniature probe. The 30° conical probe tapered from a root diameter of 3.2 mm to a tip diameter of 0.82 mm. Uncertainties in the total pressure data was estimated to be 7.5%. The mechanical and calibration details of the probe as well as further uncertainty estimates were given by Milanovic and Kalkhoran [33]. Measurements were carried out at 7° and 12° angles of attack, at the trailing edge and half-chord downstream. The test parameters satisfied the condition of the subsonic leading edge. Only the mutually perpendicular traverses through the vortex core were made in the supersonic flow. The minimum step size in the traverses was one millimeter; thus, the supersonic and low-speed data have comparable spatial resolution with respect to the planform size.

In both experiments, surveys were carried out on the port side of the planform. In the following, the coordinate origin is located at the apex of the trailing edge (Fig. 1). "Streamwise" coordinate (x) is along the direction of the free stream. "Spanwise" coordinate (y) is in the horizontal direction parallel to the trailing edge. The third, referred to as the "transverse" coordinate (z) is in the out-of-page direction. For most of the data, distances are nondimensionalized by the half-span of the trailing edge, s. Streamwise measurement locations are referred to, in keeping with common practice, in terms of the chord (c). The appropriate cross reference in terms of the half-span (s) is provided in the figure captions. All velocities are normalized by the free-stream velocity (u_∞).

3 Results and Discussions

3.1 Flow-Field Surveys at Low-Speed. Measurements were made at low speed for both 7° and 12° angles of attack at six locations, $x/c=0$, 0.06, 0.13, 0.25, 0.5, and 0.64. For brevity, detailed flow-field maps only for the 12° case are presented in Figs. 2–5. Total pressure (P_0) distributions are shown in Fig. 2. The data are given in the format of a loss coefficient, $(P_0-P_{0,\infty})/q$, where q is the dynamic head and $P_{0,\infty}$ is the total pressure in the free stream (El-Ramly and Rainbird [34]). As stated earlier, the surveys capture the port side half of the wake; $y/s=1$ denotes the symmetry plane (Fig. 1). The rollup and the evolution of the primary vortex can be seen clearly. Significantly lower pressures characterize its core. At the trailing edge, the loss coefficient in the core has a value of −0.95. Another low-pressure region is observed underneath the primary vortex, most likely due to the combination of a secondary vortex and the viscous wake from the trailing edge. For the first two survey stations, the latter structure also has a pronounced total pressure deficit. With increasing downstream distance it diffuses while merging with the primary vortex. By the last survey station the primary vortex has become the salient feature of the wake.

In Fig. 3, contours of turbulence intensity (u'/u_∞) are shown. The cross-stream velocity vector fields are superimposed in this and the remaining flow-field maps (Figs. 4 and 5). Turbulence intensity in the vortex core at the trailing edge plane is 11%. The viscous wake from the trailing edge and the shear layer from the leading edge are also discernible. These manifest as a highly turbulent sheet of fluid wrapping around the primary vortex. The shear layer and the viscous wake are ingested by the primary vortex farther downstream, consistent with the evolution seen in Fig. 2. The turbulence intensity in the core at the final survey station is about 0.16, representing a significant increase of 45%. High turbulence intensity found in the core has often been attributed to vortex meandering. However, the present data display a concentrated vortex core throughout the measurement domain. This suggests a relatively steady vortex since large-scale meandering would smear the distributions. On the other hand, the wrapping of turbulent fluid from the shear layer underneath is evident. With increasing distance downstream, turbulent fluid from outside is brought in and deposited in the core. Thus, the entrainment of turbulent fluid from the surrounding must also contribute to and indeed could be the main mechanism for the high turbulence in the core.

In Fig. 4, streamwise vorticity ($\omega_x c/u_\infty$) contours are shown. The primary vortex with the negative (clockwise) sense persists in the flow. At the upstream locations a secondary vortex structure of opposite sign is clearly seen. The opposite senses of the swirl can also be discerned from the vector fields. By a half-chord downstream the secondary vortex has completely disappeared, as also observed with the pressure contours (Fig. 2). The magnitude of vorticity in the primary vortex has also decreased rapidly, by about a factor of 3, within the same distance. The ingestion of the surrounding turbulent fluid into the core and diffusion are likely responsible for the observed decrease in the streamwise vorticity.

Corresponding total velocity distributions are presented in Fig. 5. The total velocity represents the resultant of three components; however, it is dominated by the streamwise velocity. Again, it is observed that low momentum fluid from the wake of the trailing edge becomes entrained into the primary vortex with downstream distance. The vortex itself in general has velocity higher than that of the free stream for the first four stations, but a deficit appears farther downstream. The axial velocity characteristics in the vortex core will be addressed further in Sec. 3.2.

The streamwise evolution of various properties pertaining to the vortex core, obtained from Figs. 2–5, is summarized in Fig. 6. All magnitudes are normalized by the corresponding value at the trailing edge. The circulation ($\Gamma c/u_\infty$) was obtained by line integration of the cross-flow velocities ($\int v\,dy+\int w\,dz$) over an appropriate boundary surrounding the vortex (Foss and Zaman [31]). While the entrainment of the turbulent wake is taking place, as indicated by the increase in turbulence intensity, the total velocity is found to decrease significantly. The peak vorticity also decreases substantially while circulation remains fairly constant. These trends are analyzed further in the following section.

3.2 Comparison of High- and Low-Speed Surveys. The two flow regimes are now compared using profiles obtained along the transverse (z) and spanwise (y) axes of the vortex core. Results for $x/c=0$ and 0.5 are presented in Figs. 7–18, respectively. In order to allow the comparison with incompressible flow, the Mach number data from the supersonic experiment were converted to velocity by assuming a constant stagnation temperature. In the experiments, the probes were traversed in planes normal to the free-stream direction. Therefore, the vortex axis was not always aligned with the probe axis and thus the swirl velocity was not truly measured. The term vortex "swirl" velocity has nevertheless been used to denote cross-stream velocity components. Similarly, the term "axial" velocity has been used to denote the streamwise component. As stated earlier, the total pressure data for the low-speed case is presented as the coefficient, $(P_0-P_{0,\infty})/q$. For the supersonic regime, the definition of a corresponding pressure coefficient is not obvious. Following the format of Milanovic and Kalkhoran [32], the total pressure in the latter regime is normalized by the free-stream total pressure. Despite this difference in normalization, a comparison of the trends in the pressure variation should be valid and adequate.

3.2.1 Trailing Edge. Profiles in the transverse direction are shown in Figs. 7–9. Those in the spanwise direction are shown in Figs. 10–12. Figure 7 illustrates that both the magnitude and spatial extent of the total pressure deficit are larger at a higher angle of attack. The minimum Pitot pressure has been used in previous supersonic studies to denote the vortex center location (Brodetsky and Shevchenko [35]; Milanovic and Kalkhoran [33]). With this criterion, the core center location at Mach 2.49 can be found from Figs. 10(a) and 7(a). At $\alpha=7°$ the center is at $y/s=0.39$ and z/s

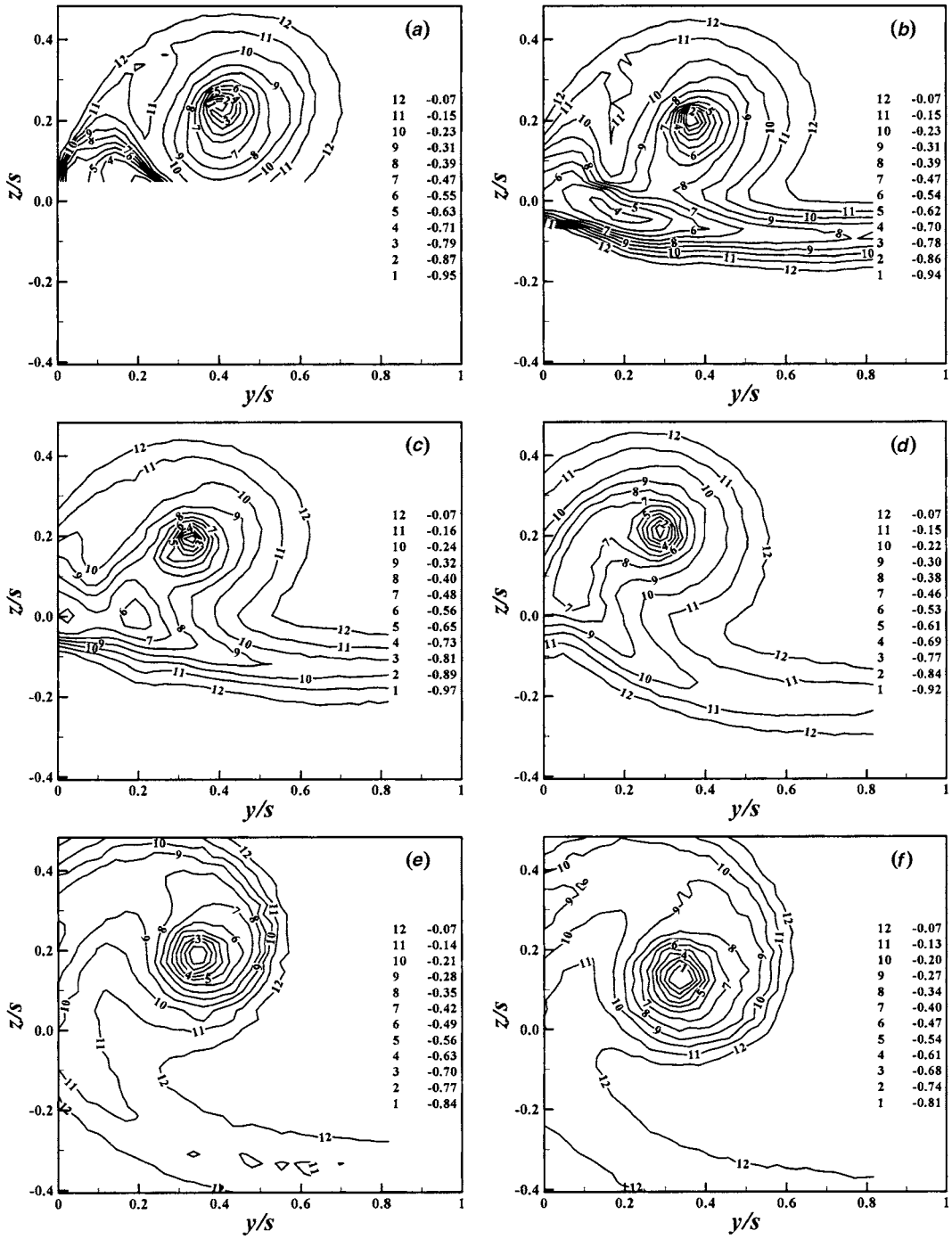

Fig. 2 Low-speed vortex wake at $\alpha=12°$; contour labels indicate total pressure loss coefficient $(P_0 - P_{0,\infty})/q$, at the following locations: (*a*) ($x/c=0$; $x/s=0$), (*b*) ($x/c=0.06$; $x/s=0.22$), (*c*) ($x/c=0.13$; $x/s=0.49$), (*d*) ($x/c=0.25$; $x/s=0.93$), (*e*) ($x/c=0.5$; $x/s=1.87$), (*f*) ($x/c=0.64$; $x/s=2.39$)

=0.13, while at $\alpha=12°$ the coordinates are (0.54, 0.21).

For the low-speed experiments, with the criterion of minimum total pressure, the coordinates of the core center $(y/s, z/s)$ are found to be at (0.34, 0.15) and (0.41, 0.24), for the 7° and 12° cases, respectively. Thus, both high- and low-speed results show the vortex moving inboard and upward relative to the wing surface, as the angle of attack is increased. However, the cores in the Mach 2.49 case are somewhat more toward the centerline of the wing and closer to the surface compared to the low-speed counterpart. The vortex core trajectories will be summarized in Sec. 3.3.

The vortex core dimensions can be characterized based on the locations of swirl velocity peaks and maximum pressure gradient as in Milanovic and Kalkhoran [33]. For the Mach 2.49 case at 7°, the core size is measured in the spanwise and transverse directions $(y/s \times z/s)$ to be 0.29×0.14. The corresponding size at 12° is 0.42×0.26. The low-speed core dimensions are found to be 0.18×0.14 for the 7° case, and 0.12×0.19 for the 12° case. The measurements in the supersonic case therefore agree with flow visualization observations that the core is stretched in the spanwise direction (Stanbrook and Squire [12]; Vorropoulos and

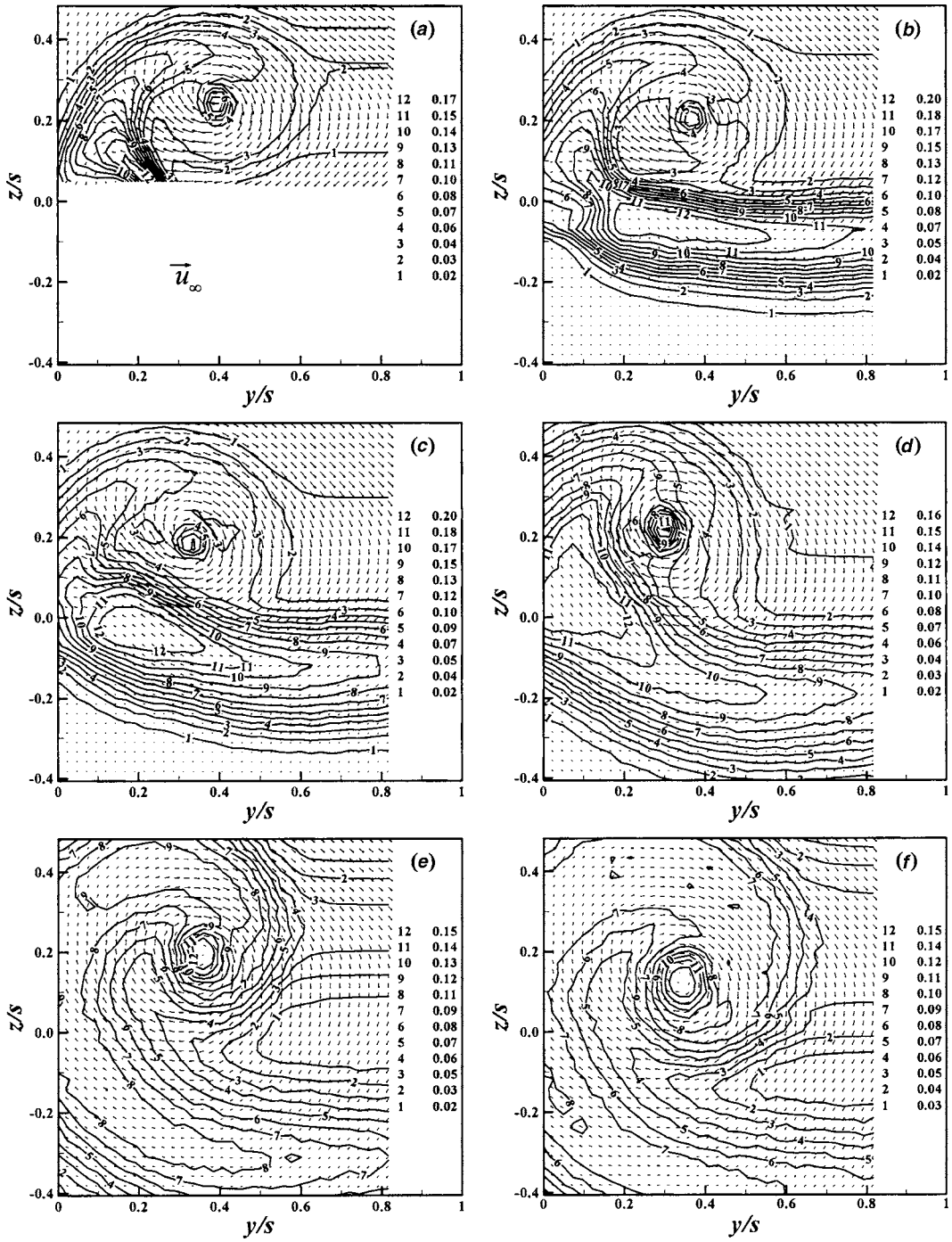

Fig. 3 Low-speed vortex wake at α=12°; contour labels indicate turbulence intensity, u'/u_∞, at the following locations: (*a*) (x/c=0; x/s=0), (*b*) (x/c=0.06; x/s=0.22), (*c*) (x/c=0.13; x/s=0.49), (*d*) (x/c=0.25; x/s=0.93), (*e*) (x/c=0.5; x/s=1.87), (*f*) (x/c=0.64; x/s=2.39)

Wendt [29]; McGregor [30]). Note that the low-speed results do not exhibit such a pronounced stretching. The core becomes flattened at high speed conceivably because the vortex is sandwiched between the planform and the expanding flow above (Stanbrook and Squire [12]).

The spanwise profiles of total pressure shown in Fig. 10 also reveal the presence of secondary vortices in both regimes, as indicated by the smaller pressure dips (Milanovic and Kalkhoran [32,33]). These are to the left of the primary vortices. The secondary vortices, found in the normalized spanwise range of 0.1–0.2, are characterized by opposite gradients in the transverse velocity (Fig. 11). Recall from the low-speed data that vorticity was of an opposite sense for the primary and secondary vortices at this x location.

Thus, the flow fields for the two regimes so far are found to be similar in many details. However, the streamwise velocity distributions differ considerably (Figs. 9 and 12). The supersonic case features velocity deficit in the core with values below that of the free stream. A higher angle of attack results in a larger deficit. This

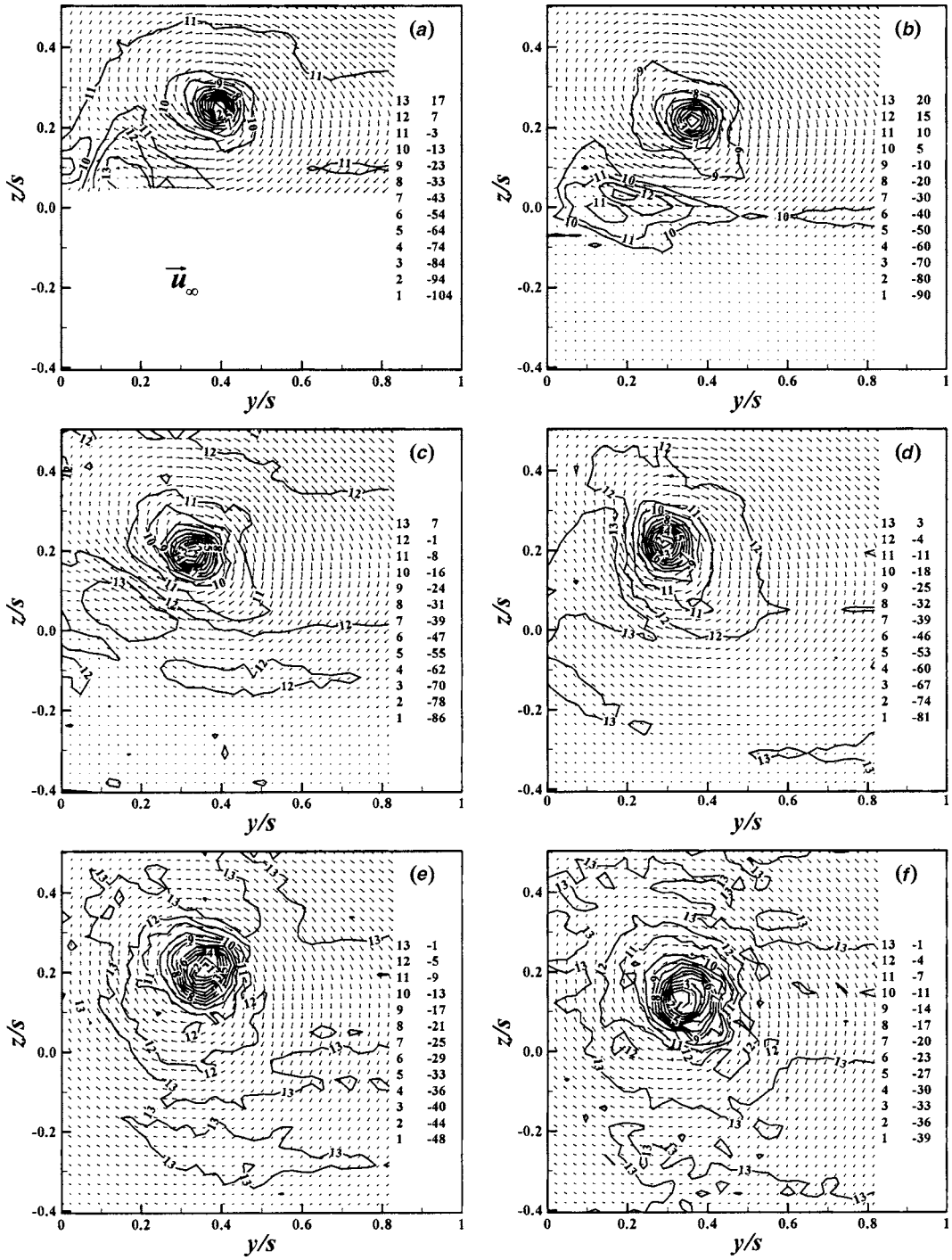

Fig. 4 Low-speed vortex wake at α=12°; contour labels indicate normalized streamwise vorticity, $\omega_x c/u_\infty$, at the following locations: (*a*) (*x*/*c*=0; *x*/*s*=0), (*b*) (*x*/*c*=0.06; *x*/*s*=0.22), (*c*) (*x*/*c*=0.13; *x*/*s*=0.49), (*d*) (*x*/*c*=0.25; *x*/*s*=0.93), (*e*) (*x*/*c*=0.5; *x*/*s*=1.87), (*f*) (*x*/*c*=0.64; *x*/*s*=2.39)

is apparent in the transverse profiles of Fig. 9(*a*). Low-speed data shown in Fig. 9(*b*) indicate a different trend. An increase in the angle of attack increases the axial velocity in the core. A clearer contrast with the high-speed case is that the velocity around the core exceeds that of the free stream. The streamwise velocity in and around the core has an important consequence on vortex breakdown for both supersonic and incompressible flows. A vortex with axial velocity in the core lower than that of the free stream is more susceptible to breakdown. The required deceleration to reach the stagnation point at breakdown is less than that for the case with a uniform or an overshoot/jet-like profile (Délery et al. [36]; Nedungadi and Lewis [37]; Mahesh [38]; Kalkhoran & Smart [39]).

3.2.2 Half-Chord From Trailing Edge. Low-speed and supersonic data at half-chord downstream are compared in Figs. 13–18, in a similar manner as done in Figs. 7–12. Pressure and velocity measurements provided core center locations and dimensions. As before, core center coordinates are given in terms of $(y/s, z/s)$. At Mach 2.49, they are (0.37, 0.08) at α=7° and (0.48, 0.11) at α

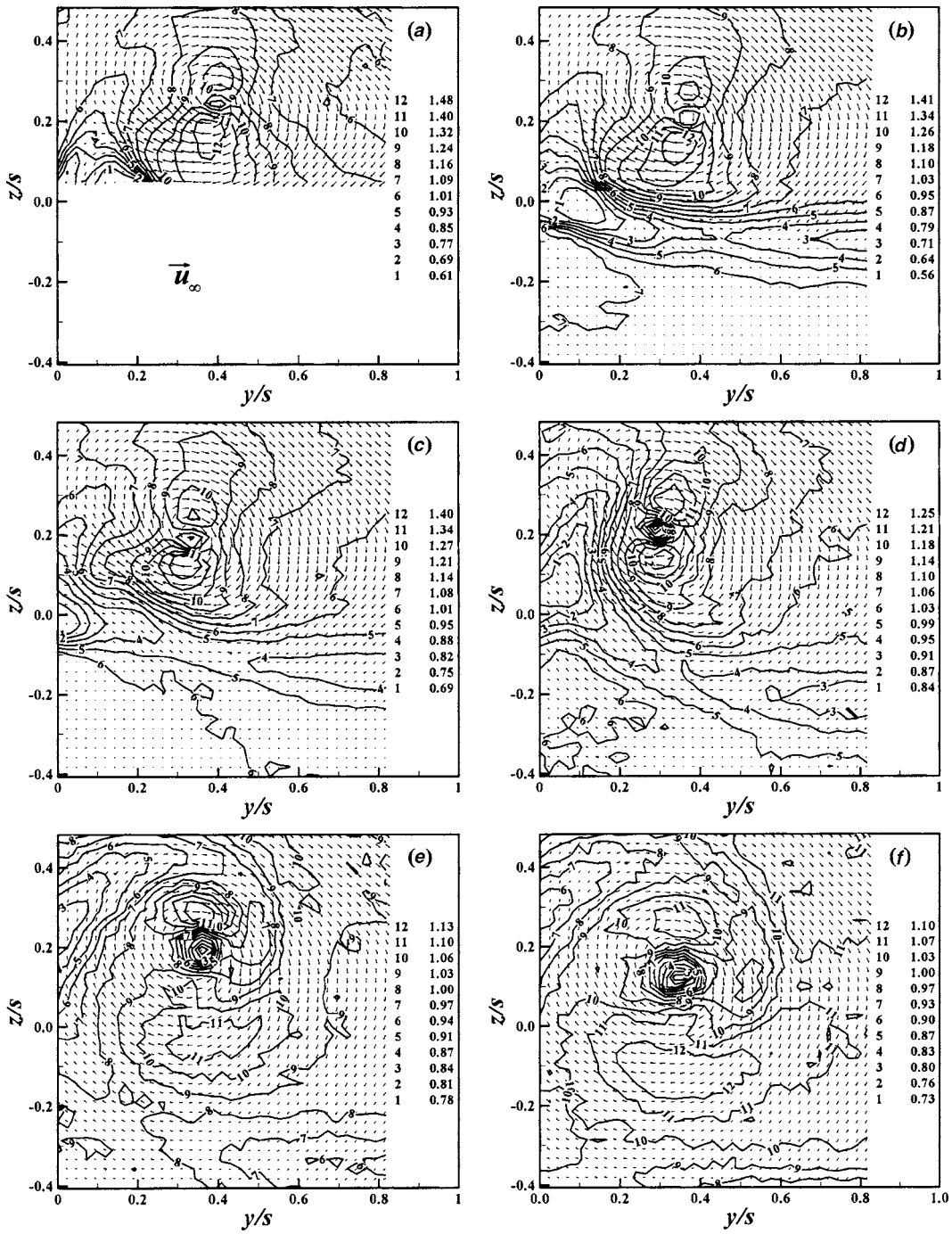

Fig. 5 Low-speed vortex wake at $\alpha=12°$ contour labels indicate normalized total velocity, $(u^2+v^2+w^2)^{1/2}/u_\infty$, at the following locations: (*a*) ($x/c=0$; $x/s=0$), (*b*) $x/c=0.06$; $x/s=0.22$, (*c*) ($x/c=0.13$; $x/s=0.49$), (*d*) ($x/c=0.25$; $x/s=0.93$), (*e*), $x/c=0.5$; $x/s=1.87$), (*f*) $x/c=0.64$; $x/s=2.39$)

$=12°$. At low speed the coordinates are (0.29, 0.17) and (0.34, 0.19). Therefore, at each angle of attack in both flow regimes, the cores have moved slightly outboard and downward with increasing downstream distance. The core sizes at Mach 2.49 are similarly found to be 0.22×0.18 at $\alpha=7°$ and 0.22×0.32 at $\alpha=12°$. At low speed, the corresponding dimensions are 0.22×0.23 at $\alpha=7°$, and 0.22×0.20 at $\alpha=12°$. While the core in the low-speed case is approximately round, at the higher incidence in the supersonic regime it is stretched significantly in the transverse direction. These data again are in agreement with the vapor-screen flow visualization results of Ganzer and Szodruch [24] for a 73° swept-back wing in a Mach 2 free stream at $\alpha=10°$. These trends are further analyzed in Sec. 3.3.

In both flow regimes, the "viscous" wake of the trailing edge is evident in the total pressure profiles (around $z/s=-0.2$ in Fig. 13, just below the vortex cores). The viscous wake has not affected the "swirl" patterns, as seen in Fig. 14. The presence of a secondary vortex is also indicated by the total pressure deficit [Fig. 16(*a*)] and the swirl velocity profiles [Fig. 17(*a*)], in the y/s range of 0.0–0.1. At low speed, the secondary vortex is not obvious either in the total pressure profiles [Fig. 16(*b*)] or in the swirl velocity profiles [Fig. 17(*b*)]. Thus, it appears that the secondary vortex generated in the supersonic case is either stronger initially or has less dissipative characteristics compared to its low-speed

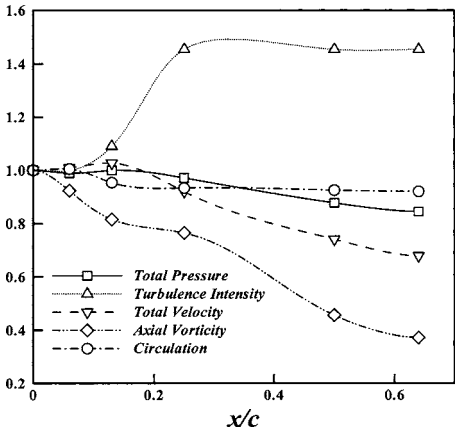

Fig. 6 Evolution of minimum and maximum values of various properties of the vortex core, normalized by respective values at the trailing edge

counterpart.

The axial velocity profiles at half-chord (Figs. 15 and 18), particularly for the high-speed case, are rather complex. This is attributed to the proximity of the viscous wake, the secondary vortex, as well as shocks emanating from the trailing edge. Shadowgraph visualization for the Mach 2.49 flow indicates that the vortices go through the shock and expansion waves before reaching the half-chord survey location. In comparison, a simple profile with the vortex wake only is visible at the low speed. It is also noted that velocities in the core at the low-speed are lower than the free-stream velocity, in contrast to the observation at the trailing edge.

The results presented so far have shown that the vortices in the two flow regimes have many similar characteristics with comparable swirl profiles. However, the axial velocity distributions differ significantly. The causes and implications of the difference in axial velocities are further explored in the following.

3.2.3 Axial Flow in the Vortex Core. It is clear that the vortex cores do not usually convect at the speed of the free stream in the near-field. This is in concurrence with the experience from previous research on wing tip vortices (see, e.g., Thompson [40]; Devenport et al. [41]; Chow et al. [42]; Anderson and Lawton [43]). When the core velocity is higher than the free-stream velocity, a vortex is said to have a jet-like profile. Similarly, a wake-like profile refers to a vortex having the core velocity lower than that of the free stream. The mechanisms affecting the axial velocity distribution within an incompressible trailing vortex was first addressed by Batchelor [44]. According to Batchelor's analysis, the axial velocity, $u(r)$, relative to the free-stream velocity (u_∞) at a given downstream location, is determined by evaluating the following equation:

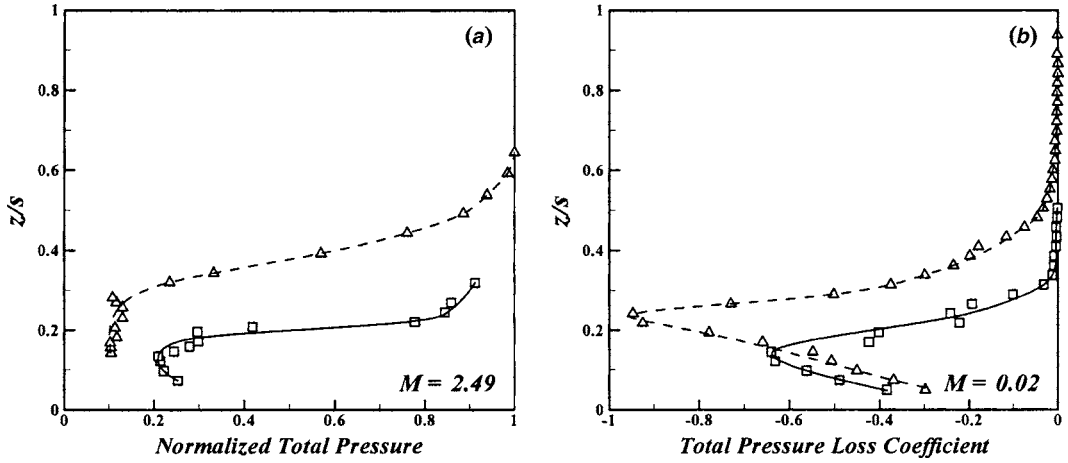

Fig. 7 A comparison of transverse profiles at the trailing edge; □ α=7° △ α=12°

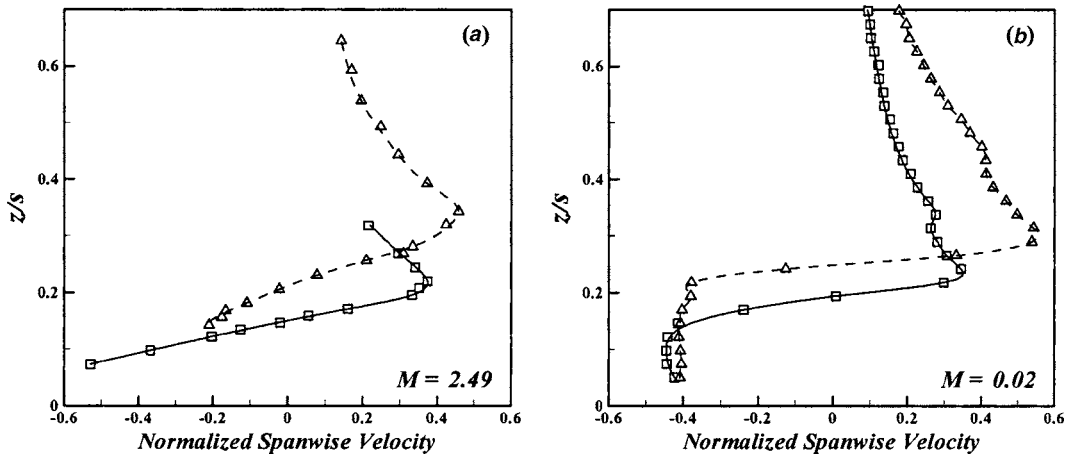

Fig. 8 The same as in Fig. 7

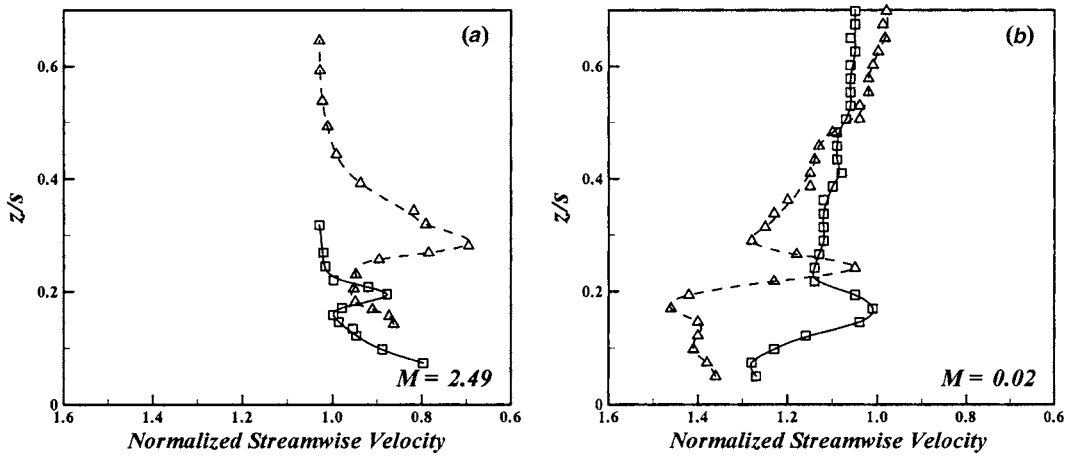

Fig. 9 The same as in Fig. 7

$$u^2 = u_\infty^2 + \int_r^\infty \frac{1}{r^2}\frac{\partial C^2}{\partial r} dr - 2\,\Delta H \tag{1}$$

where $C \equiv rw$ is the circulation parameter with w being the swirl velocity, and the last term represents the integrated total pressure loss. For a typical linear swirl profile in the core, the contribution of the integral term is positive, thereby promoting a jet-like axial flow. On the other hand, the total pressure loss retards the axial flow resulting in a wake-like profile. It should be noted that Eq. (1) was derived for wing-tip vortices, but the basic formulation is independent of the specific vortex generator.

Wang and Sforza [45] later extended the formulation to compressible flow by assuming a polytropic pressure–density relation in the core. A similar expression was obtained:

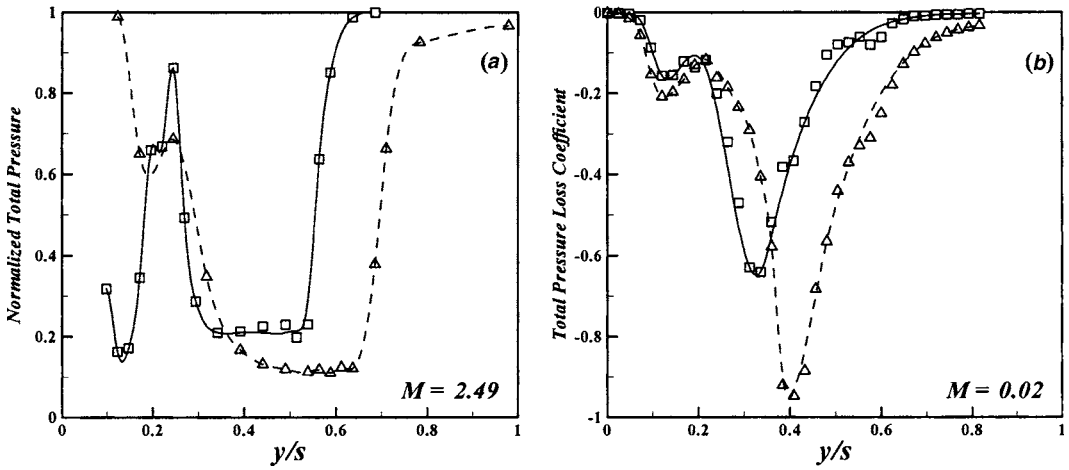

Fig. 10 A comparison of spanwise profiles at the trailing edge; □ α=7°, △ α=12°

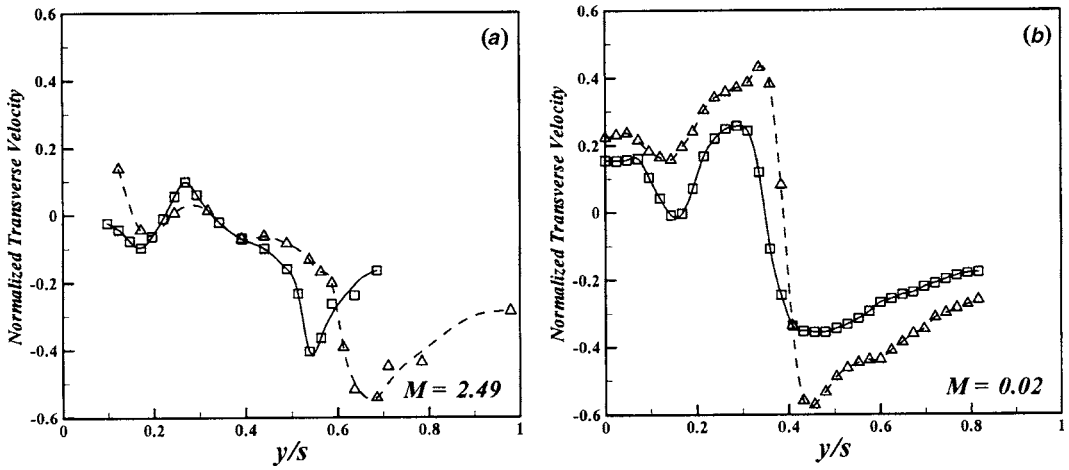

Fig. 11 The same as in Fig. 10

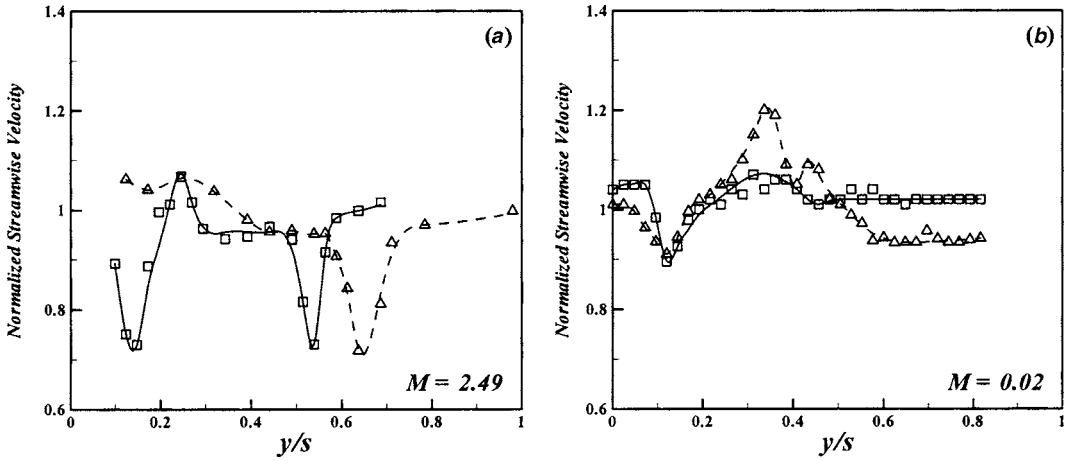

Fig. 12 The same as in Fig. 10

$$u^2 = u_\infty^2 + \left[7\left(\frac{n-1}{n}\right) - 2\right]\int_r^\infty \frac{C^2}{r^3}dr + \int_r^\infty \frac{1}{r^2}\frac{\partial C^2}{\partial r}dr - 2\,\Delta H \tag{2}$$

where n is the polytropic exponent, and the last term on the right-hand side is now the stagnation enthalpy loss. Equation (2) differs from Eq. (1) in an extra term involving the circulation parameter and the representation of the loss term. It follows that, with $1 < n < 1.4$ and $C = rw = Ar^2$ (A being a constant), the first integral of the circulation parameter is negative. However, the net contribution from the two terms involving C is positive.

Thus, in both flow regimes vortex circulation promotes a jet-like profile whereas viscous loss induces a velocity deficit. The axial flow profile is ultimately dictated by the interaction of the

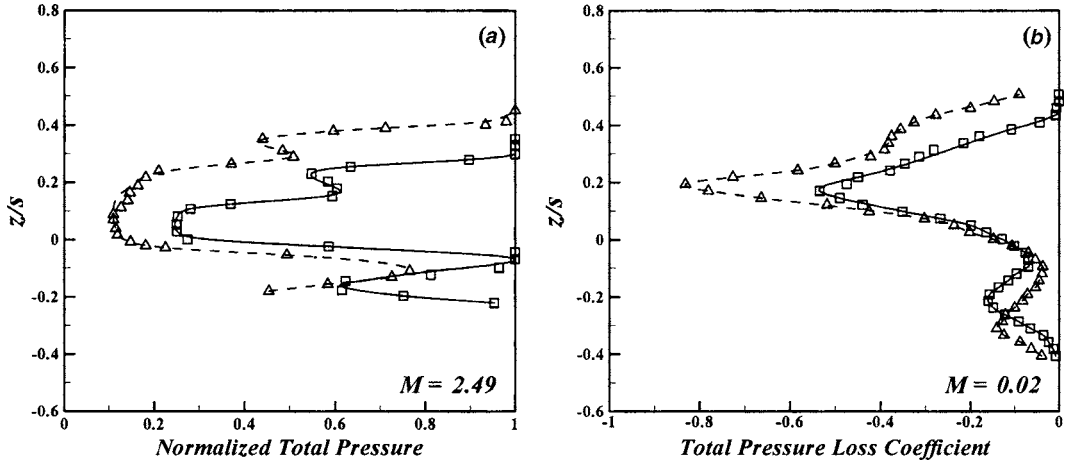

Fig. 13 A comparison of transverse profiles at half-chord downstream; □ α=7°, △ α=12°

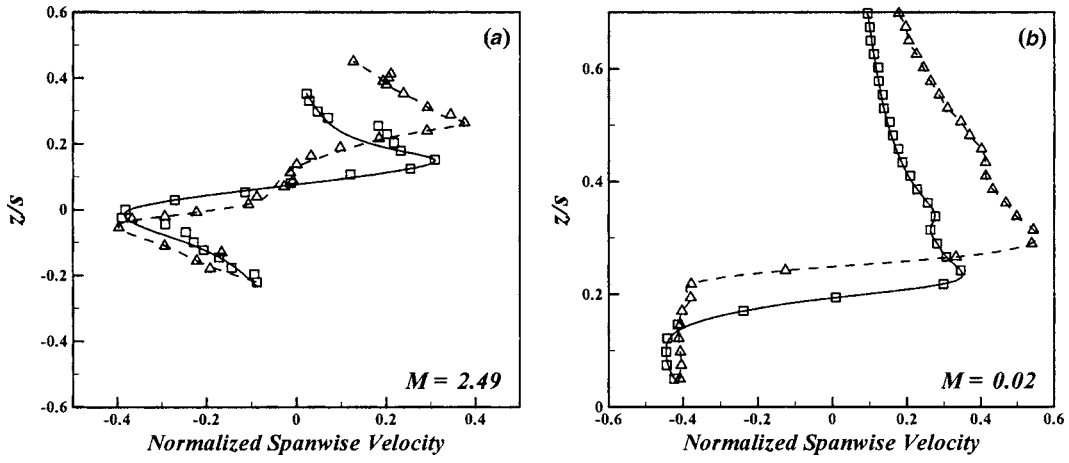

Fig. 14 The same as in Fig. 13

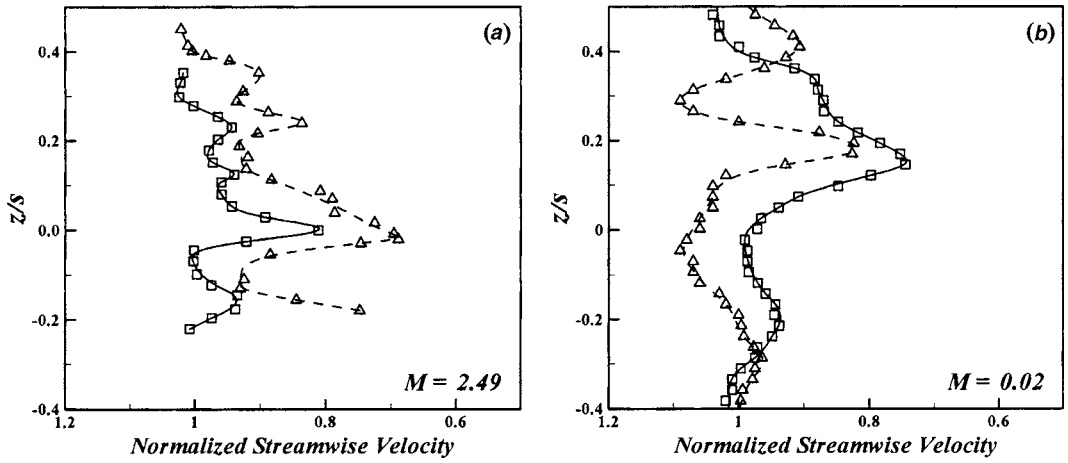

Fig. 15 The same as in Fig. 13

vortex circulation and loss stemming from entrainment of the viscous wake. It is also possible to have both velocity overshoot and deficit in the same cross-sectional profile at different radii. Although Eqs. (1) and (2) capture the physical mechanisms, they do not readily lead to a quantitative prediction due to the difficulty in the evaluation of the loss term. Nevertheless, a further qualitative assessment of the axial flow behavior can be made based on these formulations.

For identical circulation, the compressible flow would have less of a capacity to promote a jet-like axial flow due to the first term involving C in Eq. (2). Here, it is pertinent to consider the ideal amount of circulation a planform could impart into its wake. If it is assumed that the entire lift of the planform manifests itself in

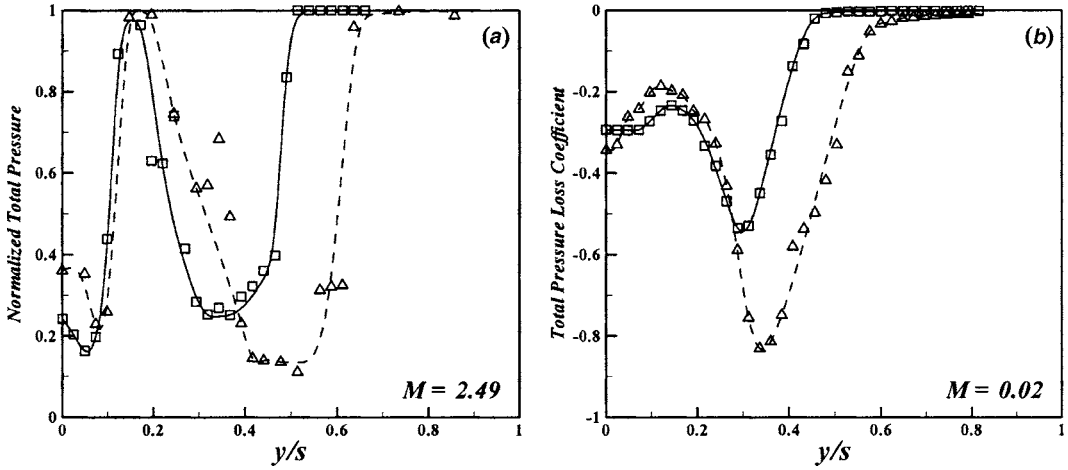

Fig. 16 A comparison of spanwise profiles at half-chord downstream; □ α=7°, △ α=12°

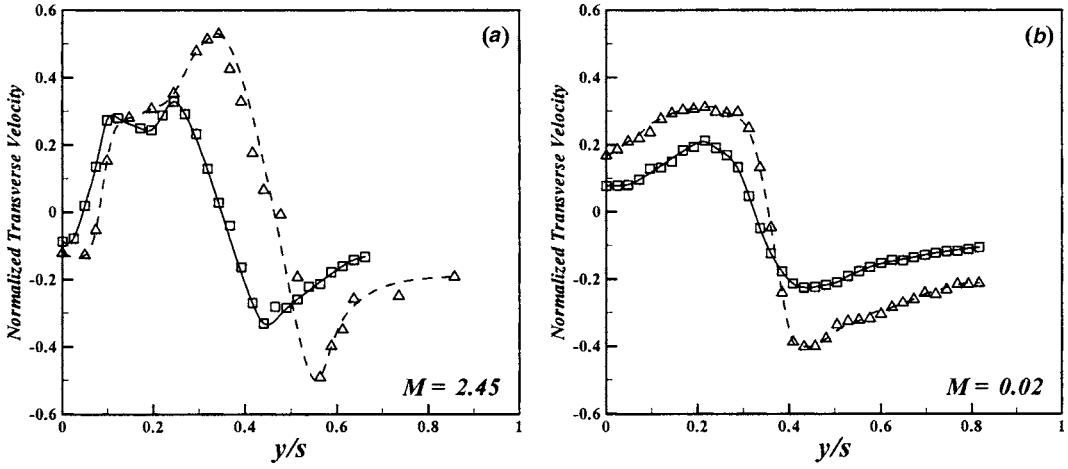

Fig. 17 The same as in Fig. 17

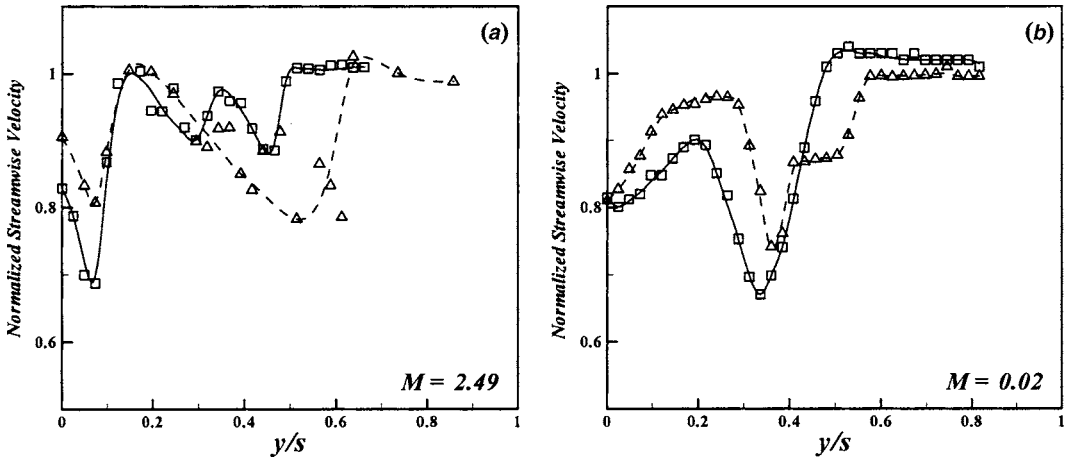

Fig. 18 The same as in Fig. 17

the vortex wake, with a Kutta–Joukowski relationship being applicable, then the nondimensional vortex circulation becomes half of the lift coefficient. Hence, the lift coefficient is an indicator of the vortex strength. The supersonic experimental data summarized by Lee and Ho [46] showed that the lift coefficient, for a 76° sweepback subsonic leading edge delta wing, varies inversely with free-stream Mach number. Hence, the circulation reduces with increasing Mach number. A reduction in C together with the effect of the first term in Eq. (2), would make the viscous loss term dominate and drive a wake-like profile in the compressible case. This is supported by the comparisons of the streamwise velocity profiles in Figs. 9, 12, 15, and 18.

A numerical study (Rizetta [47]) is worth mentioning in this connection. Using Euler, laminar, and k-ε turbulent algorithms, Rizetta simulated a wing-tip vortex in a Mach 2.5 stream. The computations provided transverse profiles through the vortex core. The results showed that the various simulations had little effect on the pressure and swirl velocity distributions, but the axial Mach number profile was different. From Euler to laminar to k-ε simulation, which represented modeling the flow with an increasing viscous effect, there was an increasing deficit in the axial Mach number in the vortex core. The Euler computation produced a mild "jet-like" profile, the laminar Navier–Stokes solution showed a deficit, and the k-ε simulation resulted in the most pronounced "wake-like" profile. In spite of questions regarding the applicability of classical turbulence models to the flow under consideration, the trend is similar to the observations made here; i.e., a wake-like axial flow in the vortex is enhanced by the introduction of viscous flow into the core (Sforza [7]).

The observations made at low speed can also be reconciled based on Eq. (1). Recall that near the trailing edge a locally "wake-like" profile is embedded in a region of velocity overshoot. The overshoot is higher at the higher angle of attack. Thus, the gain in circulation at the larger incidence must have offset the viscous loss and contributed further to the overshoot. The velocity overshoot at the trailing edge is in good agreement with past measurements (Werlé [48]). With increasing downstream distance, additional dissipative effects from the ingestion of the turbulent wake continue to compete through the ΔH term. Thus, a wake-like profile eventually evolves as seen at the half-chord downstream location.

3.3 Near-Wake Core Trajectory and Shape Summarizes. From the low-speed surveys (Sec. 3.1), vortex core trajectories and sizes are determined, using the criteria discussed in Sec. 3.2. These data are compared with the corresponding high-speed results.

Vortex trajectories on the y-z plane are compared in Fig. 19 for $\alpha=12°$. For the high-speed regime, in addition to the results of Milanovic and Kalkhoran [32] data from another study approximately matching the conditions of the present investigation are also included. The latter experiment, of Povinelli [49], involved a near-wake survey of a vortex generator in a Mach 2.5 stream. In the study we addressed enhanced mixing through the action of streamwise vortices. The delta wing shaped generator had 58.5° sweepback and the data are for an incidence angle of 14°. Even though the Mach number normal to the leading edge was supersonic, shadowgraph pictures showed detached shocks in front apparently due to the large chamfer of the model. Thus, the vortex generation process was expected to be the same as in the case of subsonic leading edge.

Figure 19 provides a view of the vortex trajectories projected on the cross-sectional plane. Each data point is marked with the measurement location x/s. A rather complex trajectory at low speed can be observed. Although the details border on the spatial resolution of the measurements, a looping behavior is quite clear within the distances examined. A similar trend was also noted at $\alpha=7°$ at the low speed (the data not shown). A looping behavior is not observed in the high-speed experiments with the given spatial resolutions. The trajectory at the low speed is plausible and can be accounted for in terms of vortex dynamics. Recall from Fig. 4 that there is a secondary vortex of opposite sign underneath the primary vortex. The induced motion of the primary/secondary vortex pair causes both to first migrate upward and away from the

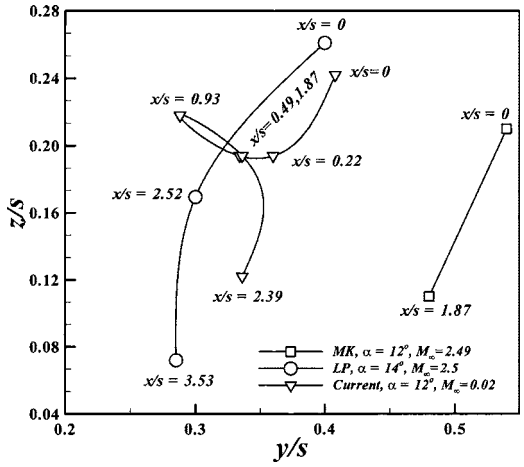

Fig. 19 Near-wake vortex core trajectories from low-speed and supersonic experiments. Cited references are (MK) Milanovic and Kalkhoran [32] and (LP) Povinelli [49].

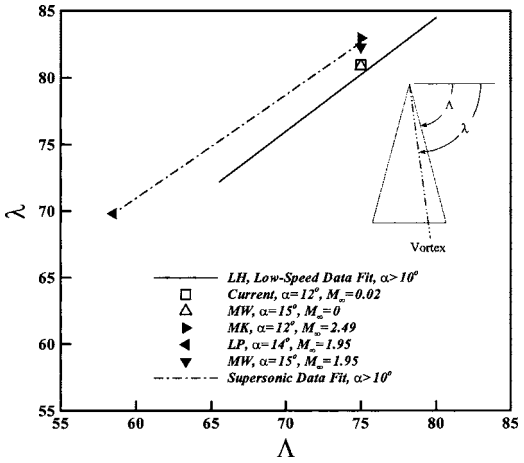

Fig. 20 The leeward vortex sweep angle, λ, for both supersonic and low-speed data, illustrating the core locations at the trailing edge. Cited references are (LH) Lee and Ho [46], (MW) Monnerie and Werlé [18], (MK) Milanovic and Kalkhoran [32], and (LP) Povinelli [49].

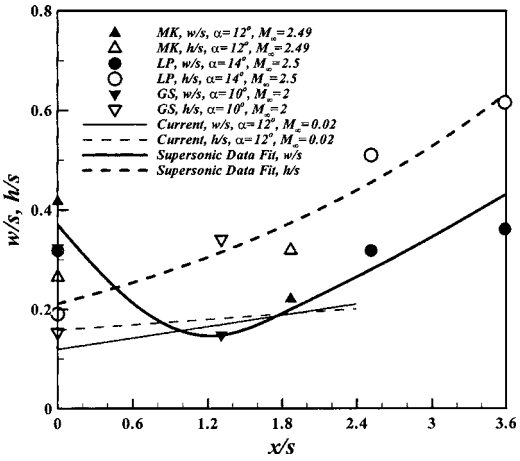

Fig. 21 Near-wake vortex core shape from low-speed and supersonic experiments. Cited references are (MK) Milanovic and Kalkhoran [32], (LP) Povinelli [49], and (GS) Ganzer and Szodruch [24].

trailing-edge apex. However, the intensity of the secondary vortex diminishes rapidly. As the secondary vortex decays, the primary vortex is left under the sole influence of its counterpart across the planform centerline. The induced velocity of the final primary vortex pair then causes a continuously downward trajectory farther downstream.

The trajectory for the 75° delta wing at the low speed is spaced outboard from its high-speed counterpart (Milanovic and Kalkhoran [32]). The vortex for the low-speed case is situated farther to the left in Fig. 19. In other words, at the higher Mach number the spacing between the two legs of the primary vortex pair is smaller. This is also seen in the near-wake data of Monnerie and Werlé [18]. It is postulated that the reduced spacing is due to the flow expansion around the leading edge that also caused the initial flattening of the core. The expanding flow squeezes the vortex down toward the wing surface as well as toward the wing centerline.

In Fig. 19, the vortex trajectories for the two supersonic cases have similar trends, but they are conspicuously spaced apart. This is due to the difference in the sweepback angle, Λ (75° vs 58.5°). The spacing between the two legs of the vortex pair does not only scale with the semispan but also depends on the chord and, thus, on the sweepback. In fact, a consistent trend emerges if the data are plotted against the sweepback angle, as illustrated in Fig. 20. Here, the solid line is a fit through the low-speed data of Lee and Ho [46], as presented in their paper. The dashed line is a straight-line fit through the three data points (dark) for supersonic flows. The open data points are from the present low-speed experiment and another low-speed experiment from the indicated reference. It is evident that the "vortex sweep angle," λ, depends directly on Λ. Note also that the curves for the supersonic and low-speed data are shifted, consistent with the outboard shift of the vortex core seen in Fig. 19.

The vortex core shape evolution for both flow regimes is summarized in Fig. 21. The spanwise width (w) and transverse height (h) of the core measured at various downstream locations (x) are shown. The data for all high-speed cases are least-squares fitted with the heavy lines. The solid line is through the width (w) data and the chain-dashed line is through the height (h) data. It is seen that the high-speed cases involve a vortex core with a much larger initial width compared to the height. The "flattened" core, as discussed earlier, is due to the expanded flow over the vortices. Downstream of the trailing edge, the vortex is free, and an "axis-switching" behavior is observed. The height becomes larger than the width. The vortex is expected to become round farther downstream. But it can be seen that the core is still elongated in the vertical direction within the measurement domain. The thinner lines in Fig. 21, with corresponding line codes, represent data for the low-speed case. In order to avoid cluttering, only the fitted curves are shown. It is seen that, overall, the core size at the low speed is smaller. Moreover, the initial asymmetry in the core dimensions is mild and the vortex rapidly develops a round shape.

4 Concluding Remarks

A quantitative comparison of delta wing vortices in the near-wake for incompressible and supersonic flows has been made. The results indicate that quantitative similarities exist in the distributions of total pressure and swirl velocity. In both flow regimes, the planform produces primary and secondary vortices with similar topological features. The overall trajectory of the vortices likewise follow a similar pattern. However, many differences are noted. At the trailing edge the vortex core at Mach 2.49 is significantly stretched in the spanwise direction. In comparison, the core in the low-speed case is approximately round. With increasing distance downstream the core in the high-speed case becomes elongated in the transverse direction, resulting in a pronounced "axis switchover." The detailed low-speed survey also reveals a looping behavior in the vortex trajectory that is not observed at high speed within the measurement resolution. The looping trajectory is due to the interaction of the primary vortex with a secondary vortex that is present close to the trailing edge. The secondary vortex disappears completely by a half-chord downstream in the low-speed case. At Mach 2.49, however, it persists farther downstream. The most conspicuous difference is noted in the axial velocity distribution within the core of the vortex. A jet-like profile observed at low-speed becomes wake-like at high speed. The details of the axial flow depend on the interaction of vortex circulation and viscous loss due to the ingestion of a turbulent wake. While the circulation promotes a jet-like profile, the viscous loss causes a velocity deficit. It is shown that with compressible flow an additional effect based on the circulation also drives the velocity deficit. Thus, with increasing compressibility a wake-like profile becomes more likely. The extrapolation of low-speed information beyond overall flow features is therefore not recommended, especially at higher angles of attack. The detailed flow maps at low speed provide a database for validating predictive tools and further insight into the evolution of the vortex wake.

Acknowledgments

The first author held a National Research Council Associateship at NASA Glenn Research Center when the low-speed experiments were performed and the manuscript was prepared. The work was supported by Aerospace Propulsion Power Research and Technology Base Program of NASA GRC. The subsequent encouragement and support from Robert Rudis, Michael Geyer, and Edward Spitzer of the Volpe Center are likewise acknowledged with appreciation. The second author gratefully acknowledges the support from NASA—Connecticut Space Grant College Consortium and the Greenberg Junior Faculty Research Grant of University of Hartford.

References

[1] Spreiter, J. R., and Sacks, A. H., 1951, "The Rolling up of the Trailing Vortex Sheet and its Effect on the Downwash Behind Wings," J. Aeronaut. Sci., **18**, pp. 21–32.
[2] Hummel, D., 1978, "On the Vortex Formation Over a Slender Wing at Large Angles of Incidence," *High Angle of Attack Aerodynamics*, AGARD-CP-247, pp. 13.1–13.17.
[3] Hiremath, B. M., Holla, V. S., and Govindaraju, S. P., 1984, "Study of Flow-Field in the Near Wake of Delta Wings," The Journal of Aeronautical Society of India, **36**, pp. 17–27.
[4] Kedzie, C. R., and Griffin, K. E., 1983, "Experimental Measurements of Wake Characteristics of Low Aspect-Ratio Delta and Flapped-Plate Planforms," USAFA-TN-83-6.
[5] Carcaillet, R., Manie, F., Pagan, D., and Solignac, J. L., 1986, "Leading Edge Vortex Flow Over a 75 Degree Swept Delta Wing—Experimental and Computational Results," *Proceedings of the 15th ICAS Congress*, London, UK, 7–12 September.
[6] Luckring, J. M., 2004, "Reynolds Number, Compressibility, and Leading-Edge Bluntness Effects on Delta Wing Aerodynamics," *Proceedings of the 24th ICAS Congress*, Yokohama, Japan, 29 August–3 September.
[7] Sforza, P. M., 1998, "Vortex-Plume Interaction Research," Fluid Dynamics Research on Supersonic Aircraft, NATO RTO-EN-4, pp. 9.1–9.20.
[8] Wood, R., Wilcox, F. J., Jr., Bauer, S. X. S., and Allen, J. M., 2000, "High Speed Vortex Flows," AIAA Paper 2000-2215.
[9] Milanovic, I. M., and Wang, F. Y., 2002, "Experimental Studies on Compressible Leading-Edge Vortices," Aerosp. Sci. Technol., **6**, pp. 383–394.
[10] Miller, D. S., and Wood, R. M., 1984, "Leeside Flows Over Delta Wings at Supersonic Speeds," J. Aircr., **21**, pp. 680–686.
[11] Seshadri, S. N., and Narayan, K. Y., 1988, "Possible Types of Flow on Lee-Surface of Delta Wings at Supersonic Speeds," Aeronaut. J., **92**, pp. 185–199.
[12] Stanbrook, A., and Squire, L. C., 1964, "Possible Types of Flow at Swept Leading Edges," Aeronaut. Q., **15**, pp. 72–82.
[13] Stromberg, A., Henze, A., Limberg, W., and Krause, E., 1996, "Investigation of Vortex Structures on Delta Wings," Z. Flugwiss. Weltraumforsch., **20**, pp. 71–79.
[14] Erickson, G. E., Peake, D. J., Del Frate, J., Skow, A. M., and Malcolm, G. N., 1987, "Water Facilities in Retrospect and Prospect—An Illuminating Tool for Vehicle Design," Aerodynamic and Related Hydrodynamic Studies Using Water Facilities, AGARD-CP-413, pp. 1.1–1.27.
[15] Kraft, E. M., 1988, "Vortex Flows," Boundary Layer Simulation and Control in Wind Tunnels, AGARD-AR-224, 338–355.
[16] Örnberg, T., 1954, "A Note on the Flow Around Delta Wings," Kungl Tekniska Högskolan Institutionen För Flygteknik KTH Aero TN 38.
[17] Rom, J., 1992, in *High Angle of Attack Aerodynamics: Subsonic, Transonic, and Supersonic Flows*, Springer-Verlag, New York, pp. 13–23.
[18] Monnerie, B., and Werlé, H., 1968, "Study of Supersonic and Hypersonic Flow About a Slender Wing at an Angle of Attack," Hypersonic Boundary Layers and Flow Fields, AGARD-CP-30, 23.1–23.19.
[19] Green, S. I., 1995, *Fluid Vortices*, Kluwer Academic, Dordrecht, the Netherlands, pp. 297–303.
[20] Centolanzi, F. J., 1959, "Measured and Theoretical Flow-Field Behind a Rectangular and a Triangular Wing up to High Angles of Attack at a Mach Number of 2.46," NASA TN D-92.
[21] Walker, H. J., and Stivers, L. S., Jr., 1950, "Investigation of the Downwash and Wake Behind a Triangular Wing of Aspect Ratio 4 at Subsonic and Supersonic Mach Numbers," NACA RM A50I14a.
[22] Wetzel, B. E., and Pfyl, F. A., 1951, "Measurements of Downwash and Sidewash Behind Cruciform Triangular Wings at Mach Number 1.4," NACA RM A51B20.
[23] Spahr, J. R., and Dickey, R. R., 1953, "Wind-Tunnel Investigation of the Vortex Wake and Downwash Field Behind Triangular Wings and Wing-Body Combinations at Supersonic Speeds," NACA RM A53D10.
[24] Ganzer, U., and Szodruch, J., 1987, "Vortex Formation over Delta, Double-Delta and Wave Rider Configurations at Supersonic Speeds," Aerodynamics of Hypersonic Lifting Vehicles, AGARD-CP-428, pp. 25.1–25.32.
[25] Fellows, K. A., and Carter, E. C., 1969, "Results and Analysis of Pressure Measurements on Two Isolated Slender Wings and Slender Wing-Body Combinations at Supersonic Speeds, Vol. 1 Analysis," *ARA Report No.* 12.
[26] Craven, A. H., and Alexander, A. J., 1963, "An Investigation of Vortex Breakdown at Mach 2," *Cranfield College of Aeronautics CoA Note Aero-158*.
[27] Wendt, J., 1982, "Compressibility Effects on Flows Around Simple Components," High Angle-of-Attack Aerodynamics, AGARD-LS-121, pp. 7.1–7.20.
[28] Stallings, R. L., Jr., 1992, "Low Aspect Ratio Wings at High Angles of Attack," *Tactical Missile Aerodynamics: General Topics*, Progress in Astronautics and Aeronautics, edited by M. J. Hemsch, **141**, pp. 251–286.
[29] Vorropoulos, G., and Wendt, J., 1983, "Laser Velocimetry Study of Compressible Effects on the Flow-Field of a Delta Wing," Aerodynamics of Vortical Type Flows in Three Dimensions, AGARD-CP-342, pp. 9.1–9.13.
[30] McGregor, I., 1962, "Development of the Vapor Screen Method of Flow Visualization in a 3 ft.$\times$3 ft. supersonic tunnel," Flow Visualization in Wind Tunnels Using Indicators, AGARDograph 70, pp. 115–164.
[31] Foss, J. K., and Zaman, K. B. M. Q., 1999, "Large- and Small-Scale Vortical Motion in a Shear Layer Perturbed by Tabs," J. Fluid Mech., **382**, pp. 307–329.
[32] Milanovic, I. M., and Kalkhoran, I. M., 2001, "Vortex-Wake Measurements of a Delta Wing in a Supersonic Stream," J. Aircr., **38**, pp. 315–325.
[33] Milanovic, I. M., and Kalkhoran, I. M., 2002, "Measurements of Leading-Edge Vortices on a 75° Delta Platform Wing at $M=2.5$," Aeronaut. J., **106**, pp. 39–49.
[34] El-Ramly, Z., and Rainbird, W. J., 1977, "Effect of Simulated Jet Engines on the Flow Field Behind a Swept-Back Wing," J. Aircr., **14**, pp. 343–349.
[35] Brodetsky, M. D., and Shevchenko, A. M., 1991, "Some Features of a Separated Flow and Supersonic Vortex Structure at the Leeside of a Delta Wing," Separated Flows and Jets, edited by V. V. Kozlov and A. V. Dovgal, *IUTAM Symposium Novosibirsk*, Springer-Verlag, Berlin Heidelberg.
[36] Délery, J., Horowitz, E., Leuchter, O., and Solignac, J.-L., 1984, "Fundamental Studies on Vortex Flows," Rech. Aerosp., **2**, pp. 1–24.
[37] Nedungadi, A., and Lewis, M. J., 1996, "Computational Study of the Flow-Fields Associated With Oblique Shock/Vortex Interactions," AIAA J., **34**, pp. 2545–2553.
[38] Mahesh, K., 1996, "A Model for the Onset of Breakdown in an Axisymmetric Compressible Vortex," Phys. Fluids, **8**, pp. 3338–3345.
[39] Kalkhoran, I. M., and Smart, M. K., 2000, "Aspects of Shock Wave-Induced Vortex Breakdown," Prog. Aerosp. Sci., **36**, pp. 63–95.
[40] Thompson, D. H., 1975, "Experimental Study of Axial Flow in Wing Tip Vortices," J. Aircr., **12**, pp. 910–911.
[41] Devenport, W. J., Rife, M. C., Liapis, S. J., and Follin, G. J., 1996, "The Structure and Development of a Wing-Tip Vortex," J. Fluid Mech., **312**, pp. 67–106.
[42] Chow, J. S., Zilliac, G. G., and Bradshaw, P., 1997, "Mean and Turbulence Measurements in the Near Field of a Wingtip Vortex," AIAA J., **35**, pp. 1561–1567.
[43] Anderson, E. A., and Lawton, T. A., 2003, "Correlation Between Vortex Strength and Axial Velocity in a Trailing Vortex," J. Aircr., **40**, pp. 699–704.
[44] Batchelor, G. K., 1964, "Axial Flow in Trailing Line Vortices," J. Fluid Mech., **20**, pp. 645–658.
[45] Wang, F. Y., and Sforza, P. M., 1997, "Near-Field Experiments on Tip Vortices at Mach 3.1," AIAA J., **35**, pp. 750–753.
[46] Lee, M., and Ho, C.-M., 1989, "Vortex Dynamics of Delta Wings," *Frontiers in Experimental Fluid Mechanics*, Springer-Verlag, Berlin, pp. 365–427.
[47] Rizetta, D. P., 1996, "Numerical Investigation of Supersonic Wing-Tip Vortices," AIAA J., **34**, pp. 1023–1028.
[48] Werlé, H., 1974, "Le Tunnel Hydrodynamique au Service de la Recherche Aérospatiale," ONERA TP-156.
[49] Povinelli, L. A., 1974, "Drag and Distribution Measurements of Single-Element Fuel Injectors for Supersonic Combustors," NASA TM X-3015.

Aspects of Shear Layer Unsteadiness in a Three-Dimensional Supersonic Wake

Alan L. Kastengren[1]
Energy Systems Division,
Argonne National Laboratory,
9700 S. Cass Ave.,
Argonne, IL 60439
e-mail: akastengren@anl.gov

J. Craig Dutton[2]
Mechanical & Aerospace Engineering
Department, The University of Texas
at Arlington, 500 West First Street,
Arlington, TX 76019

The near wake of a blunt-base cylinder at 10° angle-of-attack to a Mach 2.46 free-stream flow is visualized at several locations to study unsteady aspects of its structure. In both side-view and end-view images, the shear layer flapping grows monotonically as the shear layer develops, similar to the trends seen in a corresponding axisymmetric supersonic base flow. The interface convolution, a measure of the tortuousness of the shear layer, peaks for side-view and end-view images during recompression. The high convolution for a septum of fluid seen in the middle of the wake indicates that the septum actively entrains fluid from the recirculation region, which helps to explain the low base pressure for this wake compared to that for a corresponding axisymmetric wake. [DOI: 10.1115/1.2062727]

1 Introduction

The behavior of compressible base flows has been a subject of research interest for many years, due to their applications in the flight of aerodynamic bodies, as well as in flame-holding. Several recent base flow studies [1–5] have focused on the behavior of the free shear layer between the freestream flow and the recirculation region. The base flow shear layers are populated by large-scale turbulent structures, similar to those found in compressible planar shear layers.

Aside from the behavior of large-scale structures, another important aspect of shear layer behavior is the variability of its transverse position, known as flapping. Knowledge of flapping can help in understanding instability modes in a shear layer. Flapping also affects time-averaged velocity measurements of the shear layer, so knowledge of the extent of flapping is needed to ensure that averaged measurements in the shear layer are representative of actual flow conditions. For example, if the shear layer flapping is of the order of the shear layer thickness, average velocity data will indicate a larger shear layer thickness than is seen instantaneously. Previous studies of flapping are rather limited. Ponton and Seiner [6] studied the flapping of a jet issuing from a converging nozzle at M_j=1.3. They found that for a thin-lipped nozzle, the dominant instability mode of the jet was flapping (double helix) rather than helical, while for a thick-lipped nozzle, the jet contained both flapping and helical disturbances. Bourdon and Dutton [2] showed that in both planar and axisymmetric supersonic base flows, the flapping, normalized by the shear layer thickness, increased as the shear layer developed before recompression and from recompression to the developing wake, with slight decreases during recompression. RMS flapping values ranged from 10% to 40% of the local shear layer thickness. They also showed that the planar base flow experienced greater shear layer flapping than the axisymmetric case for both side and end views. This was attributed to axisymmetric confinement effects. Scarano and van Oudheusden [4] also noted flapping on the order of the wake width in the trailing wake of their planar base flow study.

A critically important aspect of turbulent shear layers is their capacity to mix and entrain free-stream fluid. One popular hypothesis is that fluid interfaces exhibit fractal properties. Fractal geometry results in a surface whose area increases in a self-similar manner as the scale of measurement used to measure the interface shrinks. The most important parameter in this analysis is the fractal dimension, which characterizes how quickly the area increases as the scale of measurement decreases. These techniques have been used by several researchers to measure the interfaces in passive scalar transport [7–10], as well as fluctuations in schlieren images [11] and velocity fluctuations [7].

While fractal dimension measurements are quite common, they do not lend themselves to an intuitive understanding of the behavior of a fluid interface. Instead, Bourdon and Dutton [2] measured the tortuousness of the shear layer interface, known as interface convolution, between the free-stream fluid and recirculation fluid in an axisymmetric base flow. Interface convolution is determined by comparing the length of the shear layer interface to the length for an ideal case. This quantity gives a rough indication of the potential for entrainment and mixing in a shear layer. This method was used by Glawe et al. [12] to study the structure of a jet of fluid injected in the base region of a strut in supersonic flow. Bourdon and Dutton [2] found that the convolution increased monotonically for both planar and axisymmetric base flows as the shear layer developed, with generally higher values for the planar base than for the axisymmetric base.

The literature on shear layer behavior in three-dimensional compressible wakes is very limited. Boswell and Dutton [13–15] studied a blunt-base cylinder flow field at 10° angle-of-attack to a Mach 2.46 free-stream flow. The flow along the afterbody is quite asymmetric. For example, at separation the displacement thickness of the lateral plane boundary layer is 0.0881 R, while the windward boundary layer displacement thickness is only 0.0136 R. A circumferential pressure gradient exists around the afterbody, causing flow to move from windward to leeward around the afterbody. This causes a thin boundary layer with high shear on the windward side of the afterbody. Mass builds up in the leeward part of the boundary layer, resulting in a thick boundary layer. This study also showed a marked asymmetry in the wake, with a division of the wake into two lobes after reattachment.

The current investigation examines the variability in the shear layer position (i.e., flapping), and the tortuousness of the shear layer interface for a blunt-base cylinder at 10° angle-of-attack to a

[1]Postdoctoral Research Scientist.
[2]Professor and Chair.

Contributed by the Fluids Engineering Division for publication in the JOURNAL OF FLUIDS ENGINEERING. Manuscript received by the Fluids Engineering Division August 2, 2004; final manuscript received July 5, 2005. Associate Editor: Sivaram Gogineni.

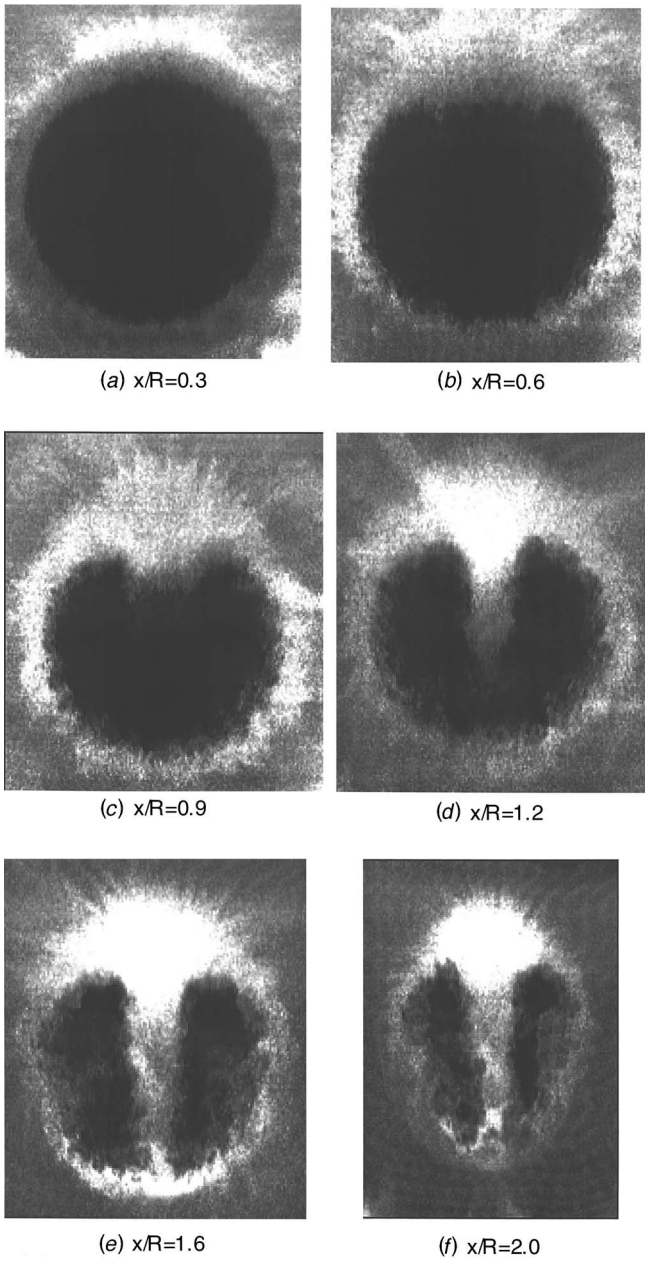

Fig. 1 Example global end-view Mie scattering images at various axial locations

supersonic free-stream flow. Time-resolved flow visualizations of the shear layer between the free-stream flow and the recirculation region are used to examine the flapping and interface tortuousness in both side-view and end-view images. While accurate time-averaged velocity data are available for this wake [15], such data are not able to describe the instantaneous behavior of the wake. The current results provide such information, giving a better understanding of the dynamics of the turbulent shear layer in this flow. These data are compared to the axisymmetric blunt-base data by Bourdon and Dutton [1,2], to show how the three-dimensional nature of the current flow impacts the structure and characteristics of the shear layer.

Extensive visualizations of this flow have also been performed [5] to examine the gross flow-field features, as well as the topology of the large-scale structures in the shear layer and trailing wake. To achieve an overall understanding of the wake topology, a set of example instantaneous global end-view images is shown

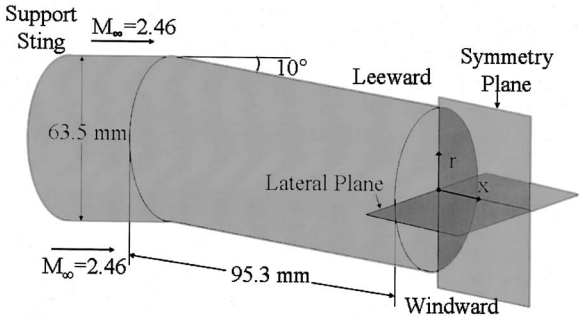

Fig. 2 Schematic of the test afterbody with added nomenclature

in Fig. 1 [5]. This set of images demonstrates that while the wake is roughly circular immediately after separation, the leeward side of the shear layer thickness quickly, forming a septum that is driven downward to eventually divide the wake into two lobes. The rapid convergence of the forming septum toward the windward part of the shear layer explains the short distance from the base surface to the rear stagnation point (reattachment length) for the current flow compared to axisymmetric base flow [15].

2 Experimental Equipment and Techniques

These experiments were conducted in an intermittent blowdown wind tunnel at the University of Illinois Gas Dynamics Laboratory. This tunnel uses an annular converging-diverging nozzle with an exit Mach number of 2.46 [16]. The stagnation temperature and pressure are 302±2 K and 545 kPa±2%, respectively. The afterbody is a cylinder 63.5 mm in diameter, with a sudden 10° bend. The length-to-radius ratio after the bend is 3.0. The afterbody is supported from upstream of the nozzle by a sting passing through the center of the nozzle. This allows the wake to be studied without interference from rear or side supports, which have been shown to significantly alter the structure of the near wake in base flows [17]. Figure 2 shows a schematic of the test body, as well as a depiction of some of the nomenclature used throughout the rest of the paper.

Visualizations of the shear layer were performed using passive-scalar Mie scattering, a commonly used technique for studying compressible shear layer structure [1–3,5,18]. In this method, liquid ethanol was injected into the supply air well upstream of the flow facility. This liquid evaporates before the flow facility, but recondenses as a fine mist of particles as the air accelerates to supersonic speeds in the facility C-D nozzle. The particles evaporate quite quickly in subsonic regions of the flow but remain stable in supersonic portions of the flow, allowing the shear layer interface to be visualized. A sheet of laser light (approximately 750 μm thick) from a pulsed Nd:YAG laser (6–8 ns duration, 40–100 mJ pulse energy) was used to scatter light from the particles. The repetition rate of the laser is 10 Hz; thus, the images in each ensemble are uncorrelated in time. The scattered light was collected by an unintensified CCD camera of 512×512 pixel resolution. The particles are roughly 50 nm in diameter [18], allowing them to quickly respond to changes in flow velocity or static temperature [19,20].

The most important source of noise in the images is due to the phenomenon of laser speckle. Laser speckle is a three-dimensional interference effect that occurs when a diffuse reflector is illuminated by coherent light. The result of speckle is additional random noise in the images. Speckle can be reduced by the use of larger aperture collecting optics. Hence, the side-view images were obtained at f/4, the largest aperture possible with the lens used for these experiments. Due to the lack of ideal optical

Table 1 Side-view imaging parameters

Region	Distance from separation x/R	Image size mm	M_c
Lateral A	0.48	$15.0\times15.0\pm0.2$	1.03
Lateral B	0.95	15.0×15.0	1.20
Lateral C	1.65	15.4×15.4	1.03
Lateral C Septum	1.65	15.0×15.0	0.48
Lateral D	1.96	25.0×25.0	0.93
Lateral E	2.57	28.1×28.1	0.69
Leeward F	0.4	13.3×13.3	
Leeward G	0.7	13.3×13.3	
Leeward H	0.9	13.3×13.3	
Windward I	0.3	13.2×13.2	1.14
Windward J	0.6	13.2×13.2	1.31
Windward K	0.9	13.2×13.2	1.37

access in the flow facility, the end-view images were obtained at an oblique angle to the laser sheet. To achieve adequate depth-of-focus, a smaller lens aperture (f/16) was used.

Two kinds of images were used for the following analysis. First, detailed images were obtained of the shear layer with the laser sheet parallel to the freestream flow (side views). Second, global views of the entire wake at a given axial location were obtained with the laser sheet parallel to the base surface (cross-sectional end views). The sizes and locations of the images are listed in Tables 1 and 2 and are shown schematically in Fig. 3. As Table 1 shows, the shear layer is moderately to highly compressible for all positions imaged; see the listed values for the convective Mach number, M_c.

At each imaging position, 600–1200 images were obtained. For the initial image processing, saturated pixels due to large ethanol particles were removed, and the effects of the uneven intensity profile of the laser sheet were corrected. Images with large numbers of excessively bright or dark pixels were rejected, as these images usually contained nonuniform seeding intensity. The effects of nonuniform seeding are usually obvious in the free stream; thus, images with unusual intensity profiles in the free stream are rejected. These criteria successfully removed most images with nonuniform seeding. After processing, 500–700 images remained for further analysis.

The analyses of the side-view and end-view images differ slightly. The first analysis of the side-view images is for the shear layer thickness and the variability in its position, also known as flapping. For each image, the columns are averaged together to create a mean intensity profile across the shear layer. The shear layer position is defined as the point whose intensity is 20% of the difference between the brightest and darkest rows, matching the definition of Bourdon and Dutton [2]. The thickness is defined as the distance between the points whose intensities are 90% and 10% of the difference between the brightest and darkest rows in the intensity profile. Figure 4 depicts this process.

Table 2 End-view imaging parameters

Distance from separation x/R	Image size mm
0.3	$91.3\times73.7\pm1.0$
0.6	87.4×68.3
0.9	82.3×69.6
1.2	76.8×64.0
1.6	70.6×60.0
2.0	70.6×60.0

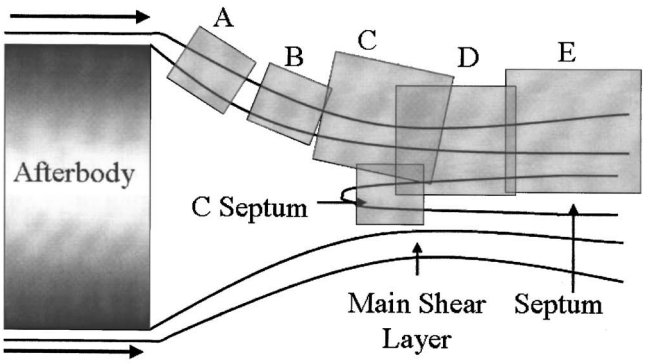

(*a*) Lateral Plane

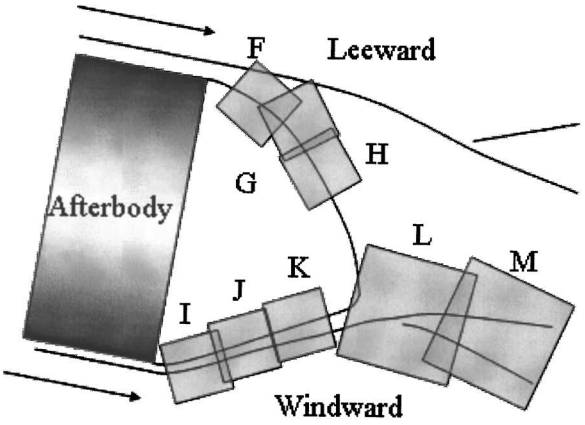

(*b*) Symmetry Plane

Fig. 3 Schematic of side-view imaging locations

The second analysis is for the interface convolution. Interface convolution analysis measures the tortuousness of the shear layer interface between the free-stream and recirculation fluid. A more tortuous interface presents more surface area across which entrainment and mixing can occur. Thus, interface convolution can be used to gauge the potential for mixing in the shear layer. Given the high Reynolds number of this flow, fully resolving all of the scales of motion in the shear layer would be very difficult, if not impossible. Thus, this analysis focuses on the tortuousness of the largest scales of motion, which are important to the initial entrainment of fluid into the shear layer. Since all scales of motion are not resolved, these data are only semi-quantitative, though they are still useful in deciphering the physical processes in this wake.

The interface convolution is quantified by the shape factor value. To find the shape factor, the image is thresholded at a particular intensity. Tests on the base flow images have shown that changing the threshold value between 10% and 20% of the free-stream intensity changes the shape factor values by less than 10%; thus, the value used for the threshold is not critical. In this study, the threshold was set at 20% of the average free-stream intensity to match the interface intensity used for the flapping analysis. The shape factor is defined as the ratio of the length of the interface between the bright and dark pixels to the minimum possible length [2,12], which for side-view images is simply the width of the frame.

For each thresholded image, isolated pixels are filtered out if fewer than 5 pixels in a 5×5 pixel neighborhood match the pixel's character (bright or dark). Random noise is the most likely cause of a pixel having a significantly different intensity than neighboring pixels; such pixels are removed to avoid unduly influencing the results. To calculate the interface length, the method

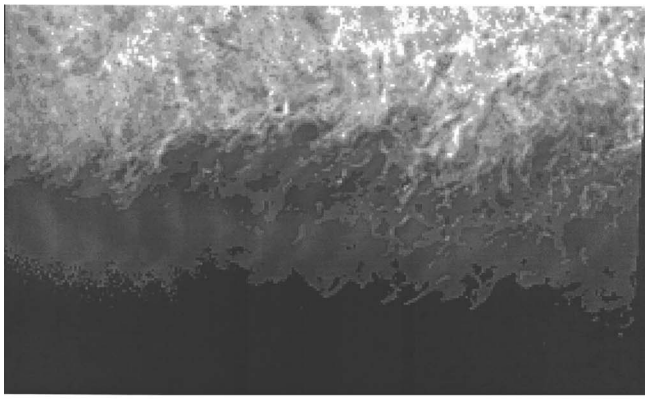

(*a*)

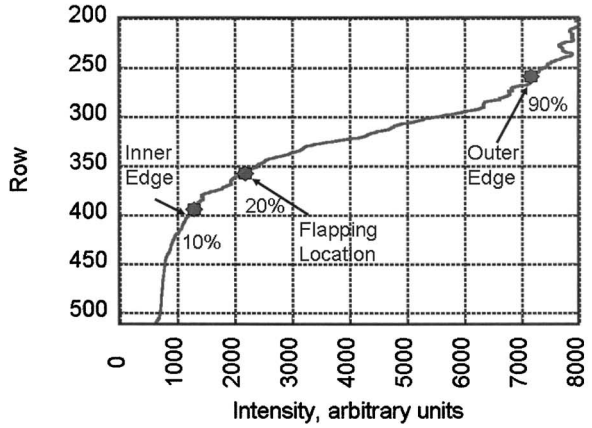

(*b*)

Fig. 4 Flapping processing example: (*a*) processed image; (*b*) average intensity profile, with shear layer inner and outer edges, as well as position for flapping calculations

described by Russ and Russ [21] and used by Sreenivasan and Meneveau [7] is applied. The process is depicted in Fig. 5. In this method, the shortest distance from each pixel in the image to the interface is calculated. One then counts the number of pixels within a certain distance of the interface; this creates a band around the interface. The area of this band is divided by the width of the band to yield the length of the interface.

This is a flexible and robust method of finding the interface length without the need for external filtering. One parameter that must be calibrated is the width of the band drawn around the interface between the bright and dark pixels. Several test cases were run with interfaces of polynomial curves and sinusoidal curves of varying amplitude and wavelength. The test results show that a band width of 8 pixels (4 pixels on each side of the interface) gives the most consistent and accurate results. Thus, for all of the data presented here, the band around the interface includes all pixels within four pixels of the actual interface.

The details of the convolution calculations are critical to obtaining reliable data. The results will be affected by such variables as speckle noise, laser sheet thickness, and filtering of the images. The authors have taken pains to reduce these effects. For example, the sheet thickness is consistent for all of the images, isolated bright or dark pixels (caused largely by speckle noise) are removed, and no outside filtering process is used. Nevertheless, the shape factor values obtained by this analysis should be treated as approximate values only.

Another topic of interest is the transverse extent over which the shear layer tortuousness occurs. If the tortuousness is due to very large structures, the interface should range over a wide transverse

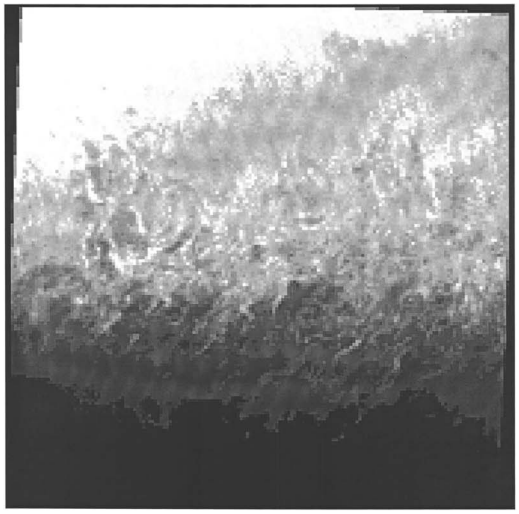

(*a*)

(*b*)

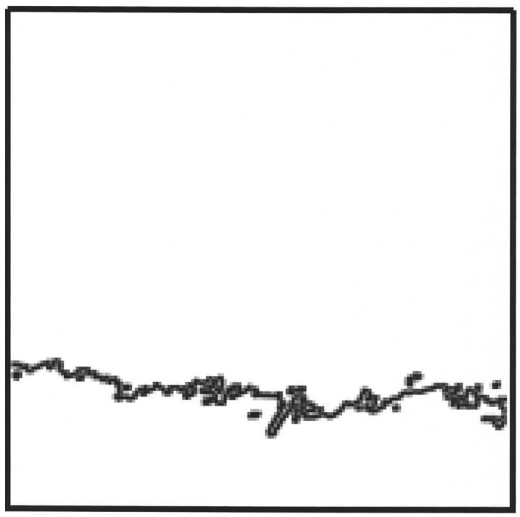

(*c*)

Fig. 5 Convolution processing example, lateral plane, position A; (*a*) processed image; (*b*) threshold image; (*c*) image showing all pixels within 4 pixels of the interface

extent on average. On the other hand, if the large-scale structures are not important, the shear layer interface will be relatively flat. To measure this behavior, an intermittency factor is used. This factor defines the fraction of realizations in which bright, supersonic fluid is found at a given transverse location. To calculate the intermittency, a simple count of the number of bright pixels in each row of the thresholded images is performed. This analysis is performed on one ensemble from the windward shear layer, one from the lateral plane, and one from the leeward part of the shear layer, to show the different behavior of the shear layer in these three areas.

For global end-view images, the flapping analysis is based on the variability in the size and position of the recirculating fluid region. In this procedure, the image is thresholded at 20% of the free-stream intensity. The number of dark pixels in the wake core is counted and the centroid of the dark region is calculated.

Convolution analysis is performed on the global end-view images in the same manner as for the side-view images. The only change is in the definition of the minimum possible interface length. As the dark fluid does not extend to the boundary of the image frame, the ideal length is now defined as the circumference of a circle with the same area that the dark fluid encompasses for each image. It should be noted that the end-view images cover a much larger region of the flow than the side-view images. Due to the lower spatial resolution, the convolution values for these images cannot be compared directly with the more detailed side-view images, though the qualitative trends should be consistent.

3 Results and Analysis

3.1 Side-View Shear Layer Flapping and Thickness Analysis. Figure 6 shows example side-view images from position B (in the developing lateral-plane shear layer) and position D (at apparent reattachment). Numerous large-scale structures can be noted in both sets of images. In most of the image ensembles, variations in the instantaneous shear layer position can be noted, but they do not appear to be large compared to the shear layer thickness.

The results of the flapping analysis confirm these observations. Plots of the trends in shear layer flapping and thickness are given in Fig. 7. As shown in Fig. 7(*a*), for all planes, the flapping (standard deviation of the shear layer position) normalized by the local shear layer thickness increases as the shear layer develops. The maximum value, however, is only 31% of the shear layer thickness. The windward plane has a higher level of flapping than the lateral plane, which in turn has much higher flapping than the leeward plane. This trend matches the structure size trends seen previously [5] that large-scale structures are very active in the windward part of the shear layer, less so in the lateral plane, and largely absent in the leeward part of the shear layer. It is logical that these flapping trends may be related to the activity of the large-scale structures in the shear layer, since the presence of a particularly large structure distorts the shear layer interface and may displace the interface from its average position. Histograms of the instantaneous shear layer position are roughly Gaussian for the main lateral shear layer. They are more distorted in the symmetry plane and septum shear layers, but no clear trends are evident.

Trends in thickness normalized by the base radius [Fig. 7(*b*)] show that the shear layer is thinner in the windward plane than in the lateral plane near separation. This is logical, since the boundary layer is thinner at separation in the windward plane than in the lateral plane [14]. The windward part of the shear layer grows more quickly, however, becoming thicker than the lateral plane shear layer near reattachment (rear stagnation point). These data match the general trends seen in the LDV velocity data for this wake [15]. Since the large-scale structures in the windward part of the shear layer have previously been shown to be more active than in the lateral plane [5], it seems consistent that the windward part of the shear layer would have a higher growth rate.

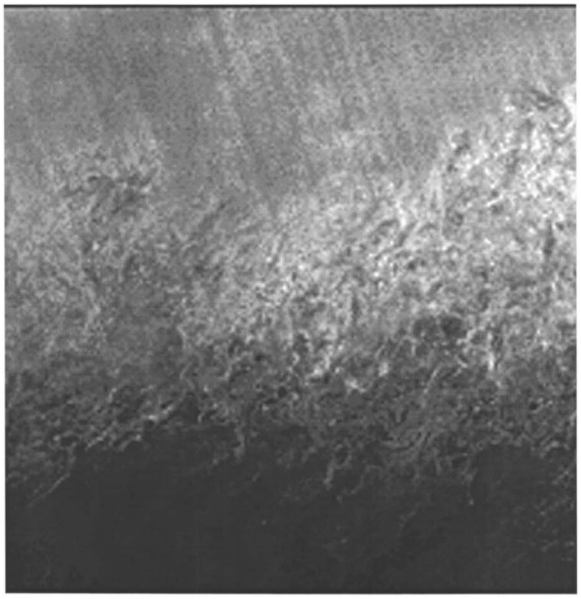

(*a*) Position B

(*b*) Position D

Fig. 6 Example side-view Mie scattering images

The leeward part of the shear layer near the base is quite thick but grows more slowly than the windward part of the shear layer, based on the limited number of available data points. The initial thickness of the shear layer seems much larger than the amount of fluid present in the leeward part of the afterbody boundary layer [14]. In addition, it is peculiar that the leeward shear layer can grow significantly, as it eventually does, since little large-scale structure activity is evident in the leeward shear layer [5]. As previous analysis has shown, however, the dynamics of the leeward part of the shear layer are most likely dominated by the influx of flow from out of the symmetry plane, explaining both the large initial thickness of the leeward shear layer and its ability to grow [5].

The lateral plane main shear layer also grows quite markedly during recompression, perhaps due to the adverse pressure gradient in this region. The thickness then falls rather dramatically

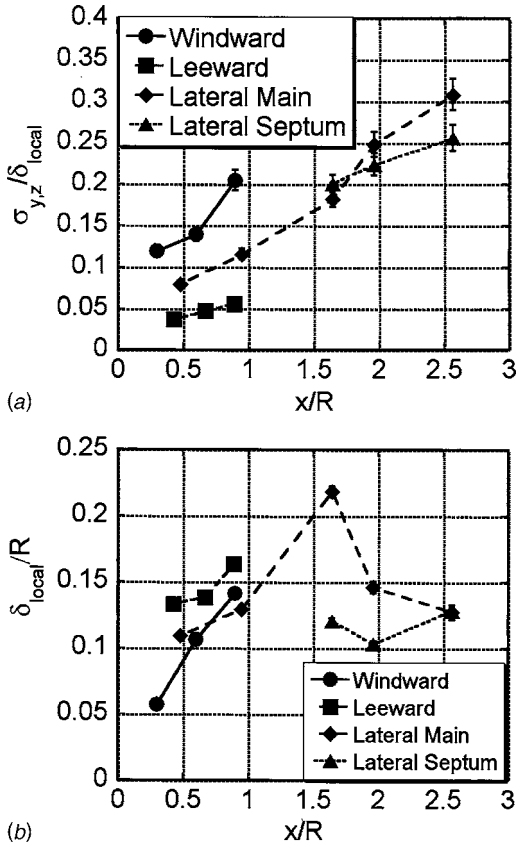

Fig. 7 Trends in side-view image shear layer flapping and thickness. (*a*) Standard deviation in the shear layer position (flapping), normalized by local shear layer thickness; (*b*) average shear layer thickness normalized by base radius

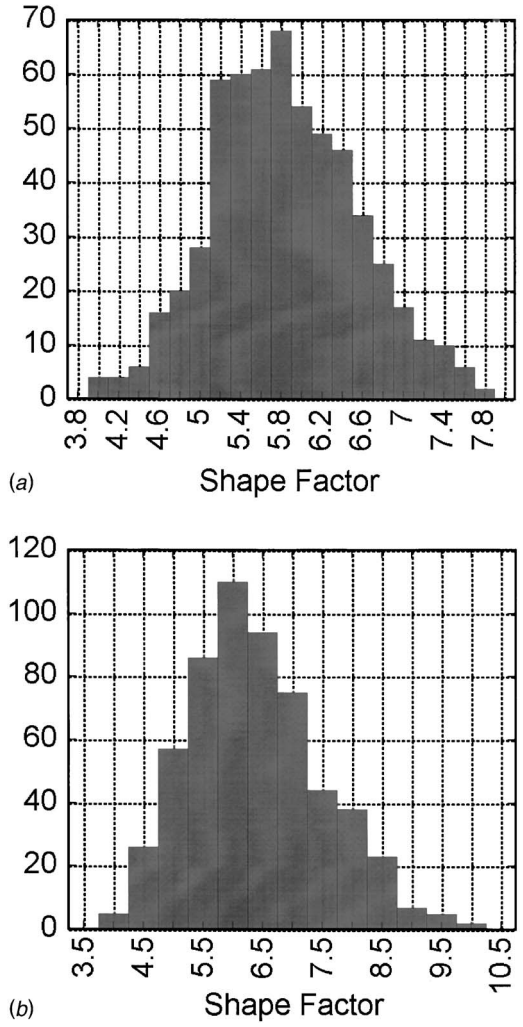

Fig. 8 Example side-view image shape factor histograms: (*a*) leeward, position G; (*b*) windward, position J

during and after reattachment. These trends are far different than those for the axisymmetric base flow of Bourdon and Dutton [2], which show a monotonic increase in the shear layer thickness throughout its development. The presence of the septum, however, limits the extent of the low-speed side of the shear layer in the current flow, while no such restriction is present in the axisymmetric base flow.

At positions C and D (see Fig. 3) the septum shear layer thickness is significantly less than for the main lateral shear layer. The septum shear layer also becomes thinner when the main shear layer converges onto the septum shear layer (apparent reattachment), perhaps due to added confinement. The thickness increases from positions D to E, however, closely matching the thickness of the main shear layer at position E.

For the lateral plane before recompression and the entire leeward plane, histograms of the individual thickness realizations (not shown) are roughly Gaussian. For the windward plane, the septum shear layer, and the lateral plane shear layer during and after recompression, the results are skewed toward deviations with larger thickness values. The reasons for this behavior remain unclear.

3.2 Side-View Interface Convolution Analysis. Some example histograms for the interface convolution in the symmetry plane are shown in Fig. 8. The interface convolution histograms for all parts of the wake are generally shaped like skewed Gaussian distributions, with the distributions skewed toward high values of the shape factor. The distributions for the windward side of the shear layer are more skewed at all positions than those for the leeward side. A possible explanation for this behavior is that occasionally a particularly large structure will be present in an image, causing a higher than average shape factor. Since the structures are larger and more active in the windward shear layer than in the leeward, particularly severely skewed distributions in the windward part of the wake would be consistent with this hypothesized mechanism [5].

A plot of the trends in the mean shape factor is shown in Fig. 9(*a*). This plot includes the values for the windward, lateral, leeward, and septum areas of the shear layer, as well as calculations for positions A–D of the axisymmetric base flow of Bourdon and Dutton [2] using the methods outlined in this paper. The interface convolution is much lower in the axisymmetric base flow than for the current three-dimensional flow. This is reasonable. The base pressure for the current three-dimensional wake is much lower than for the axisymmetric afterbody flow, indicating more vigorous entrainment of fluid out of the recirculation region for the current wake. Lower shape factor values for axisymmetric base flow are consistent with less entrainment of recirculation region fluid into the shear layer compared to the angle-of-attack wake.

For all planes, the shape factor is relatively low near separation than farther downstream indicating a low potential for entrainment and mixing near the base. This is likely due to the small size of the turbulent structures at this location. The shape factor for the windward side is much higher than for the lateral or leeward sides of the shear layer immediately after separation. The high initial shape factor value for the windward shear layer is reasonable, since a higher degree of shear is seen in the windward boundary layer compared to the lateral boundary layer [14], and one would

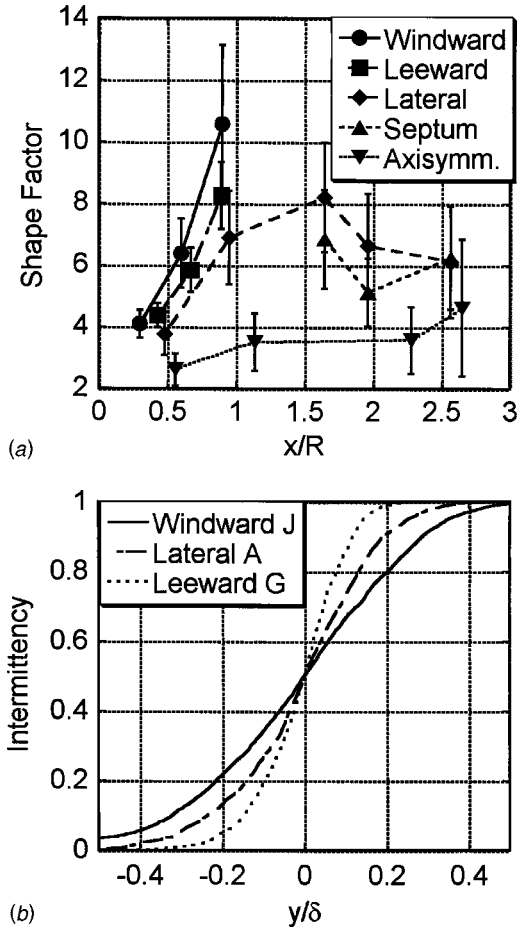

Fig. 9 (*a*) **Trends in the average shape factor for the symmetry plane, lateral plane, and axisymmetric base flow. Uncertainty bars show one standard deviation on either side of the mean.** (*b*) **Intermittency in the occurrence of supersonic fluid, as a function of transverse position for the developing shear layer.**

expect a more highly sheared flow to have a more tortuous interface. The shape factor values for the windward part of the shear layer grow much more quickly as the shear layer develops than in the lateral plane. This is logical, given the larger structures and faster structure growth in this plane [5]. The shape factor for the main lateral plane shear layer peaks at recompression and then falls as the wake develops. This indicates that the recompression process makes the large-scale structures more tortuous, which matches the appearance of the images at recompression.

The leeward plane, however, also shows greater interface convolution than the lateral plane. This is quite surprising, since large-scale structures, which should be a primary cause of high shape factor values, are not very dominant in the leeward plane. There are two potential explanations. First, numerous smaller-scale structures could create a significantly tortuous interface for the leeward shear layer, especially at low scattered intensity values, for which the structures are not as obvious by visual inspection. Second, the intensity gradient across the shear layer is much lower for the leeward part of the shear layer than for the windward or lateral parts. When coupled with speckle noise and a strict thresholding criterion, this will cause a large number of isolated bright or dark pixels in the thresholded image, which will deform the nominally straight interface and artificially inflate the shape factor value. The authors deem this second explanation the most likely, as it better matches the appearance of the example images.

These observations are supported further by the intermittency data, shown in Fig. 9(*b*). One can see that when normalized by the shear layer thickness, the windward shear layer shows the broadest intermittency plot, the lateral plane less so, and the leeward the most narrow. It is logical that the windward part of the shear layer has the broadest intermittency plot, as the large-scale structures are the largest relative to the shear layer thickness in the windward part of the shear layer [5]. It is also logical that the windward part of the shear layer would have the greatest shape factor, since there is a larger volume across which the shear layer interface can be located. The narrow intermittency plot for the leeward part of the shear layer again indicates that large-scale motions in this part of the shear layer are not important. The shear layer interface has only a small region in which it can move. Thus, it seems counterintuitive that the leeward shear layer could achieve the high shape factor values shown in Fig. 9. Again, the authors believe that these large values are an artifact caused by the unusual intensity distribution across the leeward shear layer.

The septum shear layer shape factor is generally lower than for the main shear layer, but converges to the same value at position E. The relatively high shape factor values for the septum shear layer suggest that it has significant potential for mixing and may actively entrain fluid from the recirculation region in a fashion similar to that for the main shear layer. The presence of the septum also greatly increases the surface area of the shear layer available to entrain recirculation fluid, acting to counteract the reduction in shear layer area due to the short reattachment length in the current flow compared to that for axisymmetric base flow.

This added septum area, in addition to the generally high shape factors compared to axisymmetric flow, suggests a much higher degree of turbulent mixing in the shear layer of this three-dimensional wake than in the corresponding axisymmetric wake. This turbulent mixing will cause added entrainment of recirculation region fluid into the shear layer, resulting in added removal of fluid from the recirculation region. This would explain the low base pressure for this three-dimensional case compared to that for the corresponding axisymmetric base flow [16].

3.3 End-View Wake Core Flapping and Pulsation. The region of dark, low-speed fluid in the global end-view images is subject to unsteadiness in both its size and position. This is demonstrated by the example global end-view images shown in Fig. 10. Statistics quantifying the mean values and fluctuations (standard deviation) of the wake core area are shown in Fig. 11. The wake core area normalized by the base area [Fig. 11(*a*)] decreases swiftly from separation through reattachment and trailing wake development due to the convergence of the shear layer. The standard deviation of the wake core area [Fig. 11(*b*)], which measures instantaneous area variations, monotonically increases when normalized by the average wake core area at that location. The trends show that unsteadiness in the wake core area ranges from insignificant near separation to a sizable fraction ($>25\%$) of the wake core area in the trailing wake. Given the growth of the large-scale structures as the wake develops, it is not surprising that the wake core area fluctuations become more significant as a fraction of the total wake core area downstream, due to the intermittent passage of large-scale structures. These trends largely match those seen in axisymmetric base flow, which has a similar monotonic increase in area pulsation when normalized by the local wake core area [2].

In an absolute sense (i.e., when normalized by the base area), the area pulsation increases before reattachment and decreases after reattachment. The decrease in absolute area fluctuations after reattachment is due to the sharp decrease in the average wake core area after reattachment. The agreement between these data and the data for axisymmetric flow when normalized by the base area is not as good as the agreement when the data are normalized by the local wake core area [2]. This is logical, given the grossly different structure of these two wakes.

Unsteadiness in the wake core position is also significant. Figure 12(*a*) shows a typical distribution of the wake core centroid locations across an ensemble, in this case for $x/R=1.6$. The distributions tend to be largely symmetrical about the mean centroid

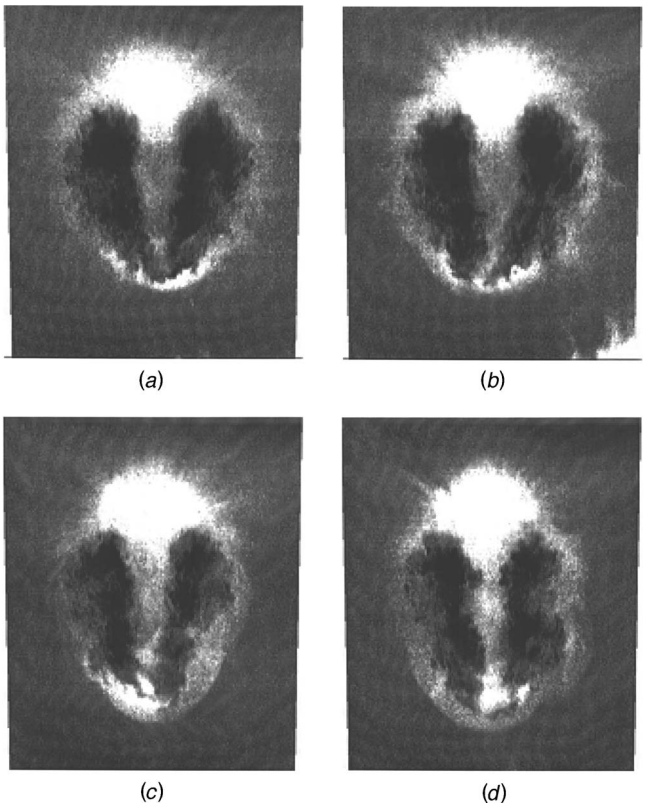

Fig. 10 Example end-view images, showing the unsteadiness of the wake core area (*a*), (*b*) $x/R=1.6$; (*c*), (*d*) $x/R=2.0$

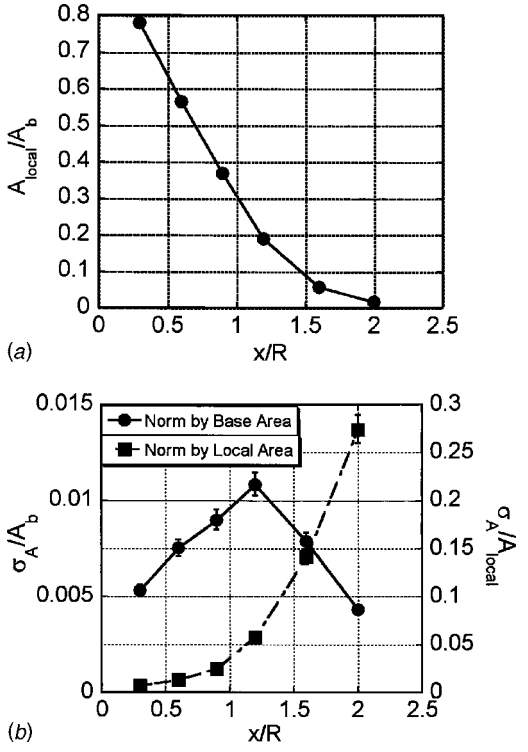

Fig. 11 Trends in global end-view wake core area: (*a*) average wake core area, normalized by base area; (*b*) wake core area standard deviation normalized by base area and local wake core area

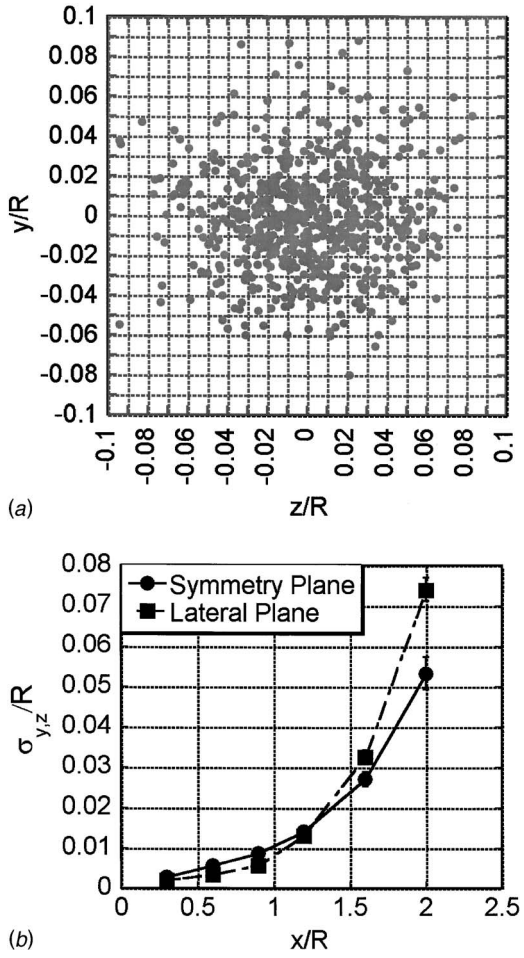

Fig. 12 Centroid displacement plots: (*a*) distribution of wake core centroid positions for global end view, $x/R=1.6$; (*b*) standard deviation of the wake core centroid displacement from the mean position in the lateral and symmetry planes for the global end views

position. Figure 12(*b*) shows the overall trends in the flapping of the wake core centroid in both the symmetry plane and lateral plane directions, shown as the standard deviation of the wake core centroid position normalized by the base radius. The overall trend is for the flapping to increase in both the symmetry plane and the lateral plane directions with downstream distance. This may again be due to the action of large-scale structures. For example, compare the two images for $x/R=2.0$ in Fig. 10. The presence of the large-scale structure at the bottom right of the wake in the second image will tend to displace the centroid of the wake core fluid toward the right. The extent of wake core flapping is very similar to the extent of side-view shear layer flapping, indicating that a significant fraction of the side-view flapping is a more global displacement of the wake, rather than a local displacement of the shear layer.

It is interesting to note that the wake core flapping is higher in the symmetry plane than in the lateral plane before reattachment, as the septum is forming, but is more significant in the lateral plane than in the symmetry plane after reattachment. Since the septum breaks the axisymmetry of the wake core as the flow nears reattachment, variations in the distance the septum has penetrated the wake core would be expected to yield large variations of the centroid position before reattachment, which naturally would occur mainly in the symmetry plane. After reattachment, the septum may act to stabilize fluctuations in the symmetry plane.

3.4 End-View Interface Convolution Analysis. Example

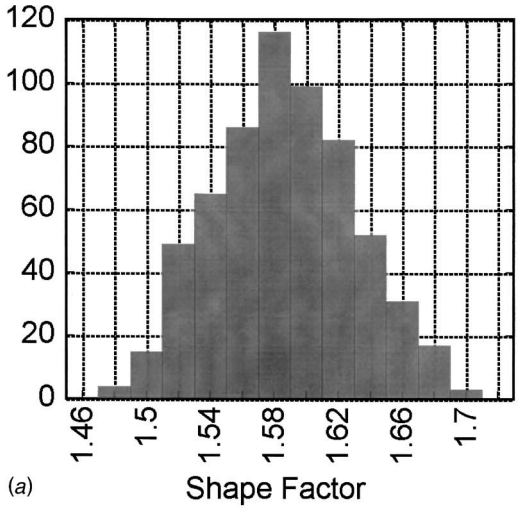

(*a*)

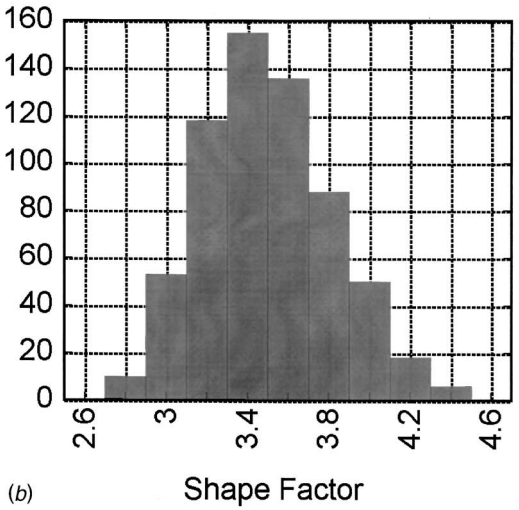

(*b*)

Fig. 13 Example end-view shape factor histograms: (*a*) $x/R=0.6$; (*b*) $x/R=1.2$

histograms of the shape factor values for the end-view images are shown in Fig. 13. Most of the histograms are reasonably symmetrical and Gaussian, like is shown in Fig. 13(*a*) for $x/R=0.6$. Near reattachment, for $x/R=0.9$ and $x/R=1.2$, the distributions are more positively skewed, like is shown in Fig. 13(*b*) for $x/R=1.2$. The distributions also quickly become much broader as the flow develops.

The trend in the end-view shape factor is shown in Fig. 14. The shape factor is relatively small near separation. This is because the shear layer is much thinner, and the large-scale structures much smaller, near separation, leading to a naturally lower shape factor. As the flow develops, the shape factor quickly rises for two reasons. First, the shear layer and the attendant large-scale structures grow. Second, the formation of the septum adds a great deal of extra interface area to the wake, further increasing the shape factor. The shape factor peaks near $x/R=1.6$, and then declines in the trailing wake. The overall trend is fairly similar to that seen in the side-view images, which also showed a peak shape factor near $x/R=1.65$.

One can also note the behavior of the variability in this data. The uncertainty bars in Fig. 14 show one standard deviation on either side of the mean. The standard deviation is very small near separation, since the large-scale structures are still quite small. As the structures grow, the fluctuations in the shape factor become much larger, during and after mean reattachment at $x/R=1.2$.

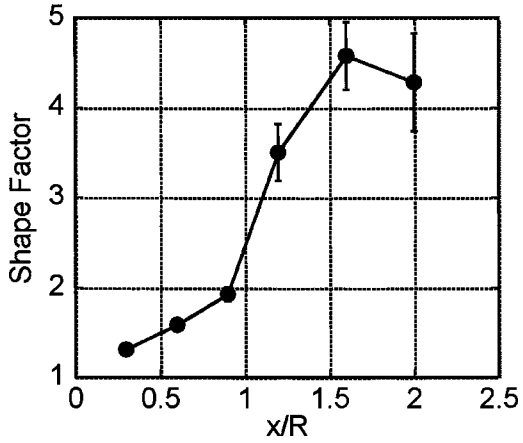

Fig. 14 End-view shape factor trends. Uncertainty bars denote one standard deviation on either side of the measured mean value.

4 Discussion

There is a close correspondence between the trends in the side-view and end-view images. Both the side-view and end-view images show similar values for the flapping of the shear layer and wake core centroid, and both sets of images show a monotonic increase in the flapping as the wake develops. Both side- and end-view images show an increase in convolution up to $x/R=1.6$, with slight declines thereafter. This seems to indicate that the dynamics of the shear layer are similar between side- and end-images. Previous studies have shown that the large-scale structures in planar shear layers become more three-dimensional as the shear layer compressibility increases. Since the shear layer in the current study is highly compressible, it seems reasonable that the structures would be highly three-dimensional.

The present data also agree with previous structure topology data for this wake [5]. For example, the windward plane contains the structures with the largest growth rate before reattachment. The flapping results also complement the time-averaged LDV velocity results in this wake [15]. The amount of side-view shear layer flapping is quite small (at most 31% of the shear layer thickness). Thus, the LDV velocity profile of the shear layer is not subject to significant smearing from flapping of the shear layer and should give an accurate measure of the average behavior of the shear layer.

It is also interesting to compare the turbulence statistics from the LDV velocity data [15] to the interface convolution results. In areas of high shape factor, we expect intense turbulent mixing, which should be reflected in high values of turbulent kinetic energy. In the angle-of-attack wake, this trend seems to hold. For example, the turbulent kinetic energy grows steadily in the windward shear layer from separation to reattachment, and is much larger in the windward part of the shear layer than the lateral part. The same trends are seen in the shape factor data. The lateral plane shape factor is maximum at lateral plane reattachment ($x/R=1.6$) and declines thereafter; the turbulent kinetic energy behaves in the same manner. Finally, near lateral plane reattachment, the main shear layer has much higher values of turbulent kinetic energy than the septum shear layer, but the values of turbulent kinetic energy tend to converge as the flow develops. The same trends are reflected in the interface convolution data. This correspondence is not perfect; the turbulent kinetic energy and shape factor trends do not agree as well for the axisymmetric wake, for example. Nevertheless, the relationship between turbulent kinetic energy and shape factor seems logical, matches much of the data for the angle-of-attack wake, and allows us to connect the LDV velocity data to the appearance of the shear layer in flow visualizations of this wake.

These data provide further evidence of the importance of the septum in the dynamics of the angle-of-attack wake. Combined with previous data on the behavior of the large-scale structures in the shear layers of this wake [5], the current data show that the septum shear layer behaves in much the same manner as the main shear layer. It has similar amounts of flapping and interface convolution, and the large-scale structures behave in much the same manner as those in the main shear layer. It therefore seems fairly certain that the septum shear layer entrains fluid from the recirculation region in much the same manner as the main shear layer. The addition of the septum to the nominally round wake adds a great deal of surface area across which entrainment can take place. Combined with the higher interface convolution in this wake compared to the corresponding axisymmetric wake, this helps to explain the sharp reduction in base pressure seen when a cylinder is tilted from zero degrees angle-of-attack to 10° [13,16].

5 Conclusions

Extensive flow visualization of a blunt-base cylinder at 10° angle-of-attack has been performed using planar Mie scattering imaging. Shear layer flapping increases monotonically as the shear layer develops for all parts of the wake. The greatest flapping was found in the windward part of the shear layer before reattachment. The side-view shape factor is greatest near recompression and reattachment for all planes, with the greatest convolution in the symmetry plane. The significant levels of interface convolution for the septum shear layer indicate that it has the potential to actively entrain recirculation fluid, which along with the generally high shape factor values for the current flow may help to explain the low base pressure in this three-dimensional flow compared to that for axisymmetric base flow. The recirculation region fluid is unsteady in both its extent and its position in end-view images. The area pulsation tends to peak around reattachment, while the flapping of the wake core increases monotonically as the flow develops. End-view interface convolution peaks at $x/R=1.6$, the same location as the peak for the side-view images.

Acknowledgment

This work was supported by the U.S. Army Research Office, Grant No. DAAD19-01-1-0367, with Dr. Thomas Doligalski as technical monitor.

Nomenclature

A_{local} = instantaneous area of the wake core
A_b = the area of the base surface
R = base radius
x = coordinate parallel to the afterbody axis
y = coordinate in the symmetry-plane direction
z = coordinate in the lateral-plane direction
δ = local shear layer thickness, as determined by flow visualizations
σ = standard deviation

References

[1] Bourdon, C. J., and Dutton, J. C., 1999, "Planar Visualizations of Large-Scale Turbulent Structures in Axisymmetric Supersonic Separated Flows," Phys. Fluids, **11**, pp. 201–213.
[2] Bourdon, C. J., and Dutton, J. C., 2000, "Shear Layer Flapping and Interface Convolution in a Separated Supersonic Flow," AIAA J., **38**, pp. 1907–1915.
[3] Smith, K. M., and Dutton, J. C., 1996, "Investigation of Large-Scale Structures in Supersonic Planar Base Flows," AIAA J., **34**, pp. 1146–1152.
[4] Scarano, F., and van Oudheusden, B., 2003, "Planar Velocity Measurements of a Two-Dimensional Compressible Wake," Exp. Fluids, **34**, pp. 430–441.
[5] Kastengren, A. L., and Dutton, J. C., 2003, "Wake Topology in a Three-Dimensional Supersonic Base Flow," AIAA J., **43**, pp. 1053–1063.
[6] Ponton, M., and Seiner, J., 1995, "Acoustic Study of B Helical Mode for Choked Axisymmetric Nozzle," AIAA J., **33**, pp. 413–420.
[7] Sreenivasan, K., and Meneveau, C., 1986, "The Fractal Facets of Turbulence," J. Fluid Mech., **173**, pp. 357–386.
[8] Lane-Serff, G., 1993, "Investigation of the Fractal Structure of Jets and Plumes," J. Fluid Mech., **249**, pp. 521–534.
[9] Catrakis, H., and Dimotakis, P., 1996, "Mixing in Turbulent Jets: Scalar Measures and Isosurface Geometry," J. Fluid Mech., **317**, pp. 369–406.
[10] Villermaux, E., and Innocenti, C., 1999, "On the Geometry of Turbulent Mixing," J. Fluid Mech., **393**, pp. 123–147.
[11] Davis, M., and Li, H., 1996, "Evaluation of Fractal Dimension for Mixing and Combustion by the Schlieren Method," Exp. Fluids, **21**, pp. 248–258.
[12] Glawe, D., Samimy, M., Nejad, A., and Chen, T., 1995, "Effects of Nozzle Geometry on Parallel Injection From the Base of an Extended Strut into a Supersonic Flow," 33rd Aerospace Sciences Meeting and Exhibit, AIAA Paper 95-0522.
[13] Boswell, B., and Dutton, J., 2001, "Flow Visualizations and Measurements of a Three-Dimensional Supersonic Separated Flow," AIAA J., **39**, pp. 113–121.
[14] Boswell, B., and Dutton, J., 2002, "Velocity Measurements in a Pressure-Driven Three-Dimensional Compressible Turbulent Boundary Layer," AIAA J., **40**, pp. 1300–1310.
[15] Boswell, B., and Dutton, J., 2003, "Velocity Measurements in a Three-Dimensional Compressible Base Flow," AIAA J., **41**, pp. 785–794.
[16] Herrin, J., and Dutton, J., 1994, "Supersonic Base Flow Experiments in the Near Wake of a Cylindrical Afterbody," AIAA J., **32**, pp. 77–83.
[17] Dayman, B., 1963, "Support Interference Effects on the Supersonic Wake," AIAA J., **1**, pp. 1921–1923.
[18] Clemens, N. T., and Mungal, M. G., 1991, "A Planar Mie Scattering Technique for Visualizing Supersonic Mixing Flows," Exp. Fluids, **11**, pp. 175–185.
[19] Samimy, M., and Lele, S., 1991, "Motion of Particles With Inertia in a Compressible Free Shear Layer," Phys. Fluids A, **3**, pp. 1915–1923.
[20] Wegener, P., Clumpner, J., and Wu, B., 1972, "Homogeneous Nucleation and Growth of Ethanol Droplets in Supersonic Flow," Phys. Fluids, **15**, pp. 1869–1876.
[21] Russ, J., and Russ, J., 1989, "Uses of the Euclidean Distance Map for the Measurement of Features in Images," J. Comput.-Assist. Microsc., **1**, pp. 343–375.

High-Speed Observation of a Cavitating Jet in Air

Hitoshi Soyama
Professor
ASME Member, Member #:2045284
e-mail: soyama@mm.mech.tohoku.ac.jp
Department of Mechanical Engineering, Tohoku University, 6-6-01 Aoba, Aramaki, Aoba-ku, Sendai 980-8579, Japan
Phone: +81-22-217-6891
Fax: +81-22-217-3758

The use of cavitation impact is a practical method for improving the fatigue strength of metals in the same way as shot peening. In the case of peening using cavitation impact, cavitation is produced by a high-speed submerged water jet with cavitation, i.e., a cavitating jet. A cavitating jet in air was successfully generated by injecting a high-speed water jet into a low-speed water jet injected into air using a concentric nozzle. In order to investigate the various appearances of cavitating jets in air, an observation was carried out using high-speed photography and high-speed video recording. In this study, periodical shading of the cavitation cloud was observed and the frequency of the shading was found to be a function of the injection pressure of the low-speed water jet. Unsteadiness of the low-speed water jet, which is related to the periodical shading of the cloud, was also observed. [DOI: 10.1115/1.2060737]

Introduction

Cavitation impact normally causes severe damage in hydraulic machinery. However, this can be utilized for modifying the surface so as to improve the fatigue strength of metallic materials [1–6] and introduce residual stress into the surface of metallic materials [7–11] in the same way as shot peening. The cavitating jet can also improve the corrosion resistance of carbon steel [12], and it can be used as a gettering technique to keep the surfaces of silicon wafers clean [13,14]. In the case of peening using cavitation, a shot is not required. Thus, peening by a cavitation impact is called "cavitation shotless peening." [3–6,10,11]. The improvement of fatigue strength by cavitation shotless peening is better than that obtained using shot peening [4,5]. Normally, the cavitation bubbles in cavitation shotless peening are generated by injecting a high-speed water jet into a water-filled chamber, and this is known as a cavitating jet. In this paper, we call this a cavitating jet in water. From the point of view of the practical use of cavitation shotless peening, the application area for a cavitating jet without a water-filled chamber is wider than the submerged situation. Several researchers had tried to produce an artificially submerged jet in air by injecting a high-speed water jet into a concentric low-speed water jet for cutting rocks or cleaning [15–17]. However, the aspect of the cavitating jet in air was not clear.

Soyama successfully generated suitable cavitating jet in air for cavitation shotless peening by injecting a high-speed water jet into a concentric low-speed water jet, which is injected directly into air without a water-filled chamber [18]. According to an erosion test on a pure aluminum specimen, the performance of the cavitating jet in air depended on the injection pressure of the low-speed water jet, and the cavitating jet in air at the optimum injection pressure had a higher impact compared with both a cavitating jet in water and a normal water jet in air [18]. The cavitating jet in air introduced more compressive residual stress into the surface of tool alloy steel [18], and improved the fatigue strength of metallic materials [19,20]. A cavitating jet in air has also been tested for peen forming to produce a curved duralumin plate for the main wing of an airplane [21].

In order to optimize the cavitating jet in air, its appearance was observed using high-speed photography with a xenon flash lamp and a high-speed video camera. As the performance of the cavitating jet in air is closely related to the injection pressure of the low-speed water jet [18], an erosion test was conducted to determine the optimum injection pressure, where the erosion rate was a maximum. The appearance of the jet was observed at various injection pressures of the low-speed water jet. It is noted that this is the first paper to report observations of a cavitating jet in air.

Experimental Facilities and Procedures

Figure 1 illustrates a schematic diagram of the apparatus used to generate the cavitating jet in air. The test nozzle consists of a nozzle for the high-speed water jet and a nozzle for the low-speed water jet, as shown in Fig. 2. The nozzles were set in a concentric configuration. The starting point of cavitation might be at the upstream corner of the nozzle throat of a high-speed water jet. The diameter of the nozzle for the high and low-speed water jets, d_H and d_L, were 1 and 20 mm, respectively. The injection pressure of the high-speed water jet p_H and low-speed water jet p_L were controlled by opening bypass valves. The injection pressures, p_H and p_L, of the nozzles were measured by pressure transducers. In the present paper, the pressure is considered to be the absolute pressure. The standoff distance s_H is defined as the distance from the upstream corner of the nozzle throat of the high-speed water jet to the surface of the test specimen. The standoff distance s_L is defined as the distance from the outlet of the nozzle of the low-speed water jet to the surface of the test specimen. In the present experiment, the distance $s_H - s_L$ was fixed at 7.5 mm. Tap water was used in the cavitating jet loop for both high-speed and low-speed water jets. The air content ratio α/α_s of test water in the tank B was measured by a dissolved oxygen meter. Here α_s is saturated air content of water. During the test, the air content ratio α/α_s and the water temperature were from 1.03 to 1.05 and from 293 K to 303 K, respectively.

The key parameter for a cavitating jet in air is the cavitation number σ. The cavitation number is defined by the injection pressure of both the high-speed water jet p_H and the low-speed water jet p_L, and the saturated vapor pressure of the test water p_v as follows:

$$\sigma = \frac{p_L - p_v}{p_H - p_L} \cong \frac{p_L}{p_H}. \tag{1}$$

In the case of a cavitating jet in air, the cavitation number can be simplified as in Eq. (1) because $p_H \gg p_L \gg p_v$.

In order to observe the appearance of cavitating jets in air, high-speed photographs were taken using a xenon flash lamp with an exposure time of 1.1 μs. To observe the unsteadiness of the cavitating jet in air, a high-speed video camera with a maximum frame speed of 100 000 frames per second was used.

Contributed by the Fluids Engineering Division for publication in the JOURNAL OF FLUIDS ENGINEERING. Manuscript received by the Fluids Engineering Division September 27, 2004; final manuscript received July 14, 2005. Associate Editor: Yoshinobu Tsujimoto.

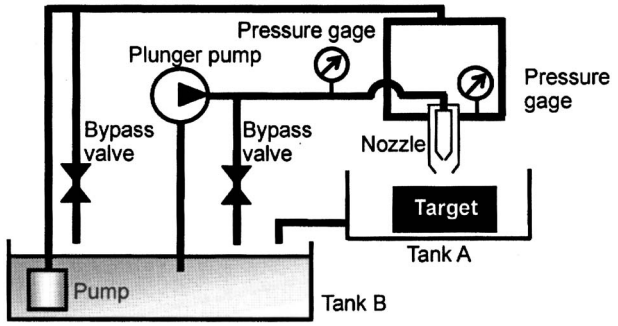

Fig. 1 Test apparatus for the cavitating jet in air

The jet's capability was investigated by measuring the mass loss induced by erosion. This assumes that the greater the mass loss, the greater the jet's capability. Specimens for the erosion test were made of pure aluminum (Japanese Industrial Standard JIS A1050). The exposure time of specimens to the jet was kept constant at 3 min. The mass loss Δm was measured at a constant injection pressure p_H=20 MPa. To optimize the cavitating jet in air, the mass loss Δm was measured as the standoff distance s_H and the injection pressure of the low-speed water jet p_L were varied. In order to measure the jet capability in the erosion test, both the aluminum specimen and the nozzle were fixed.

Results

Capability of a Cavitating Jet in Air. In order to investigate the performance of the cavitating jet in air, the mass loss Δm was plotted as a function of standoff distance s_H at various injection pressure p_L, as shown in Fig. 3. The injection pressure p_H was 20 MPa. The mass loss Δm peaks at a certain standoff distance, i.e., the optimum standoff distance, which varies with p_L. At p_L =0.14, 0.15, and 0.16 MPa, the optimum standoff distance is 30 mm. At p_L=0.17 and 0.18 MPa, this increases to 35 mm, and at p_L=0.20 MPa it is 40 mm. Thus, the optimum standoff distance

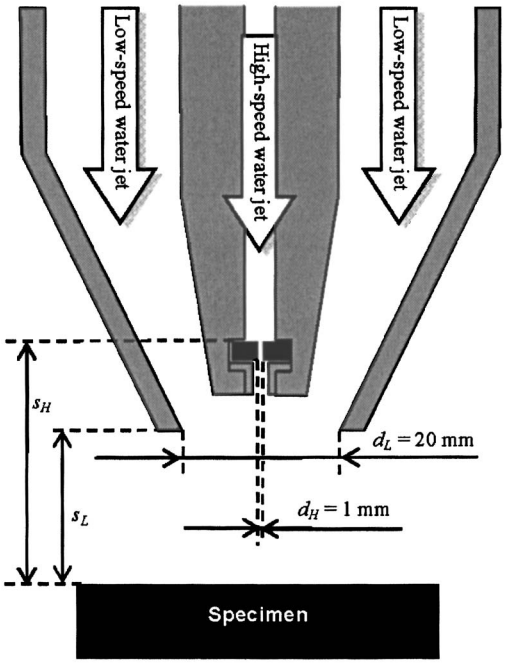

Fig. 2 Nozzle geometry

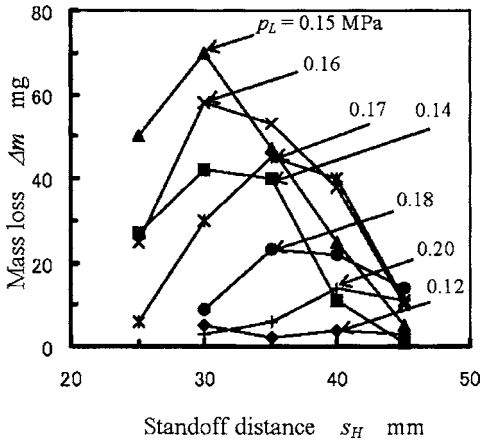

Fig. 3 Jet performance as a function of standoff distance s_H(p_H=20 MPa)

increases slightly with injection pressure p_L.

Figure 4 shows the erosion pattern at p_H=20 MPa, p_L =0.15 MPa, and s_H=30 mm, where the mass loss was a maximum. Although the center has been eroded by impinging droplets of the high-speed water jet, the main erosion region is a ring shape. The outer and inner diameters of the ring are about 20 and 10 mm, respectively. This ring erosion is typical of a cavitating jet in water [18]. The cavitation cloud impinged the surface, spread out, and then collapsed, producing impacts. This is the reason why the main erosion is formed in the shape of a ring. Thus, the ring pattern is proof of the functioning of the cavitating jet in air.

Figure 5 illustrates the mass loss Δm at the optimum standoff distance as a function of the injection pressure p_L. The data of Fig. 5 were taken from those of Fig. 4 at the optimum standoff distance. Obviously, the mass loss reaches a peak at p_L=0.15 MPa. At p_H=20 MPa and p_L=0.15 MPa, the cavitation number was 0.0075. In the case of a cavitating jet in water, the mass loss was a maximum at σ=0.01 or 0.014 [22,23]. Thus, the optimum cavitation number of the cavitating jet in air is smaller than that of a cavitating jet in water.

Appearance of a Cavitating Jet in Air. Figure 6 shows the appearance of a cavitating jet in air at p_H=20 MPa and p_L

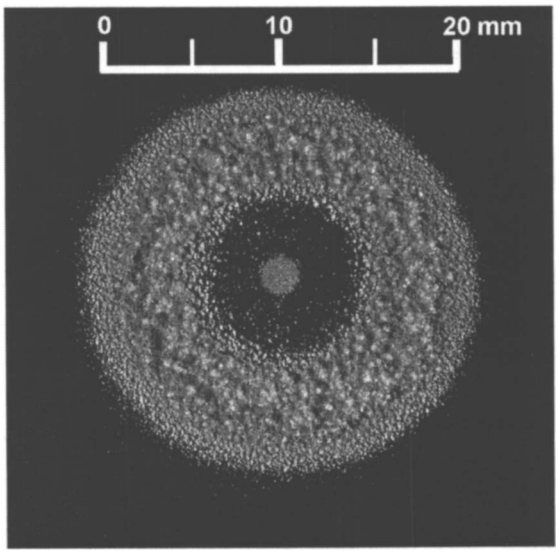

Fig. 4 Erosion pattern induced by a cavitating jet in air (p_H =20 MPa, p_L=0.15 MPa, s_H=30 mm)

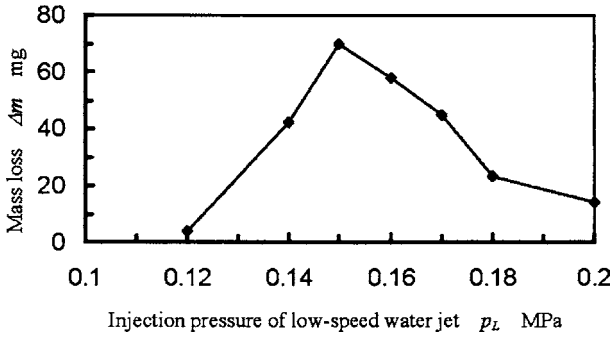

Fig. 5 Jet performance as a function of the injection pressure of the low-speed water jet p_L(p_H=20 MPa)

=0.15 MPa obtained using a xenon flash lamp. The highest impact was obtained under these conditions in the present experiment. A part of the nozzle is shown in the upper side in Fig. 6, the jet being injected downward. The surface of the low-speed water jet reveals a wavy pattern with a wavelength of about 4.6 mm. Although the wavy pattern was observed near the nozzle, the surface was continuous. As the distance from the nozzle increases, the surface is broken up and droplets are shown spilling out from the surface of the low-speed water jet. The white region seen in the center of the low-speed water jet starts from the outlet of the nozzle of low-speed water jet, and its length is about 15 mm. This white region is the cavitation cloud, which develops around the high-speed water jet. Although the cavitation cloud disappears farther downstream, another cavitation cloud can be observed, starting at a distance of 20 mm from the nozzle. This kind of breakdown of the cavitation cloud has also been observed for a cavitating jet in water [24–26]. The cavitation cloud shedding and the breakdown of the cloud of the cavitating jet in water took place periodically with a frequency in the range of 0.5 to 2 kHz [24]. This frequency depends on the injection pressure of the cavitating jet and/or the cavitation number.

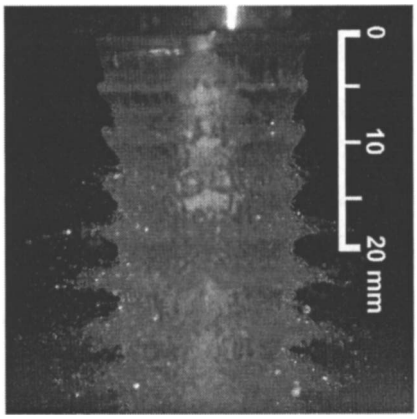

Fig. 6 Appearance of a cavitating jet in air (p_H=20 MPa, p_L =0.15 MPa)

In order to investigate the cavitation cloud shedding, a cavitating jet in air at p_H=20 MPa and p_L=0.15 MPa was observed using a high-speed video camera, as shown in Fig. 7. The frame speed was 30 000 frames per second. At t=0 ms, the wavy pattern of the low-speed water jet was observed near the nozzle. Shedding of the wave occurred downstream and the next wave appeared at the 16th frame followed by a 2nd new wave at the 31st frame. That is, the wavy pattern of the low-speed water jet appeared at each 15th frame, corresponding to a 0.5 ms time interval. When the high-speed water jet was observed, the cavitation cloud developed from t=0 to 0.3 ms and then broke up at 0.3 ms. The next cavitation cloud developed from 0.3 to 0.8 ms. At about t=0.8 ms, the cavitation cloud broke up for the second time. Thus, the breakup of the cavitation cloud occurred every 0.5 ms. The period of the breakup of the cavitation cloud was the same as that of the wavy pattern of the low-speed water jet. That is, the wavy pattern was synchronized to the periodic shedding and breakup of the cavitation cloud. The breakup or collapse of the cavitation cloud produced a pressure wave, which in turn produced the wavy pattern observed in the low-speed water jet.

In order to measure the flow velocity of the high- and low-speed water jets, the appearance in Figs. 6 and 7 was investigated. The average wavelength of the three wavy patterns near the nozzle of the low-speed water jet is about 4.6 mm in Fig. 6. The time interval of the shedding of the wavy pattern in Fig. 7 is

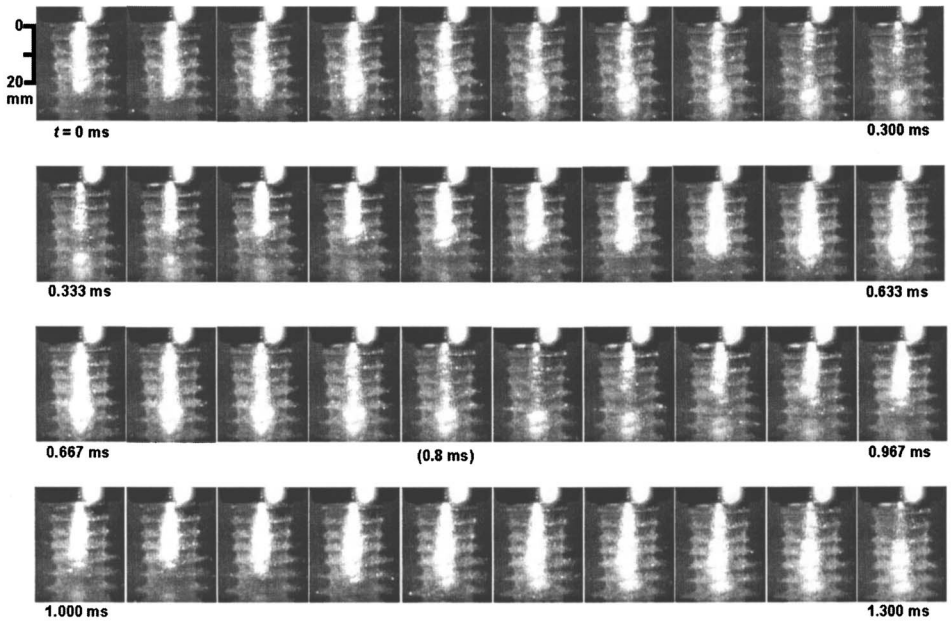

Fig. 7 Changing appearance of a cavitating jet in air with time (p_H=20 MPa, p_L=0.15 MPa)

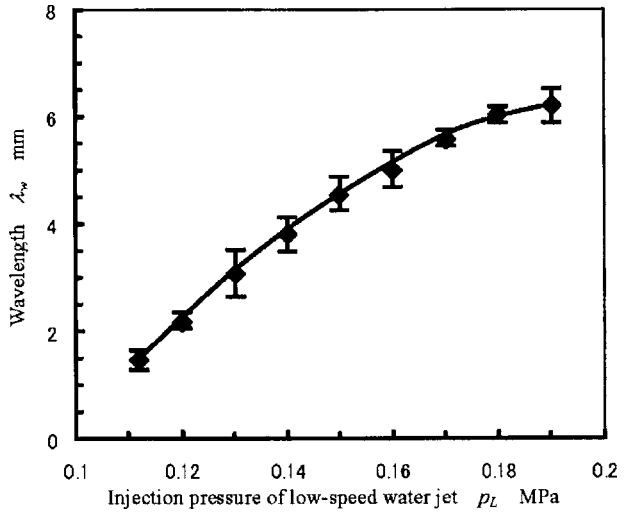

Fig. 8 Wavelength λ_w of the wavy pattern of the low-speed water jet (p_H=20 MPa)

0.5 ms, as mentioned above. The average speed of shedding of the wavy pattern is 9.2 m/s. As the injection pressure of the low-speed water jet was, in absolute pressure, 0.15 MPa, the calculated flow speed was 10 m/s, given that the relative injection pressure was 0.05 MPa. Thus, the shedding speed of the wavy pattern is about 92% of the flow velocity. Regarding the observations made using high-speed photography and the high-speed video camera under the conditions of p_H=20 MPa and p_L =0.11 MPa, the shedding speed of the wavy pattern was 4.5 m/s, calculated from the 1.5 mm wavelength and the 0.33 ms time interval of shedding. This was also 92% of the calculated velocity at the injection pressure. Thus, the time interval can be calculated from the wavelength of the wavy pattern and the flow speed near the nozzle by considering the injection pressure and the factor of 92%.

Shedding Frequency of Wavy Pattern. Figure 8 illustrates how the wavelength of the wavy pattern λ_w of a low-speed water jet varies with the injection pressure p_L. The frequency can be obtained from the wavelength, the injection pressure, and the factor of 92% mentioned above. In Fig. 8, the symbol shows the average of three measurements of the wavelength taken near to the nozzle from each of five pictures, i.e., 15 measurements in total. The bar shows the standard deviation for the 15 measurements. The wavelength increases as the injection pressure p_L increases and the rate of increase decreases as p_L increases.

Figure 9 shows the appearance of the cavitating jet in air, changing as the injection pressure p_L is changed. In all cases, the cavitation cloud can be observed at the center of the jet. As mentioned above, the wavelength λ_w increases with injection pressure p_L. At low injection pressures such as p_L=0.11 or 0.12 MPa, the low-speed water jet near the nozzle is pulled into the center by the high-speed water jet. The wavy pattern is at its most significant at around p_L=0.15 MPa. At this pressure, water is seen spilling out from the surface of the low-speed water jet. At higher injection pressure such as p_L=0.18 and 0.19 MPa, the surface of the low-speed water jet gets smoother. This means that the wavy pattern was most clearly seen when the highest impact conditions were used.

Figure 10 illustrates the variation of the shedding frequency of the wavy pattern f_w with injection pressure p_L. Data from Fig. 9 were used to obtain the data for Fig. 10. The frequency f_w was calculated from the wavelength λ_w and the flow velocity of the wavy pattern ν_w. The flow velocity ν_w is 92% of the flow velocity of the low-speed water jet, and it was obtained from the injection pressure p_L using the Bernoulli equation. The frequency f_w, calculated from the wavelength λ_w and the injection pressure p_L, is expressed in Eq. (2). Here, ρ is the density of water.

$$f_w = \frac{1}{\frac{\lambda_w}{\nu_w}} = \frac{1}{\frac{\lambda_w}{0.92\sqrt{2p_L/\rho}}}. \tag{2}$$

The frequency f_w decreases with injection pressure p_L and saturates at about p_L=0.15 MPa, as shown in Fig. 10. The frequency of the wavy pattern is nearly the same as the shedding frequency, since the breakup of the cavitation cloud is related to the wavy pattern of the low-speed water jet, as mentioned above. Thus, the decrease of f_w means that the interval of breakup increases and the cavitation cloud develops as the injection pressure p_L is increased.

Figure 11 illustrates how the shedding interval of the wavy pattern τ_w varies with the flow velocity of the low-speed water jet ν_L calculated from the injection pressure p_L using the Bernoulli equation. The shedding interval τ_w is the inverse of the frequency f_w of Fig. 10. The shedding interval τ_w increases with the flow velocity ν_L until ν_L=10 m/s, i.e., p_L=0.15 MPa and at ν_L $>$10 m/s it saturates. The increase of the shedding interval τ_w means that cavitation is developing. When cavitation develops and collapses, the cavitation impact increases normally. As the interval increases with the flow velocity until ν_L=10 m/s, the cavitation impact might also have been increasing. Since the shedding interval saturates at $\nu_L$$>$10 m/s, the cavitation cloud might break the low-speed water jet before bubble collapse, perhaps resulting in weak cavitation impact.

The cavitation length L_{cav} was decreased with the increase of the cavitation number σ at cavitating jet without an associated low-speed water jet, and it was described by following equation [27].

$$L_{cav} = c_1\sigma^{-n} \tag{3}$$

where c_1 and n are constants that depend on the shape of nozzle. c_1 and n are 2.02 and 0.78, respectively, [27]. In case of a cavitating jet, the cavitating length refers to the moving distance of cavitation cloud from the initiation point of cavitation, i.e., the upstream corner of the nozzle, to the collapsing point of cavitation. If it is assumed that the lifetime of the cavitation cloud is constant at constant p_H, the moving distance of the cavitation cloud, i.e., the cavitating length L_{cav} is proportional to the shedding speed of the cloud. Since the cavitation cloud was carried by the low-speed water jet in the case of a cavitating jet in air, the cavitating length L_{cav} was proportional to the shedding speed of the cloud, i.e., the velocity of the low-speed water jet ν_L. Thus, the cavitating length can be revealed by following equation at constant p_H.

$$L_{cav} = c_2\sigma^{-n} \times \nu_L \tag{4}$$

Here, c_2 is constant, considering c_1 and the proportional coefficient of ν_L. The decrease of L_{cav} affected by increase of ν_L was already considered in $L_{cav} \propto \sigma^{-n}$. As p_L is in absolute pressure, p_L (MPa) is described by ν_L (m/s) as follows when ρ =1000 (kg/m^3);

$$p_L = \frac{\nu_L^2}{2000} + 0.1 \tag{5}$$

At constant p_H, $\sigma \propto p_L$, then

$$L_{cav} \propto p_L^{-n} \times \nu_L \approx \frac{\nu_L}{\left(\frac{\nu_L^2}{2000} + 0.1\right)^n} \tag{6}$$

Regarding Ref. [23], which surveyed results of researchers, n is from 0.5 to 1. L_{cav} tends to a minimum at n=1, varying with ν_L. Consider L_{cav} as a function of ν_L.

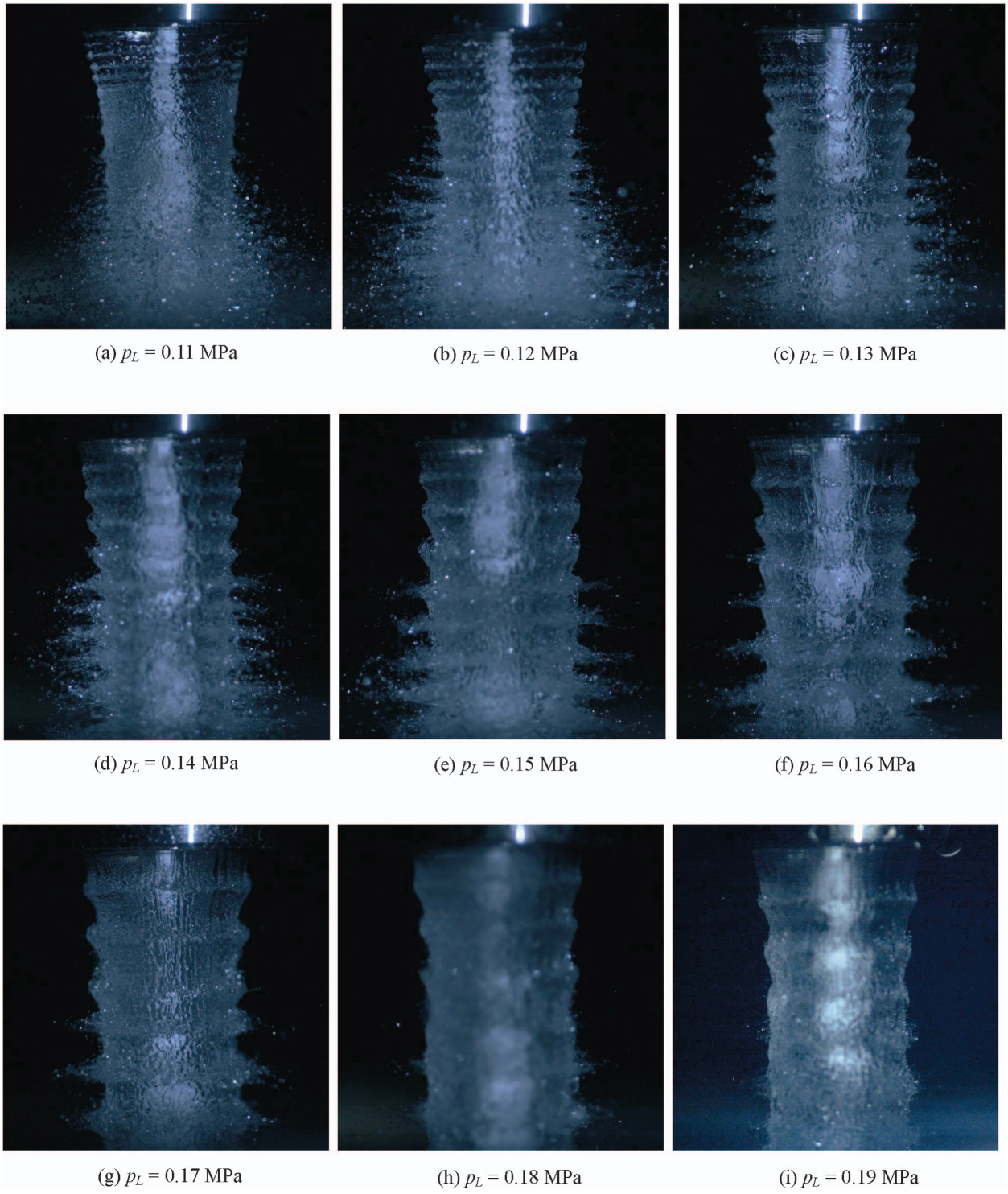

Fig. 9 Variation in the appearance of a cavitating jet in air with the injection pressure of the low-speed water jet p_L(p_H =20 MPa)

$$f(\nu_L) = \frac{\nu_L}{\frac{\nu_L^2}{2000} + 0.1} = 2000\frac{\nu_L}{\nu_L^2 + 200} \tag{7}$$

Differentiating Eq. (7),

$$f'(\nu_L) = 2000\frac{(\sqrt{200})^2 - \nu_L^2}{\nu_L^2 + (\sqrt{200})^2} \tag{8}$$

Since $\sqrt{200} \approx 14.1$, $f'(\nu_L) > 0$ at $\nu_L < 14.1$. This means that the cavitating length increased with ν_L when $\nu_L < 14.1$ m/s. This is the reason why the cavitation developed with an increase of the

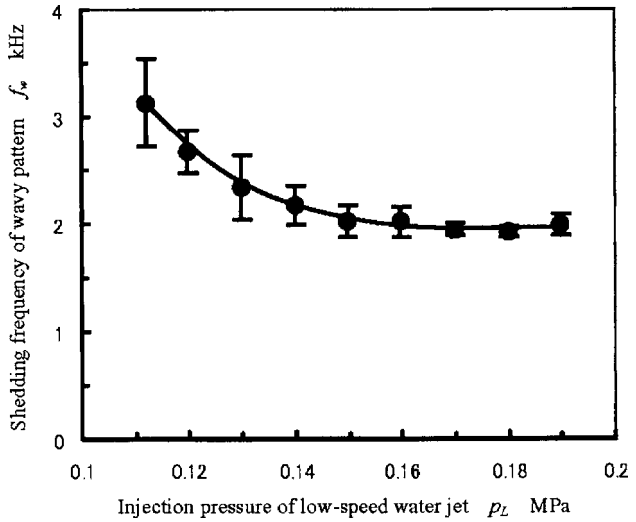

Fig. 10 Variation of the shedding frequency of the wavy pattern f_w with the injection pressure of the low-speed water jet p_L(p_H=20 MPa)

pressure of the low-speed water jet and then the cavitating length was saturated.

Conclusions

In order to investigate a cavitating jet in air, observations were made using a high-speed video camera and high-speed photography. Cavitating jets in air were successfully realized by injecting a high-speed water jet into a low-speed water jet using a concentric nozzle. In the experiment, the pressure of the high-speed water jet was kept constant at 20 MPa and the pressure of the low-speed water jet was varied from 0.11 to 0.19 MPa.

(1) The cavitating jet in air under high impact conditions shows a periodic phenomena. The cavitation cloud in a low-speed water jet shaded periodically. The low-speed water jet had a wavy surface with a frequency related to that of the cloud shedding.

(2) The frequency of the wavy pattern of low-speed water jet decreased with increasing injection pressure of the low-speed water jet.

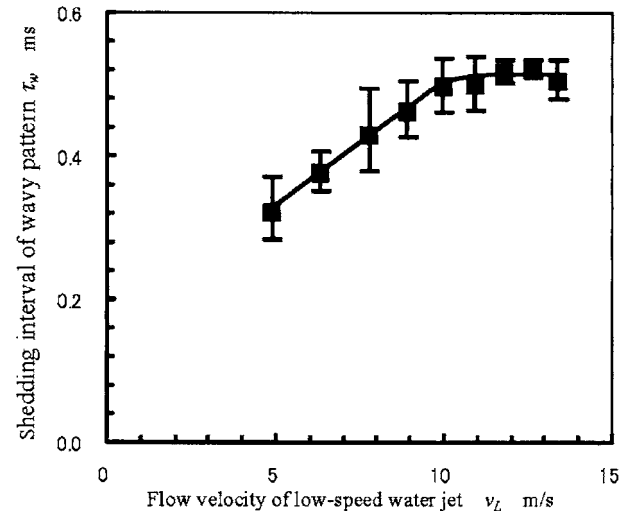

Fig. 11 Variation of the shedding interval of the wavy pattern τ_w with the flow velocity of the low-speed water jet v_L(p_H =20 MPa)

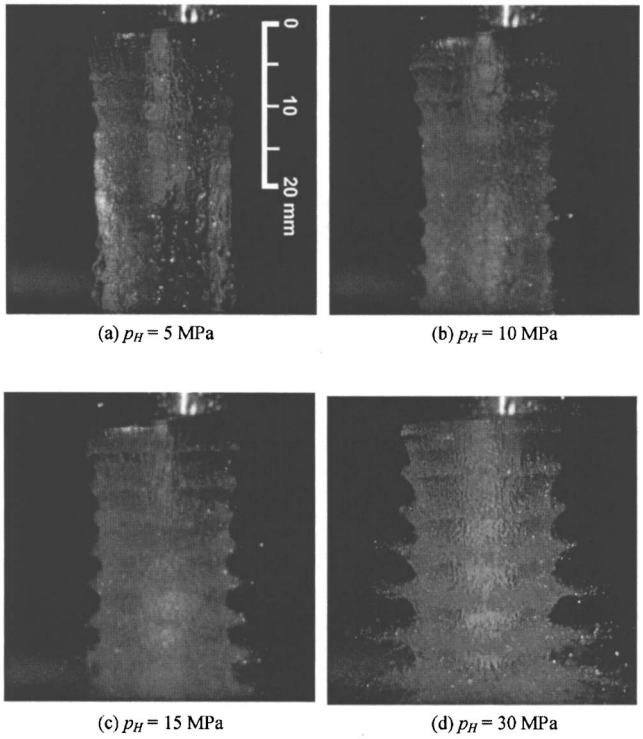

Fig. 12 Aspects of a cavitating jet in air with the injection pressure of the high-speed water jet p_L(p_L=0.15 MPa)

(3) The cavitating jet in air had a maximum capability at certain injection pressures of the low-speed water jet.

(4) The wavy pattern of the low-speed water jet was most significant under high impact conditions.

Acknowledgment

This work was partly supported by the Japan Society for the Promotion of Science under a Grant-in-Aid for Scientific Research (B)(2) 14350049 and the Ministry of Economy, Trade, and Industry under Project No. 13HC2016. The author is also grateful to Mr. Akihiro Yamaguchi, Nippon Roper Co. Ltd., for providing a high-speed video camera.

Nomenclature

d = nozzle diameter
f_w = shading frequency of wavy pattern
p = injection pressure of water jet
s = standoff distance from nozzle to impinged surface
t = time
v_L = flow velocity of low-speed water jet
v_w = flow velocity of wavy pattern
α/α_s = air content ratio of test water
α_s = saturated air content of water
Δm = mass loss
σ = cavitation number
λ_w = wavelength of wavy pattern
τ_w = shading interval of wavy pattern
H = parameter of high-speed water jet
L = parameter of low-speed water jet

Appendix: Effect of Injection Pressure of High-Speed Water Jet

Figure 12 shows the aspects of the cavitating jet in air changing with the pressure of the high-speed water jet p_H from 5 to 30 MPa

at constant p_L=0.15 MPa. For all cases, the cavitation cloud was observed in the low-speed water jet center. The cavitating length increased with p_H as same as the cavitating jet in water at constant p_L. The wavy patterns were also observed. The averaged wavelength was about 3.3 mm at p_H=5 MPa, 4.1 mm at p_H=10 MPa, 4.3 mm at p_H=15 MPa, and 5.0 mm at p_H=5 MPa, respectively. These results show that the wavelength slightly increases with p_H at constant p_L. There are two possible reasons. One of them is related to the cavitating length. In the case of a cavitating jet in water, when the cavitating length was increased, the shedding frequency of the cavitation cloud was decreased. As mentioned in the present paper, the frequency of the wavy pattern was related to the cloud shedding. Thus, the wavelength increases with p_H, as the cavitation is developed. Another reason is that the flow velocity of the low-speed water jet v_L will be increased with p_H and an increase of v_L causes a longer wavelength, as the low-speed water jet carries the wavy pattern.

References

[1] Soyama, H., 2000, "Improvement in Fatigue Strength of Silicon Manganese Steel SUP7 by Using a Cavitating Jet," JSME Int. J., Ser. A, **43**, pp. 173–178.

[2] Soyama, H., Kusaka, T., and Saka, M., 2001, "Peening by the Use of Cavitation Impacts for the Improvement of Fatigue Strength," J. Mater. Sci. Lett., **20**, pp. 1263–1265.

[3] Soyama, H., Saito, K., and Saka, M., 2002, "Improvement of Fatigue Strength of Aluminum Alloy by Cavitation Shotless Peening," J. Eng. Mater. Technol., **124**, pp. 135–139.

[4] Odhiambo, D., and Soyama, H., 2003, "Cavitation Shotless Peening for Improvement of Fatigue Strength of Carbonaized Steel," Int. J. Fatigue, **25**, pp. 1217–1222.

[5] Soyama, H., Odhiambo, D., and Saito, K., 2003, "Cavitation Shotless Peening for Improvement of Fatigue Strength," *Proceedings of the 8th International Conference on Shot Peening*, edited by L. Wagner, Wiley-VCH, Weinheim, Germany, pp. 435–440.

[6] Macodiyo, D. O., Soyama, H., and Saka, M., 2004, "Effect of Cavitation Number on the Improvement of Fatigue Strength of Carburized Steel Using Cavitation Shotless Peening," Key Eng. Mater., **261–263**, pp. 1245–1250.

[7] Soyama, H., Yamauchi, Y., Ikohagi, T., Oba, R., Sato, K., Shindo, T., and Oshima, R., 1996, "Marked Peening Effects by Highspeed Submerged-Water-Jets—Residual Stress Change on SUS304—," Journal of Jet Flow Engineering, **13**, pp. 25–32 (in Japanese).

[8] Hirano, K., Enomoto, K., Hayashi, E., and Kurosawa, K., 1996, "Effects of Water Jet Peening on Corrosion Resistance and Fatigue Strength of Type 304 Stainless Steel," J. Soc. Mater. Sci. Jpn., **45**, pp. 740–745 (in Japanese).

[9] Soyama, H., Park, J. D., and Saka, M., 2000, "Use of Cavitating Jet for Introducing Compressive Residual Stress," J. Manuf. Sci. Eng., **122**, pp. 83–89.

[10] Soyama, H., Sasaki, K., Odhiambo, D., and Saka, M., 2003, "Cavitation Shotless Peening for Surface Modification of Alloy Tool Steel," JSME Int. J., Ser. A, **46**, pp. 398–402.

[11] Soyama, H., Macodiyo, D. O., and Mall, S., 2004, "Compressive Residual Stress into Titanium Alloy Using Cavitation Shotless Peening Method," Tribol. Lett., **17**, pp. 501–504.

[12] Soyama, H., and Asahara, M., 1999, "Improvement of the Corrosion Resistance of a Carbon Steel Surface By a Cavitating Jet," J. Mater. Sci. Lett., **18**, pp. 1953–1955.

[13] Soyama, H., and Kumano, H., 2000, "Oxidation-Induced Stacking Faults Introduced by Using a Cavitating Jet for Gettering in Silicon," Electrochem. Solid-State Lett., **3**, pp. 93–94.

[14] Kumano, H., Sasaki, T., and Soyama, H., 2004, "Evaluation of the Effectiveness of Backside Damage Gettering in Silicon Introduced by a Cavitating Jet," Appl. Phys. Lett., **85**, pp. 3935–3937.

[15] Vijey, M. M., and Brierley, W. H., 1978, "Cutting Rocks and Other Materials by Cavitating and Non-Cavitating Jets," *Proceedings of the 4th International Symposium on Jet Cutting Technology*, Paper No. C5, pp. 51–66.

[16] Vickers, G. M., Harrison, P. W., and Houlston, R., 1980, "Extending the Range of Cavitating Cleaning Jets," *Proceedings of the 5th International Symposium on Jet Cutting Technology*, Paper No. J1, pp. 403–412.

[17] Vijey, M. M., Zou, C., Hu, S. G., Remisz, J., and Tavoularis, S., 1992, "A Study of the Practicality of Cavitating Water Jets," *Proceedings of 11th International Symposium on Jet Cutting Technology*, pp. 75–99.

[18] Soyama, H., 2004, "Introduction of Compressive Residual Stress Using a Cavitating Jet in Air," J. Eng. Mater. Technol., **126**, pp. 123–128.

[19] Macodiyo, D. O., Soyama, H., Saito, K., and Saka, M., 2003, "Improvement of Fatigue Strength on Duralumin by Cavitation Shotless Peening," International Conference on Advanced Technology in Experimental Mechanics, W0131 OS4, pp. 1–4.

[20] Soyama, H., and Macodiyo, D., 2004, "Improvement of Fatigue Strength by Using a Cavitating Jet in Air," *Proceedings of 2004 ASME/JSME Pressure Vessels and Piping Conference*, PVP-Vol. 472, pp. 165–169.

[21] Soyama, H., and Saito, K., 2003, "Peen Forming by Using a Cavitating Jet in Air," *Proceedings of the 7th Pacific Rim International Conference on Water Jetting Technology*, pp. 429–436.

[22] Shimizu, S., Tanioka, K., and Ikegami, N., 1997, "Erosion Induced by Ultra High Speed Cavitating Jet," *Proceedings of Spring Meeting of Hydraulics & Pneumatics*, pp. 5–8 (in Japanese).

[23] Soyama, H., 1998, "Material Testing and Surface Modification by Using Cavitating Jet," J. Soc. Mater. Sci. Jpn., **47**, pp. 381–387 (in Japanese).

[24] Soyama, H., Yamauchi, Y., Adachi, Y., Sato, K., Shindo, T., and Oba, R., 1995, "High-Speed Observations of the Cavitation Cloud around a High-Speed Submerged Water Jet," JSME Int. J., Ser. B, **38**, pp. 245–251.

[25] Soyama, H., Yamauchi, Y., Sato, K., Ikohagi, T., Oba, R., and Oshima, R., 1996, "High-Speed Observation of Ultrahigh-Speed Submerged Water Jets," Experimental Thermal and Fluid Science Exp. Therm. Fluid Sci., **12**, pp. 411–416.

[26] Soyama, H., Lichtarowicz, A., and Momma, T., 1996, "Vortex Cavitation in a Submerged Jet," *Proceedings of the 1996 ASME Fluids Engineering Division Summer Meeting*, FED-Vol. 236, pp. 415–422.

[27] ASTM G134-95, 1997, "Standard Test Method for Erosion of Solid Materials by a Cavitating Liquid Jet," Annual Book of ASTM Standards, Vol. 03.02, ASTM International, pp. 537–548.

Investigation of the Influence of Injection Rate Shaping on the Spray Characteristics in a Diesel Common Rail System Equipped with a Piston Amplifier

J. Benajes

R. Payri[1]
e-mail: rpayri@mot.upv.es
Phone: +34-963879658
Fax: +34-963877659

S. Molina

V. Soare

CMT-Motores Térmicos, Universidad Politécnica de Valencia, Valencia, Spain

The quality of the mixing process of fuel and air in a direct injection diesel engine relies heavily on the way the spray develops when injected into the combustion chamber. Among other factors, the spray development depends on the injection rate of the fuel delivered by the injector. The paper presents a study, at both a macroscopic and microscopic level, of a Diesel spray generated by a common-rail injection system featuring a piston pressure amplifier. By modifying the timing and the duration of the injector and amplifier piston actuation, it is possible to obtain high injection pressures up to 180 MPa*, and different shapes for the injection rate, which would not be achievable with a regular common rail injection system. The spray evolution produced by three different injection rate shapes (square, ramp, and boot) has been investigated in an injection test rig, by means of visualization and PDPA techniques, at different injection conditions. The main conclusions are the important effect on spray penetration of the initial injection rate evolution and the small influence of the maximum injection pressure attained at the end of the injection event. Smaller or even negligible effects have been found on the spray cone angle and on the droplet Sauter mean diameter.* [DOI: 10.1115/1.2062767]

1 Introduction

As it is well-known in the diesel engine community, the process of injecting fuel into the combustion chamber is responsible for the quality of the air/fuel mixture that is achieved [1–3]. The efficiency of combustion relies heavily on the quality of this mixture and greatly influences engine performance as well as pollutant emissions [4]. The ideal situation would be to ensure that all the injected fuel is in contact with the maximum amount of available oxygen, so that the burning of the hydrocarbons is as complete as possible, and that high local fuel concentrations were avoided, thus limiting the maximum temperatures that normally occur locally and which are well known for inducing the formation of nitrogen oxides [5].

It can consequently be stated that the main objective of injection is for the spray to come into contact with as much fresh air as possible. On the one hand, this means that through its own turbulence the spray should entrain as much air as possible and, on the other, that the droplets should be as small as possible in order to maximize the contact surface between fuel and air [6,7] and to promote evaporation. Throughout the open literature numerous studies can be found that have achieved to theoretically predict the main defining parameters of the spray: tip penetration, cone angle, and droplet size [8–10]. However, the results vary between different injection systems and conditions, and the conclusions that can be drawn are rather qualitative than quantitative, although it can be argued that the laws of penetration are quite well understood at present. It is generally acknowledged that the flow turbulence inside the orifice is one of the factors that encourage the spray to break up into droplets, as well as increasing the interaction between the spray and its ambient. The flow characteristics are influenced by the injection pressure, and consequently its variations during the injection process, as well as the injector geometry [2,8,10].

The aim of the present paper is to study experimentally the influence that the variations in fuel delivery throughout an injection cycle may have over the spray behavior [11]. Previous studies relevant to this area of research have investigated the influence of different injection strategies and injection rate shapes over engine performance and emissions [12,13]. In order to achieve different profiles for the rate shape at the beginning of injection, those studies employed different diameters for the discharge orifice in the injector's control volume.

In the present work this was achieved more flexibly with a system based on a common rail and a pressure piston amplifier. This system can deliver lower rail pressure or higher amplified pressure to the injector, and can change from one level to the other during injection. This allows for a very practical way of testing different rate shapes because no physical change to the injector is required, and could also be of interest in the engine as it would allow for very flexible injection strategies that vary with engine speed and load.

The spray is characterized by two macroscopic parameters, cone angle and tip penetration, obtained through a direct visualization method, and one microscopic parameter, the droplet size, measured with the phase Doppler particle analyzer (PDPA) technique.

2 Experimental Set-Up

2.1 Injection System. The concept of the injection system (whose sketch appears in Fig. 1) is based on the combination of a pressure amplifier piston and a regular common rail system. This system is able to supply two levels of pressure to the injector, one constant "low" pressure from the rail and one instantaneous "high" pressure from the amplifier piston. The amplifier piston is

[1]Corresponding author.

Contributed by the Fluids Engineering Division for publication in the JOURNAL OF FLUIDS ENGINEERING. Manuscript received by the Fluids Engineering Division July 21, 2004; final manuscript received: July 27, 2005. Associate Editor: Sivaram Gogineni.

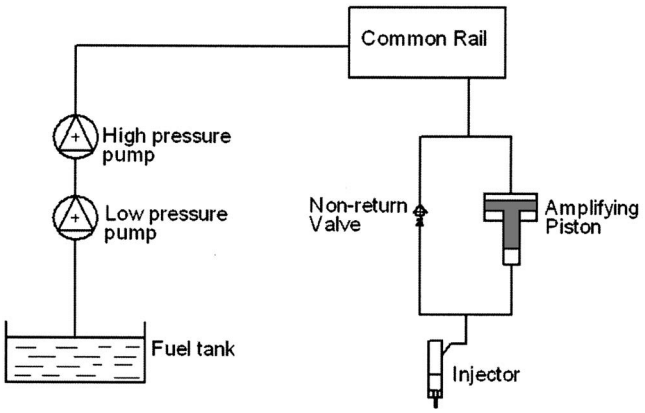

Fig. 1 Common rail injection system with piston amplifier

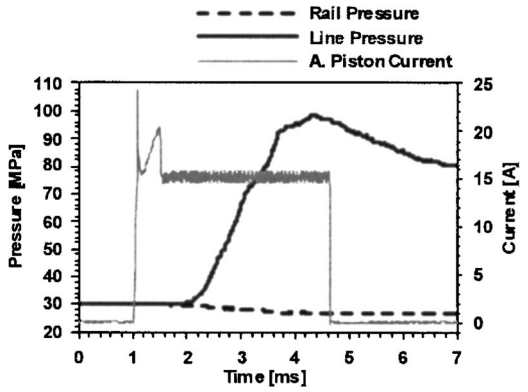

Fig. 3 Pressure evolution at the injector and piston energizing signal

activated independently of the injector, and thus the pressure evolution at the injector can be modulated with high flexibility. In principle, the injection system is able to produce different injection rate shapes, for instance a common-rail "square," "ramp," or "boot" shape. These injection rates are shown in their idealized from in Fig. 2.

The three shapes of injection rate are obtained by changing the relative timing of the piston amplifier and injector actuation. If the piston is actuated before the injector, then when the injector opens, the pressure will have already risen to the amplified value, and the profile of the injection pressure over one cycle should ideally look like the graph on the left of Fig. 2 ("square"). If the piston is actuated at almost the same instant as the injector, then the injection pressure will initially be as in the common rail and will rise progressively to the maximum value delivered by the amplifying system. This is the shape characterized as the "ramp."

Finally, if the piston is activated after the injector has opened; the injection pressure will initially rise to the rail value, remain at that value for a while and then increase again once the fuel at the amplified pressure starts being delivered. This is the "boot" case, shown on the right of Fig. 2.

In reality, however, there is a delay of about 2 ms between the moment the electrical signal is given to the amplifying piston and the moment the pressure at the injector reaches the maximum value; this requires the two energizing times to be adjusted accordingly. Figure 3 shows the evolution of the fuel pressure available to the injector when the piston amplifier is actuated.

The actual resulting rate shapes are shown in Fig. 4. The origin of the "x" axis is taken as the actual start of injection for presentation purposes, although in reality the process starts with the injector's energizing pulse, which is also used for synchronizing the camera and the flash light.

2.2 Injection Test Rig. The injection test rig (ITR) is based on a constant-volume vessel that offers better optical access than a normal engine and allows the ambient conditions in the combustion chamber at the moment of injection to be totally or partially reproduced.

The test rig is filled with a dense gas, sulphur hexa-fluoride (SF_6), which is inert thus preventing combustion. Its high molecular mass allows the density values that normally occur in a diesel engine at the moment of injection (20–60 kg/m^3) to be reached at much lower pressures (0.2–0.8 MPa). It is generally accepted that the behavior of the spray depends mainly on the density of the ambient gas rather than on its pressure, which implies that the experiments performed in such a test rig are representative of the real conditions in a Diesel engine spray [8].

The temperature inside the rig is kept constant, at 25°C. The gas is continuously scavenged at a velocity lower than 3 m/s, which is not expected to affect the diesel spray, while window fouling is avoided. The test section of the rig is shown in Fig. 5, where the three plexiglass windows allow good optical access to the injector both for the macroscopic and microscopic characterization.

In order to study the spray evolution, only one jet from the injector nozzle needs to appear in the image recorded by the camera, since the other ones are irrelevant and quite inconvenient for the purpose of this study. In fact, the ITR is difficult to operate with a multihole injector, since the additional sprays cause contamination of the windows, as they are generally directed towards them. Consequently, specially machined nozzles with fewer orifices need to be employed, if the ITR is to be kept operative for a reasonable time before it requires cleaning. In the case of the

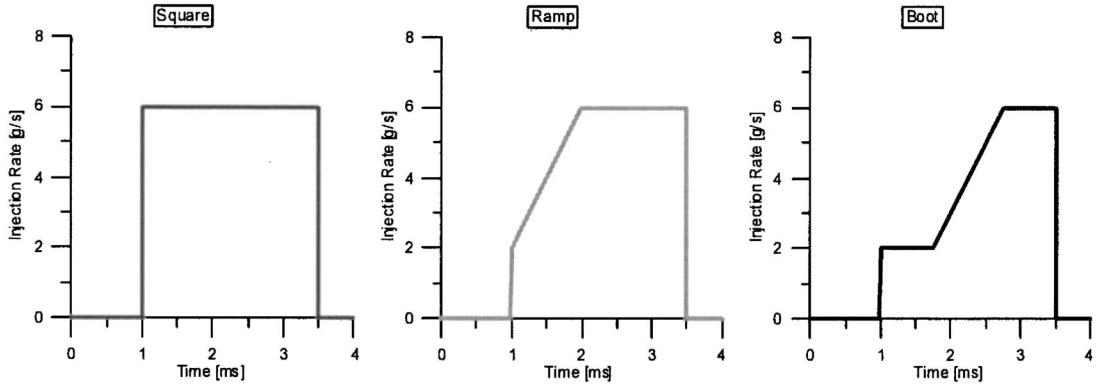

Fig. 2 "Square," "ramp," and "boot" type ideal injection rates

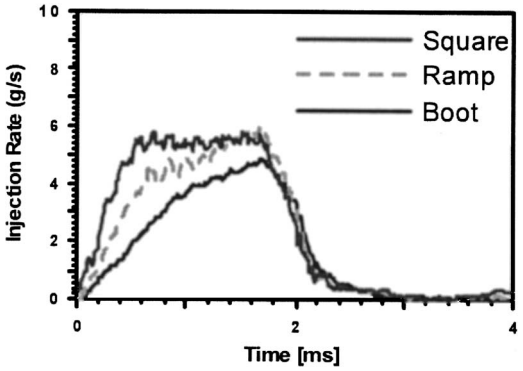

Fig. 4 Actual injection rate shapes

present study, a two-hole injector tip was used as could be seen in Fig. 5, with the two orifices diametrically opposite, in order to balance the hydraulic forces acting on the injector needle.

A Roots compressor is used to provide a maximum flow rate of 5000 l/min, with an increase of about 0.05 MPa in the vessel pressure. Two filters collect the fuel injected in order to keep the gas stream clean; the first one is cyclonic, while the second one is of higher efficiency, retaining the smaller droplets.

Several authors have employed high density gas to simulate the engine conditions [14,15]. Obviously, the use of SF6 is more likely to produce shock waves during the injection process [14], and the existence of shock waves probably modifies the spray characteristics, making the inner part of the spray to travel much faster than the leading edge [14]. However, with the available experimental set-up the visualization of shock waves was not possible, neither an evaluation of their presence.

2.3 Spray Visualization System. The images were recorded with a 12-bit color CCD camera (Pixel Fly by PCO) with a resolution of 1280×1024 pixels, and a minimum exposure time of 10 μs with a jitter of ± 5 μs. Illumination was produced by a conventional electronic flash, with controllable duration and intensity. All the experimental equipment (camera-flash-injection) was synchronized with a purpose-made electronic system, using the injector trigger signal as a reference for the image sequences. The flash was located in front of the camera while a set of light diffusers ensured homogeneous background illumination.

The flash was synchronized by means of a TTL signal generated at each revolution of the injection pump and its shot was time-delayed to illuminate the spray at different instants. Images were taken every 100 μs throughout the entire injection process showing high repeatability and very low cyclic dispersion.

The image analyzing software then reads the images pixel by pixel and, based on the difference in intensity between the background and the spray, identifies the spray position and calculates its cone angle and its penetration [16].

2.4 The Phase Doppler Particle Analyzer. The Phase Doppler analyzer was used to measure the fuel drop sizes in the spray. The instrument provides non-intrusive point measurements of droplet size and velocity simultaneously from refractive scattered light. Explanation of the PDPA principle can be found in [17].

Generally, for analyzing and presenting the results, the Sauter Mean Diameter (SMD) is used. The SMD represents the diameter of a uniform equivalent drop set with the same volume and the same surface of all drops, and thus is relevant to a number of important processes involving drop penetration or heat and mass transfer [18],

$$\mathrm{SMD} = \frac{\sum nD^3}{\sum nD^2}. \tag{1}$$

The laser-emitting equipment of the PDPA system features a 2 W water-cooled Ar^+ Laser source operated at 600 mW, a 40 MHz Bragg cell as frequency shifter and a TSI 15 mm Laser probe linked by 10 m length fiber optics. Collecting optics and electronics are those from a standard Aerometrics component system. The one-per-cycle signal given by the injection pump bench was used as a trigger for defining the beginning of the measuring temporal window. The PDPA optical components (laser-emitting and signal-receiving optics) were mounted on an *X-Y-Z* coordinate table that allows the positioning of the control volume within the spray with a precision of movement of 0.05 mm.

The only shortcoming of the method for application to diesel sprays is the inability to measure in zones of high droplet density, especially close to the injector at the spray center. Due to multiple droplets being present within the measurement volume, the light signal is difficult to be interpreted by the processor. Another problem are the droplets located between the measurement volume and the receiver as they make the propagation of light difficult. Finally, there are some droplets that cross the laser beams before these intersect to form the probe volume, and thus light intensity fluctuations are produced by reflection and refraction. All these factors obviously have a negative influence on the quality of the light signals that are to be processed [19,20].

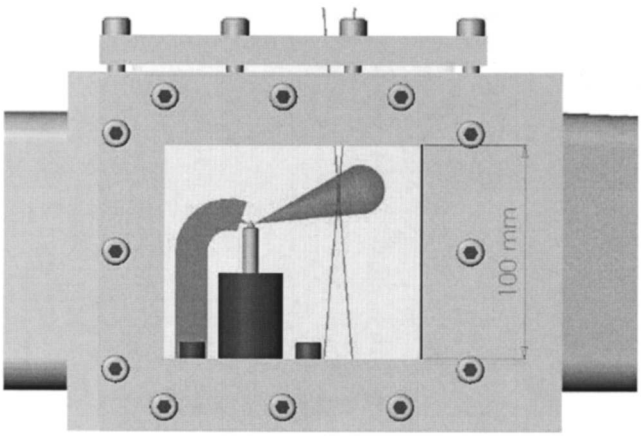

Fig. 5 The rig's testing section; there can also be noticed the laser beams for PDPA measurement, the device collecting the second spray, and a dimension for scaling

3 Test Conditions

The ambient density and temperature in the test volume were fixed throughout the experiments at 44 kg/m^3 and 25°C, respectively. In the first two parametric studies the rail pressure was 35.5 MPa and consequently the amplified pressure at the injector was 100 MPa. In the second test case the injector energizing times were changed in order to inject the same amount of fuel. In the third case the rail pressure was varied in order to modify the amplified injector pressure, and the energizing times were changed to maintain the injected quantity constant. A summary of the operating conditions is given in Table 1.

The PDPA measuring points within the spray have been chosen with the aim of revealing the possible differences occurring at different positions along the jet's axis and at different radial positions.

Figure 6 and Table 2 show all the positions at which droplet size measurements have been made. However, only the relevant results will be presented and discussed.

Table 1 Test matrix

	Pressure (MPa)		Injected Mass	Rate Shape	ET	Testing Mode	
	Rail	Amplified	(mg/orifice)		(ms)	Visualization	PDPA
1st Comparison	35.5	100	9.41	Square	2.6	X	X
	35.5	100	7.93	Ramp	2.6	X	X
	35.5	100	6.73	Boot	2.6	X	X
2nd Comparison	35.5	100	9.41	Square	2.6	X	
	35.5	100	9.37	Ramp	2.8	X	
	35.5	100	9.52	Boot	3	X	
3rd Comparison	57	160	9.65	Boot	2.35	X	X
	46.3	130	9.42	Boot	2.6	X	
	35.5	100	9.52	Boot	3	X	X

4 Experimental Results

4.1 Visualization Results. In Fig. 7 three sample pictures of the spray in the high density test rig are presented for 1000 μs after the start of injection. The differences in the spray characteristics are obvious as will be seen in the processed results. The higher the instantaneous injection rate, the higher the spray tip penetration [21,22].

The first comparison between the three injection patterns (Fig. 8) has been done by simply changing only the injection rates, as shown in Fig. 4. The results are displayed with vertical bars showing the sample standard deviation. The rail pressure (P_{rail}) was 35.5 MPa and the maximum injection pressure (P_{inj}) was 100 MPa. The injector energizing times were the same for all three cases, as well as the test rig gas density and temperature.

It should be mentioned that having the same injection duration but different injection rates, produced by different instantaneous injection pressures, means that the total fuel quantity injected per cycle is not the same. As shown in Fig. 8, these differences translate into different tip penetrations, as expected, with the *square* pattern having a faster penetration than the other two, and the *boot* the slowest one. However, no significant differences were observed in the spray cone angle [23].

The comparison presented in Fig. 9 is similar to the previous one but in this case the injector energizing time has been adjusted in order to inject the same quantity of fuel for every case [24]. Consequently, the injection duration is the shortest for the *square* pattern and the longest for the *boot*. Looking at the upper graph in Fig. 9, it can be appreciated that the area contained under the rate curves are the same, as expected, since the integral of the instantaneous rate curve provides the total mass of injected fuel per cycle.

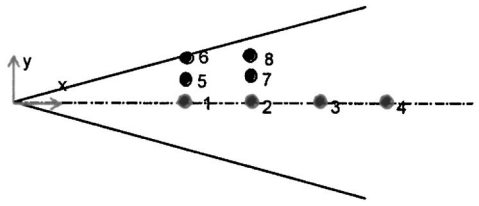

Fig. 6 PDPA measurement positions

It can be seen that in the *square* pattern the spray penetrates faster in the initial phases due to the higher fuel pressure at the beginning of injection. The same is true for the *ramp* in comparison to the *boot* pattern. However, towards the end of injection when the pressures are almost the same in all three cases, the penetration curves also become similar, conserving the differences that appear in the initial stages. The spray cone angles are the same after an initial short period, when the *boot* and *ramp* patterns exhibit higher cone angles. This corresponds to the period the injector needle is still opening and thus the injection conditions have not yet reached the quasi-steady state. *Square* reaches that state faster due to a much higher fuel pressure at the injection start.

The results presented in Fig. 10 are meant to reveal the influ-

Table 2 Position of test points within the spray

Point code	Axial Position X (mm)	Radial Position Y (mm)
1	20	0
2	30	0
3	40	0
4	50	0
5	20	1.5
6	20	3.0
7	30	1.5
8	30	3.0

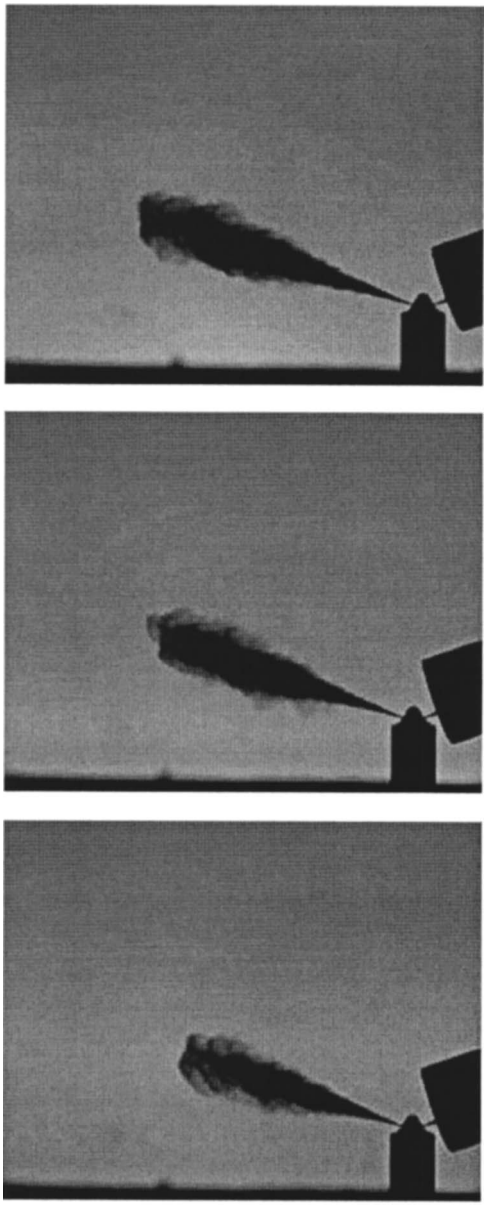

Fig. 7 Shadography image example for "square," "ramp," and "boot" (in this order, starting from above), corresponding to 1 ms after start of injection, and the test conditions from Fig. 9

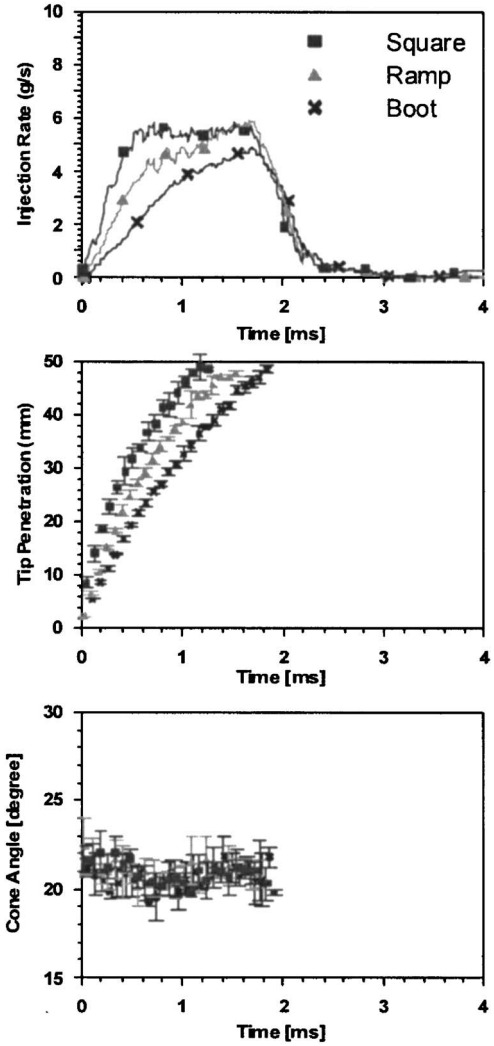

Fig. 8 Injection rate, spray cone angle, and tip penetration comparison: P_{rail}=35.5 MPa, P_{inj}=100 MPa, ET=1.6 ms

ence that injection pressure has on the spray characteristics. That is why only one injection pattern has been used, and the maximum injection pressure has been varied from 100 MPa to 160 MPa. This means that the rail pressure was in the interval between 35.5 MPa and 57 MPa. The injector energizing times were modified accordingly in order to inject the same quantity in all three cases. The results revealed that the penetration curves are similar, with the higher injection pressure leading to slightly higher penetration than the lower pressures. However, it is worth noting that in the case of injecting under *boot* pattern at 160 MPa, spray penetration is lower than the one achieved at the *square* pattern at 100 MPa. This can be easily noticed by comparing Figs. 9 and 10, both of them corresponding to *boot* pattern at 100 MPa. This means that the higher pressure at the beginning of injection in the case of the *square* pattern at 100 MPa in comparison to *boot* at 160 MPa is the most important factor in determining spray tip penetration.

The spray cone angles exhibit such close values that it would be difficult to draw a clear conclusion over a possible tendency. The angle values averaged over the entire injection cycle and over several repetitions are within 0.5° of one another regardless of the injection pressure or rate shape, with no consistent tendency between them, so it leads to the conclusion that there is no direct influence of the injection pressure over the aperture angle [22].

4.1.1 Discussion of the Visualization Results Reliability. It can be observed in the penetration graphs that the data presents very low variation, about ±1 mm, which at a 50 mm penetration represents an uncertainty interval of 4%. This variation is due to both cycle-to-cycle variations in the injection process itself, as well as the ones in the image processing. The injection process may typically vary due to fluctuations of the injection pressure, which are unlikely to be significant in the case of a common-rail system, and due to friction forces actuating on the injector needle. The opening of the needle influences the fuel flow inside the nozzle, and thus, a slightly smaller lift, not only produces a small decrease of the penetration, but also increases with a small amount the aperture angle, due to higher in-nozzle turbulence [22]. The image processing relies on a statistical method, the likelihood-ratio test [16], to separate the spray shadow from the more luminous background, and so it is inherent to introduce a small variability due to the particularities of every individual spray.

The same factors determine the variability of the observed angle. This is typically measured with two straight fits at 60% of

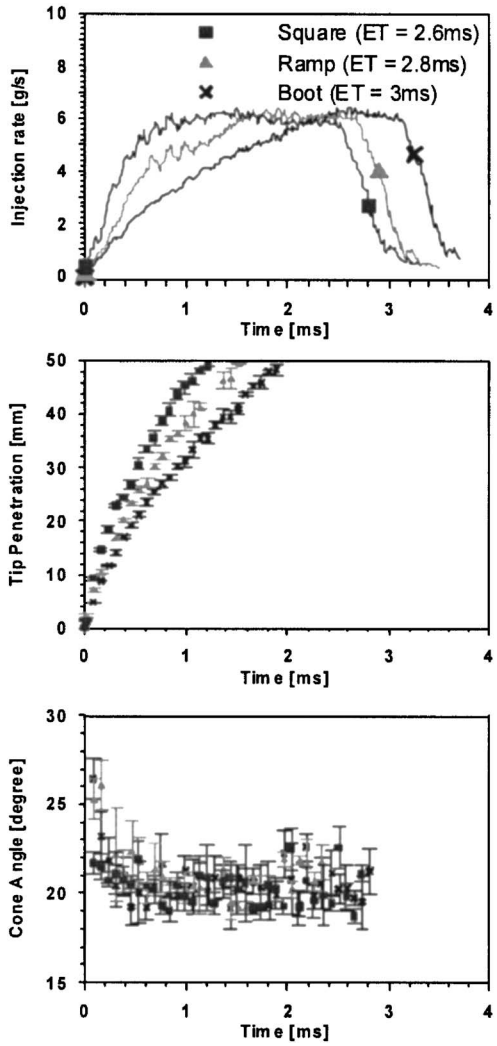

Fig. 9 Effect of different rate shapes and energizing times; P_{rail}=35.5 MPa, P_{inj}=100 MPa

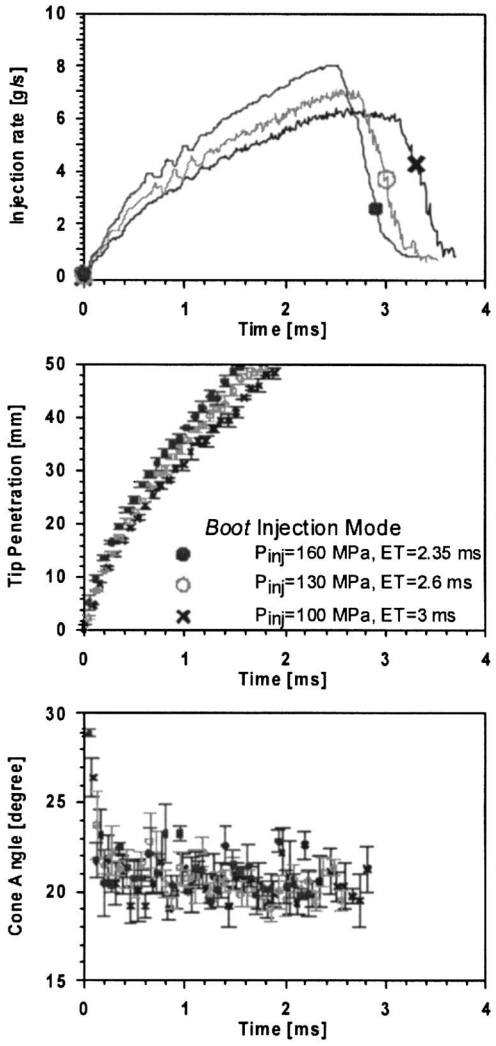

Fig. 10 Effect of different injection pressures, boot mode

the total penetration [1], and so if it was to consider the same variability as in the penetration data at either side of the spray image at 30 mm from the orifice, it would translate roughly into a 4 deg variation in spray cone angle. While this consideration leads to an obvious overestimation of the angle variability, it shows that the actual variability of about 3 deg observed in the experimental results can be considered normal, although it might seem abnormally high at first sight. It can be however concluded that the measuring angle standard deviation is greater than the differences due to rate shaping or injection pressure. In the case of the penetration data, these differences are greater than the standard measurement deviation, and thus the results could be considered as reliable and a theoretical analysis is performed in the following paragraphs.

4.1.2 Theoretical Analysis of the Penetration Results. Amongst the parameters that characterize a spray, the penetration is the one which is best understood, because its theoretical prediction is rather straightforward in comparison to the one of the angle or the droplet diameter. Hay and Jones [23] carried out a critical review of the proposed correlations for the penetration of the Diesel spray in the literature before 1972 and arrived at the conclusion that those of Wakuri et al. [25] and Dent [26] were those that best fitted the experimental results. Wakuri et al. applied conservation of momentum in a cone of constant angle over a time period, assuming that the mixture of air and fuel is homogenous, and developed an equation that will be taken as reference in the present paper,

$$S(t) = ct \cdot \Delta P^{1/4} \rho_a^{-1/4} D_0^{1/2} \tan\left(\frac{\theta}{2}\right)^{-1/2} t^{1/2} \tag{2}$$

where $S(t)$ is the time-dependent penetration, ρ_a is the ambient density, D_0 is the outlet orifice diameter, ΔP is the pressure differential, t is the time from the start of injection, and θ is the spray cone angle. The injector geometry is taken into account through the orifice diameter and the constant ct. This equation has been established for an ideal injection rate having a squared shape; therefore it would only be appropriate to use it for correlation with the penetration results obtained with the *square* injection mode. Assuming that apart from the time t, everything else can be grouped in to one constant, a general equation for the penetration could be written as

$$S(t) = k \times t^a \tag{3}$$

In this equation, the time exponent, a, should have the value of 0.5 [1] for the *square* injection mode. Trying to fit this equation with the experimental results, the value of coefficient a becomes 0.52 for the *square* rate, which is close to the value predicted by Wakuri et al., 0.59 for the *ramp* and 0.67 for the *boot*. The R^2 correlation coefficient reaches values of 0.991 for *square* and *ramp* cases and 0.995 in the case of *boot*, which implies an ex-

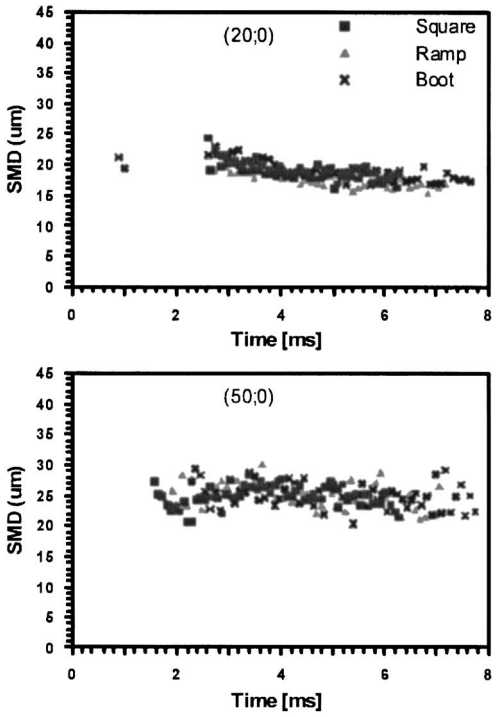

Fig. 11 On-axis PDPA results, 20 and 50 mm from injector orifice

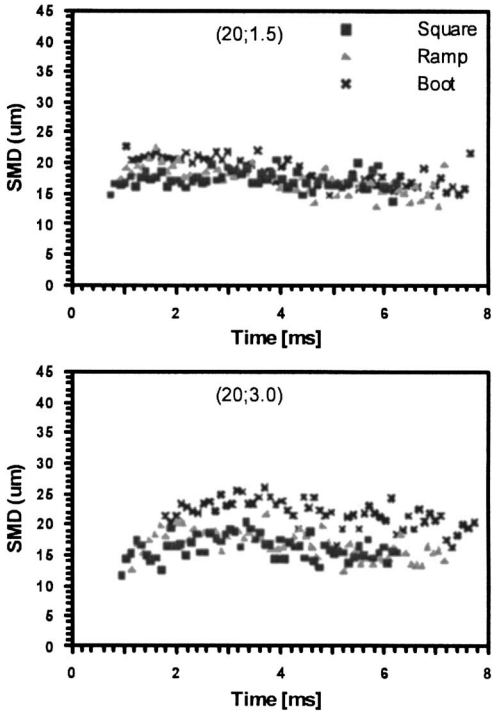

Fig. 12 Off-axis PDPA results, 20 mm from injector orifice, 1.5 and 3 mm radial distance

cellent correlation. The greater dependence on time in the penetration equation in the last two cases is expected because the pressure is time dependent too.

As far as the constant k is concerned, it takes the highest value for *square* and the lowest one for *boot*. Comparing Eqs. (2) and (3) it can be seen that k includes the pressure differential which has a higher average value over one injection event for *square* than for the other two, thus explaining the observed tendency.

It can thus be concluded that the visualization results are in good agreement with generally accepted theoretical considerations.

4.2 PDPA Results. The SMD measurements in Figs. 11 and 12 correspond to the injection conditions of Fig. 8.

The results presented in Fig. 11 correspond to points located exactly on the spray axis at a distance of 20 mm and 50 mm, respectively, from the orifice. At 20 mm the data collection starts relatively late, at around 2.5 ms after the start of injection. By comparison, at 50 mm the data collection begins earlier, which is physically impossible since the first droplets reach earlier the 20 mm point. This anomaly is explained by the fact that the jet is too dense at 20 mm in the first injection phase thus the system is not being able to collect any data.

Consequently, at 20 mm data begin to be collected only after the droplet density falls below a certain level. On the other hand, at the 50 mm point, data collection begins with the first droplets that reach the probe volume, which is proven by the fact that in the case of the *square* injection mode droplets are detected a little earlier than in the case of *ramp* or *boot*. This is in accordance with the penetration results of Fig. 8.

As far as the actual SMD values are concerned, no differences are observed. This could be because at 20 mm the data are collected late, when the injection conditions are equalized in the three cases, and at 50 mm the drops have already spent long enough in contact with the ambient gas for their size to become uniform [27].

At the 20 mm distance, measurements have also been taken off-axis (Fig. 12) where the spray density is lower and data were available as soon as the first droplets reach the probe volume. As it can be seen, at 1.5 mm distance off axis, close to the injection start, the *square* rate produces a slightly smaller SMD than the *ramp*, with *boot* producing the highest one. The operating conditions then equalize and so do the SMD's. At the 3 mm off-axis point it is clear that *boot* produces higher droplet diameter probably due to the lowest effective injection pressure.

The off-axis measurements at points (30;1.5) and (30;3.0) have revealed no diameter difference between the three injection modes. However, the droplet diameter is in general agreement with those observed and predicted in similar investigations [27,28].

A PDPA test was also performed at 40 mm from the orifice at the spray axis with the injection conditions as in Fig. 9. It is common knowledge that droplet size depends on the intensity of the breakup process at the orifice exit, which depends on the turbulence inside the nozzle. It could be argued that a short, high-pressure injection produces more turbulence than a long, lower-pressure one, so one could expect the 160 MPa injection pressure to produce lower SMD. In Fig. 13 such a difference can be seen although it is rather small. The conclusion from this figure would

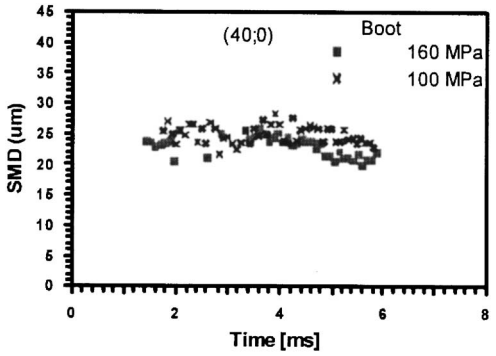

Fig. 13 Effect of injection pressure on droplet size

be that the SMD values far from the nozzle exit are not influenced by small changes in the internal flow characteristics (injection pressure) when keeping unchanged the nozzle geometry as is the case in the present work.

4.2.1 Discussion of the PDPA Results Reliability. While performing a PDPA characterization of a spray there is a set of measures that are taken to make sure the results are reliable. The first step is to choose a sampling rate frequency that fits with the velocity range going to be encountered, the purpose being to limit the possibility of sampling fake signals or noises that are outside the required range frequency. To eliminate noises that produce frequencies in the same range as the droplet velocities the most common practice is to keep the PMT voltage rather low, 400–600 mV, increase the laser power to about 1–1.2 W, and increase the burst threshold to eliminate the noise, typically 300–500 mV. Increasing the burst threshold has the disadvantage of decreasing the data rate and that it also might eliminate valid measurements. The process thus depends on the experience of the operator to find a good balance between obtaining a low-noise measurement while keeping the data rate at an acceptable level. Software wise, the phase calibration, as well as the intensity validation make sure that non-spherical droplets and other abnormalities are eliminated and that when a droplet does gets measured, it is done accurately.

The main problem occurs when multiple droplets are present within the measurement volume, because they produce a single burst signal, which cannot be processed, and thus no valid data can be collected from the denser parts of the spray. Looking at the burst efficiency, it was noticed that it was up to 70% in the tail of the spray, i.e., after the first dense front has passed, but in the first part of the spray only 5% of the droplets passing through the probe volume produced valid data. This indicates clearly that those measurements are seriously biased towards the droplets that are easier to measure, especially the slower ones.

The conclusion is that the data presented for the less dense parts of the spray reflects satisfactorily its characteristics.

5 Conclusions

The comparison between *square, ramp*, and *boot* injection rate profiles revealed that *square* always leads to higher spray tip penetration due to the higher pressure at the start of injection, even if the times are adjusted so that the same fuel quantity is injected. *Ramp* always has medium penetration and *boot* the lowest one. The spray cone angles are almost identical in the three cases showing no influence of injection rate shape or injection pressure on the value of the spray cone angle.

When the injection mode is maintained as either *ramp* or *boot* and the injection pressure and duration are varied while keeping the same injected quantity, a small difference appears in spray penetration, with higher pressures leading to faster penetration. A trend was also observed for the combination of higher injection pressure with shorter duration to produce a higher aperture angle at the beginning of the injection process when transient processes were important.

Measurements at the spray center two axial positions revealed no difference between the droplet diameters produced by the three injection rate shapes mainly due to the fact that only the spray tail was considered and not the leading edge where most differences could be foreseen.

The off-axis measurements far downstream from the orifice also showed no difference in droplet size. Nevertheless, it was noticed that closer to the orifice the higher injection pressures tended to produce droplets with slightly smaller diameter.

Acknowledgments

The authors acknowledge that part of this work was performed in the frame of the CRICE project, G3RD-CT99-0001, founded by the European Commission, and also the contribution of Mr. J. E. del Rey for the technical assistance provided throughout the experiments.

Nomenclature

CCD = charged coupled device
ct, k = constants
D = droplet diameter
D_0 = injector outlet orifice diameter
ET = energizing time
ITR = injection test rig
PDPA = phase Doppler particle analyzer
P_{inj} = injection pressure
P_{rail} = rail pressure
PMT = photomultiplier
SMD = Sauter mean diameter
$S(t)$ = time-dependent penetration
SF_6 = sulphur hexa-fluoride
t = time from the start of injection
TTL = transistor-transistor logic signal

Greek symbols

ρ_a = density in the testing section
ΔP = pressure differential
θ = spray cone angle

References

[1] Payri, F., Bermúdez, V., Payri, R., and Salvador, F. J., 2004, "The Influence of Cavitation on the Internal Flow and the Spray Characteristics in Diesel Injection Nozzles," Fuel, **83**, pp. 419–431.
[2] Macian, V., Payri, R., Margot, X., and Salvador, F. J., 2003, "A CFD Analysis of the Influence of Diesel Nozzle Geometry on the Inception of Cavitation," Atomization Sprays, **19**, pp. 579–604.
[3] Wigley, G., and Pitcher, G., 1997, "The Effect of Fuel Line Pressure and Injection Duration on Diesel Spray Formation and Structure," Proceedings of ILASS-98, pp. 83–88.
[4] Pierpont, D. A., and Reitz, R. D., 1995, "Effects of Injection Pressure and Nozzle Geometry on D.I. Diesel Emissions and Performance," SAE Paper No. 950604.
[5] Su, T. F., Chang, C. T., and Reitz, R. D., 1995, "Effects of Injection Pressure and Nozzle Geometry on Spray SMD and D.I. Emissions," SAE Paper No. 952360.
[6] Arcoumanis, C., and Gavaises, M., 1997, "Effect of Fuel Injection Processes on the Structure of Diesel Sprays," SAE Paper No. 970799.
[7] Post, S., Iyer, V., and Abraham, J., 2000, "A Study of Near-Field Entrainment in Gas Jets and Sprays Under Diesel Conditions," ASME J. Fluids Eng., **122**, pp. 385–395.
[8] Hiroyasu, T., and Arai, M., 1990, "Structures of Fuel Sprays in Diesel Engines," SAE paper No. 900475.
[9] Ruiz, F., and Chigier, N. A., 1991, "Parametric Experiments on Liquid Jet Atomization Spray Angle," Atomization Sprays, **1**, pp. 23–45.
[10] Morgan, R., Wray, J., Kennaird, D. A., Crua, C., and Heikal, M. R., 2001, "The Influence of Injector Parameters on the Formation and Break-up of a Diesel Spray," SAE Paper No. 2001-01-0529.
[11] Koo, J. Y., Hong, T. S., Shakal, J. S., and Goto, S., 1997, "Influence of Fuel Injector Nozzle Geometry on Internal and External Flow Characteristics," SAE Paper No. 970354.
[12] Nehmer, D. A., and Reitz, R. D., 1994, "Measurement of the Effect of Injection Rate and Split Injections on Diesel Engine Soot and NO_x Emissions," SAE Paper No. 940668.
[13] Tow, T. C., Pierpont, D. A., and Reitz, R. D., 1994, "Reducing Particulate and NO_x Emissions by Using Multiple Injections in a Heavy Duty D.I. Diesel Engine," SAE Paper No. 940897.
[14] MacPhee, A. G., Tate, M. W., Powell, C. F., Yue, Y., Renzi, J. R., Ercan, A., Narayam, S., Fontes, E., Walther, J., Schaller, J., Gruner, S. M., and Wang, J., 2002, "X-Ray Imaging of Shock Waves Generated by High-Pressure Fuel Sprays," Science, **295**, pp. 1261–1263.
[15] Cheong, S. K., Liu, J., Shu, D., Wang, J., and Powell, C. F., 2004, "Effects of Ambient Pressure on Dynamics of Near-Nozzle Diesel Sprays Studied by Ultrafast X-Radiography," SAE Paper No. 1004-01-2026.
[16] Pastor, J. V., Arrègle, J., and Palomares, A., 2001, "Diesel Spray Image Segmentation with a Likelihood Ratio Test," Appl. Opt., **40**, No. 17, pp. 2876–2885.
[17] Dust, F., Melling, A., and Whitelaw, J. H., 1981, *Principles and Practice of Laser-Doppler Anemometry*, 2nd ed., Academic, London.
[18] Lefebre, A. H., 1989, *Atomization and Sprays*, Hemisphere, New York, p. 151.
[19] Koo, J. Y., and Kim, J. H., 2003, "Assessment of a Phase Doppler Anemometry Technique in Dense Droplet Laden Jet," KSME Int. J., **17**, No. 7, pp. 1083–1094.
[20] Labs, J., and Parker, T., 2003, "Diesel Fuel Spray Droplet Sizes and Volume

Fractions From the Region 25 mm and Below the Orifice," Atomization Sprays, **13**, pp. 425–442.
[21] Benajes, J., Pastor, J. V., Payri, R., and Plazas, A. H., 2004, "Analysis of the Influence of Diesel Nozzle Geometry in the Injection Rate Characteristic," J. Fluids Eng., **126**, pp. 63–71.
[22] Arcoumanis, C., and Gavaises, M., 1998, "Linking Nozzle Flow with Spray Characteristics in a Diesel Fuel Injection System," Atomization Sprays, **8**, pp. 307–347.
[23] Hay, P., and Jones, P. L., 1972, "Comparison of the Various Correlations for Spray Penetration," SAE Paper No. 720776.
[24] Payri, R., Climent, H., Salvador, F. J., and Favennec, A. G., 2004, "Diesel Injection System Modelling. Methodology and Application for a First Generation Common Rail System," Proc. Inst. Mech. Eng., Part D (J. Automob. Eng.), **218**, pp. 81–91.
[25] Wakuri, Y., Fujii, M., Amitani, T., and Tsnumeya, R., 1960, "Studies of the Penetration of a Fuel Spray in a Diesel Engine," Bull. JSME, **3**(9), pp. 123–130.
[26] Dent, J. C., 1971, "A Basis for Comparison of Various Experimental Methods for Studying Spray Penetration," SAE Paper No. 710571.
[27] Hung, C. C., Martin, J. K., and Koo, J. Y., 1997, "Injection Pressure Effects Upon Droplet Behavior in Transient Diesel Sprays," SAE Technical Paper No. 970053.
[28] Cao, J., 2002, "On the Theoretical Prediction of Fuel Droplet Size Distribution in Nonreactive Diesel Sprays," J. Fluids Eng., **124**, pp. 182–185.

Level-Set Computations of Free Surface Rotational Flows

Giuseppina Colicchio[1]
School of Civil Engineering and the Environment,
University of Southampton,
Southampton, UK
e-mail: g.colicchio@insean.it

Maurizio Landrini
INSEAN,
The Italian Ship Model Basin

John R. Chaplin
School of Civil Engineering and the Environment,
University of Southampton,
Southampton, UK
e-mail: j.r.chaplin@soton.ac.uk

A numerical method is developed for modeling the violent motion and fragmentation of an interface between two fluids. The flow field is described through the solution of the Navier-Stokes equations for both fluids (in this case water and air), and the interface is captured by a Level-Set function. Particular attention is given to modeling the interface, where most of the numerical approximations are made. Novel features are that the reintialization procedure has been redefined in cells crossed by the interface; the density has been smoothed across the interface using an exponential function to obtain an equally stiff variation of the density and of its inverse; and we have used an essentially nonoscillatory scheme with a limiter whose coefficients depend on the distance function at the interface. The results of the refined scheme have been compared with those of the basic scheme and with other numerical solvers, with favorable results. Besides the case of the vertical surface-piercing plate (for which new laboratory measurements were carried out) the numerical method is applied to problems involving a dam-break and wall-impact, the interaction of a vortex with a free surface, and the deformation of a cylindrical bubble. Promising agreement with other sources of data is found in every case.
[DOI: 10.1115/1.2062707]

1 Introduction

Over the four decades since the introduction of solvers for multiphase flows [1], several strategies have been introduced for the solution of the Navier-Stokes equations in a region containing two immiscible fluids and for tracking their interface. Applications include those situations in offshore and coastal engineering and ship hydrodynamics where both the free surface and vorticity are important, or where there are strong interactions between them. Examples of both Lagrangian and Eulerian approaches to the Navier-Stokes equations can be found in the literature, where the solution is calculated respectively with reference to moving particles of each fluid [2,3], or in terms of the fluid properties and dynamics at points that are fixed in space [4–8]. There is a third class that can be considered intermediate between these two, referred to as Boundary Fitted Methods (BFM) [8]. In this case the computational domain is divided into deformable sub-domains, and the boundaries of each domain adapt themselves to the interface between the fluids.

However, in the present context the modeling of multiphase flows has been mainly based on Eulerian methods. These have the inherent advantage that a fixed mesh eliminates the need for remeshing, which otherwise becomes necessary after the interface has undergone severe deformations.

Among Eulerian schemes further distinctions can be made, according to the method used to trace the position of the interface. The most well-known techniques are referred to as the Volume of Fluid (VOF) method [5,9–11], the Level-Set (LS) method [7,12], and the Constrained Interpolation Profile (CIP) method [13,14]. Each one of these has attendant advantages and shortcomings, and progress in this field continues to benefit from comparisons that involve different numerical methods, analytical solutions (where possible) and (probably most importantly) good quality laboratory measurements. There is a shortage of suitable definitive experimental data that focus on flows involving a strongly deforming interface and on interfacial breaking. Attempts to study strong deformations were made by Lawson et al. [10], with PIV measurements around a breaking bubble. Unfortunately, for the purpose of studying regions of strong free surface deformation and fragmentation, the value of PIV (as of other techniques) is limited by the practical difficulties of making measurements in these conditions.

This paper describes a Level-Set method that includes several novel features, implemented with a finite difference Navier-Stokes solver that uses an approximate projection method for the pressure. Four test cases of increasing complexity are explored: a dam break, a rising bubble, the interaction of a vortex pair with a free surface, and the flow generated by a rapidly accelerating surface-piercing vertical plate. All are two-dimensional flows. As is customary, the term "free surface" is used here to denote the liquid/gas interface, even though, owing to the finite density of the latter (included in the computations), the surface is not strictly free.

The geometry of the fourth test problem, for which dedicated experiments were carried out, is identical to that studied in an inviscid numerical solution by Tsai and Yue [15]. Though the conditions can be defined very simply, the problem of the flow generated by the horizontal motion of a vertical surface-piercing plate encapsulates the dominant features of a wide range of surface piercing body flows: (1) strong deformation of the surface with eventual breaking and air entrainment, (2) generation of vorticity, (3) interaction of the vorticity with the surface, and (4) significant effects of surface tension. The main features described here are shown in Fig. 1.

The first three test cases focus on some of these elements under simpler conditions. In each case comparisons are made with the results of other methods and, where possible, with measurements. The results are encouraging, and demonstrate a reduction in the smoothing errors at the interface that are commonly associated with the Level-Set technique.

2 Numerical Method

2.1 Basic Equations. One approach for computing flows that involve two phases (in this case air and water) is to consider the whole domain to be a continuous field where any generic fluid property, say f (in this case the density or viscosity), takes an appropriate value in each fluid. The problems that arise from discontinuities in f can be avoided by patching the corresponding fields across the interface, that is

[1]Present address: INSEAN, The Italian Ship Model Basin.

Contributed by the Fluids Engineering Division of ASME for publication in the JOURNAL OF FLUIDS ENGINEERING. Manuscript received by the Fluids Engineering Division November 3, 2004; final manuscript received July 8, 2005. Associate Editor: Subrata Roy.

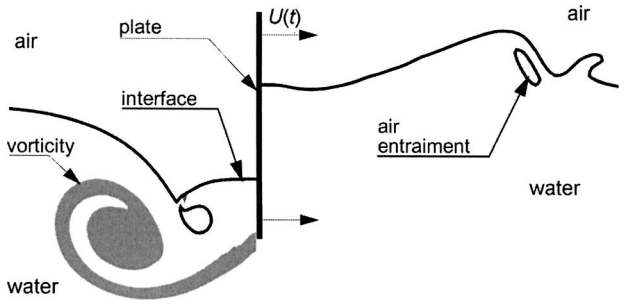

Fig. 1 Flow around a surface piercing plate accelerated horizontally from rest. The interface between air and water is strongly deformed by the movement of the plate with velocity $U(t)$. At the lower tip of the plate a region of high vorticity becomes detached (shown as a shadowed area), and interacts with the surface.

$$f = \chi f_{\text{air}} + (1-\chi) f_{\text{water}}. \tag{1}$$

A smooth transition from one phase to the other is provided by the bridge function $\chi \in [0,1]$, applied over a narrow interval around the actual interface. In this scheme, the evolution of the compound flow field is described by the Navier-Stokes equations for a single fluid of non-uniform properties and, in principle, there is no need to distinguish explicitly between the two phases. The continuity conditions for velocity and tangential stresses at the interface are automatically fulfilled, albeit in a smoothed sense, while surface tension effects have to be modeled explicitly. Clearly, most of the numerical difficulties are shifted to the treatment of the bridge function and its consequences.

In the following, we will use a Level-Set approach to define the transition from one phase to the other. The air-water interface is not explicitly followed but its position is captured as the zero level of a scalar field, defined in the whole computational domain. The field equations are discretized by a finite-difference scheme, with second-order accuracy both in time and space. The spatial discretization is based on an upwind Essentially Non-Oscillatory (ENO) scheme, and the time discretization uses an iterative predictor-corrector method, and a variable-density projection method.

The one-fluid system is governed by the Navier-Stokes equation

$$\begin{gathered} \nabla \cdot \mathbf{u} = 0 \\ \rho \frac{D\mathbf{u}}{Dt} = -\nabla p + 2\nabla \cdot \mu \mathbf{D} + \sigma \kappa \delta_s \mathbf{n} + \rho \mathbf{g} \end{gathered} \tag{2}$$

where the density ρ and the dynamic viscosity μ vary across the interface. The term $\sigma\kappa\delta_s\mathbf{n}$ is the capillary force, with σ the surface tension, $\mathbf{n}$ the normal to the interface, κ the interface curvature, and δ_S the Dirac function equal to unity on the interface and zero elsewhere. Finally

$$(\mathbf{D})_{ij} = D_{ij} = \frac{1}{2}\left(\frac{\partial u_j}{\partial x_i} + \frac{\partial u_i}{\partial x_j}\right) \tag{3}$$

is the rate of strain tensor. Within the one-fluid formulation, the conditions at an interface between two viscous fluids are automatically captured [16]. The explicit modeling of surface-tension effects is described later.

2.2 Time Discretization. A second-order approximation in time of Eq. (2) can be written as

$$\frac{\mathbf{u}^{n+1}-\mathbf{u}^n}{\Delta t} = -\frac{\nabla p^{n+1/2}}{\rho^{n+1/2}} - [(\mathbf{u}\cdot\nabla)\mathbf{u}]^{n+1/2} + \frac{[2\nabla\cdot\mu\mathbf{D}]^{n+1/2}}{\rho^{n+1/2}} + \frac{[\sigma\kappa\delta_S\mathbf{n}]^{n+1/2}}{\rho^{n+1/2}} + g \tag{4}$$

and is solved with a predictor-corrector scheme. In contrast to most implementations, here the corrector step is iterated until convergence, in order to improve stability and accuracy [17]. For brevity, we introduce the term

$$F(\mathbf{u}) = -(\mathbf{u}\cdot\nabla)\mathbf{u} + \frac{2\nabla\cdot\mu\mathbf{D}}{\rho} + g \tag{5}$$

approximated by (different) Taylor expansions in each step.

2.2.1 Predictor Step. The density and the surface tension at time step $n+1/2$ are approximated with those at time $n-1/2$, and $[F(\mathbf{u})]^{n+1/2}$ is obtained through a Taylor expansion from the previous time steps. The pressure gradient is written as

$$\frac{\nabla p_0^{n+1/2}}{\rho^{n-1/2}} = \frac{\nabla p_0^{n+1/2}}{p^{n-1/2}} - \frac{\nabla p^{n-1/2}}{\rho^{n-1/2}} + \frac{\nabla p^{n-1/2}}{\rho^{n-1/2}} \tag{6}$$

and the two-step procedure to obtain the velocity $\mathbf{u}_0^{n+1}$ reads

$$\begin{aligned} \tilde{\mathbf{u}} &= \mathbf{u}^n + \Delta t\left\{[F(\mathbf{u})]_0^{n+1/2} - \frac{\nabla p^{n-1/2}}{\rho^{n-1/2}}\right\} \\ \mathbf{u}_0^{n+1} &= \tilde{\mathbf{u}} + \Delta t\left\{\frac{\nabla p^{n-1/2}}{\rho^{n-1/2}} - \frac{\nabla p_0^{n+1/2}}{\rho^{n-1/2}} + \sigma\frac{(\kappa\delta\mathbf{n})^{n-1/2}}{\rho^{n-1/2}}\right\} \end{aligned} \tag{7}$$

For an incompressible fluid, the second equation in (7) becomes

$$\frac{\nabla\cdot\tilde{\mathbf{u}}}{\Delta t} = -\nabla\cdot\left(\frac{\nabla(p^{n-1/2}-p_0^{n+1/2})}{\rho^{n-1/2}} + \sigma\frac{(\kappa\delta\mathbf{n})^{n-1/2}}{\rho^{n-1/2}}\right). \tag{8}$$

At time step $n+1/2$, the pressure is split into two parts $p=p_{(\text{st})}+p_{(\text{nst})}$, of which the first represents that due to the pressure jump associated with surface tension at the interface,

$$\nabla^2 p_{(\text{st}),0}^{n+1/2} = \nabla\cdot(\sigma(\kappa\delta\mathbf{n})^{n-1/2}) \tag{9}$$

and is completely independent of the density distribution. The other part $p_{(\text{nst})}$ represents the pressure in the absence of surface tension and is given by

$$\nabla\cdot\left(\frac{\nabla(p^{n-1/2}-p_{(\text{nst}),0}^{n+1/2})}{\rho^{n-1/2}}\right) = -\frac{\nabla\cdot\tilde{\mathbf{u}}}{\Delta t} \tag{10}$$

The solution of the Poisson Eqs. (9) and (10) gives $p_0^{n+1/2}$, and $\mathbf{u}_0^{n+1/2}$ follows from the second equation in (7), while the viscosity and density fields are defined once the interface has been captured by the Level-Set technique discussed later. These results are used to start the iterative corrector step.

2.2.2 Corrector Step. At the kth step of the corrector, the term $[F(\mathbf{u})]_k^{n+1/2}$ is obtained by a centered Taylor expansion, and the pressure gradient is written as

$$\frac{\nabla p_{(ns),k}^{n+1/2}}{\rho_{k-1}^{n+1/2}} = \frac{\nabla p_{(ns),k-1}^{n+1/2}}{\rho_{k-1}^{n+1/2}} + \frac{\nabla p_c}{\rho_{k-1}^{n+1/2}} \tag{11}$$

where p_c is a pressure-correction term arising from the approximate projection method

$$\begin{aligned} \tilde{\mathbf{u}} &= \mathbf{u}^n + \Delta t\left\{[F(\mathbf{u})]_{k-1}^{n+1/2} - \frac{\nabla p_{k-1}^{n+1/2}}{\rho_{k-1}^{n+1/2}}\right\} \\ \mathbf{u}_k^{n+1} &= \tilde{\mathbf{u}} + \Delta t\left\{\sigma\frac{(\kappa\delta\mathbf{n})_{k-1}^{n+1/2}}{\rho_{k-1}^{n+1/2}} - \frac{\nabla p_c}{\rho_{k-1}^{n+1/2}}\right\} \end{aligned} \tag{12}$$

by solving the Poisson equations

$$\nabla^2 p_{(\mathrm{st})k}^{n+1/2} = \nabla \cdot (\sigma(\kappa \delta \mathbf{n})_{k-1}^{n+1/2})$$
$$\nabla \cdot \left(\frac{\nabla p_c}{\rho_{k-1}^{n+1/2}} \right) = \frac{\nabla \cdot \tilde{\mathbf{u}}}{\Delta t} \tag{13}$$

As before, once these Poisson equations have been solved, the velocity, density, and viscosity fields can be updated. Again, we note that density and viscosity depend on the iteration step k because of the motion of the interface. The iterative procedure is repeated until convergence is satisfied. Full details of the procedure are described by Colicchio [18]. If the corrector step were performed only once, the method would resemble the 4-step solver described in [19]. However, in the present case a pressure correction p_c, rather than a new pressure p^{n+1}, is calculated through the Poisson equation. This makes the solution more sensitive to velocity variations in successive iterations, speeds up the convergence and gives a more accurate solution.

2.3 Spatial Discretization. For the spatial discretization we have used a staggered grid, and x and y derivatives have been calculated using a second-order approximation and an ENO scheme [20]. The application of second-order ENO schemes requires the choice of a so-called "limiter function." One of the most commonly used limiters is the "minmod" which is known to be dissipative. This feature is usually accepted because it smooths the high normal gradient of the tangential velocity and further stabilizes the interface with a numerical viscosity. On the other hand the so-called "superbee" is the most suitable limiter to capture the advection of a steep function. However its indiscriminate application over the whole domain, including regions of much smoother velocity distributions within each phase, is not advisable. Though other limiters have been proposed, minmod and superbee have been used here because of their individual features, and because it is possible to implement a smooth transition from one to the other, to achieve a more accurate advection of the velocity over the whole computational domain. We have introduced a variable coefficients limiter function $m(a,b)$ in the form

$$m(a,b) = \begin{cases} 0 \text{ if } ab < 0 \\ \max[\min(f|a|,|b|),\min(f|b|,|a|)]\mathrm{sign}(a) \text{ if } ab > 0 \end{cases} \tag{14}$$

where the coefficient f is a function of the distance ϕ from the interface

$$f = \begin{cases} \cos\left(\dfrac{\phi\pi}{\delta_{\lim}}\right) + 1 & \text{if } |\phi| < \delta_{\lim} \\ 1 & \text{if } |\phi| > \delta_{\lim} \end{cases} \tag{15}$$

and $\delta_{\lim}$ is the interval of variation of the coefficients. The practical choice of $\delta_{\lim}$ will be discussed later.

We note that this formulation is valid for high Reynolds numbers. In fact, the tangential velocity would be physically smoothed by the higher fluid viscosity, and the use of a superbee scheme would produce unphysical steepening of the tangential velocities at the interface.

The algebraic systems arising from the discretization of the Poisson equations are solved by a GMRES routine.

2.4 Interface Capturing. The interface between the fluids is followed by using a Level-Set function ϕ, as introduced by Sussman et al. [12]. The value of ϕ at each of a large number of particles within a narrow region surrounding the interface (as shown in Fig. 2) is identified as its signed distance from the interface. This function is then used in defining the bridge function χ in Eq. (1) for the purpose of smoothing variables across the interface. The explicit functional form of the bridge function depends on the property in question, as discussed in the following.

First, considering the density to be a function of ϕ, the continuity equation can be written as

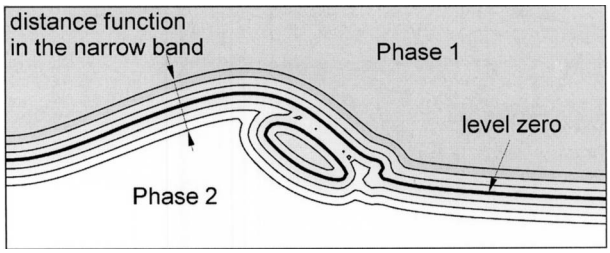

Fig. 2 The narrow region surrounding the interface in which a distance function is defined

$$\frac{\partial \rho}{\partial \phi}\left(\frac{\partial \phi}{\partial t} + u \cdot \nabla \phi \right) = 0 \tag{16}$$

from which the expression in parentheses provides a transport equation for ϕ. The Lagrangian evolution of ϕ does not preserve distance, and so a periodic reinitialization is necessary to restore its geometrical meaning. The reinitialization, as introduced by Sussman et al. [12], is based on

$$\frac{\partial \phi}{\partial \tau} + \left(\frac{\nabla \phi \cdot \nabla \phi}{|\nabla \phi|} - 1 \right) \mathrm{sign}(\phi) = 0, \tag{17}$$

where ϕ is advanced in pseudo-time τ until stationary conditions are obtained. The standard solution procedure is based on an ENO scheme for the calculation of the spatial derivatives. As shown by Russo and Smereka [21], such schemes introduce an error at the interface and this problem can be alleviated by putting

$$\phi_{ij}^{l+1} = \begin{cases} \phi_{i,j}^n - \Delta\tau[\mathrm{sign}(\phi_{i,j}^0)|\phi_{i,j}^l| - D_{i,j}] \text{ at an interface cell, and} \\ \phi_{i,j}^n - \Delta\tau\ \mathrm{sign}(\phi_{i,j}^0)\left(\dfrac{\nabla \phi_{i,j}^l \nabla\ \phi_{i,j}^l}{|\nabla \phi_{i,j}^l|} - 1 \right) \text{ elsewhere} \end{cases} \tag{18}$$

where

$$D_{i,j} = \frac{2\phi_{i,j}^0}{\sqrt{\dfrac{(\phi_{i+1,j}^0 - \phi_{i-1,j}^0)^2}{\Delta x^2} + \dfrac{(\phi_{i,j+1}^0 - \phi_{i,j-1}^0)^2}{\Delta y^2}}} \tag{19}$$

This procedure has been found to be more accurate also when the interface is split into separate branches (as in the present case of a surface piercing plate shown in Fig. 3), without the need for introducing different level-set functions. In spite of this, some numerical smoothing of the interface did occur in regions of high

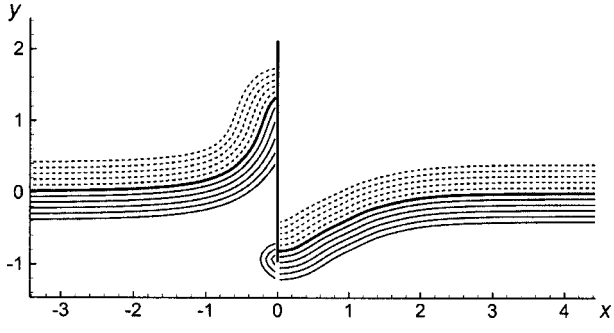

Fig. 3 Contour levels of the distance function at a time when the surface approaches the bottom edge of the plate

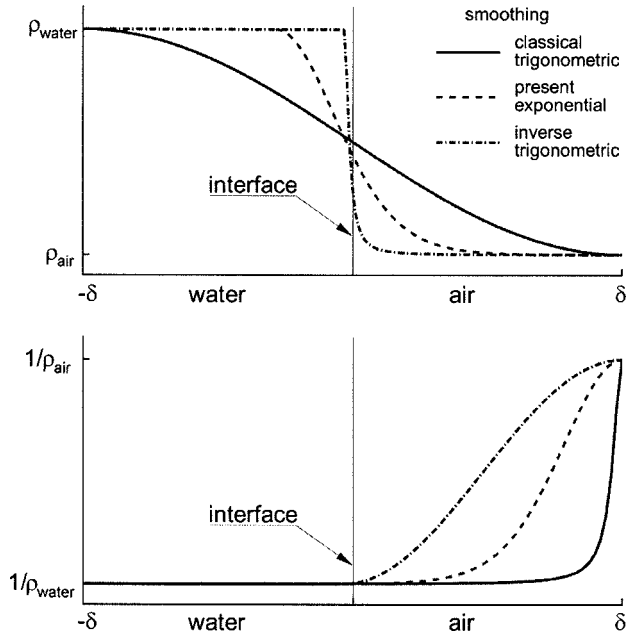

Fig. 4 Smoothing of the density and of its inverse across the interface

curvature. For such cases, a more accurate solution can be obtained by adopting

$$D_{i,j}^m = \frac{\phi_{i,j}^0}{\sqrt{A+B}}$$

$$A = \frac{\phi_{i+1,j}^0\left(\frac{1}{2}\phi_{i+1,j}^0 - \phi_{i,j}^0\right) + (\phi_{i,j}^0)^2 + \phi_{i-1,j}^0\left(\frac{1}{2}\phi_{i-1,j}^0 - \phi_{i,j}^0\right)}{\Delta x^2} \tag{20}$$

$$B = \frac{\phi_{i,j+1}^0\left(\frac{1}{2}\phi_{i,j+1}^0 - \phi_{i,j}^0\right) + (\phi_{i,j}^0)^2 + \phi_{i,j-1}^0\left(\frac{1}{2}\phi_{i,j-1}^0 - \phi_{i,j}^0\right)}{\Delta y^2}$$

but this has the drawback that it does not smooth the oscillations at the interface, and results in a poorer stability. Therefore, in the final implementation, at the interface we adopted a weighted combination of the two methods

$$\phi_{i,j}^{i+1} = \phi_{i,j}^n - \Delta\tau[(\text{sign})(\phi_{i,j}^0)|\phi_{i,j}^l| - (a_{rs}D_{i,j} + a_m D_{i,j}^m)] \tag{21}$$

and found $a_{rs}=0.8$ and $a_m=0.2$ to be suitable choices. At a wall, the level set function ϕ satisfies a symmetry boundary condition.

2.5 Smoothing Across the Interface. To avoid possibly divergent numerical oscillations, the density ρ in the region surrounding the interface has previously been defined in terms of a smooth trigonometric (bridge) function of ϕ. As a result, the transition of its inverse $1/\rho$ between $1/\rho_w$ and $1/\rho_a$ (where ρ_w and ρ_a are the densities of water and air) is shifted to the air side, and is much steeper on that side, as shown in Fig. 4. This reduces the stability of the method and the accuracy of the solution. An obvious alternative is to adopt a trigonometric smoothing of $1/\rho$, or in other words of the coefficients of the Poisson equation. However the pressure, which is the solution of this equation, is almost proportional to the density. This means that the original steepness in the transition would merely reappear in the pressure, probably to introduce oscillations and eventually instabilities in its derivatives. In the present implementation, we adopted an exponential bridge function as given in Eq. (22)

$$\rho(\phi) = \begin{cases} \rho_w \text{ if } (\phi - \delta_\rho c) < -\delta_\rho \\ \sqrt{\rho_w \rho_a}\exp\left[\frac{1}{2}\log\left(\frac{\rho_w}{\rho_a}\right)\sin\frac{\pi}{2\delta_\rho}(\phi - \delta_\rho c)\right] \\ \quad \text{if } |\phi - \delta_\rho c| < \delta_\rho \\ \rho_a \text{ if } (\phi - \delta_\rho c) > \delta_\rho \end{cases} \tag{22}$$

where the constant coefficient c is chosen to conserve the total mass according to

$$\int_{\delta_\rho(-1+c)}^{\delta_\rho(1+c)} \rho\, d\phi = \rho_w \delta_\rho(1-c) + \rho_a \delta_\rho(1+c). \tag{23}$$

For the air-water density ratio this implies $c=0.5521$. Using Eq. (22) results in a similar smoothing of the density and of its inverse, reducing the risk of oscillation both in the discretization of the Poisson equation and in the estimation of derivatives of the pressure. The difference between using Eq. (22) and the usually adopted trigonometric bridge function becomes important in the resolution of local flow details, where the mesh can be relatively coarse, and where the solution is more sensitive to the smoothing region.

In solving the conservation equations, it is the inverse of the viscosity that has to be smoothed across the interface, rather than the viscosity itself. Here we have used

$$\frac{1}{\mu}(\phi) = \begin{cases} \mu_w^{-1} \text{ if } \phi < -\delta_\mu \\ \frac{\mu_w^{-1} - \mu_a^{-1}}{2}\left(\frac{\sin(\pi\phi/\delta_\mu)}{\pi} - \frac{\phi}{\delta_\mu}\right) + \frac{\mu_w^{-1} + \mu_a^{-1}}{2} \text{ if } |\phi| < \delta_\mu \\ \mu_a - 1 \text{ if } \phi > \delta_\mu \end{cases} \tag{24}$$

Finally, the Dirac function in the surface-tension term is smoothed as

$$\delta(\phi) = \begin{cases} 0 \text{ if } |\phi| \geqslant \delta_{\text{st}} \\ \frac{1}{2\delta_{\text{st}}}\left(\cos\left(\frac{\pi\phi}{\delta_{\text{st}}}\right) - 1\right) \text{ if } |\phi| < \delta_{\text{st}} \end{cases} \tag{25}$$

In the present implementation, the half-widths δ_{lim}, δ_ρ, δ_μ, and δ_{st} of the four smoothing intervals were set constant during the computations and satisfy:

$$\delta_{\text{lim}} \geqslant \delta_\rho = \delta_\mu > \delta_{\text{st}}. \tag{26}$$

The range δ_{lim} of the variable-coefficient limiter function should be larger than δ_ρ to maintain the accuracy of the solution of the advection term in the transition region. Usually, $\delta_{\text{st}} \geqslant 0.7\Delta x$ is sufficient to prevent oscillations in the solution of the corresponding Poisson equations. Such oscillations would induce non-physical parasitic currents in both phases, though larger ones in air because of the density ratio. Therefore, if $\delta_\rho > \delta_{\text{st}}$ the gradients of p_{st} decrease more rapidly, reducing the presence of non-physical currents on the air of the interface.

The convergence and accuracy of the numerical scheme are discussed in the Appendix.

3 Results and Discussion

The flow generated by a vertical surface-piercing plate undergoing horizontal displacements has several interacting features, each of which may warrant individual attention. For this reason the numerical method described above was applied first to simpler problems, for which data are available from other sources.

3.1 The Dam Break Problem. The first test case is a dam break problem, schematically represented in Fig. 5 as an initially rectangular column of fluid of depth H and length L at rest over a

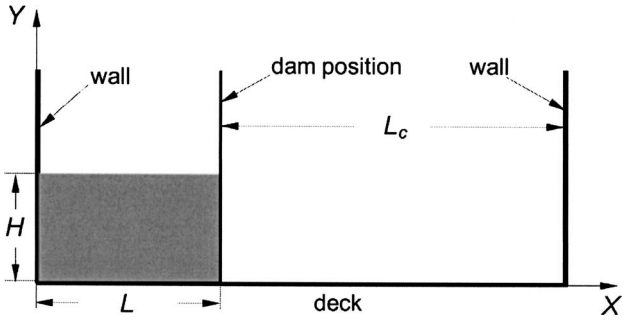

Fig. 5 Definition sketch for the dam-break problem. The shaded area represents the initial configuration of the water.

horizontal floor. On the left there is a vertical wall, on the right a vertical dam which is suddenly removed at time $t=0$. Further to the right at a distance L_c there is a second vertical wall. The origin of Cartesian coordinates (X,Y) is at the bottom left-hand corner.

The flow is characterized by the development of a tongue of liquid spreading along the floor without free-surface breaking. This problem has been widely investigated because it has practical applications and because it is a simply defined test case for verifying and validating numerical methods for handling large deformations of the free surface. The flow that develops after the liquid meets a downstream wall is more challenging and has received less attention. In this case, overturning and breaking of the free surface are observed, leading also to air entrapment.

For the dam break problem with $L/H=2$ and $L_c/H=5.4$ numerical results of two other methods were available: the Boundary Element Method (BEM) [22] and the two-phase Smoothed Particles Hydrodynamics method (SPH) [2]. The results are expressed in dimensionless form with $x=X/H$, $y=Y/H$, $\tau=t(g/H)^{1/2}$. Figure 6 shows a comparison of the free surface positions for the three different solvers at $\tau=2.2$, 2.6, 5.6, and 6.2. The displacement of the free surface is almost identical for all three schemes until the plunging jet is formed. From that point on, the flow that develops is quite violent but nevertheless the SPH and LS results remain very close. They differ from the BEM results at this stage probably because that method does not include the effect of the air underneath the jet.

The dam break problem also provides an opportunity to illustrate the differences between results of the Level-Set algorithm described above and of those present in the literature. To make the conditions as close as possible between the different solvers, the viscosity has been set to zero and free slip conditions have been implemented on the walls. For these calculations the domain has been discretized using a uniform square mesh with $\Delta x=\Delta y=1/56$. The time step was $\Delta\tau=0.002$, and the smoothing interval was $\delta=2\Delta x$.

The first difference appears as a consequence of using an exponential, rather than a trigonometric, smoothing of the density across the interface. In Fig. 7 the free surface for the two schemes are plotted at $\tau=1.59$. It can be seen that the trigonometric smoothing is characterized by instabilities near the front that are due to numerical errors, as discussed above.

The effect of different limiter functions becomes apparent at the time of the formation of the plunging jet. Figure 8(*a*) shows the free surface at $\tau=5.64$ obtained with the LS method using the variable coefficients advective scheme (Eq. (14)—plotted with a continuous line), and the minmod scheme (plotted with a broken line). Corresponding SPH results (a series of dots) agree closely with the former. In Figs. 8(*b*) and 8(*c*) the velocity field is plotted respectively for the two LS methods. It is clear that the minmod scheme has the effect of diffusing into the water the rotation that has been generated in the air.

Figure 9 shows LS results at $\tau=6.76$ obtained with different

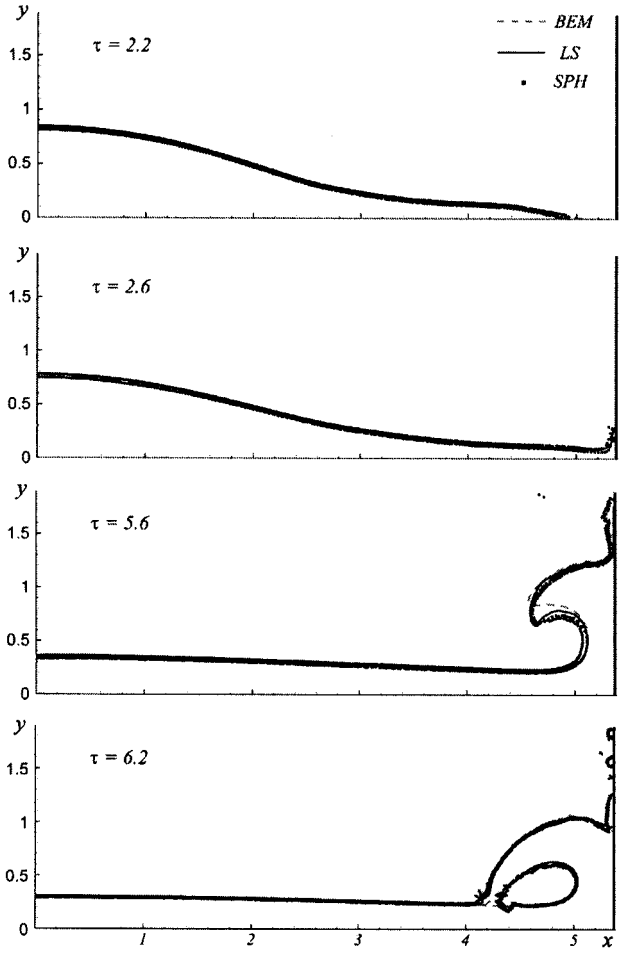

Fig. 6 Free surface evolution after the dam-break. The dashed line represents the BEM, the solid line the Level-Set, and the dotted double line the SPH.

reinitialization techniques. The broken line was obtained with the scheme described by Russo and Smereka [21], while the solid line represents the result of the present modified algorithm. The difference is most pronounced in the region against the wall on the right where a thin film of water has been smoothed out by the first technique. Using the modified algorithm a small cavity appears beneath the film, in agreement with the result of the SPH method, shown as a series of dots.

3.2 The Rising Bubble Problem. The problem of the rising bubble has been used to focus on modeling the effects of surface tension. The numerical solution of the surface tension used here is very similar to that proposed by Brackbill et al. [23] except for the splitting of that part of the pressure that is due to surface tension

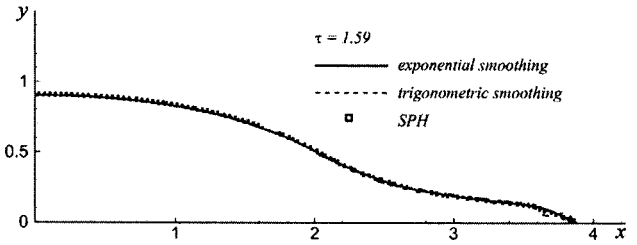

Fig. 7 Effects of different numerical schemes for smoothing at the interface in the dam break problem. Dashed line: exponential smoothing, solid line: trigonometric smoothing.

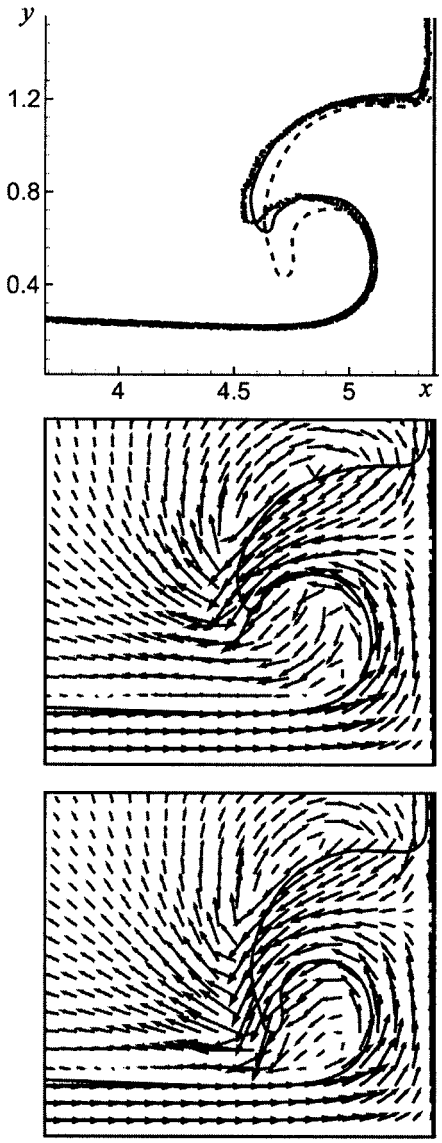

Fig. 8 Comparison of the interface location with (solid line) and without using (dashed line) the variable-coefficient limiter function. The SPH solution (dots) is used as a reference. $\tau = 5.64$.

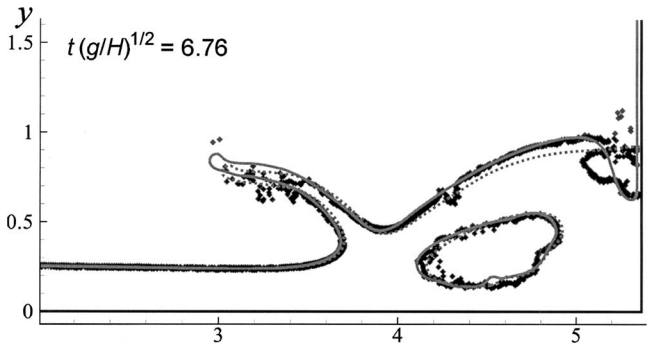

Fig. 9 Effects of different reinitialization procedures. Solid line: present reinitialization, dashed line from Russo and Smereka [21]. The two methods differ in the small cavity created at the right wall. The SPH has been used as a reference solution.

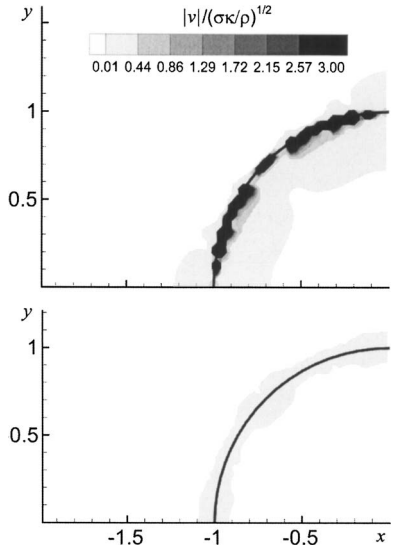

Fig. 10 Parasitic currents for different numerical solvers. Above, the classic solver (Brackbill et al. [23]); below, the present solver. $\Delta x = R/33$, $t = \Delta t = R/(2\sqrt{\sigma\kappa/\rho})$, $\delta_{st} = \delta_\rho/2 = 0.4\Delta x$.

from the other terms in the Navier-Stokes equation. To understand the numerical difference between the two schemes, the analytical solution of a flow field around a cylindrical bubble at zero gravity has been analyzed. The exact solution to this problem is zero velocity everywhere and a pressure jump across the interface that is proportional to surface tension. The numerical solution of the discrete Poisson equation introduces some numerical errors which appear as parasitic currents. Their intensity is shown in Fig. 10(*a*) for Brackbill's solver, and in Fig. 10(*b*) for the present technique. It is seen that the magnitude of the currents is reduced by an order of amplitude by the splitting technique.

A different approach is used by Liu et al. [24]; there, a sharp interface is used and the pressure jump conditions for the surface tension are imposed exactly at the interface. This methodology is challenging but particularly useful if the two phases are treated separately. In the present framework, which uses a single fluid with variable properties, the surface tension is consistently spread over a narrow region around the exact interface. The error introduced by this approximation is comparable with those associated with the advective and viscous terms.

Next the present numerical solver is applied to the rise of a cylindrical bubble like that described in the experiments by Walters and Davidson [25]. A two-dimensional bubble was formed in a water tank 9.5 mm wide by impulsively withdrawing a 25-mm-diam air-filled tube from the tank.

The problem is governed by the Reynolds number and the Weber number, and, assuming standard values for water density, viscosity and surface tension, in this case they were $\mathrm{Re} = \sqrt{gR}\rho_{water}/\mu_{water} = 1.1 \times 10^6$, and $\mathrm{We} = gR^2\rho_{water}/\sigma = 837$. Figure 11 shows both numerical and experimental results for the displacement of the interface computed with grid size $R/33$ and time step $5 \times 10^{-5}/\sqrt{g/R}$. The agreement is satisfactory throughout the whole sequence. Small differences can be explained by the effects of the glass and by the initial effect of the withdrawal of tube in the experiment (Fig. 12).

3.3 Interaction of Vorticity With a Free Surface. The third numerical test was aimed at verifying the possibility of modeling the interaction of vorticity with the free surface. The case of a rising vortex pair is analyzed, and the results compared with those from Ohring and Lugt [26]. A Reynolds number is defined in terms of the circulation of each vortex and the kinematic viscosity, $\mathrm{Re} = \Gamma\rho/2\pi\mu$, and a Froude number as $\mathrm{Fn} = \Gamma/2\pi(ga^3)^{1/2}$, where

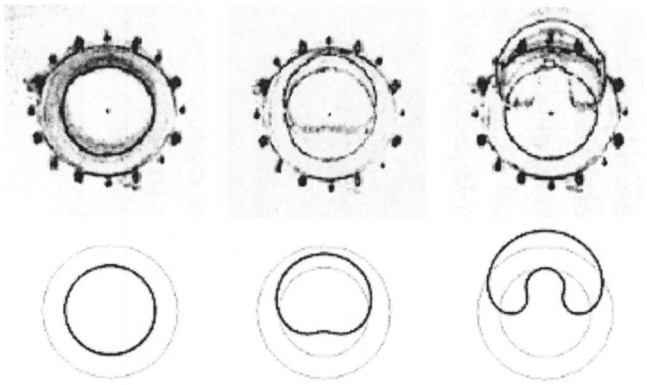

Fig. 11 2D air bubble in water. The top figures are extracted from the experiments presented by Walter and Davidson [25]. The lower figures are the numerical results. t=0.0125 s, 0.0625 s, 0.1125 s.

a is the initial distance between the vortices. In this case Re $=100$ and Fn$=0.8$; the Weber number is infinite. Time t is measured from the instant at which the vortices were at an elevation $3a$ beneath the surface.

Figure 13 presents a comparison between the results of Ohring and Lugt and those obtained here, where the same initial mesh has been used. The two methods differ in the discretization of the Navier-Stokes equation (the former is Lagrangian the latter Eulerian) and by the presence in the latter of the second phase. The agreement between the two methods is very good even though some minor differences can be seen at the moment of the formation of a region of counterclockwise vorticity (shown as dashed contour lines) close to the free surface. In this case the present method suffers from the presence of a locally coarser mesh; the Lagrangian mesh tends to be more compact at that point. But this same deformation of the mesh causes the Lagrangian method to be arrested at time $\tau=t(g/a)^{1/2}=3.475$, while the present calculation can follow the break up of the water surface above the region of strong vorticity, as shown in Fig. 14 at $\tau=4.0$ and 4.8. The grid size was $a/17$ and the time step $7\times10^{-3}/\sqrt{g/a}$.

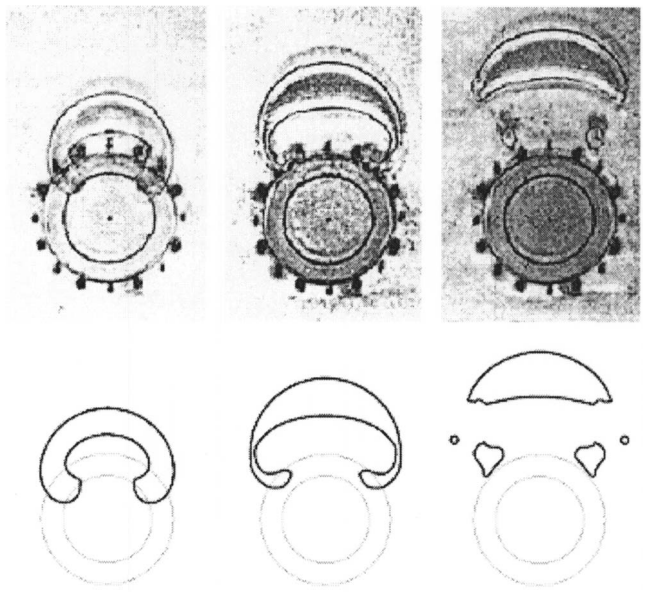

Fig. 12 See Fig. 11; t=0.1625 s, 0.2125 s, 0.2625 s

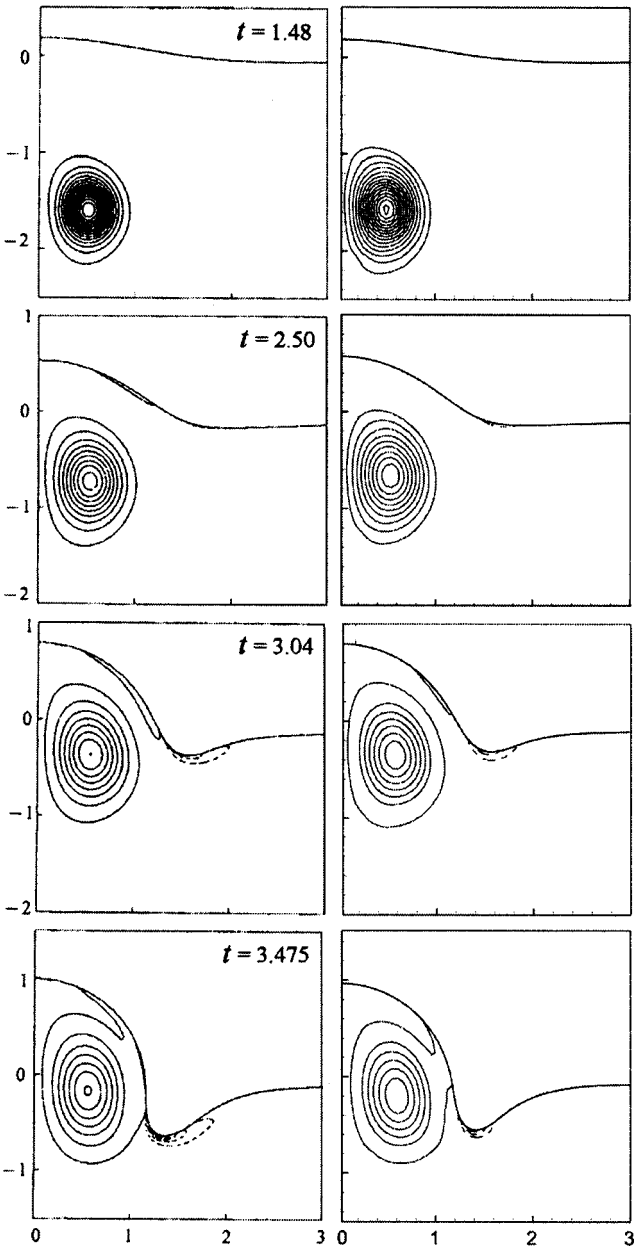

Fig. 13 Right vortex of a vortex pair rising towards a free surface. On the left the results from Ohring and Lugt [26] and on the right the present results. The continuous contours represent the clockwise rotating vorticity and the dashed contours the counterclockwise rotation.

3.4 The Surface-Piercing Plate Problem. For the purpose of comparing the results of the present numerical algorithm with measurements performed in well-defined but more challenging conditions, a simple experiment was set up with a vertical surface-piercing plate. The experiments were performed about half way along a channel that is 420 mm wide, 18 m long, with a still water depth of 700 mm, and efficient wave absorption at both ends. An aluminum vertical plate (3 mm thick) with a still water draft h of 43.7 mm was towed horizontally on a carriage, as shown in Fig. 15. Strips of soft foam on the edges of the plate provided an almost complete seal with the glass walls of the channel so that the experimental conditions were essentially two dimensional. The ratio between the water depth and the initial submergence of the plate was 16, and so for the purposes of numerical modeling it seems reasonable to assume deep water conditions. An optical

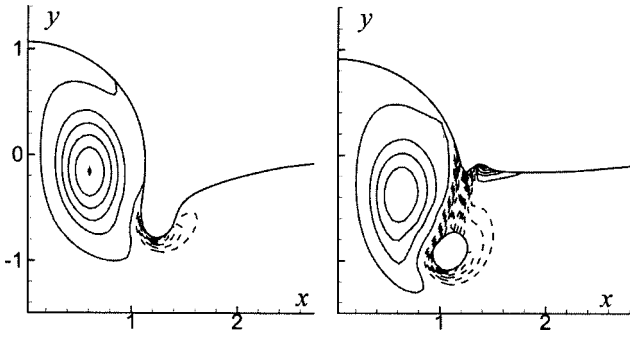

Fig. 14 Break up of the water above the vortex and formation of a region of high counterclockwise vorticity

encoder provided the displacement of the plate and the numerical simulation was driven from the same time series. The velocity of the plate for the case discussed in the following is shown in Fig. 16, reaching a maximum of $U_{max}=0.7$ m/s.

The flow was recorded from the side with a stationary high-speed video camera having a field of view 410 mm wide and 300 mm high. Fluorescent dye added to the water improved the definition of the free surface which was illuminated by a vertical laser sheet.

In Fig. 17 the deformation of the surface is shown at four instants before the impact of the plunging jet. The position of the interface in the experiment can be identified as the edge of the darker region formed by the fluorescent dye. Regions of high vorticity are made visible by the presence of bubbles that are formed by ventilation of the back of the plate. As the vortical regions are characterized by low pressure, bubbles initially remain at their centers. Since the camera was stationary, there is a parallax effect in its view of the plate during the early stages of the motion. A vertical line has been added to each image to show the position of the plate on the centerline of the channel, and in the numerical simulation.

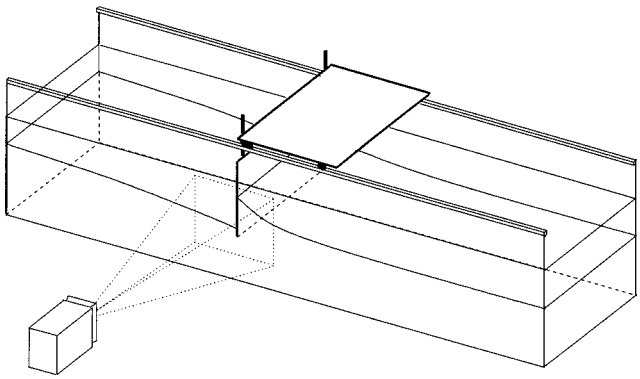

Fig. 15 Experimental arrangements

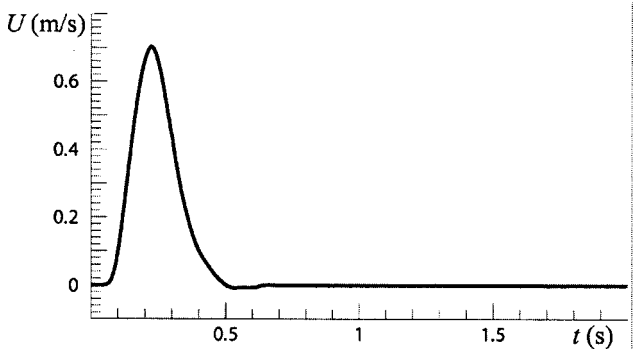

Fig. 16 Velocity of the plate in the experiments

Fig. 17 Numerical and experimental results for the flat plate moving with the velocity of Fig. 16. The shaded background represents the experiments, the water is darker grey and the free surface is almost black. The numerical results are superimposition on the experimental data. The vorticity field is highlighted in the numerical part with some contour lines; $t=0.28$ s, $t=0.34$ s, $t=0.45$ s, $t=0.52$ s.

Numerical results are superimposed in the form of a solid line representing the computed free surface, and contour lines of vorticity that detach from the bottom of the plate. These were computed with a grid size $h/35$, and time step $1.65\times10^{-4}/\sqrt{g/h}$. The overall comparison between numerical and experimental results is good, even though some differences can be seen. At $t=0.45$ s the observed jet is slightly in advance of the computed interface which is pointing further up. The difference could be due to some remaining errors in the advection of the interface, though at successive times the agreement improves again. The position of the vortical regions is captured well, as is the successive rolling up of the vortex sheet at the lower edge of the plate after $t=0.52$ s when

the plate stops.

In particular the vorticity generated at the lower tip of the plate shows a behavior similar to that described by Tsai and Yue [15] for a plate that is impulsively started. They identified three regimes, identified in terms of the Froude number $\mathrm{Fn}=U_{\max}/\sqrt{gh}$, that are related to the levels of interaction between vorticity detached at the bottom edge of the plate and free surface. In the "sub-critical" regime ($\mathrm{Fn}<0.7$), no significant interaction takes place. In the "transcritical" regime ($0.7<\mathrm{Fn}<1$), on the rear side of the plate the backwards-propagating free surface set-down interacts with the vortex sheet causing its rolling up into a series of spirals. In the supercritical regime ($\mathrm{Fn}>1$), the vortex sheet spirals result in significant interactions with the free surface.

The present case $\mathrm{Fn}=1$ (though not an impulsively started flow) is on the boundary of the transcritical and supercritical regimes and the free surface shows behavior very similar to that of the second regime. This behavior seems not to be highly affected by the steepness of the velocity-versus-time curve.

Figure 18 compares observed and predicted water surface elevations after the breaking at the front of the plate. On the whole agreement is very good. The position of the breaking and successive splash up are qualitatively very similar to the experimental data. Some differences can probably be explained partly by three-dimensional effects not visible from the side of the channel.

The prediction of the position of the vortical region is also quite accurate. After the plate has stopped, the vortex sheet detaches from it and moves downwards together with the water. After $t=0.5$ s the water flow behind the plate is deviated partially upwards with the formation of a backward plunging jet and partially downwards to flow around the lower tip of the plate. The latter convects the vorticity downwards.

4 Conclusions

A two-dimensional Level-Set method has been developed for the study of violent free surface motion. The main differences between the algorithm described here and those present in the literature are concentrated at the interface: the correction of the reinitialization technique for the Level-Set function, the introduction of an exponential smoothing of the density, the introduction of an advection scheme with variable coefficients, and the splitting of the pressure term due to surface tension. The free surface is a very sensitive area characterized by very steep gradients, and is therefore prone to the introduction of numerical errors. These errors can cause oscillations and eventually instabilities, or they can propagate from one phase to the other. The attempt that has been made here is to identify the causes of common errors and to correct them. The result is a numerical algorithm whose computational complexity has not been changed but whose stability and reliability have been markedly increased. The overall accuracy of the numerical scheme has been shown by means of comparisons with other numerical techniques and with laboratory measurements. In particular, in the complex case of a surface piercing plate moving horizontally, the features of the flow field are captured very well.

Acknowledgment

This work was supported by Ministero delle Infrastrutture e Trasporti within the Programma Sicurezza, and by the award of a scholarship to the first author from the University of Southampton.

Appendix: Accuracy and Convergence

Introduction. The accuracy and convergence of the method are examined here for the case of the dam-break problem described in Sec. 3.1. The analysis has been carried out both for local and global quantities in the following way. Given the time series of some parameter $q(t,\Delta x)$, its integral $Iq(\Delta x)$ over an interval of time $[t_0,t_f]$ is first calculated for a range of values of the discretization parameter Δx. If the exact solution $Iq(0)$ is known, the order of convergence is then equal to

$$\frac{\log\dfrac{|Iq(\Delta x_2)-Iq(0)|}{|Iq(\Delta x_1)-Iq(0)|}}{\log\dfrac{\Delta x_2}{\Delta x_1}} \tag{A1}$$

On the other hand, if the exact solution is not available, it can be approximated by applying Eq. (A1) over two different intervals in Δx, and solving

$$\frac{\log\dfrac{|Iq(\Delta x_2)-Iq(0)|}{|Iq(\Delta x_1)-Iq(0)|}}{\log\dfrac{\Delta x_2}{\Delta x_1}}=\frac{\log\dfrac{|Iq(\Delta x_3)-Iq(0)|}{|Iq(\Delta x_2)-Iq(0)|}}{\log\dfrac{\Delta x_3}{\Delta x_2}} \tag{A2}$$

for $Iq(0)$. The order of convergence can then be estimated by

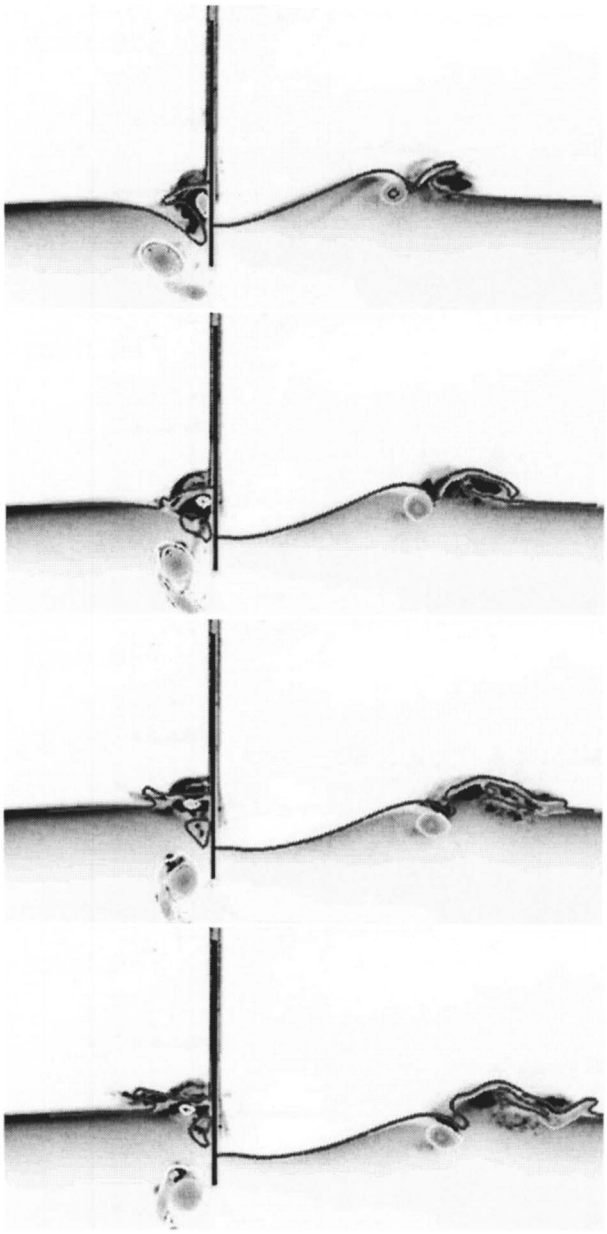

Fig. 18 Numerical and experimental results after the breaking; $t=0.64$ s, $t=0.74$ s, $t=0.80$ s, $t=0.83$ s

Table 1 Convergence of the computed horizontal position of the leading edge of the water front, and the wall pressure, with respect to Δx

Mesh	$N\times N$	$1.5N\times 1.5N$	$2N\times 2N$
Horizontal position of the water front	1.5496	1.5324	1.5283
Wall pressure at $y=0.27$	5885.90	5854.85	5824.64

substituting the result into Eq. (A1).

In the dam-break problem, three different meshes were considered: $N\times N$, $1.5N\times 1.5N$, and $2N\times 2N$, where $N=H/\Delta x=50$.

Local Parameters. The local parameters considered here are the position of the leading edge of the water front, and the pressure on the vertical wall at an elevation of $y=0.27$. The results are set out in Table 1, and indicate orders of convergence of 3.05 and 1.4, respectively. The considerable difference between these figures is explained by the fact that in the case of the position of the water front the results were computed over a time interval $(0<\tau<5.2)$ in which no wave breaking occurred. The computed pressures on the other hand were integrated over a period $(0<\tau<7.0)$ which included wave breaking, and were thus much more sensitive to small changes in the computation, as well as to the details of the interpolation needed to obtain pressures at a particular point on the wall.

Global Parameters. Three different global parameters are considered here: the total force acting on the bottom of the tank, and the mass and energy of the whole system. Changes in mass $\Delta m(\tau)$ and energy $\Delta E(\tau)$ from their initial values m_0 and E_0 are used in evaluating the accuracy of the method, since for these there is obviously an exact solution, namely zero.

The integrals $Iq(\Delta x)$ for these three global parameters are given in Table 2, leading to orders of convergence of, respectively, 3.0, 0.94, and 1.42 for the force and for variations in mass and energy.

The result for the total mass is rather poor, while a slightly better convergence is obtained for the energy. The reason for this poor convergence is shown in Figs. 19 and 20 which plot the variations of total mass and energy, respectively. Energy is lost during the violent impact against the vertical wall and also when the plunging jet in the subsequent breaking wave strikes the interface. This energy is partially recovered using the variable coefficient advective scheme, as can be seen from the difference between this and the minmod advective scheme shown in Fig. 20; but still the variation of the total energy is within a rather wide range of ±3%.

Table 2 Convergence of the force on the tank floor and changes in total mass and energy: parameters integrated over the interval $0<\tau<7.0$

Mesh	$N\times N$	$1.5N\times 1.5N$	$2N\times 2N$
Force on the tank floor	22545.644	22519.404	22508.971
Change in total mass $\Delta m/m_0$	2.3876E−3	1.6260E−3	
Change in total energy $\Delta E/E_0$	1.023E−2	5.75E−3	

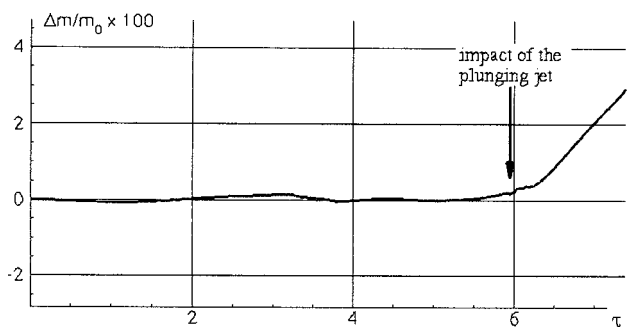

Fig. 19 Relative changes in total mass for a discretization $N\times N$

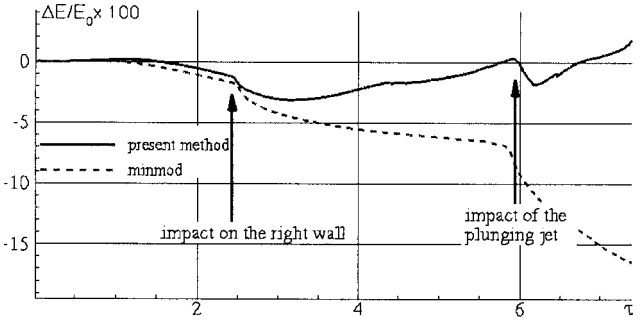

Fig. 20 Relative changes in total energy for a discretization $N\times N$

After the impact of the plunging jet on to the water below, Fig. 19 shows that there is a slight increase in computed mass. This is due to the presence of a splash up constituted of a thin layer of water whose advection becomes difficult to model both for the level set function and for the Navier-Stokes solver because of the gradients of density across it. It is also to be noted that the level set function does not identify exactly the points of intersection of the free surface with the coordinate grid. These are calculated with a postprocessor that is only first order accurate and that has a strong influence on the accuracy with which the mass can be calculated.

The Level Set Algorithm. To study the performance of the level set algorithm a classical problem has been chosen—the rotation of the Zalesak disk [27]. A disk of radius 15 and with a central gap wide 5 and long 25 rotates around a point (the origin) that is 20 below its center. The velocity components in x and y directions are, respectively,

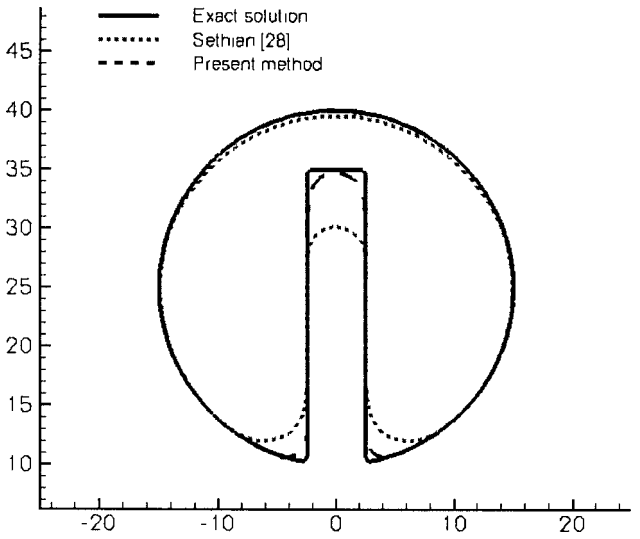

Fig. 21 Verification of the level set solutions after one revolution of the Zalesak circle

$$u = -\frac{\pi y}{314}, \quad v = \frac{\pi x}{314} \tag{A3}$$

A field 100×100 wide is discretized using $\Delta x = \Delta y = 0.5$ and a $\Delta t = 1$. In Fig. 21 the solution of the present method is compared with that obtained using the level set reinitialization described by Sethian [28]. Even though the corners of the slotted disk are not perfectly preserved the shape of this particular disk is quite well maintained.

References

[1] Harlow, F. H., and Welch, J. E., 1965, "Numerical Calculation of Time-Dependent Viscous Incompressible Flow of Fluids With Free Surface," Phys. Fluids, **8**, pp. 2182–2189.

[2] Colagrossi, A., and Landrini, M., 2002, "Numerical Simulation of 2-Phase Flows by Smoothed Particle Hydrodynamics," NuTTS, Pornichet (France).

[3] Shopov, P. J., Minev, P. D., Bazhelkov, I. B., and Zapryanov, Z. D., 1990, "Interaction of a Deformable Bubble With a Rigid Wall at Moderate Reynolds-Numbers," J. Fluid Mech., **129**, pp. 241–271.

[4] Li, W. Z., and Yan, Y. Y., 2002, "Direct-Predictor Method for Solving Steady Terminal Shape of a Gas Bubble Rising Through a Quiescent Liquid," Numer. Heat Transfer, Part B, **42**, pp. 55–71.

[5] Hirt, C. W., and Nichols, B. D., 1981, "Volume of Fluid (VOF) Method for the Dynamics of Free Boundaries," J. Comput. Phys., **39**, pp. 201–225.

[6] Scardovelli, R., and Zaleski, S., 1999, "Direct Numerical Simulation of Free-Surface and Interfacial Flow," Annu. Rev. Fluid Mech., **31**, pp. 567–603.

[7] Sussman, M., Smereka, P., and Osher, S., 1994, "A Level Set Approach for Computing Solutions to Incompressible Two Phase Flows," J. Comput. Phys., **114**, pp. 146–159.

[8] Tryggvason, G., Bunner, B., Esmaeeli, A., Juric, D., Al-Rawahi, N., Tauber, W., Han, J., Nas, S., and Jan, J. Y., 2001, "A Front-Tracking Method for the Computations of Multiphase Flow," J. Comput. Phys., **169**, pp. 798–859.

[9] Lafaurie, B., Nardone, C., Scardovelli, R., Zaleski, S., and Zanetti, G., 1994, "Modelling Merging and Fragmentation Multiphase Flows With SURFER," J. Comput. Phys., **113**, pp. 134–147.

[10] Lawson, L. J., Rudman, M., Guerra, A., and Liow, J. L., 1999, "Experimental and Numerical Comparisons of the Break-up of a Large Bubble," Exp. Fluids, **26**, pp. 524–534.

[11] Zhao, Y., Tan, H. H., and Zhang, B., 2002, "A High-Resolution Characteristics-Based Implicit Dual Time-Stepping VOF Method for Free Surface Flow Simulation on Unstructured Grids," J. Comput. Phys., **183**, pp. 233–273.

[12] Sussman, M., Almgren, A. S., Bell, J. B., Colella, P., Howell, L. H., and Welcome, M. L., 1999, "An Adaptive Level Set Approach for Incompressible Two-Phase Flow," J. Comput. Phys., **148**, pp. 81–124.

[13] Yabe, T., Xiao, F., and Utsumi, T., 2001, "The Constrained Interpolation Profile Method for Multiphase Analysis," J. Comput. Phys., **169**, pp. 556–593.

[14] Yabe, T., Ogata, Y., Takizawa, K., Kawai, T., Segawa, A., and Sakurai, K., 2002, "The Next Generation CIP as a Conservative Semi-Lagrangian Solver for Solid, Liquid and Gas," J. Comput. Appl. Math., **149**, pp. 267–277.

[15] Tsai, W. T., and Yue, D. K. P., 1993, "Interaction Between a Free Surface and a Vortex Sheet Shed in the Wake of a Surface-Piercing Plate," J. Fluid Mech., **257**, pp. 691–721.

[16] Wehausen, J. V., and Laitone, E. V., 1960, *Handbuch der Physik*, pp. 446–778.

[17] Fraigneau, Y., Guermond, J. L., and Quartapelle, L., 2001, "Approximation of Variable Density Incompressible Flows by Means of Finite Elements and Finite Volumes," Commun. Numer. Methods Eng., **17**, pp. 893–902.

[18] Colicchio, G., 2004, "Violent Disturbances and Fragmentation of Free Surfaces," School of Civil Engineering and the Environment. Southampton, University of Southampton, p. 170.

[19] Yue, W., Lin, C. L., and Patel, V. C., 2003, "Numerical Simulation of Unsteady Multidimensional Free Surface Motions by Level Set Method," Int. J. Numer. Methods Fluids, **42**, pp. 853–884.

[20] Harten, A., and Osher, S., 1987, "Uniformly High-Order Accurate Nonoscillatory Schemes. 1," SIAM (Soc. Ind. Appl. Math.) J. Numer. Anal., **24**, pp. 279–309.

[21] Russo, G., and Smereka, P., 2000, "A Remark on Computing Distance Functions," J. Comput. Phys., **163**, pp. 51–67.

[22] Greco, M., 2001, "A Two-Dimensional Study of Green-Water Loading," *Marine Hydrodynamics*, Trondheim, NTNU.

[23] Brackbill, J. U., Kothe, D. B., and Zemach, C., 1992, "A Continuum Method for Modeling Surface Tension," J. Comput. Phys., **100**, pp. 335–354.

[24] Liu, X., Fedkiw, R. P., and Kand, M., 2003, "A Boundary Condition Capturing Methods for Poisson's Equation on Irregular Domains," J. Comput. Phys., **160**, pp. 151–178.

[25] Walters, J. K., and Davidson, J. F., 1962, "The Inital Motion of a Gas Bubble Formed in an Inviscid Liquid," J. Fluid Mech., **12**, pp. 408–416.

[26] Ohring, S., and Lugt, H. J., 1991, "Interaction of a Viscous Vortex Pair With a Free-Surface," J. Fluid Mech., **227**, pp. 47–70.

[27] Zalesak, S. T., 1979, "Fully Multidimensional Flux-Corrected Transport Algorithms for Fluids," J. Comput. Phys., **31**, pp. 335–362.

[28] Sethian, J. A., 1999, *Level Set Methods and Fast Marching Methods: Evolving Interfaces in Computational Geometry, Fluid Mechanics, Computer Vision and Materials Science*, Cambridge University Press, Cambridge.

Low Reynolds Number Film Flow Down a Three-Dimensional Bumpy Surface

C. Y. Wang
Professor
Departments of Mathematics and Mechanical Engineering,
Michigan State University,
East Lansing, MI 48824
e-mail: cywang@mth.msu.edu

The slow film flow down a doubly periodic bumpy surface is studied for the first time. Perturbations on the primary variables and the complex boundary conditions lead to a system of successive equations. The secondary flow and the free surface shape depend on the wavelength of the bumps and a surface tension-inclination parameter. There exists an optimum aspect ratio of the protuberances for maximal flow rate.
[DOI: 10.1115/1.2060730]

1 Introduction

The study of a fluid film flowing down an inclined plane is basic in coating flows, film cooling, and vapor-fluid reaction processes. In many cases the plane is not smooth and flat, but has some periodic texture. Previous theoretical work on film flow on corrugated plates used perturbation methods or numerical integration. Essentially the perturbation methods assume the amplitude of the corrugations is either small compared to the thickness of the film [1–3], or when the film is thin, small compared to its wavelength [4–6]. If the amplitude is not small, numerical methods are needed [7,8].

The above sources all considered two-dimensional corrugations. For three-dimensional bumpy surfaces, which occur due to intentional texture or surface roughness, most existing methods are inapplicable. We shall assume small Reynolds number and small amplitude compared to the film thickness and use a perturbation method.

2 Formulation

Figure 1(*a*) shows a three-dimensional bumpy plate inclined at an angle γ from the horizontal. Since the surface is fully three-dimensional, a two-dimensional stream function cannot be defined and the primitive variables (velocities, pressure) need to be used. In a Cartesian coordinate system (x',y',z') let $z'=0$ represent the mean free surface of the film and let x' be the direction of steepest descent of the mean surface [Fig. 1(*b*)]. The Navier-Stokes equations are

$$u'u'_{x'}+v'u'_{y'}+w'u'_{z'}=-p'_{x'}/\rho+\nu\nabla^2u'+g\sin\gamma \tag{1}$$

$$u'v'_{x'}+v'v'_{y'}+w'v'_{z'}=-p'_{y'}/\rho+\nu\nabla^2v' \tag{2}$$

$$u'w'_{x'}+v'w'_{y'}+w'w'_{z'}=-p'_{z'}/\rho+\nu\nabla^2w'+g\cos\gamma \tag{3}$$

where (u',v',w') are Cartesian velocity components, p' is the pressure, ρ is the density, ν is the kinematic viscosity, and g is the gravitational acceleration. The continuity equation is

$$u'_{x'}+v'_{y'}+w'_{z'}=0 \tag{4}$$

The bottom surface is assumed to be doubly periodic

$$z'=a+b\sin(2\pi x'/L_1)\sin(2\pi y'/L_2) \tag{5}$$

where a is the mean thickness of the film, b is the amplitude of the bumps, and L_1,L_2 are their wavelengths in the x',y' directions, respectively. On this bottom surface, the velocities are zero

$$u'=0,\quad v'=0,\quad w'=0 \tag{6}$$

On the hitherto unknown free surface at

$$z'=bf(x',y') \tag{7}$$

the normal velocity is zero and the shear stresses are zero (in the two principal directions)

$$T'_{ns}=0,\quad T'_{nt}=0 \tag{8}$$

See the Appendix for the definition of the principal orthogonal (n,s,t) directions. The normal stress balances the ambient pressure p'_a and the surface tension

$$T'_{nn}=-p'_a-2\sigma H'(x',y') \tag{9}$$

where σ is the surface tension coefficient and H' is the mean curvature [9]

$$H'=\frac{(1+b^2f_{x'}^2)bf_{y'y'}+(1+b^2f_{y'}^2)bf_{x'x'}-2b^3f_{x'}f_{y'}f_{x'y'}}{2(1+b^2f_{x'}^2+b^2f_{y'}^2)^{3/2}} \tag{10}$$

As it stands, the problem is formidable even numerically.

We assume the Reynolds number is small and the flow is laminar and stable. When $b=0$, the bottom plate is smooth and the solution is half the Poiseuille flow

$$u'=\frac{g\sin\gamma}{2\nu}(a^2-z'^2),\quad v'=w'=0 \tag{11}$$

$$p'=p'_a+\rho g\cos\gamma z' \tag{12}$$

We shall perturb from this state. Normalize all lengths by the film depth a, all velocities by $g\sin\gamma a^2/(2\nu)$, the pressure and stress by $\rho g\sin\gamma a/2$ and drop primes. For small amplitudes, let

$$\varepsilon\equiv b/a\ll 1 \tag{13}$$

The Navier-Stokes and the continuity equations reduce to

$$R(uu_x+vu_y+wu_z)=-p_x+\nabla^2u+2 \tag{14}$$

$$R(uv_x+vv_y+wv_z)=-p_y+\nabla^2v \tag{15}$$

$$R(uw_x+vw_y+ww_z)=-p_z+\nabla^2w+2\cot\gamma \tag{16}$$

Contributed by the Fluids Engineering Division for publication in the JOURNAL OF FLUIDS ENGINEERING. Manuscript received by the Fluids Engineering Division November 8, 2004; final manuscript received May 6, 2005. Associate Editor: S. Balachandar.

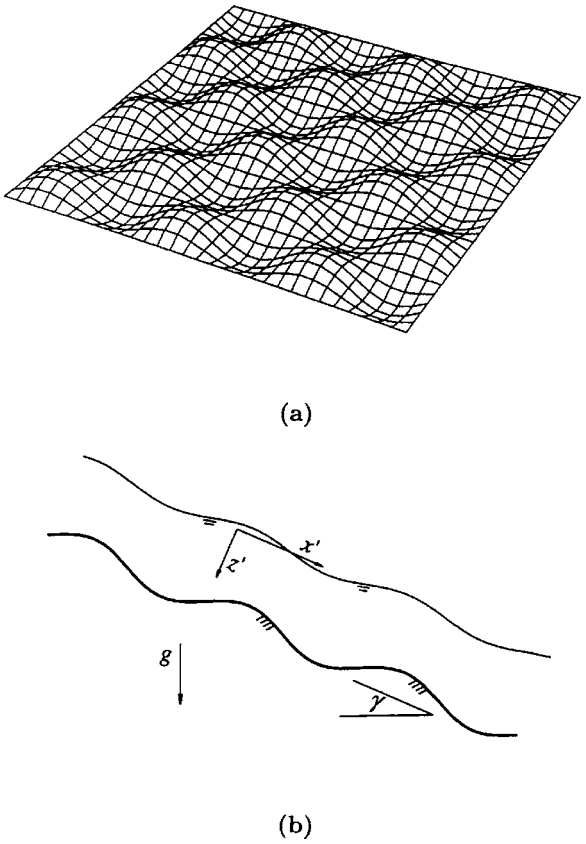

Fig. 1 (*a*) The three-dimensional bumpy surface; (*b*) A cross section of the film

$$u_x + v_y + w_z = 0 \tag{17}$$

The Reynolds number $g \sin \gamma a^3/(2\nu^2)$ is assumed to be small. Let $R=\varepsilon\eta$ where η is of order 1. The dependent variables are perturbed as follows:

$$u = 1 - z^2 + \varepsilon u_1 + \varepsilon^2 u_2 + \cdots \tag{18}$$

$$v = \varepsilon v_1 + \varepsilon^2 v_2 + \cdots \tag{19}$$

$$w = \varepsilon w_1 + \varepsilon^2 w_2 + \cdots \tag{20}$$

$$p = p_a + 2 \cot \gamma z + \varepsilon p_1 + \varepsilon^2 p_2 + \cdots \tag{21}$$

$$f = f_1(x,y) + \varepsilon f_2(x,y) + \cdots \tag{22}$$

Equations (14)–(17) yield for the first order

$$0 = -p_{1x} + \nabla^2 u_1, \tag{23}$$

$$0 = -p_{1y} + \nabla^2 v_1 \tag{24}$$

$$0 = -p_{1z} + \nabla^2 w_1 \tag{25}$$

$$u_{1x} + v_{1y} + w_{1z} = 0 \tag{26}$$

and the second order

$$\eta[(1-z^2)u_{1x} - 2z w_1] = -p_{2x} + \nabla^2 u_2 \tag{27}$$

$$\eta(1-z^2)v_{1x} = -p_{2y} + \nabla^2 v_2 \tag{28}$$

$$\eta(1-z^2)w_{1x} = -p_{2z} + \nabla^2 w_2 \tag{29}$$

$$u_{2x} + v_{2y} + w_{2z} = 0 \tag{30}$$

The boundary conditions are more complex. The velocities are zero on the bottom plate at

$$z = 1 + \varepsilon \sin(\alpha x)\sin(\beta y) \tag{31}$$

where $\alpha \equiv 2\pi a/L_1$ and $\beta \equiv 2\pi a/L_2$. Thus

$$\begin{aligned} u|_{z=1+\varepsilon \sin(\alpha x)\sin(\beta y)} = {} & u|_1 + \varepsilon \sin(\alpha x)\sin(\beta y) u_z|_1 \\ & + \varepsilon^2 \sin^2(\alpha x)\sin^2(\beta y) u_{zz}|_1/2 + \cdots = \varepsilon[u_1|_1 \\ & - 2\sin(\alpha x)\sin(\beta y)] + \varepsilon^2[u_2|_1 \\ & + \sin(\alpha x)\sin(\beta y) u_{1z}|_1 - \sin^2(\alpha x)\sin^2(\beta y)] \\ & + \cdots = 0 \end{aligned} \tag{32}$$

Similarly

$$\varepsilon v_1|_1 + \varepsilon^2[v_2|_1 + \sin(\alpha x)\sin(\beta y) v_{1z}|_1] + \cdots = 0 \tag{33}$$

$$\varepsilon w_1|_1 + \varepsilon^2[w_2|_1 + \sin(\alpha x)\sin(\beta y) w_{1z}|_1] + \cdots = 0 \tag{34}$$

On the top free surface

$$z = \varepsilon f(x,y) \tag{35}$$

the normal velocity is zero. From Eq. (A2) of the Appendix this is

$$\varepsilon f_x u + \varepsilon f_y v - w = 0 \tag{36}$$

An expansion about $z=0$ yields

$$\begin{aligned} & \varepsilon(f_{1x} - w_1|_0) + \varepsilon^2(f_{2x} + f_{1x} u_1|_0 + f_{1y} v_1|_0 - f_1 w_{1z}|_0 - w_2|_0) + \cdots \\ & = 0 \end{aligned} \tag{37}$$

Using a computer with symbolic capabilities, Eqs. (18)–(22) and (A5)–(A9) give

$$\begin{aligned} T_{nn} = {} & -p_a - 2\cot\gamma z + \varepsilon(-p_1 + 2w_{1z} + 4f_x z) + \varepsilon^2\{-p_2 - 2[f_x(u_{1z} \\ & + w_{1x}) + f_y(v_{1z} + w_{1y}) - w_{2z}]\} + \cdots \end{aligned} \tag{38}$$

$$\begin{aligned} T_{ns} = {} & 2z - \varepsilon(u_{1z} + w_{1x}) + \varepsilon^2[-u_{2z} - w_{2x} + 2f_x(u_{1x} - w_{1z}) + f_y(u_{1y} \\ & + v_{1x}) - (4f_x^2 + f_y^2)z] + \cdots \end{aligned} \tag{39}$$

$$\begin{aligned} T_{nt} = {} & -\varepsilon(v_{1z} + w_{1y}) + \varepsilon^2[-v_{2z} - w_{2y} + f_x(u_{1y} + v_{1x}) + 2f_y(v_{1y} \\ & - w_{1z}) - 4f_x f_y z] + \cdots \end{aligned} \tag{40}$$

A further expansion about $z=0$ gives

$$\begin{aligned} T_{nn}|_{\varepsilon f} = {} & -p_a + \varepsilon(2w_{1z}|_0 - p_1 - 2f_1\cot\gamma) + \varepsilon^2[2w_{2z} - p_2 \\ & - 2f_{1x}(u_{1z} + w_{1x}) - 2f_{1y}(v_{1z} + w_{1y}) + f_1(-p_{1z} + 2w_{1zz} \\ & + 4f_{1x}) - 2\cot\gamma f_2]|_0 + \cdots \end{aligned} \tag{41}$$

$$\begin{aligned} T_{ns}|_{\varepsilon f} = {} & \varepsilon(2f_1 - u_{1z} - w_{1x})|_0 + \varepsilon^2[2f_2 - u_{2z} - w_{2x} + f_{1y}(u_{1y} + v_{1x}) \\ & + 2f_{1x}(u_{1x} - w_{1z}) - f_1(u_{1zz} + w_{1xz})]|_0 + \cdots \end{aligned} \tag{42}$$

$$\begin{aligned} T_{nt}|_{\varepsilon f} = {} & -\varepsilon(v_{1z} + w_{1y})|_0 + \varepsilon^2[-v_{2z} - w_{2y} + 2f_{1y}(v_{1y} - w_{1z}) \\ & + f_{1x}(u_{1y} + v_{1x}) - f_1(v_{1zz} + w_{1yz})]|_0 + \cdots \end{aligned} \tag{43}$$

Thus the boundary conditions on the free surface is

$$T_{ns}|_{\varepsilon f} = 0, \quad T_{nt}|_{\varepsilon f} = 0 \tag{44}$$

and form Eq. (9)

$$T_{nn}|_{\varepsilon f} = -p_a - 2\lambda H \tag{45}$$

where $\lambda \equiv 2\sigma/(\rho g a^2 \sin\gamma)$ and

$$H = \varepsilon(f_{1xx} + f_{1yy})/2 + \varepsilon^2(f_{2xx} + f_{2yy})/2 + \cdots \tag{46}$$

The solution is found by solving the equations for successive orders of ε.

3 The First Order Solution

Guided by Eq. (30) and the boundary condition Eq. (32), let

$$u_1 = e^{i\alpha x}\sin(\beta y)U(z), \quad v_1 = e^{i\alpha x}\cos(\beta y)V(z), \quad w_1 = e^{i\alpha x}\sin(\beta y)W(z) \tag{47}$$

$$p_1 = e^{i\alpha x}\sin(\beta y)P(z), \quad f_1 = e^{i\alpha x}\sin(\beta y)C \tag{48}$$

where the upper case functions may be complex but the real part of the product is implied. Then Eqs. (23)–(26) yield

$$U'' - \delta^2 U - i\alpha P = 0 \tag{49}$$

$$V'' - \delta^2 V - \beta P = 0 \tag{50}$$

$$W'' - \delta^2 W - P' = 0 \tag{51}$$

$$i\alpha U - \beta V + W' = 0 \tag{52}$$

where $\delta^2 \equiv \alpha^2 + \beta^2$. From Eqs. (32)–(34), (37), (44), and (45) the boundary conditions are

$$U(1) = -2i, \quad V(1) = 0, \quad W(1) = 0 \tag{53}$$

$$i\alpha C - W(0) = 0 \tag{54}$$

$$U'(0) + i\alpha W(0) - 2C = 0 \tag{55}$$

$$V'(0) + \beta W(0) = 0 \tag{56}$$

$$2W'(0) - P(0) - 2C\cot\gamma = C\delta^2\lambda \tag{57}$$

If pressure P and the constant C are eliminated, Eqs. (49)–(57) is a set of sixth order ordinary differential equations with six boundary conditions.

Eliminate P from Eqs. (49) and (50) and also from Eqs. (50) and (51), and then substitute W and U into Eq. (52) give

$$\left(\frac{d^2}{dz^2} - \delta^2\right)^2 V = 0 \tag{58}$$

The governing equations for U and W are similar. The general solution can be written as

$$U = a_1\cosh(\delta z) + a_2\sinh(\delta z) + a_3 z\cosh(\delta z) + a_4 z\sinh(\delta z) \tag{59}$$

$$V = b_1\cosh(\delta z) + b_2\sinh(\delta z) + b_3 z\cosh(\delta z) + b_4 z\sinh(\delta z) \tag{60}$$

$$W = c_1\cosh(\delta z) + c_2\sinh(\delta z) + c_3 z\cosh(\delta z) + c_4 z\sinh(\delta z) \tag{61}$$

From Eq. (50)

$$P = \frac{2\delta}{\beta}[b_3\sinh(\delta z) + b_4\cosh(\delta z)] \tag{62}$$

Equations (59)–(62) are then back substituted into Eqs. (49)–(52). Comparing similar terms, the following independent relations are obtained

$$\beta a_3 = i\alpha b_3, \quad \beta a_4 = i\alpha b_4 \tag{63}$$

$$\beta c_3 = \delta b_4, \quad \beta c_4 = \delta b_3 \tag{64}$$

$$c_4 + \delta c_1 + i\alpha a_2 - \beta b_2 = 0 \tag{65}$$

$$c_3 + \delta c_2 + i\alpha a_1 - \beta b_1 = 0 \tag{66}$$

The boundary conditions Eqs. (53)–(57) give

$$a_1\cosh\delta + a_2\sinh\delta + a_3\cosh\delta + a_4\sinh\delta = -2i \tag{67}$$

$$b_1\cosh\delta + b_2\sinh\delta + b_3\cosh\delta + b_4\sinh\delta = 0 \tag{68}$$

$$c_1\cosh\delta + c_2\sinh\delta + c_3\cosh\delta + c_4\sinh\delta = 0 \tag{69}$$

$$c_1 = i\alpha C \tag{70}$$

$$\delta a_2 + a_3 + i\alpha c_1 = 2C \tag{71}$$

$$\delta b_2 + b_3 + \beta c_1 = 0 \tag{72}$$

$$2\delta c_2 + 2c_3 - 2\delta b_4/\beta = C(\delta^2\lambda + 2\cot\gamma) \equiv B \tag{73}$$

The unknown coefficients are solved as follows. Use Eqs. (63) and (64) to eliminate a_3, a_4, c_3, c_4 from the rest of the equations. Then Eqs. (64) and (73) give

$$c_2 = B/(2\delta) \tag{74}$$

Eliminating c_1, b_3 from Eqs. (65) and (70)–(72) yields

$$a_2 = C(\delta^2 + \beta^2)/\delta^3 \tag{75}$$

$$b_2 = i\alpha\beta C/\delta^3 \tag{76}$$

Using these results eliminate c_1 from Eqs. (69) and (72) to obtain

$$(1 - \delta\tanh\delta)b_3 - \delta b_4 = B\beta\tanh\delta/(2\delta) - \delta b_2 \tag{77}$$

After some work, Eqs. (67) and (68) give

$$\delta^2\cosh\delta b_3 + (\delta\cosh\delta + \delta^2\sinh\delta)b_4 = -2\alpha\beta - B\beta\cosh\delta/2 + \delta^2\sinh\delta b_2 \tag{78}$$

from Eqs. (77) and (78) which b_3, b_4 are obtained. The results are

$$C = -\frac{i[B\delta + \cosh\delta(4\alpha\delta - B\sinh\delta)]}{\alpha\delta[3 + 2\delta^2 + \cosh(2\delta)]} \tag{79}$$

$$a_1 = i[8\alpha\delta^2(2\alpha^2 - 3\delta + 2\alpha^2\delta^2 - 2\delta^4) + B(\beta^2 + \delta^2 + 4\alpha^2\delta^2 + 4\alpha^2\delta^4)\cosh\delta - 8\alpha\delta^4\cosh(2\delta) - B(\beta^2 + \delta^2)\cosh(3\delta) + 8B\beta^2\delta\sinh\delta + 4B\delta^3\sinh\delta + 8\alpha\delta(\beta^2 + \delta^2 + \alpha^2\delta^2)\sinh(2\delta)]/\{4\alpha\delta^4\cosh\delta[3 + 2\delta^2 + \cosh(2\delta)]\} \tag{80}$$

$$a_2 = (\beta^2 + \delta^2)C/\delta^3 \tag{81}$$

$$a_3 = \alpha^2(1 + \delta^2)C/\delta^2 \tag{82}$$

$$a_4 = i\alpha[B(1 - \delta^2) - 8\alpha\delta^2\cosh\delta - B(1 + \delta^2)\cosh(2\delta) + 8\alpha\delta(1 + \delta^2)\sinh\delta]/\{2\delta^3[3 + 2\delta^2 + \cosh(2\delta)]\} \tag{83}$$

$$b_1 = \beta[B(4\delta^4 + 4\delta^2 - 1)\cosh\delta + B\cosh(3\delta) - 8B\delta\sinh\delta + 16\alpha\delta^2(1 + \delta^2) + 8\alpha\delta(\delta^2 - 1)\sinh(2\delta)]/\{4\delta^4\cosh\delta[3 + 2\delta^2 + \cosh(2\delta)]\} \tag{84}$$

$$b_2 = i\alpha\beta C/\delta^3 \tag{85}$$

$$b_3 = -i\alpha\beta(1 + \delta^2)C/\delta^2 \tag{86}$$

$$b_4 = -i\beta a_4/\alpha \tag{87}$$

$$c_1 = i\alpha C \tag{88}$$

$$c_2 = B/(2\delta) \tag{89}$$

$$c_3 = -i\delta a_4/\alpha \tag{90}$$

$$c_4 = -i\alpha(1 + \delta^2)C/\delta \tag{91}$$

It is interesting to note that the surface tension and inclination

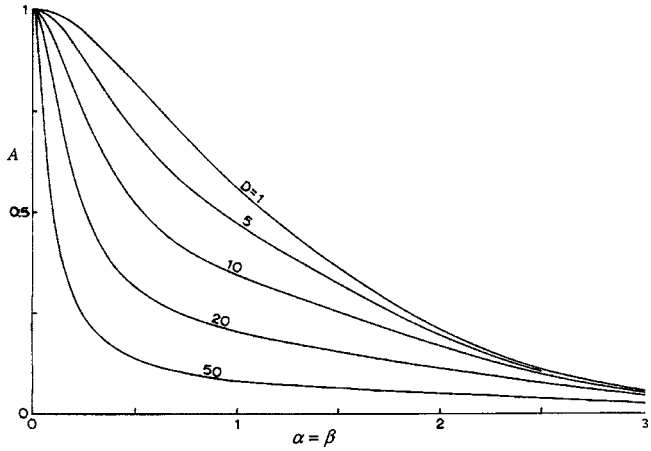

Fig. 2 Amplitude of the free surface ($\alpha=\beta$)

effects enter in the combination of

$$D \equiv \delta^2\lambda + 2\cot\gamma \tag{92}$$

Since $B=CD$ we solve for C from Eq. (79) to obtain

$$C = -iA\exp(i\phi) \tag{93}$$

where A is the amplitude and ϕ is the phase

$$A = 4\alpha\delta\cosh\delta/\sqrt{q_1^2+q_2^2}, \quad \phi = \arctan(q_2/q_1) \tag{94}$$

and

$$q_1 = \alpha\delta[3+2\delta^2+\cosh(2\delta)], \quad q_2 = (\cosh\delta\sinh\delta-\delta)D \tag{95}$$

The free surface is described by the real part of Eq. (48)

$$f_1 = A\sin(\beta y)\sin(\alpha x+\phi) \tag{96}$$

Figure 2 shows the amplitude A as a function of wave number $\alpha(=\beta)$ for various values of the parameter D. It is seen that the surface amplitude tends to one (as large as the bottom amplitude) when wave number α is small (long wave lengths), and decreases to zero with increased α. A higher surface tension or smaller inclination angle also tend to smooth out the free surface. Figure 3 shows the phase of the free surface lags behind that of the bottom surface. There is no lag for zero or infinite wave numbers, and a maximum lag exists for some wave number. Increased surface tension increases the phase lag.

The vorticity vector is given by

$$\vec{\varsigma} = \nabla\times\{u,v,w\} = \{\varepsilon e^{i\alpha x}\cos(\beta y)(\beta W - V'), -2z - \varepsilon e^{i\alpha x}\sin(\beta y) \times (i\alpha W - U'), \varepsilon e^{i\alpha x}\cos(\beta y)(i\alpha V - \beta U)\} \tag{97}$$

We see that vorticity is dominated by the Poiseuille value of $-2z$.

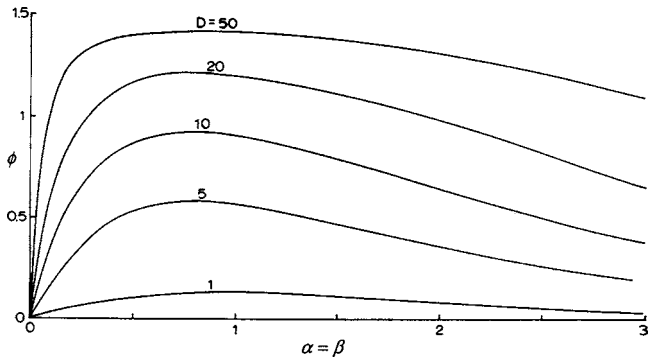

Fig. 3 Phase lag of the free surface ($\alpha=\beta$)

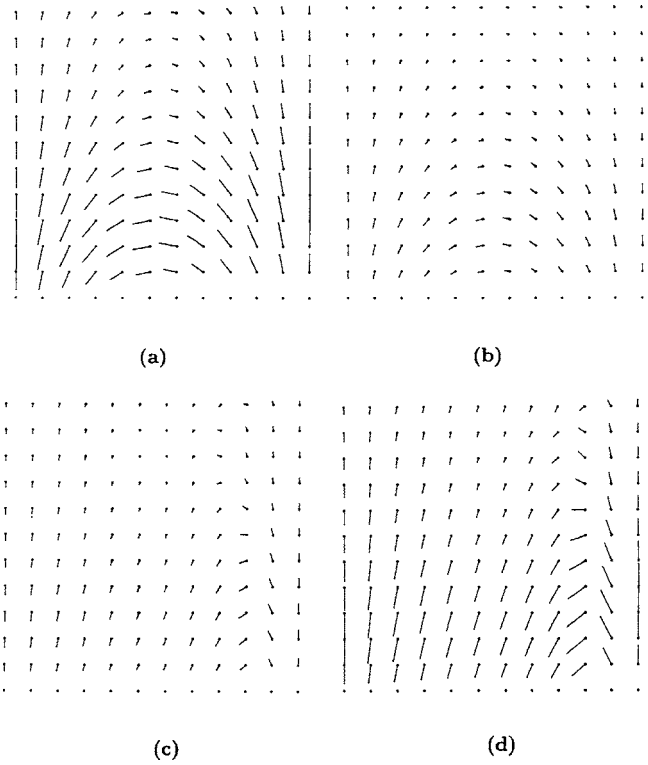

Fig. 4 Typical secondary flow velocity vectors ($\alpha=\beta=\pi$, $D=5$). The square domain is $0\leq z\leq 1$ and $-0.5\leq y\leq 0.5$; (a) $x=0$; (b) $x=0.375$; (c) $x=0.625$; (d) $x=1$.

However, the bottom three-dimensional unevenness induces vorticity in all three directions.

The flow field is also dominated by the parabolic x-direction velocity. The secondary flow caused by the bumpiness can be described by the vectors constructed by v_1 and w_1 for each constant x plane. Typical secondary velocity vectors are shown in Fig. 4. Periodic extensions in the y-directions are understood. The fluid is pushed sideways due to the three-dimensional bumps.

4 The Flow Rate

The change in flow rate due to the unevenness is of second order. Let an overbar denote the average, in one period, in both x and y directions. Since the first order solutions has no mean, the second order equations, Eqs. (27)–(30) become

$$0 = \bar{u}_{2zz}, \quad 0 = \bar{v}_{2zz}, \quad 0 = -\bar{p}_{2z} + \bar{w}_{2zz}, \quad \bar{w}_{2z} = 0 \tag{98}$$

Note the Reynolds stress terms have no mean. Due to symmetry, $\bar{v}_2=0$. Equation (98) gives

$$\bar{u}_2 = d_1 + d_2 z, \quad \bar{w}_2 = d_3, \quad \bar{p}_2 = d_4 \tag{99}$$

where the d's are constants. From Eq. (32)

$$\bar{u}_2|_1 = -\overline{\sin(\alpha x)\sin(\beta y)u_{1z}}|_1 - \overline{\sin^2(\alpha x)\sin^2(\beta y)} \tag{100}$$

or

$$d_1 + d_2 = \mathrm{Im}[U'(1)]/4 - 1/4 \tag{101}$$

Similarly from Eq. (34)

$$d_3 = \mathrm{Im}[W'(1)]/4 \tag{102}$$

Equation (42) yields

$$d_2 = \overline{[f_{1y}(u_{1y}+v_{1x})+2f_{1x}(u_{1x}-w_{1z})-f_1(u_{1zz}+w_{1xz})]}\big|_0$$
$$= \mathrm{Re}\{C^*[(\beta^2+2\alpha^2)U(0)+i\alpha\beta V(0)+i\alpha W'(0)-U''(0)]/4\} \quad (103)$$

Here C^* is the complex conjugate of C. The rest of the boundary conditions can also be satisfied. Consider first the expansion of the integral

$$I = \int_{\varepsilon f}^{1+\varepsilon g} u\,dz$$
$$= \int_0^1 u\,dz + (\varepsilon g u + \varepsilon^2 g^2 u_z/2)\big|_1 - (\varepsilon f u + \varepsilon^2 f^2 u_z/2)\big|_0 + \cdots$$
$$= \int_0^1 u_0\,dz + \varepsilon\left[\int_0^1 u_1\,dz + g u_0\big|_1 - f_1 u_0\big|_0\right]$$
$$+ \varepsilon^2\left[\int_0^1 u_2\,dz + g u_1\big|_1 + g^2 u_{0z}\big|_1/2 - (f_1 u_1 + f_2 u_0)\big|_0 - f_1^2 u_{0z}\big|_0/2\right] + \cdots \quad (104)$$

The average flow rate is then

$$\bar{F} = \overline{\int_{\varepsilon f_1+\varepsilon^2 f_2+\cdots}^{1+\varepsilon\,\sin(\alpha x)\sin(\beta y)} (u_0+\varepsilon u_1+\varepsilon^2 u_2+\cdots)\,dz}$$
$$= \int_0^1 \overline{u_0}\,dz + \varepsilon^2\left[\int_0^1 \bar{u}_2\,dz + \overline{\sin(\alpha x)\sin(\beta y)u_1\big|_1} - \overline{f_1 u_1\big|_0} - 1/4\right] + \cdots$$
$$= \tfrac{2}{3}[1-\varepsilon^2\chi+O(\varepsilon^4)] \quad (105)$$

where

$$\chi = \tfrac{3}{8}\,\mathrm{Re}[iU'(1)-iU(1)+C^*U(0)+2d_2+2] \quad (106)$$

The parameter χ, multiplied by ε^2, represents the fractional decrease in flow due to the bottom bumpiness. In order to show the effect of the aspect ratio of the bumps on the flow rate, we define

$$\kappa = \alpha\beta, \quad AR = \beta/\alpha \quad (107)$$

where κ represents inverse of the area of a bump and AR is the aspect ratio, longitudinal period to the transverse period. We find that the effect of the surface tension factor D is minimal on the flow rate. For example, for $\kappa=1$ and $AR=1$ the value of χ varies from 1.751 ($D=0.1$) to 1.789 ($D=10$). The effect of aspect ratio is much stronger. Figure 5 shows for fixed AR, χ decreases with κ. For fixed κ, χ first decreases then increases with AR. Thus an optimum AR exists for maximum flow rate (minimum κ). Table 1 shows this minimum for various κ values.

Notice that unless κ is very small, the optimum aspect ratio lies in the range of 1.5–1.8, i.e., lengthened in the flow direction.

5 Discussions

The analysis of three-dimensional film flow over a surface with periodic bumps is studied here for the first time. The problem is much more difficult than the two-dimensional flow over a wavy surface. The boundary conditions are more complicated, especially the free surface stress conditions. Also, the absence of a convenient stream function necessitates the use of many primary variables.

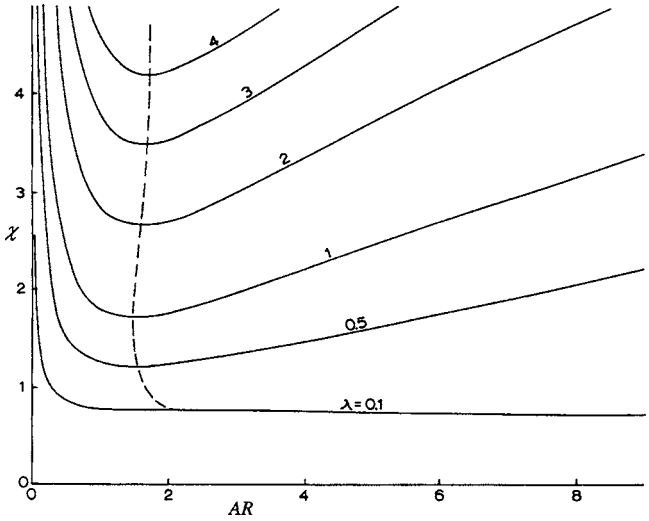

Fig. 5 The decrease in flow rate χ. Dashed curve is the locus of the optimum aspect ratio.

For small amplitude bumps on the bottom surface, the top free surface has a similar structure, but with a phase lag and decreased amplitude which are dependent on the wave length and a surface tension-inclination combination D [Eq. (92)]. The secondary transverse flow and spatial distribution of vorticity are both peculiar to three-dimensional flow.

The inertial Reynolds number terms enter the second order, but do not affect the flow rate. We find the decrease in flow is insensitive to the parameter D, but is strongly dependent on the aspect ratio and wavelength of the bottom bumps. If the bottom surface must be textured, there exists an optimum aspect ratio where the film flow can be maximized. This property would persist even when the amplitude of the bumps is not small.

In this paper the bumps are aligned with the steepest descent of the mean surface. Other periodic alignments are also possible. Effects such as surfactants or ambient surface shear can also be added.

Our results would be fundamental to future studies on film flow over textured surfaces.

Appendix: The Stress Tensors

On a three-dimensional surface

$$z = \varepsilon f(x,y) \quad (A1)$$

the outward unit normal is

$$\vec{n} = \frac{\nabla(\varepsilon f - z)}{|\nabla(\varepsilon f - z)|} = \frac{(\varepsilon f_x, \varepsilon f_y, -1)}{[1+\varepsilon^2(f_x^2+f_y^2)]^{1/2}} \quad (A2)$$

Let

Table 1 Optimum aspect ratio for minimum χ or maximum flow rate (D=1)

κ	0.05	0.1	0.25	0.5	1	2	3	4	5
$\chi_{\min}$	0.997	1.162	1.290	1.423	1.744	2.281	2.748	3.154	3.509
AR	13.8	7.68	1.66	1.53	1.49	1.55	1.64	1.71	1.77

$$\vec{s} = \frac{(1,0,\varepsilon f_x)}{[1+\varepsilon^2 f_x^2]^{1/2}} \tag{A3}$$

be a unit vector perpendicular to $\vec{n}$. The third orthonormal directions is

$$\vec{t} = \vec{s} \times \vec{n} = \frac{(-\varepsilon^2 f_x f_y, 1+\varepsilon^2 f_x^2, \varepsilon f_y)}{\{[1+\varepsilon^2(f_x^2+f_y^2)][1+\varepsilon^2 f_x^2]\}^{1/2}} \tag{A4}$$

Let $l_{xn}=(1,0,0)\cdot\vec{n}$ be the cosine of the angle between the x axis and the normal $\vec{n}$ and similarly define the other direction cosines. Tensor analysis shows the normal stress can be expressed into the Cartesian stress components

$$T_{nn} = l_{xn}^2 T_{xx} + l_{yn}^2 T_{yy} + l_{zn}^2 T_{zz} + 2l_{xn}l_{yn}T_{xy} + 2l_{xn}l_{zn}T_{xz} + 2l_{yn}l_{zn}T_{yz} \tag{A5}$$

$$T_{ns} = l_{xn}l_{xs}T_{xx} + (l_{xn}l_{zs} + l_{zn}l_{xs})T_{xz} + l_{yn}l_{xs}T_{yx} + l_{yn}l_{zs}T_{yz} + l_{zn}l_{zs}T_{zz} \tag{A6}$$

$$T_{nt} = l_{xn}l_{xt}T_{xx} + (l_{xn}l_{yt} + l_{yn}l_{xt})T_{xy} + l_{yn}l_{yt}T_{yy} + (l_{xn}l_{zt} + l_{zn}l_{xt})T_{xz} + (l_{yn}l_{zt} + l_{zn}l_{yt})T_{yz} + l_{zn}l_{zt}T_{zz} \tag{A7}$$

The Cartesian stresses are related to the velocities by

$$T_{xx} = -p + 2u_x, \quad T_{yy} = -p + 2v_y, \quad T_{zz} = -p + 2w_z \tag{A8}$$

$$T_{xy} = u_y + v_x, \quad T_{xz} = u_z + w_x, \quad T_{yz} = v_z + w_y \tag{A9}$$

References

[1] Wang, C. Y., 1981, "Liquid Film Flowing Slowly Down a Wavy Incline," AIChE J., **27**, pp. 207–212.

[2] Bontozoglou, V., and Papapolymeron, G., 1997, "Laminar Film Flow Down a Wavy Incline," Int. J. Multiphase Flow, **23**, pp. 69–79.

[3] Scholle, M., Wierschem, A., and Aksel, N., 2001, "Creeping Film Flow Down an Inclined Wavy Plane. Part I," Z. Angew. Math. Mech., **81**, pp. S487–S488.

[4] Wang, C. Y., 1984, "Thin Film Flowing Down a Curved Surface," Z. Angew. Math. Phys., **35**, pp. 532–544.

[5] Trifonov, Y. Y., 1998, "Viscous Liquid Film Flows Over Periodic Surface," Int. J. Multiphase Flow, **24**, pp. 1139–1161.

[6] Wierschem, A., Scholle, M., and Aksel, N., 2001, "Creeping Film Flow Down an Inclined Wavy Plane. Part II," Z. Angew. Math. Mech., **81**, pp. S493–S494.

[7] Pozrikidis, C., 1988, "The Flow of a Liquid Film Along a Periodic Wall," J. Fluid Mech., **188**, pp. 275–300.

[8] Bontozoglou, V., 2000, "Laminar Film Flow Along a Periodic Wall," Comput. Model. Eng. Sci., **1**, pp. 133–142.

[9] Spivak, M., 1975, *A Comprehensive Introduction to Differential Geometry*, Publish or Perish Inc., Boston, Vol. 3.

Effective Dewetting in a Microporous Particle

Yu Qiao[1]
e-mail: yqiao@uakron.edu

Xinguo Kong

Department of Civil Engineering, University of Akron, Akron, OH 44325-3905

In this paper, the kinetics of the outflow in a microporous particle infiltrated by a nonwetting liquid is analyzed in context of effective phase transformation. The "dewetting" process is considered as the nucleation, growth, and coalescence of empty pore clusters (EPCs) that starts from the interior and eventually involves the whole particle. Initially, the EPC nucleation is dominant while the influence of EPC coalescence becomes increasingly important as the EPC volume fraction increases. The dependence of the dewetting time on the pore size distribution is discussed in detail. [DOI: 10.1115/1.2060734]

1 Introduction

Since the beginning of the last century, the application of nanoporous materials in selective catalysis and adsorption processes has been an active research area [1,2]. Usually, nanoporous materials are classified as microporous materials ($r \leqslant 2$ nm), mesoporous materials ($2\ \text{nm} < r \leqslant 50\ \text{nm}$), and macroporous materials ($50\ \text{nm} < r \leqslant 1000\ \text{nm}$), with r being the pore size. The microporous materials of ultrahigh specific surface areas are particularly important to chemical, environmental, mechanical, as well as bioscience fields. They are often synthesized in the form of micropowders around $1-1000\ \mu$m diam through templating methods [3]. In the interior of these particles there are three-dimensional nanoporous structures, and the surface properties can be adjusted in broad ranges by plasma or thermochemical treatments [4].

In a variety of engineering applications and characterization procedures, the nanoporous particles are immersed in nonwetting liquids, e.g., aqueous solutions of functional chemicals [5,6]. Under a high working pressure, the capillary effect is overcome and the nanopores are filled by the liquid. The associated inflow and diffusion processes have been studied intensively, both experimentally and numerically [7–10]. As the pressure decreases, in a mesopore, the separation of the liquid and the solid can be difficult; that is, there are significant hysteresis loops in sorption isotherm curves, probably due to the difficulty in gas phase formation or the difference between contact angles of intruding and extruding liquids [7,11,12]. In microporous particles, on the other hand, the energetically favorable "outflow" will lead to a complete dewetting at the liquid-solid interface in the nanoenvironment. However, currently, most of the experimental and theoretical investigations in this area are focused on the molecular behaviors in a single nanopore. The studies on the aggregate response of the nanoporous particle are scarce.

In view of the above considerations, in this paper we will develop a pore-cluster model to relate the system performance, such as the dewetting time, to the important global design variables, such as the pore-size distribution. Since the particle size is much larger than the pore size and the orientation distribution of the nanopores is usually random, in the following discussion the confined flow is assumed to be isotropic.

2 Governing Equations

As the external pressure decreases to below the critical value p_0, the liquid confined in the nanopores in a microporous particle becomes unstable and the dewetting starts randomly at a number of points. Note that the critical pressure can be assessed as $p_0 = 2\gamma/r$, where $\gamma = \gamma_{1s} - \gamma_s$, with γ_{1s} being the solid-liquid interfacial energy and γ_s the effective surface energy of the network material. As the liquid flows out of the porous space surrounding the initiation site, an empty pore cluster (EPC) is formed and it grows along both radial and circumferential directions. Hence, the dewetting process can be considered as an effective phase transformation from filled pore clusters (FPCs) to EPCs. In the early stage, the number and average size of EPCs keep increasing as new EPCs are nucleated. As the number of EPCs reaches the peak value, it is envisioned that the EPC coalescence would become dominant.

According to the nuclear magnetic resonance (NMR) measurements as well as the atomistic simulations [13–15], there is an interface zone of the thickness of a few nanometers in a nanopore, as depicted in Fig. 1. For mesoporous or macroporous materials, the pore size is larger than the characteristic interface-zone thickness. In order to analyze the average flow rate of confined liquid $\bar{v}$, both the contributions of the interface flow and the normal flow in the interior must be taken into consideration [10,16]. For a microporous material, however, the pore size can be smaller than the thickness of interface zone and, therefore, the normal flow is negligible. Under this condition, the effective flow rate is dependent on the applied pressure p, the effective kinematics viscosity of confined liquid χ, the pore size r, as well as γ. Note that the molecular density in the interface zone is a function of γ [17]. According to the Π theorem, by assuming that the $\bar{v}$-p relationship can be described by a power-law equation, the average flow rate can be stated as

$$\frac{\gamma \bar{v}}{\chi p} = \alpha \left(\frac{pr}{\gamma} \right)^{\beta} \tag{1}$$

where α and β are system parameters. The form of Eq. (1) is compatible with the experimental observation that the average diffusion rates of confined liquids in nanoporous materials follow power-law functions [13,14]. For normal flow, $\beta = 1$; for subdiffusive flow, $\beta < 1$; and if $\beta > 1$, the flow is of a superdiffusive characteristic.

An EPC consists of a number of empty pores connected together and can be characterized by its radial depth c and the circumferential width l, as shown in Fig. 2. The collective EPCs can be characterized by the number density $n(c,l,t)$, which is defined as the number of EPCs of size $\{c,l\}$ at time t. Following the classic number density equilibrium equation, the evolution of $n(c,l,t)$ is governed by

[1]Author for correspondence.

Contributed by the Fluids Engineering Division for publication in the JOURNAL OF FLUIDS ENGINEERING. Manuscript received by the Fluids Engineering Division November 30, 2004; final manuscript received: June 8, 2005. Associate Editor: Kenneth Breuer.

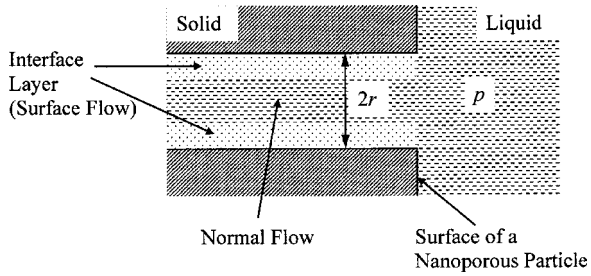

Fig. 1 Schematic diagram of the confined liquid in a nanopore

$$\frac{\partial n(c,l,t)}{\partial t}+\frac{\partial}{\partial c}[C(c,l,t)n(c,l,t)]+\frac{\partial}{\partial l}[L(c,l,t)n(c,l,t)]=n_N(c,l,t) \tag{2}$$

where C and L are the EPC growth rates along the radial and circumferential directions, respectively; and n_N is the nucleation/coalescence rate. Equation (2) describes the mass transportation between the EPCs to the saturated area.

As a first-order approximation, C and L can be taken as the average growth rate of the EPC-FPC boundary

$$C=L=\tilde{\alpha}\int_0^\infty P(r)\bar{v}\,\mathrm{d}r \tag{3}$$

where $P(r)$ is the pore size distribution, which can be considered as a lognormal function with the mean value of $\bar{r}$ and the standard deviation of σ_r; and $\tilde{\alpha}$ is a parameter accounting for the orientational correlation of the micropores. For isotropic porous structure, the directions of confined flows in nanopores are random, and therefore $\tilde{\alpha}=2/3$.

The term of n_N consists of two components

$$n_N(c,l,t)=\tilde{n}_N(c,l,t)+n_C(c,l,t) \tag{4}$$

where $\tilde{n}_N$ is caused by EPC nucleation and n_C is the component associated with EPC coalescence. The nucleation rate can be stated as

$$\tilde{n}_N(c,l,t)=\eta_0 P(c\leqslant r_0)\left[1-\frac{V(t)}{\left(\frac{4}{3}\right)\pi R^3}\right]_{c=1} \tag{5}$$

where $r_0=2\gamma/p$, R is the particle radius,

$$V(t)=\varsigma\int\int_{c,l} n(c,l,t)cl^2\mathrm{d}c\mathrm{d}l \tag{6}$$

is the total volume of EPCs, and $\eta_0=\eta_1\int_0^{r_0}P(r)\mathrm{d}r$, with ζ being a geometry factor and η_1 a parameter determined by the time resolution. For regular-shaped EPCs, $\zeta=1$. The term in the brackets in Eq. (5) is the volume fraction of FPCs.

If the distribution of the EPC nucleation sites is random, the EPC coalescence can be analyzed in the framework of conditional probability theory [18]

$$p_\mathrm{d}R/d=\sqrt{N_\mathrm{d}}(R/1-d)^{\sqrt{N_d}-1} \tag{7}$$

where p_d is the probability for two adjacent EPCs to be d apart and N_d is the total number of the EPCs in the area under consideration. When the sum of the radial depths of two EPCs equals the distance between them, the radial coalescence occurs and the associated probability is

$$f_R(d,t)=\eta p_d(R/d)\int_0^d n_\mathrm{c}(c,t)\int_0^{d-c} n_\mathrm{c}(\tilde{c},t)\mathrm{d}\tilde{c}\mathrm{d}c \tag{8}$$

where $n_c(c,t)=\int_0^\infty n(c,l,t)\mathrm{d}l$, $\eta\propto 1/N^2$ is a normalization constant, and N_d can be expressed as $N\lfloor(V/N)^{2/3}R\rfloor/\frac{4}{3}\pi R^3$, with $N=\int\int_{c,l}n(c,l,t)\mathrm{d}c\mathrm{d}l$ being the total EPC number.

The lateral coalescence, on the other hand, is dependent on the distance of the EPCs to the center of the particle r. The probability of the coalescence along the circumferential direction of two EPCs that are initially d apart is

$$f_L(r,d,t)=\eta'\cdot p_\mathrm{d}(2\pi r/d)\int_0^d n_L(l,t)\int_0^{d-l} n_L(\tilde{l},t)\mathrm{d}\tilde{l}\mathrm{d}l \tag{9}$$

where $n_L(l,t)=\int_0^\infty n(c,l,t)\mathrm{d}c$ and $\eta'\propto 1/N^2$ is a normalization constant. In Eq. (9), the effective EPC number N_d should be taken as $3Nr^2(V/N)^{1/3}/R^3$.

Consequently, the contribution of EPC coalescence is

$$n_c(c,l,t)=n_{cR}(c,l,t)+n_{cL}(c,l,t) \tag{10}$$

The two terms at right-hand side of Eq. (10) capture the effects of radial and lateral coalescences, respectively, and

$$n_{ci}(c,l,t)=N(t)[\tilde{p}_i(c,l,t)-2\hat{p}_i(c,l,t)] \tag{11}$$

where $\tilde{p}_i$ reflects the contribution of EPC formation, $\hat{p}_i$ reflects the contribution of EPC disappearance, and the subscript $i=R$ or L denotes the radial or lateral direction, respectively. These components can be stated as

$$\tilde{p}_R(c,l,t)=n_L(l,t)\int_0^R f_R(d,t)\left\{\int_0^{R-d} n_c(\tilde{c},t)\int_0^{R-d-\tilde{c}} n_c(\hat{c},t)\mathrm{d}\hat{c}\mathrm{d}\tilde{c}\right\}\mathrm{d}d \tag{12a}$$

$$\tilde{p}_L(c,l,t)=n_c(c,t)\cdot\int_0^R\int_0^r f_L(r,d,t)\times\left\{\int_0^{2\pi r-d} n_L(\tilde{l},t)\int_0^{2\pi r-d-\tilde{l}} n_L(\hat{l},t)\mathrm{d}\hat{l}\mathrm{d}\hat{l}\right\}\mathrm{d}d\mathrm{d}r \tag{12b}$$

$$\hat{p}_R(c,l,t)=n_L(l,t)\cdot\int_0^R f_R(d,t)\left[\int_0^{R-d} n_c(\tilde{c},t)\mathrm{d}\tilde{c}\Big/\, n_c(c\leqslant R)\right]\mathrm{d}d \tag{12c}$$

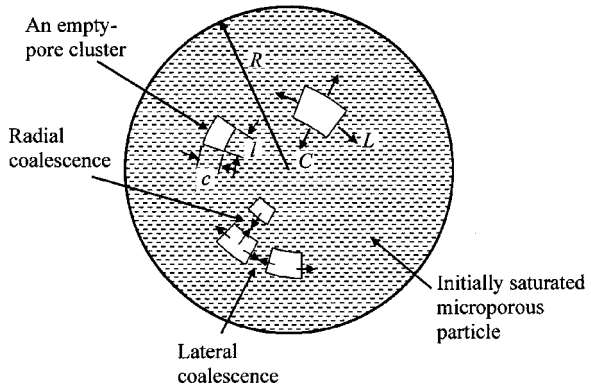

Fig. 2 Schematic diagram of a microporous particle

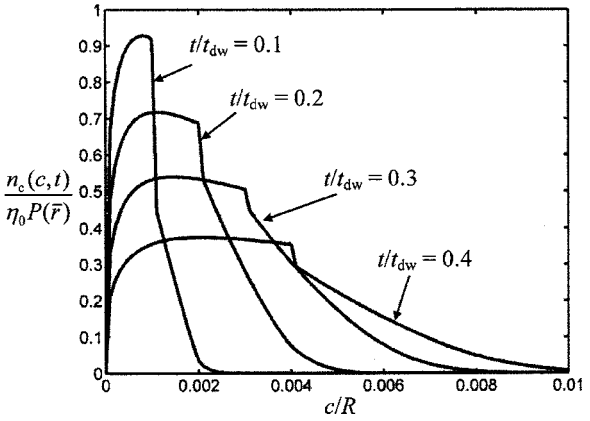

Fig. 3 Evolution of the number density of EPCs

$$\hat{p}_L(c,l,t) = n_c(c,t) \cdot \int_0^R \int_0^r f_L(d,t) \times \left[\int_0^{2\pi r - d} n_L(\tilde{l},t)\mathrm{d}\tilde{l} \Big/ n_L(c \leqslant 2\pi r) \right] \mathrm{d}d\mathrm{d}r \tag{12d}$$

Finally, the model is completed by setting the initial condition as $n(c,l,0)=0$, that is, initially the particle is fully saturated; and setting the boundary condition as $n(0,0,t)=0$.

3 Results and Discussion

Figure 3 shows the numerical results of Eqs. (3)–(12), where the average pore size $\bar{r}=1$ nm, $\sigma_r=0.3$ nm, γ is taken as 20 mJ/m^2, $p=2.0\times10^4$ Pa, and $\beta\approx1.3$. The value of ν is set to 3.2×10^{-6} m^2/s. It can be seen clearly that the $n_c(c,t)$ distribution consists of two regions separated by an abrupt drop in n_c. A similar characteristic can also be observed in the $n_L(l,t)$ distribution curves. The boundary of the two regions is close to $\int_0^t C\mathrm{d}t$, which would be the upper limit of the EPC size at time t if the EPC coalescence did not occur. The lower c region is dependent on the EPC nucleation, growth, and coalescence, while the higher c region is mostly determined by the coalescence behavior, particularly, the term of $\hat{p}_i$ in Eq. (11). The coalescence leads to the tendency of decrease in n_c in the lower c region and the increase in the higher c region. As the average size and volume fraction of EPCs increase, the coalescence becomes increasingly important and the higher c region dominates the system behavior. The height of the abrupt drop between the two regions keeps decreasing and eventually vanishes. When the effective dewetting process is completed, n_c in the lower c region is reduced to zero and there is only one EPC left in the higher c region with the size of R.

The evolution of the average EPC size $\bar{c}$ is highly nonlinear, as shown in Fig. 4. In the early stage of dewetting, before the EPC coalescence becomes pronounced, the increase in $\bar{c}$ is mostly caused by the EPC growth, which is quite slow. As t/t_{dw} reaches 0.5, $\bar{c}$ is only about 1% of R, with t_{dw} being the dewetting time. After that, with the increasing EPC volume fraction the coalescence leads to the rapid increase in $\bar{c}$ as small EPCs merge together. Compared to that of $\bar{c}$, the extent of nonlinearity of the evolution of EPC volume fraction is much lower, since EPC coalescence cannot be reflected in the V-t relation. As V rises, because of the reduction in the number of available nucleation sites, the nucleation rate is lowered, which reduces $\mathrm{d}V/\mathrm{d}t$. Furthermore, the coalescence causes a decrease in the specific area of the EPC-FPC interface, which retards the EPC growth. As a result, $V(t)$ increases with a descending rate.

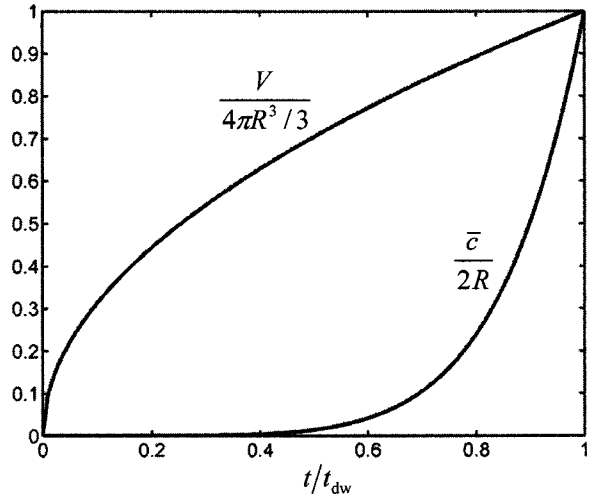

Fig. 4 Evolution of the average size and the total volume fraction of EPCs

In a number of engineering applications, the nanoporous materials work under dynamic environments with the pressure differences varying in broad ranges. The rate of pressure change $\dot{p}$ affects t_{dw} by influencing $\bar{v}$ (see Fig. 5). The characteristic time t_0 is taken as the dewetting time if the pressure were fixed at the initial value. As $\dot{p}$ increases, with everything else the same, $\bar{v}$ is higher and thus t_{dw} is lowered. Note that increasing the average pore size $\bar{r}$ and decreasing the dewetting "driving force" γ have similar effects. The dewetting time is also a function of β. When $\beta=1$, the flow rate in the nanoenvironment is proportional to r, and Eq. (2) is reduced to that of normal flow. If $\beta<1$, subdiffusive process dominates and the dewetting takes a longer time, and vice versa. It is clear that with a constant $\bar{r}$, the broader the pore-size distribution, the more large pores are involved in the EPC growth. Because $\bar{v}$ increases with r, although as σ_r rises the fraction of small pores becomes higher, the overall effect of raising σ_r is beneficial to reducing t_{dw}. However, since changing σ_r does not directly affect the EPC coalescence, and the influence of EPC growth is important only in the early stage, the σ_r dependence of t_{dw} is relatively weak.

4 Conclusion

A pore-cluster model is developed so as to provide an appropriate framework for the study on the aggregate behaviors of

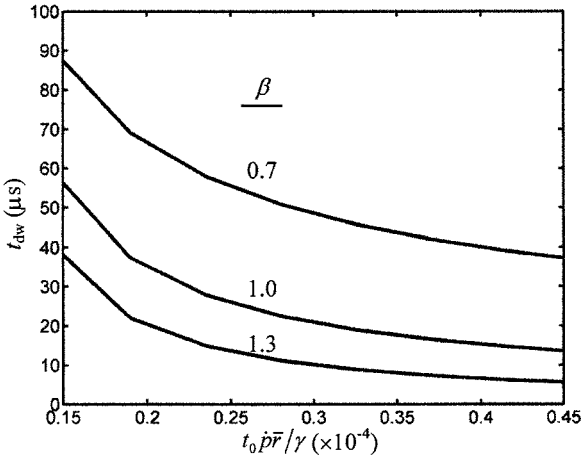

Fig. 5 Dewetting time as a function of $\dot{p}\bar{r}/\gamma$ and β

nanoporous systems. Although the details of the solid-liquid interaction and the EPC geometry are not taken into consideration and currently it is difficult to directly compare the theoretical results to experimental data, the system response (e.g., the dewetting time) can be related to the control parameters quite conveniently by the EPC number density analysis. The numerical results indicate that there exist two abruptly separated regions in the EPC number density distribution, with the lower c region formed by the EPC nucleation and the higher c region dominated by the EPC coalescence. At the early stage of dewetting, the EPC nucleation is the most important factor affecting n, whereas at the late stage the EPC coalescence results in the eventual disappearance of the lower c region and the rapid increase in average EPC size. The dewetting time decreases as the mean value or the standard deviation of pore-size distribution increases.

Acknowledgments

The theoretical analysis was supported by The National Science Foundation under Grant No. CMS-0503910 and the numerical simulation was supported by The Army Research Office under Grant No. W911NF-05-1-0288, for which we are grateful to Dr. David M. Stepp.

References

[1] Polarz, S., and Smarsly, B., 2002, "Nanoporous Materials," J. Nanosci. Nanotechnol., **2**, pp. 581–612.
[2] Kruk, M., and Jaroniec, M., 2001, "Gas Adsorption Characterization of Ordered Organic-Inorganic Nanocomposite Materials," Chem. Mater., **13**, pp. 3169–3183.
[3] Dabrowski, A., 2001, "Adsorption - From Theory to Practice," Adv. Colloid Interface Sci., **93**, pp. 135–224.
[4] Pandey, P., and Chauhan, R. S., 2001, "Membranes for Gas Separation," Prog. Polym. Sci., **26**, pp. 853–893.
[5] Kong, X., and Qiao, Y., 2005, "Improvement of Recoverability of a Nanoporous Energy Absorption System by Using Chemical Admixture," Appl. Phys. Lett., **86**, 151919
[6] Kong, X., Surani, F. B., and Qiao, Y., "Thermal Effect on Pressure Induced Infiltration of a Nanoporous System," Philos. Mag. Lett. [in the press].
[7] Borman, V. D., Crekhov, A. M., and Troyan, V. I., 2000, "Investigation of the Percolation Transition in a Nonwetting Liquid-Nanoporous Medium System," J. Exp. Theor. Phys., **91**, pp. 170–181.
[8] Degueldre, C., Scholtis, A., Laube, A., Turrero, M. J., and Thomas, B. 2003, "Study of the Pore Water Chemistry Through an Argillaceous Formation: A Paleohydrochemical Approach," Appl. Geochem., **18**, pp. 55–73.
[9] Kong, X., Surani, F. B., and Qiao, Y., "Effects of Addition of Ethanol on the Infiltration Pressure of a Mesoporous Silica," J. Mater. Res. [in the press].
[10] Qiao, Y., and Kong, X., 2005, "Modeling of Kinetics of Forced Flow in a Mesoporous Particle, Phys. Scr., **71**, pp. 27–30.
[11] Martin, T., Lefevre, B., Brunel, D., Galarneau, A., Di Renzo, F., Fajula, F., Gobin, P. F., Quinson, J. F., and Vigier, G., 2002, "Dissipative Water Intrusion in Hydrophobic MCM-41 Type Materials," Chem. Commun. (Cambridge). pp. 24–25.
[12] Grinchuk, P. S., 2002, "Large Clusters in Supercritical Percolation, Phys. Rev. E, **66**, 016124
[13] Yi, J., and Jonas, J., 1996, "Raman Study of Vibrational and Rotational Relaxation Liquid Benzene-d(6) Confined to Nanoporous Silica Glasses, J. Phys. Chem., **100**, 16789
[14] Cramer C., Cramer, C. T., Kremer, F., and Stannarius, R., 1997, "Measurement of Orientational Order and Mobility of a Nematic Liquid Crystal in Random Nanometer Confinement, J. Chem. Phys., **106**, pp. 3730–3742.
[15] Crupi, V., Magazu, D., Majolino, P., and Bellissent-Funel, M. C., 2000, "Dynamical Study of Confined Ethylene Glycol by IQENS," Physica B, **B276**, pp. 417–422.
[16] Qiao, Y., Kong, X., and Chakravarthula, S. S., 2005, "An Analysis of Aggregate Response of Confined Liquids in Nanoenvironment, J. Math. Chem., **37**, pp. 93–99.
[17] Bockris, J. O., Reddy, A. K. N., and Gamboa-Aldeco, M., 1998, *Modern Electrochemistry*. Kluwer Academic, NY.
[18] Chen, H., and Qiao, Y., "Distribution of Random Elements Subjected to a Flexible Boundary Condition, J. Appl. Math. Mech. [accepted].

Turbulent Mixing of Two Immiscible Fluids

Thierry Lemenand

Pascal Dupont

Dominique Della Valle

Hassan Peerhossaini[1]

e-mail: hassan.peerhossaini@polytech.univ-nantes.fr
Phone: +33-2-40-68-31-42
Fax: +33-2-40-68-31-41

Thermofluids & Complex Flows Research Group,
Laboratoire de Thermocinétique de Nantes,
CNRS UMR 6607, Rue Christian Pauc,
BP 50609, F-44306 Nantes, France

The emulsification process in a static mixer HEV (high-efficiency vortex) in turbulent flow is investigated. This new type of mixer generates coherent large-scale structures, enhancing momentum transfer in the bulk flow and hence providing favorable conditions for phase dispersion. We present a study of the single-phase flow that details the flow structure, based on LDV measurements, giving access on the scales of turbulence. In addition, we discuss the liquid-liquid dispersion of oil in water obtained at the exit of the mixer/emulsifier. The generation of the dispersion is characterized by the Sauter diameter and described via a size-distribution function. We are interested in a local turbulence analysis, particularly the spatial structure of the turbulence and the turbulence spectra, which give information about the turbulent dissipation rate. Finally, we discuss the emulsifier efficiency and compare the HEV performance with existing devices.
[DOI: 10.1115/1.2073247]

Keywords: Liquid-Liquid Dispersion, Turbulent Spectra, Static Mixer, Energetic Efficiency, Energy Dissipation Rate, High Efficiency Vortex (HEV), Longitudinal Vortices

1 Introduction

The global trend in chemical and manufacturing industries is towards improved energy efficiency, cleaner synthesis, reduced environmental impact, and smaller, safer, multifunctional process plants. Such concerns are the driving force for the intensification of batch processes, which are being replaced with continuous high-intensity in-line mass- and heat-transfer equipment. In this context the process-intensification (PI) approach, in which the fluid dynamics of the process is matched to the reaction in order to improve selectivity and minimize the by-products, takes on particular importance.

It is estimated that in a typical large chemical plant, between 5 and 45 million Euros are wasted every year through inefficiencies. In some cases it is estimated that optimizing reactor performance for maximum yield and selectivity would save between 0.4 and 0.8 million Euros per product per year. Overall, reactor-related problems are believed to account for between 0.5% and 3.0% of total turnover, which for European Union chemical industries amounts to 1.9 to 11.4 billion Euros per year [1].

Systems involving more than one component (or phase) contain interfaces between the components. Our ability to predict the performance of such systems is extremely limited. In addition, many multiphase processes are carried out in stirred-tank reactors. Poor flow patterns and low inhomogeneous mixing are characteristic of stirred-tank reactors and typically afford energy dissipation rates in the range 1–10 W kg^{-1}.

High selectivity requires high rates of micromixing, which need turbulent energy dissipations higher than 100 W kg^{-1}. Therefore, fast exothermic reactions when carried out in stirred tanks start before mixing is complete, leading to slow apparent rates of reaction and formation of by-products that must be separated further downline. The high-efficiency vortex (HEV) heat exchanger-reactor is selected for its capacity to generate large-scale vortex motions and enhance turbulent energy dissipation in the flow.

A typical potential application of this device in manufacturing processes is the "mixhead" of resin-injection-molding (RIM) machines. Mixing, often called the heart of RIM, is what differentiates it from other reaction-molding processes such as thermoset injection molding or sheet molding. Most mixhead designs were developed by trial and error. Even today, newly designed mixheads are mounted on a machine and a typical reaction is tried on them [2]; mixing quality is then judged by the visual appearance of the product. Therefore, understanding the basic physical phenomena underlying mixing in flows in manufacturing processes is fundamental to a predictive approach to these processes.

In this paper we give a global characterization of a special static mixer designed for use as a reactor-heat exchanger for process intensification in liquid-liquid mixing and reaction. Its design is based on curved baffles fixed on the tube walls that generate longitudinal vortices, substantially increasing transport phenomena over the simple pipe and even over some static mixers known for their high efficiency. The emulsification performance of this system, indicative of its mixing abilities, is presented in this study. Oil-in-water emulsions obtained with the static mixer are characterized by the granulometric distributions. The mean size, size distribution, and power consumption of the mixer are compared with those in some existing devices.

The turbulent characteristics of the flow in the mixer are studied extensively and the physical phenomena underlying the high efficiency of the mixer are addressed.

2 Experimental Setup and Methods

The Perspex HEV test section designed and constructed for this work (Fig. 1) is a straight tube of inner diameter 20 mm along which seven tab arrays are fixed. Each of the seven arrays consists of four trapezoidal tabs positioned at 90° to one another and fixed on the tube walls. The tabs are turbulence promoters and generate longitudinal vortical structures. The test section is 180 mm long and the distance between two successive tab arrays is 20 mm (one tube diameter).

The test section is connected to a preconditioner and postconditioner, which are 300 mm straight transparent tubes of circular inner cross section and 20 mm inner diameter. The preconditioner is used to provide a fully developed flow at the inlet of the test section, and the postconditioner to observe the effect of the test section on mixing quality.

A schematic diagram of the experimental setup is shown in Fig. 2. It consists of feed loops for oil and water. The flow rates are controlled by valves and measured with two flowmeters with overlapping ranges.

[1]Corresponding author.

Contributed by the Fluids Engineering Division for publication in the JOURNAL OF FLUIDS ENGINEERING. Manuscript received by the Fluids Engineering Division November 17, 2003; final manuscript received: June 10, 2005. Assoc. Editor: Steven Ceccio.

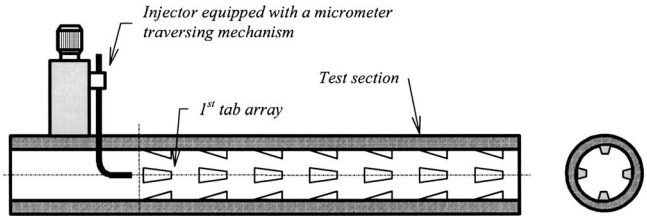

Fig. 1 Heat exchanger-reactor HEV

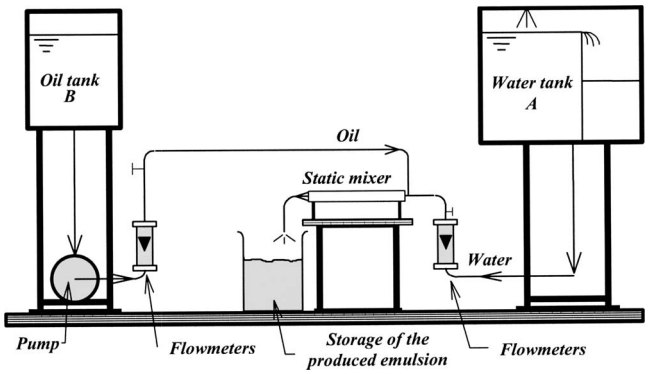

Fig. 2 Experimental setup

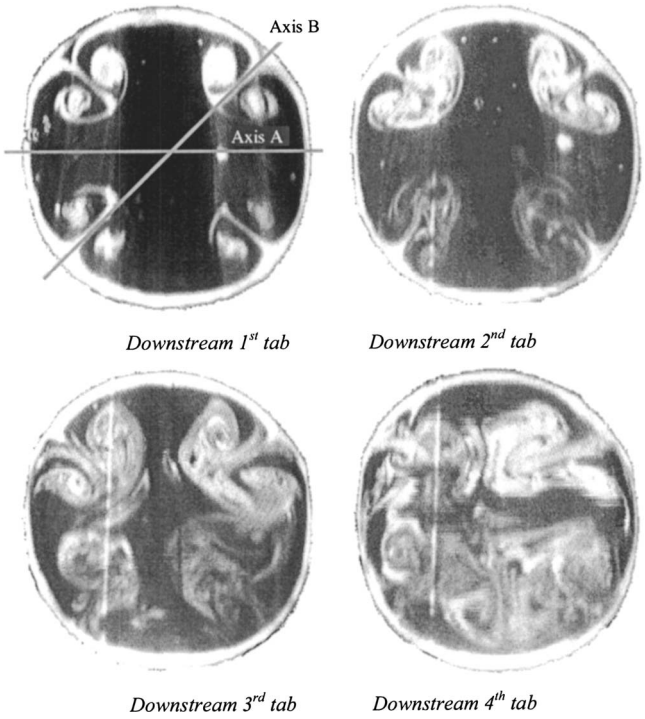

Fig. 4 Coherent structures at Re=1500

In Sec. 3, single-phase-flow results are given. The working fluid is water and flow patterns are visualized by the laser-induced fluorescence (LIF) technique. Mean and fluctuating velocity fields were measured by laser Doppler velocimetry (LDV) and particle image velocimetry (PIV). The local turbulent energy dissipation rates were hence obtained by the determination of the integral length scales. The pressure drop was measured by a differential manometer, and the temperature remained about the ambient $20°C \pm 0.5$. Experiments were run for Reynolds numbers ranging between 1500 and 15,000.

In Sec. 4, liquid-liquid phase dispersion is studied. The working fluids are water for the internal phase and an additive technical vaseline oil (Albelf ID 15) for the dispersed phase. The setup allows experiments corresponding to dispersed-phase mixing rates of up to 15%, with Reynolds numbers ranging from 7500 to 15,000. A microencapsulation, based on the isocyanate-amine polymerization reaction, is performed on the emulsion at the exit from the test section. Further details on the experimental setup and the microencapsulation technique are given by Lemenand et al. [3]. The physical properties of oil are given in Table 1.

A video-optic computer-assisted device was used for granulometric analysis (Pegase software). It was found that a sample of at least 600 droplets is needed to reach 5% precision in the Sauter diameter value. Figure 3 shows some photographs of various sampled dispersions.

3 Single-Phase-Flow Results

This section describes the flow pattern generated by the geometry tested and the turbulence properties of the single-phase flow in the mixer. Figure 4 shows LIF visualizations of the longitudinal vortices downstream of the first, second, third, and fourth tab arrays at Reynolds number Re=1500. The images were obtained while placing the camera at an angle of 45° to the axis of the (transparent) mixer. These images were then processed so as to restore the circular form of the section.

Downstream of the first tab a pair of vortices is generated that promotes radial mixing. Subsequent tabs increase the degree of mixing, although even at the last tab array special structures can

Table 1 Physical properties of oil loaded with 10% volume of encapsulation reactant

Property (20°C)	Value	Measurement method
Kinematic viscosity	30×10^{-6} m^2 s^{-1}	Mettler™ RM180 rheometer
Density	0.85	Data Technical™ picnometer
Interfacial tension with water	20×10^{-3} N m^{-1}	Krüss™ tensiometer (K12) ring method

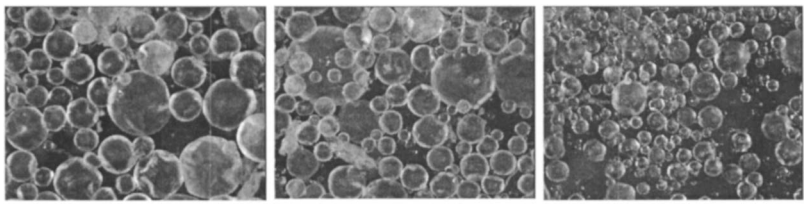

Fig. 3 Emulsion samples—optical microscopy

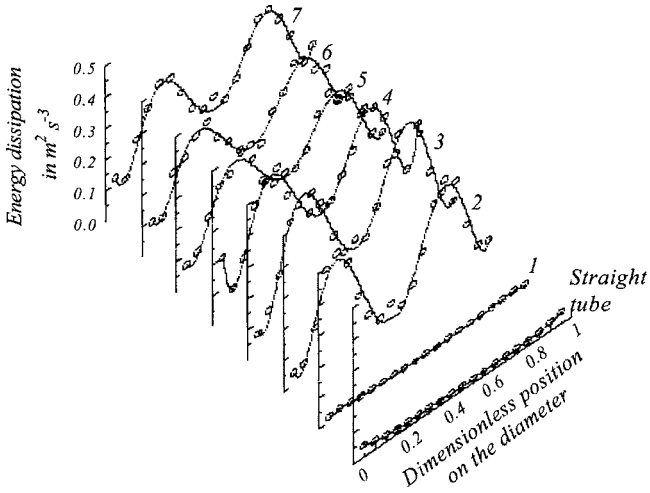

Fig. 5 Global view of evolution of mean axial velocity profile (axis *A*) at Re=15,000 [4]

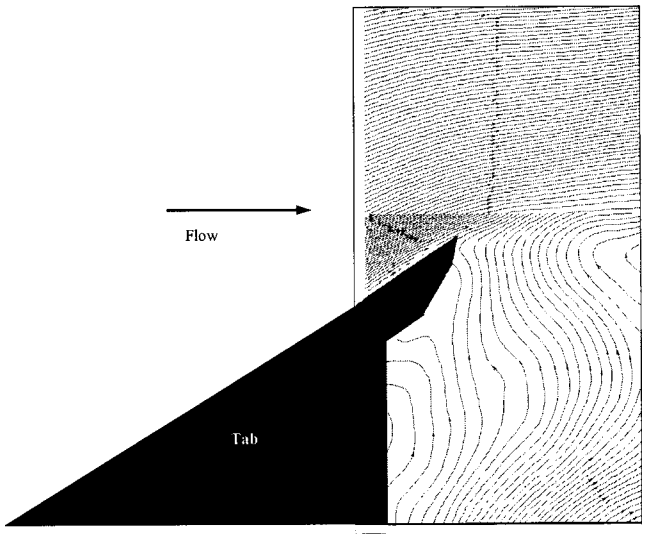

Fig. 7 Experimental streamlines downstream of the seventh baffle at Re=15,000 (PIV measurements)

still be observed. Figure 5 illustrates the axial mean velocity profiles 2 mm downstream of each tab array for flow Re=15,000 [4] along axis *A* (shown in Fig. 4). The same figure shows the velocity profile in the straight tube upstream of the first tab array. It can be seen that the first tab array has no significant effect on the mean velocity profile. However, the effect of the second tab array superposed on that of the first induces two minima (behind the tabs) in the mean velocity profile. This deformation of the velocity profile is due to the transfer of low-momentum fluid particles from the HEV wall vicinity to the core flow and is also visible downstream of the subsequent tabs.

Figure 6 shows turbulence kinetic energy (TKE) dissipation profiles 2 mm behind each tab array [5] for Reynolds number 10,000 along axis *A*. The effect of the radial velocity component in the streamwise vortices is visible here: high turbulence patterns close to the wall are transferred towards the core region, so that the TKE dissipation in the HEV center is dramatically intensified compared with the empty tube.

The TKE dissipation rate ε was computed using Batchelor's energy-cascade model [6]:

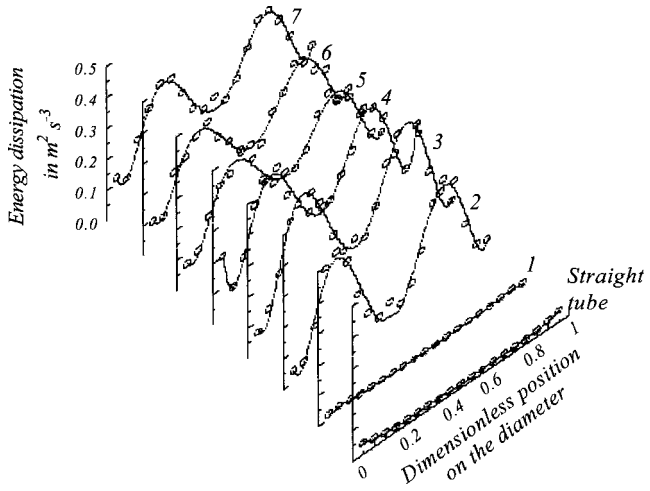

Fig. 6 Global view of the evolution of TKE dissipation profile (axis *A*) at Re=10,000 [5]

$$\varepsilon = C\frac{q^{3/2}}{l} \tag{1}$$

where l is the Prandtl mixing length and q is the turbulent kinetic energy.

Assuming that the high-frequency fluctuations involved in the energy dissipation are locally isotropic, and also that the integral macroscale Λ can approximate the length scale l, one can define the local turbulent energy dissipation by

$$\varepsilon = C\frac{\left(\frac{3}{2}\overline{u^2}\right)^{3/2}}{\Lambda} \tag{2}$$

In the present work, the integral macroscale Λ is determined from the time macroscale using Taylor's hypothesis:

$$\Lambda = U_{conv}T \tag{3}$$

where U_{conv} represents the convection velocity. This velocity was determined by using Van Doorn's expression [7] for three-dimensional flows and simplified through the following hypotheses:

1. the axial mean velocity component is much larger than the tangential and radial components,
2. the velocity fluctuation field is locally isotropic.

This model predicts fairly well the turbulent energy dissipation in grid-generated turbulence with constant $C=1.0$; however, the validity of the model for anisotropic turbulent flows may depend on the flow type [8,9]. The numerical value of C must then be determined experimentally for specific cases.

In order to estimate the numerical value of C, a series of experiments was carried out in a straight tube equipped with turbulence promoters (HEV) to measure u^2 and Λ. Then ε/C was compared to the turbulence kinetic energy dissipation ε obtained by Lawn [10] in a straight tube. This leads to a C value of 1.8, which is adopted in the latter equation.

The above description of the flow pattern allows a better understanding of the role of the tabs on the flow structure. As shown in Fig. 7, a high shear zone appears at the top of the tabs, which is the active mixing region in the device.

4 Liquid/Liquid Phase: Dispersion of Oil in an External Water Phase

HEV can be used successfully in the emulsification process. Here we focus on the granulometric characterization of oil-water emulsions obtained in a wide range of hydrodynamic conditions in the mixer. The droplets are sized using optical microscopy. The mean size, characterized by the Sauter diameter, is fitted to classical turbulent breakup models. The Sauter diameter and power consumption are compared with those in some existing devices.

4.1 Modeling Droplet Breakup in Turbulent Flow. A droplet subjected to mechanical stresses (pressure, velocity gradients, or turbulence forces) can burst into several smaller droplets. This phenomenon results from the competitive effects of the rheological and interfacial properties of the two phases, on the one hand, and mechanical forces via the flow conditions on the other. Application of the general breakup model to "noncoalesced" and inviscid systems, in homogeneous and isotropic turbulence, was tested here following the maximum drop size prediction in the Hinze-Kolmogorov theory, using a critical Weber number of order unity. Here we use the Hesketh et al. [11] presentation for this model:

$$d_{\max} = \left(\frac{\mathrm{We}_{crit}}{2}\right)^{0.6} \left(\frac{\sigma^{0.6}}{\rho_c^{0.4}\rho_d^{0.2}}\right) \varepsilon^{-0.4} \tag{4}$$

For a wide range of applications (stirred vessels, homogenizers, and the like), the breakup is fairly well predicted by a dimensionless Weber number, in formulas that may include the effect of the viscosity of the dispersed phase (the viscosity number). The dimensionless Shinnar [12] equation results from Eq. (4):

$$\frac{d_{32}}{D_H} = C_1 \mathrm{We}^{-0.6} \tag{5}$$

where the Weber number is defined as

$$\mathrm{We} = \frac{\rho_c U^2 D_H}{\sigma} \tag{6}$$

Some extensions of the basic model presented in Eq. (6) have been derived by different authors. Berkman and Calabrese [13] justified a corrective term for dilute emulsions to take into account the viscosity of the dispersed phase for a Kenics static mixer:

$$\frac{d_{32}}{D} = 0.49\left[1 + 1.38 N_{Vi}\left(\frac{d_{32}}{D}\right)^{1/3}\right]^{0.6} \mathrm{We}^{-0.6} \tag{7}$$

with the viscosity number N_{Vi} defined by

$$N_{Vi} = \frac{\mu_d U}{\sigma}\left(\frac{\rho_c}{\rho_d}\right)^{0.5} \tag{8}$$

The value of the droplet mean diameter, and thus of the interfacial area, is nevertheless modified by the volume fraction of the dispersed phase from 15% to 30%. The linear corrective term found by Pacek et al. [14] takes into account the coalescence:

$$\frac{d_{32}}{D} = C_3(1 + C_2\phi)\mathrm{We}^{-0.6} \tag{9}$$

4.2 Results and Discussion. Measurements were performed in the 0.1–0.25 l s^{-1} flow rate range, for 0%–15% oil volume fraction, in order to investigate the effect of the Weber number on droplet distribution. All experiments were performed at room temperature (18–20°C).

4.2.1 Mean and Maximum Diameter. Proportionality between the Sauter mean diameter, d_{32}, and the maximum diameter of the drops, $d_{\max}$, is the basic assumption of the turbulent breakup model [15,14]. Experimental results reveal that the diameters d_{32} and $d_{\max}$ are actually correlated according to the linear relation:

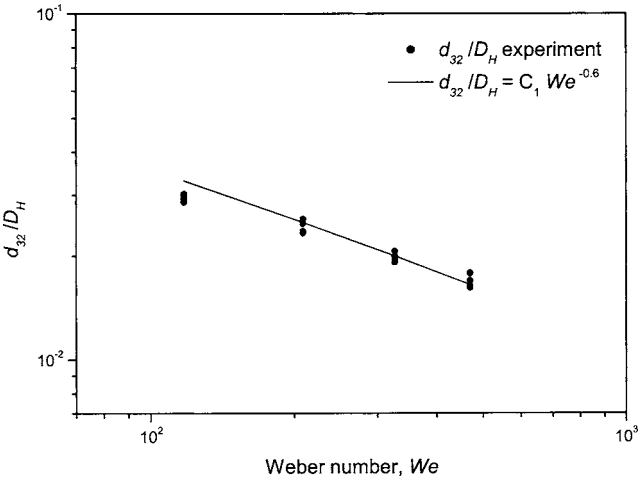

Fig. 8 Sauter diameter versus Weber number

$$d_{32} = C_4 d_{\max} \tag{10}$$

where $C_4 = 0.48$.

4.2.2 Sauter Diameter as a Function of Weber Number. The average droplet diameter strongly depends on the hydrodynamic conditions through the energy dissipation rate. The HEV measurements in Fig. 8 show fairly good agreement with this theoretical slope of -0.6 ($C_1 = 0.57$), demonstrating that turbulent disruption governs the emulsification mechanism. The fit constant is smaller than 1 (usual value), suggesting that under similar conditions the Sauter diameter is smaller in the HEV than in classical static mixers. This feature will be investigated further by analyzing the energy consumption efficiency of this device.

4.2.3 Size Distribution Function. The method proposed by Schwarz and Bezemer [16] is applied to fit the present data. The cumulative volume $V\%$ of the distribution function is modeled using a typical constant a:

$$\ln V\% = \ln 100 + \frac{a}{d_{\max}} - \frac{a}{d} \tag{11}$$

Figure 9 shows a plot for an emulsion of oil fraction 5% in which for each Reynolds number the Schwarz-Bezemer model represents the droplet size distribution in HEV, as far as the straight lines extrapolate to the same intercept.

The value of $a/d_{\max}$ is a constant (1.08) independent of the operating conditions, which is more convenient for scale-up operations than a classical log-normal distribution.

5 Local Turbulence Analysis

Previous results on the dispersion of oil in water under the combined action of mean and fluctuating velocity fields have raised the complex question of the turbulence parameters relevant in describing the ability of turbulence to split up the oil droplets. In fact, the local or mean turbulent dissipation rate measured on axis A cannot explain the low value of $d_{\max}$ given by Eq. (4). More precise turbulence measurements (on axis B) are essential to investigate the turbulent dispersion efficiency, which is related to the knowledge of its properties: first, is the turbulence in the HEV homogeneous and isotropic [Eqs. (2) and (3)], and, second, where in the device is the highest mixing efficiency concentrated?

5.1 Spatial Structure of Turbulence. The most significant effect of the tabs is to increase the turbulence energy along the tube axis. Figure 10 shows the radial profile of the turbulent rms velocity at three axial positions: x_u upstream of HEV, x_{d1} downstream of the first tab, and finally x_{d7} downstream of the seventh one.

If the distribution at x_u corresponds to an equilibrium turbulent

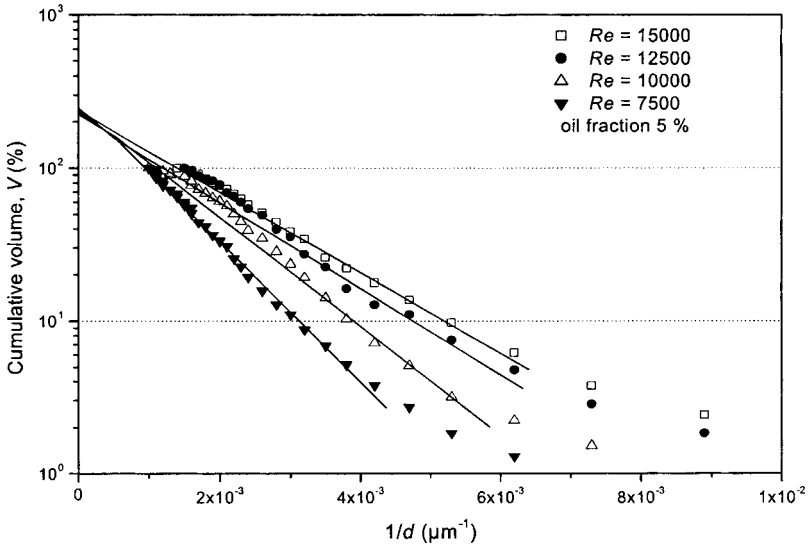

Fig. 9 Size distribution function in the Schwarz-Bezemer presentation

flow with turbulence production at the wall, turbulence is completely redistributed inside the HEV for stations x_{d1} and x_{d7}. A peak of turbulence production is observed at the top of the tabs ($y=0.37\ R$) that splits the flow in two regions of approximately equal turbulent energy: the tube core and the wake of the tabs. Obviously the level of turbulence increases downstream, reaching a plateau level that Mokrani et al. [4] have shown to be located between the second and the third tabs.

The quality of the turbulent flow was analyzed by plotting (Fig. 11) the probability density functions (pdf's) with respect to the normal law. Figure 11(*a*) shows that the pdf in the tube center does not deviate from the normal law either at x_u or at x_{d7} and deviates only transitionally after the first tab. Thus in this region the turbulence is intensified by the action of the tabs, but the distribution is not affected. Figure 11(*b*) shows the more complex situation in the wake region; here the pdf exhibits high skewness and flatness at x_{d1} and x_{d7}, indicating that the turbulence there cannot be considered homogeneous and isotropic.

A schematic description of the flow inside the HEV may require considering three zones: the turbulent core region with high mean and fluctuating velocities, the wake region with high fluctuating velocity but low mean motion, and the region of sharp shear flow

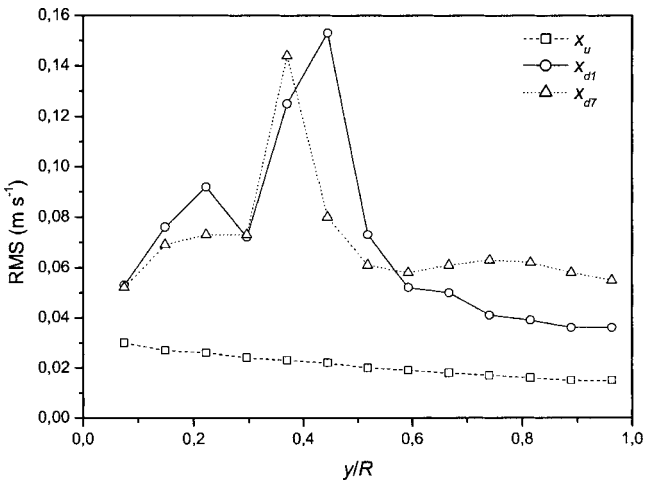

Fig. 10 Radial profiles of the rms velocity along axis *B* at axial locations x_u, x_{d1}, and x_{d7} (LDV)

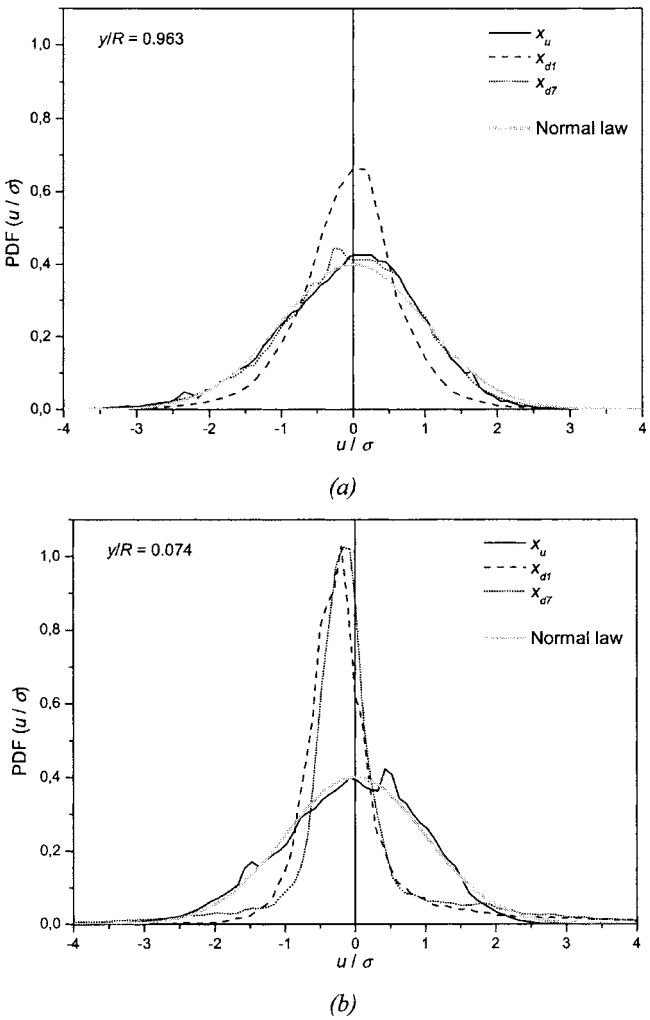

Fig. 11 Pdf of the turbulent axial velocity at the axial locations x_u, x_{d1}, and x_{d7} in (*a*) the center and (*b*) the wake regions

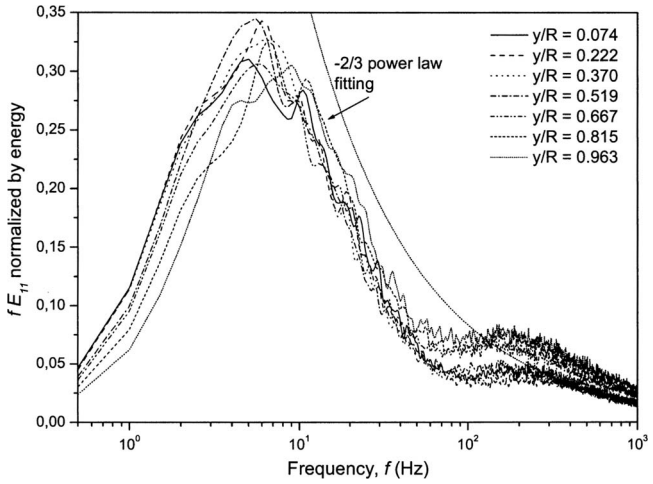

Fig. 12 Normalized premultiplied spectrum of the turbulent axial velocity in the upstream flow at different radial locations on axis *B* (LDV)

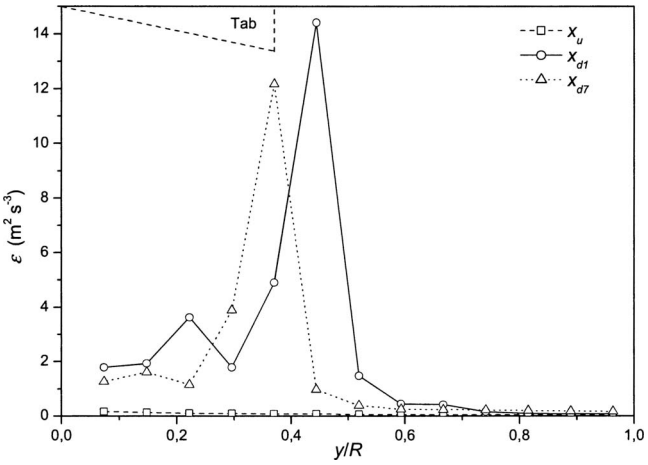

Fig. 14 Profiles of turbulent dissipation rate on axis *B* at locations x_u, x_{d1}, and x_{d7}. The limits of the tab location are added.

between them. The following sections analyze the turbulence through its spectral energy distribution and its autocorrelation function.

5.2 Turbulence Spectrum. To visualize the frequency range of energetic eddies in the turbulence, Fig. 12 plots the premultiplied spectrum $f\,E_{11}$, with f the frequency and E_{11} the power density spectrum of the axial velocity component. Then the area under the curve is proportional to the energy of the signal u'^2 and can be used to normalize them. Figure 12 compares the normalized spectra at the upstream position x_u with the $-\frac{2}{3}$ power-law curve indicating the theoretical energy cascade in the inertial range.

All curves collapse together with the same integral time scale at the point where the spectra begin to follow the $-\frac{2}{3}$ power law. The upstream turbulence inside the tube is quite homogeneous, with a simple diffusion of the turbulence energy from the wall to the center and only slight differentiation of the coherent large structures.

On the other hand, the spectra at the end of the HEV (x_{d7}) fall into different types in comparison with the upstream turbulent spectrum (Fig. 13). The most energetic flow is obviously found at the top of the tabs $y/R=0.37$ (shear flow), where the turbulence energy is produced at higher frequency than in the upstream flow. The integral time scale is roughly ten times smaller than that of x_u.

The spectrum at the center is bimodal: a large-scale peak similar to the upstream turbulence combines with a turbulent cascade at higher frequencies resulting from the radial diffusion of the shear zone. In the wake region the spectrum is more complex, with a quite large peak at roughly the same integral time scale. Thus, except in this wake region, the turbulence is well modeled by homogeneous and isotropic turbulence.

With the help of these spectra, the integral length scale is calculated by Eq. (3) and then the local turbulent dissipation rate ε as computed with Eq. (2) is plotted in Fig. 14 versus y/R at the three axial positions [even though Eqs. (2) and (3) are not completely valid below $y/R<0.37$]. The highest energy dissipation rate ε is found at the high-shear-velocity position at roughly the same radial position as the tab tip. This value will be used further to predict the mixing efficiency of this turbulence in the HEV.

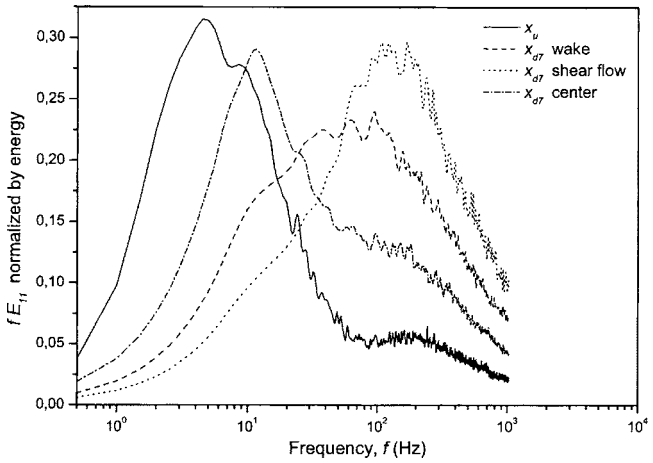

Fig. 13 Normalized premultiplied spectra at location x_{d7} (axis *B*) according to radial locations (wake, center, and shear region) compared with upstream spectrum

6 Discussion

This section examines the breakup process and the dispersion performance in order to clarify whether the TKE dissipation rate effectively governs the maximum particle diameter and to determine the energy consumption required to achieve the oil dispersion.

6.1 Energy Cost. The energy consumed in this experiment is the external pumping power necessary to propel the fluids through the static mixer, which is mostly dissipated into heat through turbulent fluctuations. As shown in Fig. 15, a small part of this energy is devoted to the potential surface energy involved in the creation of new interfacial area during emulsification:

$$E_S = \frac{\sigma A}{\rho} \tag{12}$$

The mean energy dissipation rate is computed from the total power consumption for a unit mass of the processed fluid:

$$\bar{\varepsilon} = \frac{Q\Delta P}{\rho V} = \frac{U\Delta P}{\rho L}(\mathrm{W\ kg^{-1}}) \tag{13}$$

Hence the specific energy obtained by integration over the residence time L/U is

$$E = \frac{\Delta P}{\rho}(\mathrm{J\ kg^{-1}}) \tag{14}$$

The pressure-drop values in the test section were measured and compared with the theoretical values for a simple smooth duct of

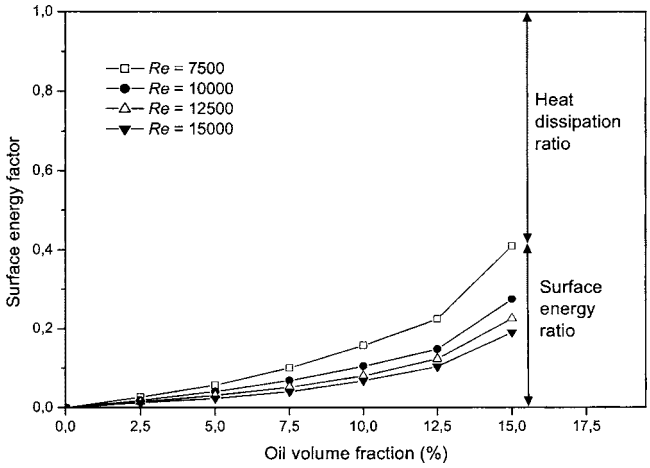

Fig. 15 Ratio of surface energy to available mechanical energy

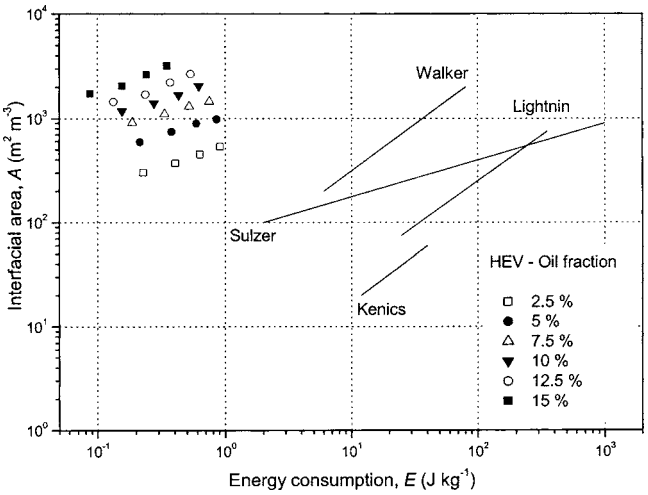

Fig. 17 Comparative energy cost of HEV

equal hydraulic diameter. The z factor, defined as the pressure-drop ratio between the HEV and the simple duct,

$$z = \left(\frac{\Delta P_{HEV,\Phi}}{\Delta P_{\text{Duct},0}} \right) \tag{15}$$

shows that the vortex generators provide up to an eightfold increase in dissipative efficiency, independent of the flow rate (Table 2).

Moreover, the pressure-drop measurements show an important decrease by increasing the oil volume concentration, because of the damping of turbulence occurring near the contact surface between the two phases [3]. The damping factor (Fig. 16) is calculated with reference to the single-phase flow in the HEV.

6.2 Efficiency. To assess the efficiency of HEV as an emulsifier, its experimentally measured energy cost is compared with those of existing devices as reported by previous investigators. Figure 17 correlates the energy spent in phase dispersion with the interfacial area generated by each system [17]. The working zone of the HEV mixer is in the small-energy range (between 0.1 and 1 J kg^{-1}) for a typical interfacial area of 300–3000 m^2 m^{-3}. This shows a good efficiency for the dispersion of immiscible liquids: a decrease in energy consumption by a factor of up to 1000 for interfacial areas around 1000 m^2 m^{-3}.

Table 2 z factor

Φ(%)	0	2.5	5	7.5	10	12.5	15
z	7.87	7.68	7.21	6.31	5.23	4.49	2.93

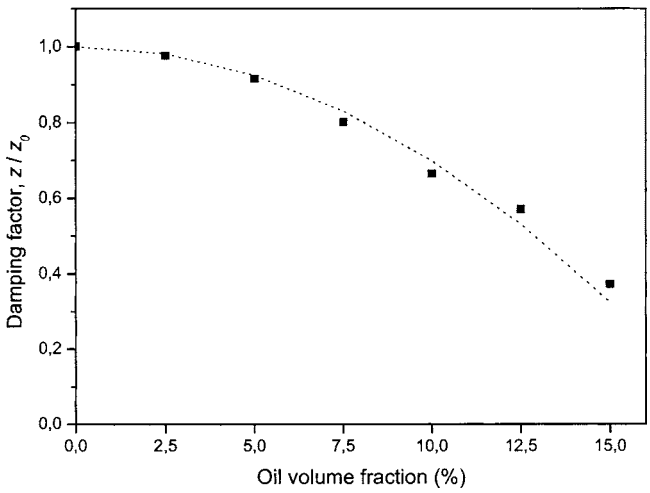

Fig. 16 Damping factor

6.3 Equilibrium Size. A large amount of laser Doppler velocimetry data was obtained and analyzed in the HEV in order to describe the turbulent energy dissipation distribution in the HEV geometry. Equation (2) was used to evaluate the energy dissipation.

The macroscale Λ was derived from the temporal autocorrelation function of the instantaneous velocity. An appropriate convection velocity was calculated by using a generalized Taylor hypothesis. Wu and Patterson [18] have already obtained satisfactory results using this method.

It is well established that in a given system, where some disruptions of the droplets occur, a maximum equilibrium droplet size is reached that can resist the turbulent forces. It is understandable that the successive divisions leading to this equilibrium size will need a "certain" time. If this time is longer than the residence time, the droplets obtained will be coarser than the predicted size, and thus the system can be optimized by increasing the residence time, for instance by adding another mixing element. The time scale proposed by some authors (Davies [19], Hesketh et al. [11]) suggests that the minimal residence time for optimal division is between 1.5 and 10 s (the characteristic time for droplet breakup is estimated at about 1 μs and a sufficient number of divisions must take place).

To analyze these features in the present system, Fig. 18 compares the experimental maximum drop size to that predicted by Eq. (4). The predicted maximum values with the mean turbulence dissipation rate are slightly higher than the measured values. This could mean that the equilibrium diameter has been reached and that the HEV mixer is long enough. Nevertheless, considering the local nature of the dissipation rate and recalling that the maximum "surviving" drop size in the flow is governed by the highest turbulence intensity, the maximum diameter was also computed from the maximum ε value. Following this hypothesis, the equilibrium seems to have been achieved. In other words, it can be concluded from this plot that the actual drop size is controlled by a dissipation rate of the order of the maximum local value. The nonuniformity of the dissipation field may explain the discrepancy between various flow configurations, and consequently the large variety of constants C in Eq. (2).

7 Conclusions

The formation of droplets in the turbulent flow of two immiscible fluids in a HEV mixer was studied. The mixing mechanism

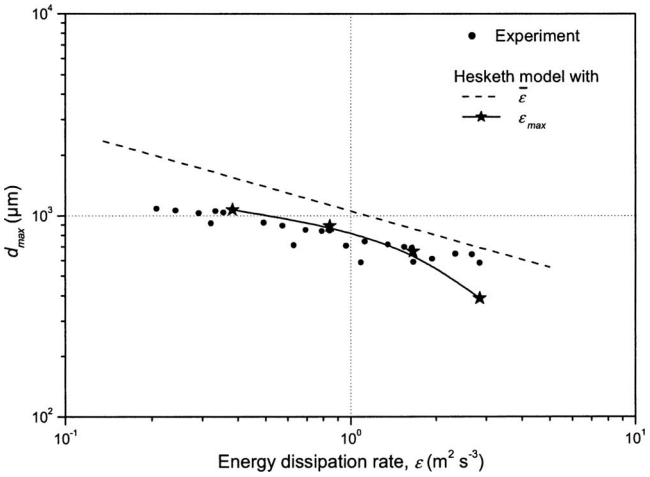

Fig. 18 Predicted equilibrium diameter using Hesketh model Eq. (4)

is the generation of a cascade of longitudinal vortices behind rows of tabs fixed in a straight tube of circular cross section. By generating extra shear in the flow, vortices increase the turbulent energy dissipation, which contributes directly to droplet breakup.

The very low energy level and the relatively high contact obtained without any surfactant show that HEV mixers have high potential for industrial applications.

Experiments carried out in low hold-up range (0%–15%) suggest that the Sauter mean diameter varies with the −0.4 power of the TKE dissipation rate [Eq. (4)], demonstrating that the dominant mechanism of emulsification is turbulent disruption.

The size distribution of the droplets obtained with HEV was modeled according to the method proposed by Schwarz and Bezemer [16]. In a log-linear coordinate system the data showed a linear relation between the cumulative volume (in %) of droplet diameters and the inverse of the bounding diameter d, verifying that the Schwarz-Bezemer model applies here.

The overall energy cost of the HEV mixer was studied. Experimental pressure-drop measurements showed that the vortex generators increase the dissipative efficiency as much as eightfold, and that this increase is independent of the flow rate. The energy consumption for generation of interfacial area with the HEV mixer was compared with those of some common static mixers. In the range of interfacial area 1000 m^2 m^{-3}, it was shown that HEV is up to 1000 times more energy efficient than other mixers.

A striking conclusion of this study is that the droplet size is controlled by the maximum turbulent kinetic energy dissipation rather that the mean turbulent kinetic energy dissipation, as commonly believed.

Nomenclature

A = interfacial area, m^2
C, C_i = constants (i=1 to 4)
D = reactor diameter, m
D_H = hydraulic diameter, m
E = specific energy, J kg^{-1}
E_s = potential surface energy, J kg^{-1}
L = static mixer length, m
N_{Vi} = Hinze's viscosity group
Q = volume flow rate, m^3 s^{-1}
ΔP = pressure drop, Pa
Re = Reynolds number
T = time macroscale, s
U = mean velocity, m s^{-1}
V = volume, m^3
$V\%$ = cumulative volume, %
We = Weber number
a = characteristic diameter, m
d = diameter, m
d_{32} = Sauter mean diameter, m
l = Prandtl mixing length, m
q = turbulent kinetic energy, m^2 s^{-2}
u = mean fluctuation velocity, m s^{-1}
x_u = axial location upstream of the mixer
x_{d1} = axial location downstream of the first tab
x_{d7} = axial location downstream of the seventh tab
z = pressure ratio

Greek Symbols

ε = energy dissipation rate, W kg^{-1}
$\bar{\varepsilon}$ = mean rate of energy dissipation, W kg^{-1}
Φ = concentration of dispersed phase, %
Λ = macro scale of turbulent fluctuations, m
μ = dynamic viscosity, Pa s
ρ = density, kg m^{-3}
σ = interfacial tension, N m^{-1}

Subscripts

c = continuous phase
$conv$ = convective
$crit$ = critical
d = dispersed phase
max = maximum
0 = Φ=0%

Dimensionless Numbers

Re = $\rho_c U D_H / \mu_c$ (Reynolds number)
We = $\rho_c U^2 D_H / \sigma$ (Weber number)

References

[1] Phillips, C. H., Lauschke, G., and Peerhossaini, H., 1997, "Experimental and numerical studies of exothermic reacting flows in a simulated heat exchanger passage," Appl. Therm. Eng., **10**, pp. 809–824.
[2] Macosko, C. W., 1989, *RIM Fundamental of Reaction Injection Molding*, Hanser Publishers, New York.
[3] Lemenand, T., Della Valle, D., Zellouf, Y., and Peerhossaini, H., 2003, "Droplets formation in turbulent mixing of two immiscible fluids in a new type of static mixer," Int. J. Multiphase Flow, **29**, pp. 813–840.
[4] Mokrani, A., Castelain, C., and Peerhossaini, H., 1995, "Experimental study of the turbulent flow inside a motionless on-line mixer," in *Process Intensification for the Chemical Industry*, C. H. Philips (ed.), BHR Ltd, pp. 115–124.
[5] Mokrani, A., Castelain, C., and Peerhossaini, H., 2005, "Experimental study of the influence of the rows of vortex generators on turbulence structure in a tube," Exp. Fluids (submitted for publication).
[6] Batchelor, G. K., 1953, *The Theory of Homogeneous Turbulence*, Cambridge University Press, Cambridge.
[7] Van Doorn, M., 1981, "On Taylor's hypothesis in turbulent shear flows", Internal note 811123, University of Missouri—Rolla.
[8] Townsend, A. A., 1976, *The Structure of Turbulent Shear Flow*, Cambridge University Press, Cambridge.
[9] Tennekes, H., and Lumley, J. L., 1997, *A First Course in Turbulence*, The MIT Press, Cambridge.
[10] Lawn, C. J., 1971, "The determination of the rate of dissipation in turbulent flow," J. Fluid Mech., **48**(3), pp. 477–505.
[11] Hesketh, R. P., Etchells, A. W., and Russell, T. W. F., 1991, "Bubble breakage in pipeline flow," Chem. Eng. Sci., **46**(1), pp. 1–9.
[12] Shinnar, R., 1961, "On the behaviour of liquid dispersions in mixing vessels," J. Fluid Mech., **10**, pp. 259–275.
[13] Berkman, P. D., and Calabrese, R. V., 1988, "Dispersion of viscous liquids by turbulent flow in a static mixer," AIChE J., **34**(4), pp. 602–609.
[14] Pacek, A. W., Man, C. C., and Nienow, W., 1998, "On the Sauter mean diameter and size distributions in turbulent liquid/liquid dispersions in a stirred vessel," Chem. Eng. Sci., **53**(11), pp. 2005–2011.
[15] Sprow, F. B., 1967, "Distribution of drop sizes produced in turbulent liquid-liquid dispersion," Chem. Eng. Sci., **22**, pp. 435–442.
[16] Schwarz, N., and Bezemer, C., 1956, Kolloid-Z., **146**, pp. 139–145.
[17] Al Taweel, A. M., and Chen, C., 1996, "A novel static mixer for the effective dispersion of immiscible liquids," Trans. Inst. Chem. Eng., Part A, **74**, pp. 445–450.
[18] Wu, H., and Patterson, G. K., 1989, "Laser-Doppler measurements of turbulent flow parameters in a stirred mixer," Chem. Eng. Sci., **44**(10), pp. 2204–2221.
[19] Davies, J. T., 1985, "Drop sizes of emulsions related to turbulent energy dissipation rates," Chem. Eng. Sci., **40**(5), pp. 839–842.

Influence of Ribbon Structure Rough Wall on the Microscale Poiseuille Flow

Haoli Wang
Doctoral Student
e-mail: wanghaoli@mailst.xjtu.edu.cn

Yuan Wang[1]
Professor
e-mail: wangyuan@mail.xjtu.edu.cn

Jiazhong Zhang
Associate Professor

Department of Fluid Engineering,
School of Energy & Power Engineering,
Xi'an Jiaotong University,
28 Xianning Western Road,
Xi'an, Shaanxi, 710049,
People's Republic of China

The regular perturbation method is introduced to investigate the influence of two-dimensional roughness on laminar flow in microchannels between two parallel plates. By superimposing a series of harmonic functions with identical dimensional amplitude as well as the same fundamental wave number, the wall roughness functions are obtained and the relative roughness can be determined as the maximal value of the product between the normalized roughness functions and a small parameter. Through modifying the fundamental wave number, the dimensionless roughness spacing is changed. Under this roughness model, the equations with respect to the disturbance stream function are obtained and analyzed numerically. The numerical results show that flowing in microchannels are more complex than that in macrochannels; there exist apparent fluctuations with streamlines and clear vortex structures in microchannels; the flow resistances are about 5–80% higher than the theoretical value under different wall-roughness parameters. Furthermore, analysis shows that the effect of roughness on the flow pattern is distinct from that on the friction factor. [DOI: 10.1115/1.2060733]

1 Introduction

Laminar flows in microchannels are significantly different from those in macrochannels, which have been shown by the fact that significant differences exist in both the friction loss and their flow pattern. One of the important reasons is believed to be the influence of the wall roughness on the flow. Much research about this has been implemented since the early 1980s and presented actively in recent years.

The experiments for laminar flow in different microchannels with the relative roughness from 0.016 to >0.05 were implemented by Wu and Little [1], Mala and Li [2], Celeta et al. [3], Li et al. [4], Papautsky et al. [5], Jiang et al. [6], and Stanley [7]. The results show that the flow resistances are about 10–90% higher than the theoretical values in most experiment data, and even a few of them are 350% above or 20% below the theoretical values [1,7].

In the theoretical and numerical analysis, Mala and Li [2] introduced a roughness viscosity model (RVM) based on work by Merkle et al. [8] and this model was implemented to water flowing through microtubes [2] and trapezoidal channels [9]. Kleinstreuer and Koo [10] introduced a porous medium layer (PML) mode to simulate several kinds of microscale flow. Furthermore, Du [11] numerically simulated laminar flow in rough microtubes to study the mechanism for the roughness effect. A similar research of three-dimensional flow in microchannel was conducted by Hu et al. [12]. These theoretical and numerical results show significant effects of surface roughness on both the velocity distribution and the pressure drop.

As wall roughness is a small quantity compared to the scale of microchannels, it can be regarded as slight distortions on the surface of smooth plates. There is a well-known regular perturbation method to study these flow problems [13], and it was used widely in other literatures [14,15]. In this study, the method of regular perturbation is introduced to study the influences of wall roughness on the Poiseuille flow in microchannels. In addition, the rough curves in this study are obtained by superposing a series of harmonic functions, so that the rough curves are closer to the real walls.

2 Theory

2.1 Perturbation Equation The flows in the microchannels between two parallel plates are shown in Fig. 1. The plates are presumed to have the same rough heights and distributions on both inner surfaces. The distribution functions are written as $k_s(x)=a\varepsilon f(x)$. Here, ε is a small parameter and $\varepsilon \ll 1$, $f(x)$ an arbitrary function fluctuating near its equilibrium position. In this system the curved face for the upper plate is described by $y=a[1-\varepsilon f(x)]$ and $y=a\varepsilon f(x)$ for the lower plate.

As wall roughness must be considered in microchannels, the flows become two-dimensional instead of one-dimensional. Taking wall spacing a as the characteristic length, average velocity U_0 as the characteristic velocity, and ρU_0^2 as the characteristic pressure, for a time-independent and fully developed Newtonian fluid, the dimensionless Navier-Stokes equations at interval $y \in [0, \frac{1}{2}]$ are derived as

$$\nabla \cdot \mathbf{u} = 0 \tag{1}$$

$$(\mathbf{u} \cdot \nabla)\mathbf{u} = -\nabla p + \mathrm{Re}^{-1}\nabla^2 \mathbf{u} \tag{2}$$

Boundary conditions must satisfy the no-slip and symmetry conditions, i.e.,

$$\text{at } y = \varepsilon f(x) \quad u = v = 0 \tag{3a}$$

$$\text{at } y = \frac{1}{2} \quad \frac{\partial u}{\partial y} = v = 0 \tag{3b}$$

The dimensionless stream function ψ is introduced, which satisfies the following relationship:

$$u = \partial\psi/\partial y, \quad v = -\partial\psi/\partial x \tag{4}$$

Substituting Eq. (4) into Eqs. (1) and (2), we obtain the equation of stream function along with the boundary conditions as

$$\left(\frac{\partial \psi}{\partial y}\frac{\partial}{\partial x} - \frac{\partial \psi}{\partial x}\frac{\partial}{\partial y}\right)\nabla^2\psi = \mathrm{Re}^{-1}\nabla^4\psi \tag{5}$$

[1]Corresponding author.

Contributed by the Fluids Engineering Division for publication in the JOURNAL OF FLUIDS ENGINEERING. Manuscript received by the Fluids Engineering Division January 11, 2005; final manuscript received: June 25, 2005. Assoc. Editor: Kenneth Breuer.

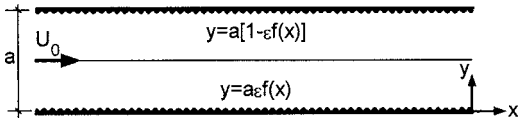

Fig. 1 Model of microchannel and the coordinate system

$$\text{at } y=\varepsilon f(x) \quad \frac{\partial\psi}{\partial x}=\frac{\partial\psi}{\partial y}=0 \tag{6a}$$

$$\text{at } y=\frac{1}{2} \quad \frac{\partial\psi}{\partial x}=\frac{\partial^2\psi}{\partial y^2}=0 \tag{6b}$$

As a small parameter appears in boundary conditions, the stream function ψ should be expanded as perturbation series

$$\psi(x,y)=\psi_0(x,y)+\varepsilon\psi_1(x,y)+O(\varepsilon^2) \tag{7}$$

and the boundary conditions at wall surface need to be expanded as Taylor series at $y=0$[13], i.e.,

$$\psi(x,y)|_{y=\varepsilon f(x)}=\psi(x,0)+\varepsilon f(x)\psi'(x,0)+O(\varepsilon^2) \tag{8}$$

Substituting Eq. (7) into Eq. (8) and emerging the like terms in ε, we have

$$\psi(x,y)|_{y=\varepsilon f(x)}=\psi_0(x,0)+\varepsilon[\psi_1(x,0)+f(x)\psi_0'(x,0)]+O(\varepsilon^2) \tag{9}$$

Substituting Eq. (9) into Eq. (6), the boundary conditions at $y=0$ and $y=1/2$ are derived as

$$\text{at } y=0 \quad \frac{\partial}{\partial x}\{\psi_0+\varepsilon[\psi_1+f(x)\psi_0']\}=\frac{\partial}{\partial y}\{\psi_0+\varepsilon[\psi_1+f(x)\psi_0']\}=0 \tag{10a}$$

$$\text{at } y=\frac{1}{2} \quad \frac{\partial}{\partial x}(\psi_0+\varepsilon\psi_1)=\frac{\partial^2}{\partial y^2}(\psi_0+\varepsilon\psi_1)=0 \tag{10b}$$

where ψ_0 and ψ_1 denote the zero-order and first-order stream functions, respectively; the superscript $(\cdot)'$ denotes $\partial/\partial y$.

Substituting Eq. (7) into Eq. (5) and emerging the like terms in ε, the equations of ψ_0 and ψ_1 along with boundary conditions (10) are rewritten as follows:

$$\left(\frac{\partial\psi_0}{\partial y}\frac{\partial}{\partial x}-\frac{\partial\psi_0}{\partial x}\frac{\partial}{\partial y}\right)\nabla^2\psi_0=\mathrm{Re}^{-1}\nabla^4\psi_0 \tag{11}$$

$$\text{at } y=0 \quad \frac{\partial\psi_0}{\partial x}=\frac{\partial\psi_0}{\partial y}=0 \tag{12a}$$

$$\text{at } y=\frac{1}{2} \quad \frac{\partial\psi_0}{\partial x}=\frac{\partial^2\psi_0}{\partial y^2}=0 \tag{12b}$$

$$\sum_{i=0}^{1}\left(\frac{\partial\psi_i}{\partial y}\frac{\partial}{\partial x}-\frac{\partial\psi_i}{\partial x}\frac{\partial}{\partial y}\right)\nabla^2\psi_{1-i}=\mathrm{Re}^{-1}\nabla^4\psi_1 \tag{13}$$

$$\text{at } y=0 \quad \frac{\partial\psi_1}{\partial x}=-\psi_{0,y}'df(x)/dx-f(x)\,\partial\psi_{0,y}'/\partial x,$$

$$\frac{\partial\psi_1}{\partial y}=-f(x)\psi_{0,y}'' \tag{14a}$$

$$\text{at } y=\frac{1}{2} \quad \frac{\partial\psi_1}{\partial x}=\frac{\partial^2\psi_1}{\partial y^2}=0 \tag{14b}$$

Since the flow is fully developed, the dimensionless zero-order velocity solution will be

$$u_0=6y(1-y) \tag{15}$$

Substituting Eq. (15) into Eqs. (13) and (14), the equation and boundary conditions of ψ_1 are reduced as

$$\left(u_0\frac{\partial}{\partial x}\nabla^2-\frac{d^2u_0}{dy^2}\frac{\partial}{\partial x}\right)\psi_1=\mathrm{Re}^{-1}\nabla^4\psi_1 \tag{16}$$

$$\text{at } y=0 \quad \frac{\partial\psi_1}{\partial x}=0, \quad \frac{\partial\psi_1}{\partial y}=-6f(x) \tag{17a}$$

$$\text{at } y=\frac{1}{2} \quad \frac{\partial\psi_1}{\partial x}=\frac{\partial^2\psi_1}{\partial y^2}=0 \tag{17b}$$

2.2 Solving of the Equation. The wall roughness varies irregularly along the x direction but presents some periodic characters. For the sake of simplicity, $f(x)$ is assumed as a periodic function which can be expanded in Fourier series. The complex form of Fourier series is as follows:

$$f(x)=\sum_{n=-\infty}^{\infty}C_n e^{i\alpha_n x} \tag{18}$$

where α_n is the wave number of the n-order harmonic function and C_n is the Fourier coefficients.

The presence of the wall roughness will lead to the disturbance of the flow field inevitably; hence, ψ_1 is no other than the first-order response function and it could be assumed as follows:

$$\psi_1(x,y)=\sum_{n=-\infty}^{\infty}\varphi_n(y)e^{i\alpha_n x} \tag{19}$$

where $\varphi_n(y)$ is the nth amplitude function with respect to y.

From Eqs. (16) and (19), the equation φ_n and its boundary conditions are derived as

$$[u_0(D^2-\alpha_n^2)-Du_0]\varphi_n=(i\alpha_n\mathrm{Re})^{-1}(D^2-\alpha_n^2)^2\varphi_n \tag{20}$$

$$\text{at } y=0 \quad \varphi_n=0, \quad D\varphi_n=-6C_n \tag{21a}$$

$$\text{at } y=\tfrac{1}{2} \quad \varphi_n=D^2\varphi_n=0 \tag{21b}$$

where the operators D and D^2 denote d/dy and d^2/dy^2, respectively. The equations should be solved by the numerical methods, and the finite difference method is employed to solve them in this study.

2.3 Model of Rough Elements. In general, a periodic function can be decomposed into a series of finite or infinite simple harmonic functions according to the theory of Fourier series. In this work, the wall roughness functions $f(x)$ are considered as the following expression:

$$f(x)=\sum_{n=1}^{N}A_n\cos(n\alpha_0 x) \tag{22}$$

where α_0 is fundamental wave number, N the number of cosine function superimposed, and A_n the amplitude of harmonic functions. We take $N=20$ in this study.

Any curve $f(x)$ displays one maximal crest (or trough) and $N-1$ lower crests (or troughs) in a period. The space between the two closest maximal crests depends on the fundamental wave number α_0 (see Fig. 2, which gives the cases of $\alpha_0=\pi, 3\pi, 5\pi$). The roughness functions are normalized according to Eqs. (23) and (24).

$$h(x)=\frac{f(x)}{f(x)_{\max}-f(x)_{\min}} \tag{23}$$

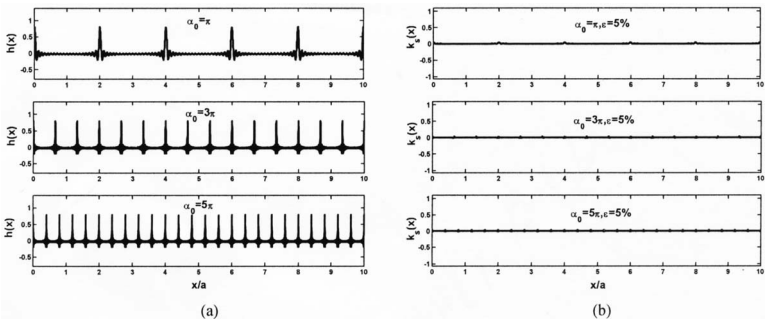

Fig. 2 Wall roughness functions with different fundamental wave numbers: (*a*) curves of $h(x)$ and (*b*) curves of $k_s(x)$

$$k_s(x) = \varepsilon h(x) \tag{24}$$

Hence, the relative roughness, which is defined as the vertical difference between the maximal crests and minimum troughs (which are adjacent), has the value ε. The dimensionless roughness spacing is $s/a = 2\pi/\alpha_0$. From Eqs. (19), (22), and (23), ψ_1 is obtained as

$$\psi_1(x,y) = \frac{\sum_{n=1}^{N} \varphi_n(y) e^{i\alpha_n x}}{f(x)_{\max} - f(x)_{\min}} + c.c. \tag{25}$$

where $c.c.$ denotes the complex conjugate. $\varphi_n(y)$ are determined by Eq. (20) and boundary conditions (21).

In this study, all dimensionless parameters are chosen as follows: (i) The relative roughness ε: 0.005, 0.01, 0.02, 0.03, and 0.05; (ii) the fundamental wave number α_0: π, 2π, 3π, 4π, 5π and the corresponding dimensionless roughness spacing s/a are 2, 1, $\frac{2}{3}$, $\frac{1}{2}$, and $\frac{2}{5}$; (iii) $A_n = 1$ for all the components of $f(x)$; and (iv) Reynolds number Re: 100–500.

2.4 Flow Pattern and Friction. The method of regular perturbation converts a physical domain into a computational domain, and physical quantities in the microchannels with rough walls are correspondingly transformed into that between two planes. The characters of flow in physical domain can be reflected well by the variables obtained in its computing counterpart. In fact, all the variable distributions are consistent in most areas of both domains except the area near walls.

2.4.1 Velocity and Vorticity. The overall velocity field in the computing domain can be written as

$$\mathbf{u} = \mathbf{u}_0 + \varepsilon \mathbf{u}_1 + O(\varepsilon^2) \tag{26}$$

The components are $u = u_0 + \varepsilon u_1$ in the x direction and $v = \varepsilon v_1$ in the y direction. Accordingly, the vorticity field is governed as follows:

$$\mathbf{\Omega} = \frac{1}{2}\left(\varepsilon \frac{\partial v_1}{\partial x} - \varepsilon \frac{\partial u_1}{\partial y} - \frac{\mathrm{d}u_0}{\mathrm{d}y}\right)\mathbf{k} \tag{27}$$

where $\mathbf{k}$ is unit vector in the z direction. Equations (26) and (27) show that velocity and vorticity in microchannel are different from the Poiseuille flow.

2.4.2 Friction Loss. For the laminar flow in macrochannels, the product between Darcy factor C_f and Reynolds number is a constant and equal to the theoretical value. In that case, friction loss comes absolutely from the wall shear stress, which can be proved by the viscous dissipation being equal to the work of wall shear stress according to

$$\Phi = \tau_0 A U_0 \tag{28}$$

where τ_0 is the shear stress of the surfaces per unit area; A the surface area and U_0 the averaged velocity; and Φ the total dissipation rate.

The perturbation analysis shows that if the wall roughness is considered, the viscous dissipations are quite different from the theoretical value. Part of the dissipations results from the wall viscous shear work and another from the perturbation velocity gradient. An increase of the viscous dissipations implies an increase of energy losses. Hence, energy loss can be obtained by the viscous dissipation rate.

For the incompressible Newtonian fluid, the total viscous dissipation rate within a given area is computed as follows (using the subscript notation):

$$\Phi = -\frac{\mu}{2}\int_V \left(\frac{\partial u_i}{\partial x_j} + \frac{\partial u_j}{\partial x_i}\right)\left(\frac{\partial u_i}{\partial x_j} + \frac{\partial u_j}{\partial x_i}\right) dV \quad (i = 1,2) \tag{29}$$

where μ is viscosity coefficient and V the volume of flow region.

According to Eq. (29), the total viscous dissipation rate of Poiseuille flow Φ_0 is computed as

$$\Phi_0 = -\mu \int_V \left(\frac{du_0}{dy}\right)^2 dV \tag{30}$$

In the case of flowing in the microchannel, the viscous dissipation rate Φ^* has the form

$$\Phi^* = -\mu \int_V \left[2\left(\varepsilon \frac{\partial u_1}{\partial x}\right)^2 + 2\left(\varepsilon \frac{\partial v_1}{\partial y}\right)^2 + \left(\frac{du_0}{dy} + \varepsilon \frac{\partial u_1}{\partial y} + \varepsilon \frac{\partial v_1}{\partial x}\right)^2\right] dV \tag{31}$$

The ratio of Darcy friction factors C_f^*/C_f is equal to the ratio of total viscous dissipations Φ^*/Φ_0 if the length in flow direction is long enough, i.e.,

$$C^* = C_f^*/C_f = \Phi^*/\Phi_0 \tag{32}$$

where C_f is the theoretical value of Darcy factor and C_f^* is the Darcy factor in the case of roughness being considered.

3 Results and Discussion

3.1 First-Order Stream Function and Velocity. It is known that both the first-order dimensionless stream function ψ_1 and velocity in transverse direction v_1 are equal to zero if the roughness is not being considered (flow in the channel between two flat plates, say); hence, their variations under the conditions of microchannels without ignoring the wall roughness will intuitively re-

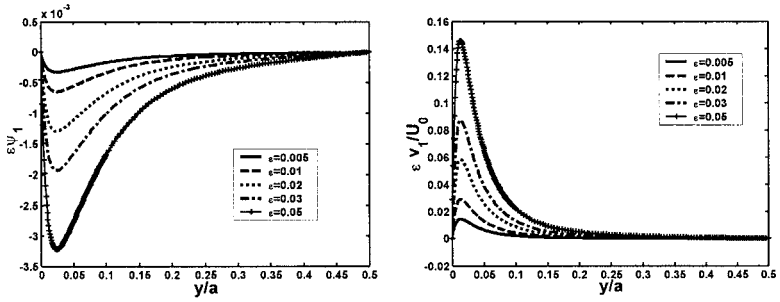

(a) (b)

Fig. 3 Variation of first-order dimensionless stream function (*a*) and velocity of the *y* direction (*b*) in a flow field at the position of rough elements under different relative roughness when $\alpha_0=2\pi$

flect the influence of roughness on the flow.

The evolution of the first-order dimensionless stream function and velocity of v_1 in flow field at the position of rough element can be seen in Figs. 3–6, and Fig. 3 presents the evolution of the stream function and velocity under different relative roughness. The results show that greater relative roughness will have a more important influence on flow field.

The influence of the dimensionless rough spacing on the flow pattern is presented in Fig. 4, which shows that the first-order stream-function curves gradually become flat with the decrease of the dimensionless spacing (Fig. 4(*a*)), but the change rate of perturbation velocity increases (Fig. 4(*b*)). The reason for that is the average kinetic energy of main flow increases as the rough spacing decreases. Thus, the disturbances are more difficult to transmit toward the center of flow field, whereas at the same time the more strong shearing action forms in the flow field due to the increment of disturbance frequency per unit length in the flow direction.

Figure 5 presents the influence of the Reynolds number on the stream function and velocity without changing the wall roughness parameters. The results show that both the disturbed area of flow field and the amplitude of disturbance quantities (ψ_1 and v_1) decrease with augmentation of Reynolds number. The explanation for this is that an increase in the Reynolds number will lead to an increase in the average kinetic energy of the main flow so that the effects of wall roughness on the flow pattern will be weakened. It can be noted from Fig. 5(*b*) that the change rate of perturbation velocity increases, to some extent, with an increase of the Reynolds number, which indicates that the viscous dissipations will increase with the augmentation of the Reynolds number.

3.2 Characters of Flow Field. Distributions of stream function near walls and velocity field in half of the channel of the

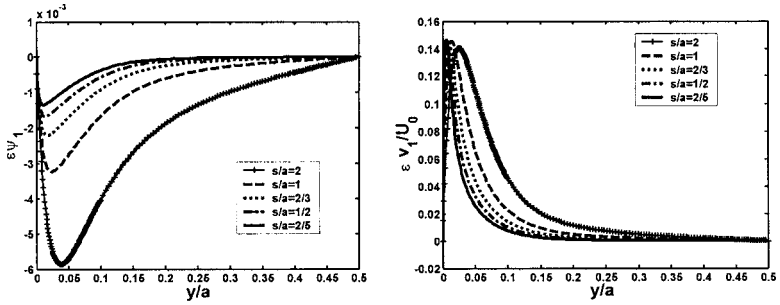

(a) (b)

Fig. 4 Variation of first-order dimensionless stream function (*a*) and velocity in the *y* direction (*b*) in a flow field at the position of rough elements under different spacing when $\alpha_0=2\pi$ and $\varepsilon=0.05$

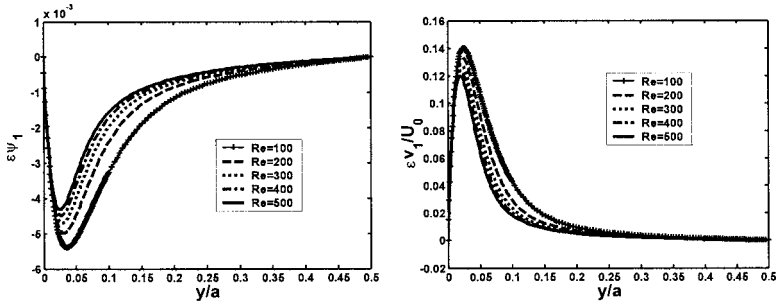

(a) (b)

Fig. 5 First-order dimensionless stream function (*a*) and velocity in the *y* direction (*b*) influenced by the Reynolds number

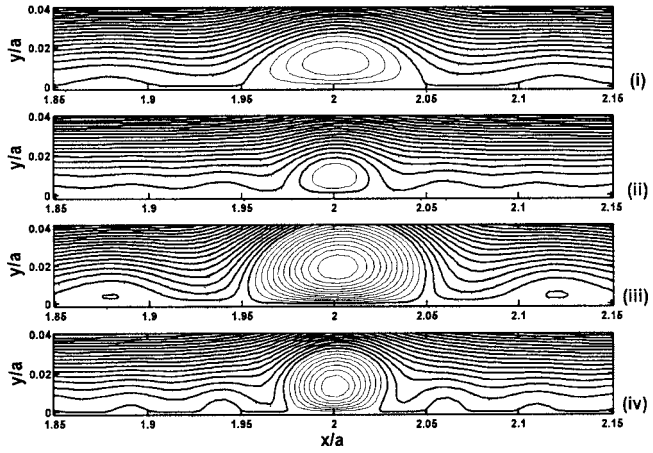

Fig. 6 Distributions of stream function and near-wall vortex structures at Re=100: (i) ε=0.02, s/a=2; (ii) ε=0.02, s/a=1; (iii) ε=0.05, s/a=2; and (iv) ε=0.05, s/a=1

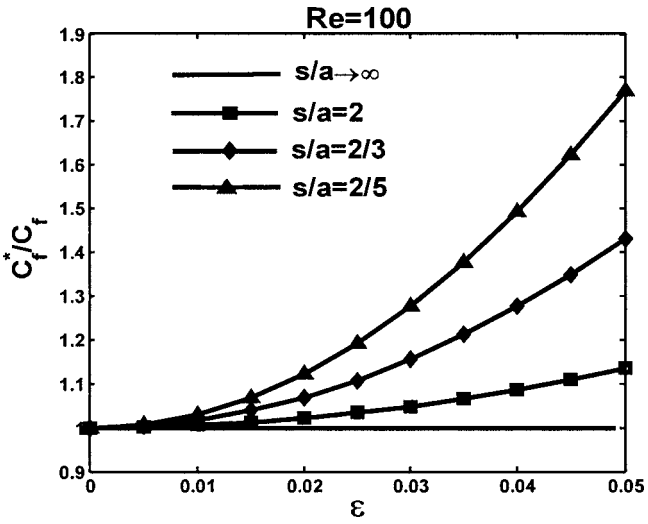

Fig. 8 Friction factors influenced by the relative roughness

computing domain are given in Figs. 6 and 7, respectively. Figure 6 presents the distributions of stream function near the walls (within the range of 0–0.04 in the y direction) with the relative wall roughness being 2% and 5% as well as the dimensionless spacing being 1 and 2, respectively. It is clear that, in the computing domain, apparent vortex structures exist in the flow field near the walls, and the sizes of vortexes are different with the different roughness parameters. Appearance of vortexes can be attributed to the direction of perturbation velocity $\mathbf{u}_1$ being opposite to that of the main flow at the positions of rough elements because of rough walls being converted into "flat" walls by the method of Taylor series expansion. Thus, it can be seen that the disturbances and viscous dissipations are the most intense at the positions of vortexes in flow field. Figures 7(a) and 7(b) show that velocities on the "flat" wall surface are not zero [16]. The values and directions of velocities are variable, and the variations are gradually submerged by the main flow in the course of being apart from the wall.

3.3 Influences on the Friction Factor. It can be seen in Figs. 8–10 that the friction factor ratios C^* are within 2, which are close to most of the experimental values mentioned above. Figures 8 and 9 present the influences of relative roughness and dimensionless spacing on friction factor, respectively. It can be seen that relative roughness and dimensionless rough spacing are two key parameters influencing the friction factor. If the relative roughness increases or the dimensionless rough spacing decreases, the friction factors will increase. This can be attributed to the fact that both the intensity and frequency of wall disturbance augment so that the viscous dissipation rate increases. For the inverse conditions, as the wall surface tends toward flatness, the dissipation rate consequently decreases.

The influence of the Reynolds number on the friction factor is shown in Fig. 10, which indicates that the friction factor increases to some extent with increments of the Reynolds number from 100 to 500. The conclusion is consistent with that from Fig. 5(b). It is implied that the product between the friction factor and Reynolds number deviates from the theoretical value, which is the constant 96 for Poiseuille flow.

4 Conclusions

The perturbation method is an effective method to study the influence of wall roughness on the flow in microchannels. In this study, the wall roughness curve is modeled by superimposing a series of harmonic functions and the corresponding perturbation equations of stream function are derived. By the technique of spatial spectral decomposition for the first-order stream function, a group of ordinary difference equations are presented and approached numerically. The results show that the wall relative roughness, dimensionless roughness spacing, as well as Reynolds number are several important factors on the flow patterns and friction losses.

If the dimensionless spacing of rough elements and the Reynolds number decrease or the relative roughness increases, then the disturbed area will be larger. If the relative roughness and Reynolds number increase or the nondimensional spacing decreases, then the friction factor will increase. These results show

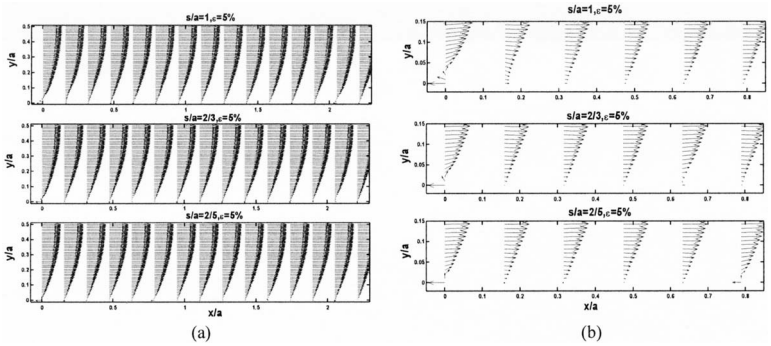

Fig. 7 Velocity fields under different wall parameters in full region (a) and in the near-wall region (b)

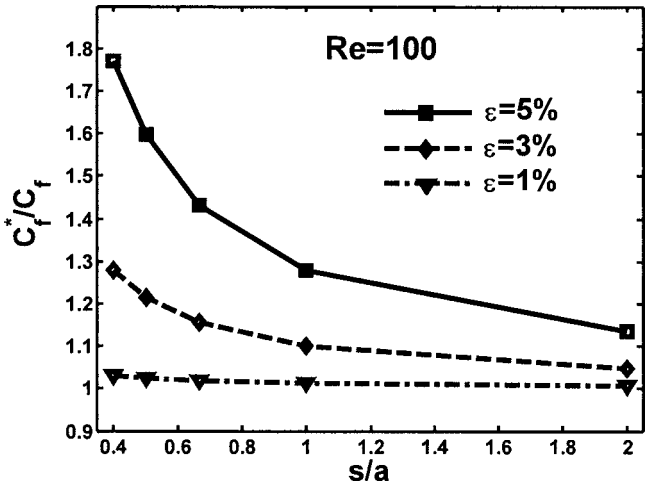

Fig. 9 Friction factors influenced by the dimensionless roughness spacing

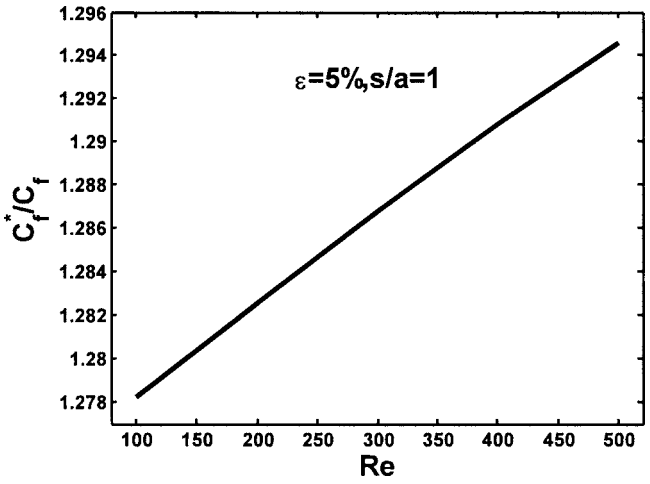

Fig. 10 Friction factors influenced by Reynolds number

that the influence of wall roughness on the flow pattern is different from that on the friction factor. The influence of roughness on flow pattern depends on the kinetic energy of main flow, whereas the effect of roughness on the friction factor depends on the energy dissipation of fluid. In this study a conclusion can be drawn that the effect of roughness should not be ignored unless the relative roughness is $<1\%$.

The method given in this paper can be extended to the analysis of the influence of three-dimensional rough elements on flow in microducts or microtubes. That will be our next study.

Acknowledgment

The authors want to express their thanks to the Chinese Research Fund for the Doctoral Program of Higher Education (No. 20030698004).

Nomenclature

k_s = distribution function of wall roughness, m
a = spacing between two plates, m
ε = small parameter, relative roughness
f = periodic function
U_0 = average velocity, m/s
ρ = density of fluid, kg/m^3
p = dimensionless pressure
Re = Reynolds number
ψ = dimensionless stream function
ψ_0 = zero-order dimensionless stream function
ψ_1 = first-order dimensionless stream function
u_0 = zero-order velocity in x direction, m/s
u_1 = first-order velocity in x direction, m/s
v_1 = first-order velocity in y direction, m/s
C_n, A_n = Fourier coefficient
φ_n = dimensionless wave amplitude of first-order stream function
α_n = wave number
α_0 = fundamental wave number
N = number of superposed harmonic function
h = normalized rough elements height
$\mathbf{u}$ = velocity vector, m/s
$\mathbf{\Omega}$ = vortical vector, 1/s
$\mathbf{k}$ = unit vector in z direction
Φ = dissipation rate, kg/m s^3
Φ_0 = dissipation rate of Poisueille flow, kg/m s^3
Φ^* = dissipation rate of flow in rough channel, kg/m s^3
τ_0 = shear stress of wall, N/m^2
μ = viscosity coefficient, kg/m s
s = spacing of rough elements, m
C_f = Darcy factor of Poisueille flow
C_f^* = Darcy factor of flow in rough channel
x = flow direction
y = transverse direction

References

[1] Wu, P. Y., and Little, W. A., 1983, "Measurement of Friction Factors for the Low of Gases in Very Fine Channels Used for Microminiature Joule—Thomson Refrigerators," Cryogenics, **23**(5), pp. 273–277.
[2] Mala, G. M., and Li, D. Q., 1999, "Flow Characteristics of Water in Microtubes," Int. J. Heat Fluid Flow, **20**, pp. 142–148.
[3] Celata, G. P., Cumo, M., Gulielmi, M., and Zummo, G., 2000, "Experimental Investigation of Hydraulic and Single Phase Heat Transfer in 0.130 mm Capillary Tube," *Proc. Int. Conf. Heat Transfer and Transport Phenomena in Microscale*, Begell House, NY, pp. 108–113.
[4] Li, Z. X., Du, D. X., and Guo, Z. Y., 2000, "Experimental Study on Flow Characteristics of Liquid in Circular Microtubes," *Proc. of Int. Conf. on Heat Transfer and Transport Phenomena in Microscale*, Begell House, NY, pp. 162–167.
[5] Papautsky, I., Brazile, J., Ameel, T., and Frazier, A. B., 1999, "Laminar Fluid Behavior in Microchannels Using Micropolar Fluid Theory," Sens. Actuators, A, **73**(2), pp. 101–108.
[6] Jiang X. N., Zhou, Z. Y., Yao, J., Li, Y., and Ye, X. Y., 1995, "Micro-fluid Flow in Microchannel," *Transducers'95*, Stockholm, June 25–29. pp. 317–320.
[7] Stanley, R. S., 1997, "Two-phase Flow in Microchannels," Ph.D. thesis, Louisiana Tech. University, Ruston, LA.
[8] Merkle, C. L., Kubota, T., and Ko, D. R. S., 1974, "An Analytical Study of the Effects of Surface Roughness on Boundary-Layer Transition," AF OÅce of Scien. Res. Space and Missile Sys. Org., AD/A004786.
[9] Qu, W. L., Mala, G. M., and Li, D. Q., 2000, "Pressure-Driven Water Flows in Trapezoidal Silicon Microchannels," Int. J. Heat Mass Transfer, **43**, pp. 353–364.
[10] Kleinstreuer, C., and Koo, L., 2004, "Computational Analysis of Wall Roughness Effects for Liquid Flow in Micro-Conduits," ASME J. Fluids Eng., **126**(1), pp. 1–9.
[11] Du, D. X., 2000, "Effect of Compressibility and Roughness on Flow and Heat Transfer in Microtubes," Doctoral degree dissertation, Tsinghua University (in Chinese).
[12] Hu, Y. D., Werner, C., and Li, D. Q., 2003, "Influence of Three Dimensional Roughness on Pressure-Driven Flow Through Microchannels," ASME J. Fluids Eng., **125**, pp. 871–879.
[13] Van Dyke, M., 1964, *Perturbation Methods in Fluid Mechanics*, Academic Press, NY.
[14] Töeren, H., 1983, "Drag on Eccentrically Positioned Spheres Translating and Rotating in Tubes," J. Fluid Mech., **129**, pp. 77–90.
[15] Bontozoglou, V., and Papapolymerou, G., 1997, "Laminar Film Flow Down a Wavy Incline," Int. J. Multiphase Flow, **23**(1), pp. 69–79.
[16] Michael, J. M., and Stephen, H. D., 1994, "Slip Over Rough and Coated Surface," J. Fluid Mech., **273**, pp. 801–817.

Skin Friction Correlation for Smooth and Rough Wall Turbulent Boundary Layers

D. J. Bergstrom

O. G. Akinlade

Department of Mechanical Engineering,
University of Saskatchewan,
57 Campus Drive, Saskatoon, SK, Canada,
S7N 5A9

M. F. Tachie

Department of Mechanical and Industrial Engineering,
University of Manitoba, Winnipeg, MB, Canada,
R3T 2N2

In this paper, we propose a novel skin friction correlation for a zero pressure gradient turbulent boundary layer over surfaces with different roughness characteristics. The experimental data sets were obtained on a hydraulically smooth and ten different rough surfaces created from sand paper, perforated sheet, and woven wire mesh. The physical size and geometry of the roughness elements and freestream velocity were chosen to encompass both transitionally rough and fully rough flow regimes. The flow Reynolds number based on momentum thickness ranged from 3730 to 13,550. We propose a correlation that relates the skin friction, C_f, to the ratio of the displacement and boundary layer thicknesses, δ^*/δ, which is valid for both smooth and rough wall flows. The results indicate that the ratio $C_f^{1/2}/(\delta^*/\delta)$ is approximately constant, irrespective of the Reynolds number and surface condition. [DOI: 10.1115/1.2073288]

Introduction

Accurate determination of the skin friction on smooth and rough surfaces continues to be an important research topic in the near-wall turbulence community. Many reliable techniques for estimating the skin friction (or wall shear stress) have been developed for a smooth wall turbulent boundary layer including use of the momentum integral equation, correlations based on total pressure measurements at the surface (i.e., using a Preston tube), and oil-film interferometry. Indirect methods based on fitting to the mean velocity profile have also been employed to determine the skin friction. These include the "classical" Clauser technique, and fitting profiles based on either a defect law or power law. Using either direct or indirect methods, a number of correlations (e.g., Schultz-Grunow [1], Coles [2], Osaka et al. [3], and Tachie et al. [4]) have been developed to allow the prediction of skin friction on a smooth surface for practical applications. The objective of this study is to develop a correlation that is useful for the prediction of skin friction on both smooth and rough surfaces. To the authors' knowledge, a single correlation, which can predict the skin friction coefficient for smooth, transitionally rough, and fully rough flow regimes, has yet to be reported in the literature.

Numerous investigations have been made of turbulent boundary layer flow over rough surfaces with the aim of understanding the complexity arising from the effects of surface roughness [5–9]. These rough wall studies have shown that the effects of surface roughness on the mean flow can be generalized to consist of an increase in the skin friction value and an associated roughness shift, ΔU^+, to the logarithmic velocity profile. However, it is difficult to directly measure local skin friction values on rough surfaces. Instead, the indirect methods noted above have also been employed to estimate the skin friction in rough wall turbulent boundary layers. For fully developed duct flow, the balance between the pressure gradient and surface shear stress enables the skin friction to be readily determined. This has enabled the development of such engineering tools as the Moody chart, which has been extensively employed to predict the friction factor in both smooth- and rough-walled ducts. For a rough wall turbulent boundary layer, an interpolation formula for skin friction was derived by Prandtl and Schlichting [10] based on the sand grain roughness experiments of Nikuradse [11]. Mills and Huang [12] compared this formulation with some experimental data sets for fully rough flows over sand grain roughness and found that it gave an average error of 17.5 percent. They attributed the discrepancy to the failure of the formulation to account for the wake component of the mean velocity profile. Acharya et al. [13] combined the velocity defect law used by Rotta [14] and the semi-logarithmic law used by Clauser [15] for a rough wall to derive a linear relationship for the skin friction on a rough surface. They tested the correlation on four different surfaces. The data obtained from two surfaces collapsed onto a single line, while the other two data sets collapsed onto a different curve. They were not able to account for the presence of two different curves.

Analyzing rough wall boundary layer flows using profile-fitting methods requires some assumption regarding the mean velocity profile. Probably the most common plotting technique for determining the friction velocity, U_τ, is that of Clauser, in which a logarithmic profile is fitted to the experimental data for the mean velocity in the overlap region to obtain U_τ, which can then be used to determine the skin friction coefficient, $C_f=2(U_\tau/U_e)^2$, where U_e is the freestream velocity. For a turbulent boundary layer, other factors, such as freestream turbulence intensity, can also influence the skin friction characteristics. As an alternative to the Clauser technique, Finley et al. [16] proposed to use the velocity defect law in terms of a formulation that does not implicitly fix the strength of the wake, Π, but rather allows its value to be optimized while ensuring a reliable determination of the friction velocity. This method was subsequently used by Granville [17] and Krogstad et al. [18]. In this case, the mean defect profile is given by

$$U_e^+ - U^+ = \frac{2\Pi}{\kappa}\left[w(1) - w\left(\frac{y}{\delta}\right)\right] - \frac{1}{\kappa}\ln\left(\frac{y}{\delta}\right) \tag{1}$$

where y is the wall normal distance, δ is the boundary layer thickness, and w is the wake function. A distinct advantage of using the defect profile, especially for high Reynolds number flows, is that velocity data outside the inner layer can be included. Akinlade and Bergstrom [19] recently examined various methods used to determine the friction velocity, U_τ, on both smooth and rough surfaces. They concluded that for a rough wall boundary layer, profile fitting based on a defect law gave slightly better results for C_f than did the Clauser technique.

Due to unsatisfactory and often incomplete agreement with experimental data, and also for theoretical reasons, several research-

Contributed by the Fluids Engineering Division for publication in the JOURNAL OF FLUIDS ENGINEERING. Manuscript received by the Fluids Engineering Division August 12, 2004; final manuscript received: April 28, 2005. Associate Editor: Michael Plesniak.

ers have investigated alternatives to the classical logarithmic law (Barenblatt [20], George and Castillo [21], and Afzal [22]). They proposed power law formulations, which can also be used to determine the skin friction on a smooth surface. Some of these formulations have been extended to turbulent boundary layers over rough surfaces (e.g., Bergstrom et al. [9], Kotey et al. [23], and Akinlade and Bergstrom [19]). Since the topic of this paper is not primarily related to power law formulations, we leave this issue for future consideration.

Recently, Zagarola and Smits [24] introduced an outer velocity scale, which is proportional to the mass flux deficit in the boundary layer. They also proposed an equivalent outer velocity scale for a smooth wall turbulent boundary layer as follows:

$$U_o = U_e \int_0^1 \left(1 - \frac{U}{U_e}\right) d\left(\frac{y}{\delta}\right) = U_e \frac{\delta^*}{\delta} \tag{2}$$

where δ^* is the displacement thickness. This outer velocity scale has been used to successfully collapse the mean velocity defect profiles on both smooth [25] and rough surfaces [26,27]. A distinct advantage of this outer scale over other scaling parameters (i.e., friction velocity, U_τ, and freestream velocity, U_e) is that it accommodates the effects of surface roughness.

Recall that Clauser [15] showed that a boundary layer with a constant turbulence equilibrium parameter could be scaled with a single parameter. He defined a thickness parameter for equilibrium flow, also known as the defect thickness, Δ, as follows:

$$\Delta = \int_0^\infty \frac{U_e - U}{U_\tau} dy = \delta^* \lambda \tag{3}$$

where $\lambda = \sqrt{2/C_f}$ is related to the local skin friction. The velocity profiles were then scaled with y/Δ, and an integral shape factor G which remains constant in an equilibrium boundary layer was defined as follows:

$$G = \frac{1}{\Delta} \int_o^\infty \left(\frac{U_e - U}{U_\tau}\right)^2 dy \tag{4}$$

where G and λ are related to the ordinary Karmán-type shape factor, H, by the following expression,

$$H = \frac{\delta^*}{\theta} = \left(1 - \frac{G}{\lambda}\right)^{-1} \tag{5}$$

and θ is the momentum thickness. Equation (3) can be rearranged as follows:

$$C_f^{1/2} = \frac{\sqrt{2}}{\Delta} \delta^* \tag{6}$$

Multiplying the right-hand side by δ/δ leads to the following equivalent expression:

$$C_f^{1/2} = \sqrt{2} \left(\frac{\delta}{\Delta}\right) \left(\frac{\delta^*}{\delta}\right) \tag{7}$$

Zagarola and Smits [24] noted that at high Reynolds number $C_f^{1/2} \sim \delta^*/\delta$ for a smooth wall turbulent boundary layer. In view of this observation, one might conjecture that the ratio δ/Δ is invariant for general classes of turbulent boundary layer flows. In our study, this hypothesis will be explored for both smooth and rough surfaces.

In the present study, we measured the velocity fields and estimated the skin friction in zero pressure gradient turbulent boundary layers on a smooth surface and ten different rough surfaces. The physical size and geometry of the roughness elements were chosen to encompass both transitionally and fully rough flow regimes. The skin friction data for both smooth and rough surfaces appear to collapse onto a single curve which represents a novel correlation for $C_f^{1/2}$ as a function of δ^*/δ.

Summary of Experiments

The experiments were conducted in a low-speed, closed-return wind tunnel for Reynolds numbers based on momentum thickness ranging from 3730 to 13,550. The test section was 1.96 m long, and the flow enters the high-speed test section (HSTS) from the low-speed test section through a 7:1 contraction. The longitudinal freestream turbulence intensity was approximately 0.4%, and the nonuniformity of the freestream mean velocity field outside the test section wall boundary layers was less than 0.5%. A 1.67 m long, 1.16 m wide, and 25 mm thick flat plate was mounted on the bottom of the test section. The smooth surface (SM) was created on a medium density fiber (MDF) board, for which the large-scale deviation was less than ±0.5 mm from the horizontal plane. The average roughness height, R_a, for the MDF board was measured and found to be 3.82 μm. As will be shown later, this roughness was sufficiently small to qualify the MDF board as hydraulically smooth. A trip strip made of sand paper (36-d grit) was placed across the width of the plate; the trip strip was 75 mm wide and located 15 mm from the leading edge. The trip ensured an early transition to turbulence and was used in all the experiments in order to maintain consistent development of the turbulent boundary layer.

The rough surfaces used in the present study consisted of the following ten roughness elements attached to the reference MDF board:

A. Four different sand grain surfaces made of sand papers, namely, 120d-grit (SGS), 80d-grit (SGM), 60d-grit (SGML), and 40d-grit (SGL).

B.
   (i) a 0.76 mm thick perforated steel sheet (PS) with circular holes 1.2 mm in diameter spaced 3.4 mm between centers giving an openness ratio of 22%;
   (ii) a 0.9 mm thick perforated steel sheet (PM) with circular holes 1.6 mm in diameter spaced 2.43 mm between centers giving an openness ratio of 41%;
   (iii) a 0.9 mm thick perforated steel sheet (PL) with circular holes 2 mm in diameter spaced 2.81 mm between centers giving an openness ratio of 45%.

C.
   (i) a stainless steel woven wire mesh (WMS) consisting of 0.36 mm diameter wire laid out 1.68 mm on center to give an openness ratio of 44%;
   (ii) a stainless steel woven wire mesh (WMM) consisting of 0.58 mm diameter wire laid out 1.77 mm on center to give an openness ratio of 30%;
   (iii) a stainless steel woven wire mesh (WML) consisting of 1.04 mm diameter wire laid out 3.68 mm on center to give an openness ratio of 35%.

In the present study, the thickness of the perforated plate and the diameter of the wire mesh were used as the roughness height, k. For example, the 0.9 mm thick perforated sheet has a roughness height of $k=0.9$ mm, while the woven wire mesh with a wire diameter of 1.04 mm has a roughness height of $k=2.08$ mm, which is equal to twice the diameter of the wire following Furuya and Fujita [28]. Note that the choice of roughness height is somewhat arbitrary and possibly ambiguous; it should not be confused with the equivalent sand grain roughness, k_{eq}, calculated from the roughness shift. A Pitot probe with an outer diameter of $d_p = 0.60$ mm was used to measure the mean velocity across the boundary layer at a section 1300 mm (downstream) from the leading edge. The Pitot probe, which was connected to a Datametric Barocell Differential Pressure Sensor, was carefully aligned to the flow to eliminate any errors caused by yaw. The pressure signal was digitized using a 16-bit A/D converter at a sampling frequency of 500 Hz; 10,000 samples were taken at each wall normal

Table 1 Summary of skin friction coefficient and flow conditions for a smooth surface

	$U_e(m/s)$	Re_θ	δ (mm)	δ^* (mm)	$C_f\times10^3$	H	Π
SM1	15.4	3730	36.9	5.40	3.16	1.33	0.490
SM2	25.5	5680	33.7	4.91	2.90	1.32	0.501
SM3	35.9	7720	33.0	4.68	2.71	1.31	0.520
SM4	44.2	10360	32.5	4.50	2.56	1.29	0.525

position. Corrections were applied to the data following MacMillan [29], in which the value of $0.15d_p$ was added to the y coordinate. However, as noted by Perry et al. [30], for viscous distances from the wall greater than $y^+=100$, the corrections tend to be insignificant. In our own case, only a very few data points fall within $30<y^+<100$ for both smooth and rough wall flows, indicating that MacMillan's correction had little impact on the overall results. In the present experiment, four different Reynolds numbers were obtained for each surface by varying the freestream velocity, U_e, from approximately 15 to 45 m/s. The nominal freestream pressure gradient was −10 Pa/m. This pressure gradient corresponded to a Clauser equilibrium parameter $[\beta=(\delta^*/\tau_w)dP/dx]$ of approximately −0.015, −0.012, −0.013, and −0.012 for the highest Reynolds number data on smooth (SM4), perforated sheet (PL4), sand paper (SGL4), and wire mesh (WML4) surfaces, respectively. In addition, the acceleration parameter $[K=\nu(dU_e/dx)U_e^2]$ for the experiment ranged between 1.5×10^{-8} and 4.5×10^{-8}. Based on these values, we concluded that the pressure gradient measured in the wind tunnel for all experiments was approximately zero.

In order to estimate the 95% precision and bias confidence limits, we adopted the procedure given by Coleman and Steele [31]. Precision uncertainty estimates for the velocity measurements were made through repeatability tests. Four replicate velocity profiles were taken on both a smooth and a rough surface. The systematic error, which represents the bias uncertainty, was obtained from the instrumentation used in the measurements, which includes a Datametrics 600A-1000T-S13-H21X-4 absolute pressure transducer, Datametrics 590D-10W-V1X-4D differential pressure transducer, and copper-constantan thermocouple (type T). The estimated bias errors were combined with the precision uncertainties to calculate the overall uncertainties for the measured quantities. For our experiment, the boundary layer thickness δ was considered to be the location above the surface at which the local mean velocity was 99% of the freestream value. We estimate the uncertainties in both δ and δ^* to be ±5%. Very close to the wall, the uncertainty in the local velocity was approximately ±2%, while the estimated uncertainty in the freestream velocity was ±0.75%. The uncertainty in the skin friction coefficient, C_f, was estimated to be ±5% and ±9% for the smooth and rough surfaces, respectively. Error bars have been included on Figs. 2–5 and 8 to indicate the level of uncertainty.

Determination of the Friction Velocity

Our research group has previously used the profile fitting method of Krogstad et al. [18] in studies of rough wall boundary layer flows (e.g., Tachie et al. [8], Bergstrom et al. [32], and Akinlade et al. [27]). It assumes the existence of a log-law and a functional form of the wake, but it allows the strength of the wake to vary. The wake function used in Eq. (1) is expressed as follows:

$$w\left(\frac{y}{\delta}\right)=\frac{1}{2\Pi}[(1+6\Pi)-(1+4\Pi)(y/\delta)]\left(\frac{y}{\delta}\right)^2 \tag{8}$$

This method was also employed to determine the friction velocity on the smooth surface. The method originally used by Krogstad et al. [18] also involved an optimization for the virtual origin, ε, which represents the virtual location of the wall relative to the nominal top of the roughness elements. When the value of the friction velocity, U_τ, obtained from the defect profile was used to fit a log-law to the experimental data, as the surface became rougher the velocity profile tended to become slightly concave near the wall. In order to eliminate this anomaly, the log-law was enforced for the data points nearest the wall by increasing the wall datum shift. For the roughness elements considered in this study, we estimated the maximum value of ε^+ to be 82. Although this method is somewhat arbitrary in its forcing of a log law at the bottom of the inner layer, it had the advantage of yielding C_f values for fully rough flow that exhibited minimal variation with Re_θ.

Table 1 presents a summary of the freestream velocity, Reynolds number based on momentum thickness, boundary layer thickness, displacement thickness, skin friction coefficient, and strength of the wake for the smooth surface. The friction velocity obtained from the smooth surface at the highest Reynolds number was used to estimate a roughness Reynolds number, k^+, which was less than 1. This estimate was based on the average roughness height, R_a, for the MDF board, and qualifies the MDF board as hydraulically smooth. For the rough surfaces, the ratio of roughness height to boundary layer thickness, k/δ, roughness shift, ΔU^+, roughness Reynolds number, $k^+(=kU_\tau/\nu)$, and the equivalent sand grain roughness Reynolds number, k_{eq}^+, are given in Tables 2–4. The equivalent sand grain roughness Reynolds number, k_{eq}^+, was obtained from the relation used by Raupach et al. [6]. Following them, the flow regimes based on the equivalent sand grain roughness Reynolds number, k_{eq}^+, were defined as follows: $k_{eq}^+<5$ (hydraulically smooth), $5<k_{eq}^+<70$ (transitional), and $k_{eq}^+>70$ (fully rough) [6]. Based on the values of k_{eq}^+, transitionally rough flows were obtained for two perforated sheets (PS and PM) and three sand grain roughnesses (SGS, SGM, and SGML 1, 2, and 3), while fully rough flow was achieved for one perforated sheet (PL), two sand grain roughnesses (SGML 4 and SGL), and all three woven wire mesh surfaces used in the experiments. The ratio of k^+ to k/δ yields the Reynolds number based on boundary layer thickness, δ^+. Jimenez [33] suggested that the Reynolds

Table 2 Summary of skin friction coefficient and flow conditions for perforated sheet

	$U_e(m/s)$	Re_θ	δ (mm)	δ^* (mm)	k/δ	$C_f\times10^3$	H	Π	ΔU^+	k^+	k_{eq}^+
PS1	15.3	4030	38.2	6.26	0.020	3.62	1.41	0.511	2.0	29	9
PS2	25.5	5870	35.3	5.34	0.022	3.34	1.39	0.541	2.2	48	10
PS3	36.5	8080	34.0	5.22	0.022	3.15	1.39	0.590	2.4	66	11
PS4	44.5	9130	32.7	4.86	0.023	2.96	1.38	0.592	2.5	78	12
PM1	15.2	3840	35.8	6.04	0.025	3.75	1.43	0.530	2.4	36	11
PM2	25.4	6030	33.5	5.78	0.027	4.09	1.45	0.535	4.4	62	26
PM3	36.2	8130	31.8	5.45	0.028	3.95	1.44	0.540	4.8	87	30
PM4	44.3	10280	31.3	5.58	0.029	3.87	1.44	0.550	5.4	105	38
PL1	15.4	4600	39.4	7.90	0.023	5.58	1.58	0.540	7.2	44	79
PL2	25.2	6780	34.7	7.26	0.026	5.35	1.56	0.555	7.7	70	97
PL3	35.1	9190	34.6	6.83	0.026	5.26	1.55	0.557	8.3	96	127
PL4	44.2	11460	34.4	6.63	0.026	5.19	1.54	0.560	8.7	122	149

Table 3 Summary of skin friction coefficient and flow conditions for sand grain

	Ue (m/s)	Re_θ	δ (mm)	δ^* (mm)	k/δ	$C_f \times 10^3$	H	Π	ΔU^+	k^+	k_{eq}^+
SGS1	15.8	3810	35.6	5.56	0.005	3.50	1.41	0.500	2.0	7	9
SGS2	26.0	5670	32.1	5.23	0.006	3.59	1.41	0.534	3.4	12	17
SGS3	36.1	8030	31.7	5.35	0.006	3.70	1.42	0.536	4.4	17	26
SGS4	45.3	10360	32.0	5.45	0.006	3.78	1.42	0.540	5.3	22	37
SGM1	16.1	3960	34.6	5.90	0.009	3.98	1.45	0.500	3.5	13	18
SGM2	25.0	6000	33.3	5.80	0.009	4.15	1.45	0.535	5.0	21	33
SGM3	35.5	8700	33.7	5.89	0.009	4.02	1.45	0.580	5.5	29	40
SGM4	44.4	10930	33.5	5.99	0.009	3.91	1.45	0.590	5.9	36	47
SGML1	15.5	4150	36.7	6.77	0.010	4.65	1.51	0.512	5.3	17	37
SGML2	25.2	6530	34.2	6.37	0.011	4.40	1.49	0.571	6.2	27	53
SGML3	35.3	9320	33.7	6.51	0.011	4.24	1.48	0.590	6.6	37	63
SGML4	45.1	11920	34.0	6.40	0.011	4.18	1.47	0.620	7.0	46	74
SGL1	15.4	4670	39.3	7.91	0.012	5.65	1.58	0.540	7.5	24	89
SGL2	25.5	7000	37.8	7.44	0.013	5.46	1.57	0.548	8.3	38	124
SGL3	35.6	9790	35.2	7.24	0.014	5.31	1.55	0.551	8.5	52	137
SGL4	44.1	12140	35.7	7.33	0.013	5.18	1.56	0.556	9.0	64	169

number based on boundary layer thickness, δ^+, should be greater than 4000 as a condition for a well-defined rough wall turbulent boundary layer. In the present study, the Reynolds numbers based on boundary thickness for all fully rough flows at the highest Reynolds number are greater than 4000. The other criterion considered by Jimenez [33] was that the blockage ratio, k/δ, be sufficiently small, i.e., $k/\delta < 0.025$ for similarity laws to be expected and perhaps $k/\delta < 0.0125$ for the mechanisms of normal wall turbulence to prevail. In our case, for the fully rough flows, the sand grain roughness (SGL) approximately meets this criterion, while the wire mesh does not. Recall that for the wire mesh, the roughness height, k, was equal to twice the wire diameter which may tend to exaggerate the blockage ratio. The values of Π for the rough surfaces are typically larger than for the smooth surface, and for each rough surface, the value of Π is observed to increase as the roughness shift increases. This is one example of the effect of surface roughness extending into the outer region. The values of the skin friction coefficient, C_f, and displacement thickness, δ^*, obtained for the rough surfaces are also higher than those of the smooth surface. For the hydraulically smooth and fully rough flows, the displacement thickness δ^* decreases with increasing Reynolds number. For the transitionally rough flow, the displacement thickness δ^* on PS and PM also decreases with increasing Reynolds number, while those on the sand grain surfaces behave somewhat differently. This is an example of the variability existing between the roughnesses created by different surfaces. For both the smooth and rough surfaces, the shape factor, H, does not vary significantly with increasing Reynolds number. This observation is similar to that of Gad-el Hak and Bandyopadhyay [34] in the case of a smooth surface, and also that of Furuya and Fujita [28] and Schultz and Flack [35] for a rough surface.

Results and Discussion

Figures 1(*a*) and 1(*b*) present the mean velocity profiles for smooth and rough surfaces at the highest Reynolds number using outer coordinates. Figure 1(*a*) shows the mean velocity profiles

Table 4 Summary of skin friction coefficient and flow conditions for wire mesh

	Ue (m/s)	Re_θ	δ (mm)	δ^* (mm)	k/δ	$C_f \times 10^3$	H	Π	ΔU^+	k^+	k_{eq}^+
WMS1	15.6	4670	38.5	7.85	0.019	5.60	1.55	0.551	7.3	35	82
WMS2	25.6	7250	36.9	7.68	0.020	5.42	1.56	0.589	8.5	56	134
WMS3	35.6	9570	34.8	7.43	0.021	5.35	1.56	0.595	9.1	78	177
WMS4	44.8	12110	33.8	7.08	0.021	5.28	1.53	0.595	9.3	99	186
WMM1	16.0	4950	39.6	8.25	0.029	5.68	1.57	0.577	7.8	59	101
WMM2	25.7	7560	36.4	7.80	0.032	5.55	1.57	0.604	8.8	94	156
WMM3	36.6	10090	35.5	7.35	0.033	5.33	1.56	0.625	9.2	133	183
WMM4	44.7	12260	34.8	7.34	0.033	5.22	1.55	0.645	9.4	156	191
WML1	15.4	5040	39.6	9.01	0.053	6.64	1.66	0.589	9.8	111	229
WML2	25.6	7840	36.7	8.44	0.057	6.49	1.65	0.627	10.5	185	314
WML3	35.6	10630	36.8	8.41	0.056	6.37	1.65	0.642	11.0	249	382
WML4	44.7	13550	37.4	8.43	0.056	6.29	1.65	0.650	11.6	314	488

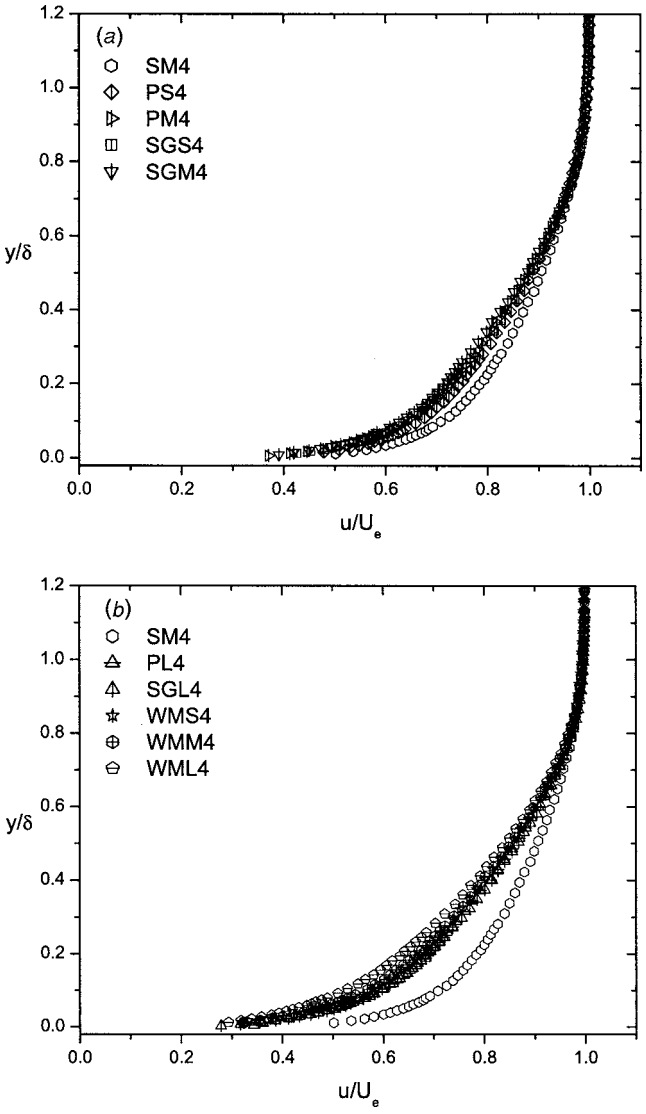

Fig. 1 Mean velocity profiles using outer coordinates: (*a*) smooth and transitionally rough and (*b*) smooth and fully rough

for smooth and nominal transitionally rough flows (based on k_{eq}^+ values), while fully rough flows are presented in Fig. 1(*b*). The effect of surface roughness increases the skin friction drag, which causes the mean velocity profile on a rough surface to be "less full" when compared to that on a smooth surface. As indicated in Figs. 1(*a*) and 1(*b*), the fully rough flow exhibits a higher deviation from the smooth profile than does the transitionally rough flow. Figures 2(*a*) and 2(*b*) compare the mean velocity profiles at the highest Reynolds number for the smooth and rough surfaces using inner coordinates. As expected, the effect of surface roughness is to increase the friction velocity resulting in a downward-right shift of the mean velocity profiles. Comparison between Figs. 2(*a*) and 2(*b*) indicates that the fully rough flow exhibits a significantly larger velocity shift, ΔU^+, than the transitionally rough flow. By definition, ΔU^+ is zero for a smooth surface. The present experimental results also indicate that as the surface roughness increases, the linear region of the overlap region becomes relatively narrow. A similar observation was reported by Bergstrom et al. [9]. As indicated in Fig. 2, the rough surface exhibits a stronger wake component than does the smooth surface. This is evidence that the effect of surface roughness extends into

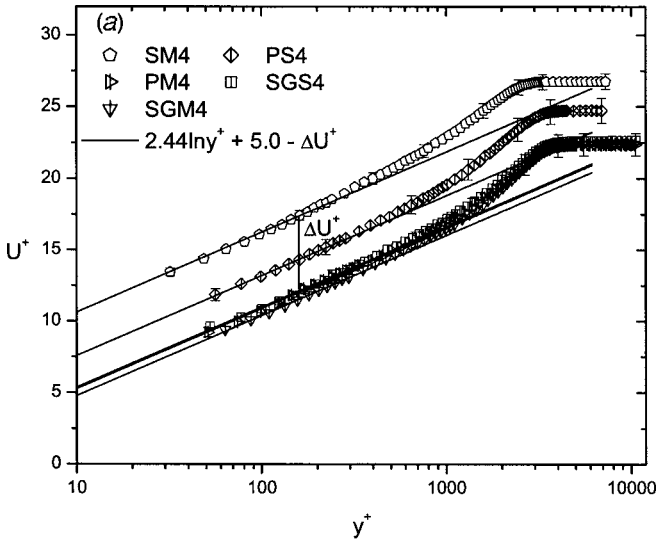

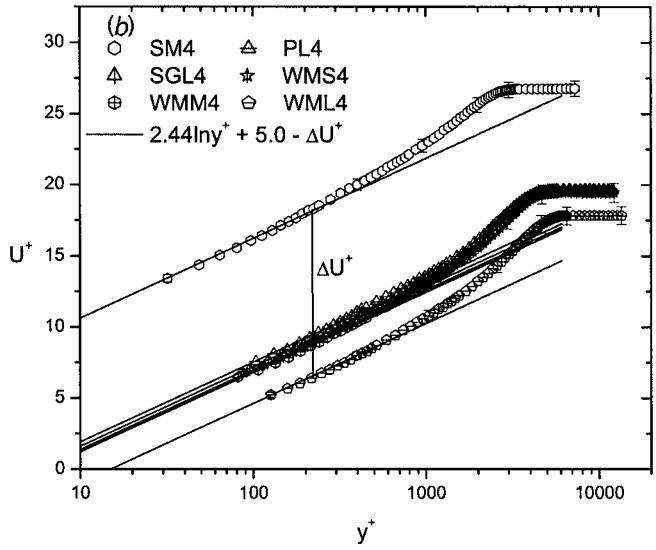

Fig. 2 Mean velocity profiles using inner coordinates: (*a*) smooth and transitionally rough and (*b*) smooth and fully rough

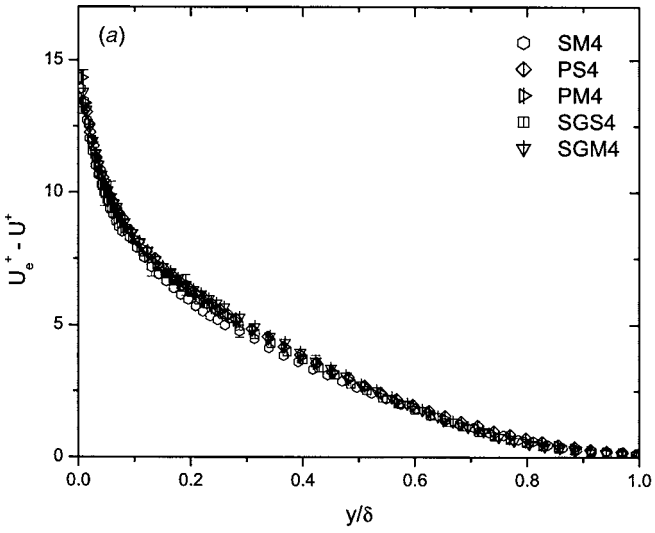

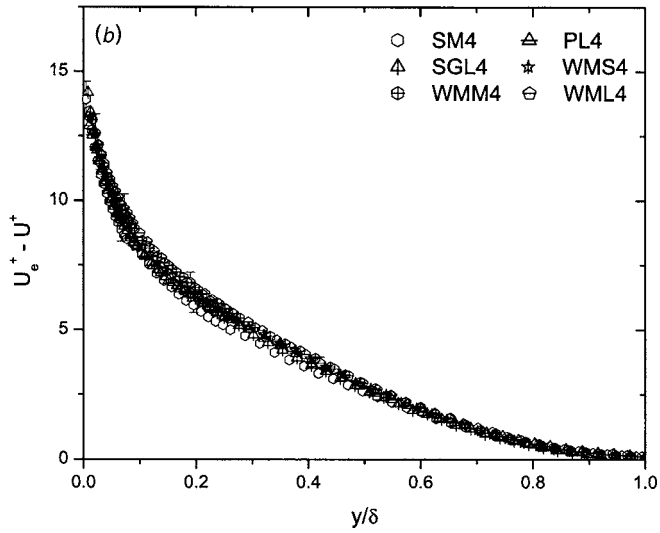

Fig. 3 Mean velocity defect profiles using inner coordinates: (*a*) smooth and transitionally rough; (*b*) smooth and fully rough

the outer region of the flow. However, the transport mechanisms related to this effect are still not well understood.

Figures 3(*a*) and 3(*b*) present the mean velocity defect profiles for the smooth and rough surfaces, where the friction velocity, U_τ, and the boundary layer thickness, δ, are used to scale the velocity and wall-normal distance, respectively. For the transitionally and fully rough flows, the defect profile is displaced slightly upward by the surface roughness. Similar to the conclusions of Krogstad et al. [18], Tachie et al. [8], and Akinlade et al. [27], the velocity profiles for the different surfaces are distinct from each other not only in the wall region but also over a significant part of the outer region of the boundary layer.

Figure 4 compares the skin friction coefficient obtained for a smooth wall with the correlation proposed by Osaka et al. [3] and the somewhat older but still widely used correlation of Coles [2]. We have also included the skin friction data of Purtell et al. [36] and DeGraaff and Eaton [37] obtained in a zero pressure gradient turbulent boundary layer at $460 \leqslant \mathrm{Re}_\theta \leqslant 5100$ and $1430 \leqslant \mathrm{Re}_\theta \leqslant 13,000$, respectively. The comparison shows that the present skin friction values are in good agreement with the correlation of Osaka et al. [3] as well as the experimental data of Purtell et al. [36] and DeGraaff and Eaton [37]. At lower values of Re_θ, the correlation of Coles [2] tends to be higher than the experimental data, although still within the experimental uncertainty. It appears unlikely that our data would trend up with increasing Re_θ to the same degree as that of DeGraaff and Eaton [37].

In order to confirm the friction velocity obtained by fitting to the defect profile, the relation between the shape factor and skin friction is presented in Fig. 5. Both Bandyopadhyay [38] and Furuya and Fujita [28] used this method to indirectly check the skin friction obtained from a profile fitting technique. Furuya and Fujita [28] plotted the relation between the shape factor, H, and skin friction as given in Eq. (5); they used the value of $G=6.3$ for a smooth surface and $G=7.0$ for a rough surface. For these values of G, Eq. (5) is plotted in Fig. 5, together with the experimental data for smooth and rough wall flows. As clearly shown, the measurements closely align with each of the curves based on Eq. (5). This gives us confidence that our profile fitting technique is valid for both smooth and rough surfaces.

Figures 6(*a*) and 6(*b*) present the variation of the skin friction coefficient, C_f, for smooth and rough surfaces with Reynolds number. Figure 6(*a*) shows the behavior of the skin friction coefficient, C_f, for the hydraulically smooth and nominal transitionally rough flows. In the latter case, the skin friction can be as much as 55% higher than that on the smooth surface. The behavior of the

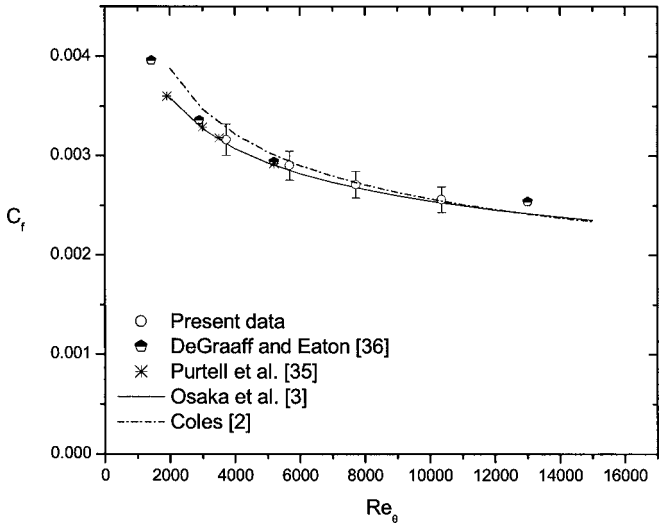

Fig. 4 Variation of skin friction coefficient for a smooth surface with Reynolds number

skin friction on surfaces that exhibited a nominal transitionally rough flow regime varied. For example, in the case of PS, the value of C_f decreased with Reynolds number, which is the same as for the hydraulically smooth surface. However, the C_f values on PM and SGM initially increase by 9% and 4%, respectively, and thereafter decrease as the Reynolds number increases. In the case of SGS, the skin friction coefficient, C_f, increases throughout with increasing Reynolds number. If we consider the measurement uncertainty of approximately ±9%, then the C_f values of PM, SGS, and SGM do not vary significantly over the range of Re_θ considered, whereas for PS we observe a systematic decrease with Reynolds number. The behavior observed for PS can be linked to the small openness ratio, which enables it to show characteristics indicative of a hydraulically smooth surface. Figure 6(*b*) presents the skin friction coefficient, C_f, for the hydraulically smooth and fully rough flows at different Reynolds numbers. We have also included the skin friction coefficient data for SGML in Fig. 6(*b*), which only became fully rough at the highest Reynolds number. Even though the k_{eq}^+ values would classify it as nominal transitionally rough, the overall variation appears to better match that of the fully rough surfaces. The wire mesh (WML) exhibits

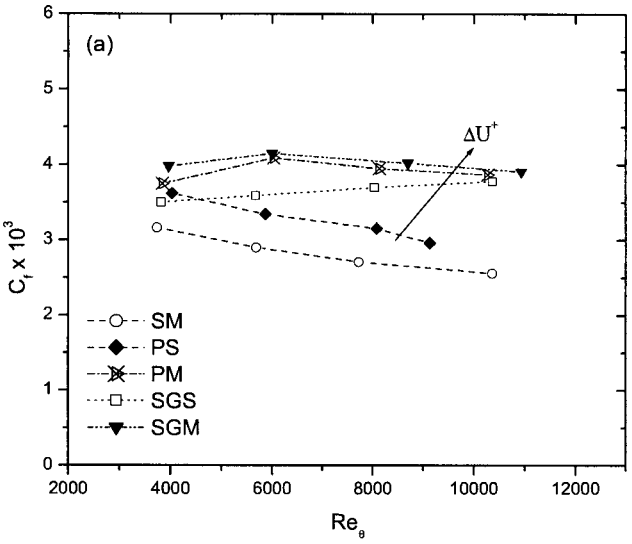

Fig. 6 Variation of skin friction coefficient with Reynolds number: (*a*) smooth and transitionally rough and (*b*) smooth and fully rough

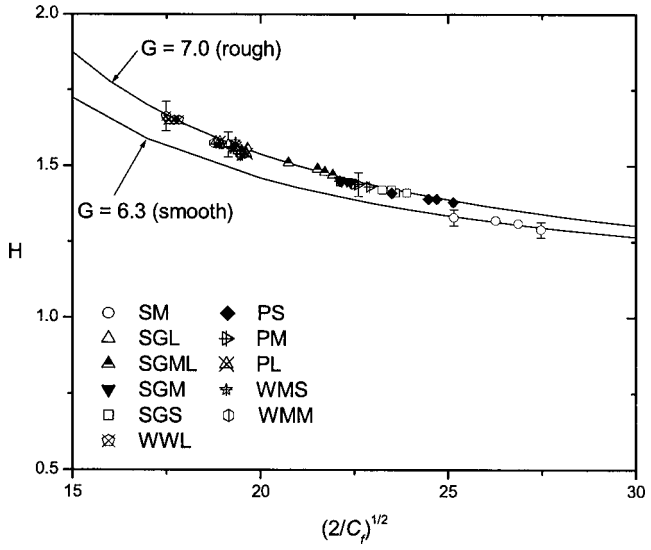

Fig. 5 Relation of shape factor to skin friction coefficient

the largest increase in C_f over the range of Reynolds numbers considered, almost 146% higher than that on the smooth surface. Again, the maximum variation in C_f for each surface is within or close to the experimental uncertainty. For the fully rough flows, each surface exhibits minimal variation of C_f with Reynolds number, although C_f varies greatly among the different surfaces.

Figure 7 presents the variation of the modified skin friction coefficient, $C_f^{1/2}/(\delta^*/\delta)$, with Reynolds number for the flows summarized in Tables 1–4. We have also included the skin friction coefficient data of DeGraaff and Eaton [37] on a smooth surface, as well as that of Antonia and Krogstad [39] on a wire mesh at Reynolds number ranging from 3120 to 22,860. One immediately observes that the modified skin friction coefficient data for all the surfaces considered are confined within a narrow range of values, irrespective of Reynolds numbers. Recalling Eq. (7), the behavior observed in Fig. 7 implies that for the ZPG turbulent boundary layers considered, the ratio δ/Δ is approximately independent of both Reynolds number and surface roughness.

If we make this approximation, i.e., that δ/Δ is approximately constant and $C_f^{1/2}$ varies in a linear manner with δ^*/δ, and plot the experimental data for all surface conditions and Reynolds numbers, we obtain the behavior shown in Fig. 8. In general, as rough-

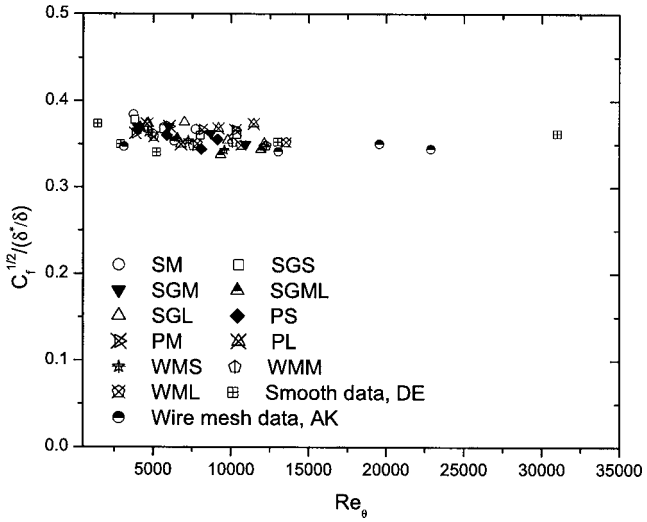

Fig. 7 Variation of mixed skin friction coefficient for smooth and rough surfaces with Reynolds number (DE and AK denote DeGraaf and Eaton [37] and Antonia and Krogstad [39], respectively)

ness increases the value of the ratio δ^*/δ, the skin friction similarly increases. The skin friction coefficient data sets for each surface appear to collapse onto a linear curve for which we propose the following correlation:

$$c_f^{1/2} = (0.360 \pm 0.025)\left(\frac{\delta^*}{\delta}\right) \tag{9}$$

An assessment of goodness-of-fit using a chi-squared distribution at a 95% confidence level indicates that Eq. (9) does an excellent job of correlating the experimental data over a Reynolds number range of $1430 \leqslant Re_\theta \leqslant 31{,}000$. Note that the multiplicative constant in Eq. (9) equals the average value of $C_f^{1/2}/(\delta^*/\delta)$ in Fig. 7. The smooth wall skin friction data of DeGraaff and Eaton [37], as well as the rough wall data of Antonia and Krogstad [39], are also included in Fig. 8 and show good agreement with the proposed correlation within the experimental uncertainty. The above correlation implies that the skin friction can be estimated from knowledge of the displacement and boundary layer thicknesses for a wide range of Reynolds number and different surface conditions.

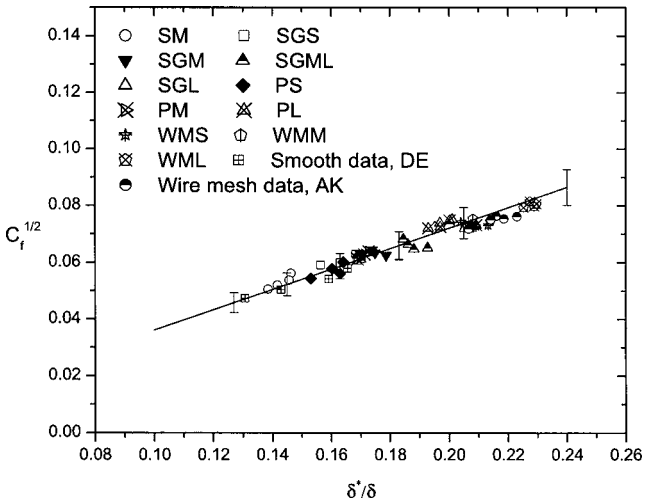

Fig. 8 Variation of skin friction coefficient for smooth and rough surfaces with length scale ratio [solid line represents Eq. (9)]

Conclusions

The present paper reports a relatively large matrix of data sets for turbulent boundary layers on one smooth and ten rough surfaces. We propose a new skin friction correlation given by Eq. (9) for zero pressure gradient turbulent boundary layers. The correlation has the advantage of predicting the skin friction in hydraulically smooth, transitionally rough, and fully rough flows. The length scale ratio, δ^*/δ, was employed to account for the effects of Reynolds number and surface roughness, such that the skin friction coefficient data collapse onto a single curve. This result is a further evidence of the special role of the length scale ratio δ^*/δ in scaling the velocity field in turbulent boundary layers. A more comprehensive assessment of the validity of the correlation requires further investigation using other types of surface geometries and a wider range of Reynolds numbers based on boundary layer thickness.

Acknowledgments

Financial support in terms of research grants from the Natural Sciences and Engineering Research Council of Canada to D.J.B. and M.F.T, and a University of Saskatchewan scholarship to O.G.A. is gratefully acknowledged. The authors thank the reviewers of the paper for their comments and suggestions, many of which have been reflected in the final version of the paper.

References

[1] Schultz-Grunow, 1941, "New Frictional Resistant Law for Smooth Plates," NACA TM 986.
[2] Coles, D., 1962, "The Turbulent Layer in a Compressible Fluid," The Rand Corp., Rep. R-403-PR.
[3] Osaka, H., Kameda, T., and Mochizyki, S., 1998, "Re-examination of the Reynolds Number Effects on the Mean Flow Quantities in a Smooth Wall Turbulent Boundary Layers," JSME Int. J., Ser. B, **41**(5), pp. 802–811.
[4] Tachie, M. F., Bergstrom, D. J., Balachandar, R., and Ramachandran, S., 2001, "Skin Friction Correlation in Open Channel Boundary Layers," ASME J. Fluids Eng., **123**, pp. 953–956.
[5] Bandyopadhyay, P. R., and Watson, R. D., 1988, "Structure of Rough-wall Turbulent Boundary Layers," Phys. Fluids, **31**, pp. 1877–1883.
[6] Raupauch, M. R., Antonia, R. A., and Rajagopalan, S., 1991, "Rough-Wall Turbulent Boundary Layers," Appl. Mech. Rev., **44**, pp. 1–25.
[7] Antonia, R. A., and Krogstad, P. A., 2001, "Effect of Different Surface Roughnesses on a Turbulent Boundary Layer," Fluid Dyn. Res., **28**, pp. 139–157.
[8] Tachie, M. F., Bergstrom, D. J., and Balachandar, R., 2000, "Rough Wall Turbulent Boundary Layers in Shallow Open Channel Flow," ASME J. Fluids Eng., **122**, pp. 533–541.
[9] Bergstrom, D. J., Tachie, M. F., and Balachandar, R., 2001, "Application of Power Laws to Low Reynolds Number Boundary Layers on Smooth and Rough Surfaces," Phys. Fluids, **13**, pp. 3277–3284.
[10] Prandtl, L., and Schlichting, H., 1934, "Das Wiederstandagesetz rouher Platten," Werft Reederere Hafen, **15**, pp. 1–4.
[11] Nikuradse, J., 1933, "Strömungsgesetze in rauhen Rohen," Forsch. Arb. Ing.-Wes. No. 361.
[12] Mills, A. F., and Huang, X., 1983, "On the Skin Friction Coefficient for a Fully Rough Flat Plate," ASME J. Fluids Eng., **105**, pp. 364–365.
[13] Acharya, M., Bornstein, J., and Escudier, M. P., 1986, "Turbulent Boundary Layers on Rough Surfaces," Exp. Fluids, **4**, pp. 33–47.
[14] Rotta, J. C., 1962, "Turbulent Boundary Layers in Incompressible Flow," Prog. Aeronaut. Sci., **2**, pp. 1–220.
[15] Clauser, F. H., 1954, "Turbulent Boundary Layers in Adverse Pressure Gradient," J. Aeronaut. Sci., **21**, pp. 91–108.
[16] Finley, P. J., Chong Phoe, K., and Jeck Pohn, Ch., 1966, "Velocity Measurements in a Thin Turbulent Wake Layer," Houille Blanche, **21**, pp. 713–721.
[17] Granville, P. S., 1976, "A Modified Law of the Wake for Turbulent Shear Layers," ASME J. Fluids Eng., **29**, pp. 578–580.
[18] Krogstad, P. A., Antonia, R. A., and Browne, L. W. B., 1992, "Comparison Between Rough and Smooth Wall Turbulent Boundary Layers," J. Fluid Mech., **245**, pp. 599–617.
[19] Akinlade, O. G., and Bergstrom, D. J., 2003, "Skin Friction Estimates in Rough Wall Turbulent Boundary Layers Using Logarithmic and Power Law Profiles," 4th International Symposium on Turbulence, Heat and Mass Transfer, Turkey, pp. 139–146.
[20] Barenblatt, G. I., 1993, "Scaling Laws for Fully Developed Shear Flow: Part 1, Basic Hypothesis and Analysis," J. Fluid Mech., **248**, pp. 513–520.
[21] George, W. K., and Castillo, L., 1997, "Zero Pressure Gradient Turbulent Boundary Layer," Appl. Mech. Rev., **50**, pp. 689–729.
[22] Afzal, N., 2001, "Power Law and Log Law Velocity Profiles in Fully Developed Turbulent Boundary Layer Flow: Equivalent Relations at Large Reynolds Numbers," Acta Mech., **151**, pp. 195–216.

[23] Kotey, N. A., Bergstrom, D. J., and Tachie, M. F., 2003, "Power Laws for Rough Wall Turbulent Boundary Layers," Phys. Fluids, **15**, pp. 1396–1404.
[24] Zagarola, M. V., and Smits, A. J., 1998, "A New Mean Velocity Scale for Turbulent Boundary Layers," ASME Paper No. FEDSM98-4950.
[25] Castillo, L., and Walker, D. J., 2002, "Effect of Upstream Conditions on the Outer Flow of Turbulent Boundary Layers," AIAA J., **40**, pp. 1292–1299.
[26] Seo, J., 2003, "Investigation of the Upstream Conditions and Surface Roughness in Turbulent Boundary Layer," Ph.D. thesis, Department of Mechanical and Aeronautical Engineering, Rensselaer Polytechnic Institute, NY.
[27] Akinlade, O. G., Bergstrom, D. J., Tachie, M. F., and Castillo, L., 2004, "Outer Flow Scaling of Smooth and Rough Wall Turbulent Boundary Layers," Exp. Fluids, **37**, pp. 604–612.
[28] Furuya, Y., and Fujita, H., 1967, "Turbulent Boundary Layers on a Wire Screen," Bull. JSME, **10**, pp. 77–86.
[29] MacMillan, F. A., 1956, "Experiments on Pitot-Tubes in Shear Flow," Aero. Res. Counc. R. & M. 3028.
[30] Perry, A. E., Hafez, S., and Chong, M. S., 2001, "A Possible Reinterpretation of the Princeton Superpipe Data," J. Fluid Mech., **439**, pp. 395–401.
[31] Coleman, H. W., and Steele, W. G., 1999, *Experimentation and Uncertainty Analysis for Engineers*, 2nd ed., Wiley, New York.
[32] Bergstrom, D. J., Kotey, N. A., and Tachie, M. F., 2002, "The Effect of Surface Roughness on the Mean Velocity Profile in a Turbulent Boundary Layer," ASME J. Fluids Eng., **124**, pp. 664–670.
[33] Jimenez, J., 2004, "Turbulent Flows over Rough Wall," Annu. Rev. Fluid Mech., **36**, pp. 173–196.
[34] Gad-el-Hak, M., and Bandyopadhyay, P. R., 1994, "Reynolds Number Effects in Wall-Bounded Flows," Appl. Mech. Rev., **47**, pp. 307–364.
[35] Schultz, M. P., and Flack, K. A., 2003, "Turbulent Boundary Layers over Surface Smoothed by Sanding," ASME J. Fluids Eng., **125**, pp. 863–870.
[36] Purtell, L. P., Klebanoff, P. S., and Buckley, F. T., 1981, "Turbulent Boundary Layer at Low Reynolds Number," Phys. Fluids, **24**, pp. 802–811.
[37] DeGraaff, D. B., and Eaton, J. K., 2000, "Reynolds-Number Scaling of the Flat-Plate Turbulent Boundary Layer," J. Fluid Mech., **422**, pp. 319–346.
[38] Bandyopadhyay, P. R., 1987, "Rough-Wall Turbulent Boundary Layers in the Transition Regime," J. Fluid Mech., **180**, pp. 231–266.
[39] Antonia, R. A., and Krogstad, P-A., 1993, "Scaling of the Bursting Period in Turbulent Rough Wall Boundary Layers," Exp. Fluids, **15**, pp. 82–84.

The Development Lengths of Laminar Pipe and Channel Flows

F. Durst

S. Ray[1]

B. Ünsal

O. A. Bayoumi

Institute of Fluid Mechanics,
Friedrich Alexander Universität Erlangen-Nürnberg,
Cauerstrasse 4, D-91058 Erlangen, Germany

The authors' research work into fully developed pulsating and oscillating laminar pipe and channel flows raised questions regarding the development length of the corresponding steady flow. For this development length, i.e., the distance from the entrance of the pipe to the axial position where the flow reaches the parabolic velocity profile of the Hagen-Poiseuille flow, a wide range of contradictory data exists. This is shown through a short review of the existing literature. Superimposed diffusion and convection, together with order of magnitude considerations, suggest that the normalized development length can be expressed as $L/D=C_0+C_1Re$ *and for* $Re\rightarrow 0$ *one obtains* $C_0=0.619$*, whereas for* $Re\rightarrow\infty$ *one obtains* $C_1=0.0567$*. This relationship is given only once in the literature and it is presumed to be valid for all Reynolds numbers. Numerical studies show that it is only valid for* $Re\rightarrow 0$ *and* $Re\rightarrow\infty$*. The development length of laminar, plane channel flow was also investigated. The authors obtained similar results to those for the pipe flow:* $L/D=C_0'+C_1'$*; Re, where* $C_0'=0.631$ *and* $C_1'=0.044$*. Finally, correlations are given to express* L/D *analytically for the entire Re range for both laminar pipe and channel flows.*
[DOI: 10.1115/1.2063088]

1 Introduction and Aim of Work

Two of the classical flows treated in introductory fluid mechanics lectures are laminar, fully developed pipe flow, in other words, the so-called Hagen-Poiseuille flow, and the corresponding plane channel flow. The development of these flows from preassigned velocity profiles require certain axial distances from the pipe or the channel inlet. Irrespective of a particular inlet velocity profile or what happens in detail at the entrance of a pipe or a channel, the physical mechanisms behind such axial development of a flow are well established and understood. Owing to the no-slip velocity condition at walls, the fluid next to the wall is immediately slowed as soon as the flow enters a pipe or a channel. This retardation near the wall spreads inwards owing to viscous effects and the slowed-down fluid close to the wall causes the fluid in the center to move faster, since the cross-sectional mass flow rate at any axial location remains constant. Ultimately, moving in the flow direction, the fully developed state of the flow is reached, i.e., the parabolic velocity distribution of the Hagen-Poiseuille flow develops. The closest location from the entrance where this phenomenon occurs defines the hydrodynamic entrance length as the distance from the inlet of the pipe to the location of the fully developed pipe flow or the corresponding position of the fully developed channel flow.

As the above explanations show, the phenomenon of laminar pipe and channel flow development is fully understood and the dependence of the development length on the Reynolds number, when derived by the type of considerations given above, must have two terms, due to the superposition of the convection and diffusion velocities. However, in spite of this, there are derivations in the literature that yield $L/D=C$ Re. This is readily illustrated in Sec. 2, where a brief literature survey is provided, indicating that there have been numerous investigations of the phenomena. Unfortunately no clear and final analysis or experimental and numerical studies exist that state precisely what the values of the constants C_0 and C_1 in the L/D-relationship should be and also whether the simple scale analysis given above is valid for all Reynolds numbers. Hence it may be concluded that the development of laminar pipe or channel flow is not correctly described in the literature. The present study was carried out in order to remedy this situation and also to provide quantitative information on the ratio of the development length to pipe diameter or channel height as a function of Reynolds number.

Owing to the situation outlined in Sec. 2, it was felt that a detailed study is needed to finalize the investigations on developing laminar pipe flow and the corresponding channel flow that eventually leads to the fully developed velocity distribution. Detailed studies in this respect were carried out, and the final results are presented in this paper. Although these investigations were performed numerically, experimentally and analytically, only the numerical part of the study was found to be really successful. The numerical studies resulted in reliable data that were evaluated and the final results are presented in Sec. 3. The experimental studies are summarized in Sec. 4 together with problems encountered also during analytical investigations of the development length of laminar pipe and channel flows. Conclusions and final remarks are provided in Sec. 5.

2 Summary of Results of Previous Investigations

There have been numerous investigations of the development length for laminar pipe flows, carried out not only using various approximate analytical methods, but also by performed numerical and experimental investigations. Good summaries of the work in the past are provided in Schlichting [1], giving special references to the publications of Schiller [2], Langhaar [3], and Sparrow [4]. Additional publications are referenced by Schmidt and Zeldin [5], followed in further studies by Lew and Fung [6]. A few years later, the development length of laminar pipe flows was looked at by Mohanty and Asthana [7]. All these publications indicate that the phenomenon of laminar flow development in the entrance region of pipe flows has attracted considerable attention in fluid mechanics research but the literature also documents that still no reliable information on $L/D=f(\mathrm{Re})$ is available.

[1]On leave from the Department of Mechanical Engineering, Jadavpur University, Kolkata- 700 032, India.

Contributed by the Fluids Engineering Division of ASME for publication in the JOURNAL OF FLUIDS ENGINEERING. Manuscript received by the Fluids Engineering Division August 16, 2004; final manuscript received: June 2, 2005. Associate Editor: Ugo Piomelli.

Table 1 Summary of publications and results of previous investigations of laminar pipe flow entrance length

No.	Authors	Year	Method	L/D
1	Boussinesq [8]	1891	Analytical, two-zone approach	0.065 Re
2	Schiller [2]	1922	Integral approach, assuming a parabolic velocity distribution within the boundary layer	0.0288 Re
3	Atkinson and Goldstein [10]	1938	Analytical, generalization of the Blasius's solution of the flat plate	0.065 Re
4	Langhaar [3]	1942	Analytical, linearized the momentum equation	0.0575 Re
5	Nikuradse [9]	1950	Experiment	0.0625 Re
6	Siegel [11]	1953	Analytical, integral approach, assuming a cubic velocity distribution within the boundary layer	0.030 Re
7	Bogue [12]	1959	Analytical, integral approach, assuming a quartic velocity distribution within the boundary layer	0.0288 Re
8	Campbell and Slattery [14]	1963	Analytical, applying a plus viscous dissipation of energy term to the entire flow	0.0675 Re
9	Collins and Schowalter [15]	1963	Analytical, developing the work of Boussinesq	0.061 Re
10	Sparrow et al. [4]	1964	Analytical, utilizing a stretched axial coordinate and introducing a mechanical energy equation	0.056 Re
11	Hornbeck [16]	1964	Numerical, initial value problems	0.057 Re
12	McComas and Eckert [17]	1965	Experimental, by relating the pressure drop to distance from the pipe entry	(0.03–0.035)Re
13	Christiansen and Lemmon [18]	1965	Numerical, by obtaining a comparative numerical solution of the momentum equation	0.0555 Re
14	Vrentas et al. [19]	1966	Numerical, boundary value problem	0.056 Re
15	McComas [20]	1967	Analytical, general method depends only on knowledge of the fully developed velocity profile	0.026 Re
16	Friedmann et al. [21]	1968	Numerical, assuming that the initial velocity profiles are concave in the core rather than uniform	0.056 Re
17	Atkinson et al. [22]	1969	Numerical, finite element method	0.59+0.056 Re
18	Lew and Fung [6]	1970	Analytical, two sets of eigenfunctions	0.065 Re(Re<1) 0.08 Re(Re>50)
19	Fargie and Martin [23]	1971	Numerical, simplified the momentum equations by employing differential and integral form	(0.049–0.068)Re
20	Chen [24]	1973	Analytical, integral momentum method	(0.052–0.068)Re
21	Gupta [25]	1977	Numerical	0.0675 Re
22	Mohanty and Asthana [7]	1979	Analytical, two-zone approach to the inlet and filled regions	0.075 Re

The number of various references cited in the above-mentioned review publications readily suggests that research on the development length for laminar pipe and channel flows is well known and the results are well documented, so that the literature survey in the present paper can concentrate only on tabulating the final results. A summary of investigations, provided in Table 1, clearly indicates that most of the studies on the development length for laminar pipe flows were carried out analytically, with some approximations. The investigations were based either on the integral form of the boundary layer equations or on the zone method, treating the flow close to the entrance of the pipe and in the far-field region separately. Results were also obtained however, by experimental and numerical investigations, as can be seen in the methods column of Table 1.

The results presented in Table 1 are not only widely scattered but also show that different relationships are suggested for the normalized development length of laminar pipe flow; i.e., both the relations $L/D=C\,\mathrm{Re}$ and $L/D=C_0+C_1\,\mathrm{Re}$ (only one publication, by Atkinson et al. [22]), correlate the development length as a function of Reynolds number. Although some of the numerical investigations suggest the first of the above relationships to be valid and provide $C\approx 0.0557$ as a consistent value, the deduced relationship $L/D=C\,\mathrm{Re}$ essentially leaves out the fact that diffusion also plays an important role in the axial direction, particularly at lower Reynolds number, and this yields: $L/D=C_0+C_1\,\mathrm{Re}$ as the "correct relationship" for L/D. This relationship was reported only by Atkinson et al. [22].

In order to obtain a better overview of the results summarized in Table 1, Fig. 1 provides information on the scatter of the entrance length coefficient C, determined by various investigators. The order of the data in this figure is presented, from left to right, in accordance with the year of publication. The results clearly show that, in general, $0.025\leq C\leq 0.08$.

Regarding the constant, C_0, in the relationship $L/D=C_0+C_1\,\mathrm{Re}$, it is worth noting that in the literature only Atkinson et al. [22] claimed that this constant is essential in the relationship for L/D. This might seem surprising since simple considerations, based on scale analysis, such as that already presented in Sec. 1, suggest that the following relations must hold:

$$\lim_{\mathrm{Re}\to 0}\left(\frac{L}{D}\right)=C_0 \text{ and } \lim_{\mathrm{Re}\to\infty}\left(\frac{L}{D}\right)=C_1\,\mathrm{Re} \tag{1}$$

All these findings from the literature regarding the development lengths of laminar pipe and channel flows are unsatisfactory and

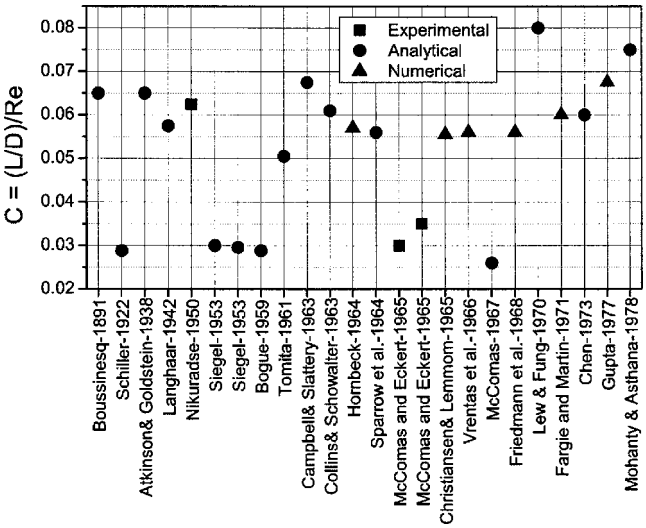

Fig. 1 The constants *C* relationship between the Reynolds number and the ratio of development length and pipe diameter

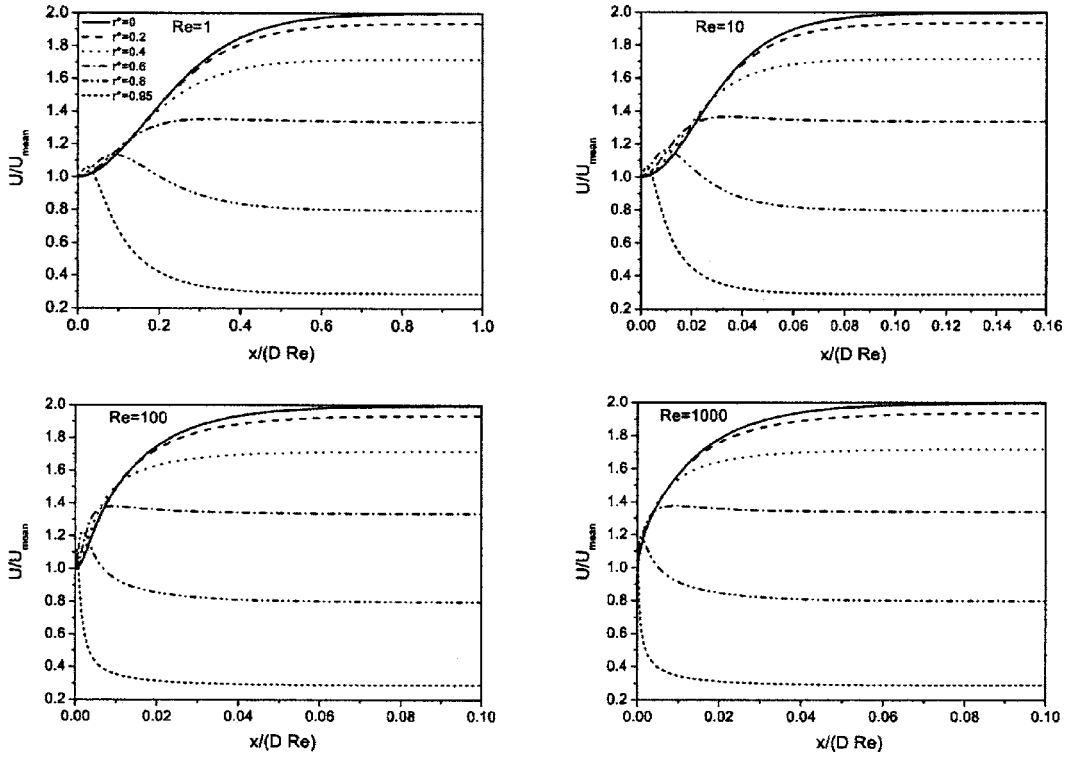

Fig. 2 Axial development of velocities at different radial positions for Re=1, 10, 100, and 1000

suggest that combined numerical, experimental and analytical (if possible) studies are essential to clarify why differences are obtained in the values of C_0 and C_1 in the L/D relationship $L/D = C_0 + C_1$ Re. Such studies and corresponding results are provided in the present paper [13,26].

3 Numerical Investigations

3.1 Equations, Boundary Condition, and Solution Procedure. The present investigations of the development of laminar pipe flow were carried out to yield numerically based data on the development length. Since, for the present investigations, a steady, laminar and developing flow was considered without swirl ($U_\theta = 0$) and fluid properties were assumed to be constant, the governing mass and momentum conservation equations were considered in axi-symmetric coordinates. These equations are as follows:

Continuity equation:

$$\frac{1}{r}\frac{\partial}{\partial r}(\rho r U_r) + \frac{\partial}{\partial z}(\rho U_z) = 0 \tag{2}$$

Axial momentum equation:

$$\rho\left(U_r\frac{\partial U_z}{\partial r} + U_z\frac{\partial U_z}{\partial z}\right) = -\frac{\partial P}{\partial z} + \mu\left[\frac{1}{r}\frac{\partial}{\partial r}\left(r\frac{\partial U_z}{\partial r}\right) + \frac{\partial^2 U_z}{\partial z^2}\right] \tag{3}$$

Radial momentum equation:

$$\rho\left(U_r\frac{\partial U_r}{\partial r} + U_z\frac{\partial U_r}{\partial z}\right) = -\frac{\partial P}{\partial r} + \mu\left[\frac{\partial}{\partial r}\left(\frac{1}{r}\frac{\partial}{\partial r}(rU_r)\right) + \frac{\partial^2 U_r}{\partial z^2}\right] \tag{4}$$

To look for a generally applicable numerical solution, all coordinates in the above equations were made dimensionless with respect to the diameter of the pipe, whereas the velocities were normalized to the constant inlet velocity (U_0), which was considered to be uniform throughout the inlet cross section. The pressure was normalized with respect to ρU_0^2.

The dimensionless governing equations were discretized by a finite (control) volume approach similar to that suggested by Ferziger and Perić [27], i.e., with a method that employs collocated variables, using the SIMPLE algorithm imposed by Patankar [28] for the pressure solution. The algebraic equations resulting from the discretization process were solved by the "Strongly Implicit Procedure" (SIP) proposed by Stone [29].

The boundary conditions before normalization, applied to the present problem, may be summarized as follows:

(1) At $z=0$, i.e., at the inlet, $U_z = U_0$ and $U_r = 0$ for every r.
(2) At $z=L_z$, the axial diffusion in both of the momentum equations was neglected, i.e., $\partial^2 U_r/\partial z^2 = \partial^2 U_z/\partial z^2 = 0$ for every r.
(3) At $r=0$, i.e., on the centerline of the pipe, a symmetry condition was imposed, i.e., $U_r = \partial U_z/\partial r = 0$ for every z.
(4) At $r=D/2$, i.e., on the walls of the pipe, no slip condition was assumed, i.e. $U_r = U_z = 0$ for every z.

With the above boundary conditions, the discretized set of differential equations was solved in a manner now well known in numerical fluid mechanics. The development length was defined as the distance from the inlet where the dimensionless centerline velocity reaches a value of 1.98 which is 1% lower than its fully developed value. In order to ensure that the development of centerline velocity actually implies true establishment of the fully developed profile in the entire cross section of the pipe, the variation of velocities at different radial positions as a function of axial distance are presented in Fig. 2 for different Reynolds numbers. The figure clearly shows that the velocities at the other radial locations attains their fully developed value much earlier than the centerline.

For the two-dimensional channel flows, the set of equations that has been solved is as follows:

Continuity equation:

Table 2 Grid independence study for circular pipe flow [$C_1=L/(D\,\mathrm{Re})$ for different grid spacings]

Re	100×20	100×40	200×40	200×80	400×80
10	0.09256	0.08881	0.08880	0.08784	0.08783
100	0.06279	0.05920	0.05922	0.05844	0.05844
1000	0.06077	0.05728	0.05723	0.05648	0.05648
4000	0.06028	0.05674	0.05677	0.05610	0.05610

$$\frac{\partial}{\partial x}(\rho U_x)+\frac{\partial}{\partial y}(\rho U_y)=0 \tag{5}$$

Axial flow momentum equation:

$$\rho\left(U_x\frac{\partial U_x}{\partial x}+U_y\frac{\partial U_x}{\partial y}\right)=-\frac{\partial P}{\partial x}+\mu\left[\frac{\partial}{\partial x}\left(\frac{\partial U_x}{\partial x}\right)+\frac{\partial}{\partial y}\left(\frac{\partial U_x}{\partial y}\right)\right] \tag{6}$$

Transverse flow momentum equation:

$$\rho\left(U_x\frac{\partial U_y}{\partial x}+U_y\frac{\partial U_y}{\partial y}\right)=-\frac{\partial P}{\partial y}+\mu\left[\frac{\partial}{\partial x}\left(\frac{\partial U_y}{\partial x}\right)+\frac{\partial}{\partial y}\left(\frac{\partial U_y}{\partial y}\right)\right] \tag{7}$$

The boundary conditions employed for the two-dimensional channel flows are similar to those imposed for flow through pipes:

(1) At $x=0$, i.e., at the inlet, $U_x=U_0$ and $U_y=0$ for every y.
(2) At $x=L_x$, the axial diffusion in both of the momentum equations was neglected, i.e., $\partial^2U_x/\partial x^2=\partial^2U_y/\partial x^2=0$ for every y.
(3) At $y=0$, i.e., on the centerline of the channel, a symmetry condition was imposed, i.e. $\partial U_x/\partial y=U_y=0$ for every x.
(4) At $y=b$, i.e., on the walls of the channel, no slip condition was assumed, i.e., $U_x=U_y=0$ for every x.

Again, a finite volume method was employed to solve this set of equations and development length was computed in a similar manner, as described for pipe flows.

For all the computations, presented in the paper, uniform grid was chosen in the cross-stream direction (r or y, as the case may be) and the numerical grid in the axial direction was varied in GP series, with a common ratio of 1.05. In order to check the accuracy of the present results, numerical computations were carried out for different grid spacing, starting from 100 (in the axial direction) $\times20$ (in the radial or cross-stream direction) to 400×80 for various Reynolds number. The development lengths, in the form of $C_1=L/(D\,\mathrm{Re})$, were monitored for each of the grids and for Reynolds number varying from 10 to 4000. The results for circular pipe are shown in Table 2. It is obvious from the table that virtually no variation was observed in the results for 200×80 and 400×80 grid up to 5 significant digits for entire range of Reynolds number. Since the emphasis in the present paper is to obtain very accurate computational data, 200×80 grid was chosen for all the final computations. Similar study for channel flow, which is not presented in the paper, yielded the same grid spacing.

3.2 Predictions and Results. As stated in the Introduction, it was the aim of the present investigations to clarify some of the widespread and partially contradictory information that is available in the literature on the development lengths of laminar pipe and channel flows. If only the convective velocity is taken into account in the flow direction and the diffusion velocity is considered only across the flow for scaling, the following order of magnitude considerations result:

$$U_z=C^*U_0 \text{ and } t_{\mathrm{diff}}=C^+\frac{D^2}{\nu}\Rightarrow\frac{L}{D}=\underbrace{C^*C^+}_{C}\frac{U_0D}{\nu} \tag{8}$$

from which one readily obtains the high Reynolds number limit of (L/D) behavior:

$$\frac{L}{D}=C\,\mathrm{Re} \tag{9}$$

Postulating this relationship to be valid also for smaller Reynolds numbers, a dependence of C on Re must result. The variation of C [$=L/(D\,\mathrm{Re})$] with Re was deduced from numerical studies on the development length of laminar pipe flow and is shown in Fig. 3. These results account for some of the scatter of C values reported in Sec. 2, i.e., wrong correlation [Eq. (9)] is fitted to the data.

The low Reynolds number limit of $L/D=f(\mathrm{Re})$ can be derived by considering only the diffusion velocity both in the axial direction and in the cross-flow direction. Such consideration yields the following relationships;

$$U_z=C^*\frac{\nu}{D} \text{ and } t_{\mathrm{diff}}=C^+\frac{D^2}{\nu}\Rightarrow\frac{L}{D}=C^*C^+=C_0 \tag{10}$$

If this consideration for the low Reynolds number limit is not taken into account, it is obvious that the constant C in Eq. (9) must increase with decreasing Reynolds number (see Fig. 3).

In the entire Reynolds number range, $0<\mathrm{Re}<\infty$, the above order of magnitude consideration can be extended by taking both the convection and the diffusion velocities in the flow direction into account, yielding

$$U_z=\left(C_0^*\frac{\nu}{D}+C_1^*U_0\right) \text{ and } t_{\mathrm{diff}}=C^+\frac{D^2}{\nu} \tag{11}$$

from which the development length may be estimated as

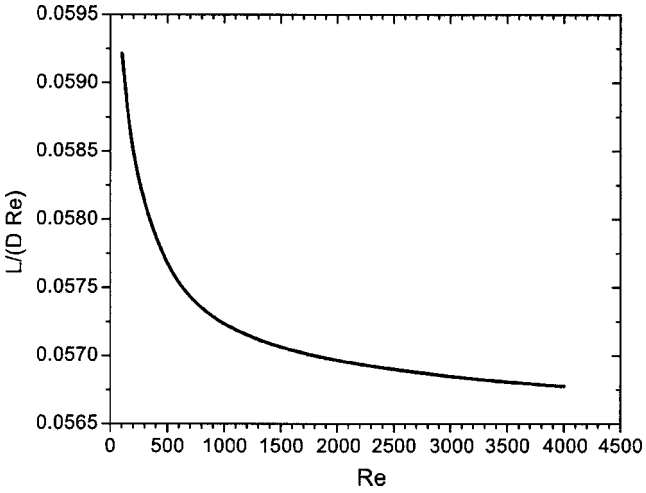

Fig. 3 Variation of constant C with Reynolds number of the pipe flow

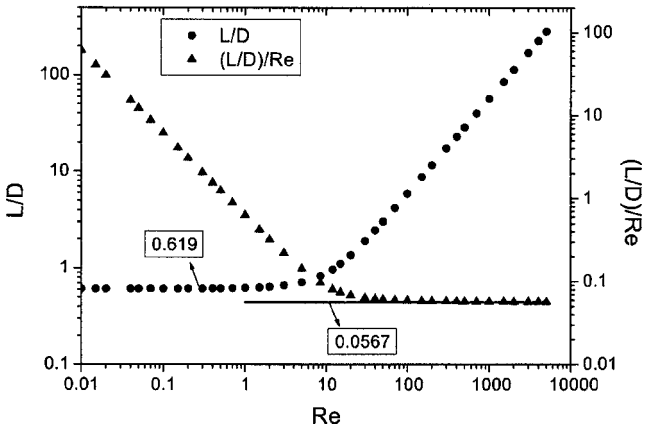

Fig. 4 Numerical results for L/D plotted to deduce C_0 and C_1 in the L/D relationship

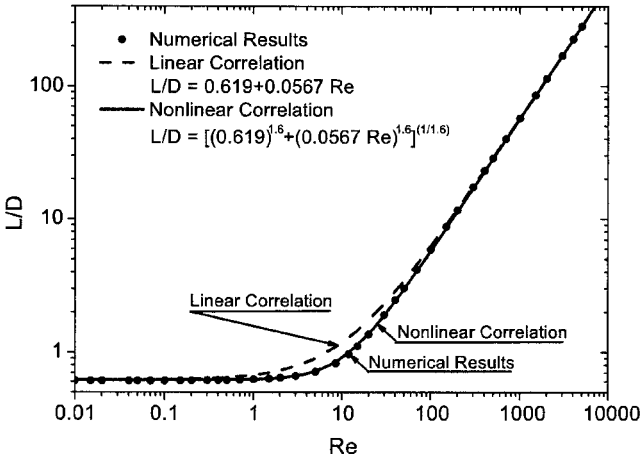

Fig. 5 Predicted development length results and comparison with the convection diffusion relationship in Eq. (14) for laminar pipe flow

$$L = U_z t_{\text{diff}} = D(C_0^* C^+ + C_1^* C^+ \text{Re}) \Rightarrow \frac{L}{D} = C_0 + C_1 \text{Re} \quad (12)$$

Fitting this function to the numerical results for L/D, one readily obtains

$$\lim_{\text{Re}\to 0}\left(\frac{L}{D}\right) = C_0 = 0.619 \quad (13)$$

The high Re numerical data are fitted to $L/(D\,\text{Re})$ to yield

$$\lim_{\text{Re}\to \infty}\left(\frac{L}{D\,\text{Re}}\right) = C_1 = 0.0567 \quad (14)$$

The numerical data for L/D and $L/(D\,\text{Re})$ are presented in Fig. 4 and also clearly indicate the limiting values given in Eq. (13) for low Reynolds numbers and in Eq. (14) for high Reynolds numbers. It may be recognized that the low Reynolds number limit takes only the diffusive momentum transport into account, whereas the high Reynolds number limit considers only the convective transport in the flow direction and the diffusive transport in the cross-flow direction.

Taking the computational results and their limiting behavior into account raises a question regarding the validity of the deduced relationship

$$\frac{L}{D} = 0.619 + 0.0567\,\text{Re} \quad (15)$$

in the range $1 \leqslant \text{Re} \leqslant 100$. In this range of Reynolds number, the nonlinearity of the convection terms in the momentum transport equation yields conditions that do not permit L/D to be simply computed by the addition of C_0 and C_1 Re terms. This can readily be seen from Fig. 5, which shows the predicted L/D correlation given by Eq. (15) (dashed line). The actual computations are given by circles. A comparison of both results suggests that, for a given Reynolds number, the actual development length of a laminar pipe flow is shorter than the length calculated from the correlation in Eq. (15). At this point, since the asymptotic behaviors of L/D in both low and high Reynolds number regimes is known, the suggestions of Churchill and Usagi [30] may be employed to correlate the data as follows:

$$\frac{L}{D} = [(0.619)^{1.6} + (0.0567\,\text{Re})^{1.6}]^{1/1.6} \quad (16)$$

The above correlation is also shown in Fig. 5, which predicts the numerical data within a maximum error of 3%.

The above-described numerical investigations of the development length for laminar pipe flow were also repeated for laminar, plane channel flow solving Eqs. (5)–(7) and the corresponding boundary conditions. As expected, the numerical computation yielded similar results. The high and low Reynolds number limits turned out to be as follows:

$$\lim_{\text{Re}\to 0}\left(\frac{L}{D}\right) = C_0 = 0.631 \quad (17)$$

$$\lim_{\text{Re}\to \infty}\left(\frac{L}{D\,\text{Re}}\right) = C_1 = 0.0442 \quad (18)$$

Atkinson et al. [10] also computed these constants and found them to be C_0=0.625 and C_1=0.044, which are in close agreement to the findings given above. However, as Fig. 6 shows, the corresponding correlation

$$L/D = 0.631 + 0.0442\,\text{Re} \quad (19)$$

again yields, for a given Reynolds number range, a development length for laminar plane channel flow that is longer than the numerically computed length. The reasons for this are principally the same as those given for the difference for the laminar pipe flow. Here also, one can fit the numerical data with the following correlation:

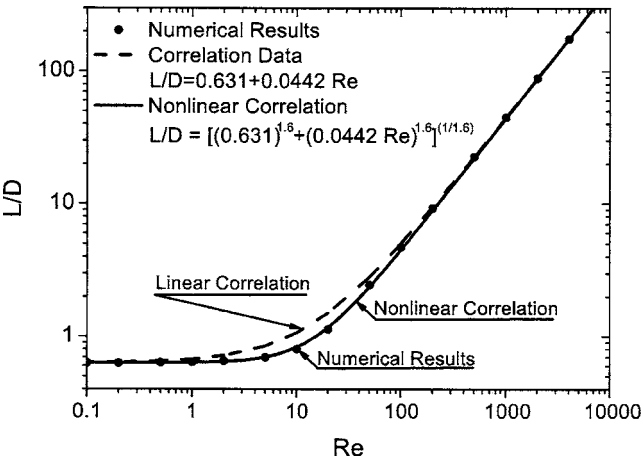

Fig. 6 Predicted development length results and comparison with convection diffusion relationship for laminar channel flow

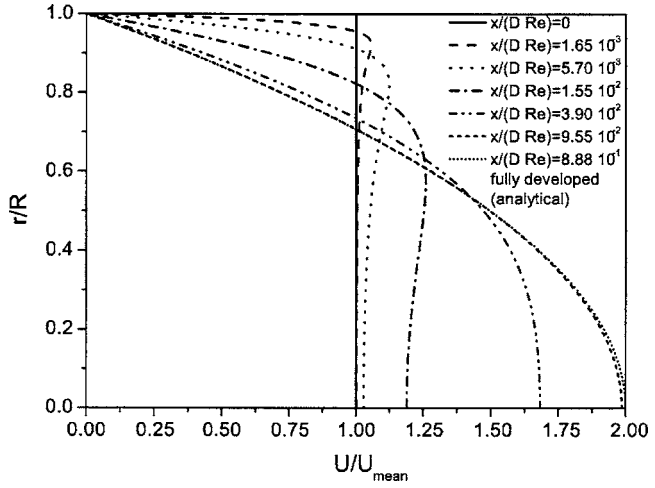

Fig. 7 Axial development of velocity profile for Re=10

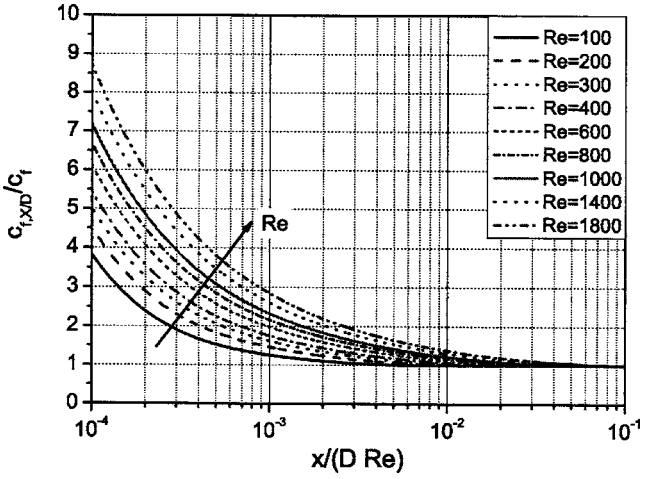

Fig. 8 Change of local skin friction factor through the entrance region of the pipe

$$\frac{L}{D} = [(0.631)^{1.6} + (0.0442\,\mathrm{Re})^{1.6}]^{1/1.6} \tag{20}$$

The above correlation is also shown in Fig. 6, which fits the computational data within 3.8%. It is also interesting that in the correlations for both pipe and channel flows [see Eqs. (16) and (20)], although the constants C_0 and C_1 vary, the exponent is the same and is equal to 1.6.

Furthermore, the change of skin friction factor ($c_{f,x/D}$) in the entrance region investigated for pipe flow. For this calculation much finer grid was used especially through the entrance region for better resolution. The results are shown for varying Re numbers in Fig. 7. The local skin friction factor ($c_{f,x/D}$) was normalized with c_f (=16/Re) and location (x/D) normalized with Re. Very sharp decrease in $c_{f,x/D}$ through the entrance region can be seen in Fig. 7.

4 Experimental and Analytical Investigations

As Table 1 shows, most of the investigations in the past, carried out to yield the development length for laminar pipe and channel flows, were carried out experimentally or analytically. The results also show (see Fig. 1) that the research, over the years, did not yield a convergence to a certain relationship for L/D for either pipe flows or channel flows. This reflects the fact that there are insurmountable difficulties in determining the development length L/D of laminar pipe and channel flows experimentally and/or analytically. To assess these difficulties, we carried out experimental investigations using an air test rig and a well set-up pipe flow test section. In the air test rig, hot-wire measurements were performed to yield the axial velocity at the exit of a pipe of given L/D (essentially pipes of fixed lengths-to-diameter ratio were employed). From a preset mass flow rate, $\dot{m}$=const and the volume flow rate was computed as $\dot{V}=\dot{m}/\rho$, where ρ was calculated from the measured air pressure and the measured air temperature of the flowing fluid using the ideal gas law. The known volume flow rate permitted the cross-sectional mean flow velocity to be determined and from this the expected maximum velocity, assuming a parabolic velocity profile, on the pipe axis was obtained:

$$U_{\mathrm{av}} = \frac{4\dot{V}}{\pi R^2} \Rightarrow U_{\max} = 2U_{\mathrm{av}} \tag{21}$$

Changing experimentally the set mass flow rate $\dot{m}$ in steps permitted the velocity on the axis to be determined at the pregiven distance L/D by means of a well-calibrated hot-wire system. When this velocity agreed within 2% with the corresponding calculated maximum velocity, the flow was assumed to be fully developed. Carrying out velocity measurements for L/D=74.67, 141.33, 208, and 274.67 permitted L/D as a function (Re) to be experimentally determined.

The L/D values obtained in this manner might be called an asymptotic assessment of L/D. These experiments revealed that any small measurement inaccuracies eventually yielded large variations of the measured Reynolds number for which a measured $U_{\max}$ was obtainable to be close to 2% of the $U_{\max}$ calculated from the preset $\dot{m}$. This fact and the strong dependence of C_1 in the expression of L/D on asymptotically measured Reynolds number might have caused, in the past, the large scatter in the experimentally determined L/D values indicated in both Table 1 and in Fig. 1.

Analytical studies were also carried out of the development length of laminar pipe and channel flows. Strictly, owing to the presence of non-linear terms in the convective transport of the momentum equations, no analytical solution is possible without further assumptions being introduced. Hence all the solution attempts available in the literature may be considered to be only "semianalytical." In order to obtain such semianalytical solutions for both the development length of the laminar pipe and channel flows, two different approaches were adopted. In the first approach, which was used by many of the early researchers, the integral momentum equation with boundary layer approximation was adopted. In this approach, the free stream velocity was considered to be the centerline velocity, which varies with the axial distance, obeying the appropriate integral mass conservation equation. With in the assumed boundary layer developing along the pipe, both parabolic and cubic velocity distributions were considered, i.e., were assumed to be valid for the L/D calculation. However, such solutions are valid only for the high Reynolds number regime, since they all neglect the contribution of the axial diffusion, which is otherwise important in the lower Reynolds number regime. Hence the applied integral momentum equation solutions can only provide an acceptable dependence of L/D on Re as given in Eq. (9). The velocity profiles at various axial locations for Re =10, are presented in Fig. 8. It is observed from the figure that at locations near to the entrance, velocity overshoots occur close to the wall. These overshoots were not taken into account in the semianalytical treatment employing boundary layer approximations, since such inflection points in the velocity distribution could not be captured by the employed parabolic or cubic profiles. Hence the evaluation of the constants, appearing in Eq. (11), by this method is also liable to be incorrect.

In the second approach, a starting flow solution was tried, where the initial condition is given by a uniform velocity distribution throughout the entire pipe cross section. In this problem the

governing equations were considered to be the same as those applicable for transient flow in the fully developed section. It was assumed that the transient term in this situation plays a similar role to that of the convection terms for steady developing flows with uniform inlet velocity. From the transient velocity distribution (which may be obtained in terms of an infinite series of cosine and sine terms), the time required to achieve the steady-state condition (to be precise, when the velocity distribution reaches 99% of that of the steady fully developed solution) was calculated. Using this time and the average axial velocity, the distance travelled by an average fluid particle to reach a steady state was obtained. This distance was considered to be development length, and this can only be correct if the assumption regarding the convection term is correct. However, it was observed that the solution not only provides the dependence given in Eq. (9), but also overpredicts the development length by a factor of 2. Hence, from the present effort to obtain an analytical solution for the development length through pipes, it may be concluded that no analytical (or even semianalytical) solution is possible which correctly predicts the dependence of L/D in both the lower and higher Reynolds number regimes.

5 Conclusions and Final Remarks

Investigations of the development length of laminar pipe and channel flows have been carried out extensively and various reports of relevant work are available in the literature. In spite of this, no analytical expressions exist that correctly describe the development length for both types of flow. This encouraged the present work employing numerical, experimental and analytical methods. Only the numerical investigations were successful, yielding the following analytical relationships for the correlation length:

$$\text{Pipe flow: } \frac{L}{D} = [(0.619)^{1.6} + (0.0567\,\mathrm{Re})^{1.6}]^{1/1.6} \tag{22}$$

$$\text{Channel flow: } \frac{L}{D} = [(0.631)^{1.6} + (0.0442\,\mathrm{Re})^{1.6}]^{1/1.6} \tag{23}$$

Mostly in the literature the correlation $L/D = C\,\mathrm{Re}$ was used. This correlation neglects the diffusion transport in axial direction and in the paper it is shown that it should be replaced by $L/D = C_0 + C_1\,\mathrm{Re}$. However, this correlation does not correctly describe the development length in the region $1 \leqslant \mathrm{Re} \leqslant 100$. Hence the above analytical correlations are suggested to compute L/D for channel and pipe flows of different Reynolds numbers.

The authors feel that the results presented in this paper close the long ongoing research work on the development length of laminar pipe and plane channel flows.

References

[1] Schlichting, H., 1979, *Boundary Layer Theory*, McGraw-Hill, NY.

[2] Schiller, L., 1922, "Die Entwicklung der laminaren Geschwindigkeitsverteilung und ihre Bedeutung für Ähnlichkeitsmessungen," Z. Angew. Math. Mech., **2**, pp. 96–106.

[3] Langhaar, H. L., 1942, "Steady flow in the transition length of a straight tube," J. Appl. Mech., **9**, pp. 55–58

[4] Sparrow, E. M., Lin, S. H., and Lundgren, T. S., 1964, "Flow development in the hydrodynamic entrance region of tubes and ducts," Phys. Fluids, **7**(3), pp. 338–347.

[5] Schmidt, F. W., and Zeldin, 1969, "Laminar flow in inlet sections of tubes and ducts," AIChE J., **15**(4), pp. 612–614.

[6] Lew, H. S., and Fung, Y. C., 1970, "Entry flow into blood vessels at arbitrary Reynolds number," J. Biomech., **3**, p. 23.

[7] Mohanty, A. K., and Asthana, B. L., 1979, "Laminar flow in the entrance region of a smooth pipe," J. Fluid Mech., **90**, pp. 433–449

[8] Boussinesq, J., 1891, "Sur la maniere don't les vitesses, dans un tube cylindrique de section circulaire, evase a son entrée, se distribuent depuis entrée jusqu'aux endroits ou se trouve etabli un regime uniforme," Compt. Rend., **113**, pp. 49–51.

[9] Nikuradse, J., 1950, *Applied Hydro and Aerodynamics*, McGraw-Hill, NY, p. 27.

[10] Atkinson, B., and Goldstein, S., 1938, *Unpublished work described in Modern Developments in Fluid Dynamics*, Oxford University Press, Oxford, Vol. 1, p. 304.

[11] Siegel, R., 1953, "The effect of heating on boundary layer transition for liquid flow in a tube," Sc.D. thesis, Massachusetts Institute of Technology, Cambridge, MA.

[12] Bogue, D. C., 1959, "Entrance effects and prediction of turbulence in non Newtonian flow," Ind. Eng. Chem., **51**(7), p. 874–878.

[13] Tomita, 1959, Soc. Chem. Engrs. Japan, **23**, pp. 525–529.

[14] Campbell, W. D., and Slattery, J. C., 1963, "Flow in the entrance of a tube," ASME J. Basic Eng., Series D, **85**(1), pp. 41–46.

[15] Collins, M., and Schowalter, W. R., 1963, "Behaviour of non-Newtonian fluids in the inlet region of a channel," AIChE J., **9**, pp. 98–102.

[16] Hornbeck, R. W., 1964 "Laminar flow in the entrance region of a pipe," Appl. Sci. Res., Sect. A, **13**, pp. 224–236.

[17] McComas, S. T., and Eckert, E. R. G., 1965, "Laminar pressure drop associated with the continuum entrance region and for slip flow in a circular tube," ASME J. Appl. Mech., **32**, p. 765–770.

[18] Christiansen, E. B., and Lemmom, H. E., 1965, "Entrance region flow," AIChE J., **11**(6), pp. 995–999.

[19] Vrentas, J. S., Duda J. L., and Bargeron, K. G., 1966, "Effect of Axial Diffusion of Vorticity on Flow Development in Circular Conduits," AIChE J., **12**, pp. 837–844.

[20] McComas, S. T., 1967, "Hydrodynamic entrance lengths for ducts of arbitrary cross section," J. Basic Eng., **89**, pp. 847–856.

[21] Friedmann, M., Gillis, J., and Liron, N., 1968, "Laminar flow in a pipe at low and moderate Reynolds numbers," Appl. Sci. Res., **19**(6), pp. 426–433.

[22] Atkinson, B., Brocklebank, M. P., Card C. C. H., and Smith, J. M., 1969, "Low Reynolds number developing flows," AIChE J., **15**, pp. 548–553.

[23] Fargie, D., and Martin, B. W., 1971, "Developing laminar flow in a pipe of circular cross section," Proc. R. Soc. London, Ser. A, **321**, pp. 461–476.

[24] Chen, R. Y., 1973, "Flow in the entrance region at low Reynolds numbers," J. Fluids Eng., **95**, pp. 153–158.

[25] Gupta, R. C., 1977, "Laminar flow in the entrance of a tube," Appl. Sci. Res., **33**, p. 1–10.

[26] Durst, F., Heim, U., Ünsal, B., and Kullik, G., 2003, "Mass flow rate control system for time-dependent laminar and turbulent flow investigations," Meas. Sci. Technol., **14**, p. 893.

[27] Ferziger, J. H., and Perić, M., 1999, *Computational Methods for Fluid Dynamics*, 2nd ed., Springer, Berlin.

[28] Patankar, S. V., 1980, *Numerical Heat Transfer and Fluid Flow*, Hemisphere, WA, D.C.

[29] Stone, H. L., 1968, "Iterative solution of implicit approximations of multidimensional partial differential equations," SIAM (Soc. Ind. Appl. Math.) J. Numer. Anal., **5**, pp. 530–541.

[30] Churchill, S. W., and Usagi, R., 1972, "A general expression for the correlation of rates of heat transfer and other phenomenon," AIChE J., **18**, pp. 1121–1132.

Parallel DSMC Simulation of a Single Under-Expanded Free Orifice Jet From Transition to Near-Continuum Regime

J.-S. Wu
Phone: 886-3-573-1693
Fax: 886-3-572-0634
e-mail: chongsin@faculty.nctu.edu.tw

S.-Y. Chou

U.-M. Lee

Y.-L. Shao

Y.-Y. Lian

Department of Mechanical Engineering, National Chiao-Tung University, Hsinchu 30050, Taiwan

This paper describes the numerical analysis of the flow structure of a single underexpanded argon free jet issuing into a lower-pressure or vacuum environment using the parallel three-dimensional direct simulation Monte Carlo (DSMC) method employing dynamic domain decomposition. Unstructured and tetrahedral solution-based refined mesh depending on the local mean free path is used to improve the resolution of solution. Simulated Knudsen numbers of the stagnation conditions based on orifice diameter, Reynolds numbers based on the conditions at the orifice exit, and stagnation-to-background pressure ratios are in the range of 0.0005–0.1, 7–1472, and 5–∞, respectively, where "∞" represents vacuum condition in the background environment. Results show that centerline density decays in a rate proportional to the inverse of the square of the axial distance (z^{-2}) from the orifice for all ranges of flow in the current study. The more rarefied the background condition is, the longer the z^{-2}-regime is. In addition, a distinct flow structure, including barrel shock, Mach disk and jet boundary, is clearly identified as the Knudsen number reaches as low as 0.001. Predicted location and size of Mach disk in the near-continuum limit (Kn=0.001, 0.0005) are found to be in reasonable agreement with experimental results in the continuum regime. [DOI: 10.1115/1.2062807]

Introduction

Many industrial processes requires the use of high-speed underexpanded jets to either provide impulse or deliver the interested gas species to the designated region or provide high-density cooling to specific heated wall (due to small area of jet impingement and higher velocities of impact). Practical examples include the use of jets for rocket exhausts at high altitude and attitude control on satellite, cooling of Micro-Electro-Mechanical-Systems (MEMS) devices, fine particle deposition and removal, in inkjet printing technology, showerhead (periodic array of microjets) for materials processing, among others [[1], and the reference cited therein]. The nozzle used to generate the under-expanded jet can be either a simple thin sonic orifice or converging-diverging (Laval) nozzle [2]. The latter design can create uniform supersonic jets with desirable flow properties. For example, one such property is a highly uniform pressure along the centerline of the jet that extends many nozzle diameters downstream (inviscid potential core). Of course, this design may also present some significant drawbacks, including difficulties of manufacturing and high noise level. Previous studies have shown that these drawbacks may be removed if the nozzle is miniaturized [2]. However, manufacturing this kind of nozzle is not straightforward at all.

On the other hand, *thin sonic orifice*, having a minimum cross-sectional area at the exit, represents the simplest type of micronozzle. One of the obvious advantages of using the orifice lies upon the simplicity of manufacturing and maintenance. This type of orifice generates an *underexpanded sonic jet* if the pressure ratio of chamber to background is approximately larger than 2, which is often the case in practical applications. However, the axial pressure distribution resulting from the orifice microjet varies significantly within the first few orifice diameters. The inviscid potential core of the supersonic jet dissipates and the resulting subsonic flow decays rapidly, which may be advantageous for mixing purpose. The situation is even more complicated due to rarefaction if the background environment is at low-pressure or near-vacuum. Thus, understanding of the flow characteristics of the free orifice underexpanded sonic jets is important when applying them to these practical situations.

A single underexpanded orifice jet issuing into a quiescent environment has been studied extensively in the past, but most studies were either emphasizing upon the experimental visualization of the flow structure [[3,9], and references cited therein] or simple analytical solution [4,5]. Very few simulation studies were done, especially when rarefaction effects are considered [12]. The main features of the continuum free jet in the near field include a Mach disk, barrel shock and free jet boundary [1]. Behind the Mach disk, subsonic core and supersonic outer flow are bounded by a slip line, which emanates from the triple point. The triple point is the intersection location of barrel shock and Mach disk. The barrel shock intersects with the Mach disk and then reflects as an oblique shock.

Several theoretical researches [4,5] studied the flow structures, especially the diameter or location of the Mach disk. However, there is no satisfied analytical method available to predict the entire structure of an underexpanded sonic jet. Numerical solutions using method of characteristics [6,7] predicted the inviscid jet boundary and the intercepting shock, but were generally not able to predict the formation of Mach disk. Instead, experiments using flow visualization were able to capture the location and diameter of the Mach disk. Ashkenas and Sherman [8] measured the Mach disk position using electron beam visualization in the continuum limit. They proposed a well-known correlation as $x_M/D=0.67(p_0/p_b)^{1/2}$, where x_M is the Mach disk position, p_0 is the source pressure, and p_b is the background pressure. Later, in the same group of Sherman [9], they measured the Mach disk position and diameter of a highly underexpanded sonic jet, considering high-pressure ratios, high stagnation pressures, temperature variations and geometries of solid boundary in the nozzle lip

Contributed by the Fluids Engineering Division for publication in the JOURNAL OF FLUIDS ENGINEERING. Manuscript received by the Fluids Engineering Division March 5, 2004; final manuscript received: June 26, 2005. Associate Editor: Fernando Grinstein.

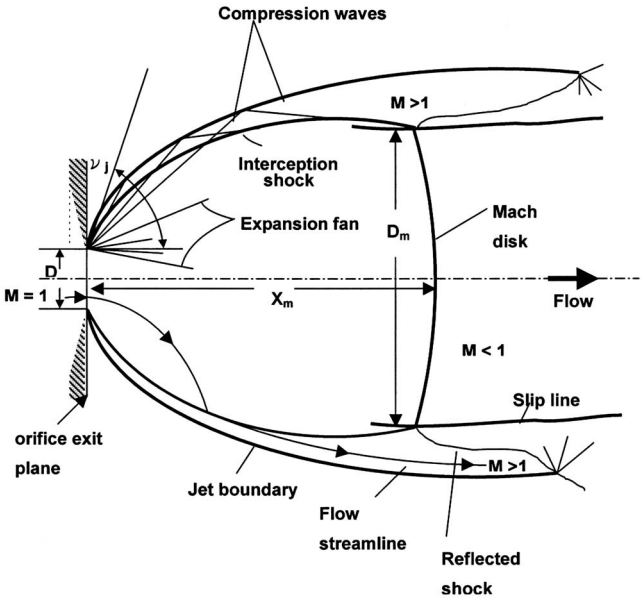

Fig. 1 Flow structure of a single under-expanded orifice jet in the continuum regimen [1]

region. Results showed that Mach disk location was insensitive to the variations of (a) γ, (b) condensation, (c) nozzle lip geometry, (d) absolute pressure level.

Muntz et al. [10] proposed a rarefaction parameter $D(p_o p_b)^{1/2}/T_0$ to classify the structure of a free jet expanding into a region of finite background pressure. This rarefaction parameter is in fact proportional to the inverse of $(p_o/p_b)^{1/2}$ Kn, which combines the effects of pressure ratio and rarefaction. The structures of free jet can be classified into three flow regimes: continuum, transition, and scattering, according to the degree of continuum to rarefied upstream. In this scattering flow regime, any evidence of continuum gas dynamic features disappears [2]. In this regime, the shock envelope has completely vanishes and the gas density smoothly passes to the background density through scattering process. Only the DSMC method [11] is capable of simulating such flow field, although it is well known that it is very computational expensive. Usami and Teshima [12] did an experiment using mass-sampling technique for mass flow measurements in an underexpanded orifice jet. Flow field was then simulated by the DSMC method and reasonable agreement was found as compared with experiments, although the treatment of outflow boundary conditions is problematic due to the assumption of mean zero velocities in the DSMC simulation and near-uniform mesh. It is rather difficult to simulate this type of flow field since the density varies very much from the orifice to the outer boundaries, which makes the selection of both the time-step size and cell size very challenging in the DSMC simulation.

In summary, numerical studies along this line are relatively few or unsatisfied, especially the rarefaction effects caused by the low-pressure stagnation condition and low-pressure background, in which the N-S equations break down. In addition, the flow may reach hypersonic speed ahead of the Mach disk (or highly thermal nonequilibrium) for larger pressure ratio, which makes the simulation using N-S equation difficult. Thus, in the current study we shall use the DSMC method to systematically study the flow structure of the underexpanded sonic jets at different flow conditions with Knudsen numbers in the range of 0.0005–0.1 and Reynolds numbers in the range of 7–1472, both defined using orifice size and upstream stagnation conditions of pressure and temperature (Fig. 1). Transition to turbulence is not considered in the current simulation due to the low Reynolds-number flows. Simulated results are then compared with experimental data available in the literature.

The paper begins with descriptions of numerical method and procedures (Table 1). Then, results are presented along with appropriate discussions. Finally, conclusions of this study are presented.

Numerical Method and Procedures

In the current study, the single under-expanded free jet flow is intrinsically axisymmetric. However, the three-dimensional DSMC code was used instead of the axisymmetric DSMC code because of the following two reasons. First, it is well known that the accuracy near the axis deteriorates if the cell size becomes small (thus, small cell volume) due to insufficient samplings,

Table 1 Corresponding values of the rarefaction parameter for test conditions

Po / Pb	Kn			
	0.0005	**0.001**	**0.01**	**0.1**
5	**15.98**	**7.991**	**0.799**	**0.0790**
10	**11.30**	**5.651**	**0.565**	**0.0560**
20	**7.992**	**3.995**	**0.399**	**0.0390**
50	**5.050**	**2.527**	**0.253**	**0.0253**
100	**3.570**	**1.787**	**0.179**	**0.0179**
150	**2.920**	**1.459**	**0.146**	**0.0146**
200	**2.530**	**1.264**	**0.126**	**0.0126**
250	**2.260**	**1.130**	**0.113**	**0.0113**
500	**1.600**	**0.799**	**0.080**	**0.0080**
1000	**1.130**	**0.565**	**0.057**	**0.0057**
2500	**0.710**	**0.357**	**0.036**	**0.0036**
5000	**0.510**	**0.253**	**0.025**	**0.0025**
7500	**0.410**	**0.206**	**0.020**	**0.0020**
10000	**0.360**	**0.179**	**0.018**	**0.0018**
∞	0.000	0.000	0.000	0.0000

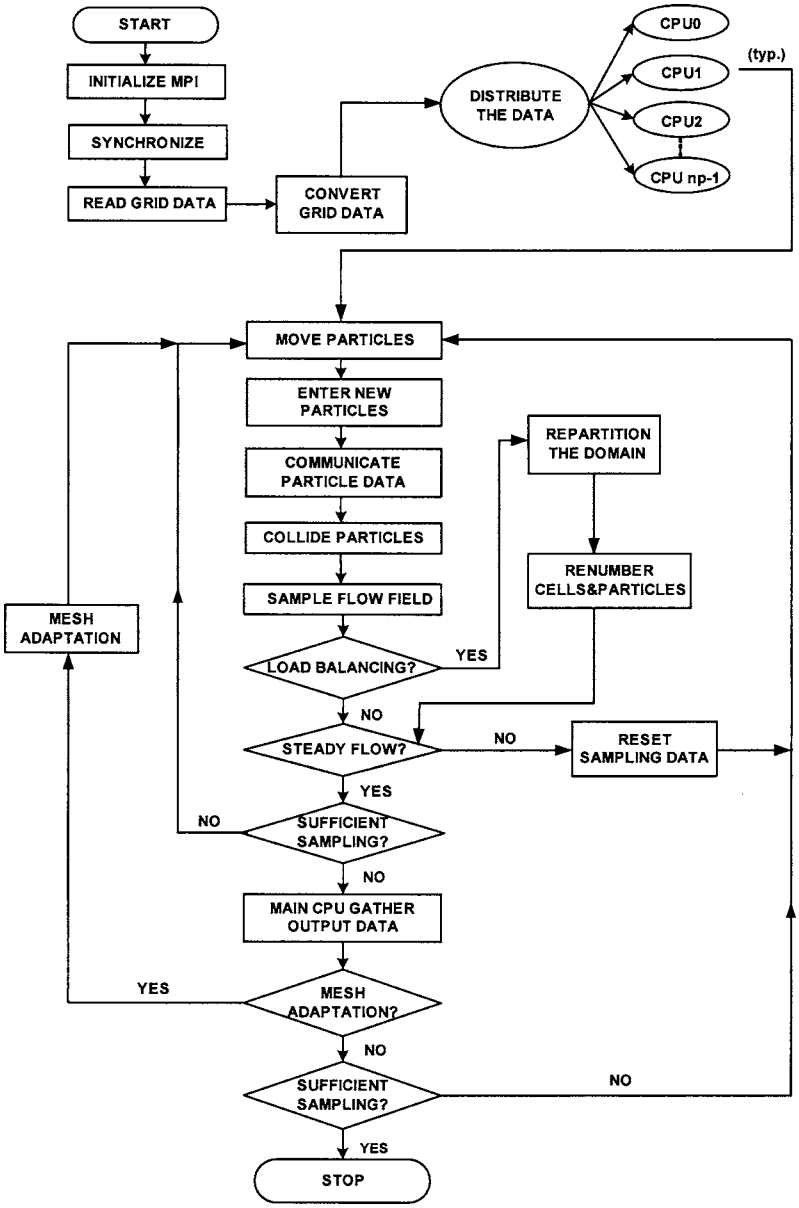

Fig. 2 Flow chart of the parallel DSMC method (PDSC) with mesh refinement

which often contradicts with the requirements of spatial resolution. In addition, position-based (e.g., radial) particle (or cell) weighting [11] used to remove this inaccuracy often induce other problems, such as random walk, whose effect is hard to evaluate before simulation. However, use of the three-dimensional DSMC code will naturally remove this constraint, although the computational load is higher than the axisymmetric DSMC code in essence. Nevertheless, it can be relieved to greater extent by taking the advantage of the symmetric conditions and efficient parallel processing, which will be shown clearly later. Second, maintaining both the axisymmetric and three-dimensional DSMC codes can be very time-consuming and tedious. Especially, we are interested in applying this 3D code to compute multiple jet interaction in the near future. The DSMC method and the parallel DSMC code (PDSC) [13] used in the current study are described as follows in turn.

The DSMC Method. The direct simulation Monte Carlo method (DSMC) [11] is a particle method for the simulation of gas flows. The gas is modeled at the microscopic level using simulated particles which each represents a large number of physical molecules or atoms. The physics of the gas are modeled through the motion of particles and collisions between them. Mass, momentum and energy transports are considered at the particle level. The method is statistical in essence. Physical events such as collisions are handled probabilistically using largely phenomenological models, which are designed to reproduce real fluid behavior when examined at the macroscopic level. General procedures of the DSMC method consist of four major steps: moving, indexing, collision and sampling. In the current study, we use VHS molecular model [11] to reproduce real fluid behavior as well as no time counter (NTC) [11] for the collision mechanics. Since monatomic gas (argon) is simulated, no energy-exchange model is required. Details of the procedures and the consequences of the computational approximations regarding DSMC can be found in Bird [11].

The Parallel DSMC Method. In the present study, we have utilized the previous developed ***P***arallel three-dimensional ***DS***MC ***C***ode (PDSC) [13], which features unstructured adaptive mesh

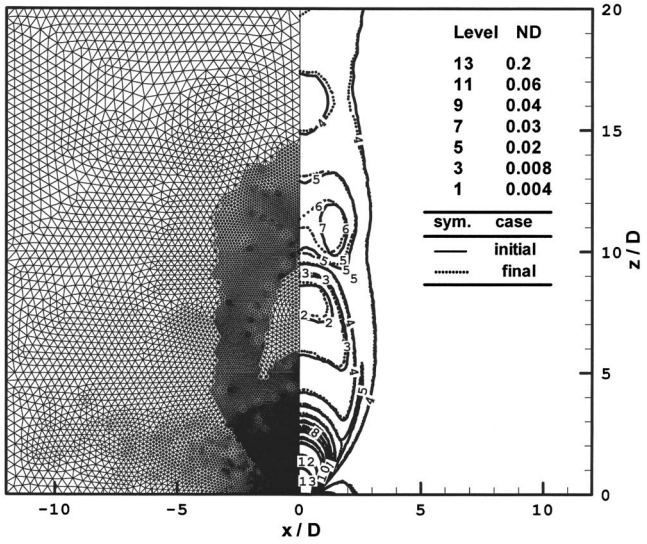

Fig. 3 Surface mesh and its isodensity distribution on a 1/16-domain of a single jet (Kn=0.001, PR=150) (initial: 149, 168 cells; level-2: 1,109,411 cells)

refinement [14,17], parallel implementation on memory-distributed machines using dynamical domain decomposition [15,16], variable time-step method [13,17], and boundary-pressure iterative scheme [19]. Details of all features of the PDSC can be found in these references and will be only briefly described here for completeness, considering the specific application in the current study.

Overall computational procedures of the PDSC can be summarized schematically in Fig. 2. The parallel DSMC method is implemented on an unstructured tetrahedral mesh using the particle ray-tracing technique [17,18], which takes the advantage of the cell connectivity information. Variable time-step approach is used by enforcing mass, momentum and energy conservations when simulation particles cross the interface between cells [13,17]. Mean velocities and temperatures at the outflow boundaries can be obtained by iteratively enforcing the specified pressure boundary conditions [19]. During the simulation, the mesh *h-refinement* technique (adding local grid points) with cell-quality control is used to repeatedly improve the cell distribution according to the solution, based on some adaptation criteria (for example, "density" in the current study) [13,14]. Multilevel graph-partitioning technique [20] is used to dynamically redecompose the computational domain to balance the workload among processors [15,16]. Stop at Rise (SAR) [21] scheme is used to determine when to repartition the computational domain by defining a degradation function, which represents the average idle time per time step for each processor including the cost of repartition. Communication of particle data between processors only occurs when particle hits the inter-processor boundary, while communication of cell data only occurs when repartitioning the domain takes effect. Data for communication is sent and received as a whole to reduce the communicational time between processors.

The current parallel code, in the Single Program Multiple Data (SPMD) paradigm, is implemented on the parallel memory-distributed system, e.g., PC-cluster system (one master processor and 23 slave processors with each having 2.4 GHz AMD, 0.5 G RAM, and Giga-bit ethernet in our laboratory). This code is highly portable since the standard message-passing interface (MPI) is used to communicate information among processors. Results presented in the following are obtained using 23 processors unless otherwise specified.

Table 3 List of computing domains for Kn=0.0005 and 0.001

PR	x/D	z/D
5	3	5
10,20	3	10
50-200	6	20
250-∞	20	60

Results and Discussions

Before the detailed discussion of computational results the single orifice jet interested in the current study, we would like to mention that the parallel DSMC code [13] that we are using has been verified for a parallel twin-jet interaction at similar Knudsen number (Kn=0.00385) by comparing well with the experimental data in Ref. [13]. This nevertheless justifies our usage of the parallel DSMC code [13].

Flow Conditions and Simulation Conditions. A single jet, issuing into a chamber region at specified background pressure, is simulated in the current study. Monatomic argon gas is used as the

Table 2 Simulation conditions for Kn=0.0005

Kn=0.0005							
PR	total computing cells	total particles	averaged particles per cell	total iterations	transition iterations	sampling iterations	reference time scale
5	1,147,279	12,575,099	11	40,000	6,000	34,000	1E-10
10	1,182,070	13,512,907	11	40,000	6,000	34,000	1E-10
20	1,136,273	12,647,114	11	40,000	6,000	34,000	1E-10
50	1,254,763	18,512,998	15	40,000	6,000	34,000	1E-11
250	990,371	19,007,100	19	40,000	6,000	34,000	1E-9
500	950,590	9,871,825	10	40,000	6,000	34,000	1E-9
1000	99,7421	9,458,497	9	40,000	6,000	34,000	1E-9
2500	988,688	8,058,022	8	40,000	6,000	34,000	1E-9
5000	964,351	6,698,308	7	40,000	6,000	34,000	1E-9
∞	968,080	8,498,017	9	40,000	6,000	34,000	1E-9

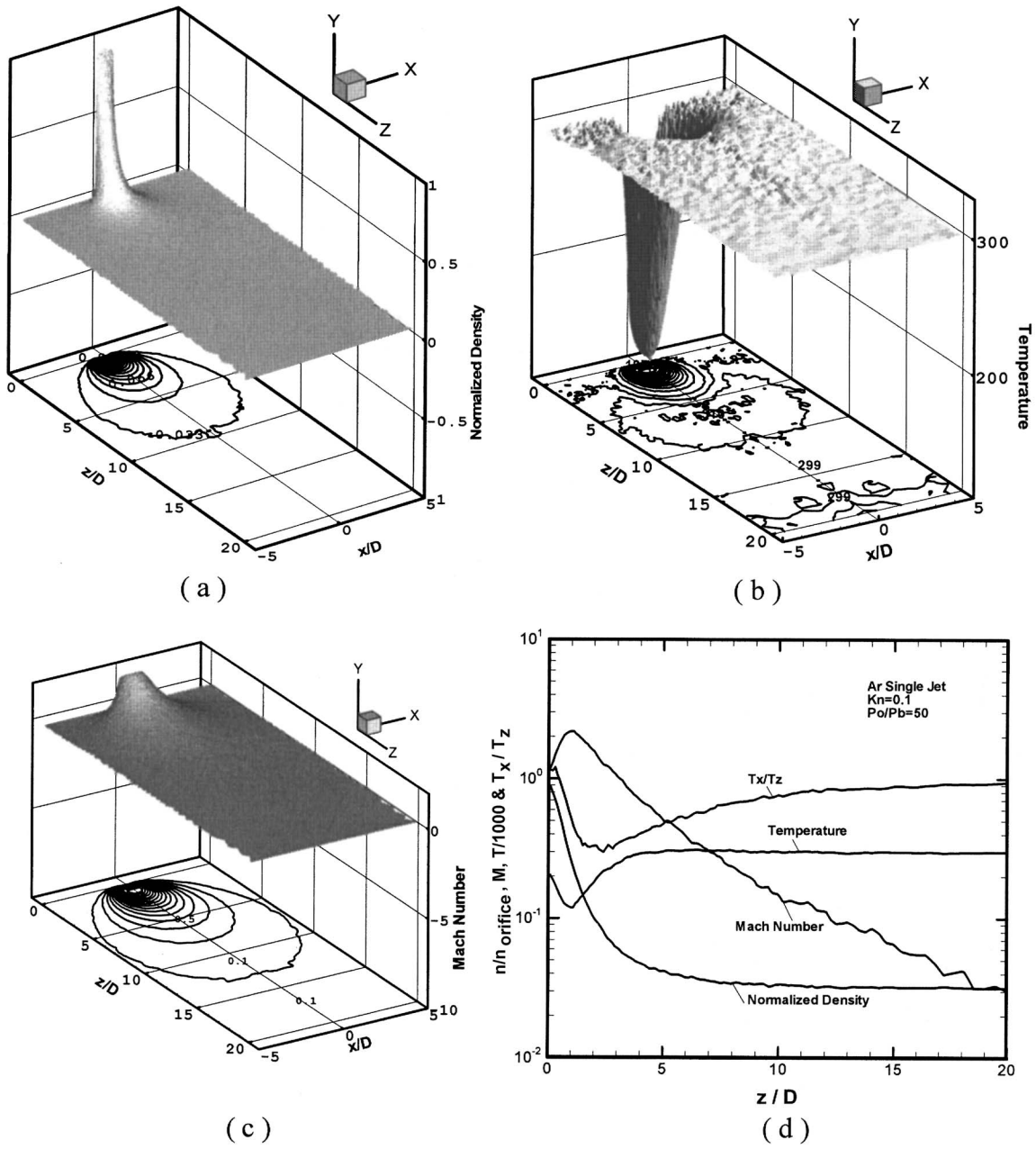

Fig. 4 Properties distribution at Kn=0.1, PR=50 of underexpanded argon jet (*y*=0 plane) (a) normalized density; (b) temperature; (c) Mach number; (d) data along centerline

working gas to preclude any complexities caused by the energy exchange among internal degrees of freedom. Orifice size used for generating the under-expanded free jet is 500 μm in diameter. Uniform sonic flow condition at the exit of the thin orifice is assumed, although viscous effects may be present in this low Reynolds-number flow regime that we are interested in. However, it is well known that for highly underexpanded free jets, the high supersonic region only weakly depends on the transonic conditions at the orifice [8]. Thus, inviscid gas dynamics (quasi-1D) is used to define the exit conditions at the orifice using the assumption. Parametric studies, varying Knudsen numbers ($\mathrm{Kn}=\lambda_{\mathrm{upstream}}/d_{\mathrm{orifice}}$) in the range of 0.0005–0.1 and stagnation-to-background pressure ratios ($\mathrm{PR}=p_0/p_b$) in the range of $5-\infty$, are considered. Corresponding upstream (stagnation) pressures and temperature are in the range of 107–21,446 Pa and 300 K, respectively. Pressure and temperature at outflow boundaries are fixed as specified background pressure and 300 K, respectively. Resulting Reynolds number defined using the conditions at the orifice exit is in the range of 7–1472, which is very low as compared with previous studies [8] that considered the macro jets in the continuum regime (upstream). Thus, the possibility of transition from laminar to turbulence is not considered in the current simulation.

We first run some typical cases (at same Knudsen number) to observe if the steady state is reached by observing if the total number of particles is approximately constant. We then decide the number of time steps (iterations) required to reach steady state conservatively by putting some safety factor, e.g., 2–3 times the number of iterations to reach approximate constant particle numbers. For convenience, we often use the same number of iterations (time steps) for representing the transient periods at different pressure ratios for the same Knudsen number. We believe this should be safe for all the cases considered that steady state has been reached for sampling.

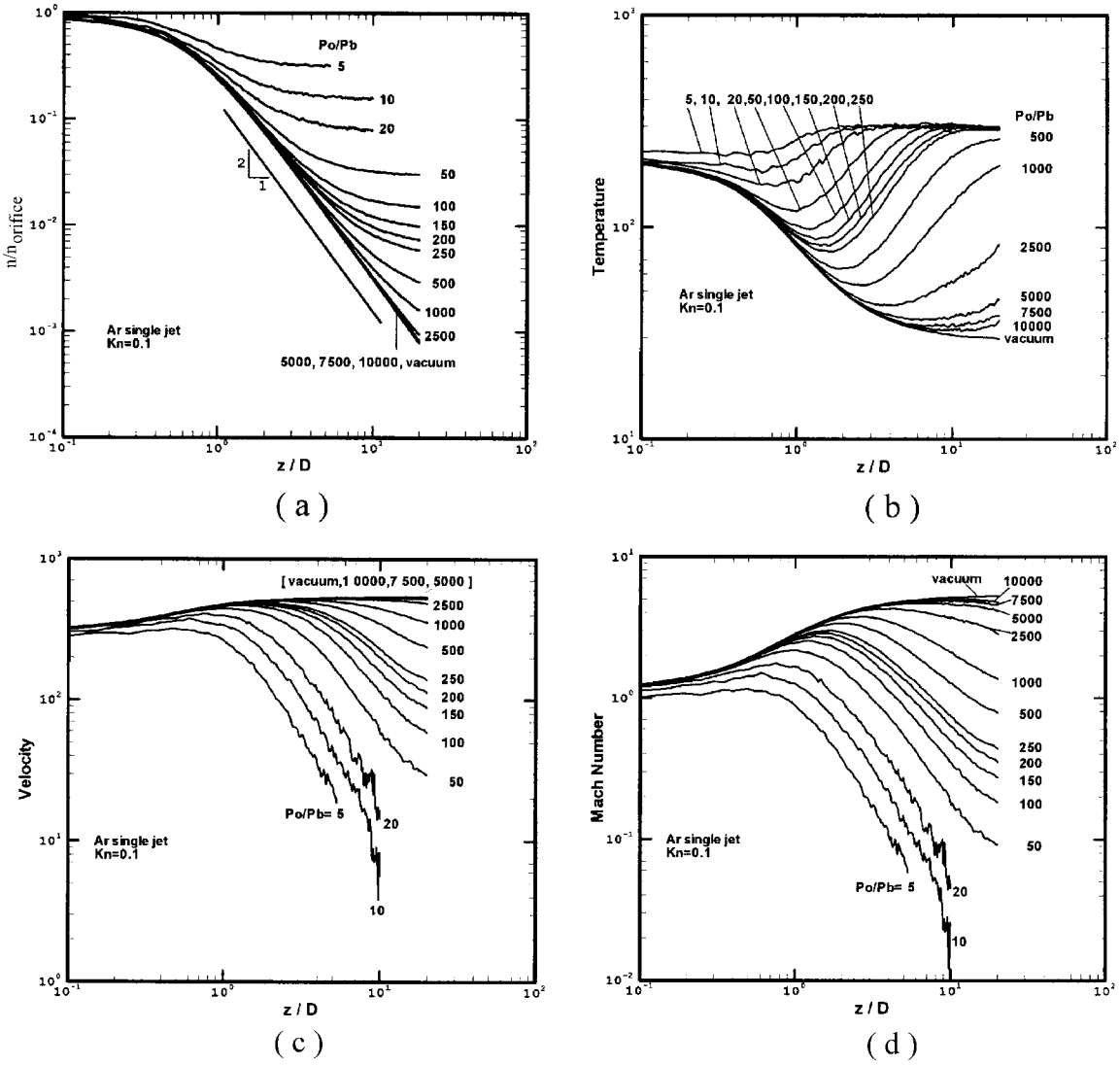

Fig. 5 Centerline normalized density, temperature, velocity, and Mach number distributions at different pressure ratios (Kn=0.1)

Typical refined unstructured mesh at the final level (level-2) along with the distribution of isodensity is shown in Fig. 3 (Kn =0.001, PR=150). It clearly shows that the mesh is automatically refined near the high-density regions. In this specific case, the number of cells increases from 149,168 cells initially to 1,109,411 cells at level-2 mesh refinement. Total number of particles in this case is approximately 10 millions. Resulting number of particles per cell is on the order of 10, except in the region near the orifice exit (~2). In general, the number of simulated particles is in the range of 0.1 million (Kn=0.1, PR=∞) to 19 million (Kn =0.0005, PR=250), while the number of time steps (iterations) for sampling is about 34,000 for each case. Detailed simulation conditions for the most challenging case (Kn=0.0005) are listed in Table 2. The number of particles used in this Kn=0.0005 case is on the order of 10 million. The reference time step (1E-10) represents the smallest time step used in the computational domain due to the high-density region, thus, very small cell, near the exit of the orifice. The mean velocities at the outer boundaries are obtained during the simulation by iteratively enforcing the specified pressure that uses the concept of flux conservation through the boundaries, which is similar to that in [19]. Temperatures at the outflow boundaries are set as 300 K. Since the flow is axisymmetric, only 1/16 of the physical domain is considered, where the specular boundary condition is imposed on each of the sliced plane. Results using this sliced domain are found to be in excellent agreement with those using full domain. In general, the larger the pressure ratio is, the larger the computational domain is required. Detailed sizes of computational domain for Kn=0.0005 and Kn=0.001 at different pressure ratios are listed in Table 3 for reference. In the following, we will discuss the effects of pressure ratio and rarefaction on the general flow structures, when presenting the simulation results.

Effects of Pressure Ratio

Kn=0.1. Before looking into the effects of pressure ratio, we first present the typical distributions of the normalized density, temperature and Mach number at the sliced plane ($y=0$) that are illustrated in Figs. 4(*a*)–4(*c*), respectively, for Kn=0.1 and PR =50. Centerline distribution of the above parameters (up to z/D =20) along with the ratio of thermal nonequilibrium (T_x/T_z) is also shown together in Fig. 4(*d*) for the convenience of comparison. Results at this flow condition show that the density monotonically decreases very rapidly outward in all directions from the orifice exit due to the lower pressure in the background (~0.03 of the value at the orifice exit). Temperature decreases due to rapid expansion near the orifice region, reaching as low as 12 K at

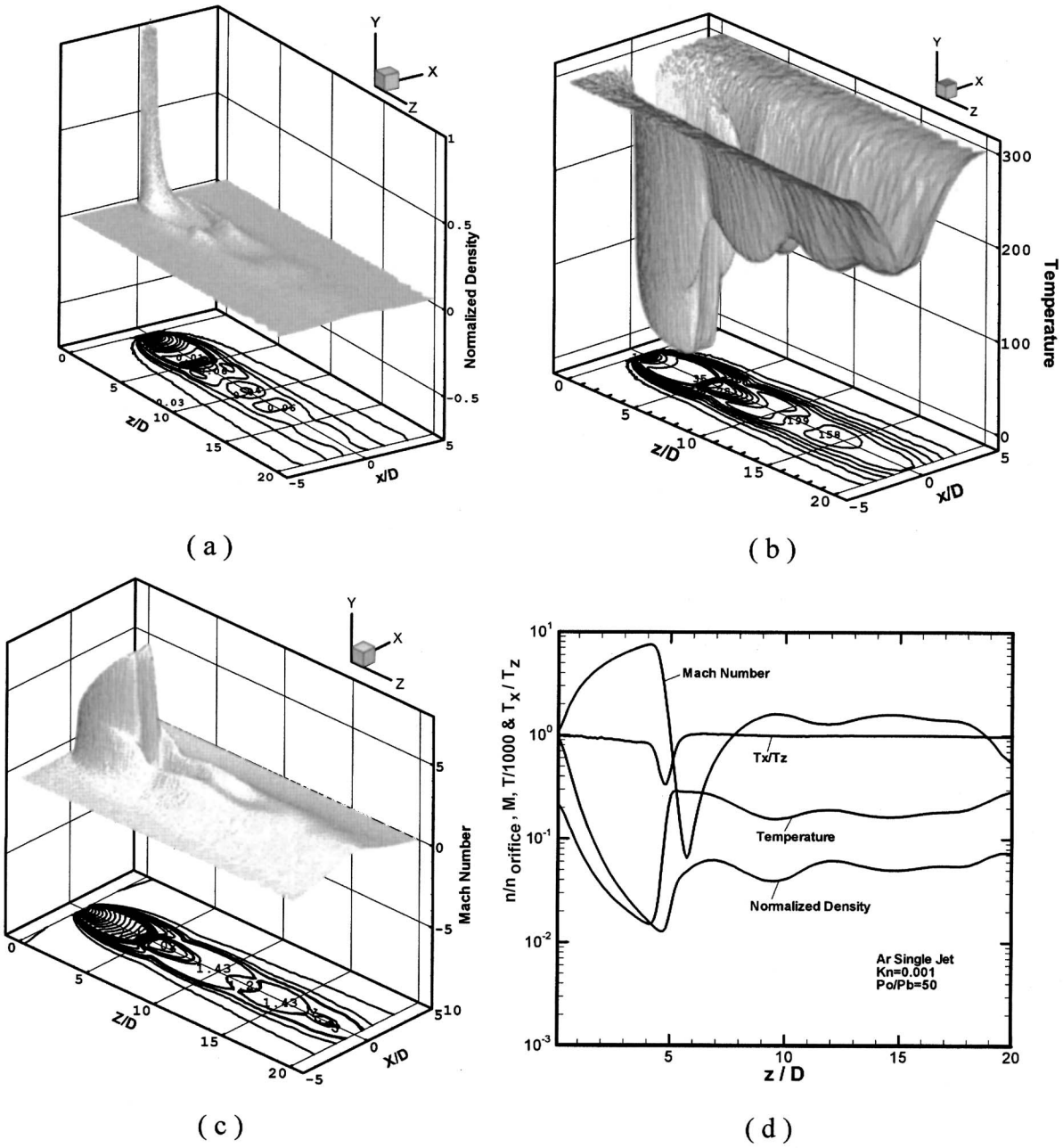

Fig. 6 Properties distribution at Kn=0.001, PR=50 of argon jet (*y*=0 plane) (a) normalized density; (b) temperature; (c) Mach number; (d) data along centerline

$z/D \approx 1$, and then increase to the specified background temperature, 300 K, at $z/D \approx 5$. Mach number increases up to 2.2 at about the same location ($z/D \approx 1$) and then decrease down to 0.1 at $z/D \approx 20$. The ratio of thermal nonequilibrium deviates from unity in the near orifice region with a value of 0.3 at $z/D=2.5$, which shows a strong thermal nonequilibrium exists in this flow due to rapid expansion.

Figures 5(*a*)–5(*d*) show the effects of pressure ratio to the centerline distributions of normalized density, temperature, velocity, and Mach number, respectively, at Kn=0.1, which is in the transitional regime. Pressure ratio in the current study is in the range of $5-\infty$, which ensures the choke condition at the orifice exit. In general, density [Fig. 5(*a*)] decreases monotonically along the centerline to the background value as expected. For example, the density at $x/D=20$ decreases down to 0.1% of the value at the orifice exit for PR $\geqslant$ 5,000. In addition, normalized density data along the centerline can be fitted as $n/n_{\text{orifice}}=0.24(z/D)^{-2}$ for PR $\geqslant$ 5,000 in the current simulation range ($z/D \leqslant 20$), which is nearly the same as that obtained experimentally [8]. Note that the axial distance, where the −2-slope decay holds, begins at $x/D \approx 1$. In Fig. 5(*b*), temperature generally decreases first along the centerline due to expansion and then increases to the background temperature. Minimum temperature is in the range of 30–220 K for PR in the range of $\infty-5$. Generally, the axial distance, where the minimum temperature reaches, increases with increasing pressure ratio. In Fig. 5(*c*), centerline velocity generally increases at first and then decreases further downstream. Faster decrease in the downstream is found for lower pressure ratios, which is retarded by the existence of higher-density background gas. For higher-pressure ratios, the centerline velocity stays at nearly constant value all the way downstream (PR $\geqslant$ 5,000). In Fig. 5(*d*), Mach

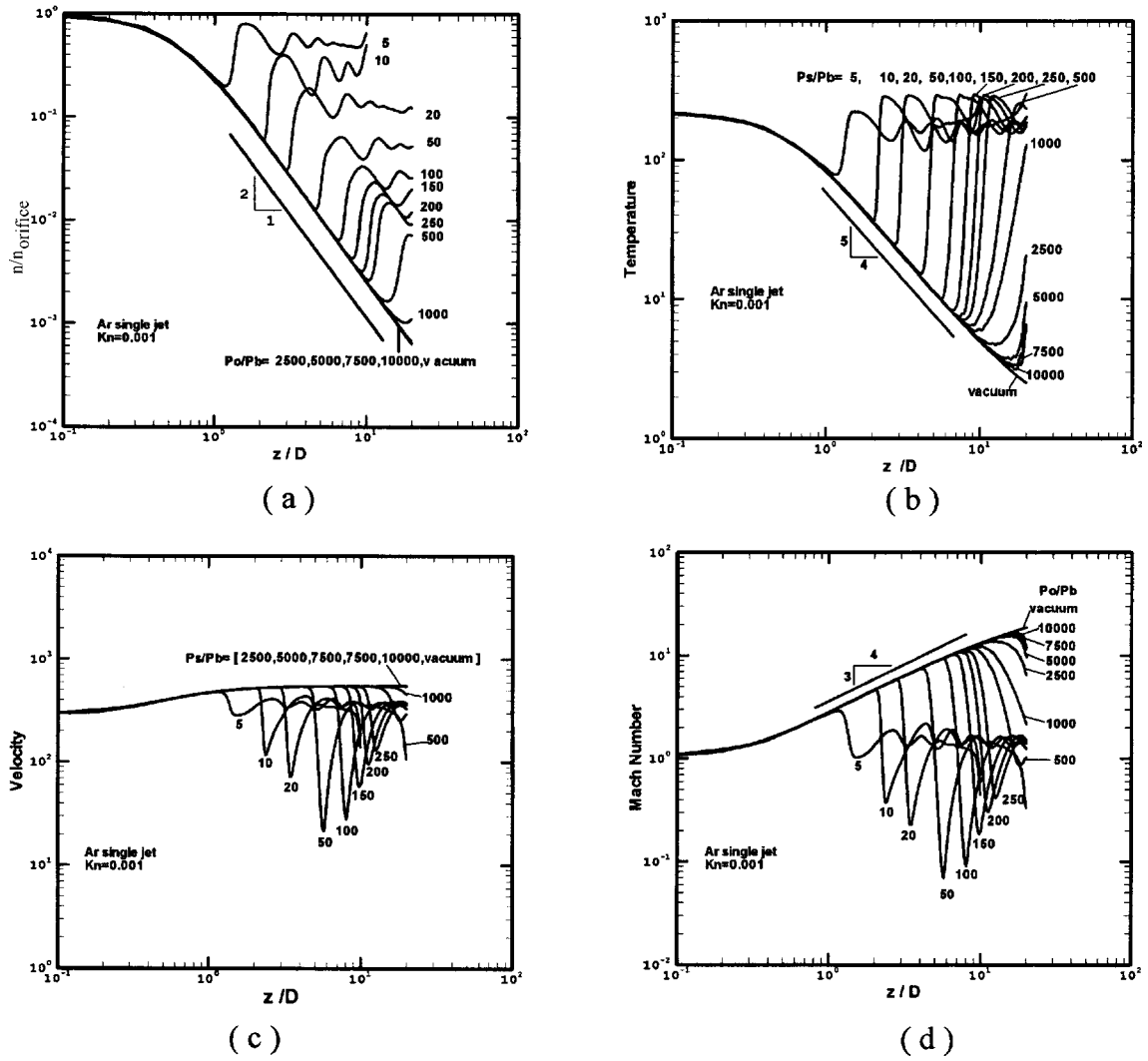

Fig. 7 Centerline normalized density, temperature, velocity and Mach number distributions at different pressure ratios (Kn=0.001)

number along the centerline generally increases to supersonic speed at first due to expansion and then decreases to low subsonic speed at far downstream for lower pressure ratios. It can be found that the change of Mach number with respect to the downstream location is generally larger than the centerline velocity because the speed of sound also varies depending on translational temperature. Note that maximum Mach number is in the range of 1.2–5 for PR in the range of 5–∞. Axial distance, where the maximum Mach number reaches, also increases with pressure ratio. In general, the above results show that at this Kn=0.1 the larger the pressure ratio, the more the gas expansion from the orifice into the background.

Kn=0.001. Typical property distributions (normalized density, temperature and Mach number) at the sliced plane ($y=0$) along with the centerline property distributions in the near-continuum regime (Kn=0.001) are illustrated in Figs. 6(*a*)–6(*d*), respectively. Unlike the case in the transitional regime (Fig. 4), a distinct cell-like flow structure, including shock and expansion waves, begins to appear. Results show that the density decreases very rapidly in the streamwise direction from the orifice exit and is approximately 1%, of the value at the orifice exit, at $z/D \approx 5$. It then increases up to 6%, of the value at the orifice exit, at $z/D \approx 7$ due to the formation of a thickened Mach disk. After this, the density decreases and increases again repeatedly, although the amplitude of alternation becomes smaller. In addition, a barrel shock circulating the core region that prevents the penetration of background gas into the core region. Due to rapid gas expansion, temperature decreases down to 15 K at location before the thickened Mach disk, and then increases to 300 K after the thickened Mach disk. It then follows the similar trend as the density variations afterwords. As for Mach number, it increases up to hypersonic speed (7.3) before the thickened Mach disk ($z/D \approx 4.5$), and drops to very low subsonic speed (0.07) right after the thickened Mach disk ($z/D \approx 5.5$). In Fig. 6(*d*), it also shows the ratio of thermal nonequilibrium (T_x/T_z) along the centerline. Results show that strong thermal nonequilibrium exists near the Mach disk location with a value of 0.3 due to strong compression of gas molecules across the shock, whose data can only be simulated using particle method as in the current study. In addition, strong thermal nonequilibrium also appears near the lips of the orifice due to rapid gas expansion, although it is not shown in the current report. In general, the cell-like flow structure begins to appear explicitly with several thickened shock structure at this near-continuum regime (Kn=0.001). The structure will be more observable as rarefaction is reduced. Comparison of the simulated Mach-disk position and diameter with experimental data in the near-continuum regime will be discussed later.

Figures 7(*a*)–7(*d*) illustrate the effects of pressure ratio (PR

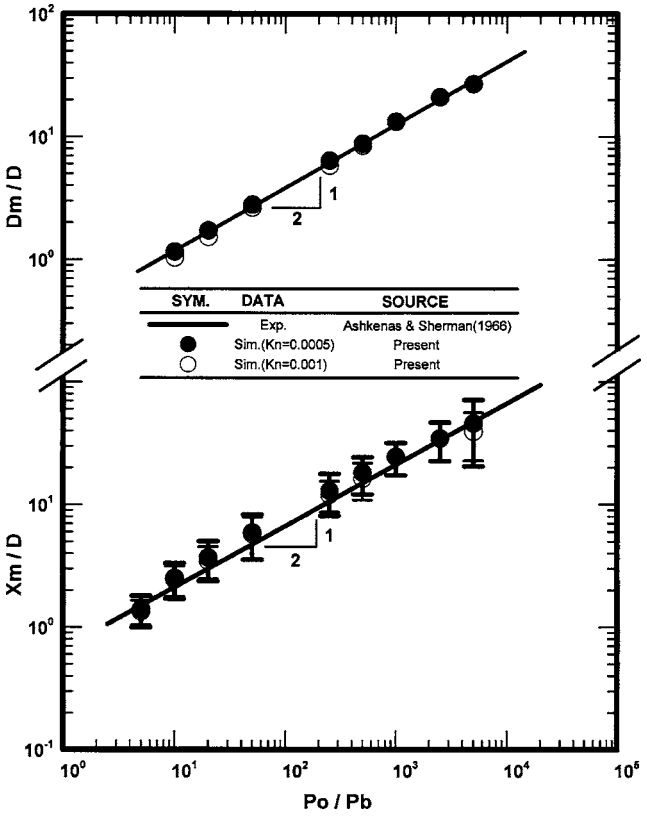

Fig. 8 Position and diameter of Mach disk as a function of pressure ratio for a single argon underexpanded jet

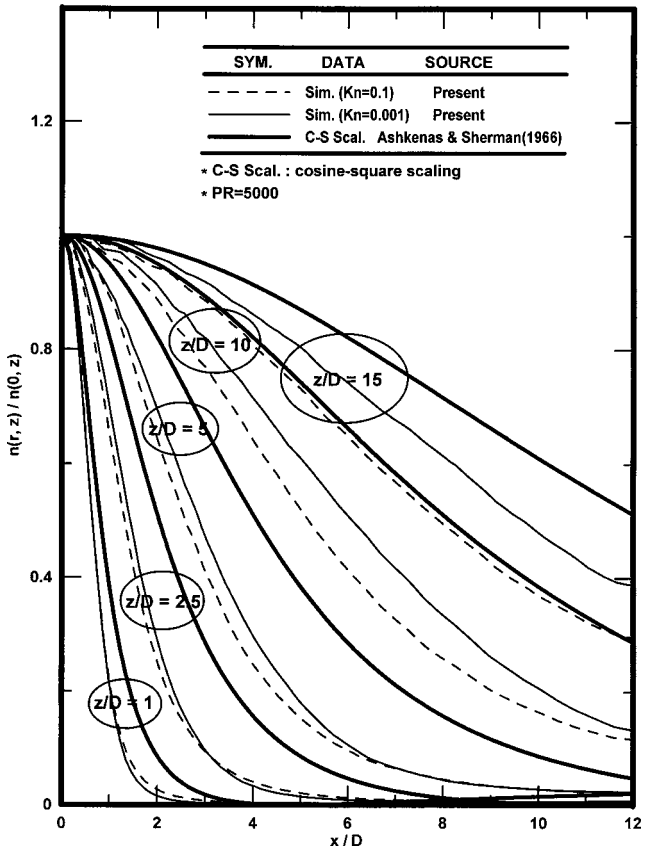

Fig. 9 Comparison of the radial profiles of normalized density at different positions at (PR=5000)

=5–∞) to the centerline distributions of normalized density, temperature, velocity and Mach number, respectively, at Kn=0.001, which is in the near-continuum regime. Again the density decreases rapidly along the centerline before the appearance of the Mach disk and scales as $n/n_{\text{orifice}}=0.24(z/D)^{-2}$ starting at $z/d \approx 1$, which is nearly the same as the case in Kn=0.1. However, Mach disk either disappears or becomes unrecognizable when PR $\geqslant$ 2500 probably due to the very rarefied flow (low background pressure) at the very downstream. We have extended the region of simulation up to $z/D=120$ for larger pressure ratios and have found the Mach disk is not clear at all. This more or less can be explained or correlated by using a rarefaction parameter, which will be shown shortly. Increase of the density across the Mach disk is generally the same in the range of 6–7 times for pressure ratios in the range of 10–500 [Fig. 7(*a*)], except the case of PR =5, in which it increases only approximately 2.5 times. For the smaller pressure ratios (PR=5,10,20) the repeated cell-like structure is comparatively clear in Figs. 7(*a*)–7(*d*), while it is smeared for the case of larger pressure ratio, which may be due to the limit of simulation domain or very lower density level at the far downstream. In addition, one distinct feature in this near-continuum regime (Kn=0.001,0.0005) is the temperature and Mach number scale approximately as $(z/D)^{-5/4}$ [Fig. 7(*b*)] and $(z/D)^{3/4}$ [Fig. 7(*d*)], respectively, before the Mach disk, which is not seen in the transitional regime (Kn=0.1,0.01). Detailed reasons resulting in these special scalings require further study. It may be due to the formation of the shock structure consisting of barrel shock and Mach disk, which prevents the penetration of background gas into the expansion region near the orifice exit. In Fig. 7(*c*), centerline velocity generally increases at first, then decreases rapidly across the Mach disk and finally increase and decrease alternatively further downstream, depending on the pressure ratios. The maximum velocity in this alternative oscillation is generally smaller than the velocity before rapid decrease. It is also found that the maximum rapid decrease of centerline velocity occurs at PR=50 in the current study. Centerline Mach number changes much more pronouncedly due to the change of centerline temperature, which is similar to the case of Kn=0.1 as presented in Fig. 5.

Figure 8 presents the comparison of the Mach-disk position and diameter, respectively, between the simulation in the near-continuum regime (Kn=0.001,0.0005) and the experimental correlation in the continuum limit [8,9,22]. Correlations of Mach-disk position and diameter were determined experimentally as $X_M/D=0.67(P_o/P_b)^{1/2}$ [8] and $D_M/D=0.24(P_o/P_b)^{1/2}$ [9], respectively. Due to the thickened Mach disk in the near-continuum regime, there are uncertainties in determining the accurate position, and especially the diameter, of the Mach disk. Nevertheless, we have defined the position of the Mach disk by locating where the minimum value of the density is. Uncertainty bars are included for the Mach-disk position in the figure for reference, while it is not shown for the Mach-disk diameter due to the difficulty of deciding the uncertainties. Nevertheless, we have measure the radial position at the Mach disk, where the density is maxima, as the Mach-disk position. Results show that the simulated data at Kn=0.001 and 0.0005 in the near-continuum limit are in reasonable agreement with the experimental correlation of Ashkenas and Sherman [8] in the continuum limit, considering the uncertainties as mentioned in the above. Similar agreement can also be found for the Mach-disk diameter as a function of the pressure ratio in Fig. 8.

Figure 9 shows the comparison of the radial profiles of normalized density for Kn=0.1 and Kn=0.001 at different positions (PR=5,000) in the inviscid core, with a simple density cosine-square scaling proposed by Ashkennas and Shermann [8] based on their experimental data. Results show the accuracy of the simple density scaling deteriorates with increasing axial position, although the simple scaling law always predicts a wider radial density profile in general. Reason for the discrepancy requires further

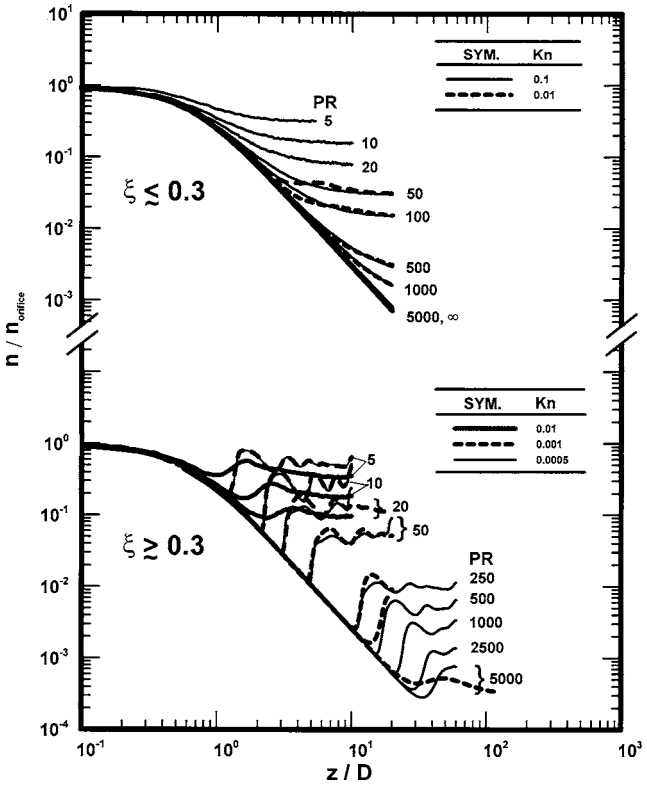

Fig. 10 Flow condition of different ξ

investigation. Flow at Kn=0.001 expands more quickly than that at Kn=0.1 at the same pressure ratio. Similar trends can be found for larger pressure ratios before the Mach disk if it exists.

In Muntz et al. [10], they proposed a rarefaction parameter $\xi = D(p_0 p_b)^{1/2}/T_0$ describing the combined effects of rarefaction and pressure ratio. It is interesting to know the correspondence between this parameter and the cases simulated cases simulated in the current study. Table 1 shows the resulting values for all the simulated cases. Equivalently, previous results can be illustrated using this rarefaction parameter and are shown in Fig. 10. Results clearly show that the cell-like structure (or the Mach disk) begins to appear as $\xi \gtrsim 0.3$ and larger. For $\xi \lesssim 0.3$ the flow can be categorized as the scattering regime as described in [10].

Conclusions

A parallel three-dimensional DSMC method using unstructured solution-based adaptive tetrahedral mesh is used to study flow structure of a single underexpanded argon free jet from transitional to near-continuum regime. In the transitional regime, gas flowing out of the orifice continues to expand to background condition if the pressure ratio is large. Otherwise, it expands first and then compress to the ambient value. In the near-continuum regime, a distinct cell-like flow structure begins to form similar to those obtained in previous experimental study in the continuum regime. Results of simulated Mach-disk position and diameter in the near-continuum regime are in reasonable agreement with previous experimental correlation in the continuum regime. In addition, highly thermal nonequilibrium both occurs across the Mach disk in the near-continuum regime and near the orifice for rapid gas expansion in the transitional regime. One last comment the authors would like to make is the statistical noise near the orifice exits, especially for the cases of Kn=0.0005 and Kn=0.001, which is the near-continuum regime. Thus, the fidelity of the data very near the orifice exit may be in doubt in the current study. From the computational viewpoint, N-S equations should be used in this high-density region instead of the DSMC method, which necessitates the hybrid of the DSMC method and the N-S solver. Preliminary progress toward this goal will be reported elsewhere [23].

Acknowledgments

The authors would like to express their sincere thanks to the computing resources provided by the National Center for High-Speed Computing of National Science Council of Taiwan. In addition, financial support by National Science Council of TAIWAN (NSC91-2212-E-009-045) is also highly appreciated.

References

[1] Phalnikar, K. A., Alvi, F. S., and Shih, C., 2001, "Behavior of Free and Impinging Supersonic Microjets," AIAA Paper No. 2001-3047.
[2] Scroggs, S. D., and Settles, G. S., 1996, "An Experimental Study of Supersonic Microjets," Exp. Fluids, **21**, pp. 401–409.
[3] Adamson, T. C., Jr., 1964, "The Structure of the Rocket Exhaust Plume Without Reaction at Various Altitudes," *Supersonic Flow, Chemical Processes and Radiation Transfer*, Pergamon, New York.
[4] Young, W. S., 1975, "Derivation of the Free-Jet Mach-Disk Location Using the Entropy-Balance Principle," Phys. Fluids, **18**, pp. 1421–1425.
[5] Eastman, D. W., and Radtket, L. P., 1963, "Location of the Normal Shock Wave in the Exhaust Plume of a Jet," AIAA J., **1**, pp. 918–919.
[6] Owen, P. L., and Thornhill, M. A., 1948, "The Flow in an Axially-Symmetric Supersonic Supersonic Jet From a Nearly Sonic Orifice Into a Vacuum," Aeronautical Research Council, ARC Technical Report No. RM-2616.
[7] Love, E. S., Grigsby, C. E., Lee, L. P., and Woodling, M. S., 1959, "Experimental and Theoretical Studies of Axisymmetric Free Jets," NSNA TR R-6.
[8] Ashkenas, H., and Sherman, F. S., 1966, "The Structure and Utilization of Supersonic Free Jets in Low Density Wind Tunnels," *Rarefied Gas Dynamics, Fourth Symposium, Vol. II*, Academic, New York, pp. 84–105.
[9] Crist, S., Sherman, P. M., and Glass, D. R., 1966, "Study of the Highly Under-Expanded Sonic Jet," AIAA J., **4**, pp. 68–71.
[10] Muntz, E. P., Hamel, B. B., and Maguire, B. L., 1970, "Some Characteristics of Exhaust Plume Rarefaction," AIAA J., **8**, pp. 1651–1658.
[11] Bird, G. A., 1994, *Molecular Gas Dynamics and the Direct Simulation of Gas Flows*, Oxford University Press, New York.
[12] Teshima, K., and Usami, M., 1997, "An Experimental Study and DSMC Simulation of Rarefied Supersonic Jets," *20th International Symposium on Rarefied Gas Dynamics*, C. Shen, ed., Bejing University Press, Beijing, pp. 567–572.
[13] Wu, J.-S., Tseng, K.-C., and Wu, F.-Y., 2004, "Parallel Three-Dimensional DSMC Method Using Mesh Refinement and Variable Time-Step Scheme," Comput. Phys. Commun., **162**(3), pp. 166–187.
[14] Wu, J.-S., Tseng, K.-C., and Kuo, C.-H., 2002, "The Direct Simulation Monte Carlo Method Using Unstructured Adaptive Mesh and Its Application," Int. J. Numer. Methods Fluids, **38**(4), pp. 351–375.
[15] Wu, J.-S., and Tseng, K.-C., 2003, "Concurrent DSMC Method Using Dynamic Domain Decomposition," *23rd International Symposium on Rarefied Gas Dynamics*, A. Ketsdever and E. Muntz, eds., AIP Conf. Proc. **663**, pp. 406–413.
[16] Wu, J.-S. and Tseng, K.-C., 2005, "Parallel DSMC Method Using Dynamic Domain Decomposition," Int. J. Numer. Methods Eng., **63**, pp. 37–76.
[17] Kannenberg, K. C., 1998, "Computational Method for the Direct Simulation Monte Carlo Technique With Application to Plume Impingement," Ph.D. thesis, Cornell University, Ithaca.
[18] Wu, J.-S., and Lian, Y.-Y., 2003, "Parallel Three-Dimensional Direct Simulation Monte Carlo Method and Its Applications," Comput. Fluids, **32**(8), pp. 1133–1160.
[19] Wu, J.-S., Lee, Fred, and Wong, S.-C., 2001, "Pressure Boundary Treatment In Micromechanical Devices Using The Direct Simulation Monte Carlo Method," JSME Int. J., Ser. B, **44**(3), pp. 439–450.
[20] Walshaw, C., Cross, M., and Everett, M., 1997, "Parallel Dynamic Graph Partitioning for Adaptive Unstructured Meshes," J. Parallel Distrib. Comput., **47**, pp. 102–108.
[21] Nicol, D. M., and Saltz, J. H., 1988, "Dynamic Remapping of Parallel Computations With Varying Resource Demands," IEEE Trans. Comput., **39**(9), pp. 1073–1087.
[22] Mirels, H., and Mullen, J. F., 1963, "Expansion of Gas Clouds and Hypersonic Jets Bounded by a Vacuum," AIAA J., **1**, pp. 596–602.
[23] Wu, J.-S., Lian, Y.-Y., Gary Cheng, and Roy Koomullil, 2005, "Development of a Parallel Hybrid Method for the DSMC and NS Solver," AIAA 43rd Aerospace Sciences Meeting and Exhibit, Reno Hilton, Jan, pp. 10–13.

A Priori Assessments of Numerical Uncertainty in Large-Eddy Simulations

Stephen A. Jordan
e-mail: jordansa@npt.nuwc.navy.mil
Naval Undersea Warfare Center,
Newport, RI 02841

Current suggestions for estimating the numerical uncertainty in solutions by the Large-Eddy Simulation (LES) methodology require either a posteriori input or reflect global assessments. In most practical applications, this approach is rather costly for the user and especially time consuming due to the CPU effort needed to reach the statistical steady state. Herein, we demonstrate two alternate a priori graphical exercises. An evaluation of the numerical uncertainty uses the turbulent quantities given by the area under the wave number spectra profiles. These profiles are easily constructed along any grid line in the flow domain prior to the collection of the turbulent statistics. One exercise involves a completion of the spectrum profile beyond the cutoff wave number to the inverse of Kolmorgorov's length scale by a model of isotropic turbulence. The other extends Richardson Extrapolation acting on multiple solutions. Sample test cases of both LES solutions and direct numerical simulations as well as published experimental data show excellent agreement between the integrated matched spectra and the respective turbulent statistics. Thus, the resultant uncertainties themselves provide a useful measure of accumulated statistical error in the resolved turbulent properties.
[DOI: 10.1115/1.2060735]

Introduction

Unquestionably, the Large-Eddy Simulation (LES) methodology has attained a comfortable level within the realm of computational fluid dynamics (CFD). Progressive journals, conferences, symposia, meetings, and the like commonly archive works dedicated to expanding our essential understanding of the methodology ranging from its rudimentary improvements to noteworthy applications. Sometimes lost in the practical computations is the most fundamental premise of the methodology, which is the full spatial and temporal resolution of the local turbulent energy scales, regardless of the complexity of the application. Without access to verifiable experimental data (for example), one can only anticipate acceptable resolution of the local turbulent quantities if this critical ingredient is satisfied throughout the flow domain of interest. Given today's most powerful supercomputers, estimating the local numerical uncertainty of the statistical turbulence in an *a posteriori* manner will claim a very high CPU requirement. Conversely, methods exist for assessing the instantaneous error by comparing volume-averaged (global) quantities, but their values can be erroneously weighted by poor resolution outside the local region of interest. Thus, not surprisingly, a common thread missing from practical applications is a systematic approach that specifically quantifies the local resolution uncertainty *a priori*.

Collectively, present treatments of error behavior provide solid advice toward improving LES solutions. One of the earliest analyses by Ghosal [1] gives a rigorous assessment of the total discretization error in terms of the finite difference stencil, aliasing from the nonlinear terms, and subgrid-scale (SGS) modeling. Using the von Kármán form of the energy spectrum, Ghosal proved masking of important modeling contributions by the discretization error when the filter width is equal to the local grid spacing, regardless of the stencil order. This observation was recently detected by Meyers et al. [2], who compared successive LES datasets of decaying homogeneous isotropic (DHI) turbulence. Moreover, Ghosal's work paved the perception for gaining grid independence where the ratio of grid spacing to filter width approaches zero. Under such an exercise, one should be aware that additional errors arise from the Leonard-type term, as noted by Rogallo and Moin [3].

One of the most revealing decompositions of solution error under grid refinement comes from the recent database analysis of DHI turbulence [2]. The total error in this case comprised only discretization and modeling errors, as given by the volume-averaged kinetic energy. Inasmuch as these separate errors in the LES computation were not necessarily the same sign, minimizing the discretization error actually degraded the total global error. This fact stems most likely from the large disparity between the model and resolved physics as governed by the filter width, as well as their complex and distinct interaction near cutoff under either *a priori* or *a posteriori* testing. In that analysis, the relative error was assessed against a parameter defined by the ratio of turbulent dissipation to the total dissipation (turbulent plus molecular). However, the Leonard-type term is also a major contributor to the total loss rate as demonstrated by Leonard [4] for DHI turbulence and Love and Leslie [5] using the grid-scale dissipation rates of Burgers' equation.

Apart from introducing a commutation error, explicit filtering of the nonlinear elements can attenuate the finite difference and aliasing errors. Through LES solutions of DHI turbulence, Lund [6] compared results of turbulent kinetic energy using the cutoff, Gaussian, and top-hat filters and clearly illustrated the independence of the filter kernel on the resolved field, provided the correct filter width ratio is used when test filtering. But subsequent solutions of the turbulent channel flow [7] revealed conflicting errors of the turbulent intensities and velocity fluctuations using a recommended minimum filter width ratio [8,9].

An analogous thrust toward answering the uncertainty issue is captured in the Grid Convergence Index (GCI) as conceived by Roache [10]. His proposed approach embodies the earlier efforts by Metha [11] and Celik et al. [12] for quantifying the numerical uncertainty in CFD predictions. The GCI is founded on the theory of a generalized Richardson Extrapolation, where the uncertainty of the CFD predictions is estimated using grid refinement. Holding the CPU expense to a minimum, a fourth-order accurate esti-

Contributed by the Fluids Engineering Division for publication in the JOURNAL OF FLUIDS ENGINEERING. Manuscript received by the Fluids Engineering Division December 15, 2004. Final manuscript received: April 26, 2005. Associate Editor: Ugo Piomelli.

mate of this error can be evaluated using two solutions; a second-order accurate method (central differences only) and uniform grids that share equivalent points in space. When deviating from these ideal conditions, certain restrictions are necessary to ensure that the accuracy of the GCI expression is higher than the CFD solutions themselves.

Although one can directly extend Richardson Extrapolation in a similar fashion to estimate the cumulative error of traditional LES solutions, it would be difficult to justify its practical significance. Each expression differs fundamentally. While sequentially finer grid solutions for the former relationship should converge on an asymptotic path toward the exact solution ($GCI \rightarrow 0$), an equivalent exercise of traditional LES solutions ultimately redefines the methodology altogether. In particular, the solutions converged toward direct numerical simulations rather than grid-independent LES. Besides being nonconservative, a third solution would be necessary in the index formula (or some equivalent expression) to fulfill the additional nonlinear terms. These terms will arise in the uncertainty relationship due to the various high-order stencils used to approximate the derivatives in the resolved-field equations. Moreover, the uncertainty estimate would be evaluated *a posteriori* (statistical steady-state solutions), which is prohibitively expensive and especially time consuming in both user labor and CPU usage. Most importantly, we should recognize that the LES computation provides useful instantaneous information that is simply unavailable in the CFD solutions targeted by the former uncertainty index. These instantaneous results should always give us the energy range of the resolved turbulent scales throughout the flow domain of interest whether we recomputed the original coarse grid channel flow of Deardolf [13] or tackle a fine-grid complex topology. For the LES methodology, we should therefore expect an alternate *a priori* approach for estimating the cumulative numerical uncertainty.

In the present work we propose a simple graphical exercise for estimating the numerical uncertainty of the LES solutions. Unlike the error analyses discussed above, this alternate technique specifically examines the uncertainty in the turbulent properties themselves rather than the individual errors of the solution methodology. The exercise actually reflects the resultant accumulation of all errors as given largely by the chosen LES formulation, solution scheme, and griddling. Conceivably, one could exploit this graphical exercise to examine a local return on global error reduction. In some respects, certain subtleties of the exercise are analogous to evaluating the GCI expression. The estimate actually touches on the earliest thoughts for designing a solution template of the turbulent flow domain that will assure full resolution of the local energy scales. The exercise is completed *a priori*, meaning time accurate solutions beyond any transient behavior but before collecting results towards a statistical steady state. This latter facet of the exercise is most attractive in view of the time saved by the user, as well as the computational effort compared to *a posteriori* exercise. The estimate exploits an empirical model for the unresolved scales to complete the wave number spectrum. Beneath the total spectrum lies the root mean square (rms) of a specific scaled turbulent quantity with a second respective quantity evaluated only up thorough wave number cutoff. Utilizing these quantities, one can easily estimate the resultant numerical uncertainty.

Herein, we will exercise two forms of the uncertainty estimate with one holding a similar expression as the GCI that does not necessarily need a spectrum model for its evaluation. The choice of the SGS model certainly affects the uncertainty estimates as well as the resolved wave number spectrum near cutoff, but the model is actually independent of the graphical exercise itself. We will demonstrate the utility of the exercise by starting with early experimental measurements of DHI turbulence and concluding with verified LES results of a turbulent wake behind a circular cylinder. These latter estimates reflect LES computations performed in the curvilinear space (nonuniform physical domain) to illustrate the resultant accumulation of other numerical uncertainties that include evaluating the metric coefficients and the corresponding Jacobian of the governing transformed equations. But before discussing specifics of the exercise, we shall take a look at the transformed LES equations, their numerical approximation, and the turbulent kinetic energy spectrum model.

Governing Equations For the Resolved Field

The governing LES equations of the resolved field are formally derived by mathematically filtering the full resolution system as given by the Navier–Stokes equations. Although the uncertainty estimates are clearly dependent on the filter operation (whether implicit or explicit), we will assume a traditional LES computation where the width of the filter kernel is coincident with the local grid spacing. The Leonard term, in particular, is absent from the LES form of the momentum equation. The present LES results reflect a stretched grid topology that required transforming the resolved-field equations to a curvilinear coordinate system (ξ, η, ζ). These equations were derived according to the procedure suggested by Jordan [14], where the first spatial operation is the transformation. This initial operation gives a set of direct numerical simulation (DNS) equations that are solved in the computational domain. Instituting the filter operation derives the respective LES equations. In this final formulation, the differentiation and filtering commute similar to the filter operation as applied to the Navier–Stokes equations in Cartesian coordinates. The resultant grid-filtered equations in curvilinear coordinates become

$$\text{Continuity:} \quad \frac{\partial \bar{U}^k}{\partial \xi^k} = 0 \tag{1a}$$

$$\text{Momentum:} \quad \frac{\partial \sqrt{\tilde{g}}\bar{u}_i}{\partial t} + \frac{\partial \bar{U}^k \bar{u}_i}{\partial \xi^k} = \frac{\partial \sqrt{\tilde{g}}\tilde{\xi}^k_{x_j}\bar{p}}{\partial \xi^k} + \frac{\partial \sigma_i^k}{\partial \xi^k} + \frac{1}{\mathrm{Re}}\frac{\partial}{\partial \xi^k}\left[\sqrt{\tilde{g}}\tilde{g}^{kl}\frac{\partial \bar{u}_i}{\partial \xi^l}\right], \tag{1b}$$

where the transformation operation redefines the real SGS stress (σ_i^k) in terms of the resolved Cartesian $(\bar{u}, \bar{v}, \bar{w})$ and contravariant $(\bar{U}, \bar{V}, \bar{W})$ velocity components; specifically, $\sigma_i^k = \bar{U}^k \bar{u}_i - \overline{U^k u_i}$. Each contravariant velocity component is evaluated in terms of their resolved counterparts in the physical domain using the definition $\bar{U}^k = \sqrt{\tilde{g}}\tilde{\xi}^k_{x_j}\bar{u}_j$. The overbar denotes the filtered variable whereas the overtilde symbolizes implicit filtering of the metric coefficients $(\tilde{\xi}^k_{x_j})$ and Jacobian $(\sqrt{\tilde{g}})$ through their numerical approximation.

By virtue of the work by Thompson et al. [15], Jordan [14] argued that the leading term of the truncation error in the resolved-field system of equations reduces by at least one order if $\tilde{\xi}^k_{x_j}$ and $\sqrt{\tilde{g}}$ are expressed analytically. Additionally, analytical treatment of the metric coefficients does not justify representing them as filtered quantities. This argument presents an interesting dilemma when using Richardson Extrapolation in an *a posteriori* manner for estimating the numerical uncertainty of the filtered quantities over nonuniform gridding. According to Roache [10], preserving a Taylor series basis of Richardson Extrapolation is secure only if the grid stretching terms are evaluated analytically. Settling this issue requires separate attention, but will not be addressed here because Richardson Extrapolation is applied by an entirely alternate exercise.

For the present LES (and DNS) results, the numerical stencils for approximating the equations in Eq. (1) combine fifth-order and fourth-order compact differencing for the convective terms, and second-order central differencing for the diffusion terms. These equations were then time advanced using the fractional step procedure where the pressure and intermediate velocity derivatives for the incompressibility constraint were approximated by standard second-order central differences and applied over a semistaggered grid strategy. Jordan [16] recommended this particular com-

bination of differencing accuracy for resolving the correct energy spectra of the turbulent scales in the near wake of a circular cylinder at a moderate Reynolds number. By comparison to previous LES solutions at the same Reynolds number, the correct spectra were resolved even with wave number cutoff near the beginning of the inertial subrange.

Energy Spectrum Model

One form for estimating the numerical uncertainty in the LES solutions requires a wave number spectrum profile through at least the dissipation range. Inasmuch as the cutoff wave number (k_c) of the traditional LES computation usually extends only beyond the energy scales, we can complete the spectrum by simplifying the generalized model of Driscoll and Kennedy [17] (DK). The DK model was developed to accurately represent the energy spectrum of isotropic turbulence, even at low wave numbers and low Reynolds numbers, where an inertial subrange may not be discernible. Verification of the DK model included both isotropic and anisotropic flows such as grid-turbulence, a circular jet, an atmospheric boundary layer, and finally a turbulent wake. Driscoll and Kennedy were clear to point out that their model cannot accurately depict highly anisotropic flows in the low-wave number range, but that the spectrum is well modeled beyond the energy range regardless of the turbulence not being isotropic. This characteristic is attractive when using the DK model for profiling the turbulent spectra over the unresolved wave numbers of traditional LES, but may not be as useful for companion methodologies, such as the Detached-Eddy Simulation [18], where the low-wave number anisotropic scales are commonly unresolved by the spatial resolution.

Driscoll and Kennedy [17] first developed a power series of the kinetic energy (E) in the universal range of the spectrum in wave number (k) space. This series models the three-dimensional energy spectrum in dimensionless form where the scaled kinetic energy is $\hat{E}=E/(\varepsilon\upsilon^5)^{1/4}$ with scaled wave number $\hat{k}=k(\upsilon^3/\varepsilon)^{1/4}$. This scaling originates from the Kolmorgorov length ($\eta=(\upsilon^3/\varepsilon)^{1/4}$] and velocity ($u_\eta=(\upsilon\varepsilon)^{1/4}$) scales where υ and ε are the kinematic viscosity and dissipation rate of the turbulent field, respectively. The series representation of the universal range spectra used herein has a more simplified form than the original DK development

$$\hat{E}(\hat{k})=\alpha\sum_{n=0}^{\infty}(c_n+c_{n-1})\hat{k}^{(2n-5)/3} \tag{2}$$

where the coefficients c_n and c_{n-1} are defined by

$$c_k=\sum_{n=0}^{r}(-1)^{m+n}a_n b_m \tag{3}$$

Within this second series $a_n=(1.5\alpha)^n/n!$ and $b_m=(1.5\alpha)^n/n!$, where the integer (m) is $m=(k\text{-}2n)/3$ and the index (r) is $r=k/2$ (even k) or $r=(k-1)/2$ (odd k); note $c_{-1}=0$, $c_0=1$, and $c_1=0$. The coefficient (α) stems from the $-5/3$ law in the inertial subrange of the energy spectra, i.e., $\hat{E}=\alpha\hat{k}^{-5/3}$.

Broadening the universal-range series [Eq. (2)] to the low-wave number range required coupling with a modified form of the von Karman energy-range model. This latter model in an extended series appears as

$$\hat{E}(\hat{k})=\sum_{n=0}^{\infty}\hat{B}_n(\hat{k}/\hat{k}_e)^{(2n-5)/3} \tag{4}$$

where the quantity $\hat{k}_e$ is the dimensionless energy-range wave number (the same scaling as $\hat{k}$). The dimensionless coefficient $\hat{B}_n$ is evaluated by requiring the expended von Kármán model to converge to the universal model series in the limit $\hat{k}\gg\hat{k}_e$. Satisfying this condition gives the total energy spectrum model over all wave numbers for an isotropic turbulent flow;

$$\hat{E}(\hat{k})=\alpha\left(\frac{\hat{k}^2}{\hat{k}_e^2+\hat{k}^2}\right)^2\sum_{n=0}^{\infty}d_n(\hat{k}_e^2+\hat{k}^2)^{(2n-5)/6} \tag{5}$$

When assessing the numerical uncertainty in the LES computation, the one-dimensional (1D) longitudinal spectrum ($\hat{E}_{11}$) is preferred over the $\hat{E}$ spectra. Under the assumption of isotropic turbulence, DK derived the series (simpler form);

$$\hat{E}_{11}(\hat{k}_1)=\alpha[h_1(\hat{k}_1)-h_1^*]-(\hat{k}_e^2+\hat{k}^2)[h_2(\hat{k}_1)-h_2^*] \tag{6a}$$

where

$$h_1(\hat{k})=\sum_{n=0}^{\infty}\left(\frac{3d_n}{5-2n}\right)(\hat{k}_e^2+\hat{k}^2)^{(2n-5)/6} \tag{6b}$$

$$h_2(\hat{k})=\sum_{n=0}^{\infty}\left(\frac{3d_n}{11-2n}\right)(\hat{k}_e^2+\hat{k}^2)^{(2n-11)/6} \tag{6c}$$

The variable h_2^* is evaluated in the limit as $\hat{k}\to\infty$. Given the present use, we will assume $\hat{E}_{11}=0$ once $k\eta=\hat{k}\geqslant 1$. Also, in this simpler form of the DK 1D model, the coefficient (d_n) is defined by $d_n=c_n+c_{n-1}$, where $d_0=d_1=1$.

Note that the present form of the spectrum model ignores two parameters Q and β, which were present in the original DK series. The parameter Q governs the profile shape in the dissipation range near $\hat{k}=1$ and β becomes important only when an inertial subrange is clearly nonexistent. Inasmuch as the numerical uncertainty (defined later) will be zero when the cutoff wave number (k_c) is equal to η, the estimate is therefore nearly free from influence by the Q parameter. With α largely unknown, DK simply chose $\alpha=1.65$ for all model fits to their test cases. But, as will be illustrated in the present applications, α is an important parameter to adequately model the unresolved spectrum beyond $\hat{k}_c$. Thus, the exercise for evaluating the numerical uncertainty assumes no overlap between the energy and dissipation ranges of the energy spectra, which renders the β parameter as unimportant.

Estimating the Numerical Uncertainty

Estimating the local numerical uncertainty of a LES computation *a priori* begins with reminding ourselves that the *rms* of a turbulent quantity can be evaluated by integrating the respective spectra over k space ($i=1,2,3$). For example, the inverse Fourier transform for the turbulent intensity ($u_i'^2$) in dimensionless form is

$$\hat{u}_i^2=\int_0^{k\eta}\hat{E}_{ii}(\hat{k}_i)d\hat{k}_i \tag{7}$$

where $\hat{u}_i=u_i'/u_\eta$, with $\hat{E}_{ii}$ representing the corresponding dimensionless energy spectra. Likewise, an analogous resolved intensity $(u_i')^r$ is acquired by integrating the energy profile up through the cutoff wave number (k_c^i),

$$(\hat{u}_i^r)^2=\int_0^{k_c\eta}\hat{E}_{ii}(\hat{k}_i)d\hat{k}_i \tag{8}$$

where $\hat{u}_i^r=(u_i')^r/u_\eta$. These intensities as referenced to the square root of the area under the three-dimensional energy spectrum are sketched in Fig. 1. Given these quantities, we can now form a conventional and local estimate of the local numerical uncertainty at the cutoff wave number as

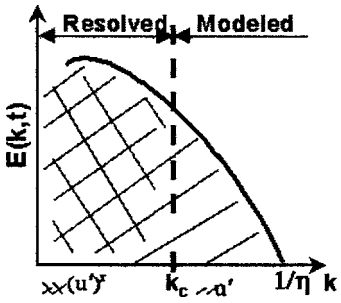

Fig. 1 Sketch showing the resolved $(u')^r$ and total (u') turbulence intensities under the energy spectrum curve

$$\hat{\delta}_i^1 = 1 - \hat{u}_i^r/\hat{u}_i \tag{9}$$

This simple expression of the uncertainty is similar to the single parameter in the CFD error estimates as derived by Roache [10]. By implementing Richardson Extrapolation a second uncertainty estimate is

$$\hat{\delta}_i^2 = (\hat{\varepsilon}_i - 1)/(\hat{r}^p - 1) \tag{10}$$

where $\hat{\varepsilon}_i = (\hat{u}_i^r)^2/(\hat{u}_i^r)^1$, $\hat{r}$ is the grid-refinement ratio, and p accounts for the order of solution accuracy. With respect to the energy spectra sketched in Fig. 1, the grid-refinement ratio in traditional LES is defined as $\hat{r} = \hat{k}_c^2/\hat{k}_c^1$ with $\hat{\Delta}_f^i = 1/2\hat{k}_c^i$ where the superscripts 1 and 2 denote the coarse and finer grids, respectively. Analogously, a LES grid-independence exercise would define the same dimensionless ratio, but the filter width (Δ_f) remains fixed, i.e., $\hat{\Delta}_f^i \geqslant 1/2\hat{k}_c^1$. Roache [10] argues (and illustrated) that the parameter $\hat{\delta}_1^1$ by itself is a poor estimate of the numerical uncertainty error in CFD solutions. But before we dispute these error estimates herein, we must first understand the meaning of $\hat{\delta}_i$ within the framework of the wave number spectrum.

The original expression for δ_i difference flow variables in the final CFD solutions at coincident grid points throughout the flow domain. As the grid spacing (h) is continuously refined $(h \to 0)$, the CFD solutions at that same coincident point are expected to converge asymptotically to the exact solution. In the context of the present k-space spectrum, the area under the curve actually represents a turbulent quantity averaged over a grid line in the flow domain. While the cutoff wave number in the spectra is the inverse of twice the grid spacing along the line $(k_c = 1/2h = 1/2\Delta_f)$, the minimum resolved wave number is given by the reciprocal of the line length. As the grid spacing is refined $(k_c \to 1/\eta)$ and/or the SGS model better represents the unresolved scales, the resolved turbulent spectra and its associated property are projected to asymptotically converge to the exact averaged value. Along the way in the former case, the spectral levels transition to those from a DNS computation where the SGS model contributions have become inconsequential.

Ostensibly, refining the grid spacing along a particular line in traditional LES should improve the numerical uncertainty of the total dimensionless spectra. Even under poor modeling of the unresolved scales, we should also expect the resolved spectra to asymptotically converge to a unique profile as $k_c \to 1/\eta$. Thus, the *a priori* exercise described herein assumes LES solutions tending toward the asymptotic convergence of both the wave number spectra as well as the resultant quantity given by the area under the curve. Emphasizing this rationale is demonstrated in Fig. 2 for the case of DHI turbulence [19], where we will assume that the wave number spectra reflects capture from a traditional LES computation. The longitudinal component in dimensional units are plotted in Fig. 2(*a*), which holds a turbulent Reynolds number (R_λ) based on Taylor's microscale (λ) of $R_\lambda = 71.6$; $R_\lambda = u'\lambda/v$. This profile clearly shows a separation of the energy and dissipation ranges. Discrete integration of the profile gives the intensity $u' = 4.21$, which compares to the measured value of $(u')_{\text{meas}} = 4.30$. A second discrete integration of the energy profile up to k_c determines the velocity quantity $(u_i')^r$. Figure 2(*b*) shows results from the uncertainty estimate [Eq. (9)] and further compares the actual error using the measured intensity. Their close agreement suggests that interrogating the wave number spectra offers a suitable means for estimating the local uncertainty. From the standpoint of convergence, only the first third of the uncertainty curve suggests a logarithmic reduction of δ_1^1 with grid refinement. Further reductions of δ_1^1 are clearly asymptotic.

An analogous argument supports nontraditional LES $(\Delta_f > h)$, where the Leonard-type term requires specific treatment in the solution methodology. We define grid convergence as holding the filter width Δ_f constant while $k_c \to 1/\eta$. An illustrative example for estimating the numerical uncertainty in nontraditional LES comes from the grid-convergence inquiry by Geurts and Frohlich [20] of DHI turbulence using Smagorinsky modeling for the SGS field. They tested four uniform LES spatial resolutions (32^3 to 96^3 grid cells) as compared to the converged DNS spacing requiring 192^3 cells. Their total energy spectra are reproduced in Fig. 3(*a*) in dimensionless form with application of Eqs. (9) and (10) to these profiles plotted in Fig. 3(*b*) for evaluating the accumulative uncertainty of the resolved turbulent kinetic energy.

An important difference between the uncertainties $\hat{\delta}_1^1$ and $\hat{\delta}_1^2$ is that the former requires the completion of the resolved profile to $k_c = 1/\eta$ as given in this example by the DNS results. We note that Meyers et al. [2] argued prefiltering versus nonfiltering the DNS spectra to evaluate the numerical error. But herein this difference is negligible $(<0.1\,\%)$ because prefiltering only attenuates the fin-

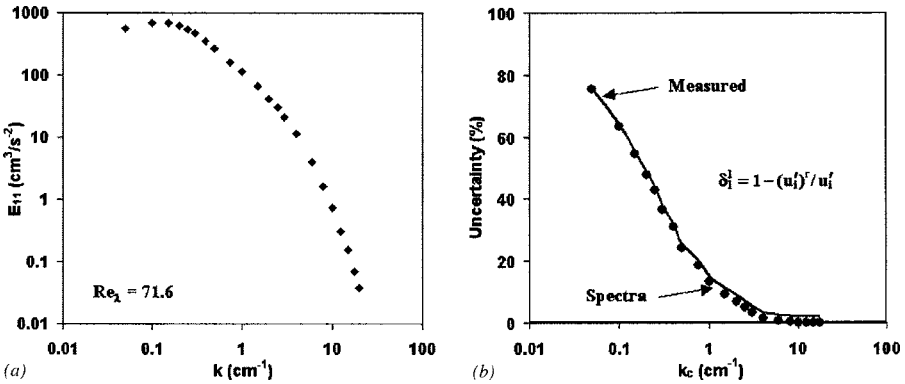

Fig. 2 Spectral energy of DHI turbulence [19] and example evaluation of the numerical uncertainty. (*a*) Dimensional energy spectra. (*b*) Percent numerical uncertainty.

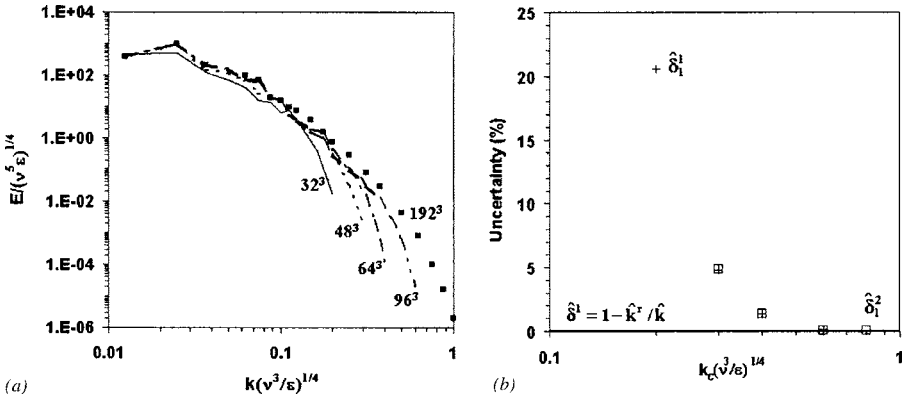

Fig. 3 LES grid-convergence study of DHI turbulence [20] and evaluation of the numerical uncertainty. (*a*) Dimensional energy spectra. (*b*) Numerical uncertainty.

est resolved scales near η. Instinctively, we would expect only $\hat{\delta}_1^1$ to be closer to the exact error as illustrated in the previous example. This presumption is simply speculative in view of the three comparisons shown in Fig. 3(*b*). The clear advantage of using the $\hat{\delta}_1^2$ expression is the immediate and reasonably accurate return on improving resolution of a local turbulent quantity by refining the respective grid spacing.

As previously mentioned, lower numerical uncertainties are equally possible by improving the representation of the unresolved scales. A first example is the very early SGS model studies of Mansour et al. [21], who tested the resolved vorticity field as a measure for forming the velocity scale of the turbulent eddy-viscosity relationship. Earlier, Ferizer [22] illustrated little difference between this scaling and that of the standard Smagorinsky model of DHI turbulence by fine-tuning the respective model coefficients. Two of their total energy spectra (VM) using very coarse gridding (16^3) are replicated in Fig. 4, where a minor reduction of the uncertainty in the turbulent kinetic energy was realized by simply tuning the model coefficient ($0.215 \rightarrow 0.230$) and improving the model differencing stencil from second to fourth order. By doubling the spatial resolution (32^3) and switching to a one-equation SGS model (OEM), the total energy spectra of Fureby et al. [23] gives more than a 50% reduction ($\hat{\delta}_1^1 \sim 0.144$) of the uncertainty over the best VM simulation. Similarity, their spectra compared to the Smagorinsky model [20] (SM) for the same grid spacing produced about a 30% drop in the numerical uncertainty of the turbulent kinetic energy.

With new insight from these applications, we can justify using the expressions in Eqs. (9) and (10) for estimating the local numerical uncertainty *a priori* of a specific turbulent quantity, including the assessment of grid convergence. Obviously, the graphical exercise is applicable to many statistical properties of the turbulent flow, simply by constructing their respective wave number spectra. A further note is necessary by once again referring to the analogous arguments of Roache [10]. The original error δ_i of the CFD solutions is really an *estimated* fractional error instead of an *actual* fractional error because the exact solution at the specific grid point is simply not known. This fact is equally understood in the present *a priori* exercise. Because the wave number spectrum is not fully resolved, the respective area under the curve is an *estimated* averaged property. The *actual* averaged property is obtained only when $\hat{k}_c \geqslant 1$.

One final argument concerns conversion of the frequency spectra at a grid point to wave number space using Taylor's hypothesis. This path offers use of the present exercise for LES solutions over unstructured gridding, where a continuous line of points may be difficult to construct through the flow domain of interest. The LES solutions toward a statistical steady state could provide enough time-dependent statistics to estimate the numerical uncertainty of the spatial resolution surrounding a particular grid point. The total time in the collected statistics should convert to a cutoff wave number beyond the energy range such that the spectrum model reliably completes the profile. One drawback with this approach is the usual appearance of spikes in the resolved spectra that identify periodic structures. These spikes and their local distortion of the profile typically deviate from smooth asymptotic convergence, which ultimately may lead to poor estimates of the numerical uncertainty.

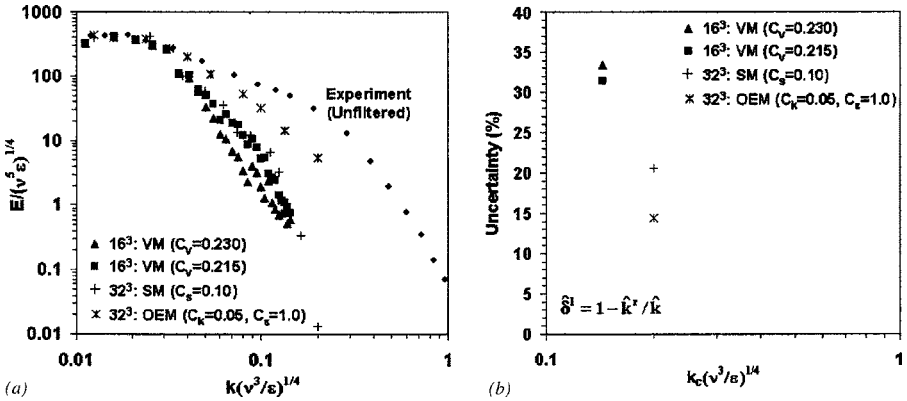

Fig. 4 SGS model study of DHI turbulence [20,21,23] and evaluation of the numerical uncertainty. (*a*) Dimensional energy spectra. (*b*) Numerical uncertainty.

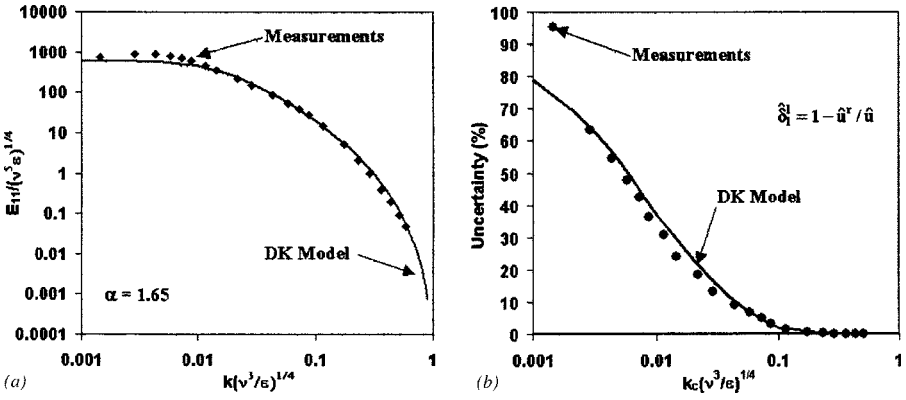

Fig. 5 DK model of isotropic turbulence [19] and model evaluation of the numerical uncertainty. (*a*) Dimensionless energy spectra. (*b*) Numerical uncertainty.

Numerical Uncertainty of Several Example Spectra

Quantifying the numerical uncertainty of LES solutions is a relatively simple exercise in view of the two expressions offered herein. Next we will see that the first estimate requires only a single profile of resolved wave number spectra, while the second asks for two solutions, each with different spatial resolutions. Neither expression cares about the discretization scheme, explicit filtering, nor the SGS model, because they operate on the turbulent quantities. Permanent adjustments in solution strategy are expected to lower the accumulated errors, and thereby improve the resultant wave number spectra. The former estimate holds no mathematical foundation while the latter estimate can be traced back to the general expression of Richardson Extrapolation. But unlike that expression, the proposed analog estimate does not require successive solutions at coincident grid points. In fact, the grid lines may not be strictly coincident because the estimate inputs are locally averaged quantities.

As discussed earlier, the completion of a single wave number spectrum beyond the resolved turbulent scales is necessary to test the numerical uncertainty *a priori*. In the absence of the full spectrum by either experimental or DNS means, we can illustrate the utility of the DK spectrum model for representing the unresolved wave numbers. As a start, we will examine its fidelity for quantifying the numerical uncertainty via fits to experimental measurements of DHI turbulence. Inasmuch as these initial exercises deal with the *assumed* converged spectrum, we will demonstrate only the conventional expression [Eq. (9)] for estimating the uncertainty.

Example DK Modeling and Numerical Uncertainty of Resolved DHI Turbulence. Comte-Bellot and Corrsin [19] collected turbulent statistics downstream of two regular mesh systems. A fit of the DK model to their energy spectra requires input for the coefficient α and the dimensionless energy wave number ($\hat{k}_c$). Assuming isotropic turbulence, Driscoll and Kennedy [17] derived the relationship $\hat{k}_c = 4.35(\alpha/\mathrm{Re}_\lambda)^{3/2}$ for evaluating the latter parameter. Upon substituting the relationship $\mathrm{Re}_\lambda = \sqrt{15}\hat{u}^2$ for the turbulent Reynolds number (also assuming isotropic turbulence), the final definition for the dimensionless energy wave number in terms of the dimensionless intensity (mean square) becomes. $\hat{k}_c = 0.57(\alpha/\hat{u}^2)^{3/2}$. Chasnov[24] listed a wide range of experimental averages for the Kolmogorov. constant α that bridge from grid turbulence to atmospheric flows ($1.34 \leqslant \alpha \leqslant 2.1$). Driscoll and Kennedy [17] found the nominal value $\alpha = 1.65$ to yield the best model fit to their tests cases of grid turbulence, a circular jet, atmospheric boundary layers, and a wake flow. The fit to isotropic grid turbulence is reconstructed in Fig. 5(*a*) with the respective uncertainty estimate plotted in Fig. 5(*b*). Outside the coarsest turbulence scales, the DK model produces nearly equivalent estimates of the numerical uncertainty as compared to the measured data. Because the coarsest wave numbers are always resolved by the spatial resolution in the LES computations (by definition), the DK model should be an excellent representation of the unresolved scales in the spectral profiles.

Estimating the Dissipation Rate (ε). The reality of most practical LES computations is the lack of accurate and local rates of dissipation (ε) for scaling the resolved spectra and wave numbers. While the resolved wave numbers are scaled by η, the spectral energy (for example) is made dimensionless using ηu_η^2. This scaling requires an approximation for ε to implement the exercise for estimating the numerical uncertainty. Within the turbulent domain of practical importance, we should consider refining the grid spacing until at least the energy range of wave numbers are well resolved in the corresponding power spectra. This requirement extends the cutoff wave number to within the upper limit of the inertial subrange of the turbulence universal range, where a dimensional analysis yields the well-known relationship $E(k) = \alpha\varepsilon^{2/3}k^{-5/3}$. A sample plot of $\alpha^{3/2}\varepsilon$ over all wave numbers is shown in Fig. 6(*a*) for the energy spectrum profile of isotropic grid-turbulence [Fig. 2(*a*)]. A plateau of points is clearly evident in the figure that clearly identifies an averaged constant slope $\alpha^{3/2}\varepsilon \approx 1550$ within the inertial subrange. Unfortunately, this average tells us that applying the nominal value $\alpha = 1.65$ results in an order-of-magnitude underestimation of the dissipation rate. The experimental value is actually closer to $\alpha = 0.48$.

As an alternate approach to finding a reasonable estimate for ε, we can substitute the term $\alpha^{3/2}\varepsilon$ into the $\hat{k}_e$ relationship for isotropic turbulence to give the form $\hat{k}_c = 0.57(\alpha^{1/4}/\hat{u}^2)^{3/2}$. Considering the range of experimental values for α and the assumption of isotropic turbulence throughout this development, we can assume $\alpha^{1/4} \sim 1.0$ to give the simpler relationship $\hat{k}_e = 0.57\hat{u}^{-3}$. This assumption affects only the low wave number fit of the DK model to the spectrum [see Fig. 6(*b*)]. Thus, altering the original DK definition for the dimensionless energy wave number should not inhibit its use to complete the spectra of the LES solutions if the energy range wave numbers are well resolved, as expected.

Continuing with the exercise for estimating ε, we will first assume ideal LES solutions that correctly resolved the grid-turbulence velocity power spectrum along arbitrary lines within the flow domain. Second, the coefficient α now becomes a free parameter whose value may be distant from the actual Kolmorgorov constant. Selecting a cutoff wave number ($k_c = 0.4$) near the upper limit of the inertial subrange gives the undervalued slope $\alpha^{3/2}\varepsilon \sim 668$ ($\mathrm{cm}^3\,\mathrm{s}^{-1}$) and $(u')^r = 15$ ($\mathrm{cm}^1\,\mathrm{s}^{-1}$). Scaling the experimental measurement data by the parameter $\alpha^{3/2}\varepsilon$ ($\hat{E}', \hat{k}'$) obvi-

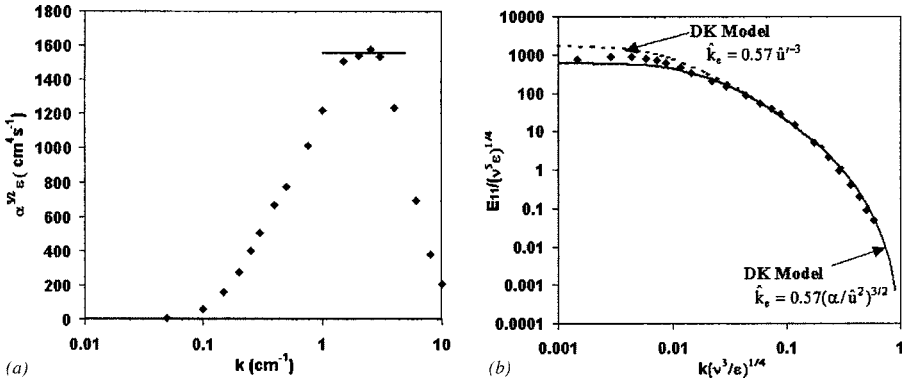

Fig. 6 Profile of subrange coefficient ($\alpha^{3/2}\varepsilon$) and DK model results using two definitions for the dimensionless energy wave number ($\hat{k}_\varepsilon$). (*a*) Coefficient $\alpha^{3/2}\varepsilon$. (*b*) Dimensionless spectral energy.

ously creates a large disparity with the DK model, as illustrated in Fig. 7(*a*). But noting that both the energy and wave number quantities are improperly scaled by the same coefficient $\alpha^{3/8}$, the ratios $(\hat{k}/\hat{k}')^{8/3}$ and $(\hat{E}/\hat{E}')^{8/3}$ permit useful estimates. A plot of these two ratios with $\hat{k}'$ and $\hat{E}'$ taken at cutoff is shown in Fig. 7(*b*), where the two curves intersect at approximately $\alpha=0.28$. Surprisingly, the corresponding rate of dissipation $\varepsilon \sim 4500$ (cm^3 s^{-1}) is close to the experimental measurement $\varepsilon \sim 4750$ (cm^3 s^{-1}). Rescaling the resolved portion of the energy spectra now shows a close match between the measurement data and the model at wave number cutoff.

Performing the same ideal exercise, but resolving all wave numbers well into the inertial subrange of the grid-turbulence data ($k_c=2.5$ cm^{-1}), produces a parameter close to the experimental value ($\alpha=0.44$). This constant coupled with the averaged slope $\alpha^{3/2}\varepsilon \sim 1550$ (cm^3 s^{-1}) of the inertial subrange gives a 12% higher rate of dissipation $\varepsilon \sim 5300$ (cm^3 s^{-1}) compared to the experimental value. But, as illustrated in Fig. 8, a modest increase in this quantity has only a minor effect on the resolved-model match to complete the dimensionless spectrum. As expected, the disparity is reduced between the $\alpha^{3/2}\varepsilon$ data scaling and model spectral energies at this higher wave number cutoff, but still required correction before evaluating the respective averaged intensities.

Estimates of Numerical Uncertainty Using the Matched Spectra of Grid Turbulence. Discrete integrations of the matched ideal spectra [Figs. 7(*a*) and 8] at various dimensionless wave numbers are illustrated in Fig. 9. At the lower cutoff wave number $\hat{k}_c=0.0145$ [Fig. 9(*a*)], $\hat{u}^r=3.20$, which is only 75% of the respective experimental value. Even if the energy levels of this grid-turbulence example are accurately captured by the computation, these estimates suggest that grid spacing short of resolving the energy range wave numbers will exceed a 20% uncertainty in the respective resolved turbulent intensities.

A distribution of the uncertainty estimates in Fig. 9(*b*) as determined by discrete integrations of the second energy spectrum (Fig. 8) suggests that nearly two-thirds of the energy spectra ($\hat{k}_c=0.07$, logarithmic scale) must be accurately captured by the computation to reduce the numerical uncertainty below 5%. The area under the joint spectrum furnishes $\hat{u}=3.91$, which is within 7% of the experimental profile. Spatial resolutions of this order appear closer to the DNS category rather than a practical LES computation.

As the turbulent Reynolds number drops, separation of the energy and dissipation ranges in the wave number spectra eventually becomes undetectable. Comte-Bellot and Corrsin [19] published one such profile ($R_\lambda=48.6$), where the energy range holds nearly one-half of the resolvable wave numbers (log scale) and the inertial subrange is confined to a very narrow band. Matching that experimental data with the DK model fails when the cutoff wave number is well inside the energy range. This breakdown is a direct consequence of treating two unknowns in the exercise. In particular, the α parameter becomes unrealistically low. At a higher cutoff wave number an acceptable match is possible, as depicted in

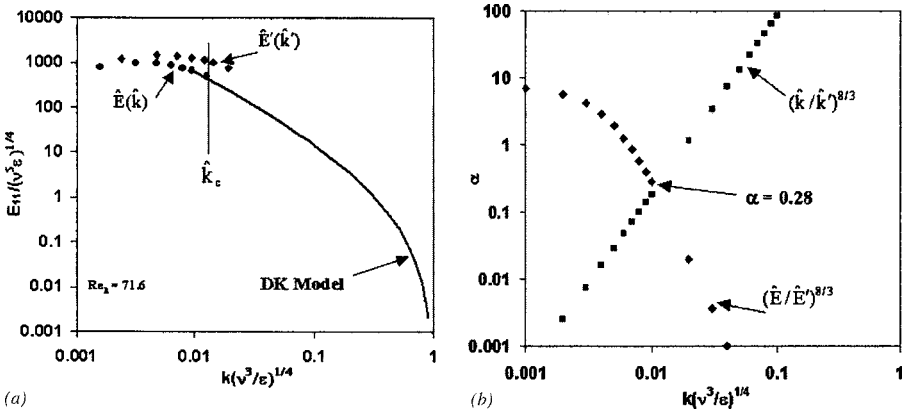

Fig. 7 Spectral energy and Kolmorgorov coefficient for estimating numerical uncertainty of grid turbulence at low-wave number cutoff. (*a*) Dimensionless spectral energy. (*b*) Kolmorgorov coefficient.

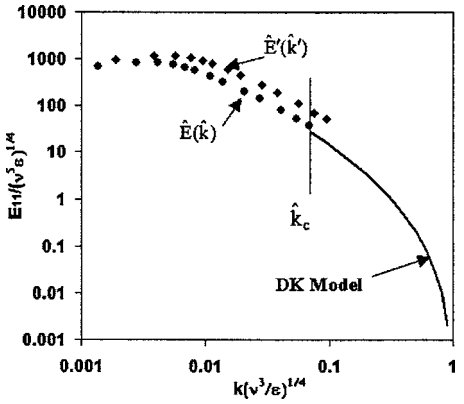

Fig. 8 Resolved-model spectra of grid-turbulence at high-wave number cutoff

Fig. 10(*a*). Again, presupposing that the LES computation has accurately resolved this latter profile, Fig. 10(*b*) shows the estimates of numerical uncertainty at various cutoff wave numbers. Good agreement between the resolved-model estimates and the actual experimental data lends strong confidence in this exercise, even when the inertial subrange is narrow banded. At $\hat{k}_c$, the experimental and resolved-model uncertainties are just over and under 10%, respectively. Reaching these error levels (at best) seems tolerable for a traditional LES computation. Moreover, they demonstrate that the user can assess the local numerical uncertainty associated with the generated grid spacing for properly resolving the local energy scales of the turbulent field.

Example Estimate of Numerical Uncertainty in the Turbulent Channel. The turbulent channel flow was one of the first engineering applications for demonstrating the LES methodology [13]. Since then, much statistical information has appeared in the literature of this simple geometry, as computed by both the DNS and LES methodologies. One such computation ($Re_\tau = 180$) was reported by Kim et al. [25], who used a spectral solution strategy and a $192 \times 129 \times 160$ grid in the streamwise, normal, and spanwise directions, respectively. Piomelli et al. [26] conducted numerous LES computations of this flow for the specific purpose of exploring SGS model consistency. To further demonstrate the versatility of the DK model to finish the wave number spectrum profile, we will use the coarse grid LES results at location $y^+ = 12.93$.

Figure 11(*a*) shows the resolved uncorrected and corrected ($\alpha = 0.86$) results as well as the DK model portion of the dimensionless energy spectrum. These total spectra reflect the summation of the resolved and SGS model contributions. The cutoff wave number resolves slightly more than one-half of the spectrum (log scaling). Notice that the DK model matches the total spectra at a slightly lower wave number to circumvent the modest overdamping of the finest resolved scales. Estimates of the numerical uncertainty at increasing $\hat{k}_c$ are illustrated in Fig. 11(*b*) using the conventional expression. These estimates indicate that resolving the energy scales of the channel turbulence at this y^+ location will yield about a 10% uncertainty in the respective intensities when using the filtered DNS profile to evaluate $\hat{v}$. A discrete integration of the matched profile gave the dimensionless intensity $\hat{v} = 4.96$, which closely agrees with the statistical value $\hat{v} = 5.61$.

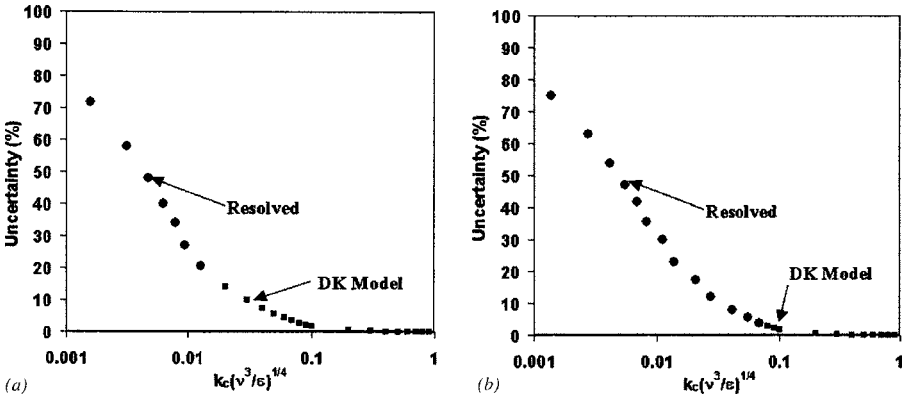

Fig. 9 Two ideal examples for estimating the numerical uncertainty of LES resolved grid turbulence. (*a*) Low wave number cutoff. (*b*) High wave number cutoff.

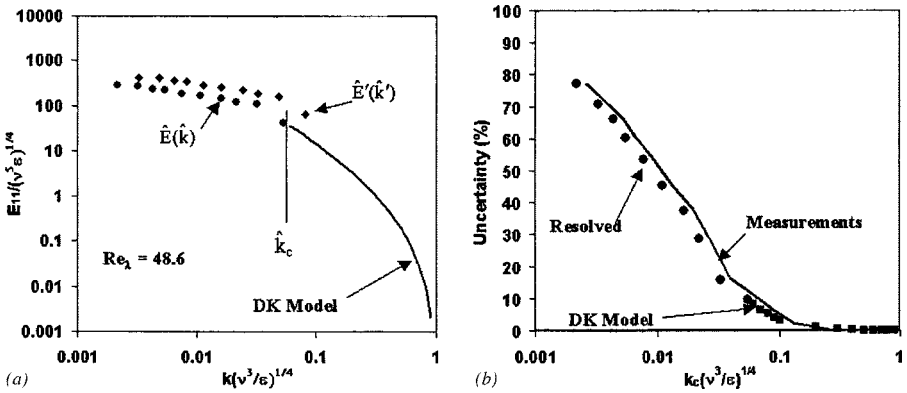

Fig. 10 Match and numerical uncertainty between measurement spectral energy data and DK model. (*a*) Energy spectrum. (*b*) Numerical uncertainty.

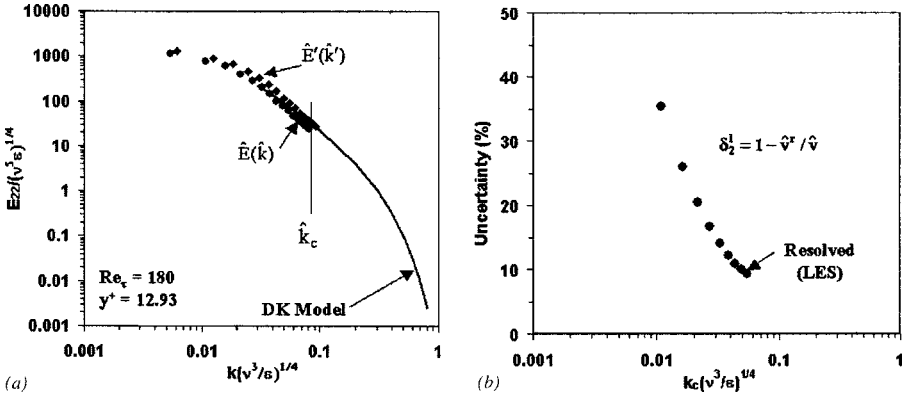

Fig. 11 Resolved-model match of energy spectrum and numerical uncertainty of the turbulent channel. (*a*) Energy spectrum. (*b*) Numerical uncertainty.

Estimates of Numerical Uncertainty in the Cylinder Wake. The spatial resolution generated for bluff-body flows provides an excellent test bed for exercising the numerical uncertainty expressions. Typically, the grids are structured with clustering toward the body surface—a good conical example being the spacing topology generated to resolve the turbulent wake of a circular cylinder. Herein, we will focus specifically on the experimental measurements and numerical computations at Reynolds number Re $=3900$, which is based on the free-stream velocity (U) and body diameter (D). Briefly, this flow possesses three distinct zones downstream of the cylinder; the immediate formation region, bounded by the upper and lower separated shear layers (where transition to turbulence occurs), followed by the turbulent Karman vortex street.

Jordan [27] claimed DNS resolution within the formation region of the near wake using a $321\times241\times64$ structured grid; circumferential, radial, and spanwise points, respectively. Downstream of this region, the grid resolution coarsened beyond DNS standards, but remained computational stable via the dissipative element inherent in the radial approximation stencil of the nonlinear terms. Only the radial grid spacing was nonuniform as the circumferential lines were clustered exponentially toward the cylinder periphery. Figure 12(*a*) shows the instantaneous longitudinal energy spectrum of the DNS results taken along the circumferential line $r/D=1.5$ (referenced to the cylinder center, where $r/D=0$). The spectrum profile depicts a snapshot of the computation prior to collection of the instantaneous quantities toward the statistical steady state, which were further smoothed using 64 spanwise averages. The profile suggests that the inertial subrange is well resolved with the cutoff wave number at $k_cD=13.34$. A reduction of the resolved energy levels gave the model constant near unity ($\alpha\sim0.97$) and therefore less than a 5% difference in the spectrum scaling using either the coefficient $\alpha^{3/2}\varepsilon$ or the rate of dissipation itself. The match between the resolved field and the DK model is shown in Fig. 12(*b*) and compared to the dimensionless experimental data of Ong and Wallace, [28] taken along the wake centerline at $r/D=5.0$. Keeping in mind that the area under the resolved-model spectra represents a statistical average along the circumferential line, discrete integrations of both profiles gave comparable values for the turbulent intensity; $\hat{u}=5.02$ vs $(\hat{u})_{\text{meas}}=5.20$.

Figure 13 shows distribution of the estimated numerical uncertainty of the resolved turbulent intensity at increasing cutoff wave numbers. At the dimensionless cutoff wave number ($\hat{k}_c=0.13$) more than two-thirds of the energy spectrum was well resolved by the grid spacing at $r/D=1.5$. Fine spatial resolution at this level apparently falls under the DNS category where the estimated uncertainty of the streamwise intensity falls below 1% (conventional expression). However, comparisons between the DNS and experimentally measured statistics place the averaged uncertainty at 4.4%. As noted earlier, other statistical properties can be assessed for their numerical uncertainty. For example, Fig. 13(*b*) illustrates the wave number distribution of the dimensionless dissipation rate along line $r/D=1.5$. Although the spatial resolution adequately captured the dominant dissipation scales within the formation region, the numerical uncertainty of the averaged rms value was approximately 20%.

Once the transient behavior of the turbulent field settles, profiles of the wave number spectra can be viewed anywhere within

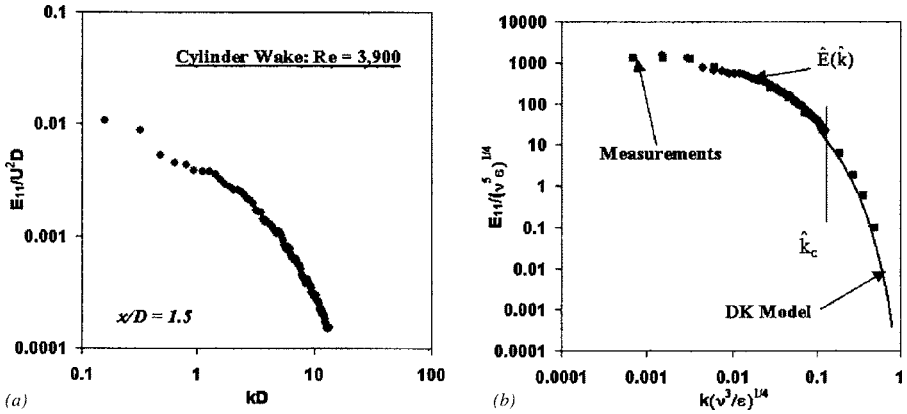

Fig. 12 Spectral energy and resolved-model match inside the formation region of the cylinder near wake; Re=3900. (*a*) Resolved energy spectrum. (*b*) Resolved-model match.

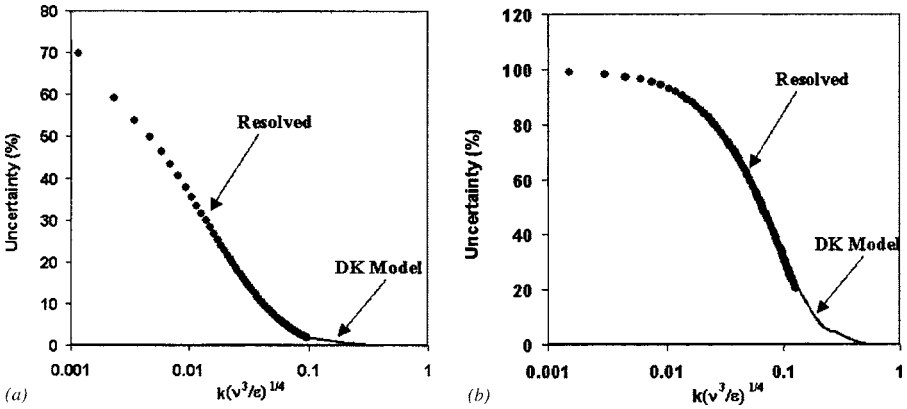

Fig. 13 Estimates of numerical uncertainty for DNS computation inside the formation region of the cylinder near wake (r/D=1.5); Re=3900. (*a*) Streamwise intensity. (*b*) Dissipation.

the flow domain. Obviously, many statistically independent averages are necessary to smooth the profiles. Although explicit operators or low-pass filters are other options for smoothing a specific profile, averaging is the preferred choice for producing realistic spectra. One should note that these averages are easily available when using the instantaneous DNS or LES results that vary over space and/or time. The profiles are also practical leading indicators of excessive or insufficient dissipation near wave number cutoff before continuing the computation. A good example of excessive numerical dissipation is the cylinder wake LES computation of Beaudan and Moin [29] (BM), who tested fifth-order accurate upwinding for the convective derivative. Their total spectrum is reproduced in Fig. 14 (converted to wave number space using Taylor's hypothesis) and shows about one-half of the wave numbers (log scaling) resolved by the grid spacing. But the profile clearly depicts excessive dissipation over the finest resolved scales and would be impossible to match ($\alpha \sim 0.0016$) with the DK model near the cutoff wave number.

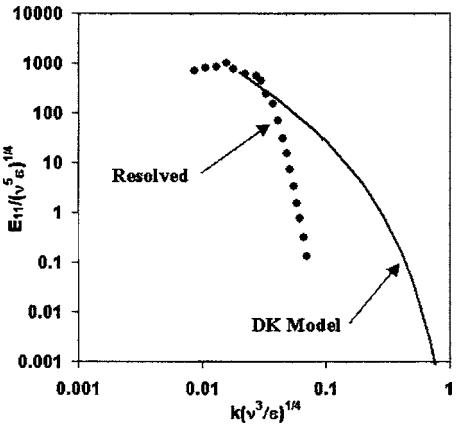

Fig. 14 Example spectrum profile [26] showing match with the DK spectrum model

Inasmuch as the energy scales in the spectrum appear sufficiently resolved by the BM computation, a suitable fit of the DK model is possible at a much lower wave number ($\hat{k} \sim 0.03, \alpha \sim 1.0$). Integrating this match gives an uncertainty of 21% for the total streamwise Reynolds stress, which is only slightly conservative when compared to the actual statistical error ($\sim 17\%$) using the experimental measurements. The point clearly emphasized in this example is the applicability of this graphical exercise to reach a favorable estimate of the numerical uncertainty when experimental data (or the like) are simply unavailable for statistical comparison.

Continuing with token exercises for estimating the numerical uncertainty, we will examine the wave number spectra generated within the Kaŕmán vortex street of the cylinder wake. These LES results were computed over a $161 \times 121 \times 32$ coarse grid with a compact fifth-order stencil approximating the convective derivative to maintain stability. The dynamic Smagorinsky model characterized the unresolved scales. A profile of the instantaneous total

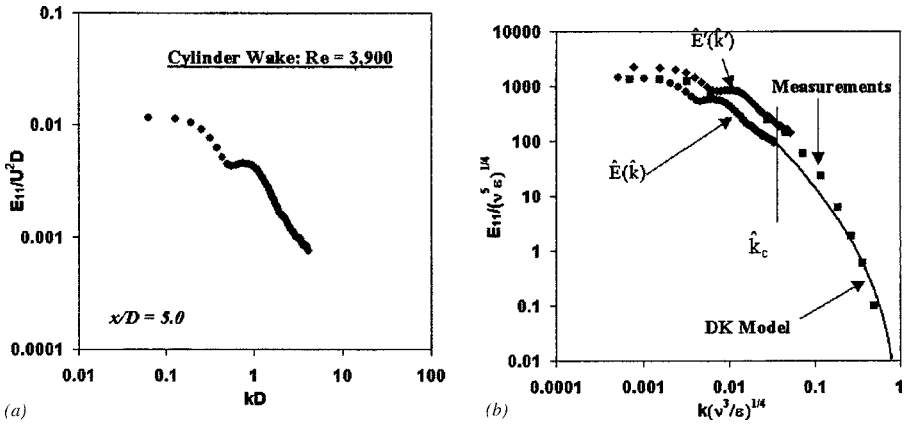

Fig. 15 Spectral energy for estimating numerical uncertainty of turbulent wake at low-wave number cutoff. (*a*) Spectral energy. (*b*) Resolved-model match.

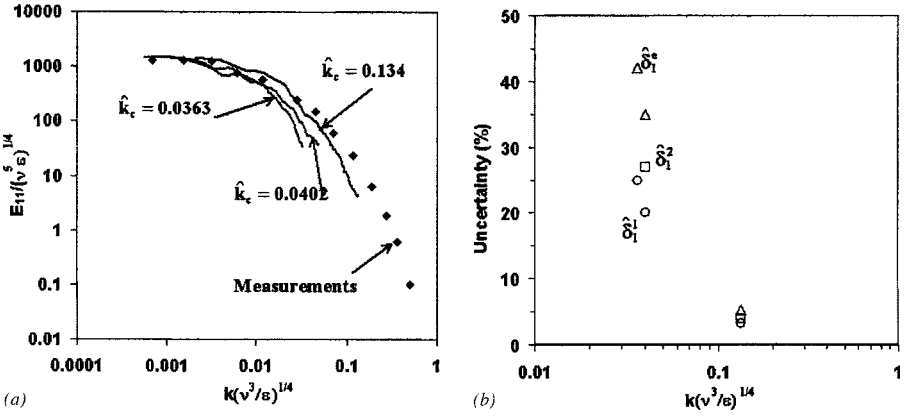

Fig. 16 Improved resolved-model match of wake spectral energy through grid refinement. (*a*) Spectral energy. (*b*) Numerical uncertainties

energy spectrum along circumferential line $r/D=5.0$ is shown in Fig. 15(*a*). Again, the spectrum denotes several snapshots of the LES computation that were taken before storing the wake statistics. Specifically, this rather poor energy profile depicts statistically independent spanwise and time averages over one shedding cycle with a dimensionless turnover time $\Delta t\, U/D=0.5$. By comparison, the approximate Kolmorgorov time scale (τ) is $\tau=0.3$ s in this LES computation. A graphical determination of the Kolmorgorov constant gave a dimensionless rate of dissipation $\varepsilon D/U^3 \sim 0.0038$. At first glance, this value compares favorable to the experimental value $(\varepsilon D/U^3)_{\text{meas}} \sim 0.0028$.

A correction of the profile and its match to the DK model is shown in Fig. 15(*b*) and suggests that in comparison to the experimental measurements, the resolved energy levels are largely underestimated by this LES computation at five diameters downstream. Besides the dissipative nature of the discretization stencil, the grid spacing simply does not fully resolve all wave numbers, defining the energy range of the spectrum. This under-resolved spectrum is clearly reflected in the uncertainty estimates of the averaged streamwise intensity ($\hat{u}$). At the matched wave number $\hat{k}=0.009$, the averaged estimate of uncertainty based on the wave number spectrum is 27%, which compares to an actual error of 51% using the measured streamwise intensities at wake location $r/D=5$. This rather large disparity between the spectrum and actual estimates underscores the versatility of the DK model to match even poorly resolved spectra. One should note that comparisons to the experimental evidence should not be necessary to realize that the energy scales were severely under-resolved by this LES computation at $r/D=5$. But with that observation, one should caution that the respective estimates of numerical uncertainty are much less reliable.

Staying with the cylinder wake test case at $r/D=5$, Fig. 16 shows the resolved turbulence from a grid-convergence exercise of traditional LES solutions. Additionally, the approximations of the circumferential and spanwise components of the convective derivative were switched to fourth-order compact differences. The base grid $161\times121\times32$ appears to produce a cutoff wave number ($\hat{k}_c=0.0363$) within the inertial subrange of the energy spectrum, but still indicates substantial damping of the finest resolved scales. The corresponding uncertainty estimate of the matched profile based on the conventional expression is $\hat{\delta}_1^1=25\%$, which is still far removed from the actual error $\hat{\delta}_1^e=42\%$ [Fig. 16(*b*)]. Increasing the spatial resolution by over 10% ($161\times133\times32$ grid) only slightly lowered these values to $\hat{\delta}_1^1=20\%$ and $\hat{\delta}_1^e=35\%$, respectively. By nearly doubling the circumferential grid points and carefully clustering them within the near wake ($\hat{k}_c=0.134$), both the uncertainty estimate and actual error of the streamwise intensity ($\hat{u}_{\text{rms}}$) averaged along line $r/D=5$ fall below 6%.

Once two solutions at different grid resolutions are available, the second expression [Eq. (10)] is preferred for estimating the numerical uncertainty. Completing the spectrum profile is not necessary to estimate $\hat{\delta}_1^2$. The parameters $p=2$ (second order) and $\hat{r}=1.11$ of the first spatial refinement substantially improved the uncertainty estimate ($\hat{\delta}_1^2=27\%$) of the streamwise intensity when compared to $\hat{\delta}_1^e=35\%$. Both of these values are plotted in Fig. 16(*b*) along with those of the finest grid, where the second expression clearly estimated the numerical uncertainty closer to the actual error; 4% and 5.3%, respectively. This latter grid refinement actually mimics the circumferential spacing needed to perform the DNS computation in the cylinder formation region (Fig. 12). As noted earlier, spatial refinement suggests a logarithmic decrease of uncertainty, starting from high unacceptable levels followed by asymptotic reductions when $\hat{\delta}_1<10\%$.

Final Remarks

Too often LES results serve a practical purpose without an estimate of their numerical uncertainty. This deficiency is not unforeseen because the uncertainty expressions offered for general CFD solutions are far too expensive for the LES methodology in light of the user effort and CPU time required to conduct grid-refinement studies *a posteriori*. Whereas sound *a priori* strategies have been established for error reduction of LES solutions, they typically view the volume-averaged global character of uncertainty and may be tainted by local regions of poor resolution. Herein, the graphical exercises for quantifying the numerical uncertainty of practical LES computations are local and executed before collecting the instantaneous results toward statistical steady state. *A priori* checks of numerical uncertainty are possible throughout the specific flow domain of interest by utilizing the dimensionless turbulent properties as given by the area under the respective wave number spectrum. Although the present token examples focused essentially on the numerical uncertainty of the turbulence intensity, other turbulent properties are certainly open for analogous studies. Gauging the turbulent quantities is practical because they reflect the accumulated error whose many specific contributors may be of opposite sign. Realistically, this exercise can offer a local assessment of the LES solution strategies toward the total error reduction.

Assessing the numerical uncertainties of a particular LES computation prior to its path toward statistical steady state lends both qualitative and quantitative confidence in the final results. One can observe whether resolution of the energy range wave numbers are satisfied while gaining insight into the uncertainties expected of the resolved statistical quantities. Working with a single LES so-

lution requires completion of the resolved spectrum by the DK model, and ultimately gives a minimum conventional estimate. The limited testing herein showed that excessive damping (or prior cutoff) of the resolved energy range spectra lead to very high levels of numerical uncertainty in the primary turbulent quantities and demands a correction before continuing the computation. With generation of a second solution, the expression founded on Richardson Extrapolation will give much better estimates of the actual error in the final turbulent statistics.

A notable caution of the proposed graphical exercise recognizes the inability of the DK model to characterize the low-wave number spectra of turbulent regions holding strong anisotropy. Fits between the resolved and DK model profiles are smooth and reliable when the low-wave number anisotropic scales through the energy range are adequately resolved largely by the solution strategy. Driscoll and Kennedy [17] illustrated this fact by adequately fitting their model to the measurements outside the energy range of a circular jet ($R_\lambda = 540$), where the flow was still anisotropic. With this perception in mind, the process should not be hampered by high-Re flows. Broadband separation of the energy and dissipation scales that are indicative of high-Re turbulence calls for a dominant participation from the DK model, principally through the inertial subrange. Finally, one should note that the proposed exercise for quantifying the numerical uncertainty in LES solutions requires subsequent testing over a wider variety of turbulent flows. Moreover, the evaluations should demonstrate a high correlation with the recommended tactics, leading to a global error reduction.

Acknowledgments

The author gratefully acknowledges the support of the Office of Naval Research (Dr. Ronald D. Joslin, Program Officers), Contract No. N0001404WX20106. The computational work was supported in part by a grant of HPCMP resources from the Arctic Region Supercomputing Center (ARSC) and the Naval Oceanographic Office Major Shared Resource Center (NAVO MRSC).

References

[1] Ghosal, S., 1995, "Analysis of Discretization Errors in LES," *Annual Research Briefs*, Center for Turbulence Research, Stanford University, pp. 3–24.
[2] Meyers, J., Geurts, B. J., and Baelmans, M., 2003, "Database Analysis of Errors in Large-Eddy Simulation," Phys. Fluids, **15**, pp. 2740–2755.
[3] Rogallo, R. S., and Moin, P., 1984, "Numerical Simulation of Turbulent Flows," Annu. Rev. Fluid Mech., **16**, pp. 99–137.
[4] Leonard, A., 1974, "Energy Cascade in Large-Eddy Simulations of Turbulent Fluid Flows," Adv. Geophys., **18A**, pp. 237–248.
[5] Love, M. D., and Leslie, D. C., 1979, "Studies of Subgrid Scale Modeling with Classical Closures and Burgers Equation," *Turbulent Shear Flows I*, Springer-Verlag, Berlin, pp. 352–369.
[6] Lund, T. S., 1997, "On the Use of Discrete Filters for Large-Eddy Simulation," *Annual Research Briefs*, Center for Turbulence Research, Stanford University, pp. 83–95.
[7] Gullbrand, J., 2002, "Grid-Independent Large-Eddy Simulation in Turbulent Channel Flow Using Three-Dimensional Explicit Filtering," *Annual Research Briefs*, Center for Turbulence Research, Stanford University, pp. 167–178.
[8] Antonopoulos-Domis, M., 1981, "Large-Eddy Simulation of a Passive Scalar in Isotropic Turbulence," J. Fluid Mech., **104**, pp. 55–79.
[9] Chow, F. K., and Moin, P., 2003, "A Further Study of Numerical Errors in Large-Eddy Simulations," J. Comput. Phys., **184**, pp. 366–380.
[10] Roache, P. J., 1994, "Perspective: A Method for Uniform Reporting of Grid Refinement Studies," J. Fluids Eng., **148**, pp. 322–340.
[11] Mehta, U. B., 1991, "Some Aspects of Uncertainty in Computational Fluid Dynamics Results," ASME J. Fluids Eng., **113**, pp. 538–543.
[12] Celik, I., Chen, C. J., Roache, P. J., and Scheuerer, G., 1993, *Symposium on Quantification of Uncertainty in Computational Fluids Dynamic*, FED Vol. 158, ASME Fluids Engineering Division Summer Meeting, Washington, DC, 20–24 June.
[13] Deardoff, J. W., 1970, "A Numerical Study of Three-Dimensional Turbulent Channel Flow at Large Reynolds Number," J. Fluid Mech., **41**, pp. 453–480.
[14] Jordan, S. A., 1999, "A Large-Eddy Simulation Methodology in Generalized Curvilinear Coordinates," J. Comput. Phys., **148**, pp. 322–340.
[15] Thompson, J. F., Warsi, Z. U. A., and Mastin, C. W., 1985, *Numerical Grid Generation*, Elsevier Science, New York.
[16] Jordan, S. A., 2003, "Resolving Turbulent Wakes," J. Fluids Eng., **125**, pp. 823–834.
[17] Driscoll, R. J., and Kennedy, L. A., 1983, "A Model for the Turbulent Energy Spectrum," Phys. Fluids, **26**, pp. 1228–1233.
[18] Travin, A., Shur, M., Strelets, M., and Spalart, P., 1999, "Detached-Eddy Simulation Past a Circular Cylinder," Flow, Turbul. Combust., **63**, pp. 293–313.
[19] Comte-Bellot, G., and Corrin, S., 1971, "Space Eulerian Time Correlation of Full- and Narrow-Band Velocity Signals in Grid-Generated, 'Isotropic' Turbulence," J. Fluid Mech., **48**, pp. 273–337.
[20] Geurts, B. J., and Frohlich, J., 2002, "A Framework for Predicting Accuracy Limitations in Large-Eddy Simulation," Phys. Fluids, **14**, pp. L41–L44.
[21] Mansour, N. N., Moin, P., Reynolds, W. C., and Ferizer, J. H., 1979, "Improved Methods for Large-Eddy Simulation of Turbulence," *Turbulent Shear Flows I*, Springer-Verlag, Berlin, pp. 188–199.
[22] Ferziger, J. H., 1977, "Large Eddy Simulation of Turbulent Flows," AIAA J., **15**, pp. 1261–1267.
[23] Fureby, C., Tabor, G., Weller, H. G., and Gosman, A. D., 1996, "A Comparative Study of Subgrid Scale Models in Homogeneous Isotropic Turbulence," Phys. Fluids, **9**, pp. 1416–1429.
[24] Chasnov, J. R., 1991, "Simulation of the Kolmorgorov Inertial Subrange Using an Improved Subgrid Model," Phys. Fluids A, **3**, pp. 188–199.
[25] Kim, J., Moin, P., and Moser, R. D., 1987, "Turbulent Statistics in Fully Developed Channel Flow at Low Reynolds Number," J. Fluid Mech., **177**, pp. 133–166.
[26] Poimelli, U., Ferziger, J. H., and Moin, P., 1987, "Models For Large Eddy Simulations of Turbulent Channel Flows Including Transpiration," Report TF-32, Stanford University.
[27] Jordan, S. A., 2001, "Dynamic Subgrid-Scale Modeling for Large-Eddy Simulations in Complex Topologies," J. Fluids Eng., **123**, pp. 1–10.
[28] Ong, L., and Wallace, J., 1996, "The Velocity Field of the Turbulent Very Near Wake of a Circular Cylinder," Exp. Fluids, **333**, pp. 375–402.
[29] Beaudan, P., and Moin, P., 1994, "Numerical Experiments on the Flow Past a Circular Cylinder at Sub-Critical Reynolds Number," Report No. TF-62, Stanford, University, Stanford, CA.

A Practical Combined Computation Method of Mean Through-Flow for 3D Inverse Design of Hydraulic Turbomachinery Blades

Guoyi Peng
Assistant Professor
Department of Mechanical Systems Engineering,
Toyama Prefectural University,
Toyama, 939-0398, Japan
e-mail: peng@pu-toyama.ac.jp

A practical combined computation method of the circumferentially averaged mean through-flow is presented for 3D inverse computations of hydraulic turbomachinery blades to consider the influence of interrelated hydraulic components. A comprehensive computation domain including the runner blades and related components is adopted and the mean flow is calculated altogether by solving a set of rotational flow governing equations simultaneously. The method has been applied to the case of Kaplan turbine. Computational results were compared to experimental data and their agreement was confirmed. Numerical investigation indicates that the mean flow is dependent on the configuration of guide vanes and the effect of runner blades reaches to the far upstream. The importance of properly taking account of the effect of blade geometry and the influence of interrelated hydraulic components is demonstrated. [DOI: 10.1115/1.2062787]

1 Introduction

With great advances in computational fluid dynamics (CFD) and rapid increasing of computing capacity, the numerical simulation gets to be used as a common tool of direct flow analysis in turbomachinery, and is frequently used to predict the performance of turbomachinery runner a/or impeller under design and off-design conditions, where unfavorable flow phenomena such as flow separation may take place against the influence of an adverse pressure gradient, by solving Reynolds averaged Navier-Stokes equations [1–3]. It becomes also possible to investigate the interaction of rotational runner blades and related stationary hydraulic components by simultaneous computation of flow passing through different flow regions [4,5]. However, the direct flow analysis of CFD does not directly propose a blade geometry generating favorable flow pattern. Although it is possible to search out a blade geometry through iterative computations of blade geometry modification and direct flow analysis for different geometry by applying three dimensional Navier-Stokes solutions [6] as well as optimization approaches such as sensitive evaluations [7,8] and genetic algorithm [9], the so-called direct method is time consuming for the difficulty to define a well-purposed blade geometry modification from varying parameters of flow field in practical blade design. So, global optimization framework utilizing statistical training data was developed to save the computation cost by combining the neural network and the polynomial-based response surface method [10,11]. On the other hand, despite the great advance in direct flow analysis the real inverse methods by which the geometry of blades is directly calculated according to design specifications of flow features given as input is still dependent on empiricism still as stated in Refs. [12,13] because, for one reason, so many of design parameters is usually defined semiempirically and, for another reason, inverse methods so far developed treat the runner a/o impeller as an isolated component and the necessary boundary conditions of inflow and outflow are given empirically according to statistical data [12–14]. In this way the flow passing through interrelated components of turbomachinery is treated separately and the influence of interrelated hydraulic components is neglected. In most cases of turbomachinery such as axial flow hydraulic turbines the runner a/o impeller is usually located in an irregular flow passage. The inflow and the outflow of runner a/o impeller are dependent on the configuration of interrelated hydraulic components and further affected by the geometry of blades [15–17]. As the blade geometry is an unknown parameter to be found in the inverse problem it becomes a difficult work to exactly define essential inflow a/o outflow conditions for inverse computation of runner blades.

Regarding to the case of hydraulic turbines, the runner is tightly set between the wicket gate and the draft tube. The inlet and the outlet of runner blades locate in areas where the flow is far from uniform. In conventional computations treating the runner separately the inflow and the outflow conditions of runner blades are usually defined empirically according to certain experimental statistic data. Due to the limitation of experimental data it is nearly impossible to obtain all experimental data for various runner blades. Especially for the inverse problem of blade geometry design, there is no exact experimental data can be referenced since the geometry of blades, which is highly influential in the inflow and the outflow, is quite an unknown parameter to be calculated. In addition, the inflow is also dependent on the geometry of flow passage and the configuration of guide vanes. It is essential to take account of the effect of related components such as guide vanes in order to design a better runner with good performance.

Concerning the inverse design of turbomachinery blades many papers were published in past years and available three-dimensional (3D) models developed may be mainly classified into two categories of quasi-3D (Q3D) and fully-3D (F3D) ones. For the difficulty of inverse problem these models were developed basically under assumption of inviscid flow considering that the effect of fluid viscosity mainly dominates in a thin layer near to solid boundaries in actual machines [18]. Based on Wu's theory of two-type stream surfaces [19,20], Q3D inverse models such as Refs. [21,22] were developed by iterative calculation of a mean hub-to-tip (S_{2m}) stream surface and a series of blade-to-blade (S_1) stream surfaces. Q3D inverse methods based on S_1 surface or S_{2m}

Contributed by the Fluids Engineering Division for publication in the JOURNAL OF FLUIDS ENGINEERING. Manuscript received by the Fluids Engineering Division January 23, 2004; final manuscript received July 1, 2005. Associate Editor: Jinkook Lee.

surface were extended to various type of turbomachinery [13,23,24]. With the combined method of predictive calculation on S_{2m} surface and corrective design on S_1 surface [24] the iterative computation time was reduced also. In order to consider the effect of circumferential flow fully-3D models such as Refs. [25,26] were developed based on Tan et al.'s works [27], where the 3D flow is decomposed into a circumferentially averaged mean flow and a circumferential periodic flow by using of the Clebsh formula. The F3D method was extended to many extended cases [28–30] and an inviscid-viscous interaction method was developed by introducing viscous effect indirectly considering the effect of viscosity in low specific speed impeller [14]. According to above descriptions we understand that both Q3D and F3D inverse methods for blade design of turbomachinery are based on a representative mean through flow, and the determination of mean flow becomes a primary problem that exerts a direct influence on the accuracy of inverse computation. On the other hand, the interaction between rotational runner a/o impeller blades and related stator vanes may be split into an unsteady component working in the circumferentially periodic flow and a steady component, which works in the mean through flow and has a main influence on the steady performance of runner blades. Under this background the present work has made a try to take account of the steady component of the interaction between rotor blades and stator vanes in the inverse design of blade geometry by improving the computation of mean through flow.

The particular attention of present paper is focused on the methodology of mean through-flow computation and a combined computation method (CCM-S_{2m}) of the circumferentially averaged mean flow is proposed for the 3D inverse computations of hydraulic turbomachinery blades. In order to take account of the interaction of interrelated hydraulic components a comprehensive computation domain including the runner blades and related hydraulic components is adopted, and the circumferentially averaged mean through-flow is calculated as a whole by solving a set of rotational flow governing equations in different regions simultaneously from systematic viewpoint. The difficulty of defining inflow a/o outflow condition of runner blades encountered in conventional computations, then, is surmounted consequently. The method has been applied to the case of Kaplan hydraulic turbine where the flow passage turns sharply from the radial to the axial direction. Computational results of spiral flow in bladeless passage were compared to experimental data and the reliability was proved by their good agreement. The interaction between interrelated hydraulic components was further investigated numerically. The result reveals that the mean flow through Kaplan blades is dependent on the configuration of guide vanes and the effect of runner blades reaches to the far upstream. The importance of properly taking account of the effect of blade geometry and the influence of interrelated hydraulic components in the inverse design of runner blades is demonstrated.

2 Mathematical Model of Circumferentially Averaged Mean Flow Computation

Figure 1 shows the scheme of hydraulic turbomachinery to be researched, where a relative cylindrical coordinate system denoted by (r,θ,z) and a relative orthogonal curvilinear coordinate system denoted by $(x_1,x_2,x_3=\theta)$ are adopted. For defining of representative mean through-flow a circumferentially averaging operation is defined as follows:

$$\bar{f}=\frac{1}{\theta_p-\theta_s}\int_{\theta_s}^{\theta_p} f(x_1,x_2,x_3=\theta)d\theta \tag{1}$$

where f denotes an arbitrary function of physical quantity. θ_p and θ_s denote the angular coordinate of the pressure surface and the suction surface of two adjacent blades. Related to the average $\bar{f}$, a circumferentially periodic fluctuation $\tilde{f}$ is written to be $\tilde{f}=f-\bar{f}$ and

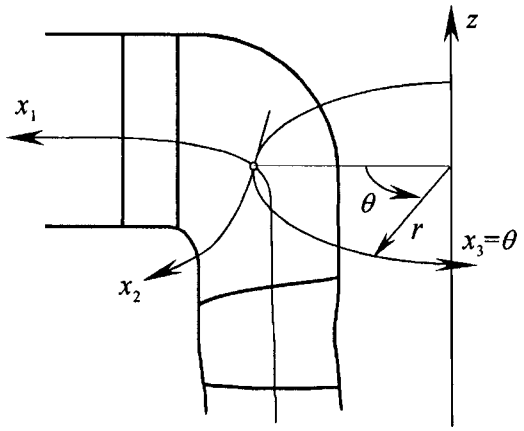

Fig. 1 Curvilinear coordinates relative to hydraulic blades

we understand that $\bar{\tilde{f}}\equiv 0$. Based on the definition given above the average of a partial difference in the general curvilinear coordinates is derived as follows:

$$\overline{\frac{\partial f}{\partial x_i}}=\frac{\partial(\Theta\bar{f})}{\Theta\partial x_i}-\frac{1}{\Theta}\Delta_{ps}\left(f(x_1,x_2,\theta)\frac{\partial\theta}{\partial x_i}\right) \tag{2}$$

where $i=1,2$ and $\Theta=\theta_p-\theta_s$, which denotes the angular distance of two adjacent blades. Δ_{ps} is an operator here giving the difference of a function from the suction surface to the pressure surface. Concerning the gradient of blade surface, any one of the pressure or the suction blade surface is expressed by the following covert function,

$$S(x_1,x_2,x_3=\theta)=x_3-\theta(x_1,x_2)=0 \tag{3}$$

Its normal vector $\boldsymbol{n}$ lies in the direction of gradient ∇S, and they may be related by following equations:

$$\frac{n_1}{\partial S/(h_1\partial x_1)}=\frac{n_2}{\partial S/(h_2\partial x_2)}=\frac{n_3}{\partial S/(h_3\partial x_3)} \tag{4}$$

where n_1, n_2, n_2 and n_3 denote three components of $\boldsymbol{n}$, and h_1, h_2, and h_3 do three metric-scale factors called Lame coefficient in coordinate directions, respectively. According to the covert function given in Eq. (3) the gradients of blade surface (pressure a/o suction) are then derived as follows:

$$\frac{\partial\theta}{\partial x_i}=-\frac{h_i n_i}{h_3 n_3} \tag{5}$$

Thus, the average of partial differences is written into following unified form by taking Eq. (5) into Eq. (2) in consideration of that $\partial\bar{f}/\partial\theta=0$,

$$\overline{\frac{\partial f}{\partial x_i}}=\frac{\partial(\Theta\bar{f})}{\Theta\partial x_i}+\frac{h_i}{\Theta h_3 n_3}\Delta_{ps}(f(x_1,x_2,x_3=\theta)n_i),\quad (i=1,2,3) \tag{6}$$

2.1 Mean Flow Governing Equations in Blade Region. Concerning the flow in hydraulic turbomachinery experimental results demonstrated that the effect of fluid viscosity is limited within a thin layer near solid walls and its influence on the global flow property is very small [18]. Following to the actual state of 3D inverse design computation the assumption of inviscid flow is adopted here and the viscous effect in thin boundary layer is neglected also [31]. Then the continuity and momentum equations of relatively steady three-dimensional rotational flow in hydraulic blades are given as follows:

$$\nabla\cdot\boldsymbol{w}=0 \tag{7}$$

$$\boldsymbol{w} \times (\nabla \times \boldsymbol{v}) = \nabla E_r \tag{8}$$

in which

$$E_r = E_i - \omega v_\theta r$$

where E_r denotes the relative total enthalpy per unit mass. $E_i = v^2/2 + p/\rho + gz$ does the absolute enthalpy per unit mass determined by the inflow, which is nearly a constant at the far inlet of wicket gate. Applying the circumferentially averaging operation to Eq. (7) and introducing Eq. (6) we obtain the following continuity equation of averaged mean flow considering the fact that the relative velocity aligns with the pressure surface or the suction surface of blade everywhere,

$$\nabla \cdot (B_f \bar{\boldsymbol{w}}] = 0 \tag{9}$$

where $B_f = N_b(\theta_p - \theta_s)/2\pi$, and it represents the blockage coefficient of blades. According to above equation a stream function for the averaged mean flow is then defined as follows:

$$\frac{\partial \psi}{\partial x_1} = B_f h_2 h_3 \bar{w}_1, \quad \frac{\partial \psi}{\partial x_2} = -B_f h_1 h_3 \bar{w}_2 \tag{10}$$

Next, the circumferentially averaging operation is applied to Eq. (8) similarly and the following equation is then derived:

$$\bar{\boldsymbol{w}} \times (\overline{\nabla \times \boldsymbol{v}}) + \overline{\tilde{\boldsymbol{w}} \times \tilde{\Omega}} = \overline{\nabla E_r} \tag{11}$$

where $\Omega = \nabla v$ and $\tilde{\Omega}$ denotes the circumferentially periodic component of flow vorticity. The second term represents the contribution of circumferential flow fluctuation to the mean flow, which is the average of the production of two circumferentially fluctuating variables whose average closes to zero. It is a high order small value compared to the first term on the left-hand side and thought to be negligible. Rewriting the above equation into the differential form and introducing Eq. (6) we obtain the following equation arranged in vector form:

$$\bar{\boldsymbol{w}} \times (\nabla \times \bar{\boldsymbol{v}}) = -\boldsymbol{F}_b + \nabla \bar{E}_r \tag{12}$$

where

$$\boldsymbol{F}_b = \frac{1}{\Theta h_3 n_3} \bar{\boldsymbol{w}} \times \Delta_{ps}(\boldsymbol{n} \times \tilde{\boldsymbol{v}})$$

The term represents the action of runner blades to the circumferentially averaged mean flow, and it may be understood to be a blade force uniformly acted on per unit mass of working fluid. Since the compound vector $\bar{\boldsymbol{w}} \times (\boldsymbol{n} \times \tilde{\boldsymbol{v}})$ lays in the direction of $\boldsymbol{n}$, the unit normal of blade surface, $\boldsymbol{F}_b$ is known to be the blade force [31] working in the normal direction of mean stream surface approximately.

Similarly, we may express the mean stream surface in the following form of covert function:

$$S_{2m}(x_1, x_2, x_3 = \theta) = \theta - \varphi(x_1, x_2) \tag{13}$$

where $\varphi(x_1, x_2)$ denotes the angular coordinate of mean stream surface. The unit normal vector of the mean stream surface is then given to be,

$$\boldsymbol{n}_m = \nabla S_{2m} / |\nabla S_{2m}| \tag{14}$$

Multiplying Eq. (12) by the above normal vector we may project the governing equation into the mean stream surface, and its expression is simplified to the following form for the fact that $\boldsymbol{F}_b \times \boldsymbol{n}_m \approx 0$.

$$[\bar{\boldsymbol{w}} \times (\nabla \times \bar{\boldsymbol{v}})] \times \boldsymbol{n}_m = \nabla \bar{E}_r \times \boldsymbol{n}_m \tag{15}$$

According to the principle of vector analysis the left-hand side may be written to,

$$[\bar{\boldsymbol{w}} \times (\nabla \times \bar{\boldsymbol{v}})] \times \boldsymbol{n}_m = (\bar{\boldsymbol{w}} \cdot \boldsymbol{n}_m) \nabla \times \bar{\boldsymbol{v}} - [(\nabla \times \bar{\boldsymbol{v}}) \cdot \boldsymbol{n}_m] \bar{\boldsymbol{w}} \tag{16}$$

in which $\bar{\boldsymbol{w}} \cdot \boldsymbol{n}_m = 0$ since the relative mean velocity aligns with the mean stream surface everywhere. Taking Eq. (16) into Eq. (15) and then multiplying Eq. (15) by $\bar{\boldsymbol{w}}$ we further project the equation to the relative flow direction, and then it is simplified to,

$$-(\nabla \times \bar{\boldsymbol{v}}) \cdot \boldsymbol{n}_m = [(\nabla \bar{E}_r \times \boldsymbol{n}_m) \cdot \bar{\boldsymbol{w}}]/w^2 \tag{17}$$

Introducing Eq. (14) and arranging above equation we obtain the following partial difference equation given in the general coordinate system $(x_1, x_2, x_3 = \theta)$,

$$\frac{1}{h_1 h_2}\left(\frac{\partial(h_1 \bar{v}_1)}{\partial x_2} - \frac{\partial(h_2 \bar{v}_2)}{\partial x_1}\right) = \frac{h_3 \partial \varphi}{h_2 \partial x_2}\frac{\partial(h_3 \bar{v}_3)}{h_3 h_1 \partial x_1} - \frac{h_3 \partial \varphi}{h_1 \partial x_1}\frac{\partial(h_3 \bar{v}_3)}{h_3 h_2 \partial x_2} + \frac{1}{\bar{w}^2}\left[\frac{\partial \bar{E}_r}{h_1 \partial x_1}\left(-\bar{w}_3 \frac{h_3 \partial \varphi}{h_2 \partial x_2} - \bar{w}_2\right) - \frac{\partial \bar{E}_r}{h_2 \partial x_2}\left(-\bar{w}_3 \frac{h_3 \partial \varphi}{h_1 \partial x_1} - \bar{w}_1\right)\right] \tag{18}$$

In the right-handed cylindrical coordinates (z, r, θ) where the Lami coefficients are known to be that $(h_1 = 1,\ h_2 = 1,\ h_3 = r)$, the equation is written as follows:

$$\frac{\partial \bar{w}_z}{\partial r} - \frac{\partial \bar{w}_r}{\partial z} = \frac{\partial \varphi}{\partial r}\frac{\partial(\bar{v}_\theta r)}{\partial z} - \frac{\partial \varphi}{\partial z}\frac{\partial(\bar{v}_\theta r)}{\partial r} + \frac{1}{\bar{w}^2}\left[\frac{\partial \bar{E}_r}{\partial r}\left(\bar{w}_r + \bar{w}_\theta \frac{r \partial \varphi}{\partial z}\right) - \frac{\partial \bar{E}_r}{\partial z}\left(\bar{w}_r + \bar{w}_\theta \frac{r \partial \varphi}{\partial r}\right)\right] \tag{19}$$

where $\bar{w}^2 = \bar{w}_r^2 + \bar{w}_\theta^2 + \bar{w}_z^2$. The parameter $(\bar{v}_\theta r)$ is called the mean swirl velocity or the mean velocity torque, which is usually defined as design specification of inverse computation. By introducing the stream function defined in Eq. (10), the following stream function equation governing the mean through-flow in blade region is derived:

$$\frac{\partial}{\partial r}\left(\frac{1}{r B_f}\frac{\partial \psi}{\partial r}\right) + \frac{\partial}{\partial z}\left(\frac{1}{r B_f}\frac{\partial \psi}{\partial z}\right) = \frac{\partial \varphi}{\partial r}\frac{\partial(\bar{v}_\theta r)}{\partial z} - \frac{\partial \varphi}{\partial z}\frac{\partial(\bar{v}_\theta r)}{\partial r} + \frac{1}{\bar{w}^2}\left[\frac{\partial \bar{E}_r}{\partial r}\left(\bar{w}_r + \bar{w}_\theta \frac{r \partial \varphi}{\partial z}\right) - \frac{\partial \bar{E}_r}{\partial z}\left(\bar{w}_r + \bar{w}_\theta \frac{r \partial \varphi}{\partial r}\right)\right] \tag{20}$$

This elliptic partial difference equation should be solved subjected to boundary conditions at the tip and hub walls as well as given flow conditions at the inlet and outlet of runner blades. As stated in the preceding section the inflow a/o outflow of runner blades are not only dependent on the configuration of related hydraulic components but also influenced by the geometry of blades to be designed. To surmount this difficulty and take account of the interaction of related components a comprehensive computation domain including the rotational runner blades and stationary guide vanes is adopted and the mean flow through different flow regions is calculated as a whole.

2.2 Mean Flow Governing Equation in Region of Guide Vanes. As for the flow passing through stationary guide vanes, the rotational speed of blade system reduces to zero. So, the enthalpy per unit mass keeps to a constant everywhere although the swirl velocity varies under the action of guide vanes. According to Eqs. (9) and (12) then mean flow governing equation in region of stationary guide vanes is derived as follows similarly:

$$\frac{\partial}{\partial r}\left(\frac{1}{rB_f}\frac{\partial \psi}{\partial r}\right)+\frac{\partial}{\partial z}\left(\frac{1}{rB_f}\frac{\partial \psi}{\partial z}\right)=\frac{\partial \varphi}{\partial r}\frac{\partial(\bar{v}_\theta r)}{\partial z}-\frac{\partial \varphi}{\partial z}\frac{\partial(\bar{v}_\theta r)}{\partial r} \quad (21)$$

Here φ denotes the angular coordinate of mean stream surface, which is approximately parallel to the mean surface of guide vane. B_f does the blockage coefficient of guide vanes.

2.3 Mean Flow Governing Equation in Bladeless Region. In a bladeless region of flow passage, the working fluid receives no external action. The enthalpy of per unit mass is approximately constant everywhere in this area. Thus, the absolute flow in the bladeless region becomes a spiral flow, and the equation of motion is known to be $\boldsymbol{v}\times(\nabla\times\boldsymbol{v})=0$. Taking the averaging operation similarly, we obtain the following mean flow governing equation in the same form:

$$\bar{\boldsymbol{v}}\times(\nabla\times\bar{\boldsymbol{v}})=0 \quad (22)$$

This vector equation can be written to scalar ones in three coordinate directions, and the flow governing equation in meridional surface is derived as follow by arranging flow equations in x_1 and x_2 directions.

$$(\bar{v}_1^2+\bar{v}_2^2)\mathrm{rot}_3\,\bar{\boldsymbol{v}}-\bar{v}_3^2(\bar{v}_2\,\mathrm{rot}_2\,\bar{\boldsymbol{v}}+\bar{v}_1\,\mathrm{rot}_1\,\bar{\boldsymbol{v}})=0 \quad (23)$$

where rot denotes the curl operator of a vector. Referencing the stream function given by Eq. (9) where the blade blockage coefficient becomes 1.0 in the bladeless region, we derive the mean flow governing equation in the bladeless region as follows:

$$\frac{\partial}{\partial r}\left(\frac{1}{r}\frac{\partial \psi}{\partial r}\right)+\frac{\partial}{\partial z}\left(\frac{1}{r}\frac{\partial \psi}{\partial z}\right)=\frac{\bar{v}_\theta r}{\bar{v}_m^2 r^2}\left(\bar{v}_r\frac{\partial(\bar{v}_\theta r)}{\partial z}-\bar{v}_z\frac{\partial(\bar{v}_\theta r)}{\partial r}\right) \quad (24)$$

where $\bar{v}_m^2=\bar{v}_r^2+\bar{v}_z^2$, represents the mean meridional velocity. This equation includes an unknown parameter $\bar{v}_\theta r$ and one more equation is needed to close it. This requirement can be met by using the other scalar equation of Eq. (22) in the circumferential direction, which is written to be,

$$\bar{v}_1\,\mathrm{rot}_2\,\bar{\boldsymbol{v}}-\bar{v}_2\,\mathrm{rot}_1\,\bar{\boldsymbol{v}}=0 \quad (25)$$

By employing a local orthogonal curvilinear coordinates ($x_1=m$, x_2, $x_3=\theta$), where m is a coordinate long meridional streamlines of the mean flow and x_2 does the orthogonal one, the above equation is simplified to the following form:

$$d(\bar{v}_\theta r)/dm=0 \quad (26)$$

It means that the angular momentum of per unit mass is a constant along streamline in the bladeless region. Then, the distribution of $\bar{v}_\theta r$ can be determined along streamlines according to its initial values prescribed at the inlet boundary. As the distribution of streamlines depends on the computation result Eq. (24) should be solved iteratively.

2.4 Closure of Mean Flow Governing Equations. Equation (20) of the mean flow in blade region includes six variables of ψ, $\bar{w}_z$, $\bar{w}_r$, $\bar{w}_\theta$, φ, and $\bar{v}_\theta r$. Considering Eq. (10) and the relation that $\bar{v}_\theta=\bar{w}_\theta+\omega r$, we know that the equation contain three independent variables, ψ, φ, and $\bar{v}_\theta r$ only. For the positive problem of flow simulation $\bar{v}_\theta r$ is an unknown parameter but the angular coordinate $\varphi(r,z)$ of mean stream surface, which is close to the blade camber geometry, is a given parameter. For the inverse problem φ is an unknown variable to be found but $\bar{v}_\theta r$ is defined as a design specification instead. Thus, Eq. (20) contains two independent variables and one additional equation is needed to close it properly. Equation (21) does also. This requirement can be met by introducing the equation of mean stream surface where the local relative velocity should always align with the stream surface, which is written to be $\bar{\boldsymbol{w}}\cdot\nabla S_{2m}=0$. From that we obtain the following equation of mean stream surface relating φ and $\bar{v}_\theta r$,

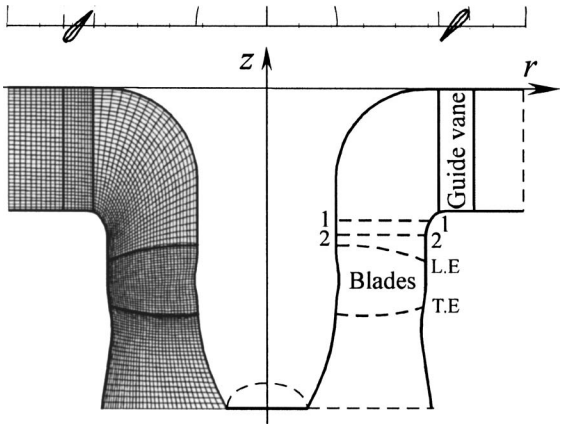

Fig. 2 Schematic diagram of computation configuration and computational grid

$$\bar{w}_r\frac{\partial \varphi}{\partial r}+\bar{w}_z\frac{\partial \varphi}{\partial z}=\frac{1}{r^2}(\bar{v}_\theta r-\omega r^2) \quad (27)$$

For the convenience of numerical computation, it is often written in the flowing form along streamline.

$$\bar{w}_m r^2\frac{d\varphi}{dm}=\bar{v}_\theta r-\omega r^2 \quad (28)$$

Then the geometry of blade mean surface can be calculated according to the design specification of $\bar{v}_\theta r$ distribution for the inverse problem, or $\bar{v}_\theta r$ can be calculated according to blade geometry for the positive problem.

2.5 Numerical Discretization and Application to 3D Inverse Computation. Equations (20), (21), and (24) constitute a set of equations governing the circumferentially averaged mean through flow. The right-hand side of these equations includes implicit parameters φ (to be calculated in the inverse problem) or $\bar{v}_\theta r$ (to be calculated in the positive problem), and they should be solved iteratively. These equations are two-dimensional ones concerning r and z only and can be solved numerically in the meridional surface. Considering the stability of numerical computation these elliptic equations were solved by finite element method here. A structure mesh of eight-node quadrilateral elements was employed and the partial differential equations of stream function were discretized by Galerkin's weighted integral method using the dual quadratic polynomial interpolation, which is proved to be of the second order accuracy of element size [32].

The above combined computation procedure calculate the circumferentially averaged mean flow through thurbomachinery by solving a set of governing equations in different flow regions simultaneously. The method is more reasonable and easily applicable to Q3D and F3D inverse computations. The present procedure may be directly applied to fully-3D models calculating 3D internal flow by superposition of a mean through flow and a circumferentially periodic flow [28,29]. By taking the circumferentially averaged flow as a representative S_{2m} flow the present procedure can be easily introduced into quasi-3D inverse models calculating 3D internal flow through iterations of a mean S_{2m} stream surface and a series of symmetric S_1 stream surfaces evaluating the circumferential flow property [24].

3 Computation Results and Discussion

The described procedure was applied to the case of a high specific speed Kaplan blades. Figure 2 shows a schematic configuration of the Kaplan turbine system, where the meridional passage turning sharply from the radial direction to the axial direction and the flow out of guide vanes is strong rotational. Basic working

parameters of under the design condition are given to be that: the volumetric flow rate $Q=0.21\ m^3/s$, the rotational frequency $\omega=1.95\ s^{-1}$ for a model runner whose diameter $D=1.0$ m, and working head $H=1.0$ m. As for the geometry configuration the diameter of pitch circle for guide vane distribution $D_0=1.16D$ and the height of guide vane (span length) $B_0=0.375D$. The guide vane is standard symmetric one and the opening of wicket gate is about 35%. A general computation domain was taken from the far upstream of the wicket gate to the far downstream of runner blades and a body fitted grid arrangement was employed as shown in Fig. 2. The number of runner blades was selected to be $N_b=6$ according to statistic data, and the geometry shape of blades was designed by iteration computations of the mean through flow with a series of S_1 surfaces. For the comprehensive computation domain a given value of stream function was directly defined at the hub and the tip walls. At the inlet in front of guide vanes the flow is approximately in the normal direction and the normal gradient of ψ was given to be zero. At the outlet boundary located in irregular expansion area of flow passage it is difficult to define an exact flow condition directly. In view of the fact that the flow discharges naturally [33] a Neumann condition was imposed by giving that $\partial\psi/\partial n=\bar{v}_r(r)$, where $\bar{v}_r(r)$ is a temporary distribution function of radial velocity component, and the distribution function was adjusted iteratively so as the outflow aligns to the hub and the tip walls.

The mean flow calculation was carried out with body-fitted quadrilateral grids shown in Fig. 2 by under relaxation iteration of meridional streamlines. The convergence criterion was given to be that the relative error of stream function is smaller than the convergence accuracy of $\varepsilon=1.0\times10^{-3}$. Regarding the resolution of computational mesh the effect of cell number density was verified by adjusting the number of element cells. Three kinds of similar computational mesh denoted as A, B, and C, whose total number of cell nodes is, respectively, 51×17, 75×25, and 101×33 in the streamline direction and the quasiorthogonal direction, were used to verify the numerical property. Computational results demonstrated that the numerical error caused by mesh size reduces to below the given convergence accuracy when the total number of cell nodes is increased to 101×33. Thus, grid C with acceptable computation accuracy was adopted hereafter.

3.1 Meridional Spiral Flow Without Effect of Runner Blades. To validate the reliability of present procedure the spiral flow without effect of runner blades was calculated at first, and computational results were compared with experimental data. The computation was performed under the given design condition when a runner is not assembled. Figure 3 shows the computational result of meridional streamline distribution in the case without runner blades by dashed lines. The figure demonstrates that the flow behind wicket gate approaches to the hub wall under the rotational effect of spiral flow. Figures 4(*a*) and 4(*b*) show the distribution of mean velocity in the radial direction at the cross sections 1-1 and 2-2 shown in Fig. 2, where the inflow condition of runner blades is usually defined in conventional computations. The abscissa represents the relative radial position from the hub to the tip and the ordinate does three components of the circumferentially averaged velocity normalized by $\bar{v}_{m0}$, the mean meridional velocity at the inlet of computation domain. The hollow symbols represent computational results obtained with different meshes. The solid symbol represents circumferentially averaged velocity obtained experimentally on a standard water turbine test rig without assembling of model runner [33]. The experiment was performed under given working head and wicket gate opening, and the velocity was measured by Pitot probes with accuracy of ±2.0% from four axisymmetric positions in the cross sections 1-1 and 2-2. The figure demonstrates that computational results converge with increase of node number and coincide with experimental ones except near the hub and the tip walls, where computational results are greater than experimental ones about 2.5%. The

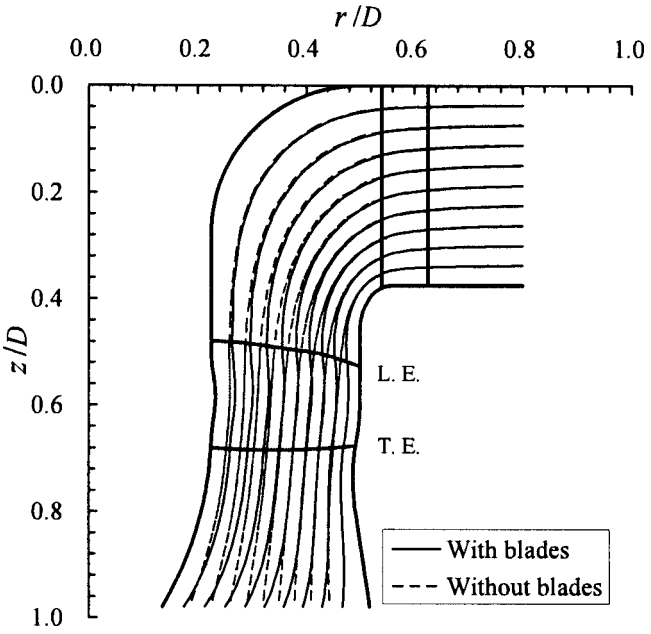

Fig. 3 Distribution of meridional streamline in cases with and without runner blades

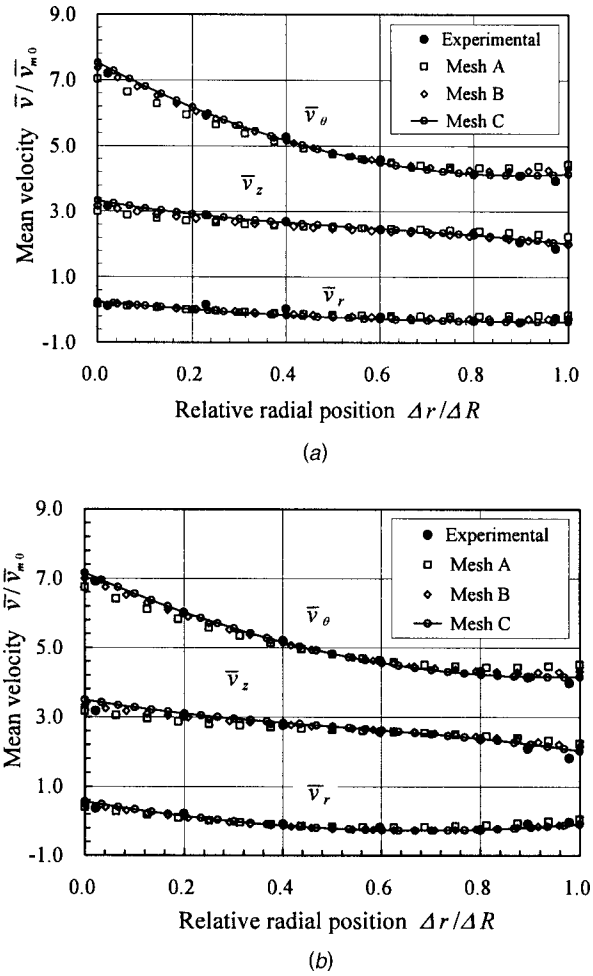

Fig. 4 Comparison of computational results by different meshes and experimental data: distribution of circumferentially averaged mean velocity in the radial direction: (*a*) at section 1-1 and (*b*) at section 2-2

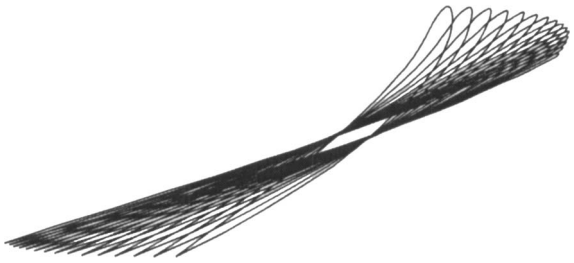

Fig. 5 Blade geometry on cylindrical sections

dispersion may be due to the difficulty of velocity measuring near a solid wall. Thereby, the reliability of numerical computation has been confirmed.

3.2 Effect of Runner Blades. With respect to the effect of runner blades the circumferentially averaged mean flow was further investigated under condition when a runner is assembled to the given position shown in Fig. 2. The runner was designed by quasi-3D inverse method employing the above combined computation procedure of mean through flow. Figure 5 shows the geometry of runner blades calculated for the design specification of swirl velocity distributions shown in Fig. 6 by open circles. As comparison the final mean swirl velocity distribution in the designed runner blades, which was obtained through flow analysis, is shown in Fig. 6 by solid lines. The abscissa s represents the relative streamline cooridnate from leading edge to the trailing edge and the ordinate does the swirl velocity normalized by the average variation of swirl velocity from the inlet to the outlet of runner blades, $\Delta(\bar{v}_\theta r)$. Figure 6 indicates that the swirl velocity distribution coincides with specified one and the designed runner meets the requirement of output well.

Concerning the mean through flow under the effect of runner blades Fig. 3 shows the distribution of meridional streamlines in the case with runner blades by solid lines. The figure indicates that the flow in blade region becomes much uniform under the effect of runner blades compared to the case without runner blades. The alteration of streamlines extends to the upstream of runner blades close to the turn of meridional flow passage. Figures 7(*a*) and 7(*b*) show the variation of meridional velocity along streamlines in cases with and without runner blades, respectively. According to the result we understand that the meridional velocity in the blade region decreases near the hub but increases near the tip under the effect of runner blades. So, the distribution of streamlines becomes much uniform compared to the case without runner blades. However, in the bladeless region behind runner blades the meridional velocity increases intensively near the hub wall for the rotational effect of spiral flow, and the velocity in area near to the boss

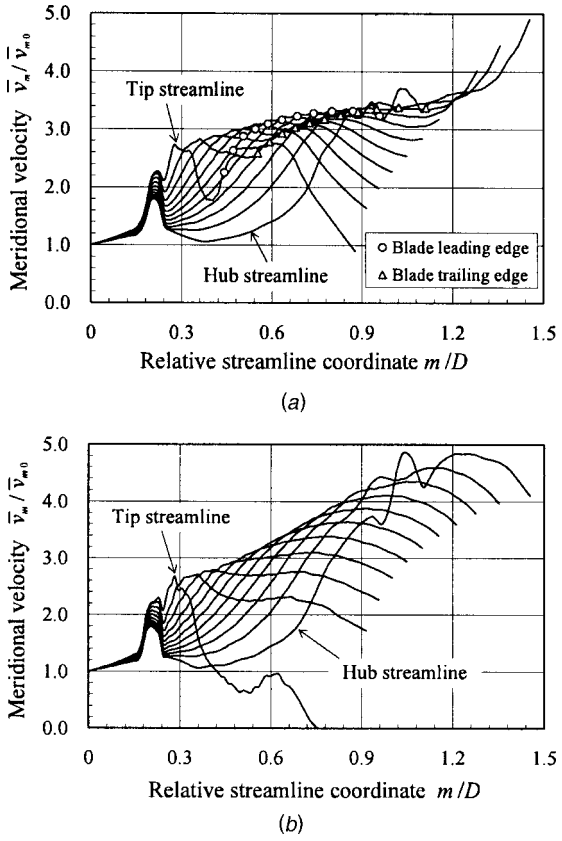

Fig. 7 Distribution of meridional velocity along streamlines in cases with and without the runner blades: (*a*) in the case with runner blades and (*b*) in the case without runner blades

cover becomes much higher. This may be the reason why the cavitation inception is practically easy to take place around the boss cover in Kaplan turbines.

Figure 8 shows the distribution of meridional velocity in the radial direction at the cross sections 1-1 and 2-2 in the case with runner blades by solid lines marked with circles and triangles, respectively. The abscissa represents the relative radial position and the ordinate does the mean meridional velocity. For comparison meridional velocity distribution in the case without runner blades is shown by dashed line. The figure demonstrates that the meridional velocity of free spiral flow without effect of runner blades decreases monotonously from the hub to the tip, and the variation at the section 2-2 is greater than that at the section 1-1 located at the upstream. Under the effect of runner blades the

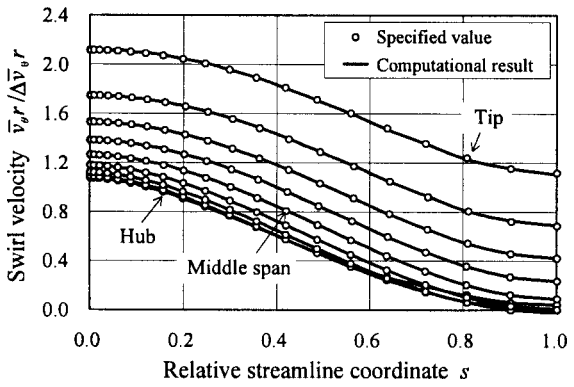

Fig. 6 Mean swirl velocity distribution in the blade region

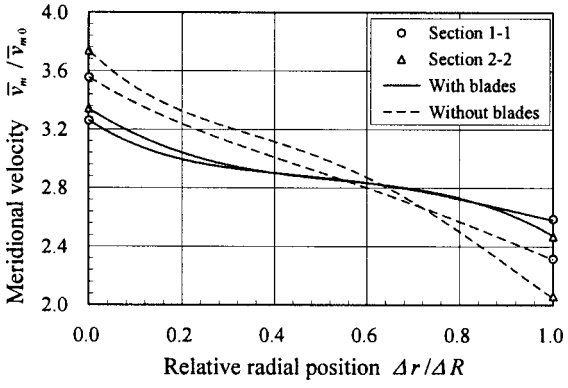

Fig. 8 Meridional velocity distribution at sections 1-1 and 2-2

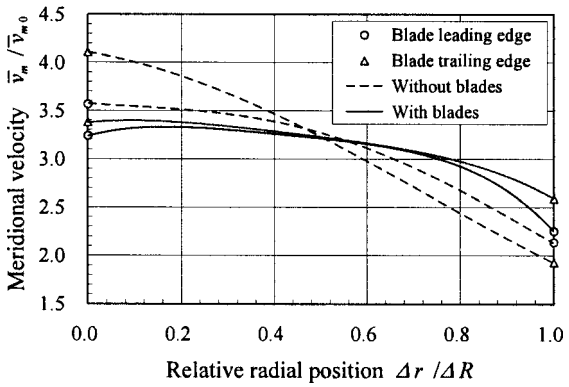

Fig. 9 Meridional velocity distribution along blade leading and trailing edges

meridional velocity in the cross sections 1-1 and 2-2 becomes much uniform for the constraint of runner blades. The difference of meridional velocity under conditions with and without runner blades is about 17.5% at the cross section 2-2, and reaches to 12.3% at the cross section 1-1 yet. Figure 9 shows the distribution of meridional velocity along the blade leading and trailing edges in the case with runner blades by solid line marked with circle and triangles, respectively. For comparison meridional velocity distributions in the case without runner blades are shown by dashed line, which varies much intensively than that in the cross sections 1-1 and 2-2 located at its upstream. In the case with runner blades the distribution of meridional velocity becomes uniform due to the constraint of runner blades. The maximum difference of meridional velocity under conditions with and without runner blades is about 20% at the blade leading edge, and increase to 25% at the blade trailing edge.

3.3 Effect of Guide Vanes. With respect to the effect of guide vanes the swirl velocity distribution along the trailing edge of guide vane has a decisive influence on the mean flow through runner blades, and the outflow of wicket gate is dependent upon the configuration of guide vanes. The guide vane height B_0 and the pitch circle diameter D_0 of guide vane distribution are main two parameters of wicket gate configuration and their effects on the mean through flow were investigated numerically. When B_0 was increased from $0.375D$ to $0.4D$ and $0.425D$ the swirl velocity distribution along the trailing edge of guide vane varies slightly with a little increase in the gradient near the bottom wall. But when D_0 was increased from $1.16D$ to $1.2D$ and $1.25D$ the swirl velocity profile out of wicket gate changes greatly. Figure 10 shows the distribution of swirl velocity along the trailing edge of guide vane when D_0 equals to $1.16D$, $1.2D$, and $1.25D$, respectively. The gradient of swirl velocity in the normal direction of streamlines varies greatly near the bottom ring with the increase of D_0, and then the vorticity of mean through flow into runner blades changes a lot. The necessity of considering the effect of guide vane configuration in the inverse design of blade geometry is demonstrated. The result reveals that a proper enlargement of D_0 is advantageous to improve the blade twist and beneficial to eliminate blade trailing vortex sheets and thereby to reduce the exit energy loss of designed runner [34].

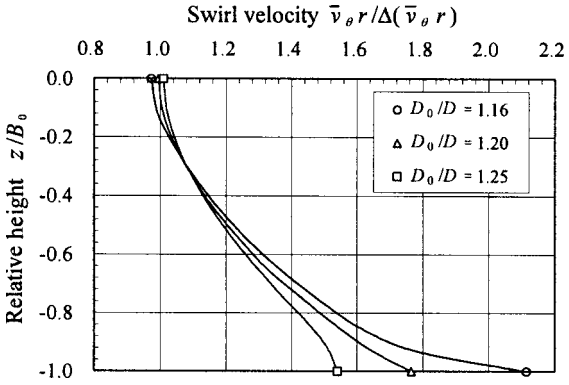

Fig. 10 Swirl velocity distribution along the trailing edge of the guide vane

The above results demonstrate that the mean flow through hydraulic turbine is dependent upon the configuration of guide vanes and the geometry of runner blades. The effect of runner blades is not only limited within the blade region and its rear area but reaches to the upstream. It is of great significance to consider the effect of blade geometry and the influence of related hydraulic components in the inverse design of runner blades in order to obtain a runner of good performance. The present combined computation method deals with the mean flow through different regions of interrelated hydraulic components as a whole. It enables us to take account of the interaction of runner blades and related hydraulic component. The difficulty of defining inflow condition of runner blades, which is encountered in conventional computations treating the runner as an isolated component, has been surmounted consequently. Although above results pertain to axial flow hydraulic turbine system the method is applicable to other hydraulic runner a/o impeller blades. Actually, the present procedure has been applied to hydraulic design of multiphase rotodynamic pump stage consisted of a helical-axial impeller and a diffuser. Experimental results demonstrated that the designed pump has a maximum hydraulic efficiency of 44.0%, which is prominently higher compared to similar pumps, and it works normally in a wide flow rate range until the gas volume fraction increases to 50%. The validity of present procedure is further proved and the detail is reported in Ref. [35].

4 Conclusions

A combined computation method of the circumferentially averaged mean through flow has been proposed for three-dimensional inverse computations of hydraulic turbomachinery blades to take account of the interaction of interrelated hydraulic components. A comprehensive computation domain including runner blades and related components is adopted, and the mean flow passing through rotational runner blades and stationary components is calculated as a whole by simultaneously solving a set of flow governing equations newly derived. By this way the interaction of runner blades and related hydraulic components is taken into account and the difficulty of defining inflow condition of runner blades encountered in conventional inverse computations is surmounted.

The method has been applied to the case of Kaplan turbine and the influence of interrelated hydraulic components was investigated. Computational results of spiral flow in the case without runner blades were compared with experimental data and the validity of computation was confirmed by their good agreement. Numerical investigation indicates that the mean flow through Kaplan blades is dependent on the configuration of guide vanes and influenced greatly by the geometry of runner blades as well. The effect of runner blades is not only limited to the blade region but reaches to the upstream also. The importance of properly taking account of the effect of runner blades and the influence of interrelated hydraulic components in the inverse design computation of hydraulic blades is demonstrated.

The present procedure is directly applicable to 3D inverse design computations of hydraulic blades, and the method enables us to consider the circumferentially steady component of interaction between rotational blades and stationary vanes in the inverse design of hydraulic turbomachinery blades.

Acknowledgment

The author would like to express heartfelt thanks to Professor Ruchang Lin and Professor Shuliang Cao of Tsinghua University, People's Republic of China, for their valuable discussions and helpful advice on the verification of numerical results.

Nomenclature

B_f = blade blockage coefficient
B_0 = height of guide vane
D = diameter of runner blades
D_0 = diameter of pitch circle
E_r = relative total enthalpy per unit mass
g = gravity
H = working head
h_1, h_2, h_3 = Lame coefficients
m = meridional streamline coordinate
$\boldsymbol{n}$ = normal vector
n_s = specific speed
N_b = number of blades
p = pressure
Q = volumetric flow rate
r = radial coordinate
s = relative streamline coordinate
$\boldsymbol{v}$ = absolute velocity
$\boldsymbol{w}$ = relative velocity
$(x_1, x_2, x_3 = \theta)$ = arbitrary orthogonal curvilinear coordinate system
z = axial coordinate
ρ = density of working fluid
θ = angular coordinate
Θ = angular distance of two adjacent blades
φ = angular coordinate of mean stream surface
ψ = stream function
ω = rotational frequency
Δ_{ps} = difference operator

Subscripts

m = value at the mean stream surface
p = value at the pressure surface
r = component in the r direction
s = value at the suction surface
z = component in the z direction
θ = component in the θ direction

Superscripts

$-$ = circumferentially averaged mean value
$\sim$ = circumferentially periodic value

References

[1] He, L., and Sato, K., 2001, "Numerical Solution of Incompressible Unsteady Flows in Turbomachinery," ASME J. Fluids Eng., **123**(3), pp. 680–685.
[2] Muggli, F-A., and Holbein, P., 2002, "CFD Calculation of a Mixed Flow Pump Characteristic From Shutoff to Maximum Flow," ASME J. Fluids Eng., **124**(3), pp. 798–802.
[3] Denton, J. D., 1992, "The Calculation of Three Dimensional Viscous Flow through Multistage Trubomachines," ASME J. Turbomach., **114**(1), pp. 18–26.
[4] He, L., and Chen, T., 2002, "Analysis of Rotor-Rotor and Stator-Stator Interferences in Multi-Stage Turbomachines," ASME J. Turbomach., **124**(4), pp. 564–571.
[5] Shum, Y. K. P., and Tan, C. S., 2000, "Impeller-Diffuser Interaction in a Centrifugal Compressor," ASME J. Turbomach., **122**(4), pp. 777–786.
[6] Vu, T. C., and Shyy, W., 1990, "Viscous Flow Analysis as a Design Tool for Hydraulic Turbine Components," ASME J. Fluids Eng., **112**(1), pp. 5–11.
[7] Lee, Y.-T., Luo, L., and Bein, T. W., 2001, "Direct Method for Optimization of a Centrifugal Compressor Vaneless Diffuser," ASME J. Turbomach., **123**(1), pp. 73–79.
[8] Sorensen, D. N., Thompson, M. C., and Sorensen, J. N., 2000, "Toward Improved Rotor-Only Axial Fans-Part II: Design Optimization for Maximum Efficiency," ASME J. Fluids Eng., **122**(2), pp. 324–329.
[9] Sharatchandra, M. C., Sen, M., and Gad-el-Hak, M., 1998, "New Approach to Constrained Shape Optimization Using Genetic Algorithms," AIAA J., **36**(1), pp. 51–61.
[10] Madsen, J. I., Shyy, W., and Haftka, R. T., 2000, "Response Surface Techniques for Diffuser Shape Optimization," AIAA J., **38**(9), pp. 1512–1518.
[11] Papila, N., Shyy, W., Griffin, L. W., and Dorney, D. J., 2001, "Shape Optimization of Supersonic Turbines Using Response Surface and Neural Network Methods," AIAA Paper No. 2001-1065.
[12] Goto, A., Nohmi, M., Sakurai, T., and Sogawa, Y., 2002, "Hydrodynamic Design System of for Pumps Based on 3-D CAD, CFD, and Inverse Design Method," ASME J. Fluids Eng., **124**(2), pp. 329–335.
[13] Jenkins, R. M., and Moore, D. A., 1993, "An inverse calculation technique for quasi-three-dimensional turbomachinery cascades," Appl. Math. Comput., **57**(2), pp. 197–204.
[14] Zangeneh, M., 1994, "Inviscid-viscous interaction method for three-dimensional inverse design of centrifugal impellers," ASME J. Turbomach., **116**(2), pp. 280–290.
[15] Arndt, N., Acosta, A. J., Brennen, C. E., and Caughey, T. K., 1990, "Experimental Investigation of Rotor-Stator Interaction in a Centrifugal Pump with Several Vaned Diffusers," ASME J. Turbomach., **112**(1), pp. 98–108.
[16] González, J., Fernández, J., Blanco, E., and Santolaria, C., 2002, "Numerical Simulation of the Dynamic Effects Due to Impeller-Volute Interaction in a Centrifugal Pump," ASME J. Fluids Eng., **124**(2), pp. 348–355.
[17] Huyer, S. A., and Snarski, S. R., 2003, "Analysis of a Turbulent Propeller Inflow," ASME J. Fluids Eng., **125**(3), pp. 533–542.
[18] Esch, B. P. M., and Kruyt, N. P., 2001, "Hydraulic Performance of a Mixed-Flow Pump: Unsteady Inviscid Computations and Loss Models," ASME J. Fluids Eng., **123**(2), pp. 256–264.
[19] Wu, C. H., 1952, "A General Theory of Three-Dimensional Flow in Subsonic Turbomachines of Radial-, Axial-, and Mixed Flow Types," NACA TN-D 2604.
[20] Wang, Q. H., Zhu, G. X., and Wu, C. H., 1985, "Quasi-Three Dimensional and Fully Three-Dimensional Rotational Flow Calculation in Turbomachines," ASME J. Eng. Gas Turbines Power, **107**(2), pp. 227–285.
[21] Zhao, X. L., Sun, C. L., and Wu, C. H., 1984, "A Simple Method for Solving Three-dimensional Inverse Problem of Turbomachine Flow and Annular Constraint Condition," ASME paper No. 84-GT-198.
[22] Peng, G., Fujikwa, S., and Cao, S., 1998, "An Advanced Quasi-Three-Dimensional Inverse Computation Model for Axial Flow Pump Impeller Design," *Proceedings of the XIX IAHR Symposium-Hydraulic Machinery and Cavitation*, H. Brekke et al., eds., World Scientific, Singapore, pp. 722–733.
[23] Köller, U., and Mönig, R., 2000, "Development of Advanced Compressor Airfoils for Heavy-Duty Gas Turbines—Part I: Design and Optimization," ASME J. Turbomach., **122**(3), pp. 397–405.
[24] Peng, G., Cao, S., Ishizuka, M., and Hayama, S., 2002, "Design Optimization of Axial Flow Hydraulic Turbine Runner Part I: An Improved Q3D Inverse Method," Int. J. Numer. Methods Fluids, **39**(6), pp. 517–531.
[25] Zangeneh, M., 1991, "A Compressible Three Dimensional Blade Design Method for Radial and Mixed Flow Turbomachinery Blades," Int. J. Numer. Methods Fluids, **13**(7), pp. 599–624.
[26] Borges, J. E., 1994, "A Three-Dimensional Inverse Method for Turbomachinery: Part-1 Theory," ASME J. Turbomach., **112**(2), pp. 346–354.
[27] Tan, C. S., Hawthorne, W. R., McCune, J. E., and Wang, C., 1984, "Theory of Blade Design for Large Deflection: Part II- Annular Cascades," ASME J. Eng. Gas Turbines Power, **106**(2), pp. 354–365.
[28] Peng, G., and Lin, R., 1995, "A Three-dimensional Inverse Method for the Design of Hydraulic Runner with Rotational Coming Flow," *Fluid Machinery*, U. S. Roratgi et al., eds., ASME FED-222, pp. 161–166.
[29] Peng, G., Cao, S., Ishizuka, M., and Hayama, S., 2001, "Fully Three-Dimensional Inverse Computation of Hydraulic Impeller Using Finite Element Method," Comput. Fluids, **10**(2), pp. 247–254.
[30] Zangeneh, M., Goto, A., and Takemura, T., 1996, "Suppression of Secondary Flows in a Mixed-Flow Pump Impeller by Application of Three-Dimensional Inverse Design Method: Part 1- Design and Numerical Validation," ASME J. Turbomach., **118**(3), pp. 536–543.
[31] Lin, R., 1996, *Theory of Fluid Dynamics for Hydraulic Machinery* (in Chinese), Mechanical Industry Press, Beijing, China, pp. 43–56.
[32] Pironneau, O., 1989, *Finite Element Methods for Fluids*, Wiley, New York, pp. 145–189.
[33] Lin, R., and Peng, G., 1995, "An Advanced Numerical Simulation Method for Rotational Flow in Hydraulic Turbomachinery," *Fluid Machinery*, U. S. Roratgi et al., eds., ASME FED-222, pp. 173–176.
[34] Peng, G., Cao, S., Ishizuka, M., and Hayama, S., 2002, "Design Optimization of Axial Flow Hydraulic Turbine Runner Part II: Multi-object Constrained Optimization Method," Int. J. Numer. Methods Fluids, **39**(6), pp. 533–548.
[35] Cao, S., Peng, G., and Yu, Z., 2005, "Hydrodynamic Design of Rotodynamic Pump Impeller for Multiphase Pumping by Combined Approach of Inverse Design and CFD Analysis," ASME J. Fluids Eng., **127**(2), pp. 330–338.

Free Surface Length Scale Estimation in Hydraulic Jumps

D. Mouaze
e-mail: mouaze@meca.unicaen.fr

F. Murzyn
e-mail: murzyn@univ-mlv.fr

J. R. Chaplin
e-mail: jrc1@soton.ac.uk

School of Civil Engineering and the Environment,
University of Southampton,
Southampton SO17 1BJ,
United Kingdom

*In the context of recent work by Brocchini and Peregrine [J. Fluid Mech., **449**, pp. 225–254 (2001a); **449**, pp. 255–290 (2001b)] in this paper we aim to document free surface elevations and free surface length scales in hydraulic jumps with Froude numbers between 1.98 and 4.82. Although information on bubble size, frequency, and velocities in hydraulic jumps is available in the literature, there is not much data on the features of the free surface, or on mixing layer thickness. In the present case, measurements at the free surface have been realized with two "homemade" miniature resistive wire gauges made of two parallel* 50 μm *diameter wires* 1 mm *apart. These instruments were calibrated dynamically over a range of frequencies up to* 20 Hz. *The present results extend the range of Froude numbers for which two-phase measurements in hydraulic jumps are available. In most respects, it confirms earlier results obtained with different experimental techniques. Length scales at the free surface are deduced from a cross-correlation analysis of wire gauge measurements, and are compared with similar data obtained from images of the surface.* [DOI: 10.1115/1.2060736]

Introduction

Hydraulic jumps often occur in open channels when the transition from a supercritical to a subcritical flow is reached. It is then characterized by a strong free surface motion leading to air entrainment. The same process is important in a number of situations and applications, notably in the air–sea exchange of mass, momentum, and heat. Indeed on the upper ocean, this mechanism has a major influence on air/sea gas exchange, mixing processes, and energy dissipation. It is then relevant to investigate how the processes involved in this particular multiphase flow are affected by turbulence, bubble features, free surfaces, and their interactions [1,2].

Previous studies were mainly performed with Pitot tubes and conductivity probes (Chanson [3]), Laser Doppler Velocimetry (Waniewski et al. [4]), or Acoustic Doppler Velocimetry (Liu et al. [5]). Intrusive probes clearly suffer the disadvantage that they could affect the flow, but the nonintrusive techniques (LDV and ADV) also face strong technical limitations in such aerated conditions (due to light diffraction by bubbles).

Our goal in this paper is to present some measurements of the free surface of the jump made by means of miniature resistive wires. In this work we present also a comparison of free surface length scales deduced either from the correlation of free surface measurements or from spectral image analysis of the hydraulic jump.

The investigations were performed for four different Froude numbers ($1.98 < \mathrm{Fr} < 4.82$) in a partially developed flow. This range of small Froude number was imposed by the experimental setup configuration. For $\mathrm{Fr} > 5$, instability of the toe was observed making measurements quite complicated.

Experimental Setup

Instrumentation and Data Processing. The experiments were conducted in a 12 m long recirculating channel at the University of Southampton. The flow rate can be controlled by a regulating valve. The flume is 0.3 m wide, 0.4 m high and the roughness height of the flat bottom was measured at 0.3 mm. The jump was generated by a sluice gate whose elevation above the channel bottom could be adjusted between 3 to 9 cm with in fixed steps of 1 cm (Fig. 1). Figure 2 represents the sketch of the experiment, the position of the axis, and the parameters definition. X_{foot} is defined as the mean position of the foot of the jump.

Free Surface Measurements. Free surface elevations were measured with resistive probes. Each probe consists of two wires of 50 μm diameter, 1 mm apart. A static calibration gives a direct relationship between the surface elevation and the output voltage from a wave monitor. A dynamic calibration of these wire gauges has been made with a vibrometer in order to estimate their frequency response. The results established a cutoff frequency (−3 dB) of 12 Hz that is quite reasonable considering previous studies. Liu et al. [6] found a cutoff frequency of 7 Hz. During the hydraulic jump measurements, 640 samples were collected at a rate of 128 Hz for each position.

The free surface length scales are determined from the correlation between the signals S_i coming from two wire gauges separated in the transverse direction. The separation, r, between the wire gauges was adjusted from 3 mm to more than 100 mm to follow the whole decay of the correlation coefficient R_i:

$$R_i(AB = r) = \frac{\overline{s_{iA} \cdot s_{iB}}}{\sqrt{\overline{s_{iA}^2}}\sqrt{\overline{s_{iB}^2}}} \tag{1}$$

The free surface transverse length scale L_g is defined by:

$$L_g = \int_0^{r_{\max}} R_i(r)dr \tag{2}$$

where $r_{\max}$ is the distance r for which R_i falls to 0.

Free Surface Visualization. A high-speed monochrome camera has been used to record the water surface of the hydraulic jump. The video acquisition rate was 120 frames per second at a frame size of 648×484 pixels. For each flow condition, the images were collected over 2–4 s. This is long enough as the stability of the toe has been previously observed for $2 < \mathrm{Fr} < 5$.

The grey levels (256) of a transverse scanning line (over 500 pixels) were collected using the Matlab image processing toolbox (Fig. 3). This toolbox is a collection of functions specialized in image processing operations (such as the image analysis and enhancement or the image transformations). These functions can be part of programs in a computing environment. The grey levels along this line were recorded in a matrix for all the frames. A one-dimensional wave number spectrum was calculated for

Contributed by the Fluids Engineering Division for publication in the JOURNAL OF FLUIDS ENGINEERING. Manuscript received by the Fluids Engineering Division July 21, 2004; final manuscript received May 20, 2005. Associate Editor: Steven Ceccio.

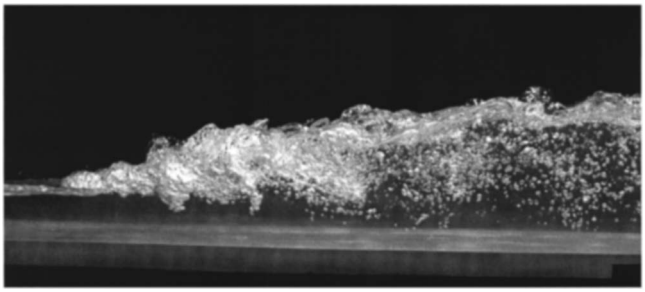

Fig. 1 Hydraulic jump in the recirculating tank (Fr=3.65)

each image. An averaged spectrum of the whole image set exhibits a series of three to four peaks that identify the characteristic wavelengths of the flow. These length scales will be compared with the free surface length scales obtained by the wire gauge correlation technique.

Both transversal and longitudinal length scales have been determined with the "wire technique" during the experiment. Unfortunately the position of the digital camera allows a comparison between two different techniques for the determination of the length scales only in the transversal direction. Further investigations are needed to find the right position of the camera in order to extend the study to the longitudinal scales.

Experimental Conditions. The incident velocity U upstream of the foot of the jump and the Froude number (Fr) were estimated from the measurements of the elevations H_2 and H_3:

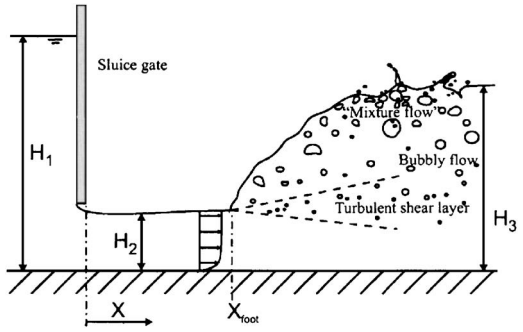

Fig. 2 Sketch of the hydraulic jump setup

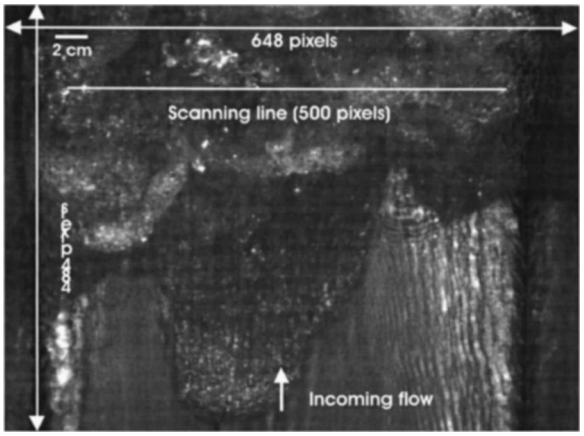

Fig. 3 Scanning line position

Table 1 Experimental conditions

Test	H_1 (m)	H_2 (m)	H_3 (m)	U (m/s)	Fr
1	0.186	0.059	0.138	1.50	1.98
2	0.200	0.046	0.137	1.64	2.43
3	0.280	0.032	0.150	2.05	3.65
4	0.320	0.021	0.133	2.19	4.82

$$\frac{H_3}{H_2} = -\frac{1}{2} + \sqrt{\frac{1}{4} + 2\,\mathrm{Fr}^2} \tag{3}$$

and

$$\mathrm{Fr} = \frac{U}{\sqrt{gH_2}} \tag{4}$$

Four set of experiments are presented in this paper, characterized by four different Froude numbers. Table 1 presents the flow conditions.

Experimental Results

The experiments were performed for a maximum incident velocity U of 2.19 m/s. An estimate of the bed boundary layer at the foot of the jump suggested a maximum thickness of $0.36H_2$. Hence, the hydraulic jump can be considered as partially developed for all flow conditions [7].

Free Surface Measurements. Time-averaged free surface elevations (η) and their standard deviations (η') are plotted against the streamwise position relative to that of the foot of the jump $(x-x_{\mathrm{foot}})/H_2$ in Fig. 4 and in Fig. 5.

These plots show three distinctive regions according to $(x-x_{\mathrm{foot}})/H_2$:

Upstream of the foot of the jump, the free surface is flat and there is no visible sign of turbulence.

At the position of the foot $[(x-x_{\mathrm{foot}})/H_2=0]$, the free surface profile grows slightly while the fluctuations profile shows a sudden strong gradient revealing the formation of the jump. The fluctuations reach a maximum and reveal an area of intensive turbulence. The bubbles generated at the foot of the jump are entrained in the shear layer and in the roller, which is characterized by large recirculation vortices. Coherent structures, reaching the free surface, are revealed by the undulations of the free surface plots and strong variations of η'. The length of this intensive turbulent area

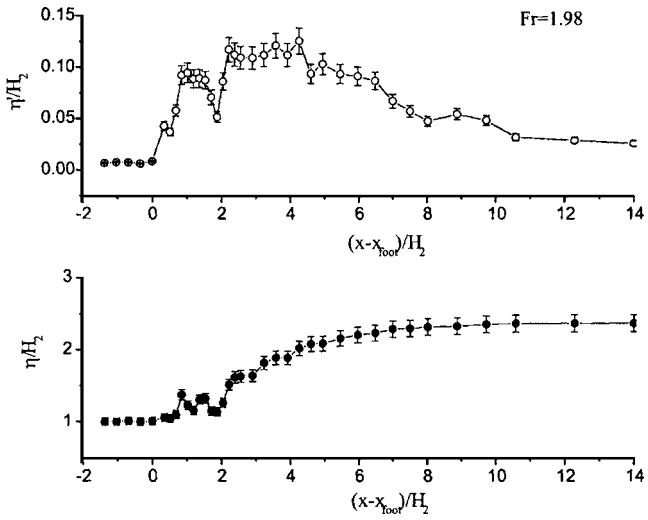

Fig. 4 Free surface and fluctuations profile for Fr=1.98

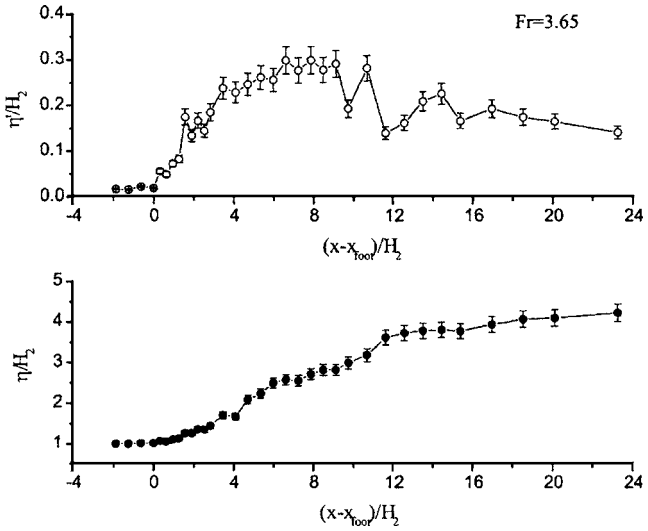

Fig. 5 Free surface and fluctuations profile for Fr=3.65

represents 25% to 30% of the total length of the jump.

Last, a large dissipative zone takes place downstream as the free surface fluctuations decrease quickly and as the free surface elevation approaches the horizontal.

Free Surface Length Scales. The following plots show a superposition of the free surface length scale estimations deduced either from the wire gauge measurements or from the video analysis.

The transverse length scale L_g grows linearly with distance downstream from the foot of the jump (Fig. 6). As the behavior of L_g does not show any obvious dependence with the Froude number, the length scale is mostly governed by the upstream water depth H_2. The results deduced from the wire gauge measurements show an increasing data scattering occurring for the highest values of $(x-x_{\text{foot}})/H_2$ as well.

The accuracy of the wire gauges is relatively high according to the calibration realized in a quite tank. Less than 5% of the error has been estimated for this experimental technique. The uncertainties are mainly due to air crossing the wires below the free surface.

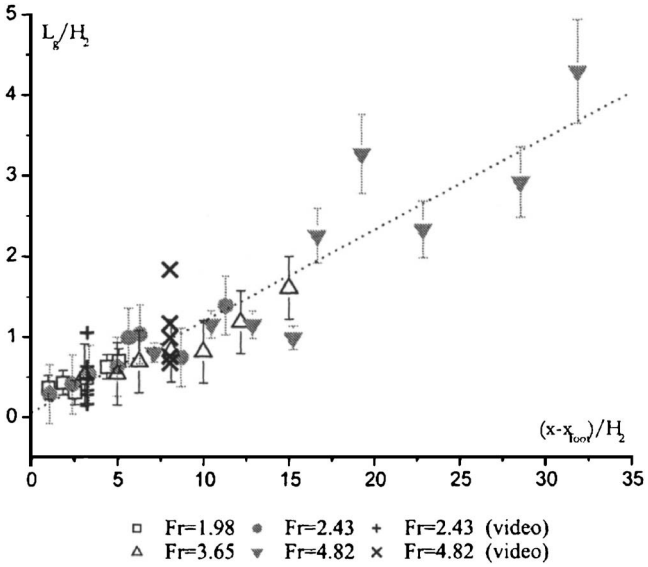

Fig. 6 Transverse free surface length scales

For the same position $(x-x_{\text{foot}})/H_2$, each cross sign in Fig. 6 refers to a peak revealed by the video spectral analysis (see the section on Experimental Setup). The calculations of L_g based on the integral of the cross-correlation coefficient R_i provides only one measure of the surface roughness scale over the whole acquisition duration at each position (120 s). The video analysis gives a range of scales over a very short time, but the averaged results stay within one standard deviation of the results obtained from the correlation technique.

Conclusion

Most previous studies in hydraulic jumps have been performed with intrusive techniques that are not necessarily well suited to aerated flow.

The free surface elevations and turbulent fluctuations show three distinctive regions along the jump, including the region just downstream of the foot (high level of turbulence).

Free surface length scales obtained from wire gauges were in reasonable agreement with those computed from a series of images of the water surface made by high-speed video from above.

Understanding the properties of the free surface turbulence is still a challenging topic [7]. Therefore this study has been extended to the case of a jet flow beneath a free surface. Knowledge on the role of the surface tension, salinity, or scale effects is still needed.

Acknowledgments

This work was supported by the EPSRC (Contract No. GR/R85068) and through a European Community Marie Curie fellowship (Contract No. HPMF-CT-2002-01897) held by the first author.

Nomenclature

ADV = Acoustic Doppler Velocimetry
C = void fraction
D_t = diffusion coefficient in the shear layer
Fr = froude number
LDV = Laser Doppler Velocimetry
L_g = free surface length scale (transversal)
r = separation between the two wire gauges
R_i = free surface correlation coefficient
S_i = signal from the wire gauge
T = total measurement duration
τ_i = duration of the air phase
U = incident velocity
X_{foot} = mean position of the jump's foot
$z_{C_{\max}}$ = position where C reaches a maximum
z_{shear} = upper limit of the turbulent shear region
z^* = lower limit of the mixing layer

References

[1] Brocchini, M., and Peregrine, D. H., 2001a, "The Dynamics of Strong Turbulence at Free Surfaces. Part 1. Description," J. Fluid Mech., **449**, pp. 225–254.
[2] Brocchini, M., and Peregrine, D. H., 2001b, "The Dynamics of Strong Turbulence at Free Surfaces. Part 2. The Boundary Conditions," J. Fluid Mech., **449**, pp. 255–290.
[3] Chanson, H., 1996, *Air Bubble Entrainment in Free-Surface Turbulent Shear Flow*, Academic, London.
[4] Waniewski, T. A., Hunter, C., and Brennen, C. E., 2001, "Bubble Measurements Downstream of Hydraulic Jumps," Int. J. Multiphase Flow, **27**, pp. 1271–1284.
[5] Liu, H. T., Katsaros, K. B., and Weissman, M. A., 1982, "Dynamic Response of Thin Wire Wave Gauges," J. Geophys. Res., **87**, pp. 5686–5698.
[6] Liu, M., Zhu, D. Z., and Rajaratnam, N., 2002, "Evaluation of ADV Measurements in Bubbly Two-Phase Flows," *Hydraulic Proceedings of the Measurements and Experimental Methods Conference*, ASCE, EWRI, Estes Park, CO.
[7] Murzyn, F., Mouaze, D., and Chaplin, J. R., 2005, "Optical Fibre Probe Measurements of Bubbly Flow in Hydraulic Jumps," Int. J. Multiphase Flow, **31**(1), pp. 141–154.

Modeling of Supercritical CO_2 Flow Through Short Tube Orifices

Chun-Lu Zhang[1]
Institute of Refrigeration and Cryogenics,
Shanghai Jiaotong University,
No. 1954 Hua Shan Road,
Shanghai 200030, China
e-mail: clzhang@sjtu.org

Liang Yang
China R&D Center,
Carrier Corporation,
#29-06 King Tower,
No.28 Xinjinqiao Road, Pudong,
Shanghai 201206, China
e-mail: liang.yang@carrier.utc.com

The transcritical cycle of carbon dioxide (CO_2) is a promising alternative approach to heat pumps and automobile air conditioners. As an expansion device, the short tube orifice in a transcritical CO_2 system usually receives supercritical fluid at the entrance and discharges a two-phase mixture at the exit. In this work, a two-fluid model (TFM) is developed for modeling the flow characteristics of supercritical CO_2 through the short tube orifice. The deviations between the TFM predictions and the measured mass flow rates are within ±20%. Meanwhile, the TFM predicts reasonable pressure, temperature, and velocity distributions along the tube length. The small values of interphase temperature difference and velocity slip indicate that the nonequilibrium characteristics of the two-phase flow of CO_2 in the short tube orifice are not significant. Consequently, the homogeneous equilibrium model reduced from the TFM gives a good prediction of the mass flow rate as well. [DOI: 10.1115/1.2060738]

1 Introduction

In recent years, after the Montreal Protocol, many development activities have been devoted to carbon dioxide (CO_2) in light of phasing out CFCs and HCFCs as working fluid refrigeration installations. CO_2 is an inert, natural fluid with no problems arising from ozone depletion, global warming, toxicity, or flammability. Since the transcritical CO_2 cycle was proposed by Lorentzen and Pettersen [1], much research on the system and components using CO_2 have been done [2–5]. Recently, Liu et al. [6] studied the flow characteristics of supercritical CO_2 through short tube orifices and developed an empirical correlation for evaluating the mass flow rate.

The short tube orifice has been widely used as a throttling and flow-rate controlling device on automobile air conditioners, residential air conditioners, and heat pumps for its simple configuration, high reliability, low cost, and ease of replacement. The transcritical expansion process of CO_2 in a short tube could be quite different from the subcritical case of other refrigerants because of the supercritical inlet condition, the large pressure drop, and the special two-phase physical properties near the critical point.

During the past few decades, many researchers have extensively investigated the performance of short tube orifices. Early studies on refrigerant two-phase flow through short tube orifices focused exclusively on R12 and R22 [7–11]. Recently, two-phase flow of alternative refrigerants through short tube orifices has been studied more [6,12–18]. In these reports, the majority of investigations have been focused on experimental data analysis and correlation, while analytical models have not been sufficiently studied. Bassiounay and O'Neal [11] employed a finite element model from a commercial finite element package to simulate single-phase flow of R22 through flexible short tubes. However, two-phase flow was not considered because there were no reasonably good two-phase finite element models available. Kim and O'Neal [13] gave a comparison of some analytical models for estimating the mass flow rate of two-phase R22 and R134a flowing through short tube orifices. Those analytical models can be categorized by the homogeneous equilibrium model (HEM), homogeneous frozen model (HFM), and nonhomogeneous equilibrium model (NEM). However, the actual two-phase flow of refrigerant through short tube orifices is nonhomogeneous and nonequilibrium. Furthermore, these models cannot describe the distributions of interphase velocity slip and temperature difference along the two-phase region.

In this work, a generalized model is developed to investigate the supercritical CO_2 flow through the short tube orifice. To describe the nonhomogeneous nonequilibrium flow characteristics of two-phase CO_2 in the tube, a two-fluid model (TFM) is employed. This model is validated by experimental data from the open literature and can help us determine the particular flow characteristics of CO_2 within the short tube orifice.

2 Model

On the basis of real physical process, the following assumptions are made: (1) steady-state flow; (2) one-dimensional and constant cross section flow; (3) adiabatic flow; and (4) negligible gravitational force. The model can be divided into four parts: two-phase region, supercritical and liquid regions, and entrance.

2.1 Two-Phase Region. A two-fluid model is used here to take the nonhomogeneous nonequilibrium flow characteristics into account. It is a six-equation model and the governing equations are as follows.

Vapor phase mass equation

$$\frac{\mathrm{d}}{\mathrm{d}z}(\varphi\rho_G u_G) = \Gamma_G \tag{1}$$

liquid phase mass equation

$$\frac{\mathrm{d}}{\mathrm{d}z}[(1-\varphi)\rho_L u_L] = \Gamma_L \tag{2}$$

vapor phase momentum equation

$$\frac{\mathrm{d}}{\mathrm{d}z}(\varphi p) + \frac{\mathrm{d}}{\mathrm{d}z}(\varphi\rho_G u_G^2) = F_{GL} + F_{Gi} \tag{3}$$

total momentum equation

$$\frac{\mathrm{d}p}{\mathrm{d}z} + \frac{\mathrm{d}}{\mathrm{d}z}(\varphi\rho_G u_G^2) + \frac{\mathrm{d}}{\mathrm{d}z}[(1-\varphi)\rho_L u_L^2] = -F_{WL} + F_{GL} + F_{LG} + F_{Gi} + F_{Li} \tag{4}$$

total energy equation

[1]Corresponding author.

Contributed by the Fluids Engineering Division for publication in the JOURNAL OF FLUIDS ENGINEERING. Manuscript received by the Fluids Engineering Division May 15, 2005; final manuscript received July 11, 2005. Associate Editor: Timothy J. O'Hern.

$$\frac{\mathrm{d}}{\mathrm{d}z}\left[\varphi\rho_G u_G\left(h_G+\frac{u_G^2}{2}\right)\right]+\frac{\mathrm{d}}{\mathrm{d}z}\left[(1-\varphi)\rho_L u_L\left(h_L+\frac{u_L^2}{2}\right)\right]=0 \quad (5)$$

energy equation of bubble growth

$$\alpha_1(T_L-T_G)A_i=GA\,\mathrm{d}x(h_G-h_L)+xGA\,\mathrm{d}h_G \quad (6)$$

where Γ_G and Γ_L are, respectively, vapor, liquid phase mass transfer rate per unit volume, $\Gamma_G=-\Gamma_L$; F_{GL} and F_{LG} are the interfacial frictional force per unit volume between vapor and liquid, $F_{GL}=-F_{LG}$; F_{Gi} and F_{Li} are interfacial momentum transfer per unit volume caused by mass transfer; F_{WL} accounts for the frictional force per unit volume between the tube wall and liquid phase, while the frictional force between the tube wall and vapor phase is neglected because the vapor phase has almost no contact with the wall except in the droplet flow regime. α_i is the interfacial heat transfer coefficient and A_i is the interfacial area.

Closure of the above governing equations requires the supplementary equations of interfacial frictional force, momentum transfer, heat transfer, bubble diameter, and void fraction in different flow patterns, etc. Some empirical equations recommended by other researchers are adopted here.

The steady-state interphase frictional force F_{GL} or F_{LG} is evaluated below [19].

$$F_{LG}=-F_{GL}=3C_{fi}\varphi^{1/2}\rho_G(u_G-u_L)|u_G-u_L|/D \quad (7)$$

where C_{fi} is interfacial fractional factor [19], $C_{fi}=0.005[1+75(1-\varphi)]$.

Furthermore, the interfacial momentum transfer F_{Gi}, F_{Li} due to mass transfer can be determined from Eqs. (8) and (9). When liquid is evaporating, its velocity is changing from u_L to u_G and the force associated with this velocity change is described with these terms.

$$F_{Gi}=-\eta\Gamma_G(u_G-u_L) \quad (8)$$

$$F_{Li}=-(1-\eta)\Gamma_L(u_L-u_G) \quad (9)$$

Wallis [20] has shown that for a reversible flow the coefficient η is 0.5.

On the other hand, F_{WL} accounts for wall friction, which is introduced from Martinelli and Nelson [21] to be

$$F_{WL}=\phi_{\mathrm{tp}}^2(\mathrm{d}p/\mathrm{d}z)_{F_{Lo}} \quad (10)$$

where $(\mathrm{d}p/\mathrm{d}z)_{F_{Lo}}$ is the friction pressure drop assuming the total flow rate to be liquid.

$$(\mathrm{d}p/\mathrm{d}z)_{F_{Lo}}=f_{Lo}G^2/(2\rho D) \quad (11)$$

f_{Lo} is calculated by the following Churchill equation [22].

$$f_{Lo}=8\left[\left(\frac{8}{\mathrm{Re}_{Lo}}\right)^{12}+\frac{1}{(A+B)^{3/2}}\right]^{1/12} \quad (12)$$

$$A=\left\{-2.457\ln\left[\left(\frac{7}{\mathrm{Re}_{Lo}}\right)^{0.9}+0.27\frac{\varepsilon}{D}\right]\right\}^{16}$$

$$B=\left(\frac{37\,530}{\mathrm{Re}_{Lo}}\right)^{16}$$

The Martinelli–Nelson two-phase multiplier ϕ_{tp}^2 is defined by

$$\phi_{\mathrm{tp}}^2=\left(\frac{1-x}{1-\varphi}\right)^{1.75} \quad (13)$$

If we assume that the equilibrium prevails between the inside and outside of the bubble before growth starts, and the initial liquid superheat can be evaluated with the Clausius–Clapeyron equation as follows:

Table 1 Interfacial area and heat transfer coefficient for different flow patterns (Ref. [19])

Flow regime	Correlations	Eq.
Bubble flow	$a=N\pi d^2=(36N\pi\varphi^2)^{1/3},\ \varphi=N\pi d^3/6$	(16)
	$\alpha_i=k_L(2+0.6\,\mathrm{Re}_b^{1/2}\,\mathrm{Pr}_L^{1/3})/d$	(17)
Churn turbulent	$a=a_b+(a_b-a_a)(\varphi-\varphi_b)/(\varphi_b-\varphi_a)$	(18)
	$\alpha_i=\alpha_a(\alpha_b)_{\varphi_b}/(\alpha_a)_{\varphi_b}$	(19)
Annular flow	$a=4\varphi^{1/2}/D$	(20)
	$\alpha_i=0.5C_{fi}\rho_L c_{pL}(u_G-u_L)\mathrm{Pr}^{-2/3}$	(21)

$$T_{\mathrm{Lsh}}=T_L-T_{\mathrm{sat}}=\frac{\nu_{LG}}{s_{LG}}\frac{4\sigma}{d_0} \quad (14)$$

where ν_{LG} is the difference in the specific volume, and s_{LG} the entropy difference between vapor and liquid. σ is the surface tension. From the available data, an initial bubble diameter d_0 may be assumed as $d_0=2.5\times10^{-5}$ m [19].

The enthalpy of superheated liquid can be evaluated by Eq. (15), where $h_L(p)$ is saturation liquid enthalpy at the pressure p.

$$h_L=h_L(p)+c_{pL}T_{\mathrm{Lsh}} \quad (15)$$

Generally, the two-phase flow can be divided into three patterns according to the value of void fraction, which are bubble flow, churn-turbulent flow, and annular flow regime. It is usually assumed that a transition from the bubbly flow to the churn-turbulent flow will occur when void fraction φ is larger than $\varphi_b=0.3$, and for φ larger than $\varphi_a=0.8$, annular flow is assumed. For the bubbly and annular flow, the interfacial area a and interfacial heat transfer coefficient α_i are calculated from Eqs. (16), (17) and (20), (21) in Table 1, respectively. However, for the churn-turbulent flow regime, we consider this particular flow regime as a transitional regime between bubbly and annular flow, so we calculate a and α_i in churn-turbulent flow by interpolation according to Eqs. (18) and (19) in Table 1.

In Table 1, a is the interfacial area per unit volume; N is the number of bubbles per unit volume and its recommended value is around 10^{11} [19]; and the interfacial area $A_i=aA\,\mathrm{d}z$, A is the cross section area of the short tube, and $\mathrm{Re}_b=\rho_L(u_G-u_L)d/\mu_L$ is the Reynolds number of the bubble.

In Eq. (18), a_a is the interfacial area per unit volume at the onset of annular flow, approximately as follows

$$a_a=4\varphi_a^{1/2}/D \quad (22)$$

Furthermore a_b is the interfacial area per unit volume at the breakdown of the bubbly flow and can be evaluated by

$$a_b=(36N\pi\varphi_b^2)^{1/3} \quad (23)$$

In Eq. (19), α_a is the annular flow heat transfer coefficient from Eq. (21) and $(\alpha_b)_{\varphi_b}$ from Eq. (17). $(\alpha_a)_{\varphi_b}$ is a pseudoheat transfer coefficient calculated from Eq. (21) at the transition point from the bubble flow to the churn-turbulent flow regime.

2.2 Supercritical and Liquid Regions. If the pressure is far below the critical pressure, the liquid density will be approximately independent of the pressure. Consequently, the temperature along the liquid region is invariant in terms of the adiabatic assumption. It brings a simple solution to the length of the region after integrating the momentum equation. In the supercritical region or the liquid region near the critical point, however, the refrigerant density is strongly dependent on the pressure as well as the temperature. A numerical solution is necessary for the following equations.

$$\frac{\mathrm{d}G}{\mathrm{d}z}=0 \quad (24)$$

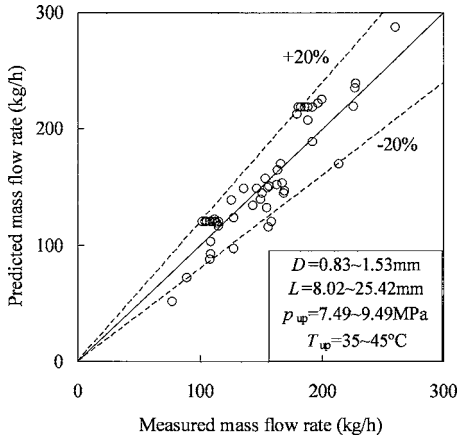

Fig. 1 A comparison of measured and TFM predicted mass flow rates

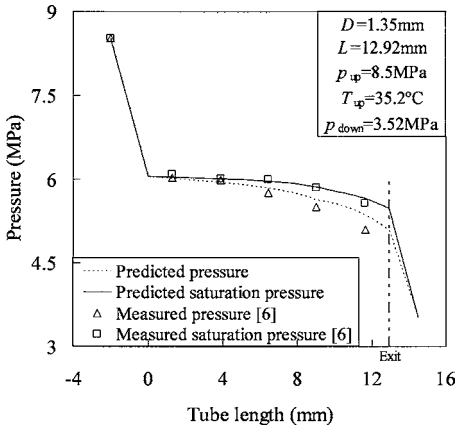

Fig. 2 Pressure distribution along a short tube orifice

$$\frac{\mathrm{d}}{\mathrm{d}z}\left(h+\frac{1}{2}G^2\nu^2\right)=0 \tag{25}$$

$$-\frac{\mathrm{d}p}{\mathrm{d}z}=G^2\frac{\mathrm{d}\nu}{\mathrm{d}z}+\frac{fG^2\nu}{2D}, \tag{26}$$

where the friction factor f is calculated by the Churchill equation (12).

2.3 Entrance. The entrance to the short tube orifice can be characterized as a sudden contraction. Since the mass flux through short tube orifices is quite high, the pressure drop at the entrance could be very large and cannot be omitted. It can be evaluated by [23]

$$\Delta p_{\mathrm{in}}=\frac{G^2\nu_L}{2}\left[\left(\frac{1}{C_c}-1\right)^2+\left(1-\frac{A^2}{A_{\mathrm{up}}^2}\right)\right]\left[1+\left(\frac{\nu_G-\nu_L}{\nu_L}\right)x\right] \tag{27}$$

$$C_C=0.544\left(\frac{A}{A_{\mathrm{up}}}\right)^3-0.242\left(\frac{A}{A_{\mathrm{up}}}\right)^2+0.111\left(\frac{A}{A_{\mathrm{up}}}\right)+0.585 \tag{28}$$

2.4 Numerical Solution. The differential equations in the above-mentioned model are discretized with the central difference method. The logic of the global algorithm is described as follows.

In the design calculation, the mass flow rate is specified and the length of the short tube is unknown. When one specifies a pressure drop for each node, the increment of length of each node is iteratively calculated by means of a Newton–Raphson algorithm. The summation of the length increments will monotonically increase until the outlet pressure reaches the discharge pressure or the length increment at some node reaches zero or a negative that indicates that the flow is choked. In short, the maximum summation of the length increments is the solution.

In the rating calculation, the tube length is specified and the mass flow rate is to be determined. It can also be iteratively estimated by means of a Newton–Raphson algorithm. For a guessed mass flow rate, one can calculate the corresponding tube length in terms of the design calculation as mentioned previously. If the calculated length equals the specified one, the mass flow rate is targeted.

3 Case Study

Experimental data from the open literature [6] are used to verify the above model. All the thermodynamic and transport properties of CO_2 and other refrigerants are evaluated by REFPROP 6.01 [24].

Figure 1 shows the comparison between the measured data and the predictions from the TFM. The measured data cover ranges of short tube inner diameters from 0.83 to 1.53 mm, short tube lengths from 8.02 to 25.42 mm, upstream pressures from 7.49 to 9.49 MPa, and upstream temperatures from 35 °C to 45 °C. The upstream state of CO_2 is generally supercritical and the downstream state is two phase. The results in Fig. 1 demonstrate that about 90% of the data fall within ±20% of the predicted values.

Figure 2 shows the comparison of the measured and predicted pressure distributions along a short tube. Because the vapor is saturated and the liquid is superheated in the two-phase region, the actual pressure is lower than the saturation pressure corresponding to the liquid temperature. The pressure difference reaches a maximum at the exit plane of the short tube. In addition, the pressure drop at the entrance is so large that the upstream supercritical fluid could turn to a subcritical liquid or two-phase mixture quickly near the entrance. As shown in Fig. 2, the TFM can give a good prediction of the pressure distribution along the short tube. It supports the further study on the nonhomogeneous and nonequilibrium flow characteristics of CO_2 through short tube orifices.

Figure 3 demonstrates the vapor and liquid velocities along a

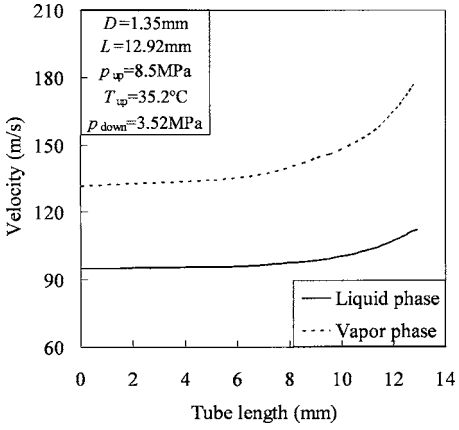

Fig. 3 Velocity distribution of phases along a short tube orifice

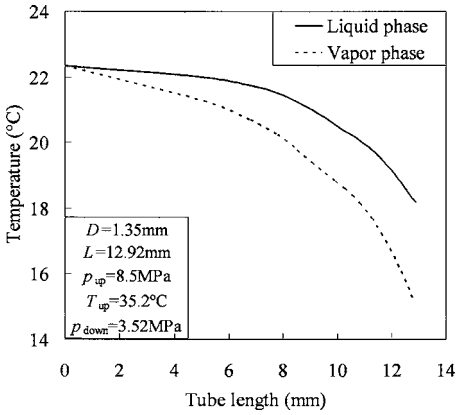

Fig. 4 Temperature distribution of phases along a short tube orifice

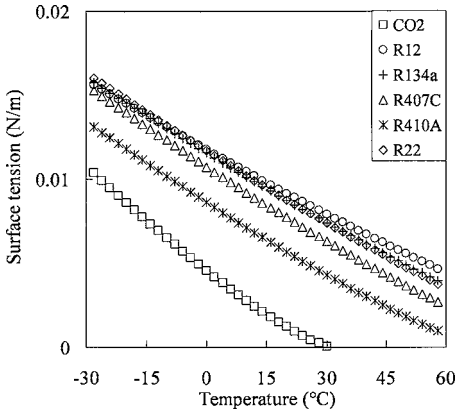

Fig. 6 Surface tensions of different refrigerants

short tube, while Fig. 4 demonstrates the vapor and liquid temperatures along a short tube. All the distributions are provided by the TFM under the same calculation conditions as shown in Fig. 2. In Fig. 3, although the absolute value of the interphase velocity difference is large, the slip ratio of the vapor velocity to the liquid velocity is less than 2, which indicates that the nonhomogeneous characteristic in this case is insignificant. Furthermore, as shown in Fig. 4, the interphase temperature difference is less than 3 °C, which indicates that the nonequilibrium characteristic in this case is not very significant as well.

Why the nonhomogeneous nonequilibrium characteristics of CO_2 flow through short tube orifices are not so significant? It can be theoretically interpreted in the Figs. 5 and 6 bases. Owing to the lower critical temperature, the common operating conditions of CO_2 are near the critical point. As shown in Fig. 5, the density ratio of the liquid to vapor of CO_2 is much lower than that of other refrigerants at the same temperature. In fact, the density ratio will reduce to unity at the critical point. In two-phase flow, the density ratio could be an indicator of the slip ratio between phases at the short tube exit plane [20]. The larger the density ratio, the higher the slip ratio and the more significant the nonhomogeneous characteristics will be. Therefore, the small density ratio of CO_2 near the critical point leads to a small slip ratio and weak nonhomogeneous characteristics in two-phase flow. In addition, as shown in Fig. 6, the surface tension of CO_2 is pronouncedly lower than that of other refrigerants at the same temperature. In theory, the surface tension will reduce to zero at the critical point [25]. In two-phase flow, the superheat of liquid strongly depends on the surface tension. The larger the surface tension, the higher the superheat of liquid will be. Higher superheat will make the bubble growth easier and the nonequilibrium characteristics more significant. Therefore, the small surface tension of CO_2 near the critical point leads to a small superheat of liquid and weak nonequilibrium characteristics in two-phase flow.

As a result, the homogeneous equilibrium model (HEM) for two-phase flow is expected to be a good approximant of the TFM to predict the mass flow rate of supercritical CO_2 through the short tube orifice. The HEM can be reduced from the TFM as long as we neglect the interaction between liquid and vapor phases and regard the two-phase mixture as a single fluid. In the HEM, vapor and liquid velocities are equal ($u_G=u_L=u$) and the two-phase mixture is in thermal equilibrium ($T_G=T_L=T$). Figure 7 gives the comparison of the measured mass flow rates and the predictions from the HEM. The result is similar to that of the TFM as expected and about 96% data fall into ±20% of the predicted values. Actually, it is hard to definitely say the prediction of the HEM is lower or higher than that of the TFM. In comparison with the TFM, the homogeneous assumption in the HEM will increase the mass flow rate and the thermal equilibrium assumption of the HEM will decrease the mass flow rate. Therefore the HEM prediction is just the tradeoff of these two main assumptions.

4 Conclusions

In this paper, a detailed model to describe the supercritical CO_2 flow through the short tube orifice has been developed. Particularly in the two-phase region, a two-fluid model is employed to predict and analyze the nonhomogeneous nonequilibrium characteristics. The proposed model agrees well with the experimental data for the mass flow rate and pressure distribution along the tube

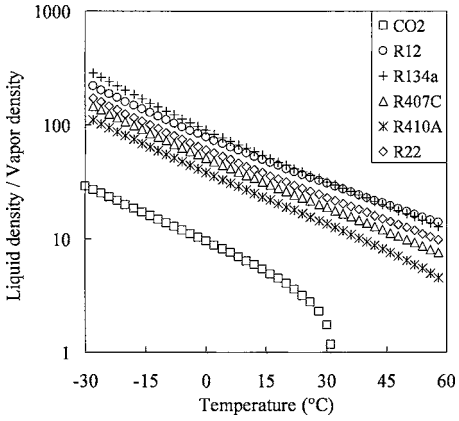

Fig. 5 Density ratios of different refrigerants

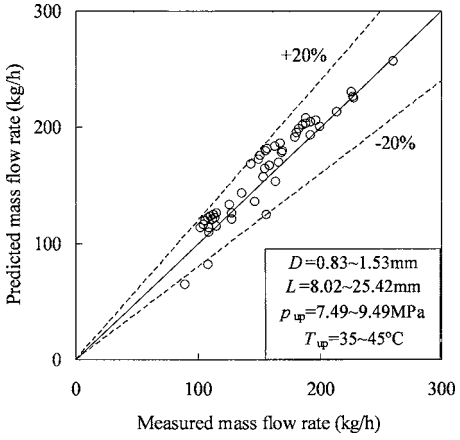

Fig. 7 A comparison of measured and HEM predicted mass flow rates

length. The simulated interphase temperature difference and velocity slip in the two-phase region are relatively small. It indicates that the nonhomogeneous nonequilibrium characteristics in this case are not significant, which generally results from the thermodynamic and transport properties near the critical point. Consequently, when we use the homogeneous equilibrium model instead of the two-fluid model to predict the mass flow rate, the accuracy is similar. It means that the designer could use the homogeneous equilibrium model as the design tool in similar cases.

Nomenclature

a = interfacial area per unit volume (m^{-1})
A = cross-section area of short tube (m^2)
c = specific heat capacity ($J\,kg^{-1}\,K^{-1}$)
C = empirical coefficient
d = bubble diameter (m)
D = inner diameter (m)
f = friction factor
G = mass flux ($kg\,s^{-1}\,m^{-2}$)
h = enthalpy ($J\,kg^{-1}$)
k = heat conductivity ($W\,m^{-1}\,K^{-1}$)
L = short tube length (m)
N = number of bubble per unit volume (m^{-3})
p = pressure (Pa)
Pr = Prandtl number
Re = Reynolds number
s = entropy ($J\,kg^{-1}\,K^{-1}$)
T = temperature (°C)
u = velocity ($m\,s^{-1}$)
v = specific volume ($m^3\,kg^{-1}$)
x = mass quality
z = direction along the tube

Greek letters

α = interfacial heat transfer coefficient between liquid and vapor phase ($W\,m^{-2}\,K^{-1}$)
Γ = interphase mass transfer rate per unit volume ($kg\,m^{-3}\,s^{-1}$)
φ = void fraction
ρ = density ($kg\,m^{-3}$)
ε = relative roughness factor (m)

Superscripts and Subscripts

a = annular flow regime
b = bubble flow regime
C = contraction
down = downstream
G = vapor phase
i = interfacial
W = tube wall
in = inlet
L = liquid phase
Lo = assume the total flow rate to be liquid
Lsh = liquid superheat
tp = two-phase
up = upstream

References

[1] Lorentzen, G., and Pettersen, J., 1993, "A New Efficient and Environmentally Benign System For Car Air-Conditioning," Int. J. Refrig., **16**, pp. 4–12.
[2] Pettersen, J., and Aarlien, R., 1998, "Progress in CO_2 Vapor Compression Systems," Therm. Sci. Eng., **6**, pp. 25–34.
[3] Pettersen, J., Hafner, A., Skaugen, G., and Rekstad, H., 1998, "Development of Compact Heat Exchangers For CO_2 Air-Conditioning Systems," Int. J. Refrig., **21**, pp. 180–193.
[4] Brown, J. S., Yana-Motta, S. F., and Domanski, P. A., 2002, "Comparative Analysis of an Automotive Air Conditioning System Operating with CO_2 and R134a," Int. J. Refrig., **25**, pp. 19–32.
[5] Thome, J. R., and Hajal, J. E., 2004, "Flow Boiling Heat Transfer to Carbon Dioxide: General Prediction Method," Int. J. Refrig., **27**, pp. 294–301.
[6] Liu, J. P., Niu, Y. M., Chen, J. P., Chen, Z. J., and Feng, X., 2004, "Experimentation and Correlation of R744 Two-Phase Flow Through Short Tubes," Exp. Therm. Fluid Sci., **28**, pp. 565–573.
[7] Davies, D., and Daniels, T. C., 1973, "Single and Two-Phase Flow of Dichlorodifluoromethane (R-12) Through Sharp-Edged Orifice," ASHRAE Trans., **79**, pp. 109–123.
[8] Mei, V. C., 1982, "Short Tube Refrigerant Restrictions," ASHRAE Trans., **88**, pp. 157–169.
[9] Aaron, D. A., and Domanski, P. A., 1990, "Experimentation Analysis and Correlation of Refrigerant-22 Flow Through Short Tube Restrictors," ASHRAE Trans., **96**, pp. 729–742.
[10] Kim, Y., and O'Neal, D. L., 1994, "Two-Phase Flow of R-22 Through Short-Tube Orifices," ASHRAE Trans., **100**, pp. 323–334.
[11] Bassiounay, R., and O'Neal, D. L., 2004, "Analysis of Refrigerant Flow and Deformation For a Flexible Short-Tube Using a Finite Element Model," Int. J. Refrig., **27**, pp. 176–183.
[12] Kim, Y., O'Neal, D. L., and Yuan, X. L., 1994, "Two-Phase Flow of HFC-134a and CFC-12 Through Short-Tube Orifices," ASHRAE Trans., **100**, pp. 582–591.
[13] Kim, Y., and O'Neal, D. L., 1995, "A Comparison of Critical Flow Models For Estimating Two-Phase Flow HCFC22 and HFC134a Through Short-Tube Orifices," Int. J. Refrig., **18**, pp. 447–455.
[14] Payne, V. W., and O'Neal, D. L., 1998, "Mass Flow Characteristic of R407C Through Short Tube Orifices," ASHRAE Trans., **104**, pp. 197–209.
[15] Payne, W. V., and O'Neal, D. L., 1999, "Multiphase Flow of Refrigerant 410A Through Short Tube Orifices," ASHRAE Trans., **105**, pp. 66–74.
[16] Singh, G. M., Hrnjak, P. S., and Bullard, C. W., 2001, "Flow of Refrigerant 134a Through Short Tubes," HVAC&R Res., **7**, pp. 245–262.
[17] Payne, V., and O'Neal, D. L., 2004, "A Mass Flow Rate Correlation For Refrigerants and Refrigerant Mixtures Flowing Through Short Tubes," HVAC&R Res., **10**, pp. 73–87.
[18] Choi, J., Chung, J. T., and Kim, Y., 2004, "A Generalized Correlation For Two-Phase Flow of Alternative Refrigerants Through Short Tube Orifices," Int. J. Refrig., **27**, pp. 393–400.
[19] Richter, H. J., 1983, "Separated Two-Phase Flow Model: Application to Critical Two-Phase Flow," Int. J. Multiphase Flow, **9**, pp. 511–530.
[20] Wallis, G. B., 1969, *One-Dimensional Two-Phase Flow*, McGraw-Hill, New York.
[21] Martinelli, R. C., and Nelson, D. B., 1948, "Prediction of Pressure Drop During Forced Circulation Boiling of Water," Trans. ASME, **70**, pp. 695–701.
[22] Churchill, S. W., 1977, "Frictional Equation Spans All Fluid Flow Regions," Chem. Eng. (Rugby, U.K.), **84**, pp. 91–92.
[23] Collier, J. G., and Thome, J. R., 1994, *Convection Boiling and Condensation*, Oxford University Press, New York.
[24] McLinden, M. O., Klein, S. A., Lemmon, E. W., and Peskin, A. P., 1998, *NIST Thermodynamic and Transport Properties of Refrigerants and Refrigerant Mixtures (REFPROP), Version 6.01*, National Institute of Standards and Technology, Gaithersburg, MD.
[25] Heide, R., 1997, "The Surface Tension of HFC Refrigerants and Mixtures," Int. J. Refrig., **20**, pp. 496–503.

The Biased Laminar By-Pass Fluidic Flowmeter

Geoffrey H. Priestman
e-mail: g.priestman@shef.ac.uk
Department of Chemical and Process Engineering,
University of Sheffield,
Mappin Street, Sheffield, S1 3JD, England

Robert F. Boucher
Office of Vice Chancellor,
University of Sheffield,
Mappin Street,
Sheffield, S1 3JD, England

This paper demonstrates that the range of a fluidic flow meter can be significantly extended by connecting it in parallel with a fixed laminar by-pass resistance. Analysis shows how for any particular specification, there is an optimum combination of meter and by-pass which maximizes the flow range. Validation tests were done in air, using a fluidic target meter integrated into a housing with a laminar by-pass of parallel rectangular cross section passages formed between flat plates. Results obtained showed excellent agreement with analytical predictions, almost doubling the operating range for the typical specification chosen, a major advance in the context of the previous research aimed at extending meter range. In principle the concept should be applicable to any flowmeter having a suitable Eulerian pressure-flow characteristic.
[DOI: 10.1115/1.2060729]

Introduction

A typical flowmeter specification, such as for a domestic gas or water meter, will effectively determine the meter size by setting an upper limit to the allowable pressure drop for operation at a required maximum flowrate, and the meter range by the further requirement to measure a specified minimum flowrate. For example a domestic gas meter can be required to measure a maximum flowrate of 6 m^3/h with a pressure drop, when tested in air, of no more than 125 Pa, and also to operate down to a minimum flow rate of 0.04 m^3/h, giving a flow range of 150:1. Such demanding specifications eliminate the use of conventional meters, such as the orifice plate or turbine meter, for which a corresponding range of just 10:1 would be difficult to achieve.

Hydrodynamic oscillating flowmeters of various designs demonstrated the potential for much larger ranges, which encouraged significant development work [1–7] in an attempt to meet domestic meter specifications. Despite much research effort, pure fluidic oscillating meters could, however, only achieve a range of about 70:1 or 80:1. A hybrid fluidic meter [4] did achieve the required range, but relied upon a thermal sensor to monitor the lower flows. More recent meter development has focused on ultrasonic meters [8], which, by using very sensitive and advanced electronic signal processing at low flows, have demonstrated the potential for a range of 150:1. The purpose of this paper is to show how the range of a meter can be significantly extended, simply by applying it in conjunction with a fixed by-pass flow resistance element. The paper focuses on a system based on a specific fluidic flowmeter, but other meters could potentially also benefit from this approach.

Minimum Limit to the Flowmeter Range

All flow meters eventually cease to be functional at a certain minimum flow rate. With orifice plates the pressure difference becomes too small to measure. Turbine meters cease to rotate due to bearing friction. Hydrodynamic oscillators, either vortex shedding or fluidic oscillating jets, cease to oscillate due to viscosity damping effects. Viscous damping becomes troublesome at low flow rates because the fluid has too little inertia to overcome it, compared to the high flowrate situation. The ratio of inertial to viscous forces is measured by Reynolds number and there is a minimum value for any hydrodynamic oscillator of a given geometry at which it will cease to function. So long as its geometry is maintained, its size may be scaled up or down but the same unique minimum Reynolds number will exist. The existence of this minimum Reynolds number, Re_{min}, permits the low flow measurement problem to be quantified as follows for the fluidic flowmeter.

Any meter will have a resistance or Euler number, Eu, independent of size, defined by

$$\mathrm{Eu} = \frac{\Delta P}{0.5\rho V^2} \tag{1}$$

where ΔP is the pressure drop, ρ the fluid density, and V a characteristic velocity. This quantification of pressure loss is traditionally applied to "Eulerian" components in which the Euler number is not a strong function of changes in flow, which is typically the case for simple resistive elements operating at high Reynolds number. At low Re when flow becomes laminar, viscous losses can often become dominant as in Eq. (5), with Eu becoming inversely proportional to Re for a pure laminar loss. In fluidic oscillating meters virtually all resistance is across a well formed nozzle expanding into a chamber, so at high flow rates Eu typically approaches unity, and is only a weak function of Re, rising only very slightly even as Re falls to below 50. This assumes a characteristic velocity V to be the average nozzle velocity, and Re based on V and the nozzle width d.

The fluidic flowmeter has a rectangular nozzle of width d and height nd, where n is called the aspect ratio. Experiments show that there is an optimum value of n for any meter design.

Since the product of velocity and nozzle area gives volume flow rate, Eq. (1) becomes

$$\mathrm{Eu} = \frac{\Delta P n^2 d^4}{0.5\rho Q^2} \tag{2}$$

At the maximum flowrate Q_{max}, the meter pressure drop is specified as ΔP_{max} and the Euler number at this maximum flowrate is defined as Eu_{max}. Note that this is not the maximum value of Eu, indeed it may be its minimum value, but this convention of subscripting with the flowrate is useful and follows previous work. Thus the meter size is given by

$$d = \left[\frac{\rho Q_{max}^2 \mathrm{Eu}_{max}}{2\Delta P_{max} n^2}\right]^{0.25} \tag{3}$$

So defining Re_{min} as corresponding to the minimum operating flowrate, Q_{min}, we obtain [9]:

Contributed by the Fluids Engineering Division for publication in the JOURNAL OF FLUIDS ENGINEERING. Manuscript received by the Fluids Engineering Division October 5, 2004; final manuscript received: July 7, 2005. Associate Editor: Volkan Otugen

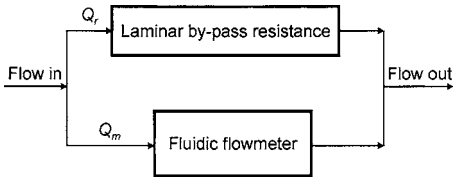

Fig. 1 Concept of by-pass resistance applied to fluidic flowmeter

$$Q_{\min} = \left[\frac{\rho Q_{\max}^2}{2\Delta P_{\max}}\right]^{0.25} \frac{\rho}{\mu} \mathrm{Re}_{\min} n^{0.5} \mathrm{Eu}_{\max}^{0.25} \tag{4}$$

The first part of Eq. (4) is seen to be entirely fixed by the meter specification and the fluid density and viscosity. Hence in order to extend the meter range the "merit parameter" represented by the three-term product at the end of the equation needs to be minimised. The specification given in the introduction requires a merit parameter value of as low as about 70, whereas a fairly optimum fluidic meter ($n=7$, $\mathrm{Eu}_{\max}=1.1$, and $\mathrm{Re}_{\min}=45$) produces the higher value of 122. Clearly a significant extension in meter range is required to apply the fluidic meter to measure domestic gas. It is shown below, however, that the range can be achieved if the meter is applied in conjunction with a fixed flow resistance.

The Biased By-Pass Concept

The description above exposes the conflicting need of a large meter size at high flow, but a small meter at low flows. One solution is to have two meters and a valve switching between them, an expensive and impracticable solution [10]. An alternative is a small meter suitable for the low flow and a by-pass pipe with a valve. When the flowrate rises the valve can be opened so that a portion of the flow by-passes the meter. It is as if the meter nozzle area has been increased. Although possible in theory, again the system is unattractive due to its complication.

The resistance of the by-pass pipe in the later case is very high (infinite) at low flowrates when it is closed and has a low value at high flowrates when it is opened. Plainly, a simple flow resistance whose resistance relative to that of the meter was high at low flows but low at high flows would be a much more attractive proposition than having a moving valve. A laminar resistance, typically comprising a bundle of small tubes, provides just such characteristics, and Fig. 1 shows how it can be applied to a flowmeter.

Although in absolute terms the resistance across a laminar element increases with flowrate, because this increase is proportional to the flowrate through it, whereas that across the flowmeter, according to Eq. (1) varies as velocity squared, neglecting the weak dependence of Eu on Re, the desired relative resistance change can be achieved across the meter flow range. Two such characteristics are plotted in Fig. 2, with arbitrary pressure and flow units. By correct choice of these resistances the following has been achieved. At low pressure drop the flowrate r through the resistance is less than that (m) through the meter. At high pressure drop, however, the situation is reversed, the flow rate R through the resistance is much greater than that (M) through the meter. Thus the laminar resistance is behaving rather like a by-pass valve which does not shut completely, but nethertheless permits a smaller meter to be used since much of the flow by-passes it at large flowrates. It remains to quantify these proposals to determine the possible range of improvement.

Modelling the Meter with By-pass Performance

The pressure drop across the laminar by-pass resistance is known theoretically and for the case of N tubes of diameter D and length L operating with fully developed flow at at a flowrate Q_r such that the Re is below 2000 we have

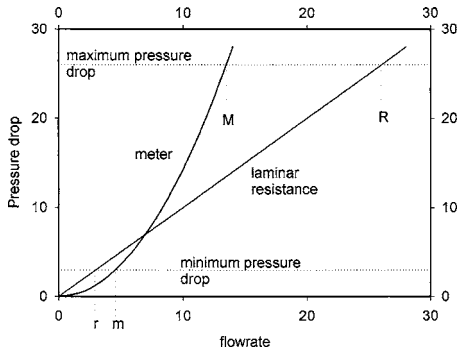

Fig. 2 Flow division for meter and laminar resistance in parallel

$$\Delta P = \frac{128 \mu L Q_r}{\rho D^4 N} \tag{5}$$

Choosing a meter size, its flow rate at the maximum pressure drop can be found from rearranging Eq. (3). The appropriate parallel laminar resistance can then be calculated such that the total combined flow at the maximum pressure drop equals the specified maximum flow. At the low flow end, the minimum meter flow is defined by the minimum operational Reynolds number:

$$Q_{m\,\min} = \frac{nd\,\mathrm{Re}_{\min}\,\mu}{\rho} \tag{6}$$

This enables the minimum operating pressure drop to be found from Eq. (1) based on an experimentally determined value of Eu. As this same pressure drop applies to the by-pass, its minimum flow, $Q_{r\min}$ can be calculated using Eq. (5), and hence the total minimum flow $Q_{\min}$ found as the sum of the two minimum flows. These calculations can be repeated for many meter sizes and the value found which gives the best flow ratio ($Q_{\max}/Q_{\min}$).

Figure 3 shows the results of such calculations done for a maximum flow specification of 6 m^3/h at a 125 Pa pressure drop and assuming a fluidic meter with $n=7$, $\mathrm{Eu}_{\max}=1.1$, $\mathrm{Eu}_{\min}=2.1$, and $\mathrm{Re}_{\min}=45$. The variation of the total minimum flow and flow range with meter nozzle size shows clearly that there is an optimum. Note that also shown is the diameter of a set of 60 by-pass tubes needed with each nozzle size to achieve the specified maximum flow. The meter alone is seen to require a nozzle size of 4.16 mm, giving a minimum flow of 0.073 m^3/h and a flow range of 82. This is to be compared with the by-pass system with a best nozzle width of 1.5 mm giving a minimum flow of 0.038 m^3/h and a flow range of 158. This clearly demonstrates the significant advantage offered by the proposed by-pass concept, with the flow range being almost double that of the meter alone. The specifica-

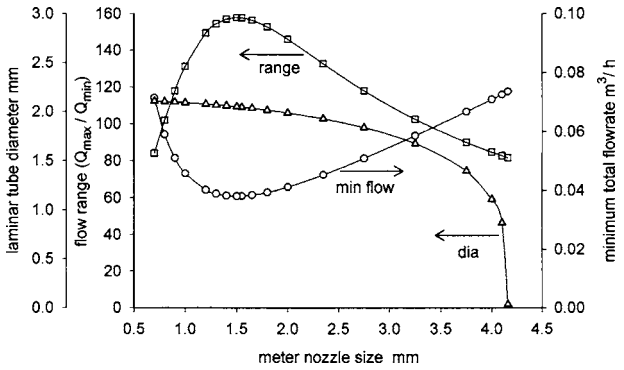

Fig. 3 Change of minimum flow, range and laminar tube diameter with nozzle size, $Q_{max}=6$ m^3/h

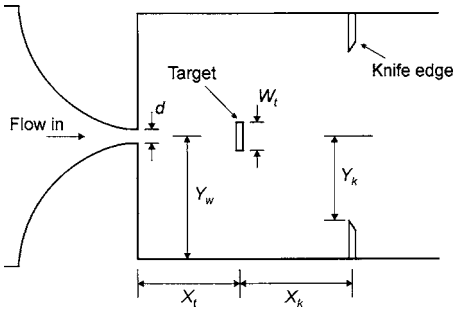

Fig. 4 Plan design of fluidic target meter

tion given earlier is now achievable and the range slightly higher than for the latest sophisticated ultrasonic meters.

It is important to note that the laminar flow resistance can, of course, be used directly as a flowmeter. Such laminar flow element or LFE meters are available commercially essentially measuring pressure drop across a section of laminar flow resistance with fully developed flow to ensure a linear calibration. Flow range depends on the pressure detection, but turndown ratios of between 50 and 100 are quoted.

It should also be noted that the by-pass principles adopted would apply to other meters limited by a minimum Reynolds number, which include vortex shedding meters and turbine meters.

The principles adopted should not be confused with regular by-pass flow metering in which a small flowmeter is placed in parallel with a large one and the small meter is used to infer the total flow [11]. In such systems it is intended that both flows should increase proportionally if possible. In the present proposal steps are taken to do the opposite, namely to force the two flows (meter and by-pass) to change disproportionately and the choice of two different types of resistance is essential to the principle.

Fluidic Meter Design and Measured Characteristics

The fluidic flowmeter selected for testing was the target meter type. The basic meter design is shown in Fig. 4, which indicates five key geometric parameters as identified in previous development work on this type of meter [2], all nondimensionalised with respect to the nozzle width d. The other key parameter is the meter depth, again normally nondimensionalised as aspect ratio, n. The nozzle width used in the test meter was 1.40 mm, with the other parameters being given in Table 1. Dimensions were measured to an accuracy of ±0.5%.

The meter was made from aluminium and tested using air at atmospheric conditions to determine its characteristics. Air flow was measured using a range of carefully calibrated rotameters, each covering overlapping flow ranges. The calibration at low flowrates was done using a stop watch and a displacement meter with volume increments of 0.005 l. The higher flow rates were calibrated against a standardized sonic orifice and gauge. The rotameter readings were adjusted against the calibration and also for variation in air density. The calibration should minimize bias error in the flow rate measurement. There was some precision uncertainty associated with using the etched rotameter tube scales, which across the flow range this was typically ±2%. Oscillation frequency was measured using a hot wire probe situated in the meter close to one of the knife edges. The signal was displayed on an oscilloscope and also sent to a frequency analyzer. The analyzer enabled frequency to be determined to a precision of ±1%

Table 1 Design of target meter tested

n	W_t	X_t	X_k	Y_w	Y_k
7	1.7	9.5	8.4	8.7	5.1

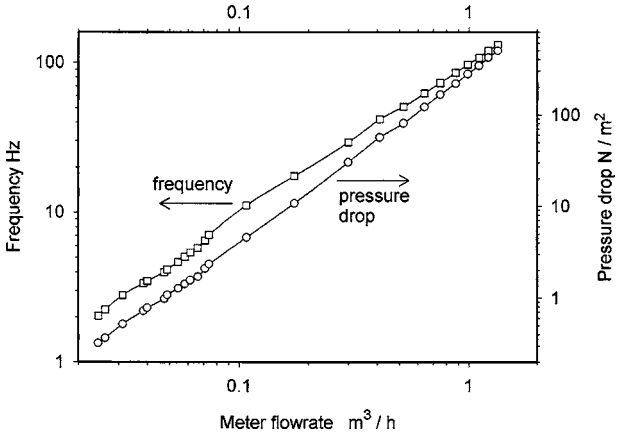

Fig. 5 Target meter operating characteristics, d=1.4 mm, n =7

with no significant bias error. In the measurement of frequency it should be noted that as the minimum operating point was approached, the signal became increasingly diminished and less defined, so determination of the exact minimum point of oscillation was made difficult. Inclined and micro manometers were used to measure total pressure drop. Careful levelling of the manometers eliminated significant bias error, but there was a reading precision uncertainty of between ±2% at the minimum flow conditions and ±1% at the maximum flow conditions. Temperature, to an accuracy of 0.2°C, and barometric pressure were recorded during each test and the air properties adjusted as appropriate. The minimum operating point was determined for both decreasing and increasing flowrate, although no significant difference was found.

In assessing the impact of experimental measurement uncertainty on the work reported it is of note that the main claim of the work is demonstrated by the comparison of data for a meter operating alone with that for the same meter operating with a by-pass resistance. The meter geometry and measurement instruments remained the same for all the tests, so the impact of any bias errors should be minimised. Also, in applying the theory to the results, empirically determined values of Re_{min}, Eu_{max}, and Eu_{min} were used, which should again tend to minimize the impact of any measurement uncertainty. The estimated uncertainty of the main dimensionless parameters used and quoted below resulting from possible measurement precision error are as follows; Re±2%, Eu_{min}±3.5%, Eu_{max}±3%, and S±2.5%.

The basic operating characteristics are plotted in Fig. 5. The minimum measured frequency was 2.04 Hz, at a flow rate of 0.0244 m^3/h. The flowrate at a pressure drop of 125 N/m^2 was 0.65 m^3/h, corresponding to a flow range of 26.5. Figure 5 shows the data plotted in nondimensional form. The meter Euler number is seen to decrease with increasing Re, from a value of 2.1 at the minimum Re to close to unity at high Re, the value corresponding to a pressure drop of 125 N/m^2 being 1.15. The minimum operational Re, below which no oscillations could be detected was 45. This is significantly less than the lowest value of 54 found in earlier work [2], however the merit parameter defined in Eq. (4) is approximately the same in each case, the other tests being for an aspect ratio of 5.

Figure 6 plots the variation with Re of the Strouhal number, defined as

$$S = \frac{fd}{V} \tag{7}$$

Ideally S should remain constant, as such a linear characteristic avoids possible calibration problems if the fluid viscosity varies. At the higher values of Re, S is seen to be reasonably constant at about 0.0065, but varies slightly at lower Re, eventually falling to

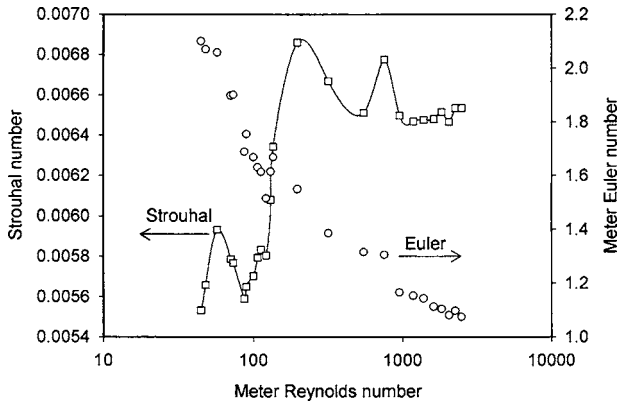

Fig. 6 Nondimensionalized operating characteristics of target meter alone, *d*=1.4 mm, *n*=7

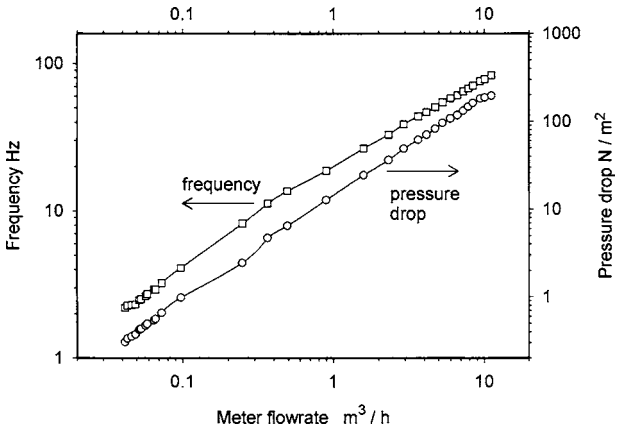

Fig. 8 Combined meter operating characteristics, *N*=17

a value of around 0.0057. The changes in Strouhal number as Re varies between about 200 and 500 are likely to be associated with changes in the oscillation mechanism, and indeed some geometries of target meter can stop oscillating in this region [2]. The geometry tested here was chosen to avoid such discontinuities and also to try and minimise the *S* variation. Both the absolute values and the shape of the *S*-Re plot generally agree with previous results [2].

Tests on an Integrated Meter and By-pass Combination

In order to demonstrate the by-pass concept, tests were done with the target meter described above combined in parallel with a laminar by-pass resistance. The system was integrated into a single rectangular cross-section housing and to facilitate design, instead of using tubes, the laminar resistance was formed by parallel stacking of rectangular plates, housed in a chamber above the meter housing. The plates were 0.54 mm thick and 110 mm long and stacked to form rectangular flow passages 0.99 mm high by 24.4 mm wide. Two arrangements were tested, having 10 and 17 passages respectively in the by-pass. Flow entered and left the meter housing through 25 mm i.d. pipes, each with a pressure tapping 50 mm from the housing.

Figure 7 plots the operating characteristics obtained for the meter with 10 passages combination. The minimum measured flowrate and frequency were 0.034 m^3/h and 2.04 Hz respectively, and the flowrate measured at a pressure drop of 125 N/m^2 was 4.53 m^3/h, corresponding to a flow range of 132. The data for the 17 passage by-pass is shown in Figure 8. With the extra by-pass passages the minimum measured flowrate and frequency were 0.042 m^3/h and 2.2 Hz, respectively, and the flowrate measured at a pressure drop of 125 N/m^2 was 6.96 m^3/h, giving a flow range of 167. Ideally the minimum meter frequency should in each case be the same as for the meter alone, which was earlier found to be 2.04 Hz. This is the case for the 10 passage system, but for the 17 passage system a slightly lower minimum flow would have been expected. This discrepancy can be attributed to the difficulty in detecting the oscillation signal as the minimum operating point is approached. The frequency against flow rate plots are seen to be well behaved for both systems. This is important as this is the calibration curve required to translate measured frequency into a flowrate. Because of the changing by-pass flow ratio the relatively constant meter Strouhal number is not expected to produce a constant frequency/flowrate ratio for the combined system. This is clearly demonstrated in Fig. 9 which shows how, as the by-pass takes an increasing flow fraction with increasing total flowrate, the ratio $f/(Q_r+Q_m)$ falls.

In order to compare the measured characteristics of the by-pass meter with the proposed model it is necessary to introduce suitable equations for the pressure drop through the rectangular by-pass passages.

For laminar flow through a rectangular duct an Euler number can be defined as follows:

$$\mathrm{Eu}_r = \left(\frac{C_f}{\mathrm{Re}_r}\right)\left(\frac{L_p}{D_h}\right) \tag{8}$$

L_p is the plate length of the passage and Re_r is based on its hydraulic diameter D_h which is found from the passage height, h and width w, thus:

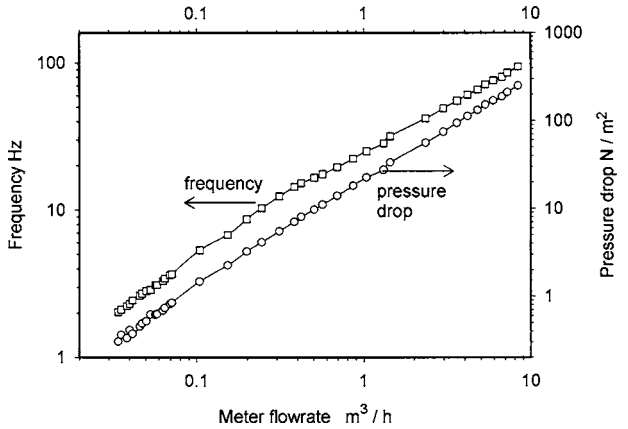

Fig. 7 Combined meter operating characteristics, *N*=10

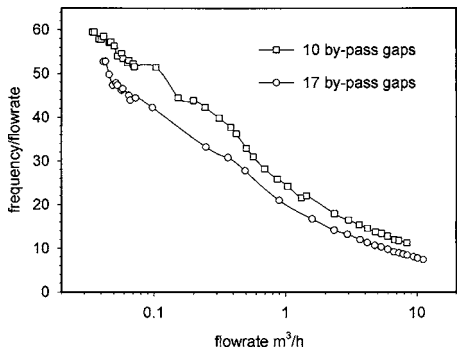

Fig. 9 Variation of frequency/flowrate with flowrate for the meter operating with 10 and 17 by-pass passages

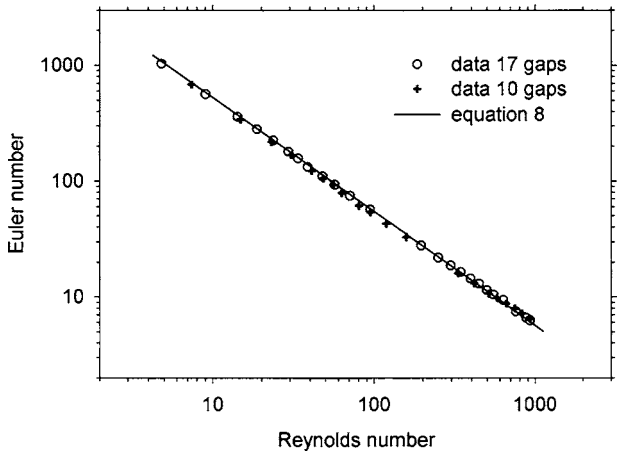

Fig. 10 Comparison of measured and theoretical laminar by-pass resistance

$$D_h = \frac{4hw}{2h + 2w} \tag{9}$$

The loss coefficient C_f is a function of passage aspect ratio, varying between 96 for an infinitely wide passage to 56 for a square one. In our case $h=0.99$ mm and $w=24.4$ mm, an aspect ratio of 0.04 which corresponds to a loss coefficient of 90.5.

Equation (8) assumes fully developed flow in the passage. At the upstream edge boundary layer development occurs which increases the pressure loss. The effect is not significant at low Re, but needs to be accounted for at the higher values. The effect can be conveniently incorporated into the analysis by adding a constant loss to Eu thus:

$$\mathrm{Eu}_r = \left(\frac{C_f}{\mathrm{Re}_r}\right)\left(\frac{L_p}{D_h}\right) + 0.7 \tag{10}$$

Figure 10 compares Eq. (10) with experimental data obtained by measuring the pressure drop across the 10 and 17 passage by-passes for a wide range of air flowrates with the meter blanked off. The agreement is seen to be very good. It is of note that the data shows no discontinuities which usefully confirms the relative calibration of the series of rotameters required to cover the large flow range tested, with no bias errors apparent between the instruments.

It is now possible to carry out an equivalent analysis to that presented in Fig. 3, but using Eq. (10) instead of Eq. (5) to represent the by-pass resistance, that is assuming rectangular passages and not tubes. To enable direct comparison with the data, the predictions are based on a design condition of a maximum flowrate of 4.53 m^3/h at a pressure drop of 125 N/m^2, being that measured for the 10 passage by-pass system. The three predicted curves plotted in Fig. 11 show how the flow range, the minimum flow rate and the required number of flow passages in the by-pass all vary with the meter size. It is of note that the maximum predicted flow range for this maximum flow corresponds to the 1.4 mm size meter with 10 passage by-pass system tested, the data for which is plotted in Fig. 11. The agreement between data and predictions is seen to be very good, with a theoretical flow range of 131 compared to a measured one of 132. Such good agreement is in part to be expected in that the calculations assume the experimentally determined values of meter Re_{min}, Eu_{max}, and Eu_{min} of 45, 1.15, and 2.1, respectively. The agreement demonstrates, however, that the model has included all appropriate parameters for this case.

For the system tested with 17 by-pass passages the flow found at 125 N/m^2 was, as expected, higher at 6.96 m^3/h, giving a flow range of 167. If the predictions plotted in Fig. 11 are recalculated

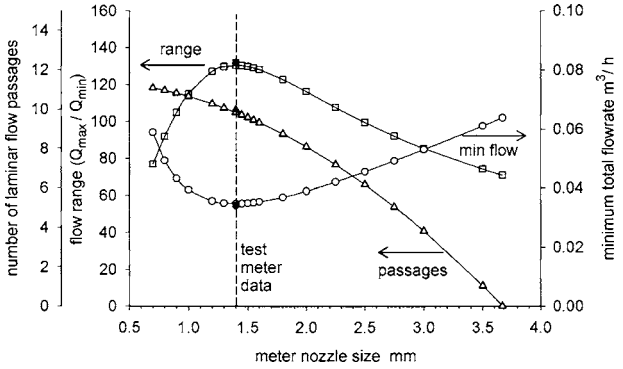

Fig. 11 Comparison of test data with predicted performance for meter with 10 laminar by-pass passages, $Q_{max}=4.53$ m^3/h

for this higher flowrate, the maximum predicted flow range is 173 and occurs for a 1.6 mm nozzle with 15.5 by-pass passages, and the predicted range for a 1.4 mm meter is 169 with 16 passages. Slight disagreement between model and data is therefore apparent. This is best illustrated by re-plotting the system model assuming a fixed meter size of 1.4 mm and calculating flow range, maximum and minimum flowrate as a function of the number of by-pass passages, as shown in Fig. 12. The 10 by-pass data is, as expected in good agreement, but the flow ratio for the 17 passage system is seen to be less than the 175 predicted. The main inaccuracy is at the maximum predicted flow rate of 7.34 m^3/h. The difference compared to the measured value is over 5% and so significantly above the precision error of 2%. This probably indicates that at this higher flowrate, the minor resistance or distribution losses associated with the flow entering or leaving the meter between the pressure tappings were starting to become significant. It is of note that repeating the calculations for the original specification used in Fig. 3 of 6.0 m^3/h at 125 N/m^2, the model still predicts an optimum size of 1.5 mm nozzle width, now operating with 13.3 by-pass passages, a minimum flowrate of 0.038 m^3/h and a range of 157, reduced slightly from the previous value of 158 due to the slight change in assumed Eu_{max} and accounting for the boundary layer development.

It is also apparent in Fig. 12 that the range of a given size of target meter can be increased by increasing the size of the by-pass. Although only one geometry will be exactly optimum, the relatively shallow slope of the flow range curve around the optimum, as illustrated in Figs. 3 and 11, means that the range does not deviate strongly from optimum as the by-pass size is changed. Thus a single target meter can be matched to several meter specifications merely by changing the by-pass resistance. It should also

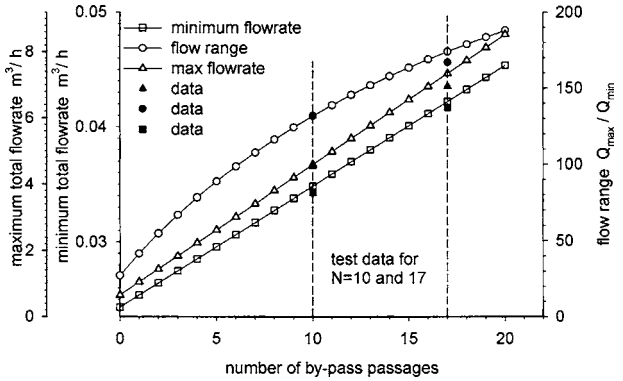

Fig. 12 Comparison of test data with predicted performance for meters with various number of laminar by-pass passages, $d=1.4$ mm

be noted that the increase in flow ratio with by-pass size shown in Fig. 12 is primarily because as the capacity of the meter increases, it is fundamentally easier to achieve a higher flow range.

Meter Application

Designing a by-pass and meter combination to match a given specification is essentially a matter of following the procedure used to generate Figs. 3 and 11, which enable meter size and by-pass geometry to be selected. This bases the meter size on the maximum flow condition, with the minimum flow then depending on the achievable range.

For applications in which the fluid is well defined, the procedure for calculating the flowrate is as follows. Given a variation of the Strouhal number with Re, in order to calculate the meter flow rate it is useful to introduce a further characterizing number, the Stokes number, defined as the product of S and Re,

$$\mathrm{St} = S \times \mathrm{Re} = \frac{fd}{V}\frac{Vd\rho}{\mu} = \frac{fd^2\rho}{\mu} \tag{11}$$

It is apparent that the meter St vs S characteristic enables the meter Strouhal number and hence velocity to be calculated from the frequency, provided the fluid properties are known. The total flow through the by-pass meter, (Q_m+Q_r), can therefore be found as follows:

(i) Measure the meter oscillation frequency f.
(ii) Calculate S from the meter St versus S characteristic.
(iii) Calculate V from S and hence find Re.
(iv) Calculate the meter pressure drop from the meter Eu versus Re characteristic.
(v) Noting that the meter and by-pass have a common pressure drop, calculate the by-pass flowrate, Q_r, from the by-pass Eu_r versus Re_r characteristic.
(vi) Calculate the meter flowrate, Q_m, from V.

This procedure requires that the necessary characteristics are stored on a processor. It also relies on knowledge of the fluid density and viscosity so the additional measurement of gas temperature and, for a gas absolute pressure, may be required. Clearly the overall accuracy of flow measurement will depend directly on the accuracy of the fluid property values used.

If a fluidic oscillating meter is being used over a relatively small flow range or is of a certain design, it may be possible to assume that the Strouhal number is independent of Re. In this case it follows from Eq. (7) that flowrate is directly proportional to measured frequency, that is each meter pulse corresponds to a given volumetric flow, and that step two in the above procedure can be simplified.

It is of note that the accuracy with which fluctuating flowrates can be measured improves if the meter frequency is raised, and that although S tends to be fixed for a given meter type, frequency increases with decreasing meter size. This is therefore a further advantage of the by-pass system as the meter size is always less than for a meter applied alone.

For operation with ill-defined fluids, this type of meter does offer some potential to operate as a "smart" meter, with further measurements enabling direct determination of both flowrate and fluid properties. The system design and operation is, however, not straightforward and is the subject of a further publication.

Conclusions

The ability of a flow meter to attain a given specification is often limited by its minimum operating point. Analysis of the characteristics of a typical fluidic flowmeter enables a merit parameter to be identified, which depends upon its minimum operating Reynolds number, its aspect ratio and its Euler number at the maximum flow condition. This demonstrates that the fluidic meter alone is unable to achieve a typical domestic gas meter specification. The connection of the fluidic meter in parallel with a simple laminar flow resistance, however, is shown to offer the potential for extending the range. Analysis of the system shows that for any particular maximum flow condition, there is an optimum combination of meter and by-pass, which maximizes the flow range. A significant increase in flow range from 82 to 158 was predicted, sufficient to meet the required specification.

To validate the model tests were done, based on a fluidic target meter. A design of meter was chosen and tested in air. The meter performance was found to be in agreement with previous work, having a continuous and reasonably flat Strouhal number-Reynolds number characteristic and a minimum operating Reynolds number of 45. The meter was integrated into a housing in parallel with a laminar by-pass of long thin passages of rectangular cross section formed between flat plates. The by-pass flow resistance was measured and seen to agree with standard laminar flow theory. Tests were done with the target meter combined with both 10 and 17 passages in the by-pass. The results obtained were in very good agreement with analytical predictions, especially for the smaller capacity system. The biased by-pass system has thus been demonstrated to significantly extend the operating range of a fluidic flowmeter, and in principle the concept should be applicable to any flowmeter having a suitable Eulerian pressure-flow characteristic.

References

[1] Boucher, R. F., McGuigan, J. A. K., and Cox, A. J., 1975, "Performance and tolerance characteristics of a fluidic volume flowmeter," 7th Cranfield Fluidic Conference (BHRA).
[2] Boucher, R. F., and Mazharoglu, C., 1988, "Low Reynolds Number Fluidic Flow Metering," J. Phys. E, **21**, pp. 977–989.
[3] Mansey, H., and Williams, D. R., 1989, "Flowmeter Based on the Trapped Vortex Pair Fluidic Oscillator," Rev. Sci. Instrum., **60**5, pp. 935–938.
[4] Sakai, K., Okabayashi, M., and Yasuda, K., 1989, "The Fluidic Flowmeter: A Gas Flowmeter Based on Fluid Dynamic Oscillation," Flow Meas. Instrum., **1**, pp. 44–50.
[5] Honda, S., and Yamasaki, H., 1985, "A new hydrodynamic oscillator type," 1st International Symposium On Fluid Control and Measurement FLUCOM'85, Tokyo.
[6] Yamasaki, H., Takahashi, A., and Honda, S., 1988, "A New Fluidic Oscillator for Flow Measurement," 2nd International Symposium On Fluid Control and Measurement, FLUCOM'88, Sheffield, pp. 16–20.
[7] Okabayashi, M., and Yamasaki, H., 1991, "Feasibility Study of New Fluidic Gas Meters, 3rd International Symposium On Fluid Control and Measurement, FLUCOM'91 San Francisco, pp. 313–318.
[8] Bignell et al., 1998, "CSIRO, Fluid Meter Construction," U.S. Patent No. US 5 728 948A
[9] Boucher, R. F., and Mazharoglu, C., 1988, "Fluidic Flowmeter Scaling Equations," 2nd International Symposium On Fluid Control and Measurement, FLUCOM'88. Sheffield, pp. 6–10.
[10] Okabayashi, M., and Haruta, M., 1985, UK Patent Application No. GB 2172996A, Osaka Gas Company.
[11] Boucher, R. F., Mazharoglu, C., Churchill, D., and Parkinson, G. J., 1991, "A Fluidic By-pass Venturimeter," in Proceedings of the 3rd International Symposium of Fluid Control, Measurement and Vizualisation (FLUCOME'91), San Francisco.

Journal of Fluids Engineering

Technical Briefs

Extended Velocity–Enthalpy Relations for Wall-Bounded and Free Shear Layers

B. W. van Oudheusden
Department of Aerospace Engineering, Delft University of Technology, P.O. Box 5058, 2600 GB Delft, The Netherlands
e-mail: B.W.vanOudheusden@LR.TUDelft.nl

The relation between the velocity and the enthalpy in steady shear flow is expressed by the Crocco–Busemann relation, which states that for adiabatic conditions the total enthalpy remains constant throughout the shear layer when the Prandtl number is one. The subject of the present Technical Brief is the rational extension of this concept in case the Prandtl number differs from one. The comparison between wall-bounded and free shear flows is studied in particular, as well as the possible application of the concept in turbulent shear flow. [DOI: 10.1115/1.2060739]

Introduction

The relation between the local values of the velocity and the enthalpy in a viscous shear flow is expressed by the so-called Crocco–Busemann (CB) relation. Such a relationship has great practical significance, both for experimental purposes, where it can be invoked to estimate flow temperature information where such is not explicitly available, as well as in numerical studies in which the temperature can be obtained from an algebraic relation rather than having to solve the energy transport equation. The background of the CB relation is essentially the similarity between momentum and heat transfer and the derivation can be found in standard textbooks [1–3]. In the present discussion its form pertinent to adiabatic flow is considered, which implies that no heat is generated inside the fluid, nor transferred across its boundaries. For these conditions the CB relation states that for steady flow a constant value of the total enthalpy H is a possible solution of the energy equation when the Prandtl number $\mathrm{Pr}=1$. Furthermore, the CB relation is applicable to turbulent flow as well, provided that also the turbulent Prandtl number Pr_T is one.

Although usually discussed primarily in the context of wall-bounded flows, the CB relation applies also to free shear flows, such as wakes and mixing layers. The subject of this Technical Brief is to investigate the rational extension of the CB concept for these different flow geometries in case the Prandtl number differs from one.

The effect of Pr on the CB relation in boundary layer flow is commonly interpreted in the sense of an incomplete recovery, in that a constant recovery factor r, different from one, is applied throughout the entire boundary layer:

$$h = h_e + r\frac{1}{2}(u_e^2 - u^2), \tag{1}$$

where the subscript "e" refers to the conditions in the adjacent inviscid free stream. The value of r is based on the recovery at the wall, which has been shown to be $r \approx \mathrm{Pr}^{1/2}$ in laminar flow, and $r \approx \mathrm{Pr}^{1/3}$ for turbulent flow [2]. The application of the recovery concept to the variation of the temperature across the shear layer suggests a conversion of kinetic into thermal energy. However, the actual background for this phenomenon is essentially the result of the combined action of mechanical and thermal diffusion [4].

The extended CB relation is exact for Couette flow [5], where $r=\mathrm{Pr}$. In the case of boundary layer flow, however, the description of Eq. (1) is only approximate and furthermore incomplete, as shown in an earlier paper [6] where an asymptotically complete extension for the CB relation in the boundary layer flow was derived. In this Technical Brief this analysis is extended to free shear layers, while also the situation of turbulent flow is addressed.

Shear Flow in Zero Pressure Gradient

In the following analysis the fluid is modeled as a perfect gas with enthalpy $h=c_pT$, with the specific heat c_p and the Prandtl number Pr taken as constants. Furthermore, laminar flow with constant material properties (density, viscosity, conductivity) in a zero pressure gradient will be considered initially, the extension to more general conditions being addressed subsequently. The effect of flow turbulence will be modeled by introducing a turbulent viscosity μ_T and Prandtl number Pr_T.

The boundary conditions imposed on the viscous flow should conform to the basic assumption that no additional energy is supplied to the flow. In the case of a wall-bounded flow hence, the wall should be stationary and without heat transfer. For free shear flows, more specifically the mixing layer between two inviscid streams, the adiabatic condition requires that all external streams have the same total enthalpy.

Laminar Flow Analysis. Laminar constant-property flow in zero-pressure gradient conditions (constant u_e and h_e) permits self-similar solutions [1,2], where nondimensional velocity and enthalpy functions are introduced:

$$f'(\eta) = \frac{u}{u_e}, \quad \theta(\eta) = \frac{h - h_e}{\frac{1}{2}u_e^2}, \quad \Theta(\eta) = \frac{H - H_e}{\frac{1}{2}u_e^2} \tag{2}$$

which depend only of the scaled transverse coordinate η:

Contributed by the Fluids Engineering Division for publication in the JOURNAL OF FLUIDS ENGINEERING. Manuscript received by the Fluids Engineering February 25, 2005; final manuscript received: May 24, 2005. Associate Editor: Subrata Roy.

$$\eta = y\sqrt{\frac{\rho u_e}{2\mu x}}. \tag{3}$$

With this transformation the following equations for f and Θ result:

$$f''' + ff'' = 0, \tag{4}$$

$$\Theta'' + \mathrm{Pr}\, f\Theta' + 2(\mathrm{Pr}-1)(f'f'')' = 0. \tag{5}$$

The boundary conditions for the adiabatic boundary layer are $f(0)=f'(0)=0$, $f'(\infty)=1$, for the velocity and $\Theta(\infty)=\Theta'(0)=0$ for the total enthalpy. For the adiabatic mixing layer we have $f(0)=0$, $f'(-\infty)=\lambda$, $f'(\infty)=1$, and $\Theta(\infty)=\Theta(-\infty)=0$. Here, $\lambda = u(-\infty)/u_e$ is the velocity ratio of the two mixing streams.

To study the effect of Prandtl number on the CB relation, the solution of the energy equation is expanded as an asymptotic series, $\Theta(\eta)=\Theta_0(\eta)+\epsilon\Theta_1(\eta)+\cdots$, with respect to the perturbation parameter $\epsilon=\mathrm{Pr}-1$. The leading-order term corresponds to the solution for $\mathrm{Pr}=1$, hence, $\Theta_0=0$. By means of regular perturbation analysis, the equation for Θ_1 is obtained as:

$$\Theta_1' + f\Theta_1' = -2(f'f'')' = -2f''^2 + 2ff'f''. \tag{6}$$

The boundary conditions are $\Theta_1(\infty)=0$ and either $\Theta_1'(0)=0$ for the boundary layer, or $\Theta_1(-\infty)=0$ for the mixing layer. The equation for Θ_1 can be solved analytically, by observing that with regard to (4), f''^{-1} can serve as an integrating factor. Taking the appropriate boundary conditions into account the solution for the boundary layer is found to be:

$$\Theta_1 = \frac{1}{2}(1-f'^2) - ff'', \tag{7}$$

while for the mixing layer we have:

$$\Theta_1 = \frac{1}{2}(1-f')(f'-\lambda) - ff''. \tag{8}$$

With the above results, the following first-order extensions of the CB relation between enthalpy and velocity can now be established.

For the boundary layer we find, up to $\mathcal{O}(\epsilon^2)$:

$$H = H_e + (r-1)\left(\frac{1}{2}(u_e^2-u^2) - \frac{\psi}{\rho}\frac{\partial u}{\partial y}\right), \tag{9}$$

where $\psi=\int \rho u\, dy$ is the streamfunction, while r can be identified with the wall recovery factor, for which the analysis yields, again up to $\mathcal{O}(\epsilon^2)$:

$$r = 1 + \frac{\epsilon}{2} = \frac{\mathrm{Pr}+1}{2} \tag{10}$$

which confirms that the expression $r=\mathrm{Pr}^{1/2}$ is an asymptotically correct first-order approximation. The static enthalpy distribution can be written as:

$$h = h_e + r\frac{1}{2}(u_e^2-u^2) + (1-r)\frac{\psi}{\rho}\frac{\partial u}{\partial y}. \tag{11}$$

A comparison shows that the classic modification of the CB relation, Eq. (1), incorporates only the first "recovery" part of the first-order term, but not the second part that expresses the energy migration toward the outer flow.

In the same way we find for the mixing layer, up to $\mathcal{O}(\epsilon^2)$:

$$H = H_e + (r-1)\left(\frac{1}{2}(u_e-u)(u-u_w) - \frac{\psi}{\rho}\frac{\partial u}{\partial y}\right) \tag{12}$$

with r given by the same relation as for the boundary layer, Eq. (10). A comparison with Eq. (9) leads to an interesting result. For the boundary layer the first part of the total enthalpy variation can be interpreted as the result of an incomplete recovery from the free-stream conditions. For the mixing layer such a direct interpretation is not valid. At most, the variation can be viewed as a kind of mixed recovery from the upper and lower free-stream conditions. The reason for this is that actually the total enthalpy defect is not caused by an incomplete recovery, but instead results from an imbalance in the transverse diffusion of mechanical and thermal energy across the shear layer.

Numerical Assessment. The performance of the extended analytical CB relations is assessed by a comparison to accurate numerical solutions obtained for a realistic value of the Prandtl number (results are given here for $\mathrm{Pr}=0.7$). The calculation results further serve to identify typical differences between wall-bounded and free shear flows. For the calculations a five-point equidistant finite-difference scheme with fourth-order accuracy was employed.

The results of the computations and analytical theory are given in Fig. 1 in terms of computed profiles of various flow properties, for three different flow cases. The top row of graphs corresponds to the Blasius boundary layer, the center and bottom row to the mixing layer with velocity ratios of $\lambda=0$ and $\lambda=0.5$, respectively. For each case, going from left to right, the first two diagrams give the velocity profile (f') and the total-enthalpy perturbation function (Θ_1), as derived from Eqs. (7) and (8). The remaining two diagrams describe the static-enthalpy profile (θ) and the total-enthalpy profile (Θ) for the case of $\mathrm{Pr}=0.7$. The solid lines give the result of the numerical computation; the dashed lines the predictions of the perturbation theory.

Discussion

As can be observed from the comparison in Fig. 1, the results of the perturbation analysis provide a good representation of the exact solutions. The solutions further clearly illustrate the nature and extent of energy separation in these shear layer flows, in particular, it is revealed how for $\mathrm{Pr}<1$ net energy is migrated from the lower- to the higher-velocity regions of the flow, for all flow configurations considered, as a result of diffusive effects (also compare the discussion in [7]). This effect is more pronounced in the boundary layer than in the mixing layers. In comparison to the shear layer with $\lambda=0$, the extent of negative energy separation is about twice as large in the boundary layer flow.

Effects of Nonsimilarity and Pressure Gradient. It has been shown elsewhere [6] that the extended CB-relation Eq. (9) for boundary layer flows apply generally to arbitrary pressure gradients. Similarly, it is easily verified that this solution can also be applied to adiabatic wake flows, provided that the conditions at both sides of the wake are equal.

For the mixing layer result, in contrast, the analysis does not permit such a generalization. The present result of Eq. (12) is therefore restricted to the constant pressure case.

Effects of Variable Properties (Compressibility). It is evident that the recovery effect becomes significant in absolute sense under conditions when for an ideal gas the fluid properties can no longer be assumed constant. This consideration may raise concern regarding the applicability of the present constant-property analysis. The effect of compressibility is conveniently studied by adapting the transformation, Eq. (3), to allow for variable properties in the following way [3,8]:

$$\eta = \frac{u_e}{\sqrt{2\int \rho_e\mu_e u_e dx}}\int \rho dy. \tag{13}$$

As discussed extensively elsewhere [9], the effect of variable properties is found to disappear from the compressible flow analysis as a result of this transformation, if Pr is approximately constant (i.e., independent of temperature, which is a reasonable as-

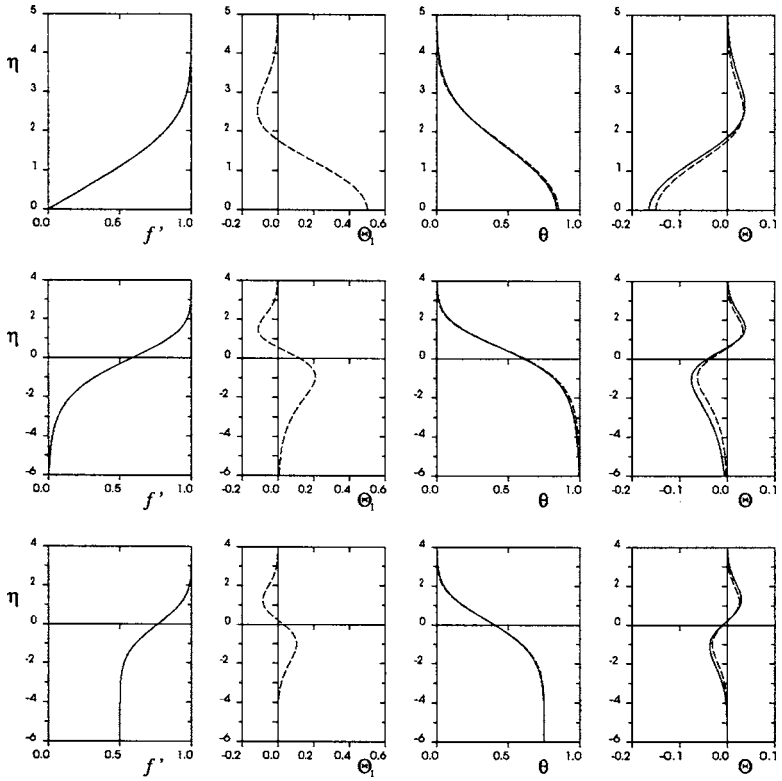

Fig. 1 Velocity and enthalpy distributions for Pr=0.7; a comparison between the numerical solution (solid) and the perturbation solution (dashed). *Top*: boundary layer; *center*: mixing layer λ=0; *bottom*: mixing layer λ=0.5.

sumption for real gases) and when further the pressure gradient is zero and when a linear relation exists between viscosity and temperature. Under these conditions, the constant-property solutions apply again, which means that in that case there are no compressibility effects on the modified CB relation and on the recovery factor [10]. These conclusions apply to wall-bounded and free shear flow alike. For more general conditions, however, compressibility influences may arise as a result of pressure gradient and a nonlinear viscosity–temperature relation [9].

A Note on the Recovery Concept in Viscous Flow. As mentioned, at least part of the modification of the CB relation can be interpreted in the sense of a recovery mechanism, i.e., a transformation of kinetic into thermal energy. It should be reminded that for inviscid flow the recovery concept is a direct consequence of energy conservation, but that in viscous flow additional diffusive effects have to be taken into account. These are the work done by the viscous stresses and the conductive diffusion of heat. The effect of the viscous stresses contains a dissipative component, which constitutes a direct energy conversion, as well as a redistributive component, which works as a pure gradient diffusion of kinetic energy in the case of a thin shear flow.

Therefore, in viscous flow the energy balance contains two different mechanisms. The first is one of convective transport in combination with a direct conversion of energy taking place along a streamline. The second mechanism is one of diffusion, predominantly in the transverse direction. For the case of a Couette flow the convective mechanism is inactive (streamwise derivatives are zero) while the diffusive mechanism yields results that are identical to an incomplete recovery from the free-stream conditions, with $r=\mathrm{Pr}$. The true physical background, however, is as stated the combined diffusive effect of viscosity and conductivity.

In general, for shear layers that develop alongside inviscid free streams (and, possibly, adiabatic walls) both effects are present, that is, the material derivative effect, which is a true and complete thermal recovery for which a recovery factor $r=1$ applies, and the diffusive effect, which is only an apparent recovery with $r=\mathrm{Pr}$. It is interesting to note that according to the present viscous flow analysis the effective recovery factor is to first-order approximation simply the average of these values; see Eq. (10).

Turbulent Flow. The situation of turbulent shear flow is of essential higher complexity than that of laminar flow, because of the combined molecular and turbulent transport effects, where even at incompressible flow conditions the turbulent viscosity and conductivity vary significantly throughout the flow field. This complication and the absence of exact analytical models for the turbulent mixing prevent a rigourous theoretical treatment unless further simplifying assumptions are introduced.

An interesting approximate result can be obtained for turbulent free shear layers. Under free shear flow conditions the molecular transport terms can be neglected, while the turbulent viscosity can be modeled as being approximately constant across the shear layer [11] and with the turbulent Prandtl number constant as well. This allows the (incompressible) turbulent shear layer then to be treated as a quasilaminar flow, having constant density but variable viscosity, with $\mu=\mu_T(x)$. Invoking the results of the above variable-property analysis then directly reveals that a transformation of the type (13) can be used to reduce the problem to that of the incompressible laminar case. As a consequence, the expressions (12) and (9) also apply to turbulent shear layers (wake and mixing layers, respectively). As in the analysis the turbulent Prandtl has to be considered the corresponding recovery factor for turbulent free shear layers is $r=\mathrm{Pr}_T^{1/2}$; typically $\mathrm{Pr}_T\approx 0.5$ in free shear flow [1].

The latter result may be surprising in the sense that, whereas in laminar flow a single recovery factor expression ($r\approx\mathrm{Pr}^{1/2}$) applies to both wall-bounded and free shear layers alike, the result for the turbulent free shear layer ($r\approx\mathrm{Pr}_T^{1/2}$) differs from that for the tur-

bulent boundary layer ($r \approx \mathrm{Pr}^{1/3}$). In this context it may therefore be clarifying to review shortly how the latter result has been theoretically justified. Analytical estimates of the turbulent recovery factor have been provided by a number of authors, Rubesin already mentioning nearly a dozen studies in his 1953 review [12]. Following the approach of Rubesin [12] or Dorrance [10], a direct relation between the local gradients in enthalpy and velocity can be established in an approximation, which in the absence of surface heat transfer takes the form of:

$$\frac{\partial h}{\partial y} = -\mathrm{Pr}_m(y) u \frac{\partial u}{\partial y}, \quad \mathrm{Pr}_m = c_p \frac{\mu + \mu_T}{k + k_T} = \frac{\mu + \mu_T}{\mu/\mathrm{Pr} + \mu_T/\mathrm{Pr}_T} \tag{14}$$

where Pr_m is the so-called "mixed Prandtl number," which is obtained as a viscosity-weighted average of the molecular and turbulent Prandtl numbers. The above result can be interpreted as a local energy recovery mechanism comparable to the differential form of Eq. (1), in which Pr_m acts as a local efficiency factor of "incremental" recovery. The wall recovery factor is computed by integrating the above relation under simplifying assumptions. In particular, using a two-layer model of the turbulent boundary layer, with a laminar sublayer with Pr constant ($\mathrm{Pr}_m = \mathrm{Pr}$) and a fully turbulent outer region with Pr_T constant ($\mathrm{Pr}_m = \mathrm{Pr}_T$), results in:

$$r = \mathrm{Pr}_T + (\mathrm{Pr} - \mathrm{Pr}_T)(u_s/u_e)^2 \tag{15}$$

where u_s is the velocity at the edge of the sublayer. Substitution of appropriate values of u_s/u_e and Pr_T (in particular, $\mathrm{Pr}_T = 1$) then permits a relation of the customary form to be reproduced.

Although the above relation is instructive for revealing the composite laminar/turbulent nature of the recovery effect in a turbulent boundary layer, in particular the important role of the viscous sublayer, it is evidently very approximate and limited in accuracy. For example, it suggests a Reynolds number effect, through the value of u_s/u_e, which is not observed in reality. Also, the use of a constant value of the turbulent Prandtl number is not appropriate for boundary layer flow. According to both experimental evidence [1–3] and DNS simulations [13], Pr_T varies significantly in the turbulent region of the boundary layer, with typical values of 0.9 or 1.0 near the wall and values of 0.5 to 0.7 near the outer edge.

It can be verified that the above analysis is essentially equivalent to assuming that the convective derivative of the total enthalpy can be neglected. This implies treating the boundary layer as a quasi-Couette flow, in which case indeed the above analysis applies exactly (cf. [14]). For the flat-plate turbulent boundary layer there is some justification for this concept in view of the fact that most of the boundary layer is described by the log law (small wake component), with the wall shear stress varying only weakly with the streamwise distance. This also implies that, although the above analysis may shed some light on the character of the recovery mechanism in the turbulent boundary layer, the energy budget is evidently not complete. By treating the boundary layer as a quasi-Couette flow, with zero convective derivates, the energy-migration term is not reproduced. A more complete description, therefore, requires the convective terms to be included. This can be conveniently expressed by applying the Crocco transformation, which, when further assuming both the shear stress $\tau(u)$ and enthalpy $h(u)$ as a function of the velocity u, allows the energy equation to be expressed as follows (see, e.g., [3]):

$$\frac{\mathrm{d}}{\mathrm{d}u}\left(\frac{1}{\mathrm{Pr}_m}\frac{\mathrm{d}h}{\mathrm{d}u}\right) + \frac{1 - \mathrm{Pr}_m}{\mathrm{Pr}_m}\frac{1}{\tau}\frac{\mathrm{d}\tau}{\mathrm{d}u}\frac{\mathrm{d}h}{\mathrm{d}u} + 1 = 0 \tag{16}$$

It can be easily observed that when either $\mathrm{Pr}_m = 1$, or when $d\tau/du = 0$ as in the case of Couette flow, the second term cancels and the equation can be analytically integrated to yield Eq. (14). This approach was further followed by Whitfield and High [15] for the case of the turbulent flat-plate boundary layer, by prescribing the relation for $\tau(u)$ explicitly. The resulting nonlinear differential equation for $h(u)$ was solved with a perturbation approach similar as in the present analysis, under the additional assumption of constant Pr_m. Selecting the value of Pr_m such that the experimental wall recovery factor was reproduced, this allowed a reasonable correspondence to be obtained to the experimental temperature–velocity relation.

In conclusion, we may consider that the structure of the extended CB relations with a recovery component and a complementing energy-migration term reflects basic energy conservation mechanisms that also apply in turbulent flow. For free shear flows there was a full justification for using the extended CB relation with constant r under the realistic assumptions of constant turbulent viscosity across the shear layer and constant turbulent Prandtl number. However, in turbulent boundary layers the energy transport is of essential mixed molecular/turbulent nature. Moreover, the turbulent Prandtl number varies significantly in the boundary layer. Therefore, it cannot be expected that the integral form of the extended CB relation with a single value of the recovery factor r can be applied to turbulent boundary layers with the same level of confidence. However, reasonable results for the temperature–velocity relation in the turbulent flat-plate boundary layer were reported in the literature when using a constant value of the mixed Prandtl number, which is equivalent to the laminar approach. This provides some support for extending the results of the laminar flow analysis to turbulent boundary layers as well.

Conclusions

The Crocco–Busemann relation expresses the relation between the velocity and the enthalpy, which occurs in steady shear flow. It describes, in particular, that for adiabatic conditions the total enthalpy remains constant throughout the shear layer, provided that $\mathrm{Pr} = 1$ but irrespective of pressure gradient and compressibility effects. For the case that $\mathrm{Pr} \neq 1$ classic theory provides an approximate extension of the CB-relation for wall-bounded flows in the form of a recovery correction.

The present analysis provides asymptotically correct first-order corrections for the Pr effect on the CB relation in laminar flow for boundary layers as well as free shear layers. For boundary layers and wakes at arbitrary free-stream conditions, the first part of this modification can indeed be written in terms of a partial thermal recovery from the local free-stream conditions, with recovery factor $r \approx \mathrm{Pr}^{1/2}$. However, as the "imperfect" recovery is due to an imbalance in diffusion, an additional term occurs, which represents the energy migration toward the outer flow. For the mixing layer a similar correction was obtained, however, the recovery component in this expression shows a mixed dependence on the velocities of both adjacent external streams. The analysis further reveals that the results can be extended to turbulent free shear layer flows, where $r \approx \mathrm{Pr}_T^{1/2}$. For turbulent boundary layers only a conceptual justification was found, as the local recovery factor actually varies across the boundary layer.

References

[1] Schlichting, H., 1979, *Boundary-Layer Theory*, 7th ed. McGraw-Hill, NY.
[2] White, F. M., 1991, *Viscous Fluid Flow*, 2nd ed. McGraw-Hill, New York.
[3] Schetz, J. A., 1993, *Boundary Layer Analysis*, Prentice–Hall, Englewood Cliffs, NJ.
[4] Eckert, E. R. G., 1986, "Energy Separation in Fluid Flows," Int. Commun. Heat Mass Transfer, **13**, pp. 127–143.
[5] Smits, A. J., and Dussauge, J. P., 1996, *Turbulent Shear Layers in Compressible Flow*, American Institute of Physics, Woodbury, NY.
[6] Van Oudheusden, B. W., 1997, "A Complete Crocco Integral for Two-Dimensional Laminar Boundary Layer Flow Over an Adiabatic Wall for Prandtl Numbers Near Unity," J. Fluid Mech., **353**, pp. 313–330.
[7] Van Oudheusden, B. W., 2005, "Energy Separation in Steady Separated Wake Flow," J. Fluids Eng., **127**, pp. 611–614.

[8] Anderson, J. D., 1989, *Hypersonic and High Temperature Gas Dynamics*, McGraw-Hill, New York.
[9] Van Oudheusden, B. W., 2004, "Compressibility Effects on the Extended Crocco Relation and the Thermal Recovery Factor in Laminar Boundary Layer Flow," J. Fluids Eng., **126**, pp. 32–41.
[10] Dorrance, W. H., 1962, *Viscous Hypersonic Flow*, McGraw-Hill, New York.
[11] Tennekes, H., and Lumley, J. L., 1972, *A First Course in Turbulence*, MIT Press, Cambridge, MA.
[12] Rubesin, M. W., 1953, "A Modified Reynolds Analogy for the Compressible Turbulent Boundary Layer on a Flat Plate," NACA Technical Note 2917.
[13] Guarini, S. E., Moser, R. D., Shariff, K., and Wray, A., 2000, "Direct Numerical Simulation of a Supersonic Turbulent Boundary Layer at Mach 2.5," J. Fluid Mech., **414**, pp. 1–33.
[14] Van Oudheusden, B. W., 2004, "The Reference Temperature Method Reconsidered and its Relation to Compressible Couette Flow," IUTAM Symposium on One Hundred Years of Boundary Layer Research, Göttingen, Germany, August 2004.
[15] Whitfield, D. L., and High, M. D., 1977, "Velocity–Temperature Relations in Turbulent Boundary Layers with Nonunity Prandtl Numbers," AIAA J., **15**, pp. 431–434.

Experimental Methods for Hydrodynamic Characterization of a Very Large Water Tunnel

Joel T. Park
Naval Surface Warfare Center Carderock Division
West Bethesda, MD 20817-5700
e-mail: joel.park@navy.mil

J. Michael Cutbirth
U. S. Navy William B. Morgan Large Cavitation Channel
Memphis, TN 38113-0428

Wesley H. Brewer
Fluid Physics International,
Starkville, MS 39759

The methodology for hydrodynamic characterization of a very large water tunnel is described. Results are presented for the U. S. Navy William B. Morgan Large Cavitation Channel in Memphis, Tennessee, the world's largest water tunnel. Three key characteristics of tunnel velocity were measured: temporal stability, spatial uniformity, and turbulence. The velocity stability at a single point for run times greater than 2 h was measured as ±0.15% at the 95% confidence level for velocities from 0.5 to 18 m/s*(1.6–59* ft/s*). The spatial nonuniformity for the axial velocity component was ±0.34 to ±0.60% for velocities from 3 to 16* m/s*(9.8–52* ft/s*). The relative turbulence intensity was measured as 0.2–0.5% depending on tunnel velocity.*
[DOI: 10.1115/1.2060740]

Introduction

A methodology has been developed for the hydrodynamic characterization of a very large-scale water tunnel. Results of the experimental methods are described for the U. S. Navy William B. Morgan Large Cavitation Channel (LCC) in Memphis, Tennessee, the largest closed circuit water tunnel in the world. The design and early performance measurements were described initially by Etter and Wilson [1,2]. The geometry and dimensions of the channel are shown schematically in Fig. 1. This paper is an abbreviated version of a paper originally presented at the Fourth ASME/JSME Joint Fluids Engineering Conference [3]. Additional details are documented in Park et al. [4].

Uncertainty Estimates in LDA Calibration

The Laser Doppler Anemometer (LDA) system at the LCC for the measurements in this paper consists of four Dantec BSA 57N11 signal processors, three fiber optic probes, two Spectra Physics 6 W argon-ion lasers (models 2016 and 2017), a Dantec three-dimensional traverse with remote control, and Dantec Flow software. A single component fiber optic probe monitors tunnel speed in a window near the test section entrance. A two-component optical head is mounted on a three-dimensional traversing system for the measurement of local velocity for models and an empty test section. The traverse has a range of 1200 mm (3.9 ft) in the y and z directions and 1300 mm (4.3 ft) in the x direction where x is positive in the direction of flow, y is positive toward the viewer in Fig. 1, and z is positive in the vertical direction. For the y direction, the software contains a magnification factor for the index of refraction of water; consequently, the traverse range in water in the y direction is 1600 mm (5.2 ft). The controller for the traversing system and motors is an Isel-Schrittmotor-Controller C142-4.1, while the drive motors are stepper motors. The stepper motors have a resolution of $\pm 5\ \mu\text{m}(0.20\times 10^{-3}$ in).

A typical calibration uncertainty in velocity for the LDA was ±25 mm/s (±1 in./s) at the 95% confidence level from a rotating disk. The uncertainty in the regression analysis of the data based upon statistical calibration theory from Scheffe [5] and Carroll et al. [6] was usually ±10 mm/s (±0.4 in./s). Details of the uncertainty estimates are describe in Park et al. [3,4].

Tunnel Velocity

Long-Term Temporal Stability. The long-term velocity stability of velocity in the test section has been quantified with a number of measurements. These measurements are summarized in Fig. 2. For the more recent measurements, the uncertainty in velocity from variations in flow speed at 0.5 to 18 m/s (1.6–59 ft/s) is ±0.15% at the 95% confidence level for run durations greater than 2 h.

Tunnel Velocity From Pump Speed. LDA is the most accurate method for the measurement of tunnel velocity. The channel operators adjusted the velocity by digitally setting the pump speed in rpm. The pump speed can be set within ±0.01 rpm. From a linear fit of the data, the slope for an empty test section is 0.320 m/s/rpm with an intercept of −0.164 m/s. From the slope of this curve (0.32 m/s/rpm), tunnel speed can be adjusted within one or two iterations for a precise set-point velocity by LDA.

Although the concept of presenting data as residuals is not particularly original, data as residuals are rarely applied by experimentalists in fluid mechanics. The concept of residuals is usually presented in statistics texts such as Ross [7]. For an adequate straight line curve fit, the data should be randomly distributed about zero, which did not occur in this case. An additional benefit of the residuals is that the size of the error bars is evident for highly precise data. The error bars would be smaller than the size of the symbols on a standard linear plot of the data.

The data were reevaluated with two different curve fits. From a commercial computer code, "TableCurve2D," an optimal curve fit was computed to be a power law with an exponent of 1.04. The results are presented in Fig. 3. As the figure indicates, the prediction limit at the 95% confidence level of the nonlinear fit is about ±0.02 m/s (0.8 in./s). This value is not significantly larger than the data scatter in the LDA calibration. The uncertainty in the velocity from LDA is only slightly larger than the prediction limit. At the lower velocities below about 2 m/s (6.6 ft/s), the data are linear with nearly the same slope of 0.32 m/s/rpm(1.0 ft/s/rpm). After tunnel speed is calibrated by the method in Fig. 3, tunnel speed can be reproduced by rpm setting almost within the uncertainty of the LDA calibration.

With a model in the tunnel, the velocity calibration from pump speed will be different from an empty test section. However, the tunnel speed can be set to a precise speed by LDA within one or two iterations from the empty test section data. Additionally, a powered model will also influence velocity. The propeller acts as a pump and adds an incremental velocity of about 0.5% in comparison to the dummy hub case at 12.2 m/s (40 ft/s), a typical test condition for a submarine model.

Velocity Nonuniformity

One of the measures of hydrodynamic performance is velocity nonuniformity. The design specification for the LCC was 1% [1,2]. Comprehensive measurements of velocity uniformity have been conducted by a two-component fiber optic probe with a 1600

Contributed by the Fluids Engineering Division for publication in the JOURNAL OF FLUIDS ENGINEERING. Manuscript received by the Fluids Engineering Division September 16, 2003; final manuscript received: July 22, 2005. Review conducted by: Joseph Katz.

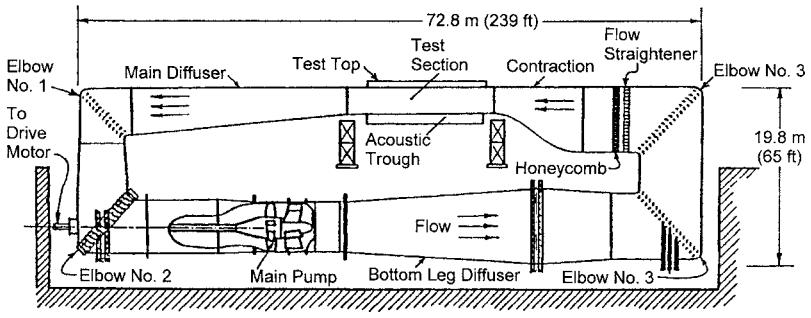

Fig. 1 Schematic drawing of the LCC

mm lens. In these measurements, the survey area was 1000 mm high by 1550 mm wide (3.3 by 5.1 ft) with a resolution of 50 by 50 mm (2.0 in). The survey area was 17% of the test section cross-sectional area. The velocity measurement at each position was an average of 1000 samples. The total number of survey positions was 672, where the number of survey positions outside the boundary layer was typically 650.

Summaries of the results are shown in Fig. 4 for the axial and vertical components. The vertical velocity has a variation of nominally 2% with a minimum value of 1.8%. The minimum variation of axial velocity was 0.34%. The variation was systematically lower in bay 4 near the center of the test section in comparison to bay 2 near the entrance with a nominal value of 0.4%. Bay 4 is the region of the tunnel where most models are installed.

Typical contour plots for the data summarized in Fig. 4 are shown in Fig. 5. For these contour plots, the spatial coordinates are nondimensionalized with the channel half width, $h/2$. The gray scale in Fig. 5 for the axial component is in increments of 0.005 (0.5%) for the local mean velocity relative to the centerline velocity (U/U_o). Typically, only three levels are observed for bay 2 while bay 4 has only two. The gray-scale variation is consistent with the statistics where the velocity variation is about 0.5% in bay 2 but 0.4% in bay 4.

Turbulence

Experimental Methods. The primary method for the measurement of turbulence in a water tunnel is by hot-film anemometry with a constant temperature anemometer (CTA). The background noise level of LDA is about 1%; consequently, a LDA cannot measure the anticipated turbulence of 0.1%. One of the difficulties with CTA is the low operating temperature required in water. Changes in water temperature will affect results. Additional details on the effect of temperature and calibration in water are described by Bruun [8].

Since water temperature increases from the energy from the pump, data acquisition was greatly simplified through acquisition of the data in a single set of measurements. That is, calibration data and turbulence data were acquired from the same set of data. Additionally, the sensitivity of the bridge voltage for the CTA greatly diminishes with increasing velocity. The maximum value reported in the literature for calibration in water is about 6 m/s (20 ft/s) [8]. The solution at Penn State was to measure the turbulence in the plenum chamber and extrapolate the results by theory to the test section [9].

For direct measurements of turbulence in the test section, a head-form fixture attached to a submarine strut was modified to accept a TSI probe support (1159AJ) and conical film probe (1230W). The outer diameter of the adapter was 50.8 mm (2.0 in.). The calibration velocity for the hot film was provided by the LDA located 2 mm (0.08 in.) upstream of the conical tip. The CTA was a TSI IFA 300, which had been modified by TSI to provide proper frequency response of the conical film and probe support with a 4.6 m (15 ft) cable for operation in water. Also, the tunnel water was deaerated to 10% saturation of oxygen for prevention of bubble problems on the probe. Additional details are described by Park et al. [3,4].

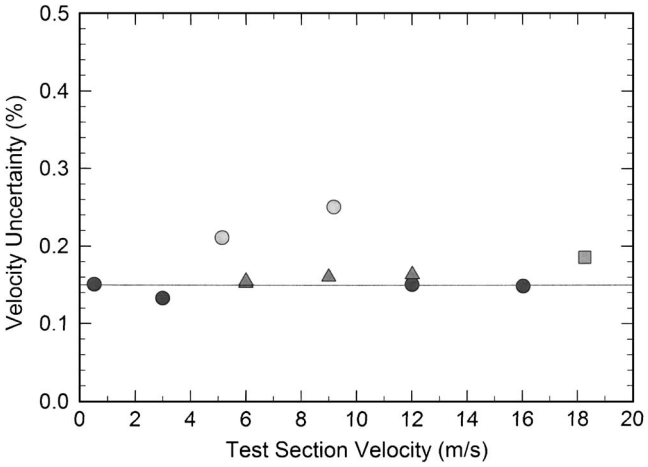

Fig. 2 Long-term temporal stability of LCC test section velocity. Symbols:—0.15% reference line, light gray circles, Aerometrics July 98, gray squares, Dantec BSA Nov. 99, dark gray circles, Dantec BSA Oct. 00 & Jan. 01, ▲ Dantec BSA May 01.

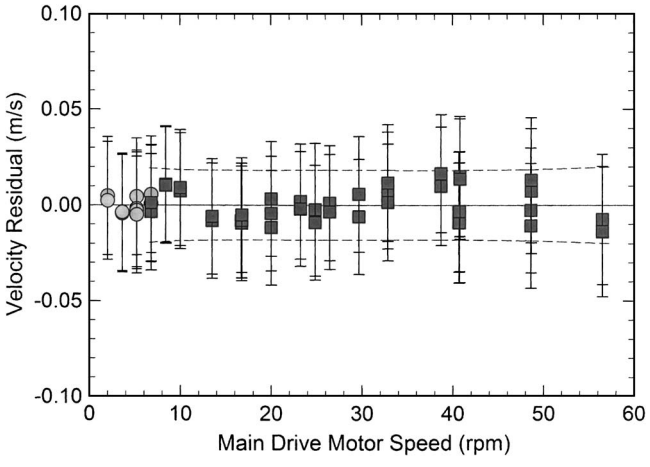

Fig. 3 Tunnel velocity from main pump speed. Residuals of power-law fit. Low range intercept: −0.1314 m/s, slope: 0.3231 m/s/rpm, r: 0.999 973, high range intercept: 0.0679 m/s, slope: 0.2449, exponent: 1.0359, r=0.999 9983. Symbols: --- ±95% prediction limit, light gray circles, LDA data, linear fit, gray squares, LDA data, power-law fit.

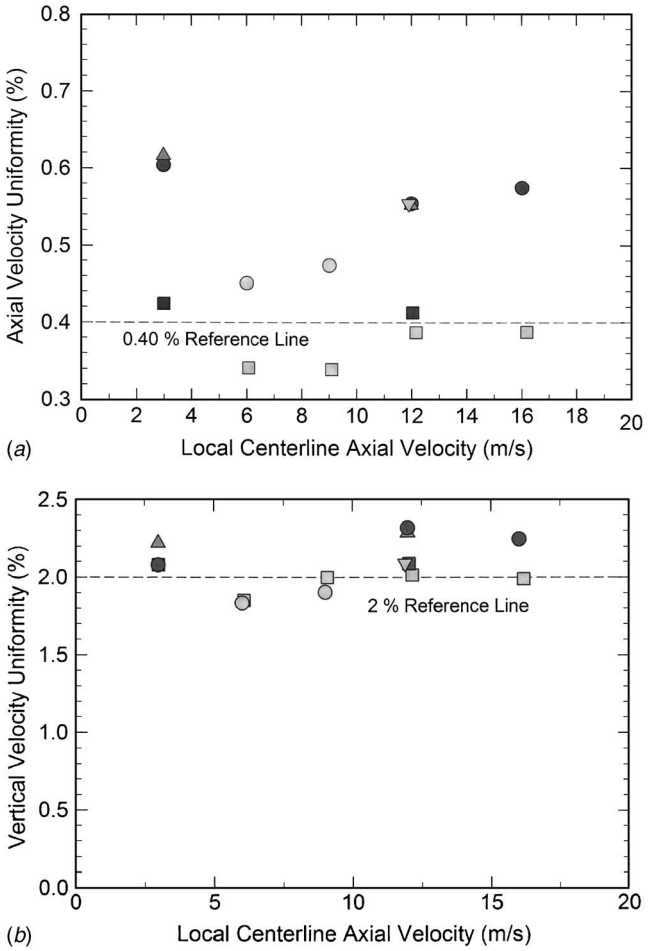

Fig. 4 Summary of spatial variation of tunnel velocity. Symbols: gray upside down triangle, Bay 2, window 1, Dec. 98, dark gray circles, Bay 2, window 1, Jan. 01, light gray circles, Bay 2, window 1, May 01, light gray triangle, Bay 2, seeder on, Jan. 01, dark gray squares, Bay 4, window 1, Jan. 01, light gray squares, Bay 4, window 1, May 01. (a) Axial velocity, (b) vertical velocity.

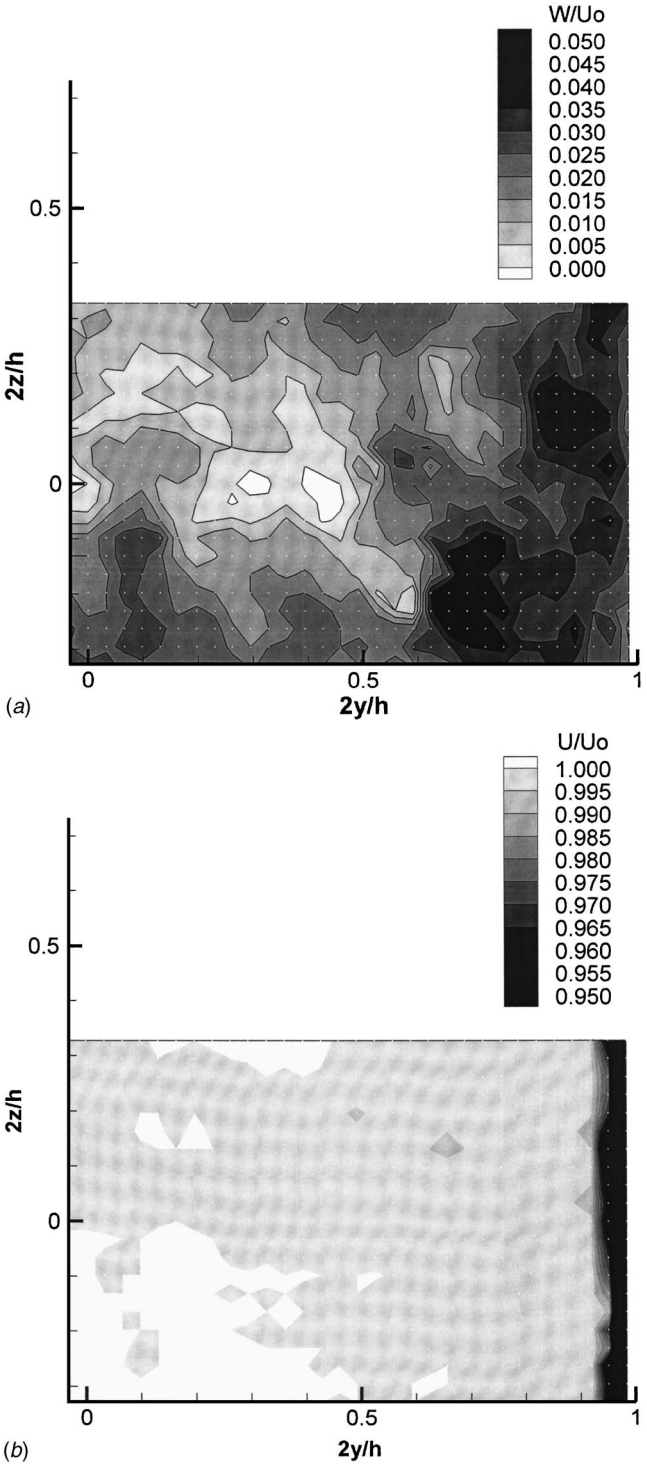

Fig. 5 Contour plots for test section in bay 4 window 1 at 16.2 m/s (53 ft/s) in May 2001. (a) Vertical velocity component, (b) axial velocity component.

Experimental Results. The reference velocity for the hot-film calibration was the LDA. The inflow to the hot-film probe was characterized by measurements 2 mm (0.08 in.) upstream of the probe tip with the LDA. Measurements were performed within a non-dimensional radius of six probe-fixture radii for the vertical and axial velocity components. The vertical and axial velocity components were referenced to a measurement 1 m (3.3 ft) from the centerline. The local velocity ratio was very nearly one. The most significant feature is the downward velocity below the centerline. The minimum measured value was −2.5% or −1.4° flow angle for three tunnel velocity conditions of 5, 10, and 15 m/s (16, 33, and 49 ft/s).

High-resolution measurements were also completed in a small region at the probe tip with a maximum non-dimensional radius of 0.2. This radius is the same order of magnitude as the length of the LDA probe volume, which was about 0.26 of the probe fixture radius. The purpose of this measurement was to resolve the effect of the probe on the flowfield nearer the probe tip. The minimum axial velocity near the probe tip was measured as 0.97 of the reference velocity or 3% below the reference for three tunnel velocities (5, 10, and 15 m/s or 16, 33, and 49 ft/s).

The test section turbulence was measured by both a TSI IFA-300 and Dantec StreamLine CTA. The frequency response of the TSI CTA is fixed by factory settings and was adjusted at the factory for the probe and probe support combination in water. The frequency response of the Dantec CTA was adjustable through software. The measured values were 96 kHz for the TSI CTA and 140 kHz for the Dantec unit.

The experimental results are presented in Fig. 6. As the figure indicates, good agreement in the turbulence data was obtained for the two CTAs. The turbulence had a maximum of about 0.49% at 2 m/s (6.6 ft/s) and a minimum of 0.17% at 0.5 m/s (1.6 ft/s). A gradual increase occurred in turbulence with increasing velocity

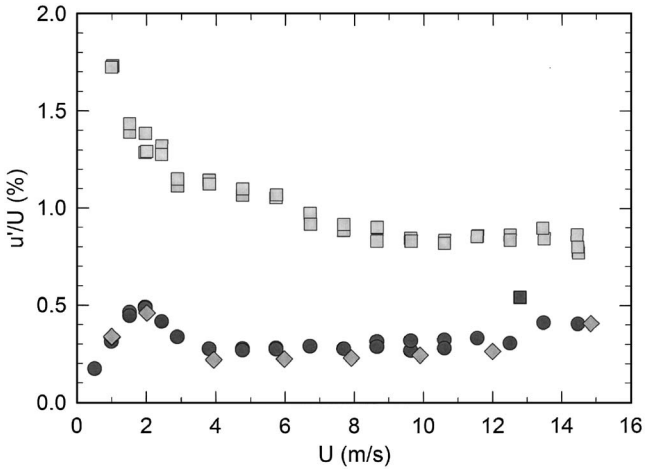

Fig. 6 Test section turbulence from hot film in comparison to LDA noise. Symbols: dark gray circles, TSI CTA data, gray diamond, Dantec CTA data, light gray squares, LDA noise, gray squares, LDA noise, LCC OWD.

above 4 m/s (13 ft/s) from 0.22% to 0.41% at 15 m/s (49 ft/s).

Also as the figure shows, the background noise level of the LDA is significantly larger than the results obtained by CTA. The minimum noise level was 0.77%, which occurred at the highest tunnel velocity, where the value measured by CTA was 0.41% or approximately half of the LDA value. During an LCC open water dynamometer (OWD) experiment, the relative turbulence intensity in the freestream was measured as 0.54% at 12.79 m/s (42 ft/s), which is one of the lowest values measured by the LDA system for the LCC. In comparison, the hot-film measured 0.31% at 12.50 m/s (41 ft/s) as shown in Fig. 6.

Velocity spectra for the IFA 300 were computed with the TSI Thermal Pro software. The data were averaged in 8192 sample record lengths. The frequency resolution was between 0.244 and 2.44 Hz with the resolution increasing with tunnel velocity and sample rate. Examples of the spectra are presented in Fig. 7 for velocities of 0.5 (1.6 ft/s) and 14.5 m/s (47.6 ft/s), respectively. The frequency is nondimensionalized with the measured cutoff frequency of the turbulence, that is, the frequency where the energy from the turbulence runs into the noise floor of the instrument. In most cases, the frequency at the minimum magnitude of spectrum was selected.

The spectra are quite smooth with the exception of instrument noise spikes at the higher frequencies. For reference, the first three large noise spikes in Fig. 7(*a*) for 0.5 m/s (1.6 ft/s) are at 30, 60 (line frequency), and 180 Hz or f/f_c=0.122, 0.246, and 0.737. A frequency spike at 180 Hz or f/f_c=0.054 is barely discernable in Fig. 7(*b*) for 14.5 m/s (47.6 ft/s). The results are similar for other velocities including 9 m/s (30 ft/s), where an audible resonant frequency can be heard. No resonant frequency spikes were observed in any spectra. The pump for the tunnel is a seven-bladed propeller. The blade frequency at 9 m/s (30 ft/s) tunnel velocity was 3.0 Hz in comparison to the frequency resolution of 1.2 Hz. The blade-passage frequencies for the various tunnel speeds were greater than the frequency resolution of the spectra, and they are not evident in any of the spectra.

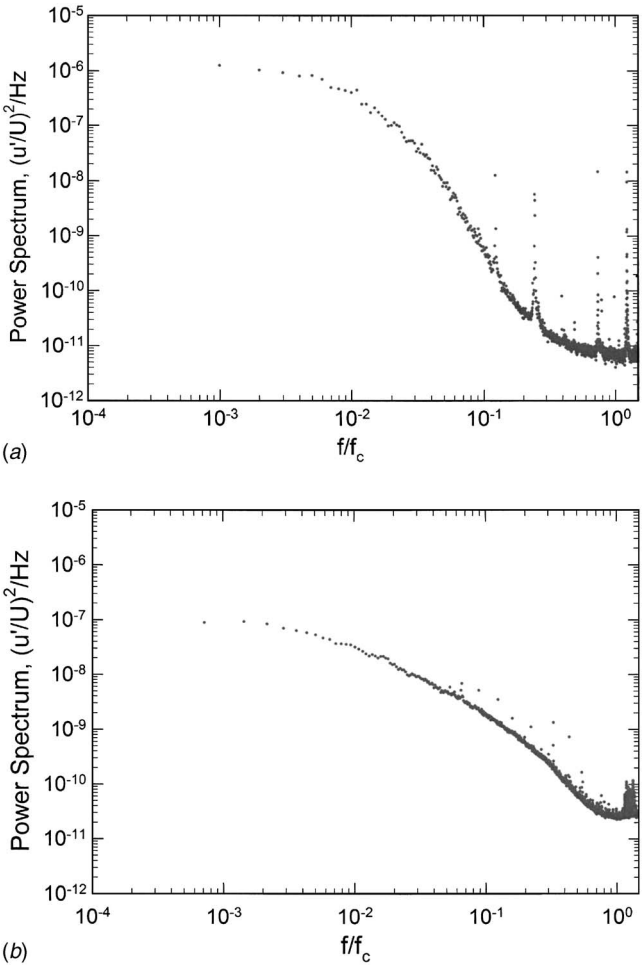

Fig. 7 Velocity frequency spectra for low and high tunnel velocities. (a) Mean velocity 0.505 m/s (1.6 ft/s), u'/U=0.17%, f_c=244 Hz, Δf=0.244 Hz (b) Mean velocity 14.47 m/s (47.6 ft/s), u'/U=0.40%, f_c=3376 Hz, Δf=2.441 Hz.

Conclusions

Experimental methods have been described for the hydrodynamic characterization of a very large water tunnel. As an example of the methodology, comprehensive experimental results and data analysis have been presented on the hydrodynamic performance of the William B. Morgan Large Cavitation Channel. This research represents several years of data accumulation. The results demonstrate a very high quality of hydrodynamic performance and are probably the most comprehensive data ever presented for any water flow test facility. For the most part, performance equals or exceeds design specifications. The results should be a useful guide for future experiments at the LCC and characterization of other water tunnels. Additional details are described in Park et al. [4].

Acknowledgments

The support and encouragement by Dr. William B. Morgan, former directorate head of Hydromechanics (Code 50) over the last several years, is gratefully acknowledged. Dr. Morgan also provided some very valuable comments for this paper. William G. Day, Jr., former department head of Code 5100, has more recently provided support and encouragement for the writing of this paper. Robert J. Etter of Code 5400 developed the ideas for the support structure for the hot-film probe for the measurement of the tunnel turbulence and supervised the fabrication of the hardware. Dr. George Papadopolous, formerly of Dantec Dynamics, assisted with the Dantec instrumentation for the turbulence measurements. The excellent support by the LCC Operations staff for the measurements is gratefully acknowledged. The research documented in this paper was primarily financed by LCC operations and maintenance funds. Finally, this paper is dedicated to James N. Blanton

(b. 1961 - d. 2003), who supplied the technical leadership and foundation for many of the experiments during his tenure at the LCC.

References

[1] Etter, R. J., and Wilson, M. B., 1992, "The Large Cavitation Channel," *Proceedings of the 23rd American Towing Tank Conference*, University of New Orleans, New Orleans, LA, pp. 243–252.

[2] Etter, R. J., and Wilson, M. B., 1993, "Testing Ship Designs in a Water Tunnel," Mech. Eng. (Am. Soc. Mech. Eng.) **115**(10), pp. 74–80.

[3] Park, J. T., Cutbirth, J. M., and Brewer, W. H., 2003, "Hydrodynamic Performance of the Large Cavitation Channel (LCC)," Paper FEDSM2003-45599, *Fourth ASME/JSME Joint Fluids Engineering Conference*, Honolulu.

[4] Park, J. T., Cutbirth, J. M., and Brewer, W. H., 2002, "Hydrodynamic Performance of the Large Cavitation Channel (LCC)," NSWCCD-50-TR—2002/068, Naval Surface Warfare Center, Carderock Division, West Bethesda, MD.

[5] Scheffe, H., 1973, "A Statistical Theory of Calibration," Ann. Stat., **1**(1), pp. 1–37.

[6] Carroll, R. J., Spiegelman, C. H., and Sacks, J., 1988, "A Quick and Easy Multiple-Use Calibration-Curve Procedure," Technometrics, **30**(2), pp. 137–141.

[7] Ross, S. M., 1987, *Introduction to Probability and Statistics for Engineers and Scientists*, Wiley, New York.

[8] Bruun, H. H., 1995, *Hot-Wire Anemometry*, Oxford University Press, Oxford.

[9] Robbins, B. E., 1978. "Water Tunnel Turbulence Measurements Behind a Honeycomb," J. Hydronaut., **12**(3), pp. 122–128.

Pseudocylinder Parametrization For Mine Impact Burial Prediction

Peter C. Chu[1]
e-mail: pcchu@nps.edu

Chenwu Fan

Naval Ocean Analysis and Prediction Laboratory, Naval Postgraduate School, Monterey, CA 93943

1 Introduction

The United States military has undergone numerous changes since the end of the Cold War. Specifically, the U.S. Navy experienced a shift in the area of engagement from the "blue water" (water depth greater than 100 m) to littoral regions of the world. The sea mines become the big threat in the naval operations. Within the past 15 years three U.S. ships, the USS Samuel B. Roberts (FFG-58), Tripoli (LPH-10), and Princeton (CG-59) have fallen victim to mines. The total ship damage was $125 million while the mines cost approximately $30 ,000 [1].

Let (x,y) be the horizontal coordinates and z the vertical coordinate. A two-dimensional model (called IMPACT28) was developed to predict the mine's movement in the (x,z) cross section [2]. The model contains two momentum equations (in x and z directions) and one moment of the momentum equation (in the y direction), and predicts the mine's center of mass (COM) position in the (x,z) plane and the rotation (i.e., the mine's orientation) around the y axis. Since the mine's movement in IMPACT28 is strictly in the (x,z) plane, it is very hard to include the motion of fluid in the two-dimensional model, because it is impossible to lay a mine in the same direction of the fluid velocity. In the littoral zone, the water velocity is not negligible. The application of the two-dimensional model for the operational use is limited.

Recently, a three-dimensional recursive model (IMPACT35) has been developed to predict the rigid cylinder's (or cylindrical mine's) translation velocity and orientation in fluid involving nonlinear dynamics, fluid–structure interaction, and instability theory [3–5]. However, the Navy operational mines are usually not cylindrical. The existing model should be extended from the cylindrical mines to more general shapes of mines with nose and tail.

2 Mine's Location and Orientation

For an axially symmetric cylinder, the centers of mass (COM) $\mathbf{X}$ and center of volume (COV) $\mathbf{B}$ are on the mine's main axis (Fig. 1). Let (L,R,χ) represent the mine's length, radius, and the distance between the two points $(\mathbf{X},\mathbf{B})$. The positive χ values refer to the nose-down case, i.e., the point $\mathbf{X}$ is lower than the point $\mathbf{B}$. Let $F_{\mathrm{E}}(\mathrm{O},\mathbf{i},\mathbf{j},\mathbf{k})$ be the earth-fixed coordinate (E coordinate) with the origin "O," and three axes: x, y axes (horizontal) with the unit vectors $(\mathbf{i},\mathbf{j})$ and z axis (vertical) with the unit vector $\mathbf{k}$ (upward positive). The position of the cylinder is represented by the position of the COM,

$$\mathbf{X} = x\mathbf{i} + y\mathbf{j} + z\mathbf{k}, \tag{1}$$

which is a translation of the cylinder. The translation velocity is given by

$$\frac{d\mathbf{X}}{dt} = \mathbf{V}, \quad \mathbf{V} = (u,v,w). \tag{2}$$

Let the orientation of the mine's main axis (pointing downward) is given by $\mathbf{i}_{\mathrm{M}}$. The angle between $\mathbf{i}_{\mathrm{M}}$ and $\mathbf{k}$ is denoted by $\psi_2+\pi/2$. The projection of the vector $\mathbf{i}_{\mathrm{M}}$ onto the (x,y) plane creates an angle (ψ_3) between the projection and the x axis (Fig. 2). The mine rotates around the main axis (i.e., $\mathbf{i}_{\mathrm{M}}$) with an angle of ψ_1. The three angles (ψ_1,ψ_2,ψ_3) determine the mine's orientation.

Three coordinate systems are used to calculate the forces and torques: earth-fixed coordinate (E coordinate), the cylinder's main axis following the coordinate (M coordinate), and the hydrodynamic force following the coordinate (F coordinate) [3]. The origin of both M and F coordinates is at COM. The hydrodynamic forces and torques are easily computed using the F coordinate. The cylinder's moments of gyration are simply represented using the M coordinate.

3 Pseudocylinder Parametrization

For a near-cylindrical mine with a nose and tail falling through a single medium or multiple media, the buoyancy force and torque are relatively easy to calculate. But, the hydrodynamic forces (lift, drag) and torques are difficult to compute. A feasible way is to transform a mine with nose and tail to a cylindrical mine (i.e., called the pseudocylinder parametrization). An axially symmetric mine usually consists of three parts: cylindrical body with radius of R, nose, and tail (Fig. 3). The lengths of the mine, nose, and tail are L, L_n, and L_t. A pseudocylinder is defined with the following features: the same radius (R) of the mine's cylindrical body and the same volume as the original mine (Fig. 4). It consists of three parts: original cylindrical body, and equivalent cylinders for nose and tail. Let (Π,Π_n,Π_t) be the volumes of the mine, nose, and tail. The equivalent cylinder has length

$$L_{ne} = \frac{\Pi_n}{\pi R^2}, \tag{3}$$

for the nose, and

$$L_{te} = \frac{\Pi_t}{\pi R^2}, \tag{4}$$

for the tail. Let (c_c,c_m) be the mine's midpoint on the main axis and the COM position, and let c_{ev} be the COV of the pseudocylindrical mine (Fig. 4). The gravity is downward and passing through c_m. The buoyancy force is upward and passing through c_{ev}. Let ε_1 be the distances between c_c and c_m,

$$\varepsilon_1 = \frac{L_n - L_{ne}}{2} - \frac{L_t - L_{te}}{2}. \tag{5}$$

Let ε_2 be the displacement from c_c to c_m that is easy to determine if COM is given. Let χ be the displacement from c_{ev} to c_m that is calculate

$$\chi = \varepsilon_1 + \varepsilon_2. \tag{6}$$

Both χ and ε_2 can be positive and negative. The positive values refer to the nose-down case, i.e., the point c_m is lower than the point c_{ev} for positive χ and the point c_c is lower than the point c_{ev} for positive ε_2.

4 Impact Burial Prediction

4.1 Two-Dimensional Modeling. Let the mine be moving in the (x,z) cross section. The mine's orientation is represented by the angle (ψ_2) rotating around the y axis. The two-dimensional model (called IMPACT28) consists of two momentum equations [for (x,z)] and one moment of momentum equation (for ψ_2) (see [2])

[1]Corresponding author: Peter C Chu, Naval Postgraduate School, Monterey, CA 93943. Telephone: 1-831-656-3688; fax: 1-831-656-2712.

Contributed by the Fluids Engineering Division for publication in the JOURNAL OF FLUIDS ENGINEERING. Manuscript received by the Fluids Engineering Division January 4, 2005. Final manuscript received: August 4, 2005. Review conducted by: Joseph Katz.

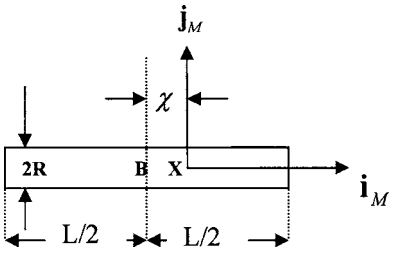

Fig. 1 Axially symmetric cylindrical mine. Here, χ is the distance between the COV (B) and COM (X), and (L,R) are the cylinder's length and radius.

$$\frac{d^2x}{dt^2} \equiv \frac{du}{dt} = \frac{F_h^x}{\rho\Pi}, \tag{7}$$

$$\frac{d^2z}{dt^2} \equiv \frac{dw}{dt} = -g + \frac{F_{nh}^z + F_h^z}{\rho\Pi}, \tag{8}$$

$$J_2\frac{d^2\psi_2}{dt} = F_{nh}^z\chi\cos\psi_2 + M_h^y, \tag{9}$$

where (F_h^x, F_h^z, F_{nh}^z) are the components of hydrodynamic and nonhydrodynamic forces; J_2 is the moment of inertia and M_h^y is the hydrodynamic torque in the y direction; and g is the gravitational acceleration. Since the mine's movement is strictly in the (x,z) plane, it is very hard to include the motion of fluid in the two-dimensional model, because it is impossible to lay a mine in the same direction of the fluid velocity. In the littoral zone, the water velocity is not negligible. The application of the two-dimensional model for the operational use is limited.

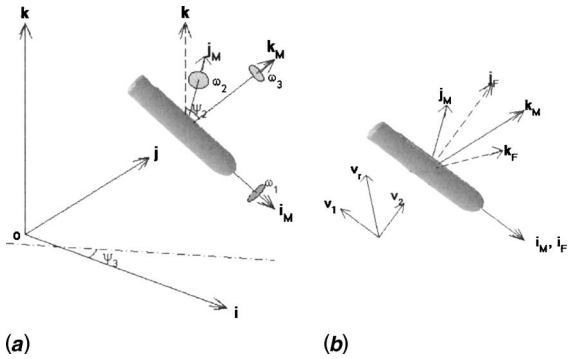

Fig. 2 Three coordinate systems

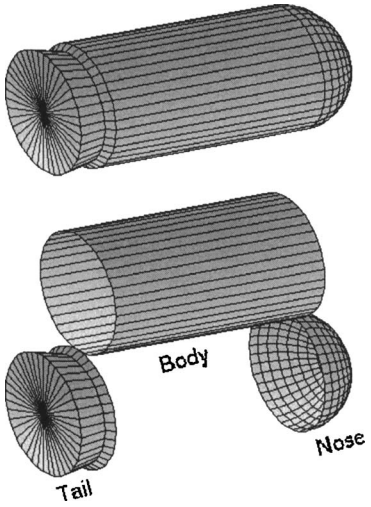

Fig. 3 Mine with nose, tail, and cylindrical body

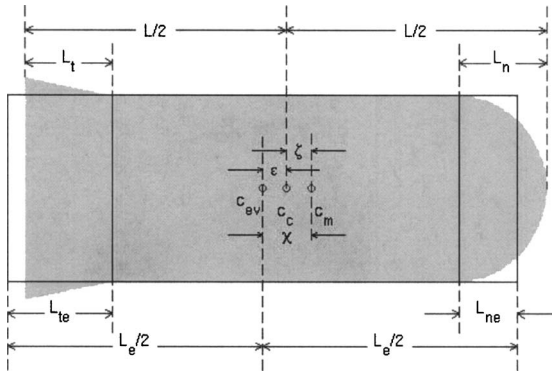

Fig. 4 Location of c_v, c_{ev}, and c_m. Here, ε is the distance between c_v and c_m; χ is the distance between c_{ev} and c_m.

4.2 Three-Dimensional Modeling. Three-dimensional model (called IMPACT35) consists of the three momentum equations for the mine's COM position

$$\frac{d^2}{dt^2}\begin{bmatrix} x \\ y \\ z \end{bmatrix} = -\begin{bmatrix} 0 \\ 0 \\ g \end{bmatrix} + \frac{\mathbf{F}_{nh} + \mathbf{F}_h}{\rho\Pi}, \tag{10}$$

which is written in the E-coordinate system. Here, Π is the mine's volume; ρ is the mine's density; $\rho\Pi = m$ is the cylinder mass; $\mathbf{F}_{nh}$ and $\mathbf{F}_h$ are integrated (over the whole volume) nonhydrodynamic and hydrodynamic forces. The moment of momentum equation for the mine's orientation (ψ_1, ψ_2, ψ_3) in the M-coordinate system is written by (see [3,5])

$$\mathbf{J}\dot{\rightarrow}\frac{d^2}{dt^2}\begin{bmatrix} \psi_1 \\ \psi_2 \\ \psi_3 \end{bmatrix} = \mathbf{M}_{nh} + \mathbf{M}_h, \tag{11}$$

where $\mathbf{J}$ is the moment of gyration tensor; and $\mathbf{M}_{nh}$ and $\mathbf{M}_h$ are the nonhydrodynamic and hydrodynamic torques. The hydrodynamic (drag and lift) forces and torques are computed using the F coordinate [3]. The sediment part is the same as that depicted in [5].

5 Mine Drop Experiments

Data from two mine drop experiments are used to verify the value added of the three-dimensional model. Exp-1 was designed to collect data on the mine's motion in the water column for various combinations of the mine's parameters. Exp-2 was designed to collect synchronized data on sediment parameters (shear strength and density) and the mine's burial depth and orientation.

5.1 Exp-1. Exp-1 was conducted at the pond (water depth: 7.92 m) of the Naval Surface Warfare Center Caderock Division, West Bethesda, Maryland in September 2001 using six model mines with a radius of 0.084 m, two lengths (1.01 m, 0.505 m), and an adjustable internal weight to change the mine's COM position (i.e., χ value) [6]. The mine shapes are fabricated from aluminum pipe with a urethane covered aluminum front plate (Fig. 5).

The controlled parameters for each drop were the L/R ratio, χ value, initial velocity ($\mathbf{V}_{in}$), and drop angle. The E-coordinate system is chosen with the origin at the corner of the swimming pool with the two sides as x and y axes and the vertical z axis. The initial injection of cylinders was in the (x,z) plane. The blunt nosed mines are released into the water from three orientations

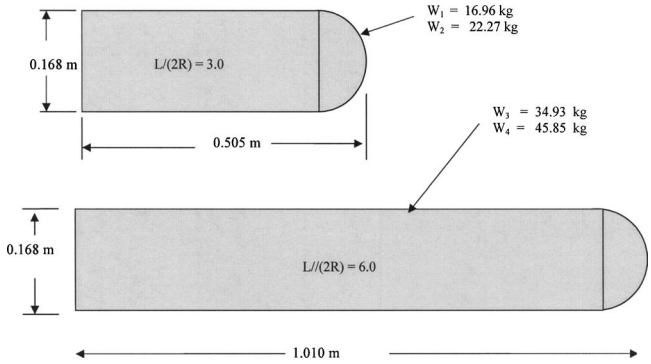

Fig. 5 Six model mines used in Carderock test pond with two different lengths

(horizontal, vertical, and 45° nose down) with a total of 42 drops. The observational data are $x(t)$, $z(t)$, and $\psi_2(t)$ in the water column. For detailed information, please contact Dr. Philip Valent at the Naval Research Laboratory Stennis Space Center (pvalent@nrlssc.navy.mil).

5.2 Exp-2. Exp-2 was conducted on the R/V John Martin on 23 May 2000 [7]. The purpose of this experiment is to collect mine burial, sediment density, and shear strength data simultaneously. The barrel with a density ratio of 1.8 was released horizontally while touching the surface with near zero velocity. The barrel was to be released 17 times. The diver would snap the quick-release shackle on the barrel and then dive down to measure the burial depth. The average depth of the water was 13 m. Before each drop, the gravity core is collected. The number of total mine drops (gravity cores) is 17. An analysis of the gravity cores was conducted at the USGS Laboratories in Menlo Park, California.

Table 1 Physical parameters of the six mines used in Exp-1

Mine	Mass (kg)	ρ (10^3 kg m^{-3})	L (m)	J_1 (kg m^2)	J_2 (J_3) (kg m^2)	χ (m)
1	16.96	1.60	0.505	0.0647	0.356	0
2	22.27	2.10	0.505	0.0806	0.477	0
3	34.93	1.60	1.010	0.1362	2.900	0
4	45.85	2.10	1.010	0.1696	3.820	0
5	45.85	2.10	1.010	0.1693	3.940	0.0045
6	45.85	2.10	1.010	0.1692	4.570	-0.077

6 Value-Added of 3D Model

6.1 Trajectory in Water Column. Improvement from IMPACT28 to IMPACT35 in predicting the cylinders' trajectory and orientation in the water column is verified using the Exp-1 data. The physical parameters of the six mines are presented in Table 1. Here, we only list three cases for illustration.

6.1.1 Near Horizontal Release. Model mine #6 is released to the water with $\psi_2=-14°$ (near horizontal, see Fig. 2). The initial conditions are given by

$$x_0 = y_0 = z_0 = 0, \quad u_0 = v_0 = w_0 = 0,$$
$$\psi_{10} = 0, \quad \psi_{20} = -14°, \quad \psi_{30} = 0, \quad \omega_{10} = \omega_{20} = \omega_{30} = 0. \tag{12}$$

Substitution of the model parameters and the initial conditions (12) into IMPACT28 and IMPACT35 leads to the prediction of the mine's translation and orientation that are compared with the data collected during Exp-1 at time steps (Fig. 6). The new 3D model (IMPACT35) simulated trajectory agrees well with the observed trajectory. Both show the same pattern and the same travel time (1.91 s) for the cylinder passing through the water column. However, the existing 2D model (IMPACT28) has less capability to predict the cylinder's movement in the water column.

6.1.2 Near 45° Release. Model mine #6 is released to the water with $\psi_2=42.2°$ (near 45°, see Fig. 2). The initial conditions are given by

$$x_0 = y_0 = z_0 = 0, \quad u_0 = v_0 = w_0 = 0,$$
$$\psi_{10} = 0, \quad \psi_{20} = 42.2°, \quad \psi_{30} = 0, \quad \omega_{10} = \omega_{20} = \omega_{30} = 0. \tag{13}$$

Substitution of the model parameters (79) and the initial conditions (81) into IMPACT28 and IMPACT35 leads to the prediction of the mine's translation and orientation that are compared with the data collected during Exp-1 at time steps (Fig. 7). The new 3D model (IMPACT35) simulated trajectory and travel time agree

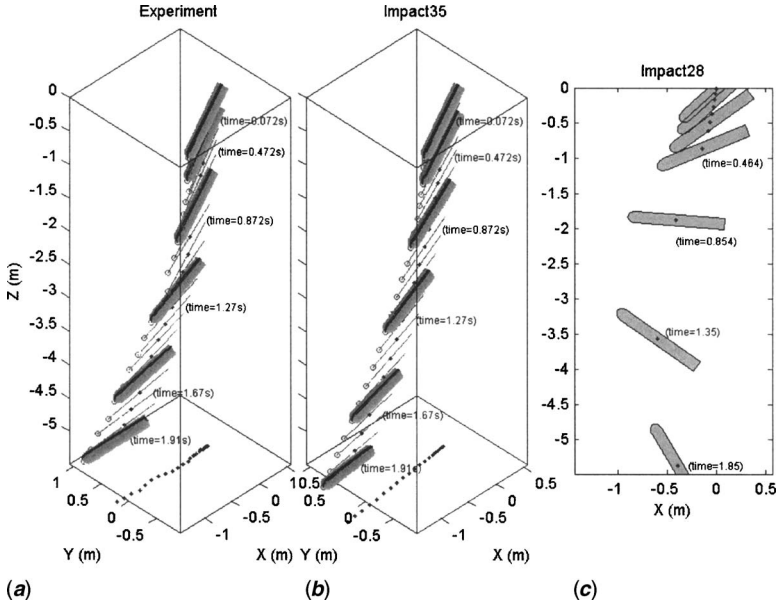

Fig. 6 Movement of Mine #6 (L=1.01 m, $\rho=2.1\times10^3$ kg m^{-3}) with χ= −0.0077 m and $\psi_2=-14.0°$ obtained from (*a*) experiment, (*b*) 3D IMPACT35 model, and (*c*) 2D Impact28 model

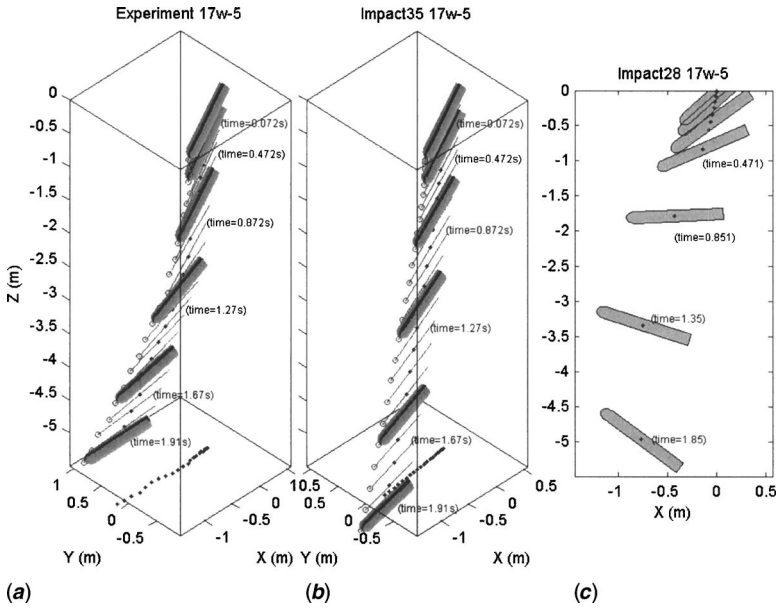

Fig. 7 Movement of Mine #5 (L=1.01 m, ρ=2.1×10^3 kg m^{-3}) with χ =0.0045 m and ψ_2=42.2° obtained from the (*a*) experiment, (*b*) 3D IMPACT35 model, and (*c*) 2D Impact28 model

well with the observed trajectory. However, the existing 2D model (IMPACT28) has less capability to predict the cylinder's movement in the water column.

6.1.3 Near Vertical Release. Model mine #2 is released to the water with ψ_2=87° (near vertical, see Fig. 2). The initial conditions are given by

$$x_0 = y_0 = z_0 = 0, \quad u_0 = v_0 = w_0 = 0,$$
$$\psi_{10} = 0, \quad \psi_{20} = 87^\circ, \quad \psi_{30} = 0, \quad \omega_{10} = \omega_{20} = \omega_{30} = 0. \tag{14}$$

The predicted cylinder's translation and orientation are compared with the data collected during Exp-1 at time steps (Fig. 8). The 3D model (IMPACT35) simulated trajectory agrees well with the observed trajectory. Both show the same straight pattern and the same travel time (1.83 s) for the cylinder passing through the water column. However, the existing 2D model (IMPACT28) does not predict the travel time well.

6.2 Burial Depth. After running the two models (IMPACT35 and IMPACT28) for each gravity core regime $[\rho_s(z), S(z)]$, the burial depths were compared with measured burial depth data (Fig. 9). As evident, IMPACT35 improves the prediction capability. The existing 2D model (IMPACT28) overpredicts the actual burial depth by an order of magnitude, on average. However, the

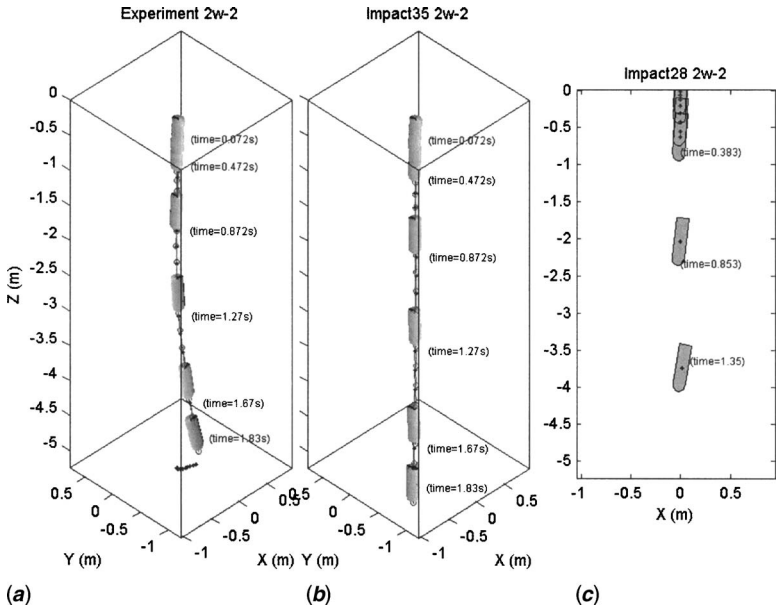

Fig. 8 Movement of cylinder #2 (L=0.505 m, ρ=2.1×10^3 kg m^{-3}) with χ=0 and ψ_2=87.0° obtained from the (*a*) experiment, (*b*) 3D IMPACT35 model, and (*c*) 2D Impact28 model

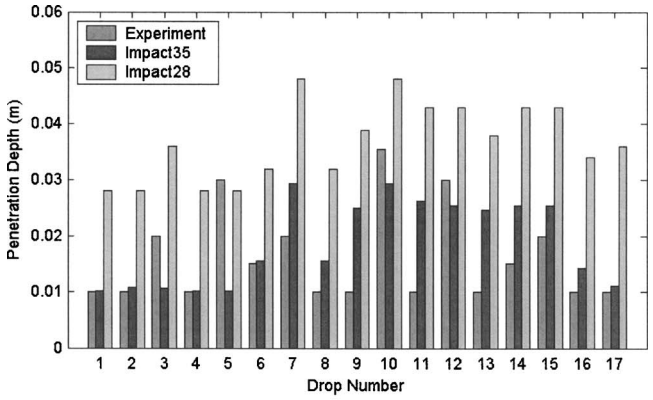

(*a*)

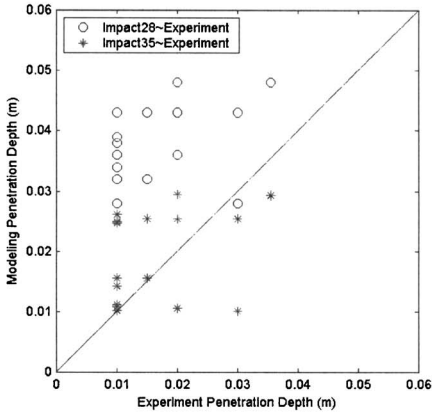

(*b*)

Fig. 9 A comparison among observed (Ext-2 data) and predicted burial depths

3D model (IMPACT35) predicts the burial depth reasonably well without evident overprediction. Since the gravity cores were taken for approximately two to three meters from the impact location, several cores were taken for each drop. This allowed an average to be calculated in order to yield more accurate data for each drop.

7 Sensitivity and Weakness of IMPACT35

IMPACT35 has two major model parameters: (1) distance (χ) between COM and COV, and (2) L/R ratio. In the two mine drop experiments, COM almost coincides with COV. Model sensitivity is tested with respect to the aspect ratio and initial release velocity using the observational data. A comparison among Figs. 6–8 shows that the model has better predictability for a large L/R ratio. When the L/R ratio is reduced, the prediction error increases.

Let ζ represent any of the five parameters $(x, y, z, \psi_2, \psi_3)$, and let (ζ_p, ζ_o) be the predicted and observed values. The difference between the two

$$\Delta\varsigma(i,t) = \varsigma_p(i,t) - \varsigma_o(i,t), \tag{15}$$

is defined as the model error. Here, the index (i) is the case number. The root-mean-square error (RMSE) for IMPACT35 is defined by

$$\mathrm{RMSE}(t) = \sqrt{\frac{1}{N(t)}\sum_i [\Delta\varsigma(i,t)]^2}, \tag{16}$$

where $N(t)$ is the total number of observational data at the falling time t. Figure 10(a) shows that $N(t)$ is around 40 as $t<1.5$ s and reduces quickly with time as $t>1.5$ s. For $t>2.5$ s, the observational data points are less than 10. RMSEs of the (x, y, z, ψ_2) prediction are very low when $t<1.5$ s and increases drastically when $t>1.5$ s. The large values of RMSE as $t>1.5$ s may also be related to less observational data (Fig. 10).

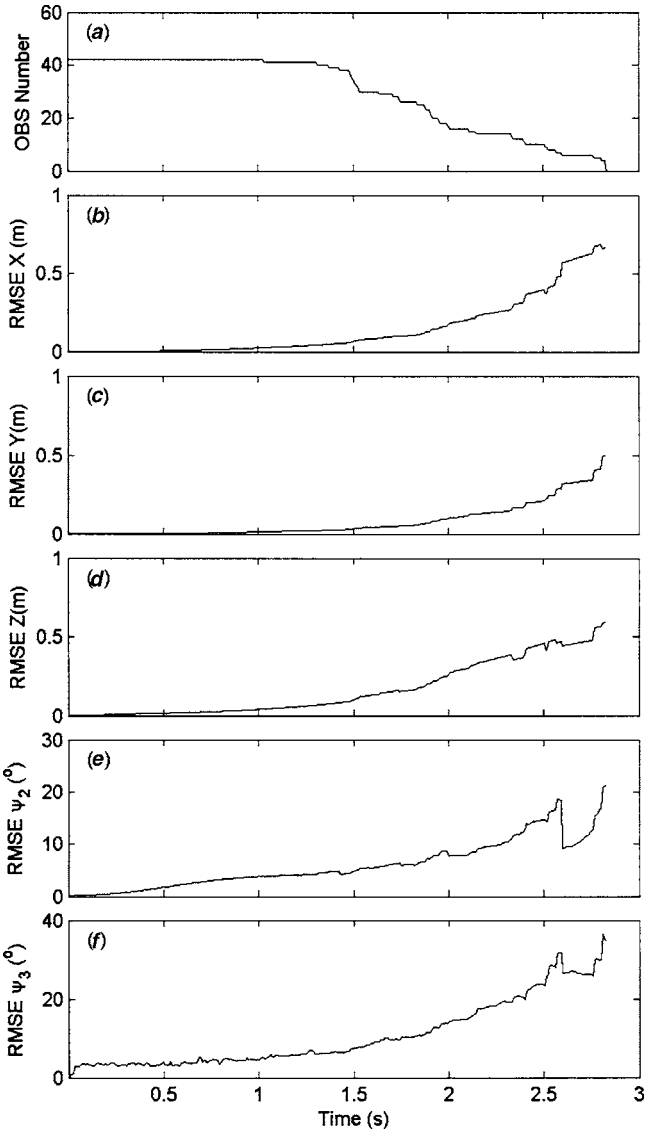

Fig. 10 Dependence of (*a*) observational data number, and of root-mean-square errors of the prediction for (*b*) *x*, (*c*) *y*, (*d*) *z*, (*e*) ψ_2, (*f*) ψ_3 on the mines' falling time.

Although the number of observational data may affect RMSE (Fig. 10), a tendency of RMSE growing with time does exist. For example, a RMSE of z increases from 0 at $t=0$ to 0.1 m at $t=1.5$ s. If we set

$$\mathrm{RMSE}_z \leqslant 0.4 \text{ m}, \tag{17}$$

as the tolerance level, IMPACT35 has capability within 6 s. In Exp-1, it takes around 3 s for the mines falling in the pond (water depth: 7.92 m) of the Naval Surface Warfare Center Caderock Division. Therefore, at a water column depth of about 16 m, IMPACT35 becomes unable to make reliable predictions.

Another weakness of the current version of IMPACT35 is only for near-cylindrical mines. The hypothesis used in this study is that the mine can be parametrized into a pseudocylinder. The model neglects the effect of the mine shape and only addresses only the effect of the L/R ratio, χ, and density. The effect of mine shape is a significant issue if the model is used operationally,

because the most popular mines such as Rockan and Manta are not near cylindrical. The most important issue is to determine the hydrodynamic (drag and lift) force and torque for noncylindrical mines. There is no existing formula for calculating the drag and lift forces and torques for noncylindrical objects. The conformal projection may be used to transfer the noncylindrical mine into an "equivalent" cylindrical mine. In the model development, the nonlinear instability and model sensitivity should be studied. Within the correct physics of the model there is a possibility of chaotic behavior. The chaotic features will be handled by the instability and predictability analyses.

To overcome such a weakness, test data are crucial to include the mine shape. Since it is not likely to conduct full-size mine experiments with varying mine shapes, controlled reduced-size mine impact experiments are needed. The reduced size model mines with various shapes (Rockan, Manta, Korean, Bowen mines) should be conducted similar to the past experiments for the cylindrical mines.

8 Conclusions

(1) Pseudo-cylinder parametrization is presented and included into the recently developed 3D model (IMPACT35) to predict the translation and orientation of falling mine with near cylindrical shape through air, water, and sediment. After the pseudocylinder parametrization, the drag and lift forces and torques can be easily calculated using the existing formulas to calculate the drag and lift coefficients.

(2) A model-data comparison shows that IMPACT35 improves the prediction capability drastically versus the 2D model (IMPACT28) with an order of error reduction in the mine burial depth, more accurate cylinder track (depth and orientation) prediction, and more accurate travel time of the cylinder through air–water–sediment.

(3) The root-mean-square error of IMPACT35 grows with time. If the error in predicting vertical position of COM is required less than 0.4 m, at a water column depth of about 16 m, IMPACT35 becomes unable to make reliable predictions.

(4) Pseudocylinder parametrization is valid only for near-cylindrical mines. The effect of the mine shape (rather than near-cylindrical) is a significant issue if IMPACT35 is used operationally, because the most popular mines such as Rockan and Manta are not near-cylindrical. To overcome the weakness, test data are crucial to include the mine shape. Reduced size mines with various shapes (Rockan, Manta, Korean, Bowen mines) should be conducted similar to the past experiments for the cylindrical or near-cylindrical mines.

Acknowledgments

The office of Naval Research Marine Geosciences Program (No. N0001403WR20178 and No. N0001404WR20067), Naval Oceanographic Office, and the Naval Postgraduate School supported this study. The authors wish to thank Dr. Philip Valent of the Naval Research Laboratory for providing data from the mine drop experiment conducted at the Naval Surface Warfare Center Caderock Division, West Bethesda, Maryland in September 2001.

References

[1] Boorda, J. M., 1999, "Mine Countermeasures—An Integral Part of Our Strategy and Our Forces," *Federation of American Scientists*, Washington D.C. (http://www.fas.org/man/dod-101/sys/ship/weaps/docs/cnopaper.htm).

[2] Hurst, R. B., 1992, "Mine Impact Burial Prediction Model—Technical Description of Recent Changes and Developments (U)," (Restricted), DSE Report No. 149, Defense Scientific Establishment, Auckland, New Zealand.

[3] Chu, P. C., Fan, C. W., Evans, A. D., and Gilles, A. F., 2004, "Triple Coordinate Transforms for Prediction of Falling Cylinder through the Water Column," ASME J. Appl. Mech., **71**, pp. 292–298.

[4] Chu, P. C., Gilles, A. F., and Fan, C. W., 2005a, "Experiment of Falling Cylinder Through the Water Column," Exp. Therm. Fluid Sci., **29**, pp. 555–568.

[5] Chu, P. C., and Fan, C. W., 2005b, "Prediction of Falling Cylinder Through Air-Water–Sediment Columns," ASME J. Appl. Mech. (in press).

[6] Valent, P. J., Holland, K. T., Green, A. W., Theophanis, S., King, C., Richardson, M. D., Bower, G. R., Congedo, P., and Lewis, W., 2002, "Observations of Velocity and Orientation of Cylindrical Shapes in Free-Fall in Water," *Fifth International Symposium on Technology and the Mine Problem*, Naval Postgraduate School, Monterey, California, 21–25 April, 2002.

[7] Smith, T. B., 2000, "Validation of the Mine Impact Burial Model Using Experimental Data," M.S. thesis, Naval Postgraduate School, Monterey, California, pp. 1–156.